frontiers | Research Topics

Recent advances in pharmaceutical analysis: applications and new challenges for the quality of medicines

Edited by
Federica Aureli, Anna Borioni, Maria-Elisa Crestoni, Birgit Hakkarainen and Constantinos K. Zacharis

Published in
Frontiers in Chemistry

ISSN 1664-8714
ISBN 978-2-8325-7085-2
DOI 10.3389/978-2-8325-7085-2

Generative AI statement
Any alternative text (Alt text) provided alongside figures in the articles in this ebook has been generated by Frontiers with the support of artificial intelligence and reasonable efforts have been made to ensure accuracy, including review by the authors wherever possible. If you identify any issues, please contact us.

About Frontiers

Frontiers is more than just an open access publisher of scholarly articles: it is a pioneering approach to the world of academia, radically improving the way scholarly research is managed. The grand vision of Frontiers is a world where all people have an equal opportunity to seek, share and generate knowledge. Frontiers provides immediate and permanent online open access to all its publications, but this alone is not enough to realize our grand goals.

Frontiers journal series

The Frontiers journal series is a multi-tier and interdisciplinary set of open-access, online journals, promising a paradigm shift from the current review, selection and dissemination processes in academic publishing. All Frontiers journals are driven by researchers for researchers; therefore, they constitute a service to the scholarly community. At the same time, the *Frontiers journal series* operates on a revolutionary invention, the tiered publishing system, initially addressing specific communities of scholars, and gradually climbing up to broader public understanding, thus serving the interests of the lay society, too.

Dedication to quality

Each Frontiers article is a landmark of the highest quality, thanks to genuinely collaborative interactions between authors and review editors, who include some of the world's best academicians. Research must be certified by peers before entering a stream of knowledge that may eventually reach the public - and shape society; therefore, Frontiers only applies the most rigorous and unbiased reviews. Frontiers revolutionizes research publishing by freely delivering the most outstanding research, evaluated with no bias from both the academic and social point of view. By applying the most advanced information technologies, Frontiers is catapulting scholarly publishing into a new generation.

What are Frontiers Research Topics?

Frontiers Research Topics are very popular trademarks of the *Frontiers journals series*: they are collections of at least ten articles, all centered on a particular subject. With their unique mix of varied contributions from Original Research to Review Articles, Frontiers Research Topics unify the most influential researchers, the latest key findings and historical advances in a hot research area.

Find out more on how to host your own Frontiers Research Topic or contribute to one as an author by contacting the Frontiers editorial office: frontiersin.org/about/contact

Recent advances in pharmaceutical analysis: applications and new challenges for the quality of medicines

Topic editors

Federica Aureli — National Institute of Health (ISS), Italy
Anna Borioni — National Institute of Health (ISS), Italy
Maria-Elisa Crestoni — Sapienza University of Rome, Italy
Birgit Hakkarainen — Medical Products Agency, Sweden
Constantinos K. Zacharis — Aristotle University of Thessaloniki, Greece

Citation

Aureli, F., Borioni, A., Crestoni, M.-E., Hakkarainen, B., Zacharis, C. K., eds. (2025). *Recent advances in pharmaceutical analysis: applications and new challenges for the quality of medicines*. Lausanne: Frontiers Media SA.
doi: 10.3389/978-2-8325-7085-2

Table of contents

05 Editorial: Recent advances in pharmaceutical analysis: applications and new challenges for the quality of medicines
Anna Borioni, Maria Elisa Crestoni, Birgit Hakkarainen, Constantinos K. Zacharis and Federica Aureli

08 Advanced modeling of pharmaceutical solubility in solvents using artificial intelligence techniques: assessment of drug candidate for nanonization processing
Turki Al Hagbani, Sameer Alshehri and Sami Bawazeer

19 Comparison of genotoxic impurities in extracted nicotine vs. synthetic nicotine
Ayesha Nisathar, Hui Chen, Xiaoli Lei, Zeyu Zeng and Jia Chen

30 Chromatographic analysis of ponatinib and its impurities: method development, validation, and identification of new degradation product
Jing Wang, Yonghong Zhu, Jisu Qin, Wenyi Wu, Rongrong Huang and Liangliang Cai

41 Chemical characterization of wheat-based waste derived from a pharmaceutical process for its potential valorization
Lidia Ciriaco, Luana Izzo, Giulia Graziani, Maria Grazia Ferraro, Marialuisa Piccolo, Roberto Ciampaglia, Barbara Maglione, Roberta Palladino, Simone Albarella, Eugenia Romano, Alberto Ritieni, Carlo Irace and Paolo Grieco

53 Research on detection methods of related substances and degradation products of the antitumor drug selpercatinib
Jingjing Xiang, Liangliang Cai, Qin Wang, Yonghong Zhu and Yong Han

64 Innovative determination of phytohormones in *Aloe vera*
Muhammad K. Hakeem, Meera Maraqa, Sampath K. Elangovan, Esam Eldin Saeed, Ajay Kumar Mishra, Khaled M. Hazzouri, Iltaf Shah and Khaled M. A. Amiri

74 The usefulness of infrared spectroscopy and X-ray powder diffraction in the analysis of falsified, illegal, and medicinal products
Anna Mocarska, Karolina Piorunska, Jan K. Maurin and Agata Blazewicz

83 Exploring imaged capillary isoelectric focusing parameters for enhanced charge variants quality control
Virginia Ghizzani, Alessandro Ascione, Federico Gonnella, Gabriella Massolini and Francesca Luciani

102 Non-destructive analysis of *Ganoderma lucidum* composition using hyperspectral imaging and machine learning
Jing Ran, Hui Xu, Zhilong Wang, Wei Zhang and Xueyuan Bai

115 Illegal and falsified medicines self-administrated in not approved post-cycle therapy after the cessation of anabolic-androgenic steroids – qualitative analysis
Agata Blazewicz, Magdalena Poplawska, Beata Daniszewska, Karolina Piorunska and Michal Karynski

132 Comprehensive and robust stability-indicating reversed phase high performance liquid chromatography (RP-HPLC) method for Rivaroxaban: synergistic integration of infrared spectroscopy and clinical pharmacology insights
Aktham Mestareehi

157 Discrimination of poisonous and medicinal plants with similar appearance (*Asarum heterotropoides* vs. *Cynanchum paniculatum*) via a fusion method of E-nose, E-tongue, LC-HR-Q-TOF-MS/MS, and electrochemical fingerprint spectra
Xin-Ru Zhang, Yue-Hua Chen, Jia-Nuo Zhang, Wen-Yu Wang, Rui-Bo Sun, Zi-Xuan Ding, Hui Zhang, Ming Xie, Ting-Guo Kang and Hui-Peng Song

179 Investigation of illicit pregabalin in seized samples from Saudi Arabia
Fatimah M. Alamri, Sultan K. Alshmmari, Monerah A. Altamimy, Ibrahim A. Al Othaim, Yahya M. Alshehri, Rayed M. Alafraa, Ahmed D. Almalki, Turki A. Alkhalifah, Taher Sahlabji, Abubakr M. Idris, Haitham Al-Hamoud, Yahya F. Jamous and Fahad S. Aldawasri

193 Quality assessment of "naturally occurring" high-percentage L-dopa commercial products proposed as dietary supplements on the Internet: from labeling to analytical findings
Federica Aureli, Maria Cristina Gaudiano, Mariangela Raimondo, Alessandro Maccelli, Domenico Di Giorgio, Marta Gramazio, Anna Borioni and Monica Bartolomei

frontiers | Frontiers in Chemistry

TYPE Editorial
PUBLISHED 19 September 2025
DOI 10.3389/fchem.2025.1699047

OPEN ACCESS

EDITED AND REVIEWED BY
Huangxian Ju,
Nanjing University, China

*CORRESPONDENCE
Federica Aureli,
federica.aureli@iss.it

RECEIVED 04 September 2025
ACCEPTED 08 September 2025
PUBLISHED 19 September 2025

CITATION
Borioni A, Crestoni ME, Hakkarainen B, Zacharis CK and Aureli F (2025) Editorial: Recent advances in pharmaceutical analysis: applications and new challenges for the quality of medicines.
Front. Chem. 13:1699047.
doi: 10.3389/fchem.2025.1699047

Editorial: Recent advances in pharmaceutical analysis: applications and new challenges for the quality of medicines

Anna Borioni[1], Maria Elisa Crestoni[2], Birgit Hakkarainen[3], Constantinos K. Zacharis[4] and Federica Aureli[1]*

[1]Chemical Medicines Unit, National Centre for the Control and Evaluation of Medicines, Istituto Superiore di Sanità, Rome, Italy, [2]Department of Chemistry and Technology of Drugs, Sapienza University of Rome, Rome, Italy, [3]Official Medicines Control Laboratory, Swedish Medical Products Agency, Uppsala, Sweden, [4]Laboratory of Pharmaceutical Analysis, Department of Pharmacy, Aristotle University of Thessaloniki, Thessaloniki, Greece

KEYWORDS

quality of medicines, multivariate analyis, illegal medicines, pharmaceutical analysis, spectroscopy, impurities, analytical methods, biotherapeutic

Editorial on the Research Topic
Recent advances in pharmaceutical analysis: applications and new challenges for the quality of medicines

This Research Topic is concerned with the exploration of the most recent advancements and developments in the field of pharmaceutical analysis, focusing on non-destructive approaches, predictive models and the application of techniques which are less frequently used in pharmaceutical analysis. The samples belonged to the legal pharmaceutical market as well as to the illegal market, being the last increasingly deceptive and difficult to spoil.

Alamri et al. applied an ultra-performance liquid chromatography-photodiode array detector (UPLC-PDA) method and a liquid chromatography tandem mass spectrometry (LC-MS/MS) method to analyse 40 samples of suspicious pregabalin samples seized from the Saudi Arabia market. The results demonstrate significant variability in pregabalin content and the presence of toxic adulterants in about 30% of the samples confirming inadequacies in illicit drug production and circulation.

Still in the field of illegal medicines, Blazewicz et al. analysed 601 samples seized from the illegal market by liquid chromatography coupled with high-resolution hybrid mass spectrometry and X-ray powder diffraction. The samples, which were reported in bodybuilding forums, were suspected to contain illegal substances such as selective estrogenic receptor modulators (SERMs), aromatase inhibitors (AIs), and preparations containing human chorionic gonadotropin (hCG). In about 65% of the samples, the declared active pharmaceutical ingredients were present, whereas in 35%, they were not. Furthermore, 6.4% of the samples in which the declared API was found, contained an additional undeclared API.

Mocarska et al. reported the applications of Attenuated total reflectance Fourier transform infrared spectroscopy and X-ray powder diffraction for analysing suspicious illegal products that have been seized by the authorities. These advantageous techniques

provide consistent, reproducible results with no environmental impact, as minimal sample preparation is required and no chemical reagents or solvents are used.

Aureli et al. described a combined approach based on Liquid Chromatography-Quadrupole Time-of-Flight Mass Spectrometry/Nuclear Magnetic Resonance spectroscopy LC-MS Q-TOF/1H-NMR to identify and quantify L-dopa in dietary supplements purchased online. The study evidenced the presence on the online market of unauthorised botanical extracts containing L-dopa and amount either as stated but also overdosed or under-dosed. Given the observed increasing public interest in levodopa discussed by the authors, these findings highlight the need to control this market.

In the above-mentioned papers multimodal analytical strategies were efficiently implemented to successfully pursue high discrimination power and method robustness. All confirmed that the declared active substances in falsified and unauthorised products may be absent, substituted, adulterated and misdosed, posing a serious threat to consumer health. There is an urgent need to inform consumers and physicians about the risks of purchasing such products, frequently available through online sources.

The importance of understanding plant-based product composition was addressed in different studies. Zhang et al. proposed a new integrated strategy based on E-nose, E-tongue, LC-HR-Q-TOF-MS/MS, and electrochemical fingerprint spectra to systematically differentiate Asarum heterotropoides (AH) from Cynanchum paniculatum (CP) a medicinal plant used in Traditional Chinese Medicine the first containing toxic ingredients. This novel synergic approach allowed identification of 25 odour components in AH and 12 odour components in CP, differentiation in bitterness and astringency between the two plants, identification of about 90 components in each plant plus further distinctions based on the electrochemical fingerprint spectra. Through the combination of electrochemical fingerprint spectra with principal component analysis (PCA) or orthogonal partial least squares-discriminant analysis (OPLS-DA), the accuracy of this method reached 100%.

Hakeem et al. focused their paper on the quantification, by LC-MS/MS, of phytohormones in *Aloe vera,* a succulent plant renowned for its diverse therapeutic effects, including anti-inflammatory and antimicrobial properties. While traditional methods for detecting phytohormones in plant extracts often fall short in terms of sensitivity, selectivity, and precision, the method here described was demonstrated suitable to quantify six phytohormones in *A. vera* samples randomly selected from diverse sources with LOQ as low as 0.04 ng/mL.

Fungi also hold a significant position in the healthcare and nutrition market. *Ganoderma lucidum* evidenced antibacterial, tumour-inhibiting, and anti-inflammatory effects. Ran et al. provided a non-destructive approach to assessing *G. lucidum* quality with a focus on the ergosterol and polysaccharide content present in the different parts of the fungus. Three machine learning models—a feedforward neural network, an extreme learning machine, and a decision tree—were tested and compared to the ergosterol and polysaccharide composition determined by chemical analysis. The extreme learning machine model provided a successful approach giving good predictions for polysaccharides and ergosterol content in *G. lucidum.*

(S)-Nicotine is a chiral alkaloid extracted from Tobacco plants which is used as addictive ingredient in smoking products. In the last few decades, synthetic (S)-nicotine has gained interest due to the straightforward manufacturing process. Nisathar et al. estimated the impurity profile of thirteen different lots of synthetic nicotine in comparison with fourteen lots of nicotine extracted from plants using an in-house reversed-phase HPLC analytical method. Similar quantities of total impurities in both synthetic and tobacco-extracted nicotine were detected though synthetic nicotine lacks some impurities such as cotinine, nornicotine, nicotine-N-oxide. Both kinds of nicotine have similar high enantiomeric purity. Nitrosamines were not detected in any synthetic or extracted nicotine lots.

Another valuable plant-derived active ingredient is phytostimulin which is extracted from wheat (*Triticum vulgare*). The process is a water-based extraction procedure with not harmful solvents but in line with the principle of reduction-reuse-recycling, Ciriaco et al. performed a chemical characterization, by UHPLC-Q-Orbitrap HRMS, of the bioactive compounds in both liquid and solid wastes from the processing of wheat and evaluated their safety and efficacy profile in human cellular models. The solid waste contained the highest phenol component represented by ferulic acid at approximately 90 mg/kg and resulted a potentially starting resource in pharmaceutical and other areas such as cosmeceuticals or food.

The following two papers focus on the analysis of anti-cancer drugs selpercatinib and ponatinib. Both are protein tyrosine kinase inhibitors with complex chemical structure and an impurity profile affecting safety and effectiveness.

Xiang et al. developed and validated a High-Performance Liquid Chromatography (HPLC) method for identifying selpercatinib and its related impurities. The experimental results and the scientific rationale underpinning the process of method development were reported in a step-by-step manner. Based on the results of stress tests the method was also validated for its capacity to detect the degradation impurity that may form under storage, and transportation of selpercatinib.

Wang et al. developed and successfully validated a robust and sensitive reverse phase HPLC method to detect the process impurity and degradation product of ponatinib. In the process a novel impurity forming under oxidative degradation was detected and its chemical structure was elucidated by HR-MS and NMR. The process underlying the method development was accurately described. The limits of quantification were found in the ng/mL range.

Rivaroxaban based medicines have anticoagulant effect and are commonly used to prevent thrombosis or inhibit the enlargement of existing blood clots. A robust, precise, and selective reversed-phase high-performance liquid chromatography (HPLC) method was developed and extensively validated by Mestareehi for analyzing Rivaroxaban in tablets. The method was demonstrated to be both stability-indicating and highly sensitive, with a limit of quantification of 1 ppm.

If patients could take a lower dosage of drugs and still achieve the same therapeutic effectiveness, the harmful effects of impurities would be reduced. To achieve this, the solubility of the active pharmaceutical ingredients in an aqueous medium at a physiological pH could be increased. Production of

nanomedicines is a possible approach and processing drugs with supercritical carbon is one of the methods for creating nanomedicines. In this view Hagbani et al. focused on the application of machine learning to model the solubility of ketoprofen in supercritical carbon dioxide by three regression techniques. A comprehensive visual representations and statistical examinations of the connections between temperature, pressure, and solubility was also provided. The results obtained in this study showed high performance of the machine learning model in prediction of drug solubility in supercritical CO_2.

Biological medicinal products are recognised as more complex than chemical medicines, requiring specific analytical techniques and a more holistic approach. Charge heterogeneity is a critical quality attribute of proteins and mAb-based drugs which is often analysed using separative techniques such as imaged capillary isoelectric focusing (icIEF).

Ghizzani et al. reviewed the icIEF advancements in the context of biotherapeutics drug development and their quality control. Key aspects, including sample preparation, capillary properties, carrier ampholytes, stabilizers, and detection are examined, and supported by recent literature. The wide range of variables that can influence this analytical method make it a suitable candidate for the development of Analytical Quality by Design approaches, according to ICH Q14 guideline and for applications of artificial intelligence in managing complex icIEF data sets.

In this Research Topic, we have provided the reader with examples of innovative approaches and application of predictive models. In the case of papers reporting more traditional methods, the analytical development and validation process is stepwise outlined. Our goal is that the Research Topic will be a source of inspiration for readers, encouraging the development of new lines of research and collaborative projects.

Author contributions

AB: Conceptualization, Writing – review and editing, Writing – original draft. MC: Writing – review and editing. BH: Writing – review and editing. CZ: Writing – review and editing. FA: Writing – original draft, Conceptualization, Writing – review and editing.

Funding

The author(s) declare that no financial support was received for the research and/or publication of this article.

Conflict of interest

The authors declare that the research was conducted in the absence of any commercial or financial relationships that could be construed as a potential conflict of interest.

The author(s) declared that they were an editorial board member of Frontiers, at the time of submission. This had no impact on the peer review process and the final decision.

Generative AI statement

The author(s) declare that no Generative AI was used in the creation of this manuscript.

Any alternative text (alt text) provided alongside figures in this article has been generated by Frontiers with the support of artificial intelligence and reasonable efforts have been made to ensure accuracy, including review by the authors wherever possible. If you identify any issues, please contact us.

Publisher's note

frontiers | Frontiers in Medicine

TYPE Original Research
PUBLISHED 22 July 2024
DOI 10.3389/fmed.2024.1435675

OPEN ACCESS

EDITED BY
Ovidiu Constantin Baltatu,
Anhembi Morumbi University, Brazil

REVIEWED BY
Kishalay Mitra,
Indian Institute of Technology Hyderabad, India
A.M. Elsawah,
Beijing Normal University–Hong Kong Baptist University United International College, China
Mahboubeh Pishnamazi,
Duy Tan University, Vietnam

*CORRESPONDENCE
Turki Al Hagbani
✉ T.alhagbani@uoh.edu.sa

RECEIVED 20 May 2024
ACCEPTED 26 June 2024
PUBLISHED 22 July 2024

CITATION
Al Hagbani T, Alshehri S and Bawazeer S (2024) Advanced modeling of pharmaceutical solubility in solvents using artificial intelligence techniques: assessment of drug candidate for nanonization processing.
Front. Med. 11:1435675.
doi: 10.3389/fmed.2024.1435675

Advanced modeling of pharmaceutical solubility in solvents using artificial intelligence techniques: assessment of drug candidate for nanonization processing

Turki Al Hagbani[1]*, Sameer Alshehri[2] and Sami Bawazeer[3]

[1]Department of Pharmaceutics, College of Pharmacy, University of Hail, Hail, Saudi Arabia, [2]Department of Pharmaceutics and Industrial Pharmacy, College of Pharmacy, Taif University, Taif, Saudi Arabia, [3]Department of Pharmaceutical Sciences, Faculty of Pharmacy, Umm Al-Qura University, Makkah, Saudi Arabia

This research is an analysis of multiple regression models developed for predicting ketoprofen solubility in supercritical carbon dioxide under different levels of T(K) and P(bar) as input features. Solubility of the drug was correlated to pressure and temperature as major operational variables. Selected models for this study are Piecewise Polynomial Regression (PPR), Kernel Ridge Regression (KRR), and Tweedie Regression (TDR). In order to improve the performance of the models, hyperparameter tuning is executed utilizing the Water Cycle Algorithm (WCA). Among, the PPR model obtained the best performance, with an R^2 score of 0.97111, alongside an MSE of 1.6867E-09 and an MAE of 3.01040E-05. Following closely, the KRR model demonstrated a good performance with an R^2 score of 0.95044, an MSE of 2.5499E-09, and an MAE of 3.49707E-05. In contrast, the TDR model produces a lower R^2 score of 0.84413 together with an MSE of 7.4249E-09 and an MAE of 5.69159E-05.

KEYWORDS

drug development, solubility prediction, optimization, machine learning, modeling

1 Introduction

Simulation and modeling of pharmaceutical processes are great tools for development of pharmaceutical manufacturing and would help for shifting from batch toward continuous manufacture mode. Process analytical technology (PAT) and process modeling are important elements of process understanding for design of continuous manufacturing in pharmaceutical area (1–3) where they can be exploited to enhance the efficiency of process and products quality. Process modeling can be performed by finding the relationships between the process parameters and critical quality attributes of finished products. Once the relationship has been established, one can implement Quality-by-Design (QbD) for improvement of process and products (4, 5). Thus, development of robust and rigorous models for pharmaceutical processing is a major challenge which should be addressed.

There are different processing routes for manufacture of solid-dosage oral products which can be optimized via process modeling and theoretical computations. For instance,

the method of wet granulation can be simulated via population balance model (PBM) to predict the granule size distribution. As the granules' properties can affect the tablet characteristics, building relationship between granule size and tablet properties can be done via process modeling which would help for process understanding (6–8).

One of the main problems in pharmaceutical area is the poor solubility of APIs (Active Pharmaceutical Ingredients) in aqueous media which makes patients to take more dosage of drugs to obtain the therapeutics effectiveness. Taking more dosages would consequently result in side effects for patients. Therefore, some techniques have been developed to enhance the solubility of APIs in aqueous media such as production of nanomedicines (9–11). The processing of drugs with supercritical carbon dioxide has been reported as one of the methods for creation of nanomedicines. This method has attracted much attention and can be considered as a green method for preparation of nanosized APIs particles. Some computational models have been developed for description of this process, where the majority of studies focus on correlation of drug solubility dataset (12–15). Machine learning models are among the most commonly used methods for correlation of solubility data which can be used for a given dataset (16, 17).

Modern data analysis now heavily depends on machine learning (ML), which provides strong instruments and methods for deriving important insights from large datasets. ML includes a range of algorithms that let computers learn from data and, in the absence of explicit programming, make predictions or decisions. These algorithms can identify patterns, relationships, and trends within data, making ML particularly useful for tasks such as regression, classification, clustering, and anomaly detection (18, 19). The ML models have been used recently for correlation of pharmaceutical solubility in supercritical solvents such as CO_2. Abouzied et al. (20) investigated the drug solubility in supercritical CO_2 using multi-layer perceptron, k-nearest neighbors, and GPR methods. A great fitting accuracy was obtained with R^2 more than 0.99 which confirmed the validity of ML models in estimating drug solubility. Support vector machine (SVM) has been one of the major methods used for evaluation of drug solubility in supercritical solvent which is useful in this area with great fitting accuracy (21).

In this paper, we focus on the application of ML to model the solubility of ketoprofen in supercritical carbon dioxide, a critical factor in pharmaceutical manufacturing processes. Accurate modeling of solubility is essential for optimizing production efficiency and ensuring the quality of pharmaceutical products. To achieve this, we employed three regression techniques:

1 Piecewise Polynomial Regression (PPR): PPR partitions the input data range into segments and applies polynomial functions to each segment, enabling a flexible and localized estimation of the regression function.
2 Kernel Ridge Regression (KRR): KRR combines ridge regression with kernel functions, enabling it to model non-linear relationships in the data by projecting it into higher-dimensional spaces.
3 Tweedie Regression (TDR): TDR is a generalized linear model capable of accommodating various distribution types, rendering it well-suited for modeling continuous, non-negative data with variance scaling with a power of the mean.

To optimize the performance of these regression models, we utilized the Water Cycle Algorithm (WCA), a nature-inspired optimization method that simulates the water cycle process to find optimal solutions. WCA has proven effective in navigating complex search spaces and identifying optimal parameter settings for various ML models.

The selected models are highly suitable for small datasets because of their adaptability and resilience in capturing complex relationships. PPR enables localized polynomial fits that can adapt to specific segments of the data, KRR effectively handles non-linearities even with limited data points using kernel functions, and TDR is designed for modeling continuous non-negative data with scalable variance. The careful application of these models, along with the Water Cycle Algorithm (WCA) for optimal parameter tuning, ensures that they are capable of delivering accurate and reliable solubility predictions despite the small dataset size.

Multiple contributions are made by this paper. First, we evaluate the three regression models for ketoprofen solubility prediction, highlighting their pros and cons. Second, we demonstrate how the Water Cycle Algorithm improves model performance by tuning hyperparameters. Finally, we present detailed dataset visualizations and statistical analyses to reveal T(K), P(bar), and solubility relationships. This study uses advanced ML techniques and robust optimization strategies to predict supercritical fluid solubility and advance pharmaceutical process optimization. Indeed, Piecewise Polynomial Regression (PPR), Kernel Ridge Regression (KRR), and Tweedie Regression (TDR) were used for the first time with the Water Cycle Algorithm (WCA) optimizer to improve the prediction accuracy of models for solubility of ketoprofen in supercritical CO_2. The models are then used for evaluation of effect of temperature and pressure on the solubility variations.

2 Data set description

The dataset includes solubility measurements at temperatures spanning from 308.15 K to 338.15 K and pressures ranging from 160 bar to 400 bar, sourced from (22). The entire data points of the dataset are shown in Table 1. So, T and P are taken as inputs of ML models, and the drug solubility has been considered as the single output for all models in this study.

Figure 1 depicts distribution plots for temperature (T), pressure (P), and ketoprofen solubility in supercritical carbon dioxide. These plots use kernel density estimates (KDE) to represent the probability density functions of the variables. The solubility distribution is right-skewed, indicating that higher solubility values occur less frequently in the dataset.

Furthermore, the violin plots in Figure 2 depict the temperature (T), pressure (P), and solubility of ketoprofen in supercritical carbon dioxide. Each plot combines a boxplot with a kernel density estimate (KDE). The KDE component shows the probability density of the data at various values, whereas the boxplot component within the violin plot displays the median, interquartile range, and potential outliers. The temperature and pressure data have relatively uniform distributions, whereas the solubility data has a more skewed distribution, indicating that solubility values vary across experimental conditions.

TABLE 1 Complete dataset of ketoprofen solubility in supercritical carbon dioxide (22).

T (K)	P (bar)	Solubility
308.15	160	2.21×10^{-5}
	200	2.56×10^{-5}
	240	2.87×10^{-5}
	280	3.21×10^{-5}
	320	3.45×10^{-5}
	360	4.23×10^{-5}
	400	4.56×10^{-5}
318.15	160	5.01×10^{-5}
	200	6.58×10^{-5}
	240	7.68×10^{-5}
	280	9.01×10^{-5}
	320	1.12×10^{-4}
	360	1.03×10^{-4}
	400	1.20×10^{-4}
328.15	160	7.01×10^{-5}
	200	1.16×10^{-4}
	240	1.75×10^{-4}
	280	2.20×10^{-4}
	320	2.54×10^{-4}
	360	3.24×10^{-4}
	400	3.59×10^{-4}
338.15	160	1.01×10^{-4}
	200	2.45×10^{-4}
	240	3.25×10^{-4}
	280	4.92×10^{-4}
	320	5.79×10^{-4}
	360	6.87×10^{-4}
	400	7.12×10^{-4}

3 Methodology

3.1 Water cycle algorithm

Inspired by the natural water cycle, the Water Cycle Algorithm (WCA) is a population-based optimization algorithm. The method relies on the water cycle, which includes evaporation, cloud formation, and precipitation. The WCA replicates this cycle to find the best solutions. Initialization, evaporation, precipitation, and river formation are key algorithm steps (23, 24).

During the initialization phase, a set of potential solutions is generated in a random manner. In this context, every solution is defined by a set of hyper-parameter values. For instance, in a function optimization scenario, these parameters may represent the input variable values (25).

The evaluation of the solutions' fitness values takes place in the evaporation phase. The fitness of a solution reflects its quality, with higher fitness values corresponding to superior solutions. These fitness values play a role in computing the evaporation rate, dictating the amount of water that evaporates from each solution (25, 26).

In the precipitation stage, the evaporated water is converted into clouds, which are subsequently dispersed randomly among the solution population. Each cloud symbolizes a potential enhancement to a solution. The fitness values of the clouds are assessed, and the most superior cloud is selected (27). The introduced steps of WCA are reiterated until a termination condition is met. The stopping criterion could involve attaining an specific fitness value, reaching a maximum number of iterations, or consuming a maximum computational time (24, 28).

Figure 3 shows the basic workflow of WCA algorithm. One of the strengths of the WCA is its capability to address multiple objectives. Multi-objective optimization finds the best solutions for conflicting goals (accuracy and generality in ML tasks). The dominance principle is used to extend the WCA to multiple goals. A solution dominates another solution if it excels in at least one objective without being inferior in any. Utilizing this idea, the WCA can identify a collection of solutions that are independent of one another (28). Natural-inspired processes give the Water Cycle Algorithm (WCA) benefits over Particle Swarm Optimization (PSO) and Differential Evolution (DE). WCA's iterative evaporation, cloud formation, and river construction balance exploration and exploitation to avoid local optima and increase convergence. Its self-adjusting evaporation rates and cloud dispersal improve performance without parameter adjustment. The robust diversification mechanism of WCA provides constant exploration of new regions, while its structured navigation of complex search spaces via river formation efficiently avoids suboptimal regions. These properties make WCA more adaptable and effective than PSO and DE.

This algorithm is used for model optimization (hyper-parameter tuning) in this study. We used deterministic optimization here while there exists methods for optimization under uncertainty (29, 30). Here, each solution consists of a combination of hyper-parameter values and one of the objective functions is the RMSE error rate of the model build on each solution which should be maximized.

Also, by selecting the architecture with the least Akaike Information Criterion (AIC) value, the models are filtered to prevent overfitting, thus promoting generalization and robustness in the forecasting models. This method already shown promising results in avoiding overfitted models (31).

3.2 Piecewise polynomial regression

Piecewise Polynomial Regression (PRR) is the process of estimating a regression function by fitting multiple polynomial functions to different segments of the dataset. In this regression model, several polynomial functions are used to approximate the regression function in specific data segments (32).

PPR divides the dataset into segments and uses polynomial functions to approximate the regression function. The foundation of this segmentation is input space partitioning. Every segment is equivalent to a polynomial function that denotes the regression relationship inside that certain interval (32, 33).

To determine the optimal piecewise polynomial estimator, the research paper suggests considering various models defined by partitions and polynomial degrees. It utilizes a penalized least squares

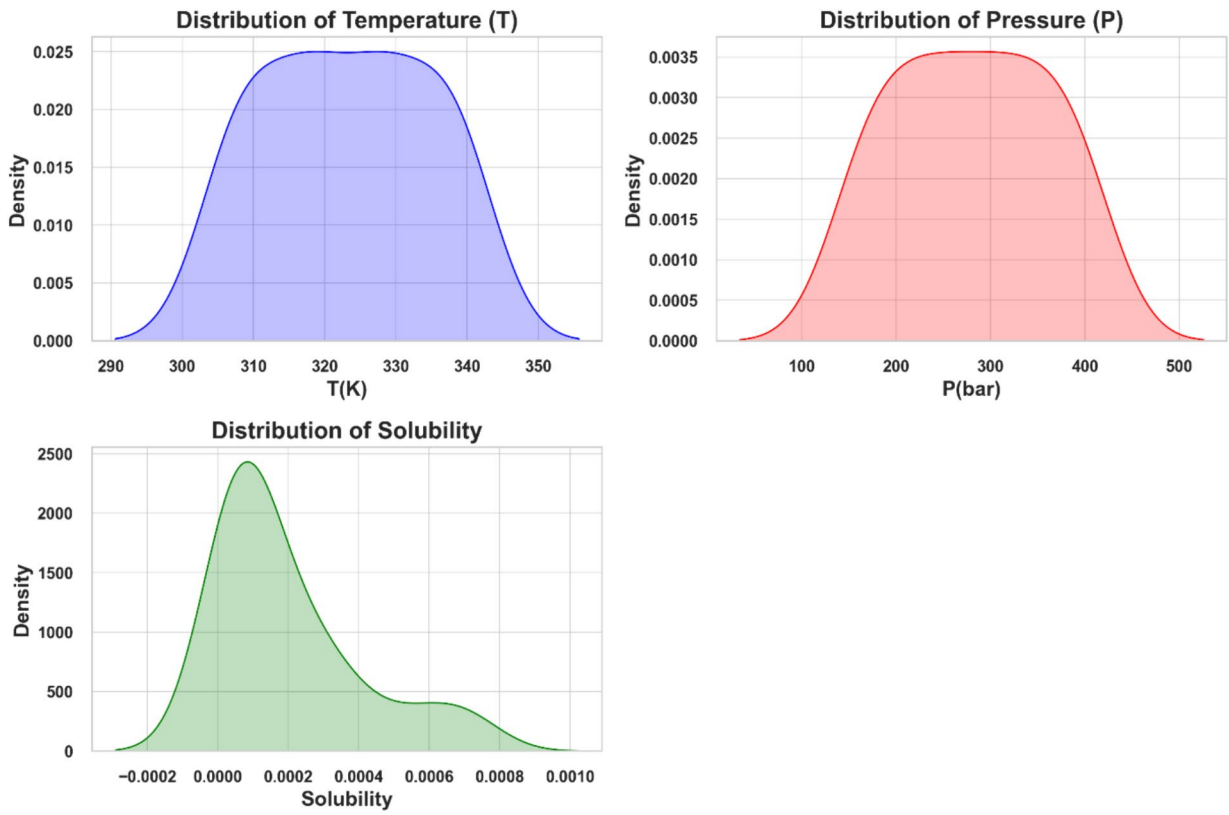

FIGURE 1
Distribution plots of temperature (T), pressure (P), and solubility of ketoprofen in supercritical CO_2.

criterion to identify the model with an estimator closely resembling the best one in terms of quadratic risk. Additionally, the study establishes a non-asymptotic risk bound to ensure the selected model's performance.

Extending the methodology to tree-structured partitions akin to those in the CART (34) algorithm offers a novel approach to constructing piecewise polynomial estimators for regression functions. This extension involves iteratively optimizing the selection of polynomial functions within each segment to best represent the underlying regression function across the entire data range.

3.3 Kernel ridge regression

The ideas of linear ridge regression are extended in the robust non-linear regression method known as kernel ridge regression (KRR). Utilizing the kernel trick, KRR adeptly captures the non-linear patterns inherent in data, rendering it applicable across diverse scenarios. The regularization mechanisms in KRR, including the ridge penalty, play a pivotal role in shaping the optimized kernel function, thereby mitigating overfitting concerns and bolstering predictive precision (35, 36).

Assume we have a dataset $\{(x_i,y_i)\}_{i=1}^{N}$ consisting of N data rows that have been sampled from a distribution P over the Cartesian product of X and the real numbers (R). The objective is to identify the best function that, with the expectation computed collectively over (X,Y) pairs, minimizes the Mean Squared Error (MSE) of the $data(f(x)-y)^2$.

The conditional mean $f^*(x):=\mathbb{E}[Y|X=x]$ is widely regarded as the most suitable function (37). Using a squared Hilbert norm penalty and the M-estimator with the lowest squares loss on the dataset is a feasible approach to forecast the unknown function f^* (37).

$$\hat{f} := \underset{f\in H}{\operatorname{argmin}}\left\{\frac{1}{N}\sum_{i=1}^{N}\left(f(x_i)-y_i\right)^2+\lambda\|f\|_H^2\right\},$$

Here, H denotes a reproducing kernel Hilbert space and $\lambda>0$ represents a regularization parameter. The kernel ridge regression estimate (referred to as KRR) serves as the estimator employed in the equation above (38).

3.4 Tweedie regression

The Tweedie regression model is a versatile tool for analyzing data that is non-negative, right-skewed, and has a high probability of being zero (39). It provides a single model that can effectively handle various types of continuous data automatically, making model selection easier during fitting.

The Tweedie regression model is predicated upon the assumption that the response variable Y follows a Tweedie distribution, denoted as $Y\sim Tw_p(u,\phi,p)$, where u represents the mean, ϕ denotes the

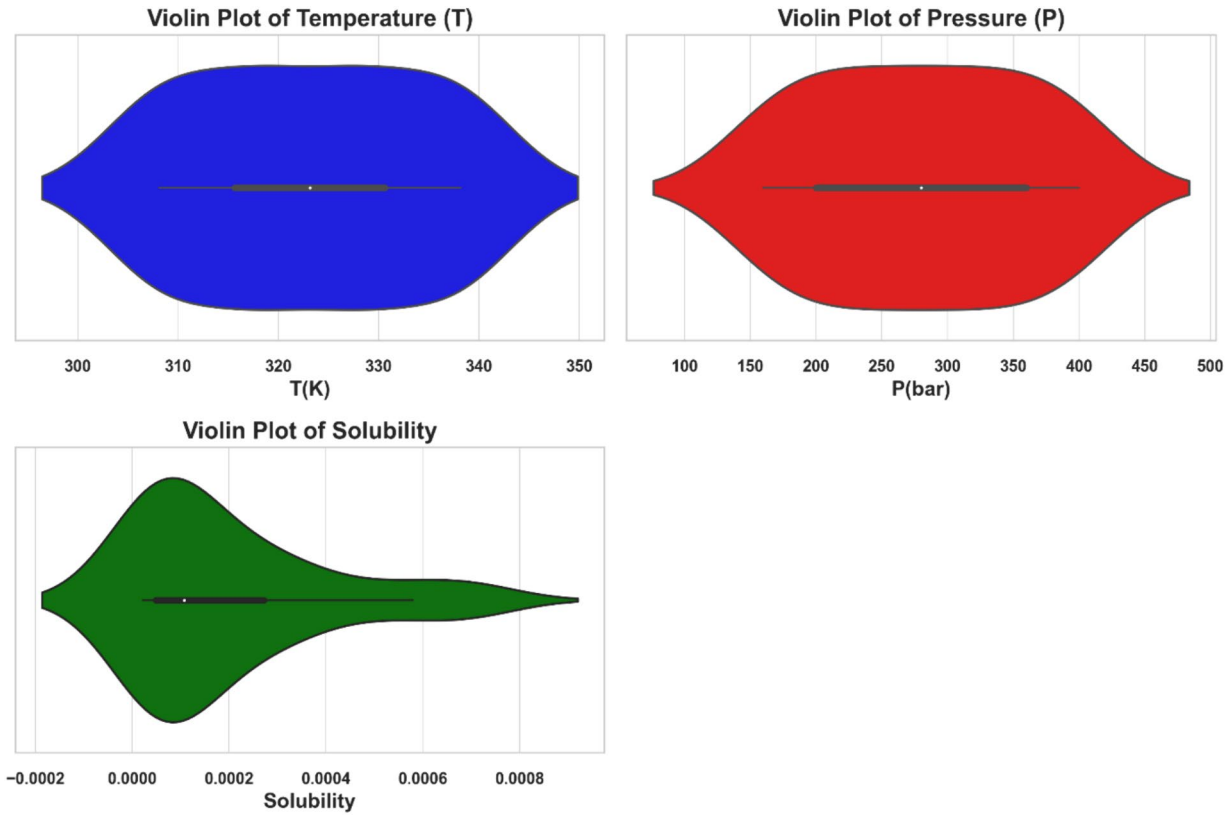

FIGURE 2
Violin plots illustrating the distributions of temperature (T), pressure (P), and the solubility of ketoprofen in supercritical CO_2.

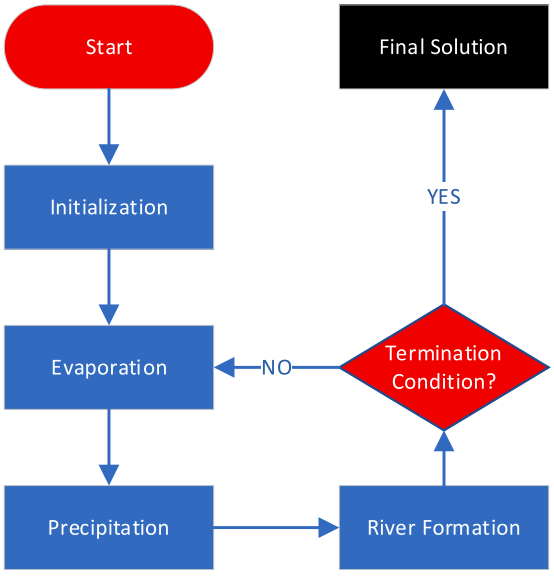

FIGURE 3
Water cycle algorithm (WCA).

dispersion parameter, and p signifies the power parameter. This model postulates a relationship between the mean and variance of Y, where the variance is proportional to the mean raised to the power parameter p, expressed as $Var(Y) = \phi u^p$. The regression parameters b are linked to the mean of Y through a specified link function $g(\cdot)$, such that $E(Y) = g(Xb)$, where X represents the design matrix. The likelihood function for the Tweedie regression model involves the probability density function of the Tweedie distribution, which entails complexity due to the presence of the power parameter p, necessitating numerical methods for its evaluation. Estimation of the regression parameters b and the dispersion parameter ϕ typically relies on maximum likelihood, quasi-likelihood, or pseudo-likelihood methods, leveraging second-moment assumptions to facilitate efficient and adaptable modeling of continuous data (39, 40).

4 Results and discussion

In this study, we implemented regression models to predict the solubility of ketoprofen in supercritical CO_2 using the provided dataset. The dataset includes measurements of temperature (T in Kelvin) and pressure (P in bar) as inputs, and solubility as the output. The regression models employed are PPR, KRR, and TDR. To optimize the hyperparameters of these models, we utilized the Water Cycle Algorithm (WCA), a robust optimization method known for its efficiency in finding optimal solutions in complex search spaces. The dataset was partitioned into training and testing subsets (80% training and 20% test) randomly, and the effectiveness of the models was gaged using a diverse set of metrics. The models are implemented on a machine with core-i7 CPU and 8Gb RAM which takes very small time

(near Realtime) for each model to be executed. The effectiveness of regression models was appraised based on the following criteria (41):

1 R^2 Score (Coefficient of Determination):

$$R^2 = 1 - \frac{\sum_{i=1}^{n}\left(Y_{\text{observed},i} - Y_{\text{predicted},i}\right)^2}{\sum_{i=1}^{n}\left(Y_{\text{observed},i} - \overline{Y_{\text{observed}}}\right)^2}$$

These metric measures how well model predictions match data. An R^2 score near 1 indicates a highly accurate model.

2 Mean squared error

$$\text{MSE} = \frac{1}{n}\sum_{i=1}^{n}\left(Y_{\text{observed},i} - Y_{\text{predicted},i}\right)^2$$

The average squared difference between the outcomes as seen in reality and those the model predicts is known as MSE. Lower MSE values indicate better model performance.

3 Mean absolute error

$$\text{MAE} = \frac{1}{n}\sum_{i=1}^{n}\left|Y_{\text{observed},i} - Y_{\text{predicted},i}\right|$$

Without taking into account the direction of the errors, MAE determines the average magnitude of errors in a set of predictions. Like MSE, lower MAE values indicate better model performance.

Table 2 summarizes the numerical findings for every regression model. The results indicate that Piecewise Polynomial Regression (PPR) outperforms both Kernel Ridge Regression (KRR) and Tweedie Regression (TDR) across all evaluation metrics. PPR achieved the highest R^2 score of 0.97111, indicating that it explains approximately 97% of the variance in solubility. Additionally, PPR had the lowest MSE (1.6867E-09) and MAE (3.01040E-05), further demonstrating its superior predictive accuracy. Figure 4 shows a comparison of predicted solubility values and their corresponding actual values using the PPR model.

The results obtained in this study showed superior performance compared to the previous machine learning models developed for prediction of drug solubility in supercritical CO_2. The accuracy reported for machine learning modeling of Hyoscine solubility in supercritical CO_2 was reported to be 2.1680E-01 for the best model in terms of RMSE which is higher than our model developed in this study (20). A RMSE value of 2.74912E-01 was reported by Almehizia et al. (42) for prediction of multiple drugs solubility in supercritical CO_2. The best model was reported to be HS-PR (Harmony Search-Polynomial Regression).

TABLE 2 Performance metrics for the regression models predicting ketoprofen solubility.

Model	R^2 Score	MSE	MAE
PPR	0.97111	1.6867E-09	3.01040E-05
KRR	0.95044	2.5499E-09	3.49707E-05
TDR	0.84413	7.4249E-09	5.69159E-05

Kernel Ridge Regression (KRR) also performed well, with an R^2 score of 0.95044, an MSE of 2.5499E-09, and an MAE of 3.49707E-05. Although KRR's performance was slightly inferior to PPR, it still showed strong predictive capabilities, making it a viable alternative for modeling ketoprofen solubility. Figure 5 compares the KRR model-predicted and corresponding actual solubility values.

Tweedie Regression (TDR) exhibited the lowest performance among the three models, with R^2 score of 0.84413, an MSE of 7.4249E-09, and an MAE of 5.69159E-05. Despite its relatively lower performance, TDR provided reasonable predictions, but it is clear that more complex models like PPR and KRR better capture the relationship between input features and solubility. The comparison between predicted and actual solubility values using the TDR model is depicted in Figure 6. Although some deviations can be observed in the testing step for this model, the overall fitting accuracy is acceptable considering the complexity of the process and dataset. Moreover, the models have been optimized in a way to minimize the risk of overprediction for the test dataset.

Ultimately, the Piecewise Polynomial Regression (PPR) model shows excellent accuracy and dependability in predicting the solubility of ketoprofen in supercritical CO_2. Comparing this model to the other models assessed in this work, it performs better because it can partition the data space and fit polynomial functions within each segment to efficiently capture the underlying patterns in the data. Figures 7, 8 illustrate, with this model, how inputs affect the solubility values. Furthermore, shown in Figure 9 is the solubility in a contour plot and three-dimensional manner as a function of T(K) and P(bar). The trend for temperature shows exponential increase of solubility with temperature rise. On the other hand, a linear trend was observed for the influence of pressure on the drug solubility (see Figure 8). Thus, the maximum amount of ketoprofen solubility is determined at the highest values of T and P based on the ML models. Indeed, there is no optimum point for the solubility, and the optimum conditions should be determined from the process cost and economic evaluations.

5 Conclusion

In this study, we successfully developed and evaluated three machine learning regression models–PPR, KRR, and TDR–to predict the solubility of ketoprofen in supercritical CO_2. By employing the Water Cycle Algorithm for hyperparameter tuning, we optimized each model's performance, demonstrating the effectiveness of this approach in enhancing predictive accuracy. Our comparative analysis revealed that PPR outperformed the other models, providing the most accurate predictions with an R^2 score of 0.97111, a MSE of 1.6867×10^{-9}, and a MAE of 3.01040×10^{-5}. This paper makes multiple contributions. Initially, we assess the three regression models used for predicting ketoprofen solubility, emphasizing their advantages and disadvantages. Furthermore, we illustrate the enhancement of model performance through the optimization of hyperparameters using the Water Cycle Algorithm. Ultimately, we provide comprehensive visual representations and statistical examinations to uncover the connections between temperature (T), pressure (P), and solubility. This study employs sophisticated machine learning techniques and resilient optimization strategies to forecast the solubility of supercritical fluids and enhance the optimization of pharmaceutical processes.

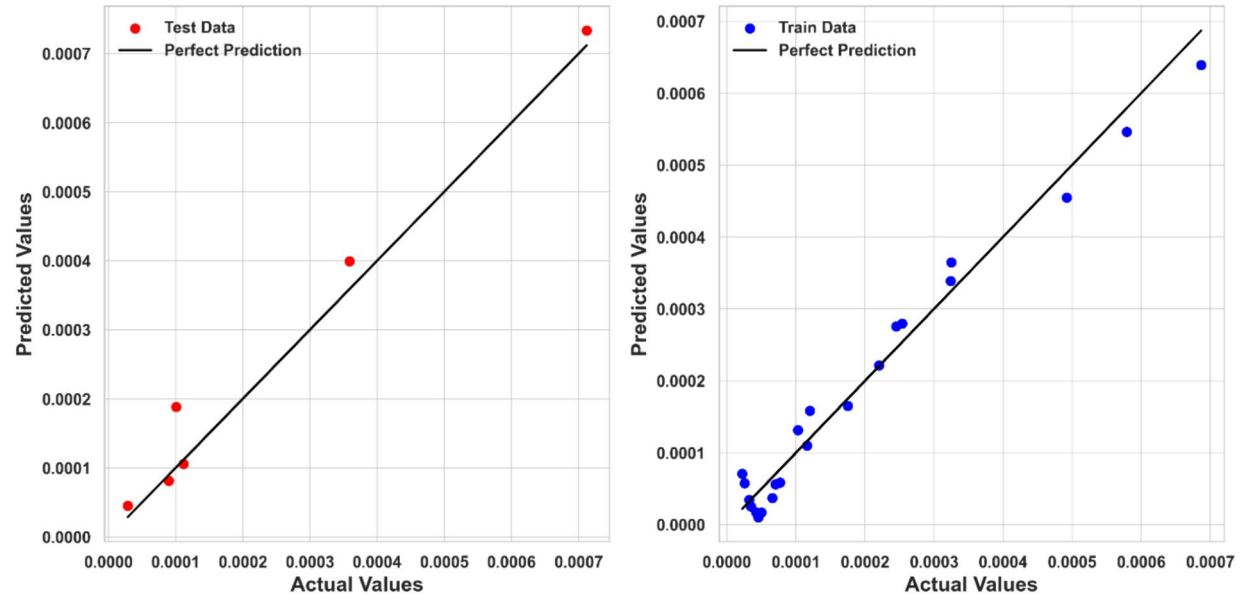

FIGURE 4
Actual and predicted values comparison (PPR model).

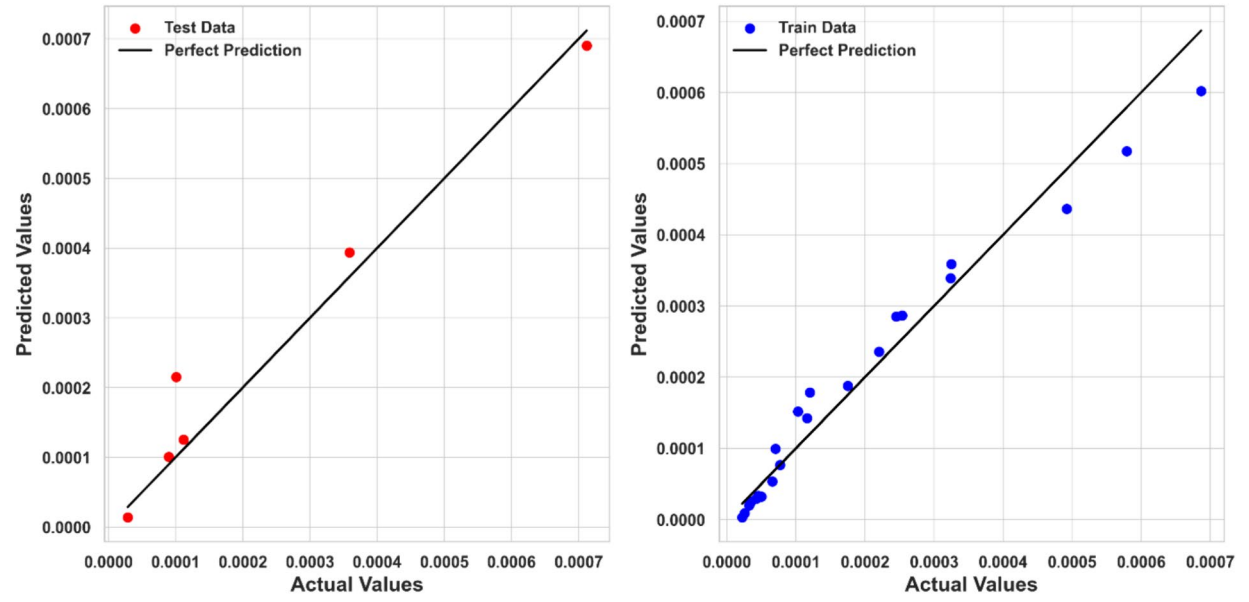

FIGURE 5
Actual and predicted values comparison (KRR model).

Data availability statement

The original contributions presented in the study are included in the article/supplementary material, further inquiries can be directed to the corresponding author/s.

Author contributions

TH: Conceptualization, Validation, Formal analysis, Writing – Review & Editing. SA: Supervision, Validation, Investigation, Resources, Writing – Review & Editing. SB: Conceptualization,

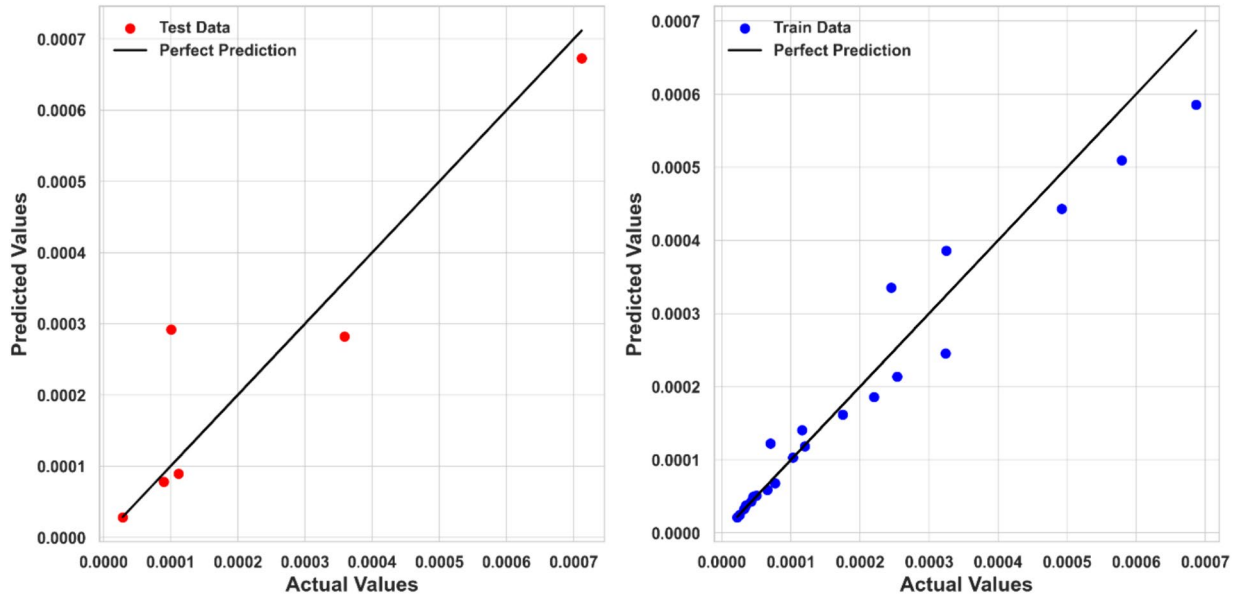

FIGURE 6
Actual and predicted values comparison (TDR model).

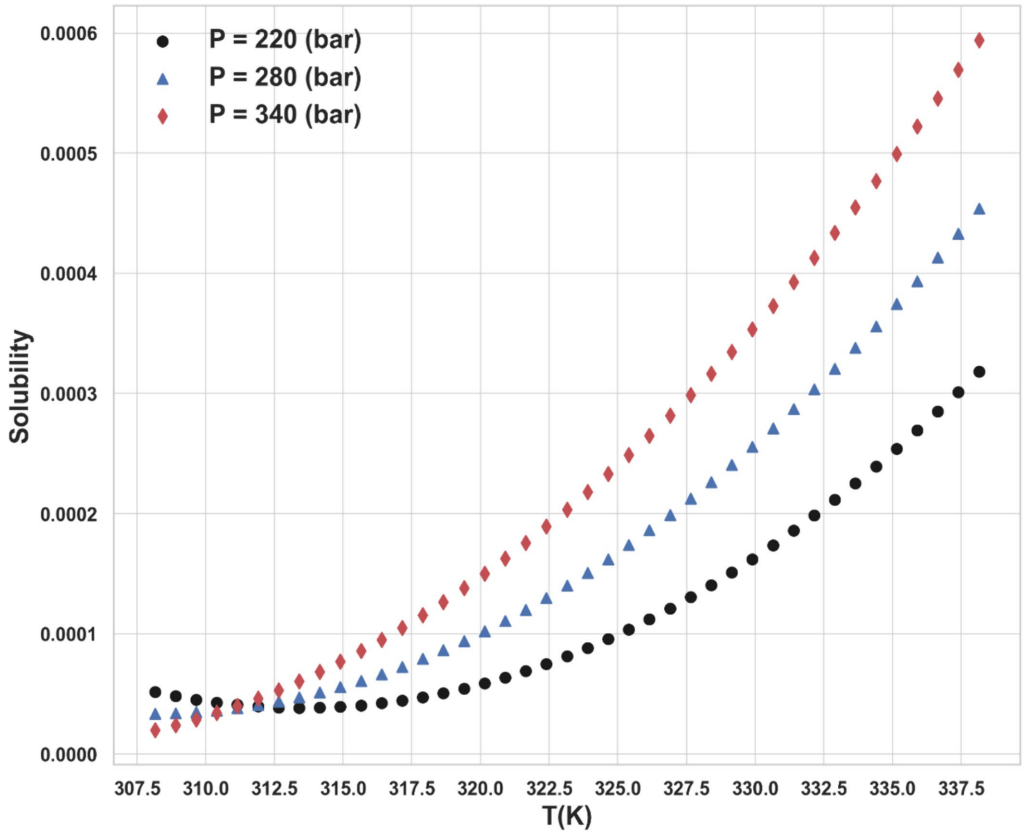

FIGURE 7
Impact of temperature on the solubility on different pressure levels.

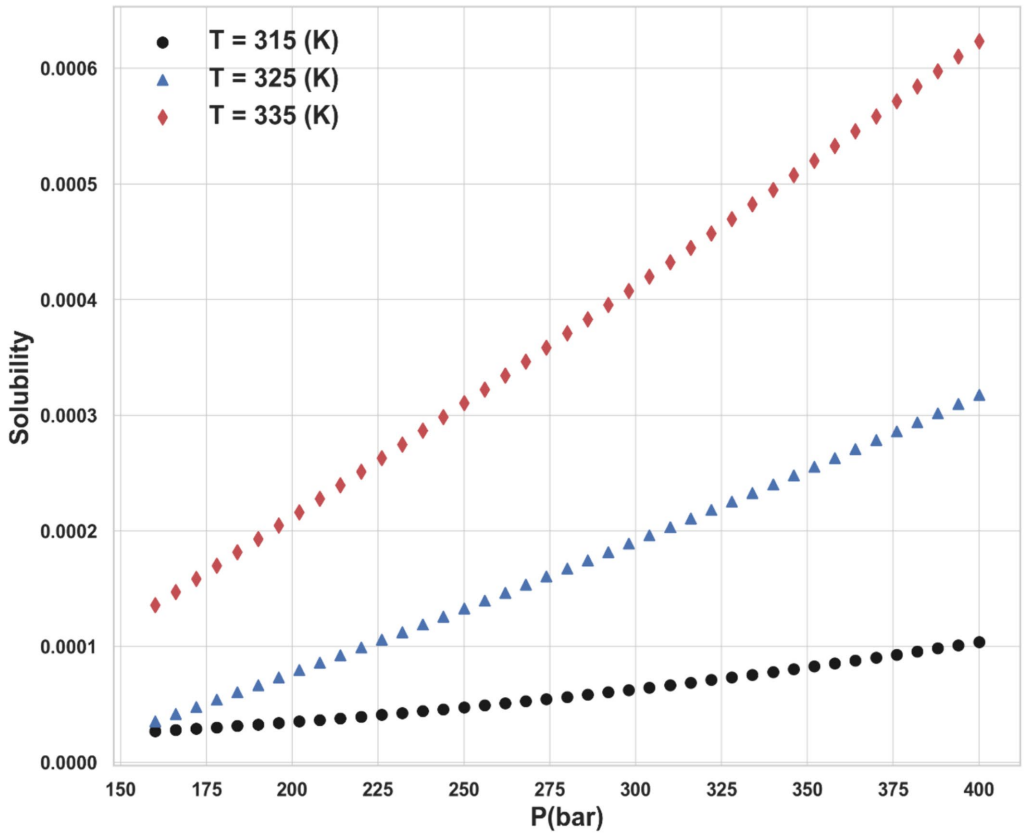

FIGURE 8
Impact of pressure on the solubility on different temperature levels.

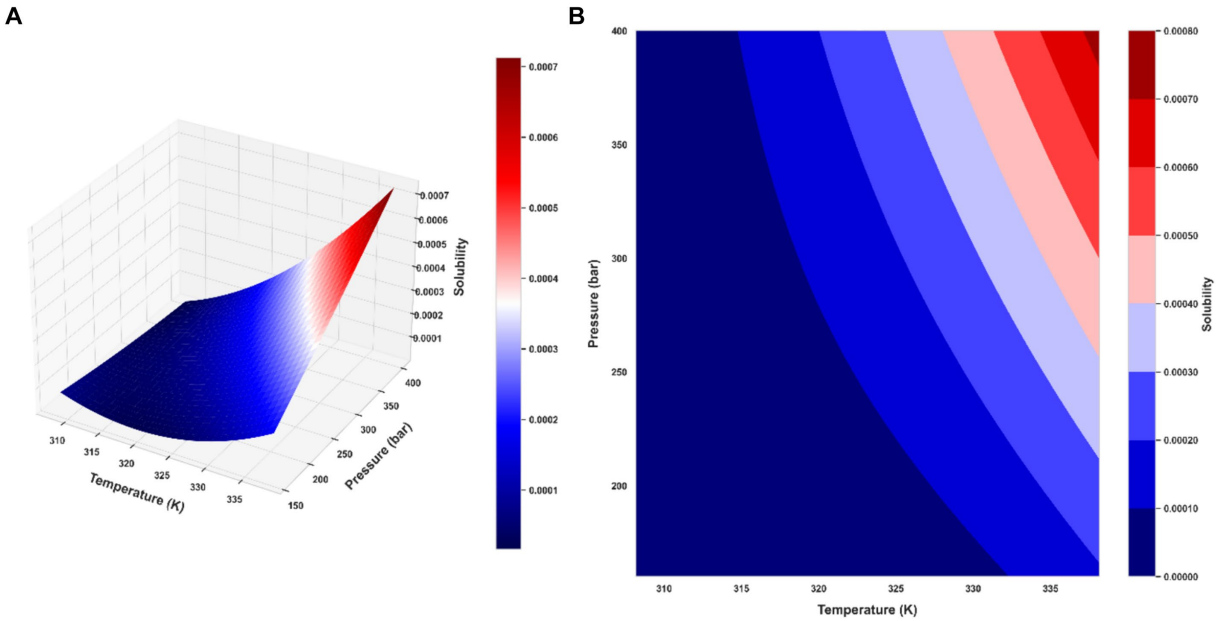

FIGURE 9
Final PPR model: **(A)** the 3D representation of predicted solubility values **(B)** contour plot of predicted solubility values.

Formal analysis, Investigation, Methodology, Resources, Validation, Visualization, Writing – original draft, Writing – review & editing.

Funding

The author(s) declare that financial support was received for the research, authorship, and/or publication of this article. This research was funded by Taif University, Saudi Arabia, Project No. (TU-DSPP-2024-61).

Acknowledgments

The authors extend their appreciation to Taif University, Saudi Arabia, for supporting this work through project number (TU-DSPP-2024-61).

Conflict of interest

The authors declare that the research was conducted in the absence of any commercial or financial relationships that could be construed as a potential conflict of interest.

Publisher's note

References

1. Hyer A, Gregory D, Kay K, le Q, Turnage J, Gupton F, et al. Continuous manufacturing of active pharmaceutical ingredients: current trends and perspectives. *Adv Synth Catal*. (2024) 366:357–89. doi: 10.1002/adsc.202301137

2. Liu P, Jin H, Chen Y, Wang D, Yan H, Wu M, et al. Process analytical technologies and self-optimization algorithms in automated pharmaceutical continuous manufacturing. *Chin Chem Lett*. (2024) 35:108877. doi: 10.1016/j.cclet.2023.108877

3. Sundarkumar V, Wang W, Mills M, Oh SW, Nagy Z, Reklaitis G. Developing a modular continuous drug product manufacturing system with real time quality Assurance for Producing Pharmaceutical Mini-Tablets. *J Pharm Sci*. (2024) 113:937–47. doi: 10.1016/j.xphs.2023.09.024

4. Camacho Vieira C, Peltonen L, Karttunen AP, Ribeiro AJ. Is it advantageous to use quality by design (QbD) to develop nanoparticle-based dosage forms for parenteral drug administration? *Int J Pharm*. (2024) 657:124163. doi: 10.1016/j.ijpharm.2024.124163

5. Simão J, Chaudhary SA, Ribeiro AJ. Implementation of quality by design (QbD) for development of bilayer tablets. *Eur J Pharm Sci*. (2023) 184:106412. doi: 10.1016/j.ejps.2023.106412

6. Barrera Jiménez AA, Matsunami K, van Hauwermeiren D, Peeters M, Stauffer F, dos Santos Schultz E, et al. Partial least squares regression to calculate population balance model parameters from material properties in continuous twin-screw wet granulation. *Int J Pharm*. (2023) 640:123040. doi: 10.1016/j.ijpharm.2023.123040

7. Bellinghausen S, Gavi E, Jerke L, Barrasso D, Salman AD, Litster JD. Model-driven design using population balance modelling for high-shear wet granulation. *Powder Technol*. (2022) 396:578–95. doi: 10.1016/j.powtec.2021.10.028

8. Muthancheri I, Chaturbedi A, Bétard A, Ramachandran R. A compartment based population balance model for the prediction of steady and induction granule growth behavior in high shear wet granulation. *Adv Powder Technol*. (2021) 32:2085–96. doi: 10.1016/j.apt.2021.04.021

9. Tong F, Wang Y, Gao H. Progress and challenges in the translation of cancer nanomedicines. *Curr Opin Biotechnol*. (2024) 85:103045. doi: 10.1016/j.copbio.2023.103045

10. Xiao Y, Zhong L, Liu J, Chen L, Wu Y, Li G. Progress and application of intelligent nanomedicine in urinary system tumors. *J. Pharm. Anal*. (2024):100964. doi: 10.1016/j.jpha.2024.100964

11. Zhang S, Li R, Jiang T, Gao Y, Zhong K, Cheng H, et al. Inhalable nanomedicine for lung cancer treatment. *Smart Mater. Med*. (2024) 5:261–80. doi: 10.1016/j.smaim.2024.04.001

12. Abdelbasset WK, Elkholi SM, Ahmed Ismail K, Alalwani TAA, Hachem K, Mohamed A, et al. Modeling and computational study on prediction of pharmaceutical solubility in supercritical CO2 for manufacture of nanomedicine for enhanced bioavailability. *J Mol Liq*. (2022) 359:119306. doi: 10.1016/j.molliq.2022.119306

13. Abourehab MAS, Salah al-Shati A, Venkatesan K, Alshehri S, Alzhrani RM, Alsubaiyel AM, et al. Theoretical investigations on the manufacture of drug nanoparticles using green supercritical processing: estimation and prediction of drug solubility in the solvent using advanced methods. *J Mol Liq*. (2022) 368:120559. doi: 10.1016/j.molliq.2022.120559

14. Bagheri H, Notej B, Shahsavari S, Hashemipour H. Supercritical carbon dioxide utilization in drug delivery: experimental study and modeling of paracetamol solubility. *Eur J Pharm Sci*. (2022) 177:106273. doi: 10.1016/j.ejps.2022.106273

15. Banchero M, Manna L. Solubility of fenamate drugs in supercritical carbon dioxide by using a semi-flow apparatus with a continuous solvent-washing step in the depressurization line. *J Supercrit Fluids*. (2016) 107:400–7. doi: 10.1016/j.supflu.2015.10.008

16. Chinh Nguyen H, Alamray F, Kamal M, Diana T, Mohamed A, Algarni M, et al. Computational prediction of drug solubility in supercritical carbon dioxide: thermodynamic and artificial intelligence modeling. *J Mol Liq*. (2022) 354:118888. doi: 10.1016/j.molliq.2022.118888

17. Kostyrin EV, Ponkratov VV, Salah Al-Shati A. Development of machine learning model and analysis study of drug solubility in supercritical solvent for green technology development. *Arab J Chem*. (2022) 15:104346. doi: 10.1016/j.arabjc.2022.104346

18. Zhou ZH. Machine learning. Berlin: Springer Nature (2021).

19. Zhong S, Zhang K, Bagheri M, Burken JG, Gu A, Li B, et al. Machine learning: new ideas and tools in environmental science and engineering. *Environ Sci Technol*. (2021) 55:12741–54. doi: 10.1021/acs.est.1c01339

20. Abouzied AS, Alshahrani SM, Hani U, Obaidullah AJ, al Awadh AA, Lahiq AA, et al. Assessment of solid-dosage drug nanonization by theoretical advanced models: modeling of solubility variations using hybrid machine learning models. *Case Stud. Therm. Eng*. (2023) 47:103101. doi: 10.1016/j.csite.2023.103101

21. Sadeghi A, Su CH, Khan A, Lutfor Rahman M, Sani Sarjadi M, Sarkar SM. Machine learning simulation of pharmaceutical solubility in supercritical carbon dioxide: prediction and experimental validation for busulfan drug. *Arab J Chem*. (2022) 15:103502. doi: 10.1016/j.arabjc.2021.103502

22. Sabegh MA, Rajaei H, Esmaeilzadeh F, Lashkarbolooki M. Solubility of ketoprofen in supercritical carbon dioxide. *J Supercrit Fluids*. (2012) 72:191–7. doi: 10.1016/j.supflu.2012.08.008

23. Abou El-Ela AA, El-Sehiemy RA, Abbas AS. Optimal placement and sizing of distributed generation and capacitor banks in distribution systems using water cycle algorithm. *IEEE Syst J*. (2018) 12:3629–36. doi: 10.1109/JSYST.2018.2796847

24. Ghazwani M, Begum MY. Computational intelligence modeling of hyoscine drug solubility and solvent density in supercritical processing: gradient boosting, extra trees, and random forest models. *Sci Rep*. (2023) 13:10046. doi: 10.1038/s41598-023-37232-8

25. Eskandar H, Sadollah A, Bahreininejad A, Hamdi M. Water cycle algorithm–A novel metaheuristic optimization method for solving constrained engineering optimization problems. *Comput Struct*. (2012) 110-111:151–66. doi: 10.1016/j.compstruc.2012.07.010

26. Sadollah A, Eskandar H, Kim JH. Water cycle algorithm for solving constrained multi-objective optimization problems. *Appl Soft Comput*. (2015) 27:279–98. doi: 10.1016/j.asoc.2014.10.042

27. Razmjooy N, Khalilpour M, Ramezani M. A new meta-heuristic optimization algorithm inspired by FIFA world cup competitions: theory and its application in PID designing for AVR system. *J Control Autom Electr Syst*. (2016) 27:419–40. doi: 10.1007/s40313-016-0242-6

28. Jafar R. M. S., Geng S., Ahmad W., Hussain S., Wang H. *A comprehensive evaluation: water cycle algorithm and its applications*. In: Bio-inspired computing: Theories and applications: 13th international conference, BIC-TA 2018, Beijing, China, November 2–4, 2018, proceedings, part II 13. Berlin: Springer. (2018).

29. Sharma S, Mahadevan J, Giri L, Mitra K. Identification of optimal flow rate for culture media, cell density, and oxygen toward maximization of virus production in a fed-batch baculovirus-insect cell system. *Biotechnol Bioeng*. (2023) 120:3529–42. doi: 10.1002/bit.28558

30. Sharma S, Keerthi PN, Giri L, Mitra K. Toward performance improvement of a Baculovirus–insect cell system under uncertain environment: A robust multiobjective dynamic optimization approach for Semibatch suspension culture. *Ind Eng Chem Res*. (2022) 62:111–25. doi: 10.1021/acs.iecr.2c03355

31. Pujari KN, Miriyala SS, Mittal P, Mitra K. Better wind forecasting using evolutionary neural architecture search driven green deep learning. *Expert Syst Appl*. (2023) 214:119063. doi: 10.1016/j.eswa.2022.119063

32. Sauve M. Piecewise polynomial estimation of a regression function. *IEEE Trans Inf Theory*. (2009) 56:597–613. doi: 10.1109/TIT.2009.2027481

33. Chaudhuri P, Huang MC, Loh WY, Yao R, et al. Piecewise-polynomial regression trees. *Stat Sin*. (1994) 4:143–67.

34. Breiman L, Friedman JH, Olshen RA, Stone CJ. Classification and regression trees. Abingdon: Routledge (2017).

35. Tandon R, Si S, Ravikumar P, Dhillon I. *Kernel ridge regression via partitioning*. arXiv (2016).

36. Welling M. *Kernel ridge regression*. Max Welling's classnotes in machine learning, pp. 1–3. (2013).

37. Byrne E, Schniter P. Sparse multinomial logistic regression via approximate message passing. *IEEE Trans Signal Process*. (2016) 64:5485–98. doi: 10.1109/TSP.2016.2593691

38. Zhang Y, Duchi J, Wainwright M. Divide and conquer kernel ridge regression. In conference on learning theory. *Proc Machine Learn Res*. 206:6245–62.

39. Bonat WH, Kokonendji CC. Flexible Tweedie regression models for continuous data. *J Stat Comput Simul*. (2017) 87:2138–52. doi: 10.1080/00949655.2017.1318876

40. Hassine A, Masmoudi A, Ghribi A. Tweedie regression model: a proposed statistical approach for modelling indoor signal path loss. *Int J Numer Modell*. (2017) 30:e2243. doi: 10.1002/jnm.2243

41. Botchkarev A. *Performance metrics (error measures) in machine learning regression, forecasting and prognostics: Properties and typology*. arXiv, (2018).

42. Almehizia AA, Naglah AM, Alkahtani HM, Hani U, Ghazwani M. Numerical optimization of drug solubility inside the supercritical carbon dioxide system using different machine learning models. *J Mol Liq*. (2023) 392:123466. doi: 10.1016/j.molliq.2023.123466

frontiers | Frontiers in Chemistry

TYPE Original Research
PUBLISHED 14 October 2024
DOI 10.3389/fchem.2024.1483868

OPEN ACCESS

EDITED BY
Serban Moldoveanu,
Independent Researcher, Greensboro, NC, United States

REVIEWED BY
Shulei Han,
China National Tobacco Quality Supervision and Test Center, China
Pawel Swit,
University of Silesia in Katowice, Poland

*CORRESPONDENCE
Ayesha Nisathar,
ayesha.nisathar@jstar-research.com
Hui Chen,
hui.chen@jstar-research.com

RECEIVED 05 September 2024
ACCEPTED 30 September 2024
PUBLISHED 14 October 2024

CITATION
Nisathar A, Chen H, Lei X, Zeng Z and Chen J (2024) Comparison of genotoxic impurities in extracted nicotine vs. synthetic nicotine. *Front. Chem.* 12:1483868. doi: 10.3389/fchem.2024.1483868

Comparison of genotoxic impurities in extracted nicotine vs. synthetic nicotine

Ayesha Nisathar[1]*, Hui Chen[1]*, Xiaoli Lei[2], Zeyu Zeng[2] and Jia Chen[2]

[1]Analytical Research Development and Quality Control, JSTAR Research Inc., Cranbury, NJ, United States, [2]Porton Pharma Solutions, Chongqing, China

Nicotine is a chiral alkaloid; nitrogen-containing organic compound that occurs naturally. (S)-nicotine is extracted from Tobacco plants and used as the key addictive ingredient in many smoking products. Synthetic nicotine has gained the interest of many smoking product manufacturers over the last few decades due to the ease and low cost of manufacturing. Another claimed advantage of synthetic nicotine is the absence of genotoxic impurities that form during the extraction process of nicotine. These impurities are other plant alkaloids, phenolic compounds, and heavy metals. Additionally, the U. S. FDA has implemented new regulations on the quality control of synthetic nicotine. However, only a very few research articles have been published on assessing the complete impurity profile of synthetic nicotine. Therefore, the need to know the composition difference between tobacco-extracted nicotine vs. synthetic nicotine is highly necessary. In this research study, the impurity profile of thirteen different lots of synthetic nicotine was compared with fourteen lots of nicotine extracted from plants using in-house analytical methods. First, the samples were tested for other alkaloids and phenols by reversed-phase High-Performance Liquid Chromatography (HPLC). Second, the chiral purity was analyzed by normal phase HPLC. Third, lead and arsenic content were tested by atomic absorption and fluorescence spectrometry. Fourth, nicotine-specific nitrosamines were tested by LC-MS. The reversed phase HPLC data suggested similar quantities of total impurities in both synthetic and tobacco-extracted nicotine (0.1%). However, synthetic nicotine lacks some impurities such as cotinine, nornicotine, and nicotine-N-oxide. Additionally, the synthetic nicotine lots used in this study have high enantiomeric purity similar to the tobacco-extracted nicotine.

KEYWORDS

chromatography, comparison, extraction, nicotine, nitrosamine, purity and impurity, synthetic

Introduction

Nicotine is an alkaloid; nitrogen-containing organic compound that occurs naturally in many plant varieties and is the key component in tobacco plants. Structurally, nicotine is a chiral molecule with a single stereocenter (Scheme 1) (Henningfield et al., 2009). Nicotine is extracted from tobacco plants and used as the key ingredient in many smoking products, such as cigarettes, cigars, smokeless tobacco, hookah tobacco, and most e-cigarettes (Robinson and Pritchard, 1992).

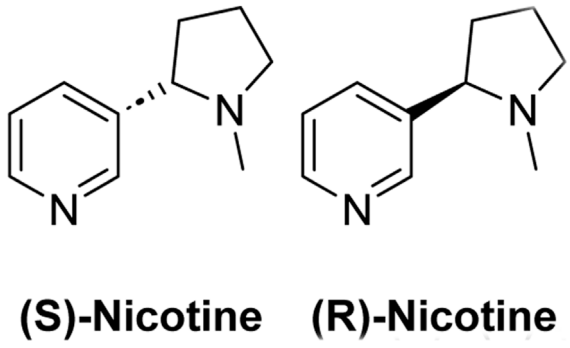

SCHEME 1
Structures of (S) and (R)-Nicotine.

The (S)-nicotine is known to be present in excess in tobacco plants and is considered a highly addictive form. While (R)-nicotine is found in less amounts in tobacco plants and considered less addictive, proper evidence confirming its addictiveness is less.

Another method to generate nicotine is chemical synthesis. Synthetic nicotine has gained the interest of many Tobacco product manufacturers over the last few decades due to the minimal regulations imposed by the FDA on synthetic Nicotine compared to tobacco plant-derived Nicotine. However, the FDA has recently implemented new controls on synthetic Nicotine. An additional advantage of synthetic Nicotine is that it the less impact on the environment such as an increased global footprint. Zafeiridou et al. evaluated the environmental impacts of Tobacco cultivation and estimated 0.2% of CO_2 global emissions from Tobacco cultivation (Zafeiridou et al., 2018). Furthermore, the Tobacco plant affects the lifespan of crop-friendly bacteria/fungi and hence causes a subsequent effect on maize crop growth (Lisuma et al., 2019). The composition of tobacco-extracted nicotine varies depending on the farming practices, climate, and which part of the plant leaf is harvested. Lisko et al. reported that many tobacco-derived nicotine products have discrepancies between labeled and actual nicotine concentrations. Furthermore, many common products contain impurity alkaloids at concentrations that exceed USP limits for impurities (Lisko et al., 2015).

The leading manufacturers of Synthetic Nicotine are Zanoprima Lifesciences, NJOY, Contraf-Nicotex-Tobacco, and Next Generation Labs. The enantiomeric purity of the final Nicotine of most of these manufacturers is poor (≤50%) and often requires a stereoselective purification step which reduces the yield of (S)-Nicotine (Jordt, 2023). Synthetic Nicotine has been used in many e-cigarettes, Nicotine pouches, and many other Tobacco products. Tobacco product manufacturers have marketed these as safe alternatives to Tobacco extracted Nicotine and attracted many younger populations (Ma et al., 2023). However, whether Synthetic Nicotine is a healthier alternative compared to Tobacco extracted Nicotine is still under debate (Kowitt et al., 2023). Porton Pharma Solutions in China has recently patented a novel Nicotine synthetic pathway that produces more of the (S)-Nicotine (Lin, 2023). The goal of this work is to compare the impurities in the Nicotine in the novel synthetic pathway with several lots of Tobacco extracted Nicotine.

According to a fact sheet released by the U. S. Department of Food and Drug Administration (FDA), other chemicals in Tobacco or Tobacco products cause more health effects than Nicotine itself. The statement is that "It's the thousands of chemicals contained in tobacco and tobacco smoke that make tobacco use so deadly. This toxic mix of chemicals—not nicotine—causes serious health effects, including fatal lung diseases and cancer" (Talhout et al., 2011). Better quality control in synthetic nicotine products is required on a global scale to ensure that customers can safely use them. Common impurities reported in tobacco-extracted nicotine are naturally occurring other alkaloids, nicotine enantiomers, nicotine-specific nitrosamines, and heavy metals.

Anatabine, β-nicotine, cotinine, myosmine, nicotine-N′-oxide, nornicotine, and anabasine are the main naturally occurring alkaloid impurities found in nicotine (Scheme 2) (Henningfield et al., 2009). Anatabine is structurally distinct from nicotine. β-nicotine is structurally related to nicotine and is considered a derivative of nicotine. The prefix "β-" indicates the position of a specific chemical bond in the molecule. Chemically, β-nicotyrine is an isomer of anatabine. Cotinine is another alkaloid impurity in nicotine, and it is also a metabolite of nicotine. Cotinine is formed when the body metabolizes nicotine, and it can also be present in tobacco. Myosmine is also structurally related to nicotine. Nornicotine is an isomer of nicotine, meaning it has the same molecular formula but a different arrangement of atoms. Anabasine is a pyridine alkaloid which is structurally related to nicotine. All of these alkaloid impurities are often present in relatively small amounts compared to nicotine, but their presence contributes to the overall alkaloid profile of tobacco (Avagyan et al., 2021).

Tobacco-specific N-nitrosamines (TSNAs) are a group of chemical compounds that are found in tobacco and tobacco smoke. N-nitrosamines are known carcinogens, meaning they have the potential to cause cancer. TSNAs are formed through a specific chemical process during the growth, curing, and processing of tobacco, as well as during the combustion of tobacco, which occurs when smoking (Konstantinou et al., 2018). Some of the key tobacco-specific N-nitrosamines are shown in Scheme 3. These include N′-Nitrosonornicotine (NNN), 4-(Methylnitrosamino)-1-(3-pyridyl)-1-butanone (NNK), N-Nitrosoanabasine (NAB), N-Nitrosoanatabine (NAT).

N′-Nitrosonornicotine (NNN): NNN is a nitrosamine compound that is formed during the curing and processing of tobacco, as well as during the smoking of tobacco products. It is known to be carcinogenic. 4-(Methylnitrosamino)-1-(3-pyridyl)-1-butanone (NNK): NNK is another important nitrosamine found in tobacco and tobacco smoke. It is known to be a potent lung carcinogen. N-Nitrosoanabasine (NAB): NAB is another nitrosamine compound related to nicotine that is found in tobacco. N-Nitrosoanatabine (NAT): NAT is a nitrosamine found in tobacco and tobacco smoke. It is a derivative of nicotine, and its presence has been identified in both unburned tobacco and mainstream smoke.

Due to the association of TSNAs with cancer, efforts have been made to reduce their levels in tobacco products and to develop methods to minimize their formation during the tobacco manufacturing process (Yalcin and de la Monte, 2016). Additionally, public health campaigns aim to raise awareness of the health risks associated with tobacco use, including exposure to TSNAs through smoking.

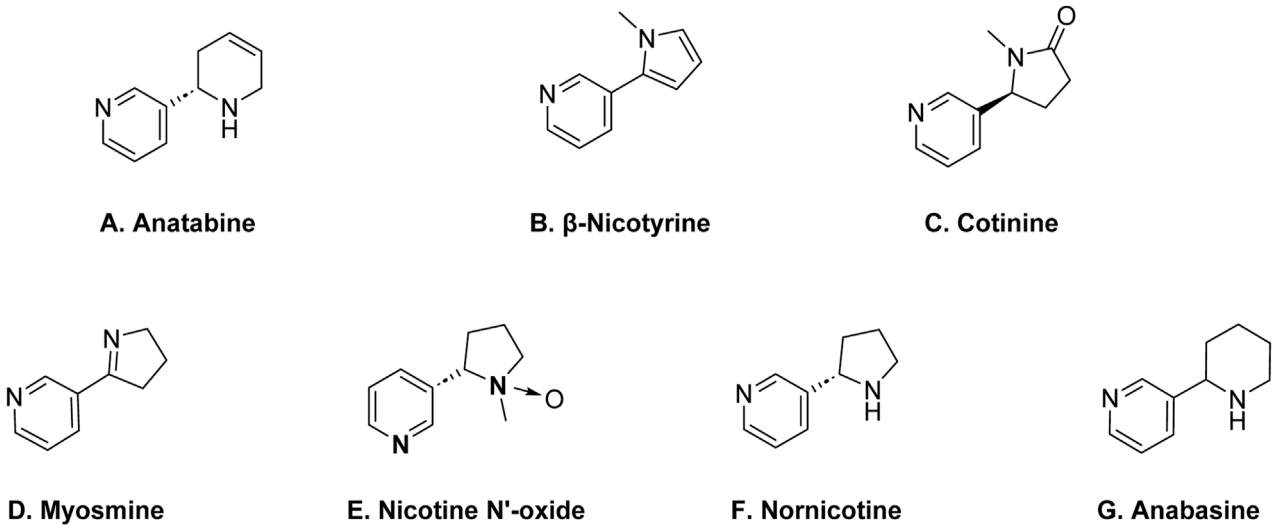

SCHEME 2
Structures of key alkaloid impurities in nicotine; **(A)** Anatabine, **(B)** β-Nicotyrine, **(C)** Cotinine, **(D)** Myosmine, **(E)** Nicotine N′-oxide, **(F)** Nornicotine, **(G)** Anabasine.

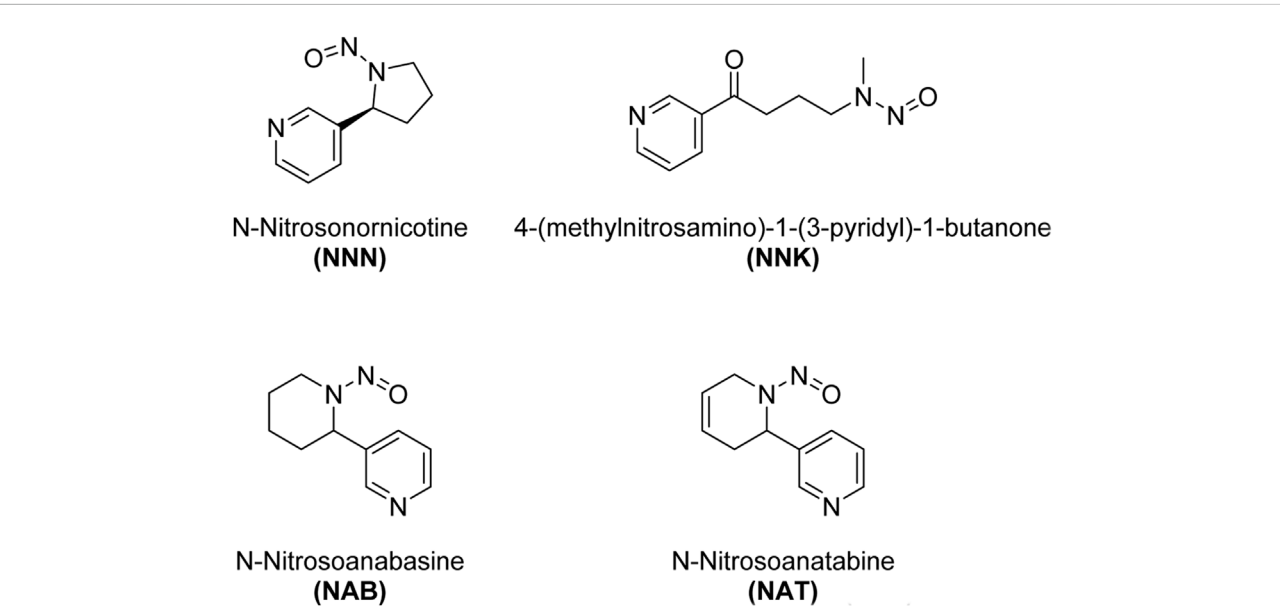

SCHEME 3
Structures of the most common nitrosamines found in nicotine.

The goal of the current research is to identify impurities in synthetic nicotine and extracted nicotine and justify the claims made by synthetic nicotine manufacturers. Additionally, synthetic nicotine used for this study is from in-house synthesized nicotine from a recently patented synthetic procedure. A similar work has been published by Cheetham and co-workers from "Enthalpy Analytical LLC" in 2022. Enthalpy analytical screened only 5 lots of synthetic Nicotine and 5 lots of Extracted Nicotine. In this study, we screened 13 different lots of Synthetic Nicotine and compared the results with 14 different lots of extracted nicotine (Cheetham et al., 2022).

Analytical methods were used to quantify the impurities in the selected Nicotine lots. European Pharmacopeia (Eu. P. 10.0) monograph method was followed for assay, purity, and impurity analysis using potentiometry and High-Performance Liquid Chromatography (HPLC) instruments, respectively. An in-house developed normal phase chiral HPLC with Diode Array Detector was used to determine enantiomeric purity. Quantification of nitrosamines was done using liquid chromatography-mass spectrometry (LC-MS). Lead and Arsenic content quantification was done using Atomic Absorption Spectrophotometer (AAS) and Atomic Fluorescence Spectrophotometer, respectively.

10.3389/fchem.2024.1483868

TABLE 1 Synthetic nicotine lot numbers and respective abbreviations.

Synthetic nicotine actual lot #	Abbreviation
205351-305-00011-P2-01	SyN-1
205351-305-00012-P2-01	SyN-2
205351-305-00013-P2-01	SyN-3
HC-1	SyN-4
HC-2	SyN-5
HC-3	SyN-6
HC-4	SyN-7
HC-5	SyN-8
HC-6	SyN-9
HC-7	SyN-10
HC-8	SyN-11
HC-9	SyN-12
HC-10	SyN-13

TABLE 2 Extracted nicotine lot numbers and respective abbreviations.

Extracted nicotine actual lot #	Abbreviation
103700-304-00006	ExN-1
103700-305-00051	ExN-2
HN-20230704	ExN-3
HN-2023062202	ExN-4
TQ-1	ExN-5
TQ-2	ExN-6
TQ-3	ExN-7
TQ-4	ExN-8
TQ-5	ExN-9
TQ-6	ExN-10
TQ-7	ExN-11
TQ-8	ExN-12
TQ-9	ExN-13
TQ-10	ExN-14

Materials and methods

Thirteen lots of synthetic Nicotine from Porton China in-house was taken and fourteen different Extracted Nicotine from local vendors in China was used. The names of the vendors will not be provided herein due to business cooperation confidentiality. Lot numbers of Synthetic Nicotine and Extracted Nicotine are provided in Tables 1, 2 below. Each lot number is abbreviated for simplicity and the respective abbreviations along with the actual lot number for synthetic nicotine and extracted nicotine batches are listed in Tables 1, 2, respectively.

Nicotine content/assay

Nicotine assay was performed according to European Pharmacopeia (Eu. P. 10.0) reference standard testing procedure. Nicotine-free base content was analyzed potentiometrically using a Mettler Toledo T5 titrator. 60 mg of the test product was accurately weighed into a 50 mL clean dry beaker and 40 mL of glacial acetic acid was added to fully dissolve. The sample was titrated with perchloric acid titration solution (0.1 mol/L) until the electrode potential stabilized as the endpoint. Each titration was conducted in duplicate. Glacial acetic acid solution without sample was titrated with perchloric acid titration solution (0.1 mol/L) until the electrode potential stabilizes as the endpoint and is used as the blank reading. Calculations were done based on the facts and the EU. P. statement that corresponds 1 mL of 0.1 mol/L perchloric acid titration solution to 0.00811 g of $C_{10}H_{14}N_2$ nicotine-free base.

Purity and related substances

Analysis of impurities present in Nicotine samples was conducted using HPLC according to Eu. P. 10.0 specifications. Agilent 1200 instrument with a DAD detector was used. Nicotine for system suitability chemical reference standard (CRS) batch 5 (catalog number Y000123, SDS product code 202300056) was used as the reference standard for the assay. The nicotine system suitability solution and nicotine test solutions were prepared according to EU guidelines.

Isomeric purity

In-house synthesized Nicotine racemate oxalate (MT117) was used as a marker to test enantiomeric purity. Agilent 1260 instrument with UV detector was used and Diacel CHIRALCEL OD-H 4.6 × 250 mm, 5 µm (part number 14325) column was used. HPLC method condition was an isocratic gradient with n-hexane-ethanol = 95:5 (v/v) mobile phase, flow 1.0 mL/min, and total run time 20 min. UV detection wavelength at 260 nm was used. The sample injection volume was 10 µL. n-hexane-ethanol = 95:5 (v/v) was used as the diluent/blank. The Isomer marker solution was prepared by weighing 50 mg of MT117 racemate oxalate and dissolved in 1 mL of 20% NaOH aqueous solution. Then, extracted it with 1.5 mL of n-hexane. The extracted MT117 racemic mixture in n-hexane solution was diluted 10 times with diluent and injected as an isomer marker solution. Nicotine sample solutions were prepared by dissolving 20 mg of the test sample in a 20 mL volumetric flask with a diluent. All the solutions were shaken well and sonicated to mix well before use.

Nicotine specific nitrosamine testing

LCMS-MRM (multiple reaction monitoring) was used for qualitative and quantitative analysis of nitrosamines. The method was adopted from the Nicotine regulatory for China. The tested N-nitrosamines are N'-Nitrosonornicotine (NNN), 4-(Methylnitrosamino)-1-(3-pyridyl)-1-butanone (NNK), N-Nitrosonornicotine (NAT), N-Nitrosoanabasine (NAB).

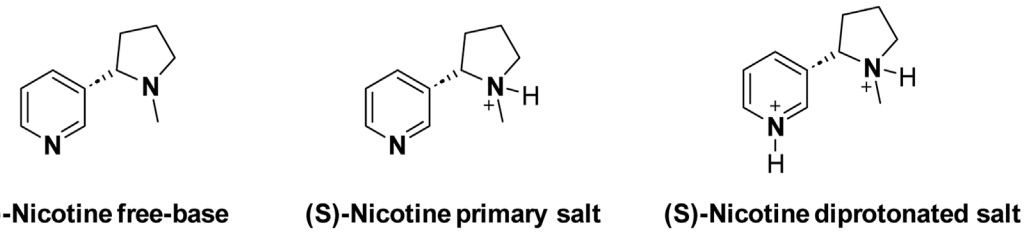

SCHEME 4
Forms of nicotine.

Deuterated N-Nitroso Nicotine (NNN-d4), Deuterated 4-sulfur nitrosamine) -1-(3-pyridinyl) -1-butone (NNK-d4), Deuterated Nitrosonornitine (NAT-d4), and deuterated (R, S)-N-Nitrostobasine (NAB-d4) was used as internal standards for NNN, NNK, NAT, and NAB respectively. Method details and sample preparation are described in the Supplementary Section S1.

Metal analysis

Lead (Pb)

Atomic Absorption Spectrophotometer, SP-3803AA, 2020-JS001 Shanghai Spectral Instrument Co., Ltd. was used for Pb analysis. Instrument parameters used for testing are described in the Supplementary Material. Pb standard solution of 1,000 mg/L from Guobiao (Beijing) Testing & Certification Co. Ltd. (lot#221008-7-1) was used to prepare a Pb standard curve of 0, 2, 5, 10, 15, 20 µg/L by diluting with Milli-Q water. The nicotine sample for testing was prepared by dissolving 0.1 g of accurately weighed sample in a beaker using nitric acid (7 mL), sulfuric acid (5 mL), perchloric acid (4 mL), and hydrogen peroxide (2 mL). 0.5 mL of this solution was added into a 25 mL volumetric flask and diluted up to the mark with Milli-Q water. The sample was shaken before testing.

Arsenic (As)

Arsenic content was analyzed by Atomic Fluorescence Spectrophotometer AFS-933 instrument. A standard solution of 100 mg/L from the Environmental Standard Institute (lot#103017-1) was used to prepare a standard dilution series of 0, 1, 2, 5, and 10 µg/L using Milli-Q water as a diluent and a linearity curve of As concentration vs. fluorescence was plotted. Nicotine samples for testing were prepared in the same manner as Pb sample preparation.

Results

Assay

Assay was conducted to determine the "free base form" content in given Nicotine lots. The free base assay in extracted nicotine serves the purpose of quantifying the amount of nicotine in its free base form within a given sample. Nicotine exists in two primary forms: free base and salt. The free base form is the unprotonated, neutral state of nicotine, while the salt form results from the combination of nicotine with an acid (Duell et al., 2018). A third form of diprotonated nicotine is another possible structure (Scheme 4). However, there's a lack of evidence to support the existence of the diprotonated nicotine form in any smoking products (El-Hellani et al., 2015; Pankow et al., 2003).

In the context of both synthetic and extracted nicotine, especially in the tobacco industry or related fields, the free base assay is crucial for several reasons. Nicotine in its free base form is more readily absorbed by the body than its salt forms (Talih et al., 2020). Therefore, knowing the concentration of free-base nicotine provides valuable information about the potential physiological impact of a given nicotine-containing product. Nicotine manufacturers use the free base assay to ensure product quality/product performance in nicotine formulations such as e-cigarettes, nicotine patches, or gums. Lastly, regular monitoring of free-base nicotine content is not only a part of quality control processes in the tobacco industry but also ensures compliance with regulations and standards. It also helps maintain product consistency and ensures that consumers receive the expected nicotine levels when using a particular product. The assay methods for determining free base nicotine levels often involve chemical analysis, such as titration or chromatography techniques (Gholap et al., 2020). Eu. P. specified potentiometric method was used to determine the free base content in synthetic and extracted nicotine samples. The nicotine-free base percentage of all the lots is tabulated in Figure 1. Both synthetic and extracted nicotine had assay percentages greater than 99.1% making them identical in nicotine form content.

Related impurities

The European Directorate for the Quality of Medicines & Health (EDQM) classifies 7 impurities (A, B, C, D, E, F, G) in the Nicotine for system suitability chemical reference standard (CRS) and hence used as an impurity's marker. The impurities are A: anatabine, B: β-nicotyrine, C: cotinine, D: myosmine, E: nicotine N′-oxide, F: nornicotine, G: anabasine. The Nicotine CRS chromatogram showing all labeled impurities is shown in Figure 2A. The retention times of impurities are A: anatabine, B: β-nicotyrine, C: cotinine, D: myosmine, E: nicotine N′-oxide, F: nornicotine, G: anabasine 13.687, 27.442, 9.340, 14.540, 4.904, 11.656 min, respectively. HPLC system suitability was assessed before sample analysis and ensured Eu. P. criteria were met. EU. P. system suitability criteria is to have a minimum resolution of 2.5 between impurity peak G and Nicotine. The system suitability

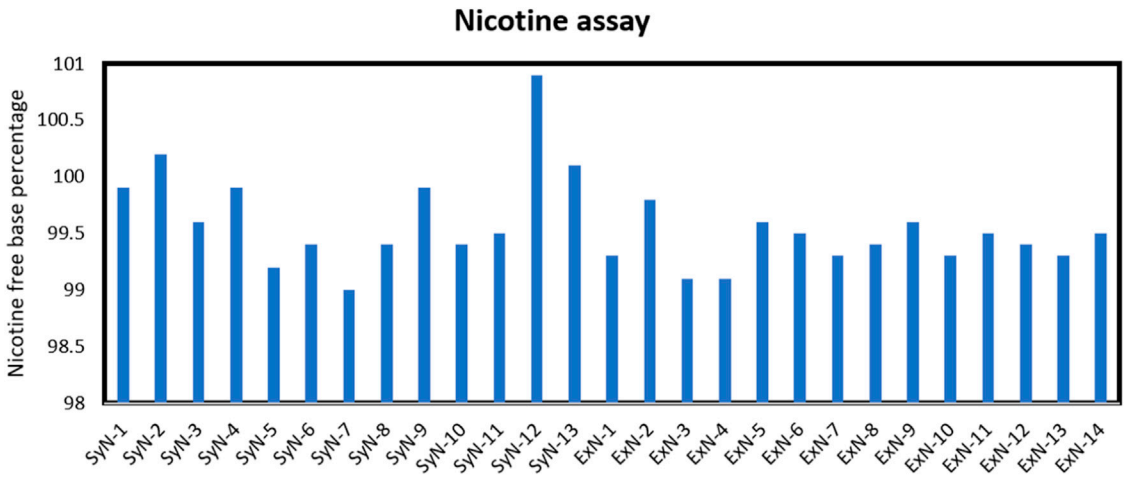

FIGURE 1
Nicotine assay percentage for synthetic and extracted nicotine lots.

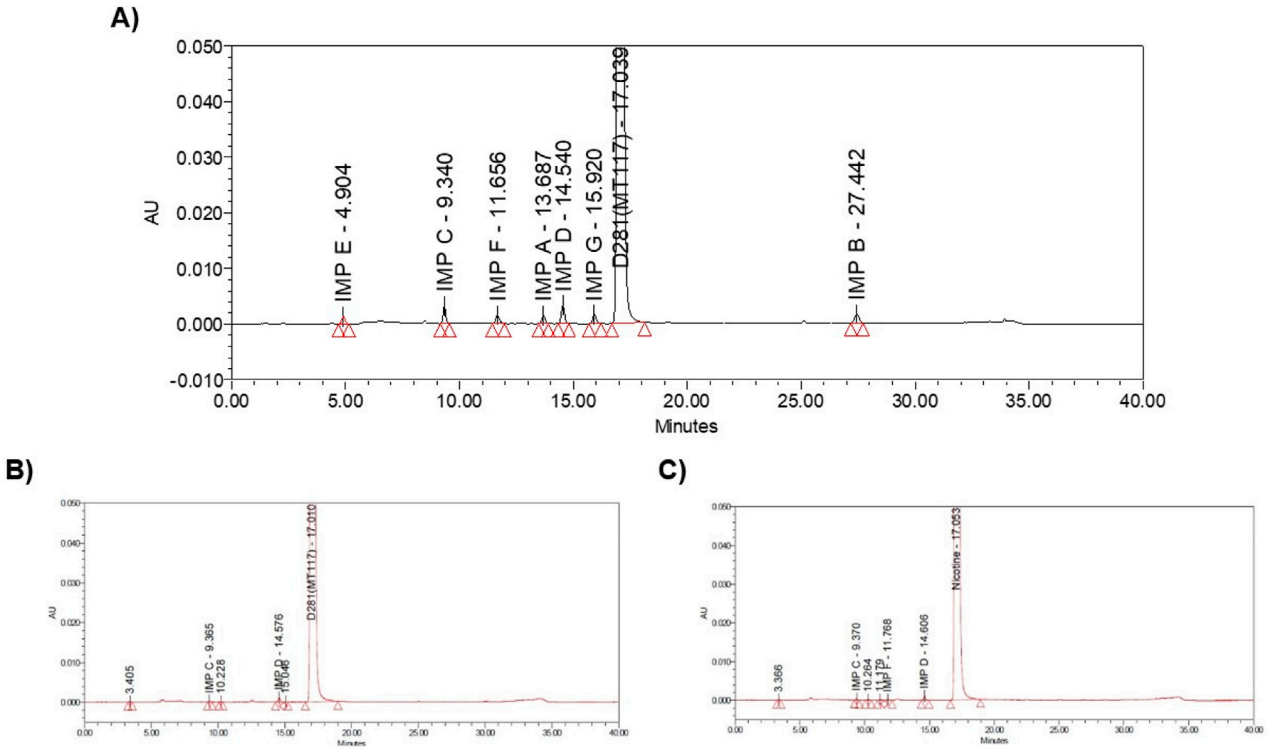

FIGURE 2
(A) Nicotine system suitability solution, **(B)** SyN-1 achiral chromatogram, **(C)** ExN-1 achiral chromatogram.

injection sequence includes two blanks, and six reference standard solutions. In addition to the EU. P. system suitability criteria satisfaction, the relative standard deviation (RSD) was checked and ensured that it is within the standard Pharmacopeial range (RSD of ≤35.0% for peaks with area percentage 0.05%–0.10%, RSD of ≤20.0% for peaks with area percentage 0.10%–0.50%, RSD of ≤10.0% for peaks with an area percentage 0.50%–1.00%). A sample chromatogram from one synthetic nicotine lot and one extracted nicotine are provided in Figures 2B, C, respectively.

All the known impurities including other impurity peaks in the chromatograms were integrated according to Eu.P. guidelines and each impurity percentage content both synthetic and extracted nicotine was tabulated, and depicted in Figures 3A–F. The area percentage of impurity cotinine vs. different synthetic and extracted nicotine lots are shown in Figure 3A. Similarly, area percentage of myosmine, nornicotine, nicotine-N-oxide, other impurities, and total impurities were plotted against different Nicotine lots and shown in Figures 3B–F, respectively. Anatabine, β-nicotyrine, and

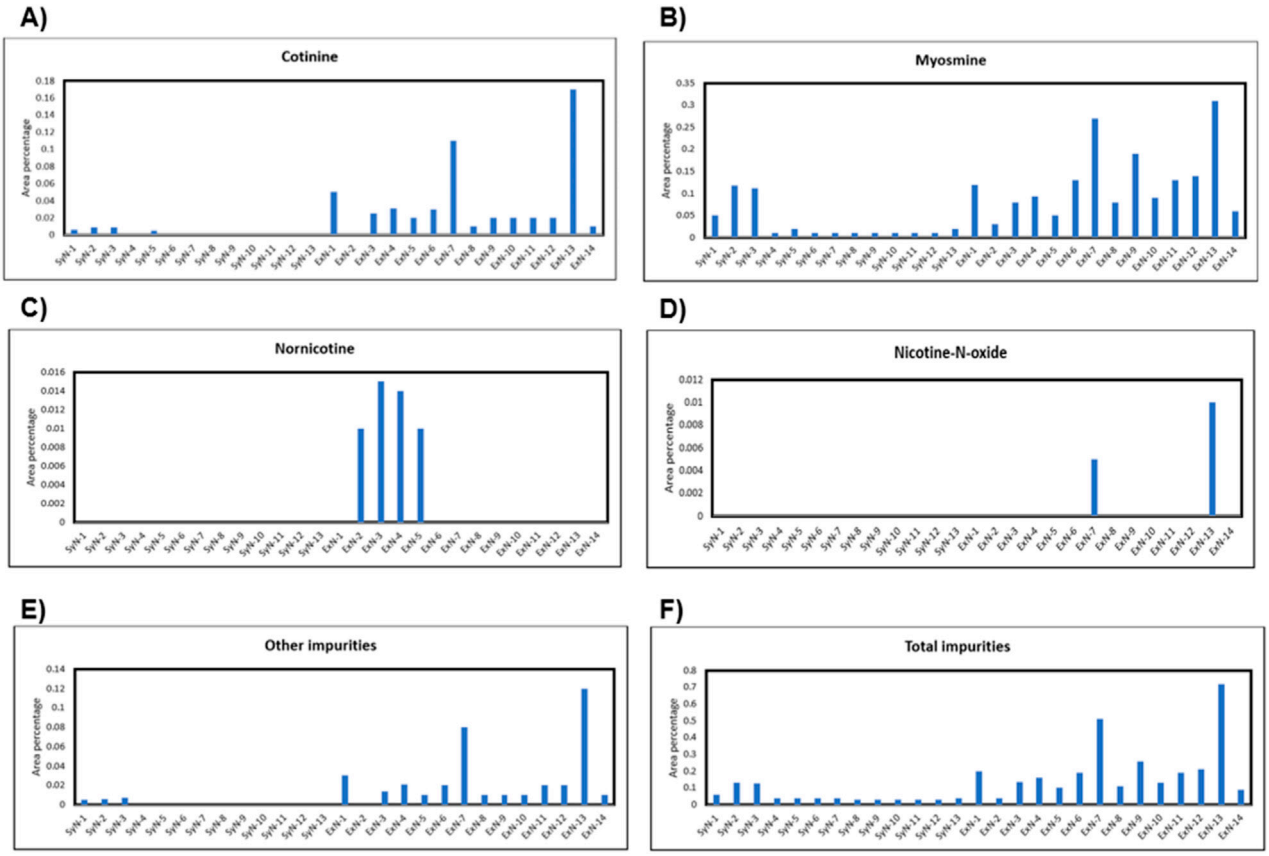

FIGURE 3
Impurity percentage in each nicotine lot vs. synthetic nicotine and extracted nicotine lot number for different impurities; **(A)** cotinine, **(B)** myosmine, **(C)** nornicotine, **(D)** nicotine-N'-oxide, **(E)** other impurities, **(F)** total impurities.

anabasine were not detected in any of the synthetic or extracted nicotine batches. Naturally occurring other alkaloids (cotinine, nornicotine, nicotine-N-oxide) were not found or found less in synthetic Nicotine. However, overall, the reversed-phase HPLC data suggested similar quantities of total impurities in both Synthetic and tobacco extracted Nicotine (0.1%).

Enantiomeric purity

(S)-Nicotine and (R)-Nicotine retention times are 5.562 and 6.219 min respectively (Figure 4A). The resolution between the two isomers was 3.9. Two sample chiral chromatograms for one synthetic nicotine and extracted nicotine are shown in Figures 4B, C, respectively. Synthetic Nicotine lots used in this study have high enantiomeric purity similar to the Tobacco extracted Nicotine (Figure 5).

Nicotine nitrosamines

Nitrosamines were not detected in any synthetic or extracted nicotine lots. See Supplementary Section S1 for details on standard curve preparation, linearity curve, sample chromatograms, and nitrosamine content results for all the samples.

Metal analysis

Lead and arsenic are heavy metals that can pose serious health risks when present in significant amounts. In the context of synthetic and extracted nicotine, it's crucial to monitor and control the levels of these contaminants, as they can have harmful effects on human health. Extracted nicotine most likely accumulates heavy metals through soil/fertilizers and synthetic nicotine via the use of heavy metal catalysts in the synthetic steps (Stephens et al., 2005). Consumption of lead can lead to a range of health issues, especially neurotoxic effects, developmental problems in children, and cardiovascular effects in adults. Even low levels of lead exposure over time can have detrimental health effects. Arsenic is a known carcinogen, and elevated levels of arsenic consumption can lead to skin, lung, bladder, and other cancers. Additionally, it can cause other health issues such as cardiovascular disease and skin lesions which are more dangerous than nicotine itself (Pappas et al., 2014). Monitoring lead and arsenic levels is part of quality control measures to ensure the consistency and safety of nicotine-containing products.

See the Supplementary Section S2 for the calculation process, lead and arsenic linearity curves, and absorbance results for each nicotine sample. The tabulated results for Pb and As in parts per million (ppm) for all the nicotine lots are shown in Figure 6.

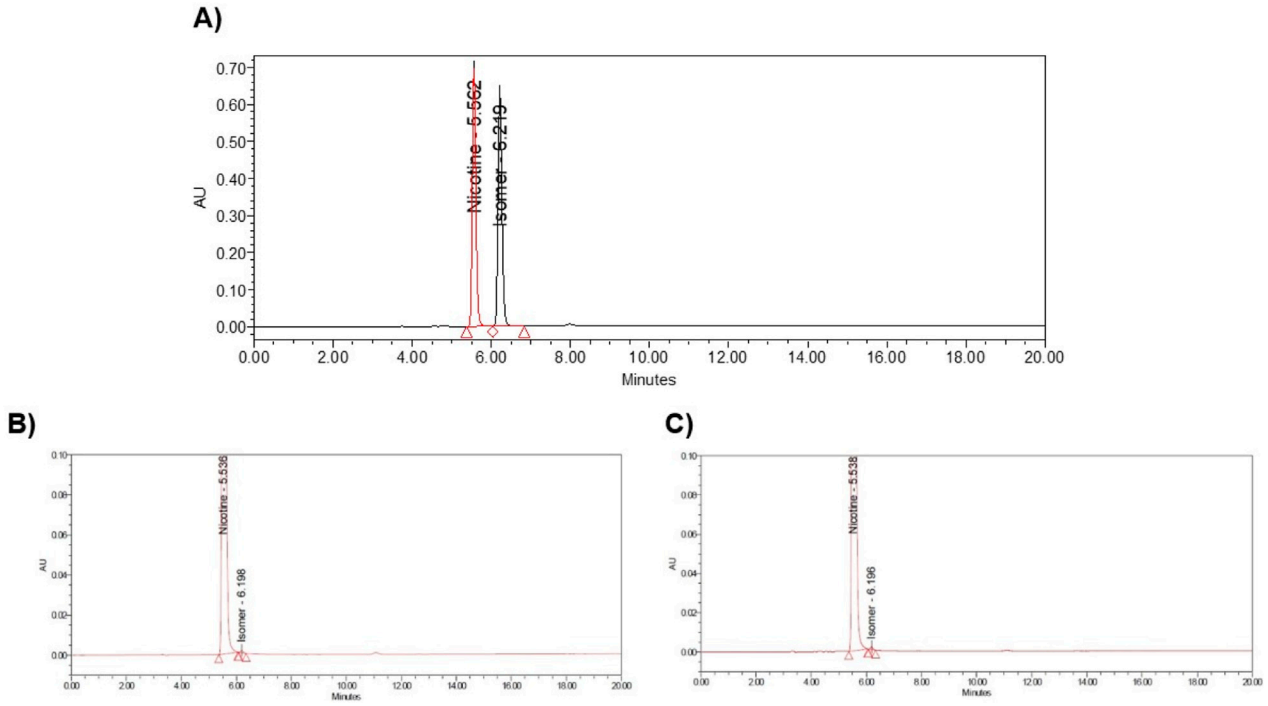

FIGURE 4
Example chromatograms of **(A)** MT117 nicotine (S) and (R) racemic marker solution, **(B)** Syn-1 chiral chromatogram, and **(C)** ExN-1 chiral chromatogram.

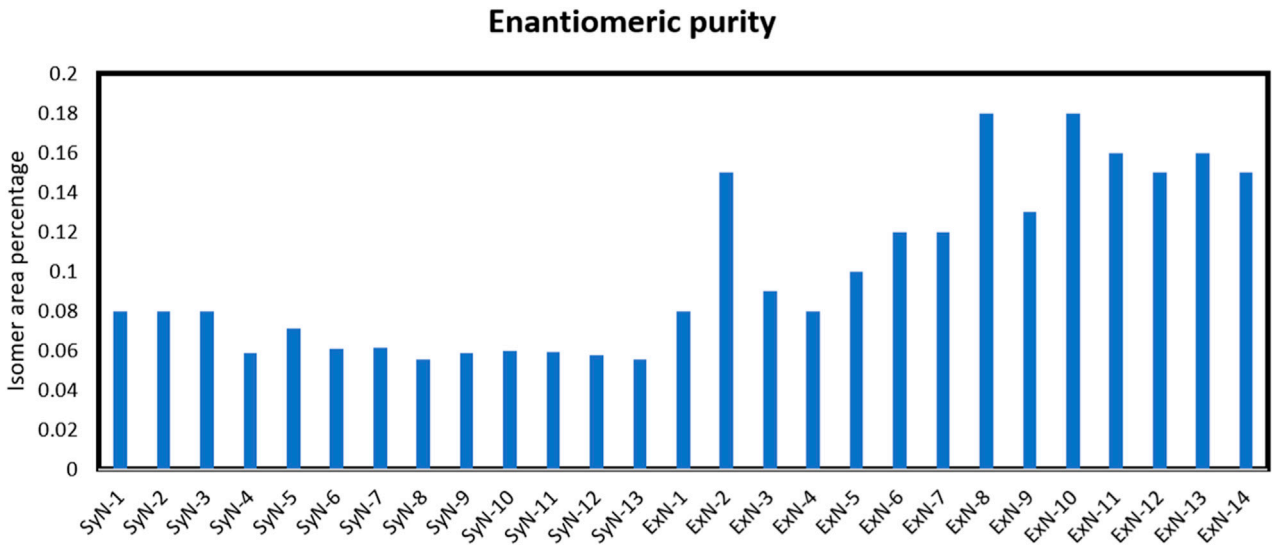

FIGURE 5
(R)-Nicotine enantiomer area percentage in synthetic and extracted nicotine lots.

Discussion and conclusion

Synthetic nicotine (SyN) has gained the interest of related product vendors over the past decade mainly due to a regulatory loophole that came into effect last year, in 2023. It has been claimed by manufacturers and vendors that SyN is purer than tobacco-extracted nicotine (ExN) due to the absence of plant residues and is less harmful. However, none of the smoking product vendors list the purity and related impurities in SyN products. Herein, a thorough evaluation of purity and impurities present in 13 Porton SyN lots in comparison to 14 ExN lots is presented for the awareness of smoking product consumers.

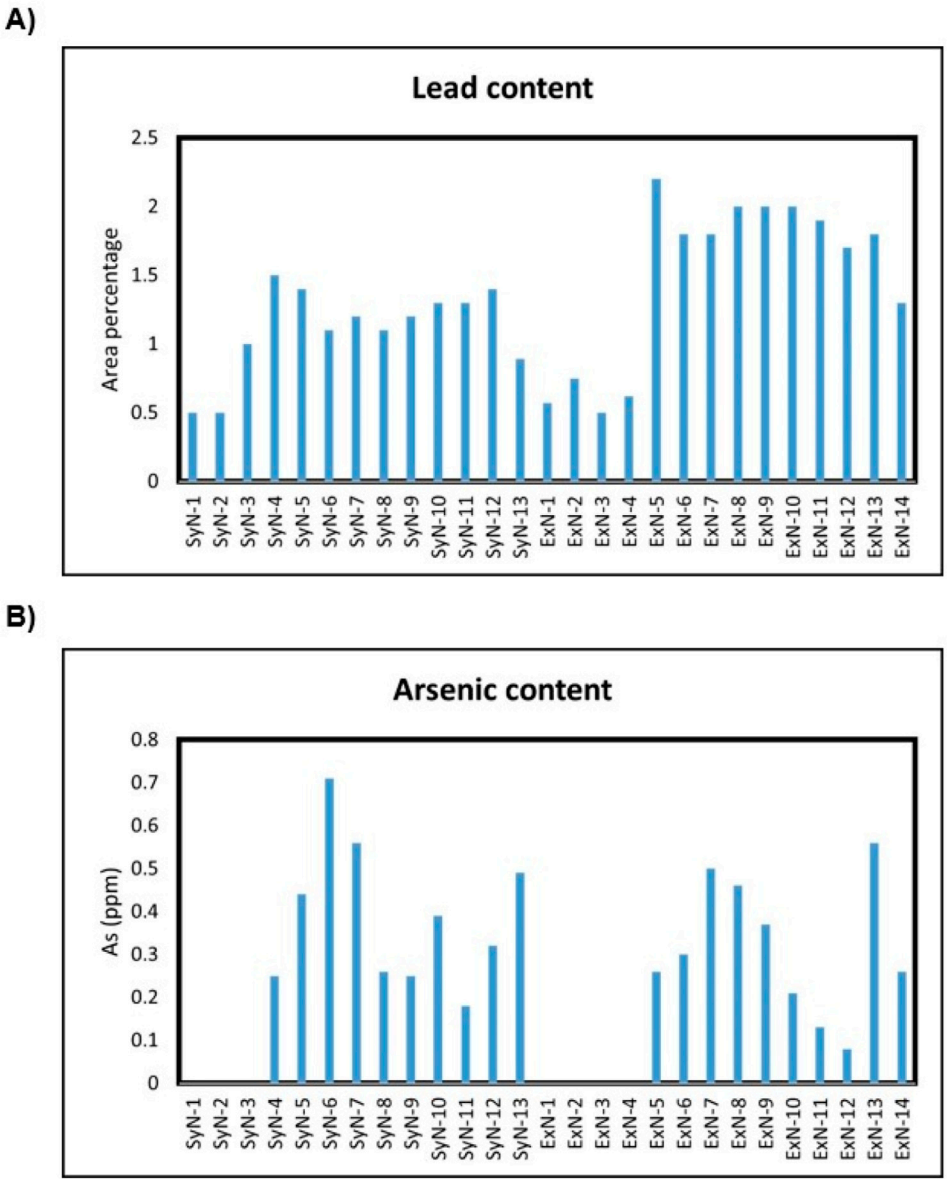

FIGURE 6
(A) Pb and **(B)** As amounts (ppm) in synthetic and extracted nicotine lots.

Both SyN and ExN lots exist in nicotine-free base form, above ~99% assay results. The enantiomeric purity of the SyN was identical to ExN and is above 99.9% of (S)-Nicotine isomer. Cotinine, Myosamine, Nornicotine, and Nicotine N-oxide, were not present or present in low amounts compared to ExN lots making SyN nicotine lots purer. Anatabine, Anabasine, and β-Nicotyrine impurities were absent in both SyN and ExN lots. The metals, lead and arsenic were found to be equal in both SyN and ExN.

Nicotine-related nitrosamine content was also tested for both SyN and ExN lots and was not detected in any lots. It was expected that ExN to contain high percentages of nitrosamine impurities as these are naturally formed in Tobacco plants/leaves during growth. Nitrosamine content in ExN depends on the maturity of Tobacco leaves at the time of harvest where pre-mature leaves do not contain nitrosamine impurities. The formation of TSNAs is influenced by various factors, including the type of tobacco, curing methods, and the conditions under which tobacco is stored. The levels of TSNAs can vary among different tobacco products and brands. Therefore, the possibility of having nitrosamines in ExN cannot be fully eliminated.

In conclusion, the Nicotine from in-house SyN lots is identical to ExN in terms of assay and enantiomeric purity. The overall impurity content in SyN was low compared to ExN with few exceptions. The key advantage of SyN is that the Tobacco leaves harvest does not depend on weather conditions and saves the land for other important vegetation cultivation. Furthermore, extracted nicotine products are often overloaded with flavor to mitigate any smell or rustic flavor incorporated during harvesting (hay-like odor, bitter,

and astringent taste). Synthetic nicotine does not require such flavoring due to the controlled nature of synthesis in a laboratory.

Additionally, it's important to note that the health risks of tobacco use extend beyond the impurities/TSNAs quantified in this work, and tobacco smoke contains numerous other harmful substances that contribute to various diseases, including respiratory and cardiovascular conditions. As a result, the best approach to minimize health risks associated with tobacco is to avoid Tobacco either extraction or synthesis approach.

One of the main limitations of this study is the availability of various SyN and ExN types due to regulatory concerns. A statistical analysis could have been carried out if more lots were available. Future work includes improving the efficiency of the methods such as developing a single High-Resolution-Mass-Spectrometry (HRMS) method to identify and quantify both alkaloid impurities and nicotine nitrosamine rather than using two methods: HPLC and LC-MS.

Data availability statement

The original contributions presented in the study are included in the article/Supplementary Material, further inquiries can be directed to the corresponding authors.

Author contributions

AN: Conceptualization, Data curation, Visualization, Writing–original draft, Writing–review and editing. HC: Conceptualization, Funding acquisition, Project administration, Supervision, Writing–original draft, Writing–review and editing. XL: Formal Analysis, Methodology, Resources, Software, Validation, Writing–original draft. ZZ: Formal Analysis, Methodology, Resources, Software, Validation, Writing–original draft. JC: Supervision, Writing–original draft.

Funding

The author(s) declare that no financial support was received for the research, authorship, and/or publication of this article.

Acknowledgments

The entire physical research work was carried out at the Chongqing, China facility of Porton United States. A part of the research work was presented at the Eastern Analytical Symposium-2023 at the Crown Plaza, Plainsboro, New Jersey.

Conflict of interest

Authors AN, and HC were employed by JSTAR Research Inc. Authors XL, ZZ, and JC were employed by Porton Pharma Solutions.

Publisher's note

Supplementary material

The Supplementary Material for this article can be found online at: https://www.frontiersin.org/articles/10.3389/fchem.2024.1483868/full#supplementary-material

References

Avagyan, R., Spasova, M., and Lindholm, J. (2021). Determination of nicotine-related impurities in nicotine pouches and tobacco-containing products by liquid chromatography–tandem mass spectrometry. *Separations* 8 (6), 77. doi:10.3390/separations8060077

Cheetham, A. G., Plunkett, S., Campbell, P., Hilldrup, J., Coffa, B. G., Gilliland, S., et al. (2022). Analysis and differentiation of tobaccoderived and synthetic nicotine products: addressing an urgent regulatory issue. *PLoS One* 17 (4), e0267049. doi:10.1371/journal.pone.0267049

Duell, A. K., Pankow, J. F., and Peyton, D. H. (2018). Free-base nicotine determination in electronic cigarette liquids by 1H NMR spectroscopy. *Chem. Res. Toxicol.* 31 (6), 431–434. doi:10.1021/acs.chemrestox.8b00097

El-Hellani, A., El-Hage, R., Baalbaki, R., Salman, R., Talih, S., Shihadeh, A., et al. (2015). Free-base and protonated nicotine in electronic cigarette liquids and aerosols. *Chem. Res. Toxicol.* 28 (8), 1532–1537. doi:10.1021/acs.chemrestox.5b00107

Gholap, V. V., Heyder, R. S., Kosmider, L., and Halquist, M. S. (2020). An analytical perspective on determination of free base nicotine in E-liquids. *J. Anal. Methods Chem.* 2020, 1–12. doi:10.1155/2020/6178570

Henningfield, J. E., London, E. D., and Pogun, S. (2009). *Handbook of experimental pharmacology, Nicotine psychopharmacology*. Heidelberg: Springer. Vol. 192.

Jordt, S. E. (2023). Synthetic nicotine has arrived. *Tob. Control. NLM (Medline)* 32, e113–e117. doi:10.1136/tobaccocontrol-2021-056626

Konstantinou, E., Fotopoulou, F., Drosos, A., Dimakopoulou, N., Zagoriti, Z., Niarchos, A., et al. (2018). Tobacco-specific nitrosamines: a literature review. *Food Chem. Toxicol.* 118, 198–203. doi:10.1016/j.fct.2018.05.008

Kowitt, S. D., Seidenberg, A. B., Gottfredson O'Shea, N. C., Ritchie, C., Galper, E. F., Sutfin, E. L., et al. (2023). Synthetic nicotine descriptors: awareness and impact on perceptions of e-cigarettes among US youth. *Tob. Control*. doi:10.1136/tc-2023-057928

Lin, W. (2023). Method for Synthesizing (S)-Nicotine. European Patent: EP 4119671A1. Publication Number: WO 2021/180019, France.

Lisko, J. G., Tran, H., Stanfill, S. B., Blount, B. C., and Watson, C. H. (2015). Chemical composition and evaluation of nicotine, tobacco alkaloids, PH, and selected flavors in E-cigarette cartridges and refill solutions. *Nicotine Tob. Res.* 17 (10), 1270–1278. doi:10.1093/ntr/ntu279

Lisuma, J. B., Mbega, E. R., and Ndakidemi, P. A. (2019). Influence of nicotine released in soils to the growth of subsequent maize crop, soil bacteria and fungi. *Int. J. Agric. Biol.*, 1–12. doi:10.17957/IJAB/15.1026

Ma, S., Qiu, Z., Chen, J., and Shang, C. (2023). Synthetic nicotine E-liquids sold in US online vape shops. *Prev. Med. Rep.* 1, 102222. doi:10.1016/j.pmedr.2023.102222

Pankow, J. F., Barsanti, K. C., and Peyton, D. H. (2003). Fraction of free-base nicotine in fresh smoke particulate matter from the eclipse "cigarette" by 1H NMR spectroscopy. *Chem. Res. Toxicol.* 16 (1), 23–27. doi:10.1021/tx020050c

Pappas, R. S., Fresquez, M. R., Martone, N., and Watson, C. H. (2014). Toxic metal concentrations in mainstream smoke from cigarettes available in the USA. *J. Anal. Toxicol.* 38 (4), 204–211. doi:10.1093/jat/bku013

Robinson, J. H., and Pritchard, W. S. (1992). The role of nicotine in tobacco use. *Psychopharmacology (Berl)* 108, 397, 407. doi:10.1007/bf02247412

Stephens, W. E., Calder, A., and Newton, J. (2005). Source and health implications of high toxic metal concentrations in illicit tobacco products. *Environ. Sci. Technol.* 39 (2), 479–488. doi:10.1021/es049038s

Talhout, R., Schulz, T., Florek, E., van Benthem, J., Wester, P., and Opperhuizen, A. (2011). Hazardous compounds in tobacco smoke. *Int. J. Environ. Res. Public Health* 8 (2), 613–628. doi:10.3390/ijerph8020613

Talih, S., Salman, R., El-Hage, R., Karaoghlanian, N., El-Hellani, A., Saliba, N., et al. (2020). Effect of free-base and protonated nicotine on nicotine yield from electronic cigarettes with varying power and liquid vehicle. *Sci. Rep.* 10 (1), 16263. doi:10.1038/s41598-020-73385-6

Yalcin, E., and de la Monte, S. (2016). Tobacco nitrosamines as culprits in disease: mechanisms reviewed. *J. Physiology Biochem.* 72, 107–120. doi:10.1007/s13105-016-0465-9

Zafeiridou, M., Hopkinson, N. S., and Voulvoulis, N. (2018). Cigarette smoking: an assessment of tobacco's global environmental footprint across its entire supply chain. *Environ. Sci. Technol.* 52 (15), 8087–8094. doi:10.1021/acs.est.8b01533

frontiers | Frontiers in Chemistry

TYPE Original Research
PUBLISHED 12 November 2024
DOI 10.3389/fchem.2024.1487108

OPEN ACCESS

EDITED BY
Roberta Risoluti,
Sapienza University of Rome, Italy

REVIEWED BY
Xueyan Zhan,
Beijing University of Chinese Medicine, China
Svante Vikingsson,
RTI International, United States

*CORRESPONDENCE
Rongrong Huang,
comic_huarong@163.com
Liangliang Cai,
cailiangliang10@163.com

†These authors have contributed equally to this work

RECEIVED 27 August 2024
ACCEPTED 30 October 2024
PUBLISHED 12 November 2024

CITATION
Wang J, Zhu Y, Qin J, Wu W, Huang R and Cai L (2024) Chromatographic analysis of ponatinib and its impurities: method development, validation, and identification of new degradation product.
Front. Chem. 12:1487108.
doi: 10.3389/fchem.2024.1487108

Chromatographic analysis of ponatinib and its impurities: method development, validation, and identification of new degradation product

Jing Wang[1†], Yonghong Zhu[2†], Jisu Qin[3], Wenyi Wu[4], Rongrong Huang[1*] and Liangliang Cai[1*]

[1]Department of Pharmacy, Affiliated Hospital of Nantong University, Nantong, China, [2]Department of Pharmacy, Affiliated Nantong Hospital of Shanghai University (The Sixth People's Hospital of Nantong), Nantong, China, [3]Department of Pharmacy, Nantong University, Nantong, China, [4]Department of quality inspection, Sinopharm holding Nantong Ltd., Nantong, China

Background: Ponatinib, a third-generation tyrosine kinase inhibitor, is employed in the management of adult chronic myeloid leukemia. Nevertheless, the presence of process impurities and degradation impurities linked to ponatinib may potentially influence its effectiveness and safety. Therefore, the objective of this research was to establish a robust liquid chromatography method and systematically validate it for the detection of substances related to ponatinib.

Methods: The separation of ponatinib and its impurities was conducted using an Agilent 5HC-C_{18} chromatographic column (4.6 mm × 250 mm, 5 μm). The mobile phase A comprised a mixture of water and acetonitrile in a 9:1 ratio, with an aqueous solution of pH 2.4 containing 2 mM potassium dihydrogen phosphate and 0.4% triethylamine. Mobile phase B, consisting of acetonitrile, was eluted in a gradient fashion. The flow rate was set at 1.0 mL/min, detection wavelength at 250 nm, column temperature at 40°C, and injection volume at 10 μL.

Results: The method demonstrated high specificity, sensitivity, solution stability, linearity, precision, accuracy, and robustness. Additionally, this research unveiled a novel compound, imp-B, generated via the oxidative degradation of ponatinib. The molecular structure of the newly discovered product was elucidated through the utilization of nuclear magnetic resonance (NMR) and high-resolution mass spectrometry (HRMS).

Conclusion: In conclusion, the chromatographic method developed in this study has the potential to be utilized for the detection of ponatinib and its impurities, thereby offering significant insights for quality assessment in ponatinib research.

KEYWORDS

ponatinib, liquid chromatography, novel compound, method development, method validation, related substances

1 Introduction

Chronic myeloid leukemia (CML) is a hematological malignancy characterized by the presence of a distinct genetic aberration referred to as the Philadelphia (Ph) chromosome (Hochhaus et al., 2020; Spagnuolo et al., 2019). This genetic aberration arises from a reciprocal translocation between chromosome 9 and chromosome 22 (Du et al., 2022; Ma et al., 2022). This genetic aberration gives rise to the formation of a chimeric fusion protein called BCR-ABL1, which exhibits uncontrolled tyrosine kinase activity (Tanaka et al., 2022). The presence of this protein induces dysregulation of signaling pathways that promote cell survival and proliferation in leukemic cells.

Tyrosine kinases are enzymes that use ATP as a phosphate donor to catalyze the phosphorylation of specific tyrosine residues in target proteins (Arshad et al., 2023; Peng and Fu, 2023). These kinases play a pivotal role in regulating a wide range of physiological and biochemical processes, including cellular growth, differentiation, and programmed cell death (apoptosis) (Alanazi et al., 2022; Mondelo-Macía et al., 2020; Richardson et al., 2023). Dysregulated expression of tyrosine kinases often results in the loss of control over cellular proliferation, consequently promoting tumorigenesis (Katayama, 2018). In response, specific tyrosine kinase inhibitors have been developed to selectively inhibit the activity of the BCR-ABL1 tyrosine kinase domain, thereby improving clinical outcomes and prognosis for patients with chronic myeloid leukemia (CML) (Hou et al., 2021; Kantarjian et al., 2021; Lin et al., 2020).

Ponatinib, a third-generation tyrosine kinase inhibitor (TKI), was approved by the Food and Drug Administration (FDA) in 2012 for treating chronic myeloid leukemia (CML) and Philadelphia chromosome-positive acute lymphoblastic leukemia (Ph+ALL) in adults (Cortes et al., 2018; Jain et al., 2019; Massaro, Molica and Breccia, 2018; Pavlovsky, et al., 2019). Previous research on ponatinib primarily focused on the drug's safety and efficacy in clinical treatment, along with its plasma drug concentration and metabolites (Abumiya, Miura and Takahashi, 2018; Cortes et al., 2018; Kidoguchi et al., 2021; Massaro et al., 2018; Yasu et al., 2018). Recent studies have specifically examined the degradation products generated during destructive testing of ponatinib (Golla et al., 2023). These degradation products are significant constituents of ponatinib-related substances. It is widely recognized that monitoring the presence of related substances is crucial in ensuring the safety, effectiveness, and overall quality of drugs (Ni et al., 2022; Pawar et al., 2024). However, to the best of our knowledge, research on the detection of ponatinib-related substances remains limited. Hence, it is necessary to develop a method for detecting ponatinib -related substances.

This research has successfully established and implemented a validated reversed-phase high-performance liquid chromatography (RP-HPLC) technique for the detecting ponatinib -related substances. The method demonstrates simplicity, sensitivity, accuracy, and robustness. In particular, it effectively separates compounds related to ponatinib, such as impurities derived from the production procedure and degradation products (imp-A, -B, -C). Following that, a thorough evaluation was performed to determine specificity, sensitivity, solution stability, linearity, precision, accuracy, and robustness. Parameters such as limits of quantification (LOQ), limits of detection (LOD), linearity, and recovery of the RP-HPLC method were evaluated. Furthermore, in the study, we discovered a novel compound designated imp-B, originating from the oxidative degradation of ponatinib. The structure of this compound was successfully determined using nuclear magnetic resonance (NMR) and high-resolution mass spectrometry (HRMS) techniques. Overall, the established RP-HPLC method represents a novel approach to advancing process development and quality evaluation of ponatinib.

2 Materials and methods

2.1 Chemicals and reagents

The compound ponatinib was obtained from MCE China (Shanghai, China). imp-A, and imp-C were obtained from Shanghai Macklin Biochemical (Shanghai, China), while imp-B was homemade by the laboratory of the authors. Merck (Darmstadt, Germany) provided HPLC-grade ACN and methanol (MeOH). Other analytical grade chemical reagents were purchased from China National Pharmaceutical Group Chemical Reagent Co., Ltd., (Beijing, China).

2.2 Instruments

For this investigation, a RP-HPLC device (Agilent 1200, Agilent, United States) and a UV-visible spectrophotometer (Cary100, Varian, United States) were utilized. Furthermore, a Milli-Q water purification system was employed.

2.3 HPLC conditions

For the separation of ponatinib and its related impurities, a 5HC-C_{18} column from Agilent (4.6 mm × 250 mm, 5 μm) was employed. Mobile phase A consisted of a water and acetonitrile (ACN) blend in a 9:1 v/v ratio. The aqueous solution contained 2 mM potassium dihydrogen phosphate solution (KH_2PO_4) and 0.4% triethylamine. Phosphoric acid adjusted the pH to 2.4. ACN was the only component of mobile phase B. The gradient elution was conducted as follows: mobile phase B maintained a constant concentration of 16% from 0 to 2 min, followed by an increase in concentration from 16% to 30% from 2 to 22 min. Subsequently, the concentration of mobile phase B further increased from 30% to 34% from 22 to 32 min. From 32 to 35 min, the concentration of mobile phase B increased to 55%, remaining constant until 42 min. Between 42 and 42.1 min, the concentration of mobile phase B decreased from 55% to 16%. Finally, from 42.1 to 50 min, mobile phase B maintained a constant concentration of 16%. The wavelength used for UV detection was 250 nm, with a flow rate of 1.0 mL/min and a sample volume of 10 μL.

2.4 Preparation and characterization of imp-B

To prepare imp-B, 200 mg of ponatinib was weighed and transferred into a 100 mL flask. Methanol (20 mL) was added to fully dissolve the powder. Subsequently, 30 mL of a 30% H_2O_2 solution was added, and the mixture underwent oxidative degradation. The reaction mixture was stirred at room temperature for 20 h before terminating the reaction with manganese dioxide. After centrifugation, the supernatant was decanted, and the crude product was obtained by freeze drying.

The imp-B crude product was purified using a preparative column (Agilent Eclipse XDB-C_{18}, 250 mm × 9.4 mm, 5 μm). The mobile phase consisted of a 75% methanol-water solution. The elution time was 6 min, and the flow rate was set at 4 mL/min.

To determine the structure of imp-B, nuclear magnetic resonance (^{1}H NMR, ^{13}C NMR and 2D NMR) and high-resolution mass spectrometry (HRMS) were employed for analysis. The procedure is as follows: dissolve 10 mg of imp-B or 20 mg of imp-B in DMSO-d6 for ^{1}H NMR, ^{13}C NMR and 2D NMR analysis. Prior to mass spectrometry analysis, the imp-B sample was diluted to a concentration of 100 ng/mL with a 50% methanol-water solution before being injected into the mass spectrometer.

2.5 Preparation of stock solution

2.5.1 Preparation of ponatinib stock solution

To prepare a stock solution of ponatinib, approximately 10 mg of ponatinib should be weighed accurately and placed in a 20 mL volumetric flask. Then, 10 mL of 50% methanol solution is added, and the mixture is sonicated to dissolve the ponatinib. The solution is then diluted to the mark with a 50% methanol solution to obtain a stock solution with a concentration of approximately 0.5 mg/mL.

2.5.2 Preparation of ponatinib-related substances stock solution

To prepare standard stock solutions of known impurities (imp-A, -B, -C), 10 mg of each impurity must be accurately weighed and transferred into separate 20 mL volumetric flasks. A mixed solution of methanol and water, with a volume ratio of 50:50 (v/v), is then added to each flask, followed by ultrasonic treatment to ensure complete dissolution of the impurities. The flasks are then filled to the mark with the mixed solution of methanol and water to achieve impurity standard stock solutions with a concentration of approximately 0.5 mg/mL.

2.6 Preparation of mixed solutions and system suitability solutions

To formulate a composite solution of ponatinib bulk drug and its related substances, approximately 10 mg of the ponatinib bulk drug was carefully measured and transferred into a 20 mL volumetric flask. Subsequently, 0.2 mL of reference standard stock solutions containing imp-A, imp-B, and imp -C were introduced. Following this, the solution was further diluted to a final volume of 20 mL by combining equal volumes of methanol and water in a proportion of 50:50 (v/v).

The system suitability solution was prepared by combining equal volumes of acidic and oxidative degradation solutions. The specific steps are as follows: Initially, accurately weigh 10 mg of ponatinib and transfer it into a 20 mL volumetric flask. Subsequently, add 10 mL of methanol to the flask to dissolve the ponatinib. Following this, add 5 mL of 1 M hydrochloric acid solution to the mixture and maintain the reaction at 70°C for 12 h. Upon completion of the reaction, neutralize the solution by adjusting the pH to 7 with 1 M sodium hydroxide. Lastly, dilute the reaction mixture to 20 mL with a 50:50 mixture of methanol (MeOH) and water (H_2O) (v/v).

A 10 mg measurement of ponatinib bulk drug was accurately added to a 20 mL volumetric bottle and dissolved in 10 mL of methanol. It was then combined with a 1 M hydrochloric acid solution and reacted at 70°C for 12 h. Subsequently, it was diluted to a total volume of 20 mL using a mixture of MeOH and H_2O in a 50/50 ratio (v/v). Likewise, an additional 10 mg of ponatinib was weighed and then mixed with 10 mL of methanol. Subsequently, it was introduced into a 10 mL solution of H_2O_2 (3%) and underwent a reaction at ambient temperature for a duration of 20 h. After the reaction was completed, any residual H_2O_2 was decomposed using MnO_2. The MnO_2 was then separated through filtration, and the resulting solution was subjected to freeze-drying. Ultimately, the oxidative degradation product was isolated and dissolved in a 50:50 (v/v) mixture of methanol (MeOH) and water (H_2O).

2.7 Preparation of the sample solution

To prepare the sample solution, accurately weigh approximately 10 mg of ponatinib bulk drug and dissolve it in 20 mL of a 50:50 methanol-water solution (v/v). This procedure results in a sample solution with an estimated concentration of 0.5 mg/mL.

2.8 Method validation

2.8.1 Specificity

To establish RP-HPLC, it is necessary to fully separate ponatinib from its associated compounds. Consequently, the evaluation of the method's specificity was conducted. According to the chromatographic conditions under Section 2.3, solvents, system suitability solutions, and mixed impurity solutions were injected separately.

2.8.2 Forced degradation experiments

For the degradation test, approximately 10 mg of ponatinib was accurately weighed and transferred into a 20 mL volumetric flask. It was then dissolved in methanol and exposed to various degradation conditions: acid and alkali hydrolysis, oxidation, photolysis, and heat degradation.

The acid degradation test includes treating the ponatinib solution with 1 mol/L HCl for 5 days at 60°C, while the alkaline degradation test involves treatment with 1 mol/L NaOH for 7 h at

60°C. The oxidation degradation test involves treating the ponatinib solution with a 3% H_2O_2 solution for 2 h.

The ponatinib sample underwent heat degradation at 150°C for 6 days, and light degradation was induced by exposing it to an LED tube with an intensity of 4,500 lx for 20 days. The volume was adjusted to 20 mL using a MeOH/H_2O (v/v 1:1) mixture, and analysis followed the instructions in Section 2.3.

2.8.3 Sensitivity

The sensitivity of the detection method was assessed by determining the LOD and LOQ. Initially, the ponatinib standard stock solution and stock solutions of related substances were sequentially diluted and injected into the sample as per the procedure outlined in Section 2.3. Subsequently, the signal-to-noise ratio (S/N) was calculated, and the concentrations corresponding to S/N ratios of 3:1 and 10:1 were determined as the LOD and LOQ, respectively.

2.8.4 Stability of the solution

For the stability study, the ponatinib sample solution was analyzed at specific time intervals ranging from 0 to 24 h (0, 1, 2, 4, 6, 8, 12, and 24 h). To assess the sample solution's stability, changes in impurity quantities, maximum concentrations of individual impurities, and overall impurity content were compared.

2.8.5 Linearity and range

The concentration of the provided sample solution of ponatinib (0.5 mg/mL) was defined as 100%. An examination was conducted to determine the linear correlation between ponatinib and its impurities in the concentration range from the quantitative limit to 2.0%. The standard stock solution of ponatinib and its known impurities (imp- A, -B and-C) was diluted using a 50% methanol-water solution to obtain various test solution concentrations, which were then analyzed through injection. A standard curve was generated with concentration on the *X*-axis and peak area on the *Y*-axis to calculate the regression equation.

2.8.6 Precision and repeatability

To assess the accuracy of the instrument, the mixed impurity solution mentioned was injected six times consecutively, employing the high-performance liquid chromatography conditions outlined in Section 2.3. Simultaneous recording of chromatograms was performed, followed by calculation of the RSD values for both the retention time and peak area.

To assess the repeatability of this method, six mixed sample solutions were prepared following the procedure outlined in Section 2.6. Subsequently, injection detection was performed using the chromatographic conditions specified in Section 2.3, and the chromatograms were recorded.

2.8.7 Accuracy

The investigation focused on the recovery rates of ponatinib-associated compounds at three different levels: 50%, 100%, and 150%. The concentration of the related substance at the 100% level was 1 μg/mL. To achieve these concentrations, varying volumes of impurity stock solutions were added to the ponatinib sample solution. Each concentration sample was prepared in triplicate. Subsequently, the samples were injected, and the recovery calculation was conducted.

2.8.8 Robustness

To assess the method's robustness, we identified the suitable solution of the system across different chromatographic conditions. Chromatographic parameters encompassed the initial mobile phase A-B ratio, detection wavelength, column temperature, flow rate, mobile phase pH, and column type. Table 3 outlines the specific robustness criteria.

3 Results

3.1 Method development

The synthesis of ponatinib, a potent TKI inhibitor, follows the pathway of patent W020110539338 as depicted in Supplementary Figure S1. Various starting materials and intermediates are utilized in the synthetic pathway of ponatinib. Forced degradation tests revealed three primary compounds associated with ponatinib: imp-A, imp-B, and imp-C. The chemical structures of ponatinib, imp-A, imp-B, and imp-C are depicted in Figure 1. imp-A is a process-related impurity, whereas imp-C serves not only as a process impurity but also as an alkaline degradation product of ponatinib. Furthermore, imp-B is a novel compound resulting from the oxidative degradation of ponatinib. Its structure was unequivocally established using nuclear magnetic resonance and mass spectrometry. A method employing reversed phase high performance liquid chromatography (RP-HPLC) was developed to determine the concentrations of ponatinib-related substance.

To optimize the method, we systematically investigated the effects of solvent, detection wavelength, mobile phase composition, and elution method on sample separation. To choose an appropriate solvent, ponatinib was dissolved in methanol (MeOH) and acetonitrile (ACN). The findings indicated that ponatinib exhibited low solubility in ACN but was completely soluble in MeOH. Consequently, we conducted additional research on ponatinib in a 1:1 MeOH/H_2O (v/v) solution and observed that it can dissolve at a concentration of 0.5 mg/mL without any evidence of turbidity. Subsequently, we investigated the influence of the MeOH/H_2O (v/v 1:1) solvent on the stability, peak shape, and resolution of ponatinib. The results demonstrated that the use of MeOH/H_2O (v/v 1:1) as the solvent did not result in any significant changes in the impurities of ponatinib over a 72-h period. Additionally, the symmetry factor of the ponatinib peak was 1.12 and the minimum resolution between it and nearby impurity peaks was greater than 1.5. Consequently, MeOH/H_2O (v/v 1:1) was ultimately selected as the solvent for this study.

To determine the optimal absorption wavelength, a solution of ponatinib standard stock and its associated compounds were diluted by a factor of 50 and then analyzed using UV-VIS scanning within the 200–400 nm range. Supplementary Figure S2 displays the acquired ultraviolet spectra, which unveil significant absorption around 250 nm for ponatinib and its associated compounds. Therefore, the wavelength of 250 nm was selected for detection in this research.

10.3389/fchem.2024.1487108

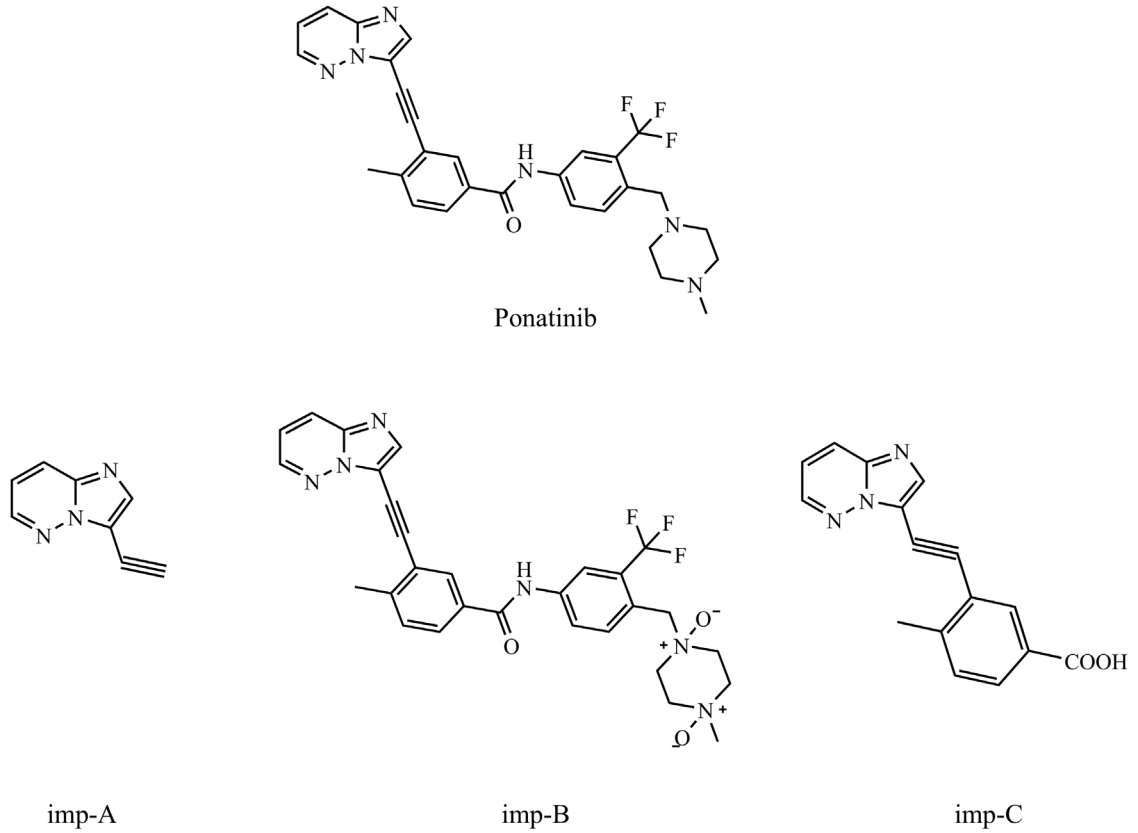

FIGURE 1
Chemical structures of ponatinib, imp-A, imp-B and imp-C.

Due to the significant presence of difficult-to-separate impurities in the system suitability solution, this solution was chosen for method development. Initially, different proportions of mobile phase B to mobile phase A (80:20; 60:40) were employed for isocratic elution. The results indicated that the impurities overlapped on the chromatogram, with a limited number of impurities, and the separation degrees both among impurities and between the impurities and the main peak failed to meet the requirements (Figures 2A, B).

Owing to the number of impurities in the system suitability solution, achieving separation of individual impurities using isocratic elution proves challenging. Consequently, the adoption of a gradient elution method was deemed suitable. Initially, gradient condition 1 (0~2 min, 10%B→10%B; 2~20 min, 10%B→90%B; 20~30 min, 90%B→90%B; 30~30.1 min, 90%B→10%B; 30.1~40 min, 10%B→10%B) was utilized for analysis, as depicted in Figure 2C. The minimum separation degree between impurities was 1.15, and between impurities and the main peak was 1.85, which did not meet the specified requirements. Subsequently, the gradient rate was optimized by decreasing the rate of change. Sample analysis was conducted using gradient conditions 2 (0~2 min, 10%B→10%B; 2~30 min, 10%B→90%B; 30~35 min, 90%B→90%B; 35~35.1 min, 90%B→10%B; 35.1~45 min, 10%B→10%B) and conditions 3 (0~2 min, 20%B→20%B; 2~30 min, 20%B→75%B; 30~35 min, 75%B→75%B; 35~35.1 min, 75%B→20%B; 35.1~45 min, 20% B→20%B), resulting in notable improvement in separation degrees between impurities and between impurities and the main peak on the chromatogram. However, these improvements did not suffice to meet the specified requirements (Figures 2D, E). After several rounds of optimization, the conditions described in Section 2.3 were identified as the definitive chromatographic conditions for the product. These conditions achieved a minimum separation degree of 1.62 among impurities and 1.8 between the impurities and the main peak, thereby meeting the required detection standards.

3.2 Method validation

3.2.1 Specificity

The chromatogram of the system suitability solutions was shown in Figure 2F. Results indicated resolutions of 6.23 and 6.93 between the main peak and adjacent impurity peaks, respectively, exceeding the threshold value of 1.5. Additionally, the minimum separation between impurity peaks was 1.75, exceeding the threshold value of 1.2.

The chromatogram of the mixed impurity solutions was shown in Figure 3. Peaks 1-4 represent imp-A, imp-B, imp-C, and ponatinib in that order. Supplementary Table S1 contains the retention time (RT), relative retention time (RRT), and resolution. The satisfactory separation (>1.5) between these impurities and ponatinib was observed. High-performance liquid

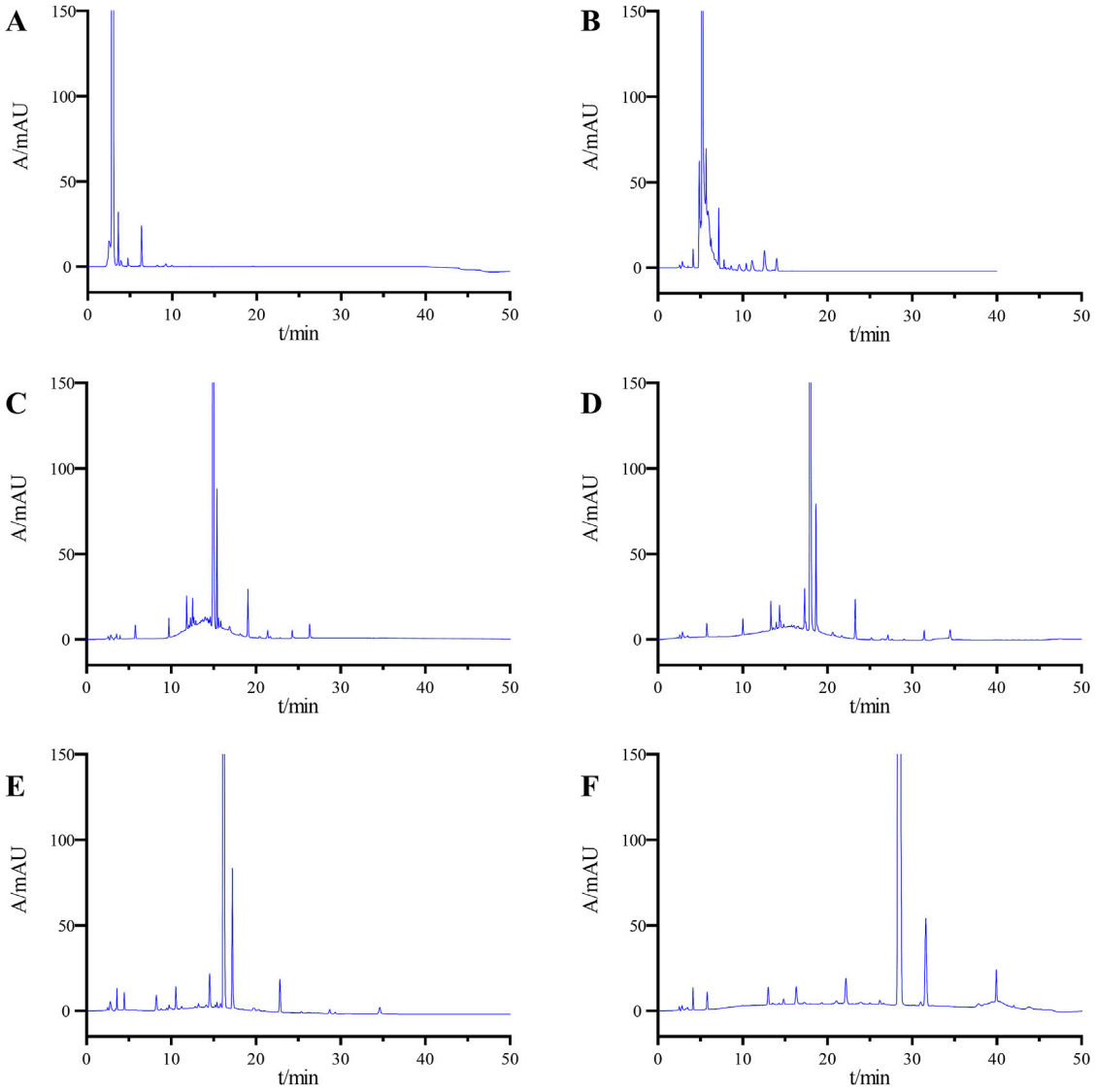

FIGURE 2
Chromatograms obtained during the optimization of the LC conditions: **(A)** ACN-H_2O (80:20), **(B)** ACN-H_2O (60:40), **(C)** gradient elution Condition 1, **(D)** gradient elution Condition 2, **(E)** gradient elution Condition 3, and **(F)** final determined gradient elution condition.

chromatography facilitated comprehensive segregation of the associated compounds.

3.2.2 Forced degradation experiments

Figure 4 presents the chromatographic findings from the forced degradation experiment, and Supplementary Table S2 assesses ponatinib's stability under these conditions, including impurity levels, main peak content, resolution between principal components and impurities, resolution between impurities, and recovery rate. Ponatinib demonstrates relative stability under high temperature and alkaline conditions but readily degrades under acidic, light and oxidative conditions.

Importantly, under varied degradation conditions, the resolution between the main peak and impurities exceeds 1.5, and between impurities, it surpasses 1.2, meeting the specified criteria. Additionally, the mass balance ranges from 96.5% to 102.1%, indicating a satisfactory material balance from 95% to 105%, a fundamental criterion for equilibrium.

3.2.3 Sensitivity evaluation

The detection limit concentrations of ponatinib and its impurities A, B, and C were determined to be 0.003, 0.002, 0.002, and 0.005 μg/mL, respectively, while the quantitation limit concentrations were 0.008, 0.005, 0.004, and 0.016 μg/mL, respectively. These results clearly demonstrate the high quantitative sensitivity of the newly developed HPLC method for related impurities present in ponatinib at concentrations exceeding 0.05%.

3.2.4 Stability of the solution

Supplementary Table S3 contains the findings from these tests. Furthermore, after exposure to ambient temperature for 24 h, the

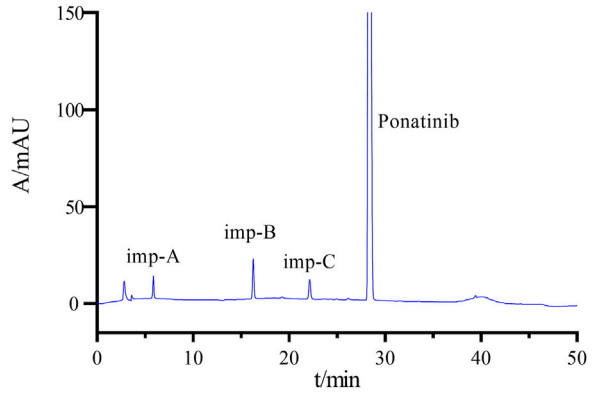

FIGURE 3
Chromatograms of mixed impurity solutions.

three parameters (number of impurities, maximum single impurity content, and total impurities content) exhibited negligible changes, confirming the stability of the sample solution at room temperature. A mixed solution containing impurities A, B, and C was prepared and allowed to equilibrate at room temperature for 24 h. Sample detection was conducted at multiple time points, revealing that the relative standard deviations (RSDs) of peak areas for ponatinib and its impurities A, B, and C were 0.85%, 1.29%, 1.72%, and 1.42%, respectively.

3.2.5 Linearity

The regression curves for ponatinib and its impurities are presented in Supplementary Figure S3. Table 1 presents the calibration curves and correlation coefficients. All correlation coefficients within the concentration range from the quantitative limit to 2.0% exceeded 0.99, meeting the experimental requirements.

3.2.6 Precision

For ponatinib and its related substances (imp-A, imp-B, imp-C), the relative standard deviations (RSDs) were 0.05%, 0.07%, 0.12%, and 0.09%, respectively. Similarly, the RSDs for the peak areas were calculated to be 0.88%, 0.67%, 1.23%, and 0.79%. It is important to mention that the entirety of RSDs were less than 2%, which suggests a significant degree of accuracy in the device.

3.2.7 Repeatability

The results indicate good repeatability of the method, with relative standard deviations (RSD) of imp-A, -B, and -C at 1.65%, 1.47%, and 1.71% respectively, all below 2%.

3.2.8 Accuracy

Table 2 presents the recovery rates of known impurities in ponatinib, which range between 90% and 110%. These findings indicate that the method exhibits a high level of accuracy.

3.2.9 Robustness

Under acceptable but fluctuating conditions, the resolution between ponatinib and its adjacent impurity peaks exceeds 1.5, while the minimum resolution between other impurity peaks also surpasses 1.2. The number and composition of impurities exhibited stability. Moreover, variations in column temperature, wavelength adjustment, and changes in mobile phase pH did not impact the detection of associated compounds. However, alterations in flow rate, chromatographic column type, and initial mobile phase ratio minimally affected retention time and resolution. Fortunately, minor modifications to these variables exerted a negligible influence on detection outcomes, thereby demonstrating the robustness of this analytical approach. Table 3 provides comprehensive information on the specific requirements for robustness performance.

3.3 Characterization of imp-B

Imp-B was prepared following the procedures outlined in Section 2.4 of the study. The resulting chromatogram in Supplementary Figure S3 showed a retention time of 8.2 min with a purity of 97.5%. Figures 5A–C present the high-resolution mass spectrum, 1D proton nuclear magnetic resonance (NMR) spectrum, and 1D carbon NMR spectrum of imp-B, respectively. Additionally, the 2D NMR spectrum is illustrated in Supplementary Figure S4. Using mass spectrometry and NMR spectroscopy techniques, we successfully elucidated the structure of imp-B (Figure 5A), which possesses a molecular weight of 564. This result was in agreement with previously reported in the literature (Golla et al., 2023).

4 Discussion

Ponatinib, a third-generation tyrosine kinase inhibitor (TKI), is utilized in the treatment of chronic myeloid leukemia and acute lymphoblastic leukemia associated with specific gene mutations (Kantarjian et al., 2022). The related substances in ponatinib, including process impurities and degradation impurities, represent critical factors influencing its safety and efficacy. Golla, V. M. et al. investigated the degradation impurities of ponatinib through degradation testing (Golla et al., 2023); however, they did not examine the process impurities generated during its synthesis. Currently, no method exists that can simultaneously detect both process impurities and degradation impurities in ponatinib. Consequently, the objective of this study is to develop a novel method capable of simultaneously detecting both process impurities and degradation impurities in ponatinib.

HPLC technology has emerged as a preferred separation technique for determining active ingredients and related substances in pharmaceutical samples, owing to its convenience, simplicity, stability, and cost-effectiveness (Zhao, et al., 2022). Furthermore, the majority of bulk drugs listed in the United States Pharmacopeia (USP) and the European Pharmacopeia (EP) utilize HPLC to detect related substances. Nevertheless, HPLC technology possesses certain limitations, including challenges in detecting impurities at very low concentrations and in separating specific chiral isomers.

Based on the synthetic process route and degradation experiments of ponatinib, we investigated its related substances. The investigation revealed that imp-A is a process impurity, imp-C

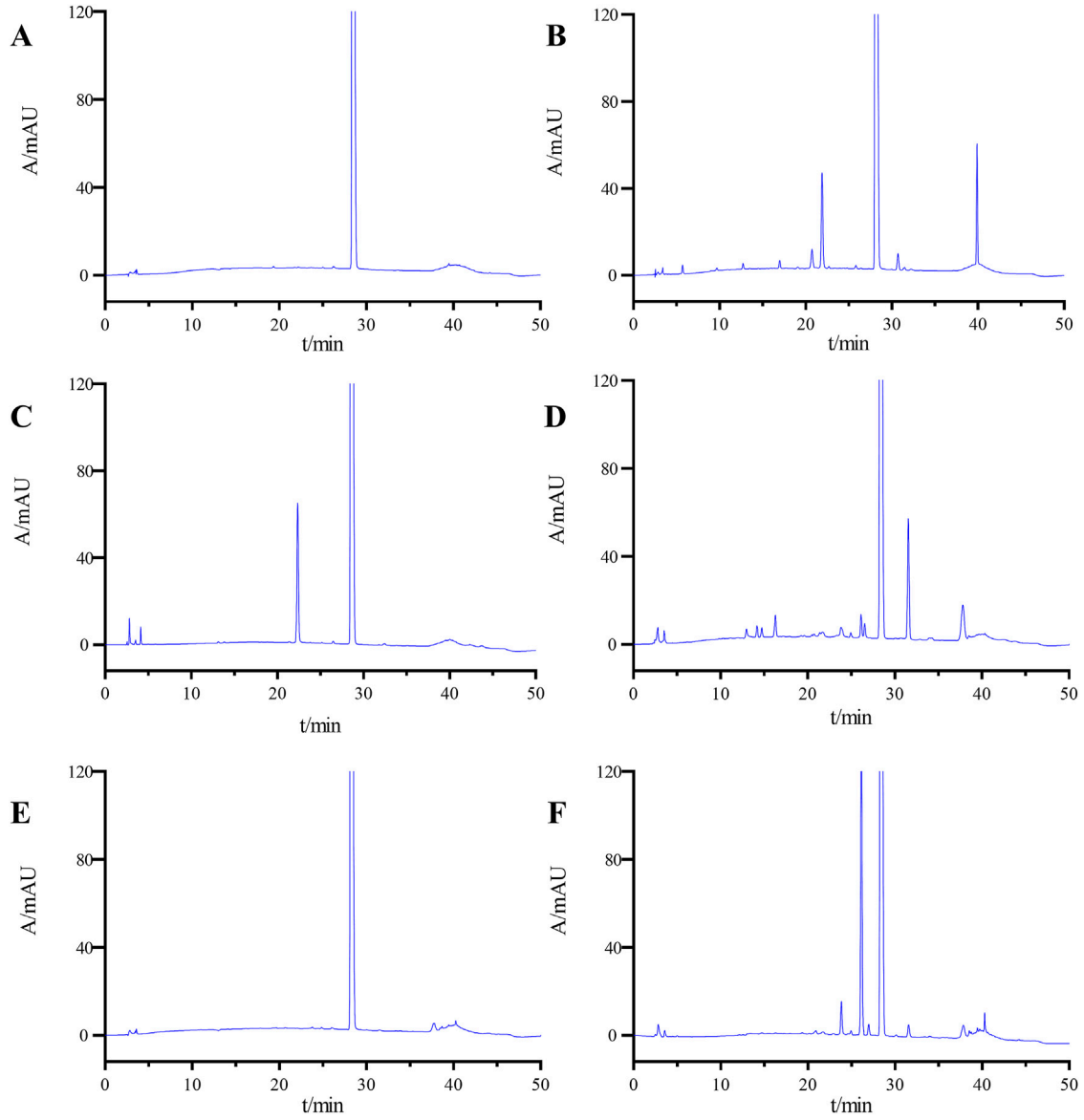

FIGURE 4
HPLC chromatograms of undegradation **(A)**, acid degradation **(B)**, base degradation **(C)**, oxidative degradation **(D)**, heat degradation **(E)**, and photolytic degradation **(F)**.

TABLE 1 Linearity of ponatinib and related substances.

Substance	Standard calibration curves	Correlation coefficient (r)
ponatinib	y = 40.53x+1.585	0.9996
imp-A	y = 16.99x+0.7561	0.9995
imp-B	y = 47.24x+0.9415	0.9996
imp-C	y = 29.63x+1.121	0.9994

serves as both a process impurity and an alkaline degradation impurity, and imp-B is formed through oxidative degradation. Structural analysis using NMR and HRMS revealed that imp-B is a previously unreported compound. While various degradation products were observed in rigorous degradation experiments, effective isolation was challenging due to either their low concentrations or their close association with adjacent components. Therefore, this study did not extensively investigate these additional degradation products, indicating the need for further exploration in future studies.

10.3389/fchem.2024.1487108

TABLE 2 Recovery of ponatinib-related substances.

Substance	Target level	Spiked conc. (μg/mL)	Determined conc. (μg/mL)	Recovery (%)	Average recovery rate (%)	RSD (%)
imp-A	50%	0.516	0.521	100.97	104.29	1.66
		0.516	0.551	106.78		
		0.516	0.541	104.84		
	100%	1.032	1.081	104.75		
		1.032	1.064	103.10		
		1.032	1.073	103.97		
	150%	1.548	1.596	103.10		
		1.548	1.637	105.75		
		1.548	1.631	105.36		
imp-B	50%	0.523	0.518	99.04	103.71	3.17
		0.523	0.545	104.21		
		0.523	0.512	97.90		
	100%	1.045	1.117	106.89		
		1.045	1.094	104.69		
		1.045	1.083	103.64		
	150%	1.568	1.677	106.95		
		1.568	1.621	103.38		
		1.568	1.673	106.70		
imp-C	50%	0.524	0.533	101.72	102.48	2.98
		0.524	0.558	106.49		
		0.524	0.511	97.52		
	100%	1.049	1.095	104.39		
		1.049	1.113	106.10		
		1.049	1.096	104.48		
	150%	1.574	1.582	100.51		
		1.574	1.594	101.27		
		1.574	1.571	99.81		

The test conditions have no change compared with that in Table 1.

TABLE 3 Test conditions of robustness.

Chromatogram conditions	The variation range of parameters
The initial proportion of mobile phases A-B (%)	86:14; 84:16; 82:18
Wavelength (nm)	245, 250, 255
Column temperature (°C)	35, 40, 45
Flow rate (mL/min)	0.9, 1.0, 1.1
Mobile phase pH	2.2, 2.4, 2.6
Chromatographic column	Waters-C_{18}, Agilent-5HC-C_{18}, Gemini-C_{18}

To establish a methodology for identifying related substances in Ponatinib, this study initially prepared a system suitability solution encompassing a wide array of process impurities and degradation products. The detection method was subsequently refined by investigating the effects of solvent selection, detection wavelength, mobile phase composition, and elution technique on the separation of related substances.

The developed method underwent validation following the guidelines of the International Council for Harmonisation of Technical Requirements for Registration of Pharmaceuticals for Human Use (ICH) Guideline Q2 (R1) (Group, 2005). The results demonstrated satisfactory performance in terms of specificity, sensitivity, solution stability, linearity, precision, accuracy, and robustness.

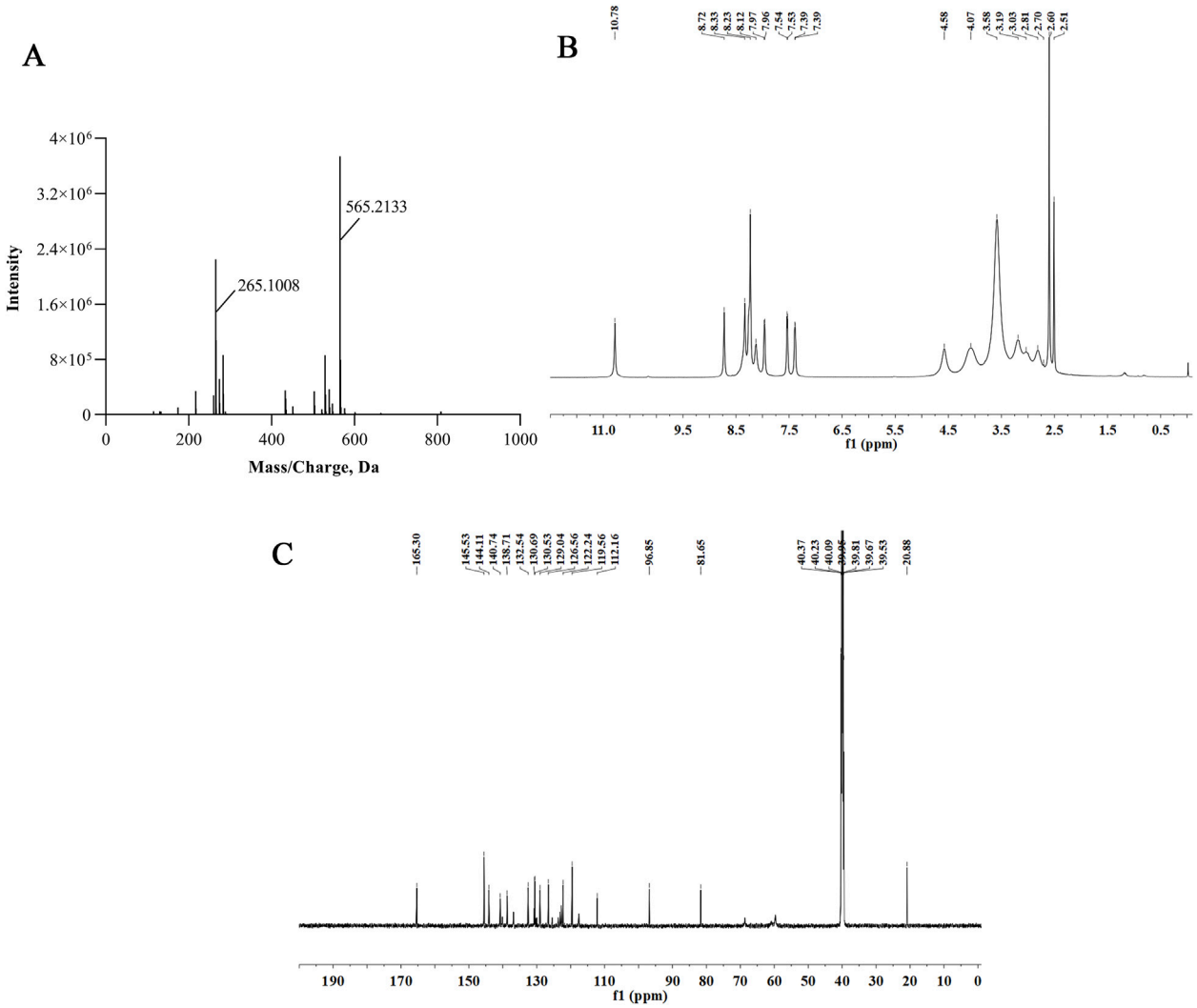

FIGURE 5
The HRMS **(A)**, ^{1}H NMR **(B)** and ^{13}C NMR **(C)** spectra of imp-B.

5 Conclusion

In this study, we developed a productive HPLC approach to detect compounds associated with ponatinib used in the treatment of CML. Furthermore, we successfully validated this detection methodology. The results demonstrate remarkable specificity, enhanced sensitivity, and satisfactory linearity, precision, repeatability, and robustness. In this study, we developed a robust HPLC method to detect compounds associated with ponatinib used in the treatment of chronic myeloid leukemia (CML). Furthermore, we successfully validated this detection methodology. The results demonstrate exceptional specificity, increased sensitivity, and satisfactory linearity, precision, repeatability, and robustness. Therefore, this study will serve as a valuable reference for the treatment of CML with ponatinib.

Data availability statement

The original contributions presented in the study are included in the article/Supplementary Material, further inquiries can be directed to the corresponding authors.

Author contributions

JW: Conceptualization, Validation, Writing–original draft. YZ: Validation, Formal Analysis, Methodology, Writing–review and editing. JQ: Validation, Investigation, Resources, Writing–original draft. WW: Investigation, Resources, Visualization, Writing–original draft. RH: Methodology, Project administration, Writing–review and editing. LC: Project administration, Writing–review and editing, Funding acquisition.

Funding

The author(s) declare that financial support was received for the research, authorship, and/or publication of this article. This work was financially supported by Nantong Social Livelihood Science and Technology Project (no.MS2023029), and Science and Technology Program of Nantong Municipal Health Commission (no. MS2022086).

Conflict of interest

Author WW was employed by Sinopharm holding Nantong Ltd.

The remaining authors declare that the research was conducted in the absence of any commercial or financial relationships that could be construed as a potential conflict of interest.

Publisher's note

Supplementary material

The Supplementary Material for this article can be found online at: https://www.frontiersin.org/articles/10.3389/fchem.2024.1487108/full#supplementary-material

References

Abumiya, M., Miura, M., and Takahashi, N. (2018). Therapeutic drug monitoring of ponatinib using a simple high-performance liquid chromatography method in Japanese patients. *Leuk. Res.* 64, 42–45. doi:10.1016/j.leukres.2017.11.012

Alanazi, W. A., Alhamami, H. N., Alharbi, M., Alhazzani, K., Alanazi, A. S., Alsanea, S., et al. (2022). Angiotensin II type 1 receptor blockade attenuates gefitinib-induced cardiac hypertrophy via adjusting angiotensin II-mediated oxidative stress and JNK/P38 MAPK pathway in a rat model. *Saudi Pharm. J.* 30 (8), 1159–1169. doi:10.1016/j.jsps.2022.06.020

Arshad, F., Ali, A., Rehman, G., Halim, S. A., Waqas, M., Khalid, A., et al. (2023). Comparative expression analysis of breakpoint cluster region-abelson oncogene in leukemia patients. *ACS Omega* 8 (6), 5975–5982. doi:10.1021/acsomega.2c07885

Cortes, J. E., Kim, D. W., Pinilla-Ibarz, J., le Coutre, P. D., Paquette, R., Chuah, C., et al. (2018). Ponatinib efficacy and safety in Philadelphia chromosome-positive leukemia: final 5-year results of the phase 2 PACE trial. *Blood* 132 (4), 393–404. doi:10.1182/blood-2016-09-739086

Du, Z., Huang, Z., Chen, X., Jiang, G., Peng, Y., Feng, W., et al. (2022). Modified dendritic cell-derived exosomes activate both NK cells and T cells through the NKG2D/NKG2D-L pathway to kill CML cells with or without T315I mutation. *Exp. Hematol. Oncol.* 11 (1), 36. doi:10.1186/s40164-022-00289-8

Golla, V. M., Kushwah, B. S., Dhiman, V., Velip, L., and Samanthula, G. (2023). LC-HRMS and NMR studies for characterization of forced degradation impurities of ponatinib, a tyrosine kinase inhibitor, insights into in-silico degradation and toxicity profiles. *J. Pharm. Biomed. Anal.* 227, 115280. doi:10.1016/j.jpba.2023.115280

Group, I. E. W. (2005). International Conference on Harmonisation of technical requirements for registration of pharmaceuticals for human use. *Validation Anal. Proced. text Methodol. Q2R1*.

Hochhaus, A., Gambacorti-Passerini, C., Abboud, C., Gjertsen, B. T., Brümmendorf, T. H., Smith, B. D., et al. (2020). Bosutinib for pretreated patients with chronic phase chronic myeloid leukemia: primary results of the phase 4 BYOND study. *Leukemia* 34 (8), 2125–2137. doi:10.1038/s41375-020-0915-9

Hou, J. Z., Ye, J. C., Pu, J. J., Liu, H., Ding, W., Zheng, H., et al. (2021). Novel agents and regimens for hematological malignancies: recent updates from 2020 ASH annual meeting. *J. Hematol. Oncol.* 14 (1), 66. doi:10.1186/s13045-021-01077-3

Jain, H., Thorat, J., Sengar, M., and Dubey, A. (2019). Ponatinib: a drug review. *Cancer Res. Stat. Treat.* 2 (2), 190–196. doi:10.4103/CRST.CRST_98_19

Kantarjian, H. M., Hughes, T. P., Larson, R. A., Kim, D. W., Issaragrisil, S., le Coutre, P., et al. (2021). Long-term outcomes with frontline nilotinib versus imatinib in newly diagnosed chronic myeloid leukemia in chronic phase: ENESTnd 10-year analysis. *Leukemia* 35 (2), 440–453. doi:10.1038/s41375-020-01111-2

Kantarjian, H. M., Jabbour, E., Deininger, M., Abruzzese, E., Apperley, J., Cortes, J., et al. (2022). Ponatinib after failure of second-generation tyrosine kinase inhibitor in resistant chronic-phase chronic myeloid leukemia. *Am. J. Hematol.* 97 (11), 1419–1426. doi:10.1002/ajh.26686

Katayama, R. (2018). Drug resistance in anaplastic lymphoma kinase-rearranged lung cancer. *Cancer Sci.* 109 (3), 572–580. doi:10.1111/cas.13504

Kidoguchi, K., Ureshino, H., Kizuka-Sano, H., Yamaguchi, K., Katsuya, H., Kubota, Y., et al. (2021). Efficacy and safety of ponatinib for patients with Philadelphia chromosome-positive acute lymphoblastic leukemia: a case series from a single institute. *Int. J. Hematol.* 114 (2), 199–204. doi:10.1007/s12185-021-03156-0

Lin, H., Rothe, K., Chen, M., Wu, A., Babaian, A., Yen, R., et al. (2020). The miR-185/PAK6 axis predicts therapy response and regulates survival of drug-resistant leukemic stem cells in CML. *Blood* 136 (5), 596–609. doi:10.1182/blood.2019003636

Ma, Y., Guo, G., Li, T., Wen, F., Yang, J., Chen, B., et al. (2022). A novel imatinib-upregulated long noncoding RNA plays a critical role in inhibition of tumor growth induced by Abl oncogenes. *Mol. Cancer* 21 (1), 5. doi:10.1186/s12943-021-01478-5

Massaro, F., Molica, M., and Breccia, M. (2018). Ponatinib: a review of efficacy and safety. *Curr. Cancer Drug Targets* 18 (9), 847–856. doi:10.2174/1568009617666171002142659

Mondelo-Macía, P., Rodríguez-López, C., Valiña, L., Aguín, S., León-Mateos, L., García-González, J., et al. (2020). Detection of MET alterations using cell free DNA and circulating tumor cells from cancer patients. *Cells* 9 (2), 522. doi:10.3390/cells9020522

Ni, R., Du, X., Huang, R., Wu, W., Xu, J., Ma, X., et al. (2022). Development and validation of a reversed-phase high-performance liquid chromatography-ultraviolet method for abemaciclib-related substance detection in bulk drugs. *J. Sep. Sci.* 45 (22), 4070–4078. doi:10.1002/jssc.202200551

Pavlovsky, C., Chan, O., Talati, C., and Pinilla-Ibarz, J. (2019). Ponatinib in the treatment of chronic myeloid leukemia and philadelphia chromosome positive acute lymphoblastic leukemia. *Future Oncol.* 15 (3), 257–269. doi:10.2217/fon-2018-0371

Pawar, R., Tivari, S., Panchani, D., and Makasana, J. A. (2024). A stability-indicating method development and validation for the determination of related substances in novel synthetic decapeptide by HPLC. *J. Pept. Sci.* 30, e3610. doi:10.1002/psc.3610

Peng, S., and Fu, Y. (2023). FYN: emerging biological roles and potential therapeutic targets in cancer. *J. Transl. Med.* 21 (1), 84. doi:10.1186/s12967-023-03930-0

Richardson, G. E., Al-Rajabi, R., Uprety, D., Hamid, A., Williamson, S. K., Baranda, J., et al. (2023). A multicenter, open-label, phase I/II study of FN-1501 in patients with advanced solid tumors. *Cancers (Basel)* 15 (9), 2553. doi:10.3390/cancers15092553

Spagnuolo, M., Regazzo, G., De Dominici, M., Sacconi, A., Pelosi, A., Korita, E., et al. (2019). Transcriptional activation of the miR-17-92 cluster is involved in the growth-promoting effects of MYB in human Ph-positive leukemia cells. *Haematologica* 104 (1), 82–92. doi:10.3324/haematol.2018.191213

Tanaka, Y., Takeda, R., Fukushima, T., Mikami, K., Tsuchiya, S., Tamura, M., et al. (2022). Eliminating chronic myeloid leukemia stem cells by IRAK1/4 inhibitors. *Nat. Commun.* 13 (1), 271. doi:10.1038/s41467-021-27928-8

Yasu, T., Momo, K., Kobayashi, S., Kuroda, S., and Tojo, A. (2018). Simple determination of plasma ponatinib concentration using HPLC. *Biol. Pharm. Bull.* 41 (2), 254–258. doi:10.1248/bpb.b17-00806

Zhao, D., Wimalasinghe, R. M., Wang, L., and Rustum, A. (2022). Development and validation of a reversed-phase high-performance liquid chromatography (RP-HPLC) method for identification, assay and estimation of related substances of ivermectin in bulk drug batches of ivermectin drug substance. *J. Chromatogr. Sci.* 60 (7), 620–632. doi:10.1093/chromsci/bmab112

frontiers | Frontiers in Chemistry

TYPE Original Research
PUBLISHED 13 November 2024
DOI 10.3389/fchem.2024.1437221

OPEN ACCESS

EDITED BY
Bikash Koli Dey,
SRM Institute of Science and Technology, India

REVIEWED BY
Md Ariful Haque,
City University of Hong Kong, Hong Kong SAR, China
Bablu Mridha,
Saveetha Medical College and Hospital, India

*CORRESPONDENCE
Paolo Grieco,
paolo.grieco@unina.it

†Deceased

RECEIVED 23 May 2024
ACCEPTED 28 October 2024
PUBLISHED 13 November 2024

CITATION
Ciriaco L, Izzo L, Graziani G, Ferraro MG, Piccolo M, Ciampaglia R, Maglione B, Palladino R, Albarella S, Romano E, Ritieni A, Irace C and Grieco P (2024) Chemical characterization of wheat-based waste derived from a pharmaceutical process for its potential valorization.
Front. Chem. 12:1437221.
doi: 10.3389/fchem.2024.1437221

Chemical characterization of wheat-based waste derived from a pharmaceutical process for its potential valorization

Lidia Ciriaco[1], Luana Izzo[1], Giulia Graziani[1], Maria Grazia Ferraro[2], Marialuisa Piccolo[3], Roberto Ciampaglia[1], Barbara Maglione[4], Roberta Palladino[4], Simone Albarella[4], Eugenia Romano[4], Alberto Ritieni[5†], Carlo Irace[3] and Paolo Grieco[1*]

[1]Department of Pharmacy, School of Medicine and Surgery, University of Naples Federico II, Naples, Italy, [2]Department of Molecular Medicine and Medical Biotechnology, University of Naples Federico II, Naples, Italy, [3]BioChem Lab, Department of Pharmacy, School of Medicine and Surgery, University of Naples Federico II, Naples, Italy, [4]Farmaceutici Damor, Naples, Italy, [5]Department of Pharmacy, University of Naples Federico II, Naples, Italy

Introduction: We report the analysis and characterization and the preliminary biological evaluation, of both liquid and solid wastes obtained from the processing of wheat (*Triticum vulgare*) to produce the most iconic phytostimulin-based pharmaceutical products. The study aims to verify whether the waste can be reused in another process and not destined to its simple destructive disposal.

Methods: In this perspective, we first carried out an in-depth chemical-physical analysis of the waste together with a biocompatibility evaluation to plan the feasible final choice of waste destination. The liquid and solid waste derived from the processing of wheat extract were analyzed and characterized through ultra-high-performance liquid chromatography coupled with high-resolution Orbitrap mass spectrometry (UHPLC-Q-Orbitrap HRMS).

Results: Results highlight that ferulic acid represent the most abundant phenolic compound for solid waste with a content of 89.782 mg/kg and dihydroferulic acid is the predominant for liquid waste (6.24 mg/L). These concentrations represent 55.87% and 84.39% of the total concentration of bioactive compounds for liquid and solid waste, respectively. The antioxidant activity registered for the solid extract was 8.598 and 7.262 mmol trolox/kg, respectively for ABTS and FRAP assays. The total phenolic content (TPC) in the liquid extract undergoes a significant percentage reduction compared to the solid waste. As regards toxicity, both liquid and solid wastes were investigated *in vitro* preclinical models of human skin (HaCaT cells and HDFa) after 24, 48, and 72 h of exposure. No cytotoxic effect was noted even at the highest tested concentration (100 µg/mL) at 72 h.

Discussion: Overall, considering its chemo-physical features and active ingredients, we believe that this waste is highly reusable as a starting material for the development of cosmeceutical products. Thus, this study allows us to

motivate the destination of the waste of the production in a recyclable raw material for additional industrial processes, thereby promoting an eco-friendly circular economy operation.

KEYWORDS

Triticum vulgare, pharmaceutical waste, biocompatibility, bioactive compounds, upcycling, UHPLC Q-orbitrap HRMS

1 Introduction

Waste derived from pharmaceutical processes is a significant problem worldwide, due to the negative effects it has on the environment, the economy, and society. In the literature, there are several scientific studies whose aim is to analyze and evaluate waste management (Sapkota and Pariatamby, 2023). Pharmaceutical waste is generated and accumulated along the various stages and practices of the production chain. The accumulation of enormous quantities of waste and by-products, not only from food and agriculture but also pharmaceuticals, often containing precious bioactive compounds, constitutes a problem of considerable interest due to its environmental impact (Vilas-Boas et al., 2021). Reducing the formation of by-products in work processes or valorizing them for the purposes of other production processes, represents today the main option to avoid environmental problems and help the economy and society. Today, various biotechnological and nanotechnological approaches are available that can be used for the valorization of by-products of natural origin with the aim of improving their potential applications (Freitas et al., 2021). Biologically active natural molecules and phytochemical compounds can be obtained directly through an extraction process rather than using a synthetic process starting from chemicals (Lemes et al., 2022). Although the extraction process allows to obtain the precious biocomponents used for therapeutic and cosmetic purposes, the destination of the wastes generated has to be considered. Wastes indeed consist of both the residues of the natural raw material and the solvents used in the extraction process.

In this context, the standard practice of "reduce, reuse and recycle" is a good strategy aiming to reduce waste in landfills, preserving natural resources and thus reducing environmental pollution (Madaan et al., 2024). Although the practice "reduce, reuse, and recycle" is useful for reducing general waste and each method has its advantages, the reuse should be the first imperative when waste comes from industrial processes. Upcycling is an innovative and creative way to give new life to old or unwanted products and materials by adding value to the product, with important benefits for the environment, society, and the economy (Sneh et al., 2024).

Upcycling helps create a circular economy, where materials can constantly be reused instead of turning into waste. This is important because it allows single-use items to be in use indefinitely. For a circular economy to be effective, manufacturers need to consider this feedback loop in the design and production of products to ensure they can be upcycled in the future.

In this scenario, the goal of our work is to valorize the use of the waste generated from the aqueous extract of the Triticum Vulgare (TVE). TVE has been proven to have biological regenerative properties useful in the wound healing. Furthermore, its processing is a simple water-based extraction procedure with not potentially toxic or harmful solvents. Thus, it can be easily ascribed to a green approach for the recovery of bioactive compounds with a reduced environmental impact (Sanguigno et al., 2018; Tito et al., 2020; Romano et al., 2023). The production of the phytostimulin-based product (Fitostimoline®, Farmaceutici Damor S.p.A., Naples, Italy) starting from wheat follows a management philosophy based on the responsible concept of reduction-reuse-recycling, aimed primarily at the sustainable management of all active processes. Although the production is not particularly excessive to create disposal problems, we were interested in analyzing this waste to verify whether it could find a more noble alternative use given that the process that leads to its production is green. Valorization and recycle of waste require an in-depth analysis in physical and chemical terms, together with the subsequent evaluation of its potential usefulness as raw material for other processes, economic feasibility, and adherence to environmental and legislative sustainability. Moving in this direction, the evaluation of biocompatibility and safety profile in human cellular models adds further value to the possibility of waste reuse. The ever-growing amount of waste from pharmaceutical activities is leading to the necessity of identifying through physicochemical analysis and biological evaluations new ways to recycle waste as raw materials in further applications. Nowadays, waste products from industrial processes have a significant economic impact due to their high presence within the European Union (Idiano et al., 2024). The aim of this work is to (i) perform a chemical characterization of bioactive compounds in both liquid and solid wastes obtained from the processing of wheat (*Triticum vulgare*) and (ii) evaluate the safety profile in human cellular models to propose this resource as a source of active components.

2 Materials and methods

2.1 Chemicals and reagents

Methanol (MeOH), ethanol (EtOH), water (UHPLC-MS grade), acetonitrile (UHPLC-MS grade), chloroform, hydrochloric acid, glacial acetic acid, formic acid (FA were purchased from Merk (Milan, Italy), whereas deionized water (<18 MX cm resistivity) was provided from a Milli-Q water purification system (Millipore, Bedford, MA, United States). The standards of polyphenols (purity >98%) were acquired from Merck group (Milan, Italy). The compound of 2,2-azinobis (3-ethylbenzothiazoline-6-sulphonic acid) diammonium salt (ABTS), ferrous chloride ($FeCl_2$), 1,1-Diphenyl-2-picrylhydrazyl (DPPH), Folin–Ciocalteu reagent, Sodium carbonate anhydrous, potassium persulfate, 2,4,6-Tris (2-pyridyl)-*s*-triazine (TPTZ), (±)-6-Hydroxy-2,5,7,8-

tetramethylchromane-2-carboxylic acid commonly called Trolox, gallic acid were acquired from Sigma Aldrich (Milan, Italy).

2.2 Sampling

Triticum vulgare was obtained through a standard manufacturing protocol of germination, under restricted conditions of temperature, light and humidity. The aqueous extract of Triticum vulgare (TVE) is produced using a newly developed extraction method patented by Farmaceutici Damor (Riccio, 2018), using a simple water-based extraction procedure with not potentially toxic or harmful solvents. Thus, it can be easily ascribed as a green approach for the recovery of bioactive compounds with a reduced environmental impact. In more detail, liquid extraction was performed from the germ wheat macerated and forced under 300 atm of pressure. The liquid sample was recovered through an ultrafiltration membrane filter with a cut-off below 30 kDa.

Wastes derived from the production process were then collected appropriately. Solid waste (SW) was generated from the exhausted solid-phase pressed while liquid waste (LW) was recovered after the ultrafiltration process. These wastes were provided by the company Farmaceutici Damor. SW was dried (to allow homogenization), ground, and subjected to analysis to investigate the profile of the polyphenolic component. Both solid and liquid wastes were analyzed for their phenolic components in different ways. LW was analyzed for evaluation of the qualitative-quantitative profile of soluble polyphenolic compounds, after filtration on 0.2-micron nylon filters and diluted with 1:10 (*v/v*) in methanol.

2.3 Polyphenolic extraction on solid waste

The polyphenolic compounds on solid waste were extracted following a procedure reported in the literature for the sprouted wheat, with little and opportune modifications (Van Hung et al., 2011). Free phenolics were extracted using 80% chilled ethanol as described in literature (Van Hung et al., 2009). Shortly, 10 mL of 80% chilled ethanol were added to a 15 mL centrifuge tube containing 1.0 g of dried sample. The content was vortex mixed and tumbled for 20 min at a room temperature before centrifugation at 4000 *g* for 5 min. The supernatant (free phenolic extracts) was collected. The residue was re-extracted twice with 10 mL of 80% chilled ethanol and all supernatants were combined. The supernatant was dried using a nitrogen evaporator (Laborata 4000; Heidolph Instruments Italia Srl, Milan, Italy) and then reconstituted with 10 mL of methanol. The extracts were then stored at −18 °C under nitrogen until analyzed.

2.4 Determination of total phenolic content (TPC)

The Folin-Ciocalteu method was used for determining the total phenolic content in accordance with the procedure reported by Izzo et al. (2020). Briefly, 500 µL of deionized water and 125 µL of the Folin-Ciocalteu reagent 2 N were added to 125 µL of extract. The tube was mixed and incubated for 6 min in dark conditions. Then, 1.25 mL of 7.5% of sodium carbonate solution and 1 mL of deionized water were added. The reaction mixture was maintained in dark conditions for 90 min. Finally, the absorbance at 760 nm was measured through a spectrophotometer system. Results were expressed as mg of gallic acid equivalents (GAE)/g of dry weight sample for solid waste and as mg of gallic acid equivalents (GAE)/mL of extract for liquid waste.

2.5 UHPLC-Q-orbitrap HRMS analysis

The qualitative and quantitative profile of bioactive compounds were performed by UHPLC (Dionex UltiMate 3000, Thermo Fisher Scientific, Waltham, MA, United States) equipped with a degassing system and an autosampler device. Analysis chromatographic was carried out with a thermostat (T = 30°C) using the Accucore aQ column (particle size 2.6 µm, 100 × 2.1 mm), (Manufacturer: Thermo Fisher Scientific). The mobile phase consisted of 0.1% acetic acid glacial in water (A) and Acetonitrile (B). The injection volume was 5 µL. Metabolites of interest were eluted by setting a flow rate of 0.4 mL/min. The gradient elution program was as follows: 0–5 min-5% B phase, 25 min-40% B phase, 25.1 min- 100% B phase, 27 min- 100% B phase, 27.1 min- 5% B phase, 35 min- 5% B phase. The total run time was 35 min, and the flow rate was 0.4 mL/min.

Mass spectrometry was performed on a Q-Exactive Orbitrap system equipped with an electrospray ionization (ESI) source operating in negative mode. The flow rates of the sheath gas, auxiliary gas and sweep gas were set at 35 arbitrary units (arb unit), 10 arb unit, respectively, with the spray voltage set to −2.8 kV under negative mode. The capillary temperature was set at 275°C, and the auxiliary gas heater temperature was 350 °C. The S-lens RF level was set at 50 V. Detection was achieved considering the exact mass with a mass error <5 ppm. Data analysis was performed using Xcalibur software 3.1.66.19. (Xcalibur, Thermo Fisher Scientific, Waltham, MA, United States).

2.6 Antioxidant activity

The antioxidant activity of the liquid waste and the extract of polyphenols obtained by the solid waste was assessed spectrophotometrically by using two different assays, namely, FRAP and ABTS. The obtained data were expressed as millimoles of Trolox Equivalents (TE)/kg of dry weight sample for solid waste and as millimoles of Trolox Equivalents (TE)/L for liquid waste.

2.6.1 ABTS assay

Free radical-scavenging activity was measured by using the method reported by Luz et al. (2018). Briefly, 9.6 mg of 2,2-azinobis (3-ethylbenzothiazoline-6-sulphonic acid) diammonium salt was solubilized in 2.5 mL of deionized water (7 mM) and 44 µL of solution of potassium persulfate ($K_2S_2O_8$; 2.45 mM) were added. The solution was kept in dark conditions at room temperature for 16 h prior to use. Afterward, $ABTS^{\cdot+}$ solution was diluted with ethanol to reach an absorbance value of 0.70 (±0.02) at 734 nm. Then, to 1 mL of $ABTS^{\cdot+}$ solution with an absorbance of 0.700 ± 0.050, 0.1 mL of opportunely diluted sample was added. After 2.5 min wait, the absorbance was immediately

measured at 734 nm. Results were expressed as mg of gallic acid equivalents (GAE)/g of dry weight sample for solid waste and as mg of gallic acid equivalents (GAE)/mL of extract for liquid waste.

2.6.2 FRAP assay

The antioxidant capacity of samples was estimated spectrophotometrically following the procedure of Benzie and Strain (1996). The ferric reducing/antioxidant power (FRAP) reagent was prepared by mixing acetate buffer (0.3 M; pH 3.6), TPTZ solution (10 mM), and ferric chloride solution (20 mM) in the proportion of 10:1:1 (v/v/v). Freshly prepared working FRAP reagent was used to perform the assay. Briefly, 0.150 mL of the appropriately diluted sample was added to 2,850 mL of FRAP reagent. The value of absorbance was recorded after 4 min at 593 nm. The method is based on the reduction of Fe^{3+} TPTZ complex (colorless complex) to Fe^{2+}-tripyridyltriazine (intense blue color complex) formed by the action of electron-donating antioxidants at low pH. Results were expressed as millimoles of Trolox Equivalents (TE)/kg of dry weight sample for solid waste and as millimoles of Trolox Equivalents (TE)/L for liquid waste.

2.7 Proximate composition analysis of solid waste

2.7.1 Water (moisture)

Water content was established via air oven drying (103°C) of samples of solid waste (5 g each per sample) until constant weight. Water values were calculated through the difference between initial weight of the sample and the constant weight of the sample, after drying process. The percent moisture was calculated by the following formula:

$$\%\ \text{moisture} = (w_1 - w_2)\ 100/w_1$$

Where w_1 = initial weight of sample; w_2 = final weight of sample (after drying).

The results are expressed as percentage of water (Stadlmayr et al., 2020).

2.7.2 Fat content evaluation

Fat extraction was carried out following the method of Folch et al. (1957) with some modifications. In brief, 1.0 g of sample was combined with 20.0 mL of a mixture chloroform/methanol (2:1 *v/v*) in a screw-top glass tube. The tubes were then shaken for 30 s before being shaken for 15 min in an orbital shaker at room temperature (~25°C). Next, the tubes were centrifuged at 1500 *g* for 15 min to then thoroughly decant the bulk of the chloroform/methanol solution, ensuring that all solid material remained at the bottom of the tube. The upper layer was covered, and the residue was extracted another time with 20.0 mL of mixture and the process was repeated. Finally, all the mixture were collected (about 40 mL) and washed with 10 mL of water. The chloroform phase was dried, and the residue was weighed. The percent crude fat was determined by using the following formula:

$$\%\ crude\ fat = Wt\ of\ chloroformic\ extract \times 100/Wt\ of\ sample$$

The fat content was then expressed as g/100 g sample.

2.7.3 Protein content evaluation

The quantitative determination of protein was carried out using the Kjeldahl, 1883, later modified by Gunning and Arnold (Pickel, 1915). In more detail, the procedure involved an initial step of mineralization of the total nitrogen in the sample, leading to the formation of ammonia, which was subsequently distilled and titrated. Concerning the volume of hydrochloric acid used, the nitrogen content is calculated. This value was then multiplied by a constant (5.7 for cereals), which allowed us to obtain the protein content value expressed as the percentage of protein per 100 g of dry sample.

2.7.4 Ash evaluation

The sample was calcined at 550°C for 2–4 h. The appearances of gray-white ash indicate complete oxidation of all organic matter in the sample. The weight loss by calcination gave the total organic matter content of the sample. The residue is the mineral part or ash (Stadlmayr et al., 2020).

2.8 Minerals content evaluation

Microwave digestion was performed for the determination of other elements in the solid sample. 500 mg of sample was transferred to a TFM®PTFE vessel with 6 mL of 65% ultrapure concentrated HNO_3 (14.33 mol/L) and 1 mL of 30% H_2O_2. The sample was subjected to digestion using a microwave (MW-AD, Ethos EZ Microwave Digester, Milestone, Shelton, CT, United States). The heating program for digestion consisted of 4 phases: phase 1 (90°C for 7 min), phase 2 (170°C for 5 min), phase 3 (210°C for 5 min) and phase 4 (210°C for 20 min). In all phases, the power was set to 1000 W. The sample was resuspended with 25 mL of bi-distilled water to undergo analysis by graphite furnace atomic absorption spectrometry (GFAAS). Analyses for arsenic, boron, calcium, chromium, cobalt, iron, manganese, selenium, copper, and zinc were performed by atomic absorption spectroscopy (AAS) according to the AOAC International, 1995. An AA-6300 atomic absorption spectrophotometer (Shimadzu, Columbia, MD, United States), equipped with an ASC-6100 autosampler (Shimadzu, Columbia, MD, United States) and a GFA-EX7i graphite furnace atomizer (Shimadzu, Columbia, MD, United States) was used. Instrument control and data analysis were performed using Multi-Element Program software (WizAArd software, Shimadzu, Columbia, MD, United States). Argon was used as the carrier gas. The AAS instrument is equipped with a hollow cathode lamp for linear sources and a deuterium lamp as a background corrector. Graphite pyrolytically coated tubes were used for the atomization step. To optimize the analytical signal, various tests were performed with different lamp intensities, sample injection volumes, and temperature ranges (1600 ◦C–1800°C for atomization).

Prior to analysis, a calibration line was performed for each analyte to be searched for using the multi-element standard prepared at concentrations of 0 µg/L (Cal Blk), 4 µg/L (Cal Std 1), 12 µg/L (Cal Std 2) and 20 µg/L (Cal Std 3). For the determination of other elements in the liquid sample from the *T. vulgare* extraction process, the microwave extraction step was not carried out, but dilutions and subsequent analysis by graphite furnace atomic

absorption spectrometry (GFAAS) was performed. The results are reported in Table 3.

2.9 Cell cultures

To evaluate the biological effects and biocompatibility profile of samples under investigation, specific bioscreens were performed on preclinical skin models by using primary and continuous cultures of both epidermal and dermal origin, representing ideal models to study cellular responses to *in vitro* treatments as well as toxicological responses.

HaCaT cells, an immortalized, nontumorigenic human keratinocyte cell line, were received from CNR (courtesy of Dr Valeria Cicatiello) to accomplish *in vitro* bioscreens. HaCaT were cultured in Dulbecco's modified Eagle's medium (DMEM; Invitrogen, Paisley, United Kingdom) containing high glucose (4.5 g/L), supplemented with 10% fetal bovine serum (FBS; Cambrex, Verviers, Belgium), L-glutamine (2 mM; Sigma, Milan, Italy), penicillin (100 U/mL; Sigma), and streptomycin (100 lg/mL; Sigma) at 37°C in a humidified 5% CO_2 atmosphere, according to ATCC recommendations (Miniaci et al., 2016). Human adult dermal fibroblasts (HDFa) were acquired by ATCC after isolation from the skin of a white male donor (PCS-201–012™). They were cultured in Fibroblast Basal Medium (ATCC) supplemented with recombinant human fibroblast growth factor (rh FGF, 5 ng/mL), L-glutamine (7.5 mM), ascorbic acid (50 µg/mL), hydrocortisone hemisuccinate (1 µg/mL), rh Insulin (5 µg/mL) and fetal bovine serum (FBS, 2%). Penicillin-Streptomycin-Amphotericin B Solution (Penicillin: 10 Units/mL, Streptomycin: 10 µg/mL, Amphotericin B: 25 ng/mL) was also added. HDFa cells were seeded at a density between 2,five to five × 10^3 cells/cm^2 and have been passed when approximately 80%–100% confluence was reached in actively proliferating cultures. Cells were cultured in a humidified 5% carbon dioxide atmosphere at 37°C, according to supplier's recommendations (Gazzillo et al., 2023).

2.10 Preparation of biological samples (LW and SW) for *in vitro* experiments

The different waste samples were subjected to distinct treatment methods based on their respective characteristics. Liquid waste (LW) samples were freeze-dried, while solid waste (SW) samples were extracted using the procedure for sprouted wheat (Van Hung et al., 2011), with some modifications. The resultant extract obtained from solid waste was dried using a rotavapor, reconstituted with 10 mL of water (UHPLC-MS grade), and subsequently freeze-dried.

2.11 Bioscreens *in vitro*

Cellular responses to samples application *in vitro* were investigated through the estimation of a "cell survival index", arising from the combination of cell viability evaluation with automated cell count (Irace et al., 2017). The cell survival index is calculated as the arithmetic mean between the percentage values derived from the MTT assay and the automated cell count. HaCaT and HDFa were inoculated in 96-well culture plates at a density of 10^4 cells/well and allowed to grow for 24 h. The medium was then replaced with fresh medium, and cells were continuously treated for 24, 48 and 72 h with a range of concentrations (5→100 µg/mL) of biological samples, i.e., liquid waste (LW) and solid waste (SW). Using the same experimental procedure, cells were also incubated with cisplatin (cDDP) as positive control for cytotoxic effects (data not shown). After *in vitro* incubations, cell viability was evaluated using the MTT assay procedure, which measures the level of mitochondrial dehydrogenase activity using the yellow 3-(4,5-dimethyl-2-thiazolyl)-2,5-diphenyl-2H-tetrazolium bromide (MTT, Sigma) as substrate. The assay is based on the redox ability of living mitochondria to convert dissolved MTT into insoluble purple formazan. Briefly, after the treatments, the medium was removed, and the cells were incubated with 20 µL/well of a MTT solution (5 mg/mL) for 1 h in a humidified 5% CO_2 incubator at 37 °C. The incubation was stopped by removing the MTT solution and by adding 100 µL/well of DMSO to solubilize the obtained formazan. Finally, the absorbance was monitored at 550 nm using a microplate reader (iMark microplate reader, Bio-Rad, Milan, Italy).

Cell number was determined by TC20 automated cell counter (Bio-Rad, Milan, Italy), providing an accurate and reproducible total count of cells and a live/dead ratio in one step by a specific dye (trypan blue) exclusion assay. Bio-Rad's TC20 automated cell counter uses disposable slides, TC20 trypan blue dye (0.4% trypan blue dye w/v in 0.81% sodium chloride and 0.06% potassium phosphate dibasic solution) and a CCD camera to count cells based on the analyses of captured images. Once the loaded slide is inserted into the slide port, the TC20 automatically focuses on the cells, detects the presence of trypan blue dye and provides the count. When cells are damaged or dead, trypan blue can enter the cell allowing living cells to be counted. Operationally, after treatments in 96-well culture plates, the medium was removed, and the cells were collected. Ten microliters of cell suspension, mixed with 0.4% trypan blue solution at 1:1 ratio, were loaded into the chambers of disposable slides. The results are expressed in terms of total cell count (number of cells per ml). If trypan blue is detected, the instrument also accounts for the dilution and shows live cell count and percent viability. Total counts and live/dead ratio from random samples for each cell line were subjected to comparisons with manual hemocytometers in control experiments. The calculation of the concentration required to inhibit the net increase in the cell number and viability by 50% (IC_{50}) is based on plots of data (n = 4 for each experiment) and repeated three times (total n = 12). IC_{50} values were calculated from a dose response curve by nonlinear regression using a curve fitting program, GraphPad Prism 8.0, and are expressed as mean values ±SEM (n = 24) of four independent experiments (Irace et al., 2017; Ferraro et al., 2023).

2.12 Cytomorphological analysis

HaCaT cells and HDF were grown on 60 mm culture dishes by plating 5 × 10^5 cells. After reaching the sub-confluence, the medium was replaced with fresh medium, and cells were continuously treated for 24, 48, and 72 h with a range of concentrations (5→100 µg/mL) of biological samples (LW and SW). After treatments, cells were

TABLE 1 Polyphenol content in solid and liquid waste. The results are displayed as average value (μg/g) for solid waste and as average (μg/mL) for liquid waste and standard deviation (SD).

Bioactive Compounds	Solid Waste	Liquid Waste
	μg/g dw	μg/mL
Ferulic acid	89.782 ± 1.626	*nf*
Dihydroferulic acid	24.934 ± 1.323	6.24 ± 0.212
Apigenin-C-hexoside-pentoside	12.398 ± 0.372	0.076 ± 0.052
Apigenin-6-arab-8-hexoside	12.167 ± 1.203	0.08 ± 0.055
Feruloyl quinic acid	7.917 ± 0.388	0.039 ± 0.02
Caffeic acid	2.715 ± 0.067	0.716 ± 0.010
Chlorogenic acid	2.299 ± 0.134	*nf*
Kaempferol-3-O-rutinoside	1.722 ± 0.095	0.022 ± 0.008
Coumaric acid-O-hexoside	1.264 ± 0.044	0.03 ± 0.002
Apigenin-C-hexoside-hexoside	1.259 ± 0.081	0.016 ± 0.008
Isoorientin-2-O-rhamnoside	1.259 ± 0.050	0.016 ± 0.007
Kaempferol-3-O-glucoside	0.768 ± 0.001	0.04 ± 0.000
Caffeic acid-O-hexoside	0.663 ± 0.082	*nf*
Naringenin	0.563 ± 0.020	0.037 ± 0.002
Sinapoyl-hexoside	0.528 ± 0.008	0.08 ± 0.002
Apigenin-7-O-glucoside	0.351 ± 0.017	0.002 ± 0.000
Total	160.697	7.394

[a]dw: dry weight.

examined by a phase-contrast microscope (Labovert microscope, Leizt) to monitor any morphological change. Microphotographs at a ×200 total magnification (×20 objective and ×10 eyepiece) were taken with a standard VCR camera (Nikon) (Ferraro et al., 2023).

2.13 Statistical analysis

Statistical analysis of data was performed by two-way ANOVA analysis (SPSS 13.0) followed by the Tukey-Kramer multiple comparison test to evaluate significant differences; *p*-values ≤0.05 were considered as significant. All the determinations were undertaken in triplicate, and results were expressed as mean ± standard deviation (SD).

3 Results

3.1 Quantification of flavonoids and phenolic compounds

The identified polyphenols (n = 16) in both solid and liquid waste were characterized using a UHPLC coupled to a high-resolution Orbitrap mass spectrometry. For the quantitative analysis calibration curves were built in appropriate solvents and regression coefficients higher than 0.990 were obtained. Quantitative analysis showed that the dominant phenolic acid identified was ferulic acid, followed by dihydroferulic acid, apigenin-6-arab-8-hexoside, feruloyl quinic acid, apigenin-C-hexoside-hexoside, chlorogenic acid, caffeic acid and others (Table 1). In the solid waste polyphenols extract, ferulic acid represents up to 55.5% of the total polyphenol content identified. In the liquid waste, dihydroferulic acid showed a reduction by 75% compared to the solid waste. A clear reduction in the content of active compounds of up to 95.4% was observed between the solid and liquid waste.

3.2 Antioxidant capacity and total phenolic content (TPC) of liquid and solid waste

The antioxidant activity of both liquid and solid wastes was assessed using two different assays (DPPH and ABTS assay). The total phenolic content (TPC) was evaluated through the Folin-Ciocalteu test. A calibration curve of inhibition, built with Trolox®, was employed as a positive control of the antioxidant assays, while gallic acid was employed to perform the calibration curve for TPC evaluation. Table 2 displays the data as millimoles of Trolox equivalent per kilogram or liter depending on the typologies of the sample is considered solid or liquid (average value and SD). In both antioxidant activity tests a higher antioxidant activity was observed for the solid extract. The total phenolic content in the liquid extract undergoes a significant percentage reduction compared to the solid waste.

3.3 Nutritional composition of solid waste

Nutritional components of the solid waste were evaluated using different techniques. The Folch method was used to evaluate the content of fat within the sample. Protein was ascertained through Kjeldahl method. The moisture of the sample was determined to express the data as content of dry material. The solid waste is composed of proteins 3.6 ± 0.3 g per 100 g, fat 2.3 ± 0.6 g per 100 g, and ash 4.1 ± 0.7 g per 100 g. The moisture in the sample was 39% ± 2.4%. The results shown were the average of three repeated measurements and were reported as average ±standard deviation.

3.4 Minerals content evaluation

Table 3 reports the results obtained from analysis by graphite furnace atomic absorption spectrometry (GFAAS). The solid waste sample was previously treated by microwave digestion, while the liquid waste was directly diluted and subjected to GFAAS analysis. All analyses were performed in triplicate, and results are expressed as averages of mg/kg and mg/L for solid and liquid waste, respectively, and are reported with standard deviations.

3.5 Bioactivity evaluation in preclinical models of human skin

Both liquid (LW) and solid (SW) wastes were investigated for their potential toxicity by well-established *in vitro* preclinical models

TABLE 2 Evaluation of the antioxidant activity through ABTS and DPPH assay and the total phenolic content (TPC) (Folin-Ciocalteu Test). The analyses were performed in triplicate and data expressed as mean ± standard deviation.

Samples	ABTS		FRAP		TPC	
	mmol trolox/kg	mmol trolox/L	mmol trolox/kg	mmol trolox/L	mg GAE/g	mg GAE/mL
Solid Waste	8.598 ± 0.053		7.262 ± 0.240		1.771 ± 0.005	
Liquid Waste		0.223 ± 0.011		0.285 ± 0.009		0.105 ± 0.000

TABLE 3 Quantitative determination of minerals in the solid and liquid waste samples.

Minerals	Solid Waste mg/Kg	SD	Liquid Waste mg/L	SD
Ammonia (NH_3)	9.25	±0.29	6.005	±0.3
Phosphate (PO_4^{3-})	30.8	±1.1	40.85	±1.05
Calcium (Ca^{++})	29.33	±2.1	18.18	±1
Magnesium (Mg^{++})	18.89	±1.8	14.5	±1.05
Sulphate (SO_4^{2-})	20.5	±0.8	41.9	±1.25
Arsenic (As^{+++})	0.0078	±0.02	0.01	±0.025
Boron (B)	<0.2	—	<0.2	—
Manganese (Mn^{++})	0.162	—	<0.0001	—
Zinc (Zn^{++})	0.159	±0.016	0.2555	±0.014
Copper (Cu^{++})	0.026	±0.005	0.0095	±0.003
Cobalt (Co^{++})	<0.0001	—	<0.0001	—
Iron (Fe^{+++})	0.0945	±0.004	0.015	±0.002
Selenium (Se)	<0.0001	—	<0.0001	—
Chromium (Cr^{+++})	0.0411	±0.008	0.0762	±0.005
Chloride (Cl^-)	3.3	±0.13	0.9	±0.065

All the determinations were performed in triplicate and results are expressed as mg/kg and mg/L means for solid and liquid wastes, respectively, and standard deviation.

of human skin. Epidermal and dermal cultures were selected for biocompatibility analysis of the biological samples under investigation Piccolo et al. (2019). Quantitative (i.e., automated cell counts) and functional (i.e., mitochondrial redox activity) assays allowed for the assessment of cellular responses to *in vitro* treatments (Ferraro et al., 2021). Overall, by targeted bioscreens a "Cell survival index" to characterize cellular viability and responses to experimental conditions was established, as fully described in the experimental section (Irace et al., 2017). Representative concentration-effect curves in the examined cellular models (HaCaT cells and HDFa) after 24, 48, and 72 h of exposure to the indicated concentrations (μg/mL) of the biological samples (LW and SW) are reported in Figure 1A. As can be clearly observed, bioscreens allow the examined samples to be defined as fully biocompatible. Indeed, no significant interference with cell viability, growth, and proliferation was observed. In line, no cytotoxic effect was noted even at the highest tested concentration (100 μg/mL) of both LW and SW following prolonged incubation times (72 h). Consequently, IC_{50} values calculated from concentration-effect curves are all higher than 100 μg/mL, indicative of a good safety profile in human cells. In addition, cytomorphological analyses on do not show noteworthy alterations in cellular morphology (Figure 1B).

4 Discussion

Recently, have been reported several studies aimed at valorizing the waste obtained from the natural matrix in the context of the upcycling economy and reduce the environmental pollution. The analysis and characterization of the phenolic compounds contained in aqueous extracts of fennel waste, pea pods and from spent coffee grounds have been already performed (Castaldo et al., 2021a; Castaldo et al. 2021b; Castaldo et al. 2021c).Valid examples of optimization of biofuel production with reduction of final waste have been already reported in literature, demonstrating that a green production process brings not only environmental but also economic benefits for companies (Sarkar et al., 2024; Mridha

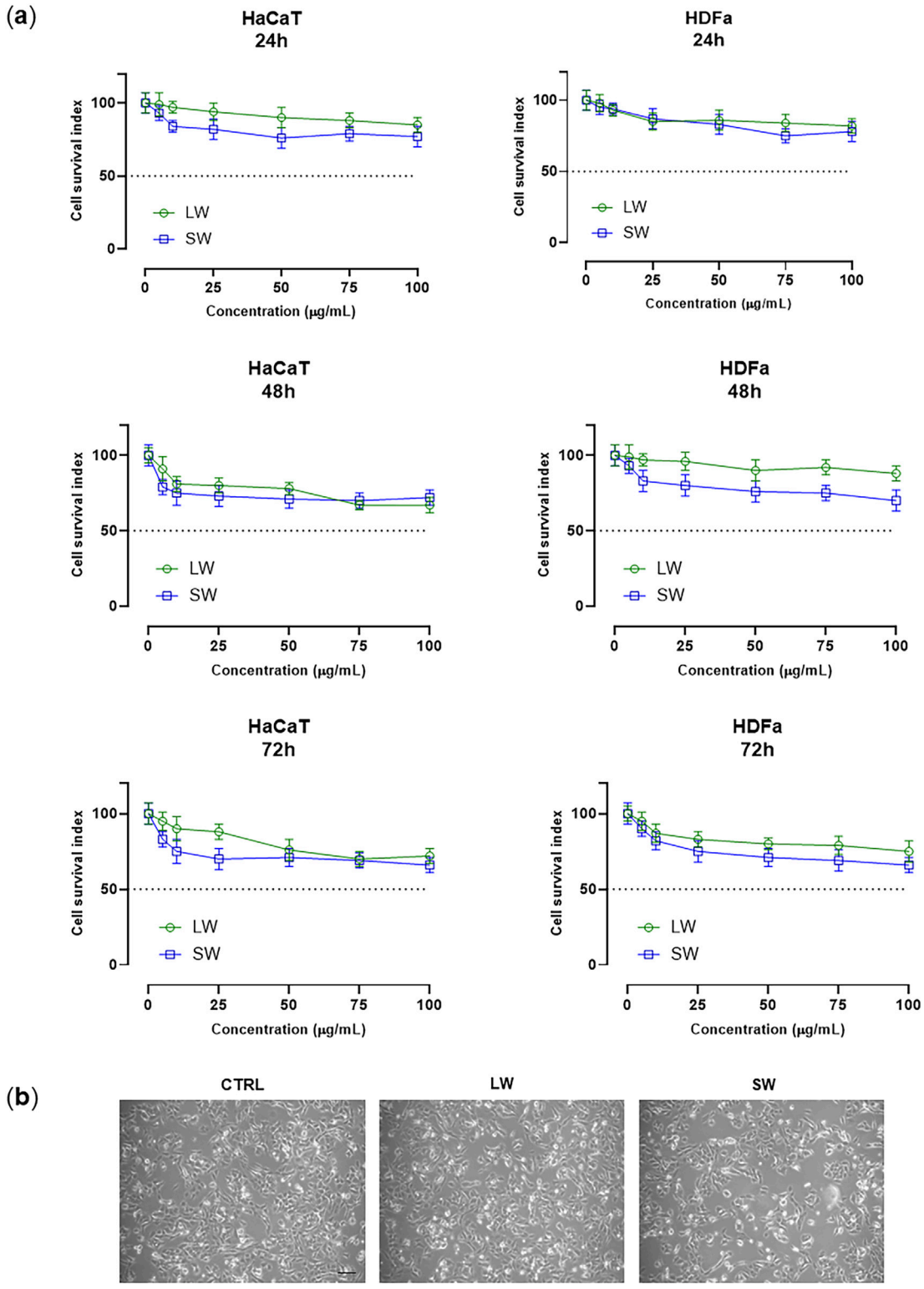

FIGURE 1
(A) Cell survival index, evaluated by the MTT assay and live/dead automated cell count, for HaCaT cells and HDFa following 24, 48, and 72 h of incubation with the indicated concentrations (0–100 µg/mL) of liquid waste (LW) and solid waste (SW), as reported in the legend. Data are expressed as a percentage of untreated control cells and are reported as mean of four independent experiments ±SEM (n = 24). The Cell Survival Index was calculated as described in the experimental section and plotted in line-graphs against the different concentrations of the tested samples. **(B)** Representative photomicrographs of HaCaT cells monolayers at ×200 total magnification (×20 objective and ×10 eyepiece) by phase-contrast microscopy after 48 h of treatment with 100 µg/mL of LW and SW, as indicated in the legend.

et al., 2024). In this context, we were motivated to analyze waste generated from the production of the aqueous extract of the Triticum Vulgare (TVE) with the aim of promoting an eco-friendly circular economy operation.

The specific extract of *T. vulgare* (TVE) is manufactured by a recently implemented extraction process (Riccio, 2018) of Farmaceutici Damor, and it is used as the active principle in pharmaceutical formulations for the treatment of decubitus ulcers, skin lesions, and burns. The company Farmaceutici Damor produces about 2–3 tons of waste each year, which compared to the production data is a relatively small amount. However, the cost of disposing of this waste could be onerous. As reported above, the extraction process adopted for the preparation of one of the most iconic pharmaceutical products based on phytostimulins, is green as it is based on the use of ecological solvents characterized by a high extraction capacity. The aqueous extract of *T. vulgare* (TVE) was obtained through a simple water-based extraction process with non-potentially toxic or harmful solvents. The use of a green extraction process in production represents an essential point for the valorization of a by-product or waste and for its potential use in a subsequent production process. The solid and liquid waste analyzed in this study represents approximately 7.5% and 5% of the entire production process. Therefore, for the entire production process, a total loss between solid and liquid of 12.5% is estimated in terms of yield of the finished product. The ratio between the solid fraction and the liquid fraction in terms of mass is of the order of 1.5 to 1.

The approach of exploiting a by-product or waste obtained as a result of an industrial process to obtain a phytochemical preparation would not only significantly reduce waste, but could also create new sources of income, thus supporting the circular economy. Ensuring environmental and economic sustainability is crucial, especially if a technical-economic assessment of the benefits obtained is carried out. From an economic and environmental point of view, to enhance the by-products of the processing of natural products, the characterization of the chemical composition and the analysis of the chemical-physical characteristics are fundamental (Espro et al., 2021).

Phenolic compounds are widely distributed in plants and have recently gained much attention due to their antioxidant activity and ability to scavenge free radicals with potential beneficial implications for human health (Muscolo et al., 2024). Phenolic compounds can be classified as secondary plant metabolites, formed by plants during their secondary metabolism (Susanti et al., 2024). Many of them are bioactive and can have antioxidant, antimicrobial, anticarcinogenic and many other beneficial health effects.

Wheat is an important component of the human diet and, therefore, may be an important source of phenolic antioxidants. In particular, ferulic acid is the predominant phenolic acid found in wheat bran, constituting approximately 90% of the total phenolic compounds (Li et al., 2024).

This observation pushed us to evaluate the by-products of wheat processing from a chemical-physical point of view to understand the potential of its reuse from a circular economy perspective. Literature shows that phenolic acids in wheat grains are mainly present in a form bound to other cereal components such as starch, cellulose, β-glucan, and pentosan (Yu et al., 2001; Vaher et al., 2010). Insoluble bound phenols can be released by basic, acidic, or enzymatic treatment of samples prior to extraction (Liyana-Pathirana and Shahidi, 2006). The identification of the main chemical constituents and the quantification of the phenolic component, almost always present in nature and endowed with antioxidant activity, represents the starting point that can favor its potential industrial exploitation.

The good antioxidant activity of the analyzed wastes, mainly due to the presence of phenols, demonstrates the possibility of recovering or reusing the phytochemical components contained in these by-products for other production processes.

The antioxidant activity of the extract obtained by solid waste is associated, as already well known for wheat, mainly with ferulic acid (Zhou et al., 2004; Klepacka and Fornal, 2006). The quali-quantitative analysis via UHPLC Q-Orbitrap HRMS of the two fractions of processing waste, i.e., solid and liquid, highlighted a different composition of the phenolic fraction. In fact, while in solid waste the phenolic fraction is mainly represented by ferulic acid, in the liquid component of waste the main phenolic component is made up of dihydroferulic acid.

Although solid and liquid waste are quite comparable in quantitative terms, the analysis carried out indicates that their chemical content is very different. This significantly affects their actual reuse value for other production processes. In fact, the in-depth chemical-physical analysis and characterization reported in this study highlighted that, regarding the nature of the phenolic substances, the solid component is mainly rich in ferulic acid (on average 90 μg/g in dry weight) and dihydroferulic acid (on average 24 μg/g in dry weight) while the liquid component is mainly represented by dihydroferulic and caffeic acid, among other things in quite limited quantities (on average 6.24 μg/mL and 0.7 μg/mL, respectively).

Comparing the results of our study with recent literature concerning the reuse and characterization of industrial waste derived from various matrices, several notable differences arise, primarily attributable to the differing biological matrices and extraction methodologies employed. Nevertheless, the existing literature presents numerous examples of waste reuse that is rich in bioactive compounds.

The investigation conducted by Sibhatu et al. (2021) explored the utilization of brewery spent grain (BSG) residues for the extraction of ferulic acid, a naturally occurring antioxidant. This extraction was optimized through an acid treatment followed by alkaline hydrolysis using sodium hydroxide (NaOH), achieving a maximum yield of 46.17 mg/100 g of ferulic acid from BSG, as determined by the Box-Behnken design.

Concentrations of ferulic acid and other active ingredients are lower than those reported in the cited studies; in fact, the data indicate that the solid component is mainly rich in ferulic acid (90 mg/kg dry weight) and dihydroferulic acid (24 mg/kg dry weight), while the liquid component contains mainly dihydroferulic acid and caffeic acid, although in relatively limited concentrations (6.24 mg/L and 0.7 mg/L, respectively). However, it is worth highlighting that the polyphenol extraction method used in our study (Van Hung et al., 2011) does not use acids or bases and is a more environmentally friendly process.

In relation to the study on fennel waste conducted by Castaldo et al. (2021a), the extract demonstrated a ferulic acid concentration of 258 mg/kg but constituting only 4.43% of the total. In contrast, analysis of coffee waste (Castaldo et al., 2021c) revealed a significantly lower ferulic acid content than our waste, 0.8 mg/kg compared to 89.78 mg/kg identified in our solid waste, indicating a

ferulic acid concentration that is 100 times higher in our samples. Despite this disparity, coffee waste showed a potential application in the preparation of fortified biscuits.

It is imperative to underscore that, in terms of bioactive compounds, particularly within polyphenolic extracts, it is essential to consider the full spectrum of compounds present, as they may exert synergistic effects. Consequently, we contend that the extraction of polyphenols without the isolation of a single bioactive compound is more advantageous, especially in light of our objective to adhere to principles of the circular economy, which advocate for the minimization of the number of steps and processes involved. The analysis carried out gives solid waste a higher recovery value than liquid waste due to the higher phenol content. In fact, ferulic acid contained mainly in solid waste could find use as a raw material in other production processes. For example, in the natural production of vanillin with biotechnological means and not with synthetic means, thus obtaining a product that can be labeled as "natural" and which could be an alternative both to the product obtained by extraction and to the additive obtained by synthesis, with costs of decidedly more contained production (Xu et al., 2024).

In this context, evaluations conducted in preclinical models of human skin allow both solid and liquid waste from the processing of wheat (*Triticum Vulgare*) to be defined as highly biocompatible. Indeed, cellular responses observed after *in vitro* treatments indicate an excellent safety profile of the wastes under investigation, at least in skin-derived cell. Of note are outcomes obtained in human primary cultures (HDFa) deriving directly from human skin, which represent preclinical cellular models very sensitive to xenobiotic effects and thereby particularly suitable for toxicology studies. Overall preclinical tests confirm the possibility of reusing and valorizing wastes from the industrial process to produce the phytostimulin-based therapeutics, paving the way for their potential upcoming applications in the biomedical and cosmetic field. Considering the positive feedback, we have attained in human skin cells further endorses a possible use of these materials in cosmetics, as well as raw material for the preparation of formulations for topical applications.

Recently, the use of waste was proposed for the development of cosmetic formulations. In particular, extracts obtained from clementine peels and olive leaves show to endowed 25% of antioxidant activity and no cytotoxic effects (*in vitro* studies on NCTC2544 Cells). Creams with these ingredients are stable at various temperatures and safe for human use, demonstrating good spreadability properties and pseudoplastic behaviour, promoting a circular economy and reducing environmental impact (d'Avanzo et al., 2024). In a study by Weronika et al. (2024), they investigated the potential of defatted strawberry seeds, obtained after oil extraction, as a source of phenolic compounds with cosmetic applications. The extracts, rich in tiliroside, kaempferol 3-glucoside and ellagic acid, were obtained with a mixture of water and ethanol. Chemical analyses showed antioxidant properties and cytoprotective activity against oxidative stress in human fibroblasts. The defatted strawberry seeds could therefore be used as beneficial additives for skin care products. Additionally, in a study reported by Draghici-Popa et al. (2024), grape marc, a by-product of the wine industry, they explored the use of grape-seed polyphenolic extracts to produce sunscreens. Extracts, obtained from different grape varieties (Merlot, Feteasc Neagr, Blaufränkisch, Isabella) using ethanol and acetone solutions, were analyzed for polyphenol content, antioxidant activity and sun protection factor (SPF). The best extract, from Merlot grape seeds with 70% ethanol, showed an SPF of 7.83, with stable and safe creams.

Based on this evidence reported in literature, the cosmeceutical applications represent one of a possible and potential use of the active ingredients contained in this waste. Moving in this direction, the herein-described outcome can be propaedeutic to further in-depth cellular studies aimed at a precise characterization of biocompatible waste recycling in the biomedical field. Certainly, one of the most economical valorization strategies for the reuse of this processing waste is to evaluate its potential use in the production of food supplements, and antioxidants, or used as a phytoprotective and anti-aging ingredient for cosmetic products. Therefore, the analysis and characterization of waste resulting from the production of a pharmaceutical preparation starting from wheat seeds can be seen as a strategic approach to a circular bioeconomy, where economic and practical advantages deriving from the valorization of waste can guarantee efficient recycling with a positive environmental impact.

5 Conclusion

This study allowed us to shed light on the potential characteristics of these wastes and to establish the basis for future investigations on their alternative applications, with particular attention to the solid waste containing the highest phenol component represented by ferulic acid. This result confers to the analyzed solid waste a potentially useful value as for other wastes containing phenolic compounds previously identified and reported in literature.

Although the waste obtained from the industrial process to produce phytostimulin-based pharmaceutical products is not particularly excessive to create disposal problems, the analysis aimed to verify whether it could find a more noble use. In fact, for the characteristics identified with the analysis carried out, this waste could represent a starting resource in other areas such as cosmeceuticals or food.

However, further studies are needed to validate its real applications as a base component of cosmeceutical products, since ferulic acid is a commonly recognized antioxidant and used to protect the skin from damage caused by free radicals.

Data availability statement

The raw data supporting the conclusions of this article will be made available by the authors, without undue reservation.

Ethics statement

Ethical approval was not required for the studies on humans in accordance with the local legislation and institutional

requirements because only commercially available established cell lines were used.

Author contributions

LC: Data curation, Investigation, Writing–original draft, Writing–review and editing. LI: Conceptualization, Data curation, Investigation, Methodology, Writing–original draft. GG: Data curation, Methodology, Writing–original draft. MF: Data curation, Methodology, Writing–original draft. MP: Formal Analysis, Investigation, Writing–original draft. RC: Formal Analysis, Investigation, Writing–original draft. BM: Data curation, Funding acquisition, Supervision, Writing–original draft. RP: Data curation, Methodology, Writing–original draft. SA: Formal Analysis, Investigation, Writing–review and editing. ER: Conceptualization, Formal Analysis, Investigation, Writing–original draft. AR: Writing–original draft. CI: Formal Analysis, Investigation, Writing–review and editing. PG: Conceptualization, Project administration, Supervision, Writing–original draft, Writing–review and editing.

Funding

The author(s) declare that financial support was received for the research, authorship, and/or publication of this article. This research work was supported by Farmaceutici Damor S.p.A., Naples, Italy.

Acknowledgments

The authors are grateful to the personnel of the '*FoodLab Laboratory*', Department of Pharmacy, University of Naples Federico II, Naples, Italy.

In Memoriam

Dedicated to the memory of Alberto Ritieni.

Conflict of interest

Authors BM, RP, SA, and ER were employed by Farmaceutici Damor.

The remaining authors declare that the research was conducted in the absence of any commercial or financial relationships that could be construed as a potential conflict of interest.

Publisher's note

References

AOAC International (1995). *Offcial methods of analysis of AOAC international*. 16th edition. Arlington, VA, USA: Association of Analytical Communities.

Benzie, I. F., and Strain, J. J. (1996). The ferric reducing ability of plasma (FRAP) as a measure of "antioxidant power": the FRAP assay. *Anal. Biochem.* 239 (1), 70–76. doi:10.1006/abio.1996.0292

Castaldo, L., Izzo, L., De Pascale, S., Narváez, A., Rodriguez-Carrasco, Y., and Ritieni, A. (2021a). Chemical composition, *in vitro* bioaccessibility and antioxidant activity of polyphenolic compounds from nutraceutical fennel waste extract. *Molecules* 26 (7), 1968. doi:10.3390/molecules26071968

Castaldo, L., Izzo, L., Gaspari, A., Lombardi, S., Rodríguez-Carrasco, Y., Narváez, A., et al. (2021b). Chemical composition of green pea (pisum sativum L.) pods extracts and their potential exploitation as ingredients in nutraceutical formulations. *Antioxidants* 11 (1), 105. doi:10.3390/antiox11010105

Castaldo, L., Lombardi, S., Gaspari, A., Rubino, M., Izzo, L., Narváez, A., et al. (2021c). *In vitro* bioaccessibility and antioxidant activity of polyphenolic compounds from spent coffee grounds-enriched cookies. *Foods* 10 (8), 1837. doi:10.3390/foods10081837

d'Avanzo, N., Mancuso, A., Mare, R., Silletta, A., Maurotti, S., Parisi, O. I., et al. (2024). Olive leaves and citrus peels: from waste to potential resource for cosmetic products. *Cosmetics* 11 (2), 41.

Draghici-Popa, A.-M., Buliga, D.-I., Popa, I., Tomas, S. T., Stan, R., and Boscornea, A. C. (2024). Cosmetic products with potential photoprotective effects based on natural compounds extracted from waste of the winemaking industry. *Molecules* 29 (12), 2775. doi:10.3390/molecules29122775

Espro, C., Paone, E., Mauriello, F., Gotti, R., Uliassi, E., Bolognesi, M. L., et al. (2021). Sustainable production of pharmaceutical, nutraceutical and bioactive compounds from biomass and waste. *Chem. Soc. Rev.* 50 (20), 11191–11207. doi:10.1039/d1cs00524c

Ferraro, M. G., Bocchetti, M., Riccardi, C., Trifuoggi, M., Paduano, L., Montesarchio, D., et al. (2023). Triple negative breast cancer preclinical therapeutic management by a cationic ruthenium-based nucleolipid nanosystem. *Int. J. Mol. Sci.* 24 (7), 6473. doi:10.3390/ijms24076473

Ferraro, M. G., Piccolo, M., Pezzella, A., Guerra, F., Maione, F., Tenore, G. C., et al. (2021). Promelanogenic effects by an annurca apple-based natural formulation in human primary melanocytes. *Clin. Cosmet. Investigational Dermatology* Vol. 14, 291–301. doi:10.2147/ccid.s299569

Folch, J., Lees, M., and Stanley, G. H. S. (1957). A simple method for the isolation and purification of total lipides from animal tissues. *J. Biol. Chem.* 226 (1), 497–509. doi:10.1016/s0021-9258(18)64849-5

Freitas, L. C., Barbosa, J. R., da Costa, A. L. C., Bezerra, F. W. F., Pinto, R. H. H., and de Carvalho Junior, R. N. (2021). From waste to sustainable industry: how can agro-industrial wastes help in the development of new products? *Resour. Conservation Recycl.* 169, 105466. doi:10.1016/j.resconrec.2021.105466

Gazzillo, E., Pierri, M., Colarusso, E., Chini, M. G., Ferraro, M. G., Piccolo, M., et al. (2023). Exploring the chemical space of functionalized [1, 2, 4] triazolo [4, 3-a] quinoxaline-based compounds targeting the bromodomain of BRD9. *Bioorg. Chem.* 139, 106677. doi:10.1016/j.bioorg.2023.106677

Idiano, D. 'A., Favari, D., Gastaldi, M., and Kirchherr, J. (2024). Towards circular economy indicators: evidence from the European Union. *Waste Manag. and Res.* 42, 670–680. doi:10.1177/0734242x241237171

Irace, C., Misso, G., Capuozzo, A., Piccolo, M., Riccardi, C., Luchini, A., et al. (2017). Antiproliferative effects of ruthenium-based nucleolipidic nanoaggregates in human models of breast cancer *in vitro*: insights into their mode of action. *Sci. Rep.* 7 (1), 45236. doi:10.1038/srep45236

Izzo, L., Castaldo, L., Narváez, A., Graziani, G., Gaspari, A., Rodríguez-Carrasco, Y., et al. (2020). Analysis of phenolic compounds in commercial Cannabis sativa L. inflorescences using UHPLC-Q-Orbitrap HRMS. *Molecules* 25 (3), 631. doi:10.3390/molecules25030631

Kjeldahl, J. (1883). A new method for the determination of nitrogen in organic matter. *Z. für Anal. Chem.* 22, 366–382. doi:10.1007/bf01338151

Klepacka, J., and Fornal, Ł. (2006). Ferulic acid and its position among the phenolic compounds of wheat. *Crit. Rev. Food Sci. Nutr.* 46 (8), 639–647. doi:10.1080/10408390500511821

Lemes, A. C., Egea, M. B., Oliveira Filho, J. G. d., Gautério, G. V., Ribeiro, B. D., and Coelho, M. A. Z. (2022). Biological approaches for extraction of bioactive compounds from agro-industrial by-products: a review. *Front. Bioeng. Biotechnol.* 9, 802543. doi:10.3389/fbioe.2021.802543

Li, W., Sun, X., Alfred, M. M., Yang, Q., Fang, Y., Hu, Q., et al. (2024). Effects of ferulic acid on the polymerization behavior of gluten protein and its components. *Food Hydrocoll.* 147, 109388. doi:10.1016/j.foodhyd.2023.109388

Liyana-Pathirana, C. M., and Shahidi, F. (2006). Importance of insoluble-bound phenolics to antioxidant properties of wheat. *J. Agric. food Chem.* 54 (4), 1256–1264. doi:10.1021/jf052556h

Luz, C., Izzo, L., Graziani, G., Gaspari, A., Ritieni, A., Mañes, J., et al. (2018). Evaluation of biological and antimicrobial properties of freeze-dried whey fermented by different strains of Lactobacillus plantarum. *Food and Funct.* 9 (7), 3688–3697. doi:10.1039/c8fo00535d

Madaan, G., Singh, A., Mittal, A., and Shahare, P. (2024). Reduce, reuse, recycle: circular economic principles, sustainability and entrepreneurship in developing ecosystems. *J. Small Bus. Enterp. Dev.* 31, 1041–1066. doi:10.1108/jsbed-01-2023-0009

Miniaci, M. C., Irace, C., Capuozzo, A., Piccolo, M., Di Pascale, A., Russo, A., et al. (2016). Cysteine prevents the reduction in keratin synthesis induced by iron deficiency in human keratinocytes. *J. Cell. Biochem.* 117 (2), 402–412. doi:10.1002/jcb.25286

Mridha, B., Sarkar, B., Cárdenas-Barrón, L. E., Ramana, G. V., and Yang, L. (2024). Is the advertisement policy for dual-channel profitable for retailing and consumer service of a retail management system under emissions-controlled flexible production system? *J. Retail. Consumer Serv.* 78, 103662. doi:10.1016/j.jretconser.2023.103662

Muscolo, A., Mariateresa, O., Giulio, T., and Mariateresa, R. (2024). Oxidative stress: the role of antioxidant phytochemicals in the prevention and treatment of diseases. *Int. J. Mol. Sci.* 25 (6), 3264. doi:10.3390/ijms25063264

Piccolo, M., Ferraro, M. G., Maione, F., Maisto, M., Stornaiuolo, M., Tenore, G. C., et al. (2019). Induction of hair keratins expression by an annurca apple-based nutraceutical formulation in human follicular cells. *Nutrients* 11 (12), 3041. doi:10.3390/nu11123041

Pickel, J. (1915). The kjeldahl-gunning-arnold method for nitrogen. *J. Industrial and Eng. Chem.* 7 (4), 357. doi:10.1021/ie50076a677

Riccio, R. (2018) *U.S. Patent No. 9,895,392*. Washington, DC: U.S. Patent and Trademark Office.

Romano, E., Campagnuolo, C., Palladino, R., Schiavo, G., Maglione, B., Luceri, C., et al. (2023). Technical evaluation of a new medical device based on rigenase in the treatment of chronic skin lesions. *Bioengineering* 10 (9), 1022. doi:10.3390/bioengineering10091022

Sanguigno, L., Casamassa, A., Funel, N., Minale, M., Riccio, R., Riccio, S., et al. (2018). Triticum vulgare extract exerts an anti-inflammatory action in two *in vitro* models of inflammation in microglial cells. *PLoS ONE* 13 (6), e0197493. [online]. doi:10.1371/journal.pone.0197493

Sapkota, B., and Pariatamby, A. (2023). Pharmaceutical waste management system–Are the current techniques sustainable, eco-friendly and circular? A review. *Waste Manag.* 168, 83–97. doi:10.1016/j.wasman.2023.05.052

Sarkar, B., Mridha, B., Pareek, S., and Fan, S. K. (2024). Sustainable multi-biofuel production with stochastic lead time and optimum energy utilization under flexible manufacturing. *Comput. and Industrial Eng.* 193, 110223. doi:10.1016/j.cie.2024.110223

Sibhatu, H. K., Anuradha Jabasingh, S., Yimam, A., and Ahmed, S. (2021). Ferulic acid production from brewery spent grains, an agro-industrial waste. *LWT* 135, 110009. doi:10.1016/j.lwt.2020.110009

Sneh, P. B., Chaudhary, V., Kajla, P., Balakrishnan, G., and Phimolsiripol, Y. (2024). Strategies for upcycling food waste in the food production and supply chain. *Trends Food Sci. Technol.* 143, 104314. doi:10.1016/j.tifs.2023.104314

Stadlmayr, B., Wanangwe, J., Waruhiu, C. G., Jamnadass, R., and Kehlenbeck, K. (2020). Nutritional composition of baobab (Adansonia digitata L.) fruit pulp sampled at different geographical locations in Kenya. *J. Food Compos. Analysis* 94, 103617. doi:10.1016/j.jfca.2020.103617

Susanti, I., Pratiwi, R., Rosandi, Y., and Hasanah, A. N. (2024). Separation methods of phenolic compounds from plant extract as antioxidant agents candidate. *Plants* 13 (7), 965. doi:10.3390/plants13070965

Tito, A., Massimiliano, M., Riccio, S., Grieco, F., Colucci, M. G., and Apone, F. (2020). A Triticum vulgare extract exhibits regenerating activity during the wound healing process. *Clin. Cosmet. Investigational Dermatology* 13, 21–30. doi:10.2147/ccid.s216391

Vaher, M., Matso, K., Levandi, T., Helmja, K., and Kaljurand, M. (2010). Phenolic compounds and the antioxidant activity of the bran, flour and whole grain of different wheat varieties. *Procedia Chem.* 2 (1), 76–82. doi:10.1016/j.proche.2009.12.013

Van Hung, P., Hatcher, D. W., and Barker, W. (2011). Phenolic acid composition of sprouted wheats by ultra-performance liquid chromatography (UPLC) and their antioxidant activities. *Food Chem.* 126 (4), 1896–1901. doi:10.1016/j.foodchem.2010.12.015

Van Hung, P., Maeda, T., Miyatake, K., and Morita, N. (2009). Total phenolic compounds and antioxidant capacity of wheat graded flours by polishing method. *Food Res. Int.* 42 (1), 185–190. doi:10.1016/j.foodres.2008.10.005

Vilas-Boas, A. A., Pintado, M., and Oliveira, A. L. (2021). Natural bioactive compounds from food waste: toxicity and safety concerns. *Foods* 10 (7), 1564. doi:10.3390/foods10071564

Weronika, W., Żuk, M., Sowa, I., Mazurek, B., Tyśkiewicz, K., and Wójciak, M. (2024). Recovery of bioactive components from strawberry seeds residues post oil extraction and their cosmetic potential. *Appl. Sci.* 14 (2), 783. doi:10.3390/app14020783

Xu, L., Liaqat, F., Sun, J., Khazi, M. I., Xie, R., and Zhu, D. (2024). Advances in the vanillin synthesis and biotransformation: a review. *Renew. Sustain. Energy Rev.* 189, 113905. doi:10.1016/j.rser.2023.113905

Yu, J., Vasanthan, T., and Temelli, F. (2001). Analysis of phenolic acids in barley by high-performance liquid chromatography. *J. Agric. food Chem.* 49 (9), 4352–4358. doi:10.1021/jf0013407

Zhou, K., Su, L., and Yu, L. (2004). Phytochemicals and antioxidant properties in wheat bran. *J. Agric. Food Chem.* 52 (20), 6108–6114. doi:10.1021/jf049214g

frontiers | Frontiers in Chemistry

TYPE Original Research
PUBLISHED 13 January 2025
DOI 10.3389/fchem.2024.1534132

OPEN ACCESS

EDITED BY
Serban Moldoveanu,
Independent Researcher, Greensboro,
United States

REVIEWED BY
Manivannan Madhu,
National Sun Yat-sen University, Taiwan
Kevin Honeychurch,
University of the West of England,
United Kingdom

*CORRESPONDENCE
Yong Han,
hanrong2002@163.com
Yonghong Zhu,
zyhzjy0927@163.com

RECEIVED 25 November 2024
ACCEPTED 27 December 2024
PUBLISHED 13 January 2025

CITATION
Xiang J, Cai L, Wang Q, Zhu Y and Han Y (2025) Research on detection methods of related substances and degradation products of the antitumor drug selpercatinib.
Front. Chem. 12:1534132.
doi: 10.3389/fchem.2024.1534132

Research on detection methods of related substances and degradation products of the antitumor drug selpercatinib

Jingjing Xiang[1], Liangliang Cai[2], Qin Wang[2], Yonghong Zhu[1]* and Yong Han[3]*

[1]Department of Pharmacy, Affiliated Nantong Hospital of Shanghai University (The Sixth People's Hospital of Nantong), Nantong, China, [2]Department of Pharmacy, Affiliated Hospital of Nantong University, Nantong, China, [3]Department of Oncology, Shanghai General Hospital, School of Medicine, Shanghai Jiao Tong University, Shanghai, China

Background: Selpercatinib, a selective RET kinase inhibitor, is approved for treating various cancers with RET gene mutations such as RET-rearranged thyroid cancer and non-small cell lung cancer. The presence of process-related and degradation impurities in its active pharmaceutical ingredient (API) can significantly affect its safety and effectiveness. However, research on detecting these impurities is limited.

Methods: This study developed and systematically validated a High-Performance Liquid Chromatography (HPLC) method for identifying selpercatinib and its related impurities. The method utilized a 4.6 mm × 250 mm chromatographic column with 5 μm particles, employing a flow rate of 1.0 mL/min, a detection wavelength of 235 nm, an injection volume of 10 μL, and a column temperature of 35°C. Mobile phase A was composed of a 9:1 ratio of water to acetonitrile, with the aqueous component adjusted to pH 2.5 and containing 2 mM potassium dihydrogen phosphate (KH_2PO_4) and 0.4% triethylamine. Mobile phase B was pure acetonitrile. The gradient elution program was as follows: 0–2 min, 5%B; 2–15 min, 5% to 15%B; 15–30 min, 15% to 35%B; 30–35 min, 35% to 45%B; 35–36 min, 45% to 5%B; 36–45 min, 5%B.

Results: The chromatographic method established in this study was validated according to the ICH Q2 (R1) guidelines. The developed HPLC method demonstrated excellent specificity, sensitivity, stability, linearity, precision, accuracy, and robustness. It efficiently separated the impurities present in selpercatinib, thereby confirming the method's efficacy in ensuring the purity and quality of the drug.

Conclusion: The chromatographic method established in this study can be used for the detection of selpercatinib and its impurities, providing significant reference value for the quality research of selpercatinib bulk drug and its preparations, and ensuring the safety of medication for patients.

KEYWORDS

selpercatinib, related substances, degradation products, method development, method validation, liquid chromatography

1 Introduction

Lung cancer is among the most prevalent malignant tumors globally, representing a significant threat to human health and presenting a major challenge to public health (Bade and Cruz, 2020; Zhang et al., 2023). According to the most recent statistics from the International Agency for Research on Cancer (IARC) of the World Health Organization (WHO), lung cancer ranked first in both incidence and mortality rates among 36 types of cancer across 185 countries in 2022, underscoring its extensive impact and peril (Bray et al., 2024). Among the various subtypes of lung cancer, non-small cell lung cancer (NSCLC) is the most prevalent, comprising approximately 85%–90% of all lung cancer cases (Pretelli et al., 2023; Restrepo et al., 2024). Consequently, research directed toward non-small cell lung cancer has emerged as a critical area of investigation within the field of oncology.

Currently, the primary treatment strategies for non-small cell lung cancer include surgical intervention, radiotherapy, chemotherapy, immunotherapy, and targeted therapy (Visa et al., 2024). Surgical treatment is generally applicable to patients diagnosed at an early stage, while radiotherapy is primarily used to control the growth of localized tumors. Although chemotherapy is widely utilized in advanced cases, its detrimental effects on normal cells can lead to severe side effects, significantly reducing the patient's quality of life (Liu et al., 2020; Purushothaman et al., 2020). In contrast, targeted therapy is increasingly emphasized in the medical community due to its high specificity. Targeted therapy is designed to target specific molecules or genetic mutations within cancer cells, and compared to traditional chemotherapy, its advantages include enhanced treatment efficacy, improved patient tolerance, reduced recurrence rates, and minimized side effects (Crintea et al., 2023; Cui et al., 2021). Common targeted drugs currently include EGFR inhibitors, ALK inhibitors, KRAS inhibitors, and RET inhibitors (Cooper et al., 2022; Griesinger et al., 2022; Nakajima et al., 2022; Shi et al., 2022).

RET is a transmembrane glycoprotein receptor tyrosine kinase encoded by the RET proto-oncogene, which is located on chromosome 10 (Servetto et al., 2022). This protein comprises three components: an extracellular domain, a transmembrane domain, and an intracellular tyrosine kinase domain responsible for catalytic activity. This structural configuration of the transmembrane protein facilitates the effective transmission of signals between the cell's interior and exterior. When pathogenic mutations arise in the RET gene (e.g., point mutations, gene rearrangements, fusions), RET proteins may exhibit abnormal activities that transmit aberrant signals, resulting in altered cellular behaviors such as growth, survival, invasion, and metastasis. Prolonged signaling may ultimately contribute to tumor development and progression. RET mutations have been identified in various cancer types, including medullary thyroid cancer, papillary thyroid cancer, and lung cancer—particularly non-small cell lung cancer, where RET rearrangements account for approximately 1%–2% of cases (Thein et al., 2021; Tiurin et al., 2023). At present, the treatment of lung cancers exhibiting RET alterations primarily concentrates on the development of targeted therapies. For instance, RET inhibitors, including pralsetinib and selpercatinib (also referred to as LOXO-292), have been approved for the treatment of RET fusion-positive or mutant non-small cell lung cancer (Griesinger et al., 2022; Wright, 2020).

Selpercatinib is an orally administered selective RET (rearranged during transfection) kinase inhibitor that effectively inhibits the activity of RET and its downstream phosphorylated molecules, thereby blocking cell proliferation induced by RET gene mutations (Majeed et al., 2021). Compared to previously approved multi-kinase inhibitors, selpercatinib exhibits significantly enhanced selectivity for RET, enabling more precise inhibition of cell proliferation associated with RET gene mutations. Furthermore, selpercatinib can inhibit both primary and secondary mutations, positioning it as a potential solution to address clinical drug resistance.

Currently, research on selpercatinib primarily focuses on its clinical efficacy and safety in the treatment of non-small cell lung cancer (Cheng et al., 2024; Drilon et al., 2023). At the same time, studies have employed high-performance liquid chromatography-tandem mass spectrometry (HPLC-MS/MS) to measure plasma drug concentrations in patients administered selpercatinib (Gulikers et al., 2023). Furthermore, researchers, such as Katta and Divya, have primarily focused on studying the impurities produced during forced degradation of selpercatinib and identifying their structures using liquid chromatography-mass spectrometry (LC-MS). The high-performance liquid chromatography (HPLC) method they established is only used for detecting degradation impurities with higher contents, while neglecting the separation of degradation products with unknown structures and process impurities (Katta and Thakre, 2024; Divya et al., 2024). Notably, there are currently relatively few studies on the detection of process impurities and their degradation impurities (including both known and unknown structures) in selpercatinib active pharmaceutical ingredients (API) using HPLC. Related substances in the API, including process-related impurities and degradation products, directly affect the safety and efficacy of the drug and are critical factors in pharmaceutical production and quality control. Consequently, the development of analytical methods for detecting selpercatinib and its impurities is of paramount importance.

HPLC is a widely utilized analytical technique known for its high sensitivity, high selectivity, broad applicability, accurate quantification capability, and cost-effectiveness. Currently, HPLC technology remains a commonly used method for detecting related substances in active pharmaceutical ingredients (API) (Ni et al., 2022; Zhu et al., 2024). Moreover, the majority of pharmacopoeias globally, including the United States Pharmacopeia, European Pharmacopoeia, Chinese Pharmacopoeia, Japanese Pharmacopoeia, and British Pharmacopoeia, designate liquid chromatography as the preferred analytical method for detecting related substances in APIs. At present, research regarding the detection of related substances in the API of selpercatinib remains limited. Given the potential impact of process-related impurities and degradation products in the API on the efficacy and safety of selpercatinib, there is an urgent need to develop a method capable of simultaneously detecting both process-related impurities and degradation products in selpercatinib.

In this study, we successfully established and implemented a validated reversed-phase high-performance liquid chromatography (RP-HPLC) method for the detection of related substances in selpercatinib. This method is characterized by its simplicity, sensitivity, accuracy, and robustness, particularly in effectively

separating compounds associated with selpercatinib, including impurities and degradation products generated during the manufacturing process (imp-A, imp-B, imp-C, imp-D). Subsequently, we conducted a comprehensive evaluation of the method to assess its specificity, sensitivity, solution stability, linearity, precision, accuracy, and robustness. Furthermore, we evaluated key parameters such as the limit of quantitation (LOQ), limit of detection (LOD), linearity, and recovery of the RP-HPLC method. In conclusion, the RP-HPLC method established in this study is suitable for the detection of related substances in selpercatinib, providing essential assurance regarding the safety and efficacy of the drug.

2 Materials and methods

2.1 Chemicals and reagents

Selpercatinib and its known impurities (imp-A, imp-B, imp-C and imp-D) were sourced from Aladdin Chemical Reagents Co., LTD. (Beijing, China). HPLC-grade acetonitrile (ACN) and methanol (MeOH) were obtained from Anaqua Chemicals Supply Co., Ltd. (Wilmington, United States).

2.2 Instruments

During the method development and validation process, two primary pieces of equipment were utilized: an Agilent 1200 HPLC system equipped with a UV detector, and a Shimadzu LC-20AD system with a Photodiode Array Detector.

2.3 HPLC conditions

Selpercatinib and its impurities were separated using a chromatographic column (4.6 mm × 250 mm, 5 μm) with a flow rate of 1.0 mL/min. The experiment was conducted with a detection wavelength of 235 nm, an injection volume of 10 μL, and a column temperature of 35°C. Mobile phase A was composed of water and acetonitrile in a 9:1 ratio, with the aqueous component adjusted to pH 2.5, containing 2 mM potassium dihydrogen phosphate (KH_2PO_4) and 0.4% triethylamine. In contrast, mobile phase B consisted solely of ACN. The gradient elution program was as follows: 0–2 min, 5%B → 5%B; 2–15 min, 5%B → 15%B; 15–30 min, 15%B → 35%B; 30–35 min, 35%B → 45%B; 35–36 min, 45%B → 5%B; 36–45 min, 5%B → 5%B.

2.4 Preparation of stock solution

2.4.1 Preparation of selpercatinib stock solution

Approximately 10 mg of selpercatinib was accurately weighed and transferred into a 20 mL volumetric flask. Subsequently, 15 mL of a 50% aqueous methanol solution was added to the flask and ultrasonic treatment was employed to dissolve the selpercatinib. The solution was then diluted with the 50% methanol solution to the calibration line to obtain the stock solution of selpercatinib.

2.4.2 Preparation of selpercatinib–related substance stock solutions

Approximately 10 mg of each of the four impurities of selpercatinib (Impurities A, B, C, D) was accurately weighed and placed into five separate 20 mL volumetric flasks. Subsequently, 15 mL of 50% methanol aqueous solution was added to each flask, and the impurities were dissolved using ultrasonication. The solutions were then diluted to the calibration mark with the 50% methanol aqueous solution to prepare the stock solutions of each impurity.

2.5 Preparation of mixed solutions and system suitability solutions

Selpercatinib, weighting precisely 10 mg, was accurately weighed and transferred it into a 20 mL volumetric flask. Then, the compound was dissolved in 10 mL of methanol using ultrasonication to ensure complete dissolution. Subsequently, 10 mL of 1 M hydrochloric acid (HCl) solution was added. Following this, the resulting mixture was heated at 80°C for 3 h. After the reaction is complete, the mixture was neutralized with 1 M sodium hydroxide (NaOH) solution. Next, the mixture was diluted with 50% aqueous methanol to a total volume of 20 mL, thereby obtaining the acidic degradation products.

In the same way, a further 10 mg of selpercatinib was precisely measured and placed into a different 20 mL volumetric flask. The compound was dissolved in 10 mL of methanol via ultrasonication. After achieving complete dissolution, 10 mL of 15% hydrogen peroxide solution was added. The flask was maintained in a 70°C water bath and maintain the reaction for 3 h. Upon completion of the reaction, manganese dioxide was added to terminate the reaction, and the mixture was subsequently filtered to remove the manganese dioxide. The system suitability solution was then prepared by mixing equal proportions of the aforementioned acid degradation solution and oxidative degradation solution.

2.6 Preparation of the sample solution

To prepare the sample solution, precisely 10 mg of selpercatinib was weighed and transferred into a 20 mL volumetric flask. Subsequently, 15 mL of a 50% aqueous methanol solution was measured and employed to dissolve the selpercatinib through ultrasonic treatment. Following this, the solution was further diluted with 50% aqueous methanol to the mark, resulting in a sample solution with a concentration of approximately 0.5 mg/mL.

3 Results and discussion

3.1 Method development

The synthetic route for selpercatinib is derived from the patent (WO 2018/071447A1). As illustrated in Supplementary Figure S1, the synthesis process comprises six primary steps, resulting in five intermediates. Based on the intermediates generated during the synthesis of selpercatinib and the results of their degradation

10.3389/fchem.2024.1534132

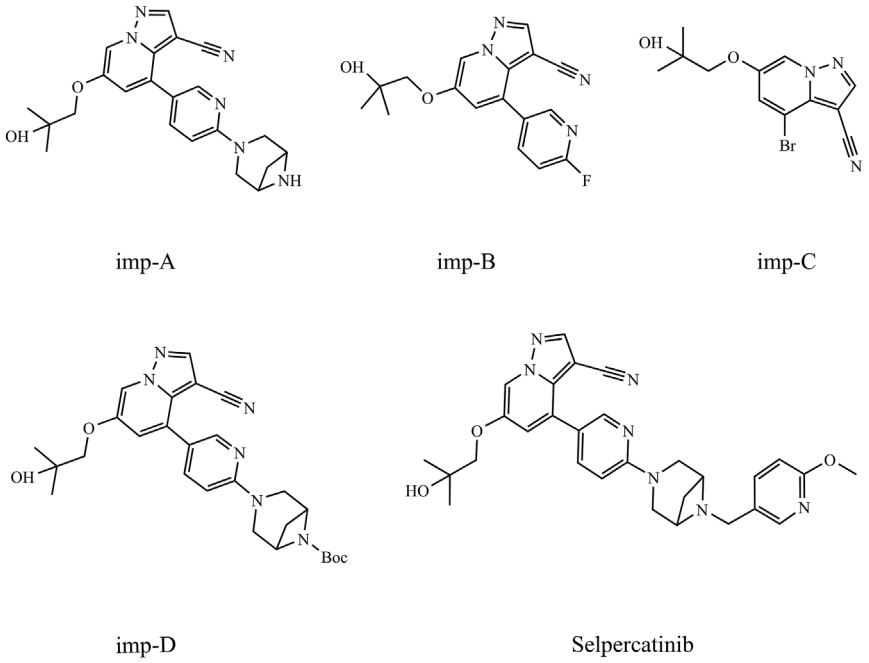

FIGURE 1
Chemical structures of selpercatinib and its known impurities.

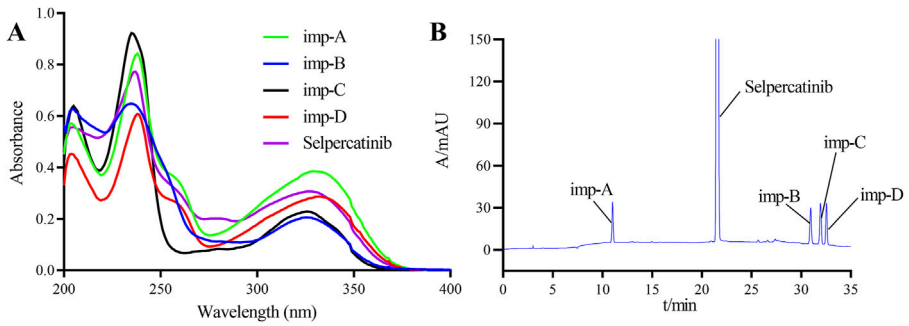

FIGURE 2
Ultraviolet spectrogram **(A)** and chromatogram **(B)** of selpercatinib and its known impurities.

experiments, this study primarily investigates four impurities, namely imp-A, imp-B, imp-C, and imp-D, whose structures are depicted in Figure 1.

It is noteworthy that during the production, storage, and transportation of selpercatinib, other degradation impurities, including unknown impurities, may be generated. The formation of these unknown impurities can be studied through forced degradation testing of the selpercatinib. Accordingly, this study aims to establish a RP-HPLC method for the simultaneous detection of known impurities and potential unknown impurities in selpercatinib.

To establish this detection method, we investigated the effects of detection wavelength, mobile phase composition, and elution mode on the separation of samples. To determine the optimal detection wavelength, the standard stock solution of selpercatinib and the stock solutions of its known impurities were diluted 50-fold, and subsequently scanned and analyzed using a UV-Vis spectrophotometer in the wavelength range of 200–400 nm. Figure 2A illustrates the UV spectra of selpercatinib and its known impurities. The results indicated that selpercatinib and its impurities exhibited two primary absorption peaks within the 200–400 nm range, located at 235 nm and 330 nm, respectively. Among these, at a wavelength of 235 nm, selpercatinib and its impurities exhibited stronger absorption and higher response signals, therefore, we determined the optimal detection wavelength to be 235 nm.

Given the high number of impurities present in the system suitability solution and the existence of difficult-to-separate impurity peak pairs, this solution was selected as the target for method development. Considering the presence of basic groups such

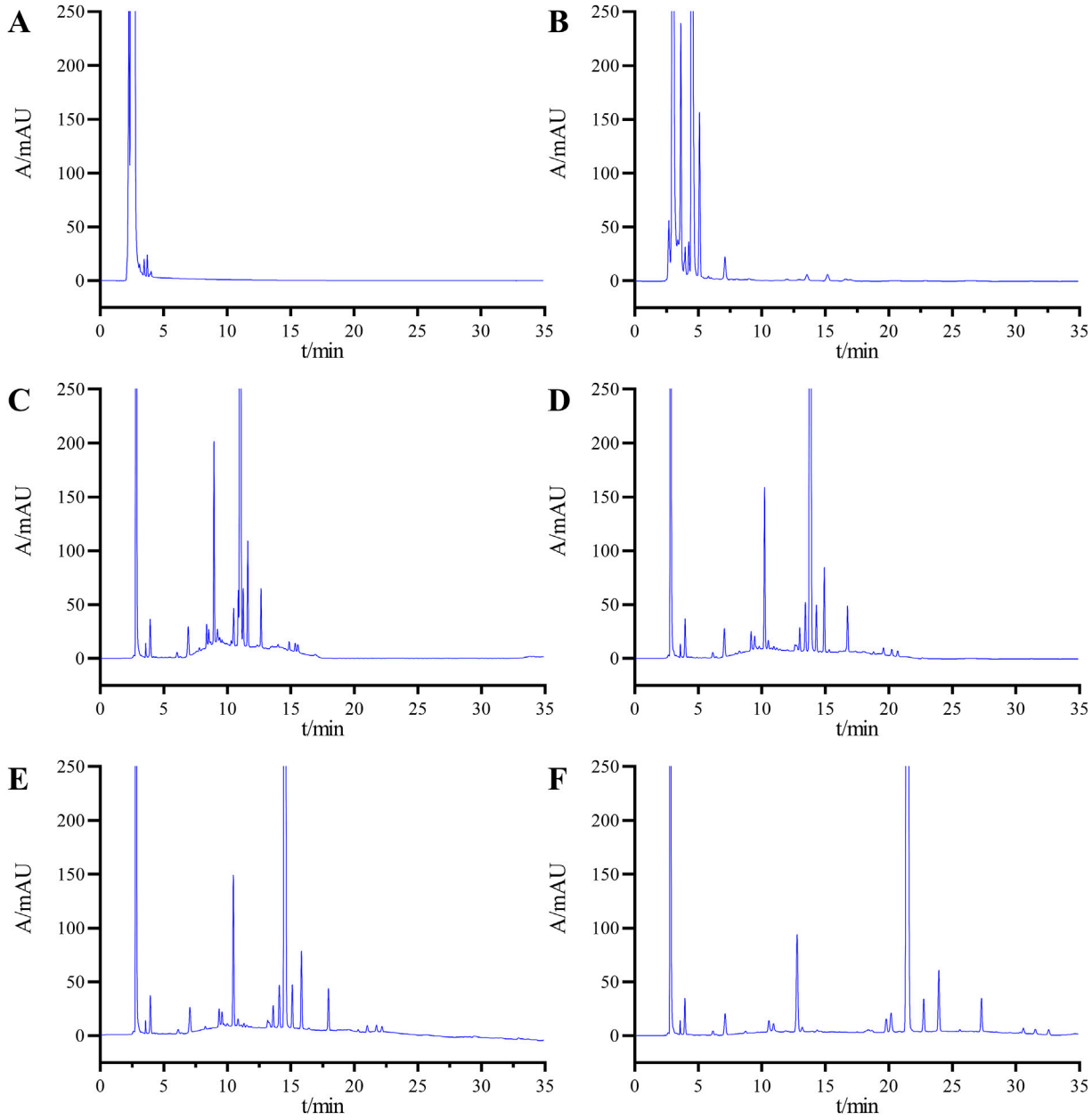

FIGURE 3
Chromatograms obtained during the optimization of the HPLLC conditions: mobile phase B and mobile phase A at ratios of 70:30 **(A)** and 30:70 **(B)**; **(C)** gradient elution condition 1; **(D)** gradient elution condition 2; **(E)** gradient elution Condition 3, and **(F)** final determined gradient elution condition.

as secondary and tertiary amines in the structures of selpercatinib and its impurities, the samples exhibit weakly basic characteristics. Based on this, we prioritized the use of phosphate solutions with buffering capabilities when selecting the mobile phase. However, during preliminary experiments, we observed tailing of the chromatographic peaks. To mitigate this phenomenon, triethylamine was added to the buffer solution. After multiple trials and optimizations, we ultimately determined the following mobile phase conditions: Mobile phase A consists 2 mmol/L KH_2PO_4 (containing 0.4% triethylamine, pH adjusted to 2.5), and contains 10% of ACN. Mobile phase B consists of ACN.

In selecting the elution method, we initially attempted an isocratic elution approach, specifically testing with mobile phase B and mobile phase A at ratios of 70:30 and 30:70, respectively. However, the chromatograms (Figures 3A,B) revealed significant overlap among the impurity peaks, and the resolution between impurities and the main peak did not meet the specified standard requirements. Given the high number of impurities with similar polarities in the system suitability solution, the isocratic elution method was found to be insufficient for achieving the desired separation effect. Consequently, we transitioned to a gradient elution scheme for further optimization attempts.

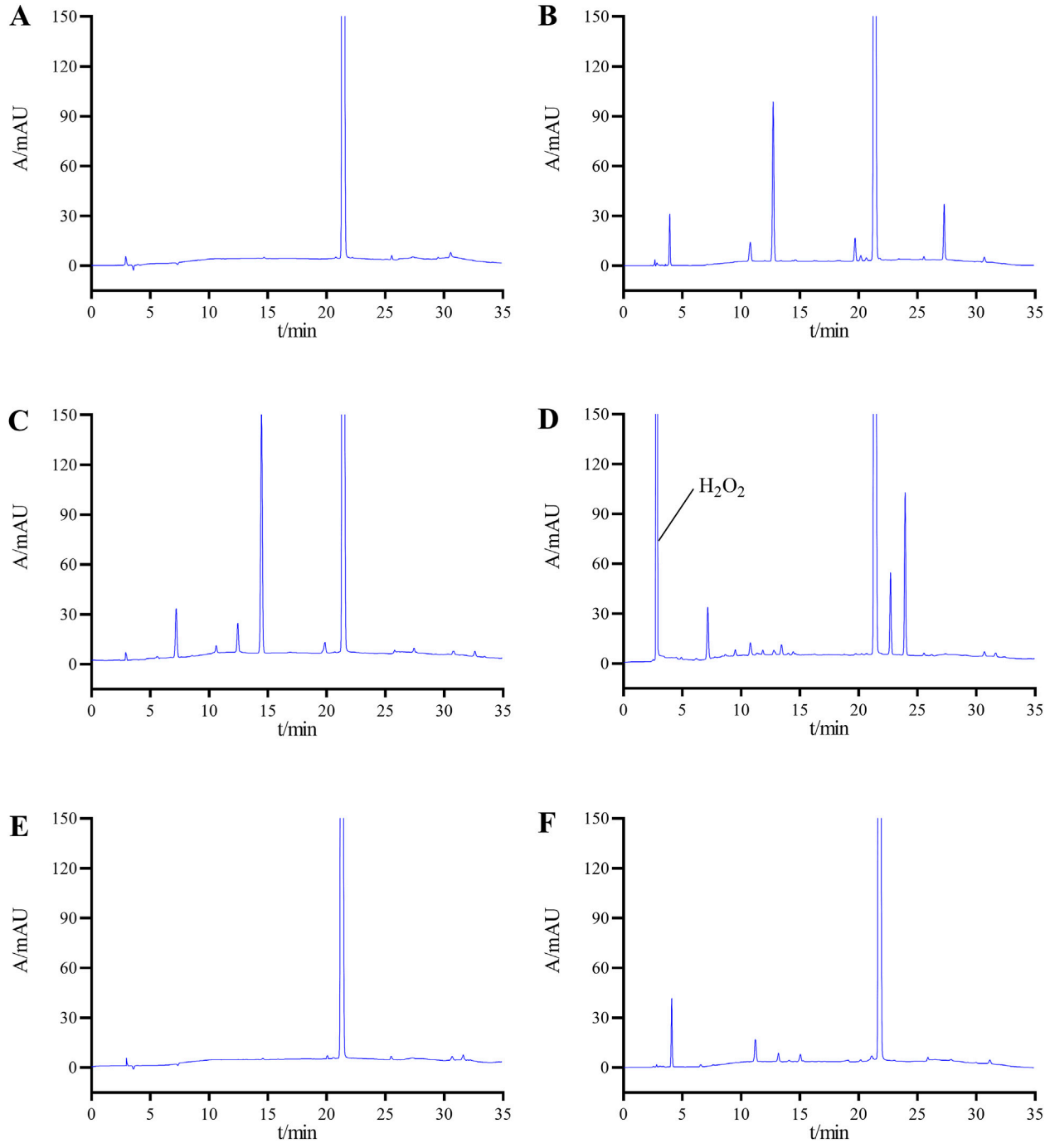

FIGURE 4
Chromatograms of selpercatinib under various degradation conditions: **(A)** undegradation; **(B)** acid-induced degradation; **(C)** base-induced degradation; **(D)** oxidative degradation; **(E)** heat degradation; **(F)** photolytic degradation.

Initially, we applied Gradient Condition 1 with the following time and composition adjustments: 0–2 min at 10%B, 2–20 min transitioning from 10%B to 90%B, 20–30 min maintaining 90%B, 30–30.1 min reverting from 90%B to 10%B, and 30.1–40 min at 10% B. As shown in Figure 3C, under this condition, the minimum resolution between impurities was 1.15, and the resolution between impurities and the main peak was 1.85, both of which failed to meet the specified requirements.

Subsequently, we further optimized the elution process by reducing the gradient change rate. We analyzed the samples using two novel gradient conditions: Gradient Condition 2, which follows the sequence 0–2 min (10%B), 2–30 min (10%B to 90%B), 30–35 min (90%B), 35–35.1 min (90%B to 10%B), and 35.1–45 min (10%B) as shown in Figure 3D; and Gradient Condition 3, which follows 0–2 min (20%B), 2–30 min (20%B to 75%B), 30–35 min (75%B), 35–35.1 min (75%B to 20%B), and 35.1–45 min

TABLE 1 Results of forced degradation tests.

Forced degradation condition	Number of impurities (>0.03%)	Content of main peak (%)	Minimum resolution between main peak and impurities	Minimum resolution among impurities	Mass balance (%)
Undegradation	3	99.74	2.30	4.48	100
Acid degradation	9	92.45	2.65	1.89	97.53
Base degradation	8	90.08	5.83	6.86	98.22
Oxidative degradation	11	90.16	6.04	2.21	97.06
Heat degradation	4	99.12	4.89	3.66	99.37
Photolytic degradation	7	97.63	2.19	7.33	98.64

(20%B) as depicted in Figure 3E. Following multiple optimization rounds, the chromatographic conditions outlined in Section 2.3 were finalized as the analytical method for sample detection. Under these conditions, the chromatogram achieved a minimum resolution of 1.62 between impurities and 4.95 between impurities and the main peak, both meeting detection standards (Figure 3F).

3.2 Method validation

The International Council for Harmonisation of Technical Requirements for Pharmaceuticals for Human Use (ICH) guideline Q2 (R1) (Group, 2005) and existing literature reports were used to guide the validation of the test method for related substances in selpercatinib (Padivitage et al., 2023).

3.2.1 Specificity

Accurately pipette 10 μL of the solvent, mixed impurity solution, and system suitability solution, respectively, and inject them into the liquid chromatograph. Conduct the sample injection analysis according to the chromatographic conditions specified in Section 2.3. The chromatogram of the mixed impurity solution is shown in Figure 2B, and the retention times of selpercatinib and its respective impurities are as follows: imp-A at 10.7988 min, selpercatinib at 21.373 min, imp-B at 30.422 min, imp-C at 31.355 min, and imp- D at 32.554 min. The minimum resolution between impurities is known to be 2.15, and the minimum resolution between impurities and selpercatinib is 28.78, both of which meet the experimental requirements (>1.5).

Figure 3F presents the system suitability chromatogram. The results indicate that the minimum resolution between the main peak and adjacent impurity peaks was 4.95, the minimum resolution between known impurities and adjacent peaks was 1.72, and the minimum resolution between unknown impurities and adjacent peaks was 1.62. All these values met the experimental requirements. In summary, these results demonstrated that the method exhibited good specificity.

3.2.2 Forced degradation experiments

The forced degradation tests for selpercatinib were primarily conducted under five conditions: acidic, alkaline, oxidative, high temperature, and photolytic. The specific conditions are as follows: Acidic degradation: Accurately weigh approximately 10 mg of selpercatinib into a 20 mL volumetric flask. Subsequently, measure 10 mL of methanol and dissolve the sample using ultrasound. Afterward, add 5 mL of 1 mol/L hydrochloric acid solution and heat at 70°C for 5 h. Once the reaction is complete, neutralize to neutrality using a 1 mol/L sodium hydroxide solution, and dilute with 50% methanol aqueous solution to the mark. Alkaline degradation: The procedure is similar to acidic degradation, but instead, use a 1 mol/L sodium hydroxide solution and heat at 50°C for 2 h. Oxidative Degradation: Use a 5% hydrogen peroxide solution and react at 50°C for 48 h. High Temperature Degradation: Firstly, weigh an appropriate amount of selpercatinib and place it in an oven set at 100°C for 6 days. Then, weigh 10 mg of selpercatinib and prepare a solution of 0.5 mg/mL concentration using 50% methanol solution. Photolytic degradation: Accurately measure 10 mg of selpercatinib and dissolve it to achieve a concentration of 0.5 mg/mL in a solvent composed of 50% methanol. Following preparation, subject the resultant solution to continuous illumination from an LED light source with an intensity of 4,500 lux for a duration of 30 days.

Figure 4 displays the chromatograms from the forced degradation study of selpercatinib. Table 1 presents the stability outcomes of selpercatinib under diverse forced degradation conditions, considering impurity count, main peak content, minimum resolution between the principal component and impurities, resolution among impurities, and mass balance. The results indicate that selpercatinib exhibits remarkable stability under high temperature and light exposure conditions, whereas it is prone to degradation under acidic, alkaline and oxidative conditions. Notably, despite the varying degradation conditions, the minimum resolution between the main peak and impurities exceeds 1.5, and the minimum resolution among impurities exceeds 1.2, both of which are in compliance with the established criteria. Additionally, the mass balance rate remains within the range of 95%–105%, which is generally considered an important standard for mass balance.

3.2.3 Sensitivity

The sensitivity of the method is evaluated by determining LOD and LOQ. The stock solutions of selpercatinib and its known impurities are diluted stepwise, followed by the calculation of signal-to-noise ratios. The corresponding concentrations are determined as LOD and LOQ when the signal-to-noise ratios reach 3:1 and 10:1, respectively. The results show that the LOD for selpercatinib and its known impurities (imp-A, imp- B, imp- C, imp-D) were 0.0022, 0.0020, 0.0030, 0.0020, and 0.0030 μg/mL, respectively, while the LOQ values were 0.0065, 0.0060, 0.0085, 0.0065, and 0.0090 μg/mL, respectively.

10.3389/fchem.2024.1534132

TABLE 2 Recovery of know impurities in selpercatinib.

Substance	Target level	Spiked conc. (μg/mL)	Determined conc. (μg/mL)	Recovery (%)	Average recovery rate (%)	RSD (%)
imp-A	50%	0.511	0.508	99.41	99.53	2.42
		0.511	0.528	103.33		
		0.511	0.499	97.65		
	100%	1.021	1.052	103.04		
		1.021	0.992	97.16		
		1.021	1.032	101.08		
	150%	1.532	1.516	98.96		
		1.532	1.492	97.39		
		1.532	1.498	97.78		
imp-B	50%	0.508	0.495	97.44	99.29	2.15
		0.508	0.512	100.79		
		0.508	0.499	98.23		
	100%	1.016	0.998	98.23		
		1.016	1.029	101.28		
		1.016	0.986	97.05		
	150%	1.524	1.506	98.82		
		1.524	1.497	98.23		
		1.524	1.578	103.54		
imp-C	50%	0.506	0.495	97.83	97.40	1.84
		0.506	0.487	96.25		
		0.506	0.511	100.99		
	100%	1.012	0.995	98.32		
		1.012	0.975	96.34		
		1.012	0.968	95.65		
	150%	1.518	1.455	95.85		
		1.518	1.462	96.31		
		1.518	1.504	99.08		
imp-D	50%	0.517	0.523	101.16	98.11	2.09
		0.517	0.508	98.26		
		0.517	0.493	95.36		
	100%	1.034	1.008	97.49		
		1.034	0.992	95.94		
		1.034	1.026	99.23		
	150%	1.551	1.493	96.26		
		1.551	1.529	98.58		
		1.551	1.562	100.71		

3.2.4 Stability of the solution

The stability of the selpercatinib sample solution was evaluated by analyzing samples at various time points: 0, 2, 4, 6, 8, 12, and 24 h. The primary focus was on changes in the number of impurities, the maximum content of individual impurities, and the total impurity content. The results of these analyses are detailed in Supplementary Table S1. The results indicate that after leaving the selpercatinib sample solution at room temperature for 24 h, there was no change in the number of impurities, and only minimal changes were observed in the maximum content of individual impurities and the total impurity content. This suggests that the sample remains stable at room temperature for 24 h.

Regarding the solution stability of known impurity samples, the solutions containing known impurities were placed at room temperature, and samples were analyzed at various time points. The results showed that the relative standard deviations (RSDs) of the peak areas for selpercatinib and its known impurities A, B, C, and D were 1.05%, 1.37%, 1.26%, and 1.68%, respectively, all of which were below the predetermined threshold of 2%. These results indicate that solutions containing these impurities remain stable within 24 h.

3.2.5 Linearity and range

This study investigated the linearity of selpercatinib and its known impurities within a range from the LOQ to 2% of the target concentration (0.5 mg/mL was defined as 100%). The stock solutions of selpercatinib and its known impurities were diluted with 50% aqueous methanol to produce test solutions at various concentrations (0.1, 0.5, 1, 2, 5, 8, 10 μg/mL), which were then injected and analyzed according to the chromatographic conditions outlined in Section 2.3. A standard curve was generated by plotting the concentration (*X*-axis) against the peak area (*Y*-axis), and the regression equation was calculated. The linear regression equations, and correlation coefficients for selpercatinib and its known impurities were presented below: Selpercatinib: y = 58.69x-2.133, r = 0.9994; imp-A: y = 59.92x-3.084, r = 0.9988; imp-B: y = 51.55x-2.071, r = 0.9993; imp-C: y = 63.59x-6.156, r = 0.9987; imp-D: y = 50.57x-3.241, r = 0.9991. Within a range from the LOQ to 2% of the target concentration (0.5 mg/mLwas defined as 100%), all correlation coefficients exceeded 0.99.

3.2.6 Precision

Take 10 μL of the mixed solution described in "2.5"and analyze it under the chromatographic conditions specified in item "2.3". Inject the sample continuously for 6 times to evaluate the precision of the instrument. The results showed that the RSDs of the retention time for selpercatinib and its known impurities (Impurities A, B, C, D) were 0.29%, 0.16%, 0.22%, 0.19%, and 0.15%, respectively. Similarly, the RSDs of peak areas were determined to be 0.75%, 0.86%, 1.08%, 0.68%, and 1.29%, respectively. Notably, all RSD values were less than 2%, indicating good precision of the instrument.

3.2.7 Repeatability

To assess the repeatability of the method, six samples containing known impurities were prepared in parallel. Analysis was then conducted according to the chromatography conditions outlined in Section 2.3. The results showed that the RSDs for impurities A, B, C, and D were 1.18%, 1.07%, 0.95%, and 1.22%, respectively. All these results were below the threshold of 2%, indicating that the method possessed good repeatability.

3.2.8 Accuracy

This study tested the recovery rates of known impurities (imp-A, imp-B, imp-C, imp-D) in selpercatinib at three different concentration levels (50%, 100%, 150%), with a reference concentration of approximately 1 μg/mL set as the 100% level. To achieve the desired concentration levels, varying volumes of stock solutions containing the known impurities were added to the selpercatinib sample solutions. Triplicate samples were prepared for each concentration level, analyzed according to the chromatographic conditions described in Section 2.3, and the recovery rates were subsequently calculated. As shown in Table 2, the recovery of all known impurities fell within the range of 90%–110%, and the RSD values for these compounds were all below 2.0%. These results clearly demonstrate the high accuracy of the method employed in this study.

3.2.9 Robustness

The robustness of the method was evaluated by small but deliberate changes to HPLC parameters including column temperature (±5°C), flow rate (±0.1 mL/min), detector wavelength (±5 nm), %B at initial change (±1%) and chromatographic columns from different manufacturers.

The minimum resolution between selpercatinib and known impurities, as well as adjacent impurities, exceeded 1.5, while the minimum resolution between unknown impurities was greater than 1.2. Both of these values fulfilled the validation requirements. Additionally, there was no significant change in the number and content of impurities. This results indicated that the method developed in this study demonstrated good robustness.

4 Conclusion

In this study, we developed a HPLC method specifically for detecting substances associated with the non-small cell lung cancer treatment drug selpercatinib, including process impurities and degradation impurities. Additionally, we conducted a comprehensive validation of this detection method, which demonstrated excellent performance in specificity, sensitivity, linearity, precision, accuracy and robustness. Therefore, the chromatographic method established in this study is of great significance for ensuring the quality of selpercatinib and enhancing the safety and efficacy of its use.

Data availability statement

The original contributions presented in the study are included in the article/Supplementary Material, further inquiries can be directed to the corresponding authors.

Author contributions

JX: Conceptualization, Formal Analysis, Investigation, Writing–original draft. LC: Formal Analysis, Methodology, Validation, Writing–original draft. QW: Investigation, Software,

Formal Analysis, Methodology, Writing–original draft. YZ: Funding acquisition, Project administration, Resources, Writing–review and editing. YH: Conceptualization, Project administration, Resources, Writing–review and editing.

Funding

The author(s) declare that financial support was received for the research, authorship, and/or publication of this article. This work was financially supported by Science and Technology Program of Nantong Municipal Health Commission (no. MS2022086) and Nantong Pharmaceutical Policy and Pharmaceutical Care Research Project (no.2023NTPA12).

Conflict of interest

The authors declare that the research was conducted in the absence of any commercial or financial relationships that could be construed as a potential conflict of interest.

Generative AI statement

The author(s) declare that no Generative AI was used in the creation of this manuscript.

Publisher's note

Supplementary material

The Supplementary Material for this article can be found online at: https://www.frontiersin.org/articles/10.3389/fchem.2024.1534132/full#supplementary-material

References

Bade, B. C., and Cruz, C. S. (2020). Lung cancer 2020: epidemiology, etiology, and prevention. *Clin. Chest Med.* 41 (1), 1–24. doi:10.1016/j.ccm.2019.10.001

Bray, F., Laversanne, M., Sung, H., Ferlay, J., Siegel, R. L., Soerjomataram, I., et al. (2024). Global cancer statistics (2022). GLOBOCAN estimates of incidence and mortality worldwide for 36 cancers in 185 countries. *CA Cancer J. Clin.* 74 (3), 229–263. doi:10.3322/caac.21834

Cheng, Y., Loong, H. H., Zhou, C., Nishino, K., Lee, D. H., Lee, S. H., et al. (2024). Efficacy and safety of 1L selpercatinib in RET fusion-positive NSCLC: LIBRETTO-431 East Asian subgroup analysis. *J. Clin. Oncol.* 42, 214. doi:10.1200/JCO.2024.42.23_suppl.214

Cooper, A. J., Sequist, L. V., and Lin, J. J. (2022). Third-generation EGFR and ALK inhibitors: mechanisms of resistance and management. *Nat. Rev. Clin. Oncol.* 19 (8), 499–514. doi:10.1038/s41571-022-00639-9

Crintea, A., Motofelea, A. C., Sovrea, A. S., Constantin, A. M., Crivii, C. B., Carpa, R., et al. (2023). Dendrimers: advancements and potential applications in cancer diagnosis and treatment-an overview. *Pharmaceutics* 15 (5), 1406. doi:10.3390/pharmaceutics15051406

Cui, G., Wu, J., Lin, J., Liu, W., Chen, P., Yu, M., et al. (2021). Graphene-based nanomaterials for breast cancer treatment: promising therapeutic strategies. *J. Nanobiotechnology* 19 (1), 211. doi:10.1186/s12951-021-00902-8

Divya, B., Prakash, J. M., Chiranjeevi, E. V., and Tadiboina, B. R. (2024). Evaluation of the genotoxic impurities of selpercatinib through HPLC and LCMS/MS identification of selpercatinib stress degradation products. *FABAD J. Pharm. Sci.* 49 (3), 449–464. doi:10.55262/fabadeczacilik.1394869

Drilon, A., Subbiah, V., Gautschi, O., Tomasini, P., de Braud, F., Solomon, B. J., et al. (2023). Selpercatinib in patients with RET fusion-positive non-small-cell lung cancer: updated safety and efficacy from the registrational LIBRETTO-001 phase I/II trial. *J. Clin. Oncol.* 41 (2), 385–394. doi:10.1200/JCO.22.00393

Griesinger, F., Curigliano, G., Thomas, M., Subbiah, V., Baik, C. S., Tan, D. S. W., et al. (2022). Safety and efficacy of pralsetinib in RET fusion-positive non-small-cell lung cancer including as first-line therapy: update from the ARROW trial. *Ann. Oncol.* 33 (11), 1168–1178. doi:10.1016/j.annonc.2022.08.002

Group, I. E. W. (2005). International Conference on Harmonisation of technical requirements for registration of pharmaceuticals for human use. *Valid. Anal. Proced. Text. Methodol. Q2R1.*

Gulikers, J. L., van Veelen, A. J., Sinkiewicz, E. M. J., de Beer, Y. M., Slikkerveer, M., Stolk, L. M. L., et al. (2023). Development and validation of an HPLC-MS/MS method to simultaneously quantify brigatinib, lorlatinib, pralsetinib and selpercatinib in human K2-EDTA plasma. *Biomed. Chromatogr.* 37 (6), e5628. doi:10.1002/bmc.5628

Katta, S. R., and Thakre, G. (2024). Characterization of degradation products of selpercatinib by mass spectrometry: optimization of stability-indicating HPLC method for separation and quantification of process related impurities of selpercatinib. *Asian J. Chem.* 36 (2), 341–352. doi:10.14233/ajchem.2024.30884

Liu, Y., Huang, W., and Cai, Z. (2020). Synthesizing AND gate minigene circuits based on CRISPReader for identification of bladder cancer cells. *Nat. Commun.* 11 (1), 5486. doi:10.1038/s41467-020-19314-7

Majeed, U., Manochakian, R., Zhao, Y., and Lou, Y. (2021). Targeted therapy in advanced non-small cell lung cancer: current advances and future trends. *J. Hematol. Oncol.* 14 (1), 108. doi:10.1186/s13045-021-01121-2

Nakajima, E. C., Drezner, N., Li, X., Mishra-Kalyani, P. S., Liu, Y., Zhao, H., et al. (2022). FDA approval summary: sotorasib for KRAS G12C-mutated metastatic NSCLC. *Clin. Cancer Res.* 28 (8), 1482–1486. doi:10.1158/1078-0432.CCR-21-3074

Ni, R., Du, X., Huang, R., Wu, W., Xu, J., Ma, X., et al. (2022). Development and validation of a reversed-phase high-performance liquid chromatography-ultraviolet method for abemaciclib-related substance detection in bulk drugs. *J. Sep. Sci.* 45 (22), 4070–4078. doi:10.1002/jssc.202200551

Padivitage, N., Tian, J., Wang, L., Zhuang, J., McAdoo, A., Zhao, D., et al. (2023). Development and validation of a stability-indicating reversed-phase HPLC method for assay and estimation of related substances of ivermectin in an oral paste. *J. Chromatogr. Sci.* 61 (2), 119–129. doi:10.1093/chromsci/bmab144

Pretelli, G., Spagnolo, C. C., Ciappina, G., Santarpia, M., and Pasello, G. (2023). Overview on therapeutic options in uncommon EGFR mutant non-small cell lung cancer (NSCLC): new lights for an unmet medical need. *Int. J. Mol. Sci.* 24 (10), 8878. doi:10.3390/ijms24108878

Purushothaman, B., Lee, J., Hong, S., and Song, J. M. (2020). Multifunctional TPP-PEG-biotin self-assembled nanoparticle drug delivery-based combination therapeutic approach for co-targeting of GRP78 and lysosome. *J. Nanobiotechnology* 18 (1), 102. doi:10.1186/s12951-020-00661-y

Restrepo, J. C., Martínez Guevara, D., Pareja López, A., Montenegro Palacios, J. F., and Liscano, Y. (2024). Identification and application of emerging biomarkers in treatment of non-small-cell lung cancer: systematic review. *Cancers (Basel)* 16 (13), 2338. doi:10.3390/cancers16132338

Servetto, A., Esposito, D., Ferrara, R., Signorelli, D., Belli, S., Napolitano, F., et al. (2022). RET rearrangements in non-small cell lung cancer: evolving treatment landscape and future challenges. *Biochim. Biophys. Acta Rev. Cancer* 1877 (6), 188810. doi:10.1016/j.bbcan.2022.188810

Shi, K., Wang, G., Pei, J., Zhang, J., Wang, J., Ouyang, L., et al. (2022). Emerging strategies to overcome resistance to third-generation EGFR inhibitors. *J. Hematol. Oncol.* 15 (1), 94. doi:10.1186/s13045-022-01311-6

Thein, K. Z., Velcheti, V., Mooers, B. H. M., Wu, J., and Subbiah, V. (2021). Precision therapy for RET-altered cancers with RET inhibitors. *Trends Cancer* 7 (12), 1074–1088. doi:10.1016/j.trecan.2021.07.003

Tiurin, V. I., Preobrazhenskaya, E. V., Mitiushkina, N. V., Romanko, A. A., Anuskina, A. A., Mulkidjan, R. S., et al. (2023). Rapid and cost-efficient detection of RET rearrangements in a large consecutive series of lung carcinomas. *Int. J. Mol. Sci.* 24 (13), 10530. doi:10.3390/ijms241310530

Visa, M. A., Abazeed, M. E., and Avella Patino, D. (2024). Integrative approaches in non-small cell lung cancer management: the role of radiotherapy. *J. Clin. Med.* 13 (15), 4296. doi:10.3390/jcm13154296

Wright, K. M. (2020). FDA approves pralsetinib for treatment of adults with metastatic RET fusion-positive NSCLC. *Oncol. (Willist. Park)* 34 (10), 406. doi:10.46883/ONC.2020.3410.0406

Zhang, Y., Vaccarella, S., Morgan, E., Li, M., Etxeberria, J., Chokunonga, E., et al. (2023). Global variations in lung cancer incidence by histological subtype in 2020: a population-based study. *Lancet Oncol.* 24 (11), 1206–1218. doi:10.1016/S1470-2045(23)00444-8

Zhu, Y., Qin, J., Wu, W., and Cai, L. (2024). Development and validation of a novel high-performance liquid chromatography (HPLC) method for the detection of related substances of pralsetinib, a new anti-lung cancer drug. *Front. Chem.* 12, 1450692. doi:10.3389/fchem.2024.1450692

frontiers | Frontiers in Chemistry

TYPE Original Research
PUBLISHED 20 January 2025
DOI 10.3389/fchem.2024.1490639

OPEN ACCESS

EDITED BY
Constantinos K. Zacharis,
Aristotle University of Thessaloniki, Greece

REVIEWED BY
Natasa P. Kalogiouri,
Aristotle University of Thessaloniki, Greece
Selva Chandrasekaran Selvaraj,
University of Illinois Chicago, United States

*CORRESPONDENCE
Iltaf Shah,
altafshah@uaeu.ac.ae
Khaled M. A. Amiri,
k.amiri@uaeu.ac.ae

RECEIVED 05 September 2024
ACCEPTED 12 December 2024
PUBLISHED 20 January 2025

CITATION
Hakeem MK, Maraqa M, Elangovan SK, Saeed EE, Mishra AK, Hazzouri KM, Shah I and Amiri KMA (2025) Innovative determination of phytohormones in *Aloe vera*. *Front. Chem.* 12:1490639. doi: 10.3389/fchem.2024.1490639

Innovative determination of phytohormones in *Aloe vera*

Muhammad K. Hakeem[1], Meera Maraqa[1], Sampath K. Elangovan[1,2], Esam Eldin Saeed[2], Ajay Kumar Mishra[2], Khaled M. Hazzouri[2], Iltaf Shah[1,2]* and Khaled M. A. Amiri[2]*

[1]Department of Chemistry, College of Science, United Arab Emirates University (UAEU), Al Ain, United Arab Emirates, [2]Khalifa Center for Genetic Engineering and Biotechnology, United Arab Emirates University, Al Ain, United Arab Emirates

Introduction: Aloe vera is widely known for its therapeutic properties, but concerns regarding the levels of phytohormones and their potential impact on human health highlight the need for advanced analytical techniques. This study aims to develop and validate a sensitive method for the determination of six key phytohormones in Aloe vera using Liquid Chromatography-Tandem Mass Spectrometry (LC-MS/MS).

Methods: A validated LC-MS/MS method was optimized for the determination and quantification of six phytohormones in Aloe vera: Abscisic Acid (ABA), Salicylic Acid (SA), Indole-3-Acetic Acid (I3AA), Gibberellic Acid (GA), 6-Benzylaminopurine (6BAP), and Isopentenyladenine (ISA). The sample extraction process and mobile phase composition were optimized to enhance chromatographic separation and mass spectrometry sensitivity. A C-18 column was used for separation, and a triple quadrupole mass spectrometer was employed for quantification. The method's performance was assessed in terms of linearity, sensitivity, and limits of detection.

Results: The LC-MS/MS method exhibited excellent linearity ($R^2 > 0.99$) and low limits of detection for all six phytohormones. Four of the six analytes were identified as predominant in Aloe vera. Quantitative analysis showed that ABA was the most abundant phytohormone, with a median concentration of 8.39 ng/mL, followed by I3AA (4.32 ng/mL), SA (3.16 ng/mL), and GA (1.55 ng/mL).

Discussion: This study provides a comprehensive and validated LC-MS/MS method for profiling phytohormones in Aloe vera. The results underscore the significant role of ABA, I3AA, SA, and GA in the plant's hormonal profile, offering a valuable tool for the analysis of phytohormonal content in Aloe vera and other plant species. The method is particularly beneficial for addressing health-related concerns regarding the presence and concentration of phytohormones in Aloe vera.

KEYWORDS

LC-MS/MS, Aloe vera, phytohormones, liquid chromatography mass spectrometry, plant hormone, method validation

Abbreviations: I3AA, Indole-3-Acetic Acid; 6BAP, 6-BenzylAminoPurine; GA, Gibberellic Acid; ISA, Isopentenyl Adenine; SA, Salicylic Acid; 2NAA, 2-Naphthalene Acetic Acid; ABA, Abscisic Acid; ng/mL, nanogram/millilitre.

Introduction

Phytohormones are natural compounds that are found in trace levels in plants. Their presence is essential in maintaining plant growth and maturation, regulating the division of cells and the differentiation of tissues, as well as controlling plant behavior because of various stimuli (Bhatt et al., 2020; Zhao et al., 2021; Pal et al., 2023; Asif et al., 2022). Phytohormones are characterized by their diverse chemical properties, but they can be poorly stable upon exposure to light or heat (Jha et al., 2022). Based on their structures and physiological functions, phytohormones are classified into six main types, entailing Auxins (Indole derived), Cytokinins (Adenine derived), Abscisic Acid (Carotenoids derived), Gibberellin (Terpene derived), Ethylene (gas derived), and Brassinosteroids (Bhatt et al., 2020; Tariq et al., 2022; Bhattacharya, 2022). Within each category, there could be several compounds with similar physiological functions. For example, Indole-3-Acetic Acid (I3AA) and 2-Naphthalene Acetic Acid (2NAA) are auxins that promote plant development in different ways, with the former promoting growth through the excessive production of roots hairs and lateral roots (Zhang et al., 2022; Etesami and Glick, 2024), while the latter is involved in the vegetative propagation of cuts in the stems or leaves (Ashok and Ravivarman, 2020; Kaviani et al., 2023). Cytokinins such as Isopentenyl Adenine Indole and 6-Benzylaminopurine play a pivotal role in regulating myriad processes associated with plant development and the cell cycle (Mangena, 2022; Butt and Gul, 2023). In addition, Abscisic Acid is a key signaling molecule in responding to a range of stimuli, involving abiotic and biotic stresses (Bharath et al., 2021; Muhammad Aslam et al., 2022). Gibberellic Acid, on the other hand, is mainly involved in activating the developmental switches in the different stages of a plant's life cycle (i.e., development from the vegetative phase to the reproductive phase) (Hernández-García et al., 2021; Katyayini et al., 2020). Moreover, Salicylic Acid not only contributes to the plant's growth but is crucial in prompting certain responses associated with plant defense (Zhong et al., 2021; Arif et al., 2020).

Aloe vera, a perennial succulent plant renowned for its diverse therapeutic properties, has captured global attention and witnessed a surge in demand within the herbal products market. It is a widely used plant that belongs to the Liliaceae family. Due to its anti-inflammatory and antimicrobial properties, Aloe vera has been utilized in traditional medicine to heal skin injuries and digestive issues (Adlakha et al., 2022; Gulati et al., 2021). Moreover, recent studies suggest its potential as an antitumor agent, further expanding its therapeutic applications (Sinha et al., 2023; Ali et al., 2020). Such therapeutic properties have advocated its extensive integration in both the pharmaceutical and the food industry (Martínez-Sánchez et al., 2020). With over 500 species of the aloe genus, only 10 species are considered of medicinal value, among which Aloe barbadensis miller is considered the most biologically active species (Leitgeb et al., 2021; Bista et al., 2020; Palaniyappan et al., 2023). The widespread use of Aloe vera in various commercial products, including cosmetics, dietary supplements, and pharmaceuticals, underscores the need for a comprehensive understanding of its chemical composition. Aloe vera's therapeutic potential is attributed to its rich chemical diversity, including polysaccharides, phenolic compounds, and bioactive molecules (Pradhan, 2023; Rajesh et al., 2023). The identification and quantification of phytohormones within Aloe vera are crucial for unraveling the intricate relationship between its chemical profile and therapeutic effects.

Phytohormones, while essential for plant physiology, have been shown to influence various physiological processes in mammals as well. For instance, compounds like salicylic acid, gibberellic acid, indole-3-acetic acid, and abscisic acid, which are found in Aloe vera, may interact with mammalian hormonal pathways, potentially affecting immune responses, metabolism, and even cancer progression (Choi and Chung, 2003; Maan et al., 2018). For instance, ABA has been shown to modulate glucose metabolism and exhibit anti-inflammatory properties, offering potential therapeutic implications for managing metabolic disorders (Gharib et al., 2024). Similarly, SA is widely recognized for its anti-inflammatory and immune-modulatory effects, which may contribute to human health when consumed through plant-based products (Thorat et al., 2023). However, excessive or imbalanced exposure to phytohormones, such as SA, could disrupt hormonal homeostasis or trigger adverse reactions, emphasizing the need for accurate and controlled quantification (Ali et al., 2024). I3AA, an auxin, has been investigated for its potential anticancer properties, with studies suggesting it may induce apoptosis in certain cancer cell lines (Phytohormones as Potential Anticancer Agents, 2024; Mukherjee et al., 2022). Meanwhile, GA has been reported to interact with mammalian signaling pathways, though its precise effects remain underexplored and warrant further investigation (Castro-Camba et al., 2022). This raises important questions about the safety and health consequences of phytohormones in Aloe vera when used in consumer products. Given the increasing incorporation of Aloe vera into products intended for human use, it is crucial to investigate its phytohormonal composition to understand the potential effects on human health. This study aims to fill this gap by systematically identifying and quantifying key phytohormones within Aloe vera, thereby providing a scientific foundation for evaluating its safety and efficacy. These findings can contribute to the development of regulatory standards and guidelines, ensuring the safety and effectiveness of Aloe vera products for consumers.

The determination of phytohormones is challenged by the extremely low concentration of these compounds in the plant tissues along with the varied concentration ranges among different plant species. Traditional methods for detecting phytohormones in plant extracts often fall short in terms of sensitivity, selectivity, and precision. In the early stage, bioassays and immunoassays were the common methods used for the determination of phytohormones (Wang et al., 2020; Jiang et al., 2020). However, these methods have been phased out due to their low sensitivity, specificity, and inability to simultaneously detect multiple plant hormones. For example, bioassays often lack the resolution required for distinguishing structurally similar compounds, while immunoassays are limited by cross-reactivity and low multiplexing capabilities. Similarly, HPLC-UV methods, while useful for single-analyte determination, fail to provide adequate sensitivity and selectivity for simultaneous analysis of diverse phytohormones in complex matrices. The inadequacies of these methods underscore the urgency of adopting advanced analytical techniques to provide more accurate and reliable

results. Significant progress in the determination of phytohormones has been witnessed in the last decade due to the advancement in the field of chromatography and mass spectroscopy (Wang et al., 2020; Recent Advances in the Chromatographic). Specifically, the integration of Liquid Chromatography-Tandem Mass Spectrometry (LC-MS/MS) emerges as a cutting-edge solution, offering unparalleled capabilities in the identification and quantification of phytohormones (Wang et al., 2020; Bisht et al., 2021; Vaidya et al., 2023; Hakeem et al., 2024; Ashraf et al., 2024). LC-MS/MS surpasses traditional approaches by enabling simultaneous determination of multiple analytes with high sensitivity and specificity, even at trace levels. Furthermore, its ability to handle complex matrices makes it particularly suitable for studying the phytohormonal profile of Aloe vera, where bioactive compounds exist in minute concentrations alongside numerous interfering substances.

However, information about the levels of phytohormones in many other plant species including Aloe vera is still limited. This gap hinders the establishment of comprehensive regulatory frameworks for herbal products, prompting the need for rigorous scientific inquiry to bridge this knowledge gap. In this context, our research addresses these critical gaps by presenting an innovative and robust LC-MS/MS methodology to detect and quantify phytohormones in Aloe vera. The developed method evaluates phytohormone levels in Aloe vera, adding to existing knowledge about their concentrations in other plants. These results may also serve as reference values for decision-making about the use of Aloe vera in commercial products. This breakthrough promises to enhance consumer safety, refine regulatory standards, and contribute significantly to the scientific understanding of Aloe vera's therapeutic composition.

Method and materials

Chemical reagents and standards

Abscisic Acid (ABA) 98%, Gibberellic Acid (GA) 90%, Indole-3-Acetic Acid (I3AA) 100%, 6-BenzylAminoPurine (6BAP) 99%, Isopentenyl Adenine (ISA) 98.5%, 2-Naphthalene Acetic Acid (2NAA) 95%, Salicylic Acid (SA) 99%, and Salicylic Acid D4 (SA-D4) (internal standard) were purchased from Sigma Aldrich (USA). LC-MS grade methanol, formic acid and acetic acid (LC-MS grade) were obtained from Supelco (Germany), Fluka (Switzerland). Milli-Q-Water obtained from in-house (UAE university).

Preparation of standard solution

Individual phytohormone standards, each weighing approximately 5.00 g, were carefully measured and dissolved in 5.00 mL of LC-MS/MS grade methanol in a volumetric flask. This resulted in a stock solution with a concentration of 1.00 mg/ml. A blend of all individual standard stock solutions was prepared using a diluent consisting of a 50:50 methanol-water to prepare an intermediate solution. This intermediate solution was then used to generate calibration standard solutions, crucial for the linearity step during the analysis. The deliberate use of methanol as the solvent ensured optimal solubility and stability of the phytohormones in the solution. This not only laid the groundwork for a reliable standard against which samples could be measured but also upheld the integrity of the phytohormones throughout the analysis.

Sample preparation and extraction of phytohormones

The quantification of phytohormones in Aloe vera was conducted with a focus on ensuring accuracy and precision throughout the analytical protocol. To achieve this, 13 Aloe vera samples were randomly selected from different sources to represent natural variability within the species. These samples were subjected to consistent environmental conditions to minimize external factors influencing phytohormone concentrations. The observed variations in phytohormone levels among these samples are indicative of the natural variability expected within a broader population. This approach allowed for a robust assessment of phytohormonal content, ensuring that the analytical results are reflective of the typical range of phytohormones found in Aloe vera plants. The samples were thoroughly washed with DI water and left to dry under ambient conditions before collecting the gel. The protocol used for sample preparation was developed by the authors, drawing on methodologies from existing literature for phytohormone analysis in plant matrices. Studies have demonstrated the efficacy of acetonitrile-based extraction solutions and acidified solvents for stabilizing phytohormones in complex plant matrices (Sutcharitchan et al., 2020). Preliminary experiments were conducted to adapt parameters such as solvent composition, sample-to-solvent ratio, and centrifugation speed to optimize analyte recovery and stability. The chosen conditions, including the use of 1% acetic acid in acetonitrile as the extraction solvent, were shown to yield consistent recoveries exceeding 95% for all target analytes. These adjustments ensured the protocol was robust and tailored specifically to Aloe vera phytohormone analysis.

The extraction process commenced with weighing 1.00 g of Aloe vera gel. To enhance accuracy, 0.05 mL of salicylic acid D4 (500.00 ng/mL), was added as an internal standard. Salicylic acid D4 was selected due to its structural and physicochemical similarity to the target phytohormones, which allows it to mimic their behavior during chromatographic separation and mass spectrometric determination. The addition of the internal standard was thoroughly optimized to ensure consistent recovery and reliable quantification across all analytes. The samples were thoroughly vortexed to ensure homogeneity. Subsequently, a solution comprising 5.00 mL with 1% acetic acid in acetonitrile was added to the sample and vortexed to ensure thorough mixing. To separate the components, the resulting mixture underwent centrifugation at 4,500 rpm for 10 min. Following centrifugation, the supernatant was meticulously filtered through a 0.45 µm filter and extracted for further analysis. The prepared solution was then injected into an LC-MS/MS instrument for a detailed analysis of the sample. The entire procedure was performed in triplicate for each Aloe vera sample, providing a robust assessment of the developed analytical protocol's precision and reliability.

TABLE 1 Qualification and quantification of MRM transition for phytohormones using LC-MS/MS.

Compound	Q1 (m/z)	Q3 (m/z)	Dwell time (ms)	Q1 pre-Bias (V)	CE (V)	Q3 pre-Bias	Ionization mode
I3AA	176.00	130.10	100	−17	−15	−22	Positive
	176.00	77.10	100	−16	−42	−15	
	176.00	103.05	100	−16	−29	−23	
2NAA	184.90	117.05	100	22	11	26	Negative
	184.90	100.05	100	20	34	38	
	184.90	141.10	100	22	10	20	
6BAP	224.05	133.15	100	24	23	26	Negative
	224.05	132.15	100	24	32	26	
	224.05	188.00	100	26	13	22	
GA	345.25	143.20	100	17	29	13	Negative
	345.25	239.20	100	17	16	30	
	345.25	221.35	100	17	25	22	
SA	137.20	93.15	100	13	21	11	Negative
	137.20	65.20	100	14	28	15	
	137.20	100.00	100	15	27	26	
ABA	263.10	153.25	100	28	12	20	Negative
	263.10	219.25	100	28	14	24	
	263.10	204.30	100	28	20	26	
SA-D4	141.10	97.10	100	14	21	12	Negative
	141.10	59.10	100	14	12	14	

Q1 pre-bias: Voltage needed to promote ionization of precursor ion, Q3 pre-bias: Voltage needed to promote ionization of product ion).

LC-MS/MS analysis and method development

LC-MS/MS analysis was carried out using Shimadzu (Japan) model LC-30AD (Nexera X2) binary pump and LCMS-8060 Shimadzu (Japan). The chromatographic separation was performed using Zorbax Eclipse Plus C18 (4.6 × 100 mm, 3.5 µm pore size) column sourced from Agilent Technologies. The mobile phase consisted of 0.01% formic acid (v/v) in a mixture of water and methanol (35:65 v/v). A 10.0 µL volume of the sample was injected, and the mobile phase flowed at a rate of 0.50 mL/min. The oven temperature was set at a constant 30°C during the analysis. The LC system was connected to a triple quadrupole mass spectrometer detector. Phytohormones underwent ionization in both positive and negative electrospray ionization (ESI) modes. Quantification was achieved through the multiple reaction monitoring (MRM) mode. In the optimization of the LC-MS/MS method, a series of standards were employed, and the resulting Multiple Reaction Monitoring (MRM) data underwent comprehensive analysis. The selection of optimal parent and daughter ions was a pivotal step in refining the method. The collision energy (CE) was carefully fine-tuned based on the relative abundance of the parent and daughter ions, as detailed in Table 1. Q1 and Q3 in Table 1 indicate the mass parent and mass product ion respectively. A detailed description of Table 1 can be found under the Supplementary Information (SI) section.

To establish the instrument's detection limits for each phytohormone, a rigorous approach was employed. Three replicates of each sample were analyzed, and the signals from each sample at the retention time of the respective phytohormone were recorded. The standard deviation of these signals was calculated. Utilizing the slope ratio between the internal standard and each phytohormone, the standard deviation values were then applied to determine the limit of detection (LOD). This method not only ensures precision in quantification but also provides a robust assessment of the sensitivity of the LC-MS/MS system in detecting trace amounts of phytohormones in Aloe vera samples.

Method validation

The validation of the testing method is crucial to determine its reliability and ability to generate accurate and valuable data. This meticulous process ensures that the analytical procedure consistently delivers results within defined parameters. The criteria employed for validation encompass selectivity, sensitivity, precision, accuracy, linearity, and matrix effect (Cheng et al., 2022; Wille et al., 2022; Williams et al., 2023). The matrix effect was evaluated to ensure that the Aloe vera matrix did not interfere significantly with analyte determination or quantification.

TABLE 2 Applied quality control measures in the determination of the target phytohormones.

Compound	Quality control (QC)	Conc. (ng/mL)	Linearity Range (ng/mL)	R^2	LOD (ng/mL)	LOQ (ng/mL)	Intraday analysis		Interday analysis	
							Accuracy (%)	RSD (%)	Accuracy (%)	RSD (%)
ASA	LOQ	0.99	0.99–203.81	0.99	0.40	1.20	105.97	10.08	101.77	6.78
	2×LOQ	1.99					103.82	4.74	100.08	6.33
	5×LOQ	4.99					100.15	2.34	98.77	5.24
GA	LOQ	2.02	2.02–411.26	0.99	0.33	1.01	90.53	4.92	87.73	14.04
	2×LOQ	4.03					90.83	9.18	97.80	8.39
	5×LOQ	10.08					95.64	3.14	95.88	4.89
I3AA	LOQ	2.07	2.07–422.40	0.98	0.27	0.83	89.96	3.71	101.66	3.78
	2×LOQ	4.14					107.12	2.02	108.37	2.69
	5×LOQ	10.35					111.34	3.44	112.51	1.68
6BAP	LOQ	2.56	2.56–522.72	0.99	0.51	1.54	84.59	7.54	83.85	10.89
	2×LOQ	5.12					97.22	12.2	95.87	4.60
	5×LOQ	12.81					100.28	1.86	97.79	1.81
ISA	LOQ	0.16	0.16–32.78	0.99	0.01	0.04	95.65	2.11	99.28	5.11
	2×LOQ	0.32					116.25	4.38	116.61	1.24
	5×LOQ	0.80					96.68	3.63	98.09	1.60
2NAA	LOQ	126.62	126.62–25840.0	0.99	36.40	110.30	101.67	4.55	105.70	9.28
	2×LOQ	253.23					100.53	1.83	104.06	5.67
	5×LOQ	633.08					101.66	2.27	104.10	2.92
SA	LOQ	1.06	1.06–216.22	0.99	0.54	1.62	90.43	14.68	110.78	9.59
	2×LOQ	2.12					89.45	9.51	99.36	5.82
	5×LOQ	5.30					86.13	4.74	94.57	3.17

Sensitivity is expressed through the limit of detection (LOD) and the limit of quantitation (LOQ). The LOD represents the lowest concentration of an analyte that can be reliably distinguished from background noise, while the LOQ is the lowest concentration that can be quantified with acceptable precision and accuracy. Both parameters were calculated using the standard deviation of the response (SD) and the slope of the calibration curve (S) as per modern guidelines (Rajmane Akash and Shinde Komal (2023)). Precision, the degree of scatter among measurements, and accuracy, the proximity of test values to actual values, were precisely evaluated. Three quality control (QC) samples (High, medium, and low) concentrations were used to evaluate both intra- and inter-day accuracy and precision. These parameters collectively ensure the consistency and reliability of the analytical method. The detailed results of the validation process are presented in Table 2. This validation demonstrates the sensitivity and robustness of the developed analytical protocol.

The results from Table 2 collectively demonstrate the method's ability to meet quality control measures, providing a foundation for accurate and reliable determination of target phytohormones in Aloe vera samples. A detailed description of Table 2 can be found in Supplementary Information (SI) section. These findings not only validate the analytical approach but also underscore its applicability in ensuring the quality and safety of Aloe vera products for consumers.

Results and discussion

Validation results

The analytical method developed for phytohormone analysis was meticulously validated and applied to Aloe vera samples. The validation process evaluated the method's selectivity, sensitivity, matrix effect, precision, and accuracy to ensure its suitability for the analysis. Matrix Effect was assessed by comparing the responses of analytes spiked into blank extracts with those spiked into pure solvent. The observed signal suppression or enhancement for all six phytohormones was within the acceptable range (80%–120%), indicating minimal interference from the Aloe vera matrix (Table 2). Further validation of the analytical method was assessed by evaluating the retention times and intensity of phytohormones. The results affirm the establishment of a robust linear relationship among the analytes, as evidenced by an

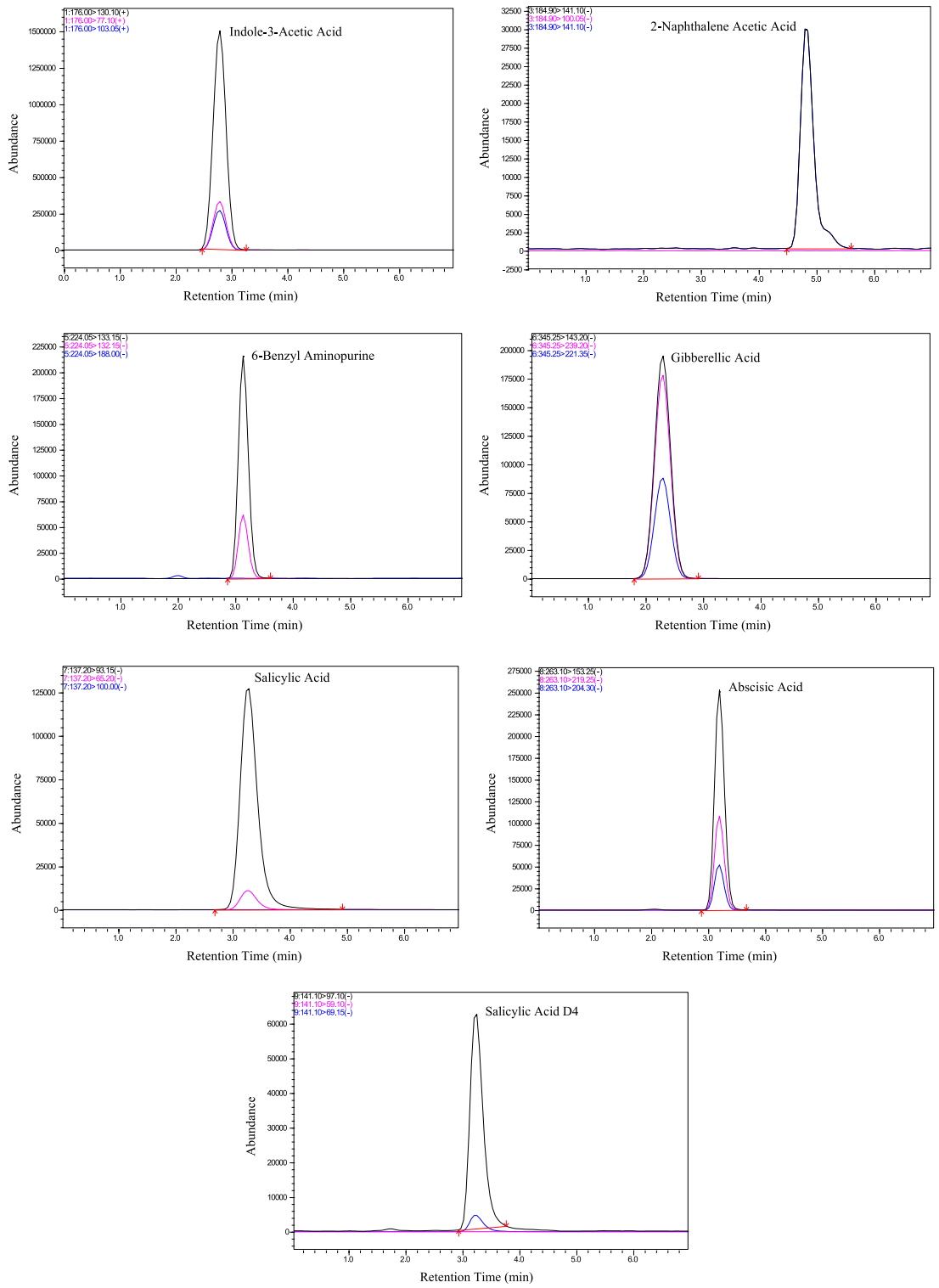

FIGURE 1
Chromatograms of the target phytohormones and internal standard.

exceptional regression value ($R^2 = 0.99$) (Supplementary Figure S1). This high degree of correlation between phytohormone concentration and signal intensity is paramount for ensuring precise and reliable quantification across a diverse concentration range. To visually represent the efficacy of the method, Figure 1 presents chromatograms depicting the chromatographic profiles of the six target phytohormones under optimal conditions. Each hormone manifests as a distinct peak at its specific retention time, demonstrating the method's ability to precisely separate and identify individual compounds. The clarity and separation of

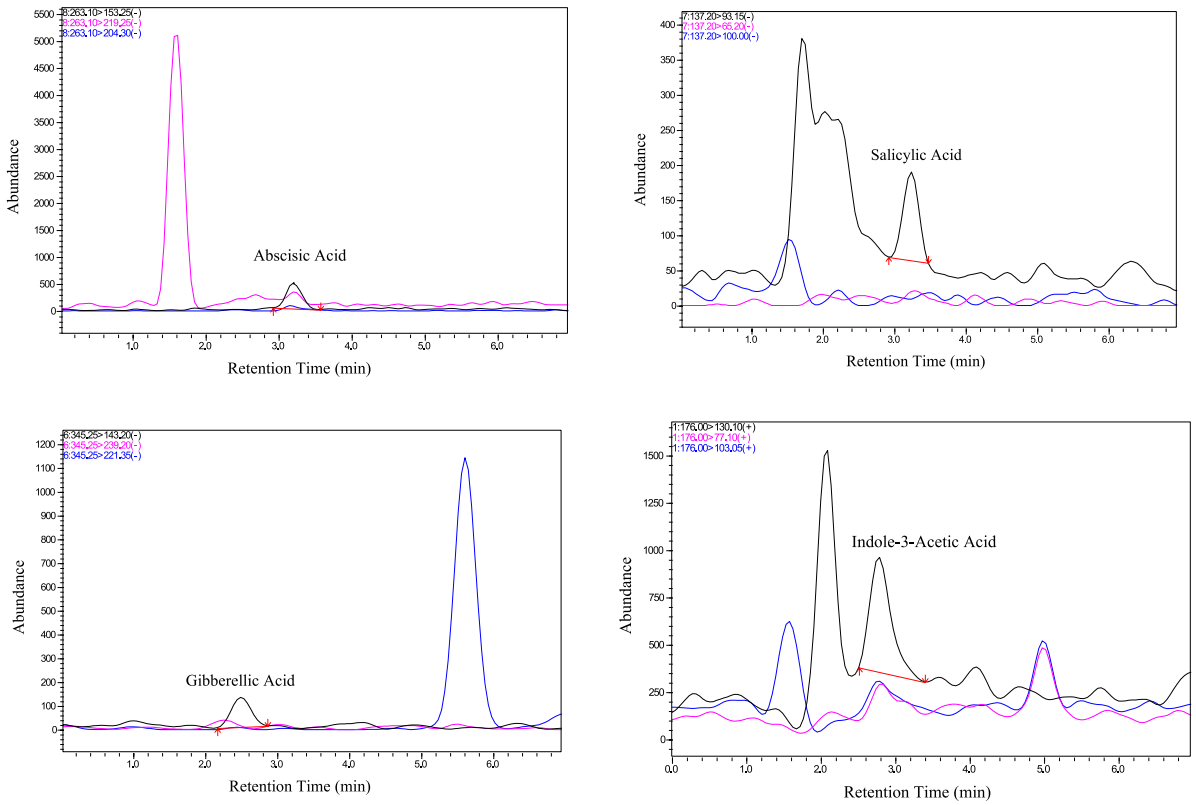

FIGURE 2
Chromatograms of the target phytohormones in real sample.

these peaks are essential for accurate quantification, ensuring that each phytohormone is distinctly identified and measured.

The chromatograms (Figure 1) reveal sharp, well-resolved peaks for all phytohormones, underscoring the method's ability to selectively quantify the target. The clarity and distinctiveness of these peaks contribute to the method's selectivity, reinforcing its efficacy in phytohormone determination. The chromatographic results not only showcase the robustness of the method but also lay the foundation for accurate quantification, thereby enhancing the reliability of the analytical approach for phytohormone analysis in plant samples.

Sample analysis

Following the successful validation of the LC-MS/MS method, it was applied to the analysis of phytohormones in Aloe vera samples. Upon analysis, it was observed that out of the six targeted phytohormones, four were successfully detected using the developed LC-MS/MS method. Figure 2 shows the chromatograms of real sample of Aloe vera highlighting the unique chemical properties of each phytohormone in terms of variations in their retention times. The observed differences in retention times, as depicted in Figure 2, offer a valuable visual tool for researchers to easily identify and distinguish individual phytohormones. This critical information contributes to the understanding of hormonal dynamics within Aloe vera, paving the way for further investigations into its therapeutic potential and adaptive responses.

The variability in concentrations among different samples highlights the heterogeneity in phytohormone composition within Aloe vera, which could be influenced by various factors such as plant age, environmental conditions, and cultivation practices. The observed concentrations provide valuable insights into the phytohormone profile of Aloe vera, contributing to a deeper understanding of its physiological and therapeutic properties. Further exploration of these variations may uncover implications for the quality and efficacy of Aloe vera products in diverse applications. In Figure 3, the box-and-whisker plots illustrate the concentrations of phytohormones in the tested Aloe vera samples, providing a comprehensive overview of overall phytohormone profile.

ABA consistently shows the highest median concentration across all samples, highlighting its dominant presence in the phytohormone composition of Aloe vera. I3AA follows, with the second-highest median concentration, underscoring its significant role in the samples. SA and GA rank third and fourth, respectively, in terms of median concentrations. The distribution and spread of the data, as depicted by the whiskers and interquartile ranges, reveal the variability within each phytohormone group. Despite these variations in median values, statistical analysis confirms that the differences in concentrations among the phytohormones are not statistically significant at a 95% confidence level. This conclusion is supported by the overlapping confidence intervals and similar

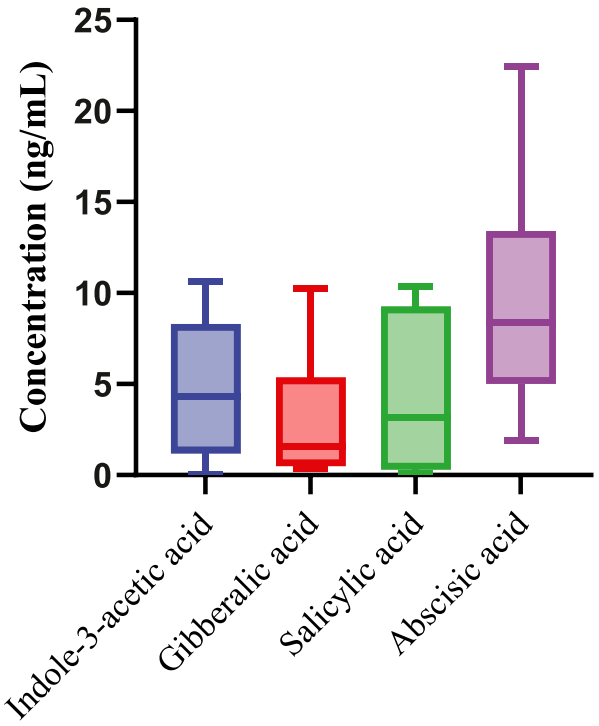

FIGURE 3
Box and Whisker plot showing concentration ranges (ng/mL) of detected phytohormones in the Aloe vera samples (N = 13).

interquartile ranges, suggesting that the observed differences fall within the normal range of variation.

This study presents a novel LC-MS/MS methodology for the comprehensive analysis of phytohormones in Aloe vera, overcoming limitations of previous approaches that predominantly focused on single analytes or employed less sensitive techniques. The optimized extraction and analytical protocols enable precise and reproducible quantification of key phytohormones, filling critical gaps in the literature regarding Aloe vera's chemical profile. By providing a detailed understanding of the phytohormonal composition, this work establishes a robust foundation for evaluating Aloe vera's therapeutic potential and safety in consumer products. These findings also highlight the complex and dynamic regulation of phytohormones in Aloe vera, emphasizing the need for further research into their roles and interactions. The methodology developed in this study provides a reliable framework for future investigations, enabling deeper insights into the biological and therapeutic significance of phytohormones in Aloe vera and other plant systems. The validated LC-MS/MS method demonstrates exceptional robustness, with the capacity to separate, detect, and quantify phytohormones with high sensitivity and selectivity. These attributes underscore its potential adaptability to other plant species, particularly those with similarly intricate biochemical compositions. The use of acidified acetonitrile as an extraction solvent and the optimized chromatographic conditions are broadly applicable to other plants with diverse phytohormonal profiles. For example, this protocol could be extended to other medicinal plants such as *Echinacea purpurea* or *Camellia sinensis*, where phytohormone analysis is crucial for understanding their therapeutic properties. Furthermore, the method's ability to analyze trace phytohormones makes it suitable for high-throughput studies in agricultural research, where the hormonal regulation of growth and stress responses across different crops is a key area of interest.

Conclusion

In the current study, we have successfully developed, optimized, and validated a robust LC-MS/MS method for the accurate determination of phytohormone concentrations in Aloe vera samples to advance our understanding of the intricate signaling mechanisms within this medicinal plant. The optimization of the LC-MS/MS method involved the systematic variation of phase composition, leading to enhanced separation and resolution of phytohormones within the complex matrix of Aloe vera. Following the guidelines established by regulatory authorities, such as the US Food and Drug Administration (FDA), our validation process rigorously examined various parameters, demonstrating the method's reliability and robustness. Compared to traditional techniques such as bioassays, immunoassays, and HPLC-UV, the LC-MS/MS method provides significant advancements in sensitivity, selectivity, and throughput. The LC-MS/MS method, with its high sensitivity (LOD as low as 0.01 ng/mL) and multiplexing capabilities, addresses these limitations and sets a new benchmark for phytohormone analysis. Our results indicate that ABA consistently emerged as the predominant hormone, followed by SA, I3AA, and GA. Variations in concentrations were observed among different samples, showcasing the heterogeneous nature of phytohormone composition in Aloe vera. Our findings stimulate further exploration, inviting researchers to delve into the world of phytohormones and their role in shaping the unique characteristics of different plants. Our findings reveal a distinct distribution of phytohormones, with ABA and SA predominating, suggesting their pivotal roles in the plant's stress response and defense mechanisms, and hint at potential gender-specific hormonal regulation. This detailed interpretation of results not only highlights the method's effectiveness but also opens new avenues for research into the physiological roles of phytohormones in Aloe vera and other medicinal plants. By establishing baseline levels of phytohormones, our study contributes to the safety evaluation of Aloe vera-based products, correlating hormonal profiles with therapeutic effects and supporting the traditional and potential new uses of Aloe vera in pharmaceuticals and nutraceuticals, thus benefiting both scientific research and consumer wellbeing.

Data availability statement

The original contributions presented in the study are included in the article/Supplementary Material, further inquiries can be directed to the corresponding author.

Author contributions

MH: Validation, Writing–original draft, Writing–review and editing. MM: Formal Analysis, Methodology, Writing–original draft, Writing–review and editing. SE: Formal Analysis, Investigation, Methodology, Validation, Writing–original draft, Writing–review and editing. ES: Validation, Writing–original draft. AM: Validation, Writing–original draft. KH: Supervision, Writing–review and editing. IS: Conceptualization, Data curation, Formal Analysis, Funding acquisition, Investigation, Methodology, Project administration, Resources, Software, Supervision, Validation, Visualization, Writing–original draft, Writing–review and editing. KA: Methodology, Supervision, Conceptualization, Project administration, Investigation, Funding acquisition, Resources, Visualization, Writing–review and editing.

Funding

The author(s) declare financial support was received for the research, authorship, and/or publication of this article. We offer our Special thanks to SURE-Plus and KCGEB UAE University for sponsoring this research.

Conflict of interest

The authors declare that the research was conducted in the absence of any commercial or financial relationships that could be construed as a potential conflict of interest.

Publisher's note

All claims expressed in this article are solely those of the authors and do not necessarily represent those of their affiliated organizations, or those of the publisher, the editors and the reviewers. Any product that may be evaluated in this article, or claim that may be made by its manufacturer, is not guaranteed or endorsed by the publisher.

Supplementary material

The Supplementary Material for this article can be found online at: https://www.frontiersin.org/articles/10.3389/fchem.2024.1490639/full#supplementary-material

References

Adlakha, K., Koul, B., and Kumar, A. (2022). Value-added products of Aloe species: panacea to several maladies. *South Afr. J. Bot.* 147, 1124–1135. doi:10.1016/j.sajb.2020.12.025

Ali, A., Kant, K., Kaur, N., Gupta, S., Jindal, P., Gill, S. S., et al. (2024). Salicylic acid: homeostasis, signalling and phytohormone crosstalk in plants under environmental challenges. *South Afr. J. Bot.* 169, 314–335. doi:10.1016/j.sajb.2024.04.012

Ali, K., Saquib, Q., Siddiqui, M. A., Ahmad, J., Al-Khedhairy, A. A., and Musarrat, J. (2020). Anti-cancer efficacy of Aloe vera capped hematite nanoparticles in human breast cancer (MCF-7) cells. *J. Drug Deliv. Sci. Technol.* 60, 102052. doi:10.1016/j.jddst.2020.102052

Arif, Y., Sami, F., Siddiqui, H., Bajguz, A., and Hayat, S. (2020). Salicylic acid in relation to other phytohormones in plant: a study towards physiology and signal transduction under challenging environment. *Environ. Exp. Bot.* 175, 104040. doi:10.1016/j.envexpbot.2020.104040

Ashok, A., and Ravivarman, J. (2020). Efficacy of naphthalene acetic acid on root promotion on vegetative propagation of Tecoma stans under mist chamber of semi-arid tropic region. *J. Pharmacogn. Phytochem.* 9 (4), 3000–3002.

Asif, R., Yasmin, R., Mustafa, M., et al. (2022). *Phytohormones as plant growth regulators and safe protectors against biotic and abiotic stress*. Plant Horm Recent Adv New Perspect Appl, 115–130.

Ashraf, D., Morsi, R., Usman, M., and Meetani, M. A. (2024). Recent Advances in the Chromatographic Analysis of Emerging Pollutants in Dairy Milk: A Review (2018–2023). *Molecules*. 29 (6), 1296. doi:10.3390/molecules29061296

Bharath, P., Gahir, S., and Raghavendra, A. S. (2021). Abscisic acid-induced stomatal closure: an important component of plant defense against abiotic and biotic stress. *Front. Plant Sci.* 12, 615114. doi:10.3389/fpls.2021.615114

Bhatt, D., Nath, M., Sharma, M., Bhatt, M. D., Bisht, D. S., and Butani, N. V. (2020). "Role of growth regulators and phytohormones in overcoming environmental stress," in *Prot chem agents amelior plant abiotic stress biochem mol perspect*, 254–279.

Bhattacharya, A. (2022). "Plant growth hormones in plants under low-temperature stress: a Review," in *Physiol process plants low temp stress*, 517–627.

Bisht, N., Gupta, A., Awasthi, P., Goel, A., Chandran, D., Sharma, N., et al. (2021). Development of a rapid LC-MS/MS method for the simultaneous quantification of various flavonoids, isoflavonoids, and phytohormones extracted from Medicago truncatula leaves. *J. Liq. Chromatogr. Relat. Technol.* 44 (15-16), 776–787. doi:10.1080/10826076.2022.2040028

Bista, R., Ghimire, A., and Subedi, S. (2020). Phytochemicals and antioxidant activities of aloe vera (aloe barbadensis). *J. Nut Sci. Heal Diet.* 1 (1), 25–36. doi:10.47890/jnshd/2020/rbista/10243803

Butt, R. S., and Gul, A. (2023). "Induction of physiological and metabolic changes in plants by plant growth regulators," in *Phytohormones and stress responsive secondary metabolites* (Elsevier), 141–159.

Castro-Camba, R., Sánchez, C., Vidal, N., and Vielba, J. M. (2022). Interactions of gibberellins with phytohormones and their role in stress responses. *Horticulturae* 8 (3), 241. doi:10.3390/horticulturae8030241

Cheng, W. L., Markus, C., Lim, C. Y., Tan, R. Z., Sethi, S. K., and Loh, T. P. (2022). Calibration practices in clinical mass spectrometry: review and recommendations. *Ann. Lab. Med.* 43 (1), 5–18. doi:10.3343/alm.2023.43.1.5

Choi, S., and Chung, M. H. (2003). A review on the relationship between Aloe vera components and their biologic effects. *Seminars Integr. Med.* 1, 53–62. doi:10.1016/s1543-1150(03)00005-x

Etesami, H., and Glick, B. R. (2024). Bacterial indole-3-acetic acid: a key regulator for plant growth, plant-microbe interactions, and agricultural adaptive resilience. *Microbiol. Res.* 281, 127602. doi:10.1016/j.micres.2024.127602

Gharib, A., Marquez, C., Meseguer-Beltran, M., Sanchez-Sarasua, S., and Sanchez-Perez, A. M. (2024). Abscisic acid, an evolutionary conserved hormone: biosynthesis, therapeutic and diagnostic applications in mammals. *Biochem. Pharmacol.* 229, 116521. doi:10.1016/j.bcp.2024.116521

Gulati, P., College, M., and Sahib, F. (2021). A review on medicinal properties of Aloe vera plant and it's profile. *Int. Res. J. Mod. Eng. Technol. Sci.* 5, 22.

Hakeem, M. K., Elangovan, S., Rafi, M., George, S., Shah, I., and Amiri, K. M. A. (2024). Advancing antibiotic residue analysis: LC-MS/MS methodology for ticarcillin degradation products in tomato leaves. *Antibiotics* 13 (2), 133. doi:10.3390/antibiotics13020133

Hernández-García, J., Briones-Moreno, A., and Blázquez, M. A. (2021). Origin and evolution of gibberellin signaling and metabolism in plants. *Semin. Cell Dev. Biol.* 109, 46–54. doi:10.1016/j.semcdb.2020.04.009

Jha, U. C., Nayyar, H., and Siddique, K. H. (2022). Role of phytohormones in regulating heat stress acclimation in agricultural crops. *J. Plant Growth Regul.* 41, 1041–1064. doi:10.1007/s00344-021-10362-x

Jiang, C., Dai, J., Han, H., Wang, C., Zhu, L., Lu, C., et al. (2020). Determination of thirteen acidic phytohormones and their analogues in tea (Camellia sinensis) leaves using ultra high performance liquid chromatography tandem mass spectrometry. *J. Chromatogr. B* 1149, 122144. doi:10.1016/j.jchromb.2020.122144

Katyayini, N. U., Rinne, P. L., Tarkowská, D., Strnad, M., and van der Schoot, C. (2020). Dual role of gibberellin in perennial shoot branching: inhibition and activation. *Front. Plant Sci.* 11, 736. doi:10.3389/fpls.2020.00736

Kaviani, B., Jamali, M., Motlagh, M. S., and Eslami, A. (2023). The effect of different levels of indole-3-butyric acid (IBA) and naphthaleneacetic acid (NAA) on the rooting of pear stem cutting. *J. Hortic. Sci.* 36 (4), 747–761.

Leitgeb, M., Kupnik, K., Knez, Ž., and Primožič, M. (2021). Enzymatic and antimicrobial activity of biologically active samples from Aloe arborescens and Aloe barbadensis. *Biology* 10 (8), 765. doi:10.3390/biology10080765

Maan, A. A., Nazir, A., Khan, M. K. I., Ahmad, T., Zia, R., Murid, M., et al. (2018). The therapeutic properties and applications of Aloe vera: a review. *J. Herb. Med.* 12, 1–10. doi:10.1016/j.hermed.2018.01.002

Mangena, P. (2022). Evolving role of synthetic cytokinin 6-benzyl adenine for drought stress tolerance in soybean (Glycine max L. Merr.). *Front. Sustain Food Syst.* 6, 992581. doi:10.3389/fsufs.2022.992581

Martínez-Sánchez, A., López-Cañavate, M. E., Guirao-Martínez, J., Roca, M. J., and Aguayo, E. (2020). Aloe vera flowers, a byproduct with great potential and wide application, depending on maturity stage. *Foods* 9 (11), 1542. doi:10.3390/foods9111542

Muhammad Aslam, M., Waseem, M., Jakada, B. H., Okal, E. J., Lei, Z., Saqib, H. S. A., et al. (2022). Mechanisms of abscisic acid-mediated drought stress responses in plants. *Int. J. Mol. Sci.* 23 (3), 1084. doi:10.3390/ijms23031084

Mukherjee, A., Gaurav, A. K., Singh, S., Yadav, S., Bhowmick, S., Abeysinghe, S., et al. (2022). The bioactive potential of phytohormones: a review. *Biotechnol. Rep.* 35, e00748. doi:10.1016/j.btre.2022.e00748

Pal, P., Ansari, S. A., Jalil, S. U., and Ansari, M. I. (2023). "Regulatory role of phytohormones in plant growth and development," in *Plant hormones in crop improvement* (Elsevier), 1–13.

Palaniyappan, S., Sridhar, A., Arumugam, M., and Ramasamy, T. (2023). Bioactive analysis of antibacterial efficacy and antioxidant potential of aloe barbadensis miller leaf extracts and exploration of secondary metabolites using GC–MS profiling. *Appl. Biochem. Biotechnol.* 196, 729–773. doi:10.1007/s12010-023-04565-z

Phytohormones as Potential Anticancer Agents (2024). *Int. J. Res. Appl. Sci. Biotechnol*. Available at: https://ijrasb.com/index.php/ijrasb/article/view/126 (Accessed November 27, 2024).

Pradhan, B. (2023). Phytochemistry, pharmacology and toxicity of aloe vera: a versatile plant with extensive therapeutic potential. *Plant Arch. 09725210* 23 (2). doi:10.51470/plantarchives.2023.v23.no2.056

Rajesh, A., Lone, S. A., Ramasubburayan, R., Sikkanthar, S., Thajuddin, N., Lee, S. Y., et al. (2023). A systemic review on Aloe vera derived natural biomaterials for wound healing applications. *Biocatal. Agric. Biotechnol.* 54, 102910. doi:10.1016/j.bcab.2023.102910

Rajmane Akash, D., and Shinde Komal, P. (2023). A Review of HPLC Method Development and Validation as per ICH Guidelines. *Asian Journal of Pharmaceutical Analysis*. 13 (2), 143–151. doi:10.52711/2231-5675.2023.00024

Sinha, L., Satyapal, G. K., and Kumar, S. (2023). Aloe vera-A medicinal plant as potential therapeutic agents for liver cancer. *Front. Med. Chem.* 10 (10), 281–289. doi:10.2174/9789815165043123100014

Sutcharitchan, C., Miao, S., Li, W., Liu, J., Zhou, H., Ma, Y., et al. (2020). High performance liquid chromatography-tandem mass spectrometry method for residue determination of 39 plant growth regulators in root and rhizome Chinese herbs. *Food Chem.* 322, 126766. doi:10.1016/j.foodchem.2020.126766

Tariq, L., Bhat, B. A., Hamdani, S. S., et al. (2022). "Plant growth regulators and their interaction with abiotic stress factors," in *Plant abiotic stress physiology: volume 2: molecular advancements* (Apple Academic Press Inc. Palm Bay), 115–136.

Thorat, J. C., Dhamal, S. V., and Dudheinamdar, P. V. (2023). Mineral-associated medicinal plants: uncovering their anti-inflammatory potential through comprehensive exploration of bioactive compounds and pharmacological activities. *J. Mines Met. Fuels* 71 (11), 2095–2109. doi:10.18311/jmmf/2023/36273

Vaidya, H., Solanki, V. H., Kansara, R. V., Desai, C., Singh, S., Patel, J., et al. (2023). Development of a novel method for multiple phytohormone analysis by UHPLC-MS/MS from bio-enriched organic fertilizer prepared using banana pseudostem sap waste. *Environ. Sci. Pollut. Res.* 30 (28), 71482–71490. doi:10.1007/s11356-022-23941-6

Wang, L., Zou, Y., Kaw, H. Y., Wang, G., Sun, H., Cai, L., et al. (2020). Recent developments and emerging trends of mass spectrometric methods in plant hormone analysis: a review. *Plant Methods* 16 (1), 54–17. doi:10.1186/s13007-020-00595-4

Wille, S. M. R., Desharnais, B., Pichini, S., Trana, A. D., Busardò, F. P., Wissenbach, D. K., et al. (2022). Liquid chromatography high-resolution mass spectrometry in forensic toxicology: what are the specifics of method development, validation and quality assurance for comprehensive screening approaches? *Curr. Pharm. Des.* 28 (15), 1230–1244. doi:10.2174/1381612828666220526152259

Williams, M. L., Olomukoro, A. A., Emmons, R. V., Godage, N. H., and Gionfriddo, E. (2023). Matrix effects demystified: strategies for resolving challenges in analytical separations of complex samples. *J. Sep. Sci.* 46 (23), 2300571. doi:10.1002/jssc.202300571

Zhang, M., Gao, C., Xu, L., Niu, H., Liu, Q., Huang, Y., et al. (2022). Melatonin and indole-3-acetic acid synergistically regulate plant growth and stress resistance. *Cells* 11 (20), 3250. doi:10.3390/cells11203250

Zhao, B., Liu, Q., Wang, B., and Yuan, F. (2021). Roles of phytohormones and their signaling pathways in leaf development and stress responses. *J. Agric. Food Chem.* 69 (12), 3566–3584. doi:10.1021/acs.jafc.0c07908

Zhong, Q., Hu, H., Fan, B., Zhu, C., and Chen, Z. (2021). Biosynthesis and roles of salicylic acid in balancing stress response and growth in plants. *Int. J. Mol. Sci.* 22 (21), 11672. doi:10.3390/ijms222111672

frontiers | Frontiers in Chemistry

TYPE Mini Review
PUBLISHED 19 February 2025
DOI 10.3389/fchem.2025.1536209

OPEN ACCESS

EDITED BY
Anna Borioni,
National Institute of Health (ISS), Italy

REVIEWED BY
Mariangela Raimondo,
National Institute of Health (ISS), Italy

*CORRESPONDENCE
Karolina Piorunska,
k.piorunska@nil.gov.pl

RECEIVED 28 November 2024
ACCEPTED 03 February 2025
PUBLISHED 19 February 2025

CITATION
Mocarska A, Piorunska K, Maurin JK and Blazewicz A (2025) The usefulness of infrared spectroscopy and X-ray powder diffraction in the analysis of falsified, illegal, and medicinal products.
Front. Chem. 13:1536209.
doi: 10.3389/fchem.2025.1536209

The usefulness of infrared spectroscopy and X-ray powder diffraction in the analysis of falsified, illegal, and medicinal products

Anna Mocarska, Karolina Piorunska*, Jan K. Maurin and Agata Blazewicz

Falsified Medicines and Medical Devices Department, National Medicines Institute, Warsaw, Poland

One way to combat the black pharmaceutical market is to exchange experience and knowledge among the laboratories involved in this fight. A beneficial approach is compiling application examples that demonstrate the development and growing potential of the two analytical techniques that are undoubtedly useful in investigating pharmacologically active ingredients found in products dangerous to consumers health and life. Attenuated total reflectance Fourier transform infrared spectroscopy and X-ray powder diffraction are nondestructive techniques substantial for examining evidence seized by the police, demanding minimal preparation of the sample. Importantly, they are among the few that do not negatively impact the environment because they do not require the production or disposal of chemical reagents or solvents, aligning with the principles of green chemistry. Both techniques provide consistent, reproducible results, essential for legal and scientific validity.

KEYWORDS

falsified medicinal products, illegal substances, API, analytical chemistry, FTIR, ATR, XRPD

1 Introduction

Although law enforcement agencies and analysts worldwide have been fighting against drug falsification for years, the market for falsified medications and the illegal use of pharmacologically active ingredients continues to thrive. Many of these products are sold without prescriptions on unregulated platforms, including websites, markets, and sex shops, often bypassing product control by being labeled, for example, as “not for human consumption” or “for research use only”. This opens up opportunities for misuse, as these drugs may contain incorrect or harmful ingredients or exist in various polymorphic forms, posing health risks. In many cases, they do not contain any active pharmaceutical ingredients (API) and consist only of excipients such as lactose, starch, sucrose, or mannitol. Falsified products are typically produced in poorly equipped laboratories, resulting in the presence of residual solvents and impurities (Sansone et al., 2021). Despite investigations and arrests, new manufacturing sites and distribution networks continue to emerge. Rapid identification of the composition of these products is crucial for law enforcement to intervene quickly and prevent the spread of these dangerous substances.

TABLE 1 Similarities and differences between ATR-FTIR and XRPD in the analysis of suspected samples.

Attenuated total reflectance infrared spectroscopy (ATR-FTIR) European Pharmacopoeia (2021), Song et al. (2020)	X-ray powder diffraction (XRPD) European Pharmacopoeia (2022), Chauhan and Chauhan (2014)
Non-destructive	
Minimal preparation needed	
Identification of salts and polymorphs	
Access to databases or reference materials is necessary	
Provides an absorption spectrum	Provides a diffraction pattern
Suitable for solid samples, liquids, gases	Suitable for solid samples
Analysis of amorphous or crystalline sample components	Analysis of crystalline sample components
Smaller sample quantity needed (a few milligrams)	Larger sample quantity needed (several hundred milligrams)
Identification of molecular structure, functional groups, bonding	Identification of crystalline structure
Short analysis time (several dozen seconds)	Longer analysis time (several dozen minutes)

The structural similarities, physicochemical properties, and multicomponent matrices of these products pose substantial analytical challenges. Consequently, various techniques have been employed to determine the composition of falsified products. Common methods include chromatography, spectroscopy, titrimetry, electrochemistry, electrophoresis, nuclear magnetic resonance (NMR), and liquid chromatography combined with mass spectrometry (LC-MS) (Rao et al., 2023; Rebiere et al., 2017). High-performance liquid chromatography and ultraviolet-visible spectrophotometry are popular for their speed and precision. Titrimetric methods, such as potentiometric titration, and electrochemical techniques, such as voltammetry, are also widely used. NMR spectroscopy provides detailed molecular information (Keizers et al., 2019), while LC-MS is preferred for comprehensive drug assays and analysis of impurities and degradation products. Nondestructive methods, such as attenuated total reflectance-Fourier transform infrared spectroscopy (ATR-FTIR) and X-ray powder diffraction (XRPD), allow the identification of components that are discarded by other techniques during dissolution or filtration processes, which is an important aspect, especially in the case of excipients. This mini-review aims to display potential of both nondestructive techniques in the field of forensic science. While they share similarities, crucial differences make them complementary, enabling a comprehensive analysis of samples (Table 1).

2 Usefulness and potential of the infrared (IR) technique in pharmaceutical analysis.

2.1 Basic properties of the IR technique and possible applications

IR spectroscopy involves changes in molecular energy due to absorbed IR radiation, causing vibrational and rotational motions. Absorbed radiation increases molecular energy, resulting in a spectrum with signals or bands. The position, intensity, and shape of these absorption bands are key characteristics. These bands correspond to the functional groups in the compound, as specific groups absorb IR radiation at defined frequencies, known as group frequencies, leading to characteristic vibrations. ATR is an IR measurement mode in which a sample is applied to a high-refractive-index crystal. Key phenomena include the reflection of the electromagnetic wave at the boundary between two media and its penetration into the lower optical density medium (European Pharmacopoeia, 2021). This technique allows for direct measurement of solid and liquid samples in less than a minute.

IR spectroscopy can analyze both mixtures and individual substances. The spectrum of a mixture is distinctive and confirms product authenticity, making it useful for examining suspected falsified products. Another purpose is to monitor changes within mixtures, such as confirming synthesis progress, decomposition, or surface adsorption. IR spectroscopy can identify different polymorphic forms of the same substance. The ATR mode is applicable for analyzing thick samples with strong absorption, as well as multilayered surface coatings and coatings on solid bodies. This technique relies on durable and chemically resistant crystals suitable for powders, solids, and even liquid samples by applying a single droplet (e.g., viscous liquids, biological materials, and aqueous solutions) (Song et al., 2020).

2.2 Application of ATR-FTIR technique in the analysis of falsified and substandard drugs

The most frequently falsified group of drugs are those used to treat erectile dysfunction (Figure 1) (Interpol, 2023). These data are reflected in the popularity of ATR-FTIR applications for testing this group of products. In a London-based study, three purported herbal

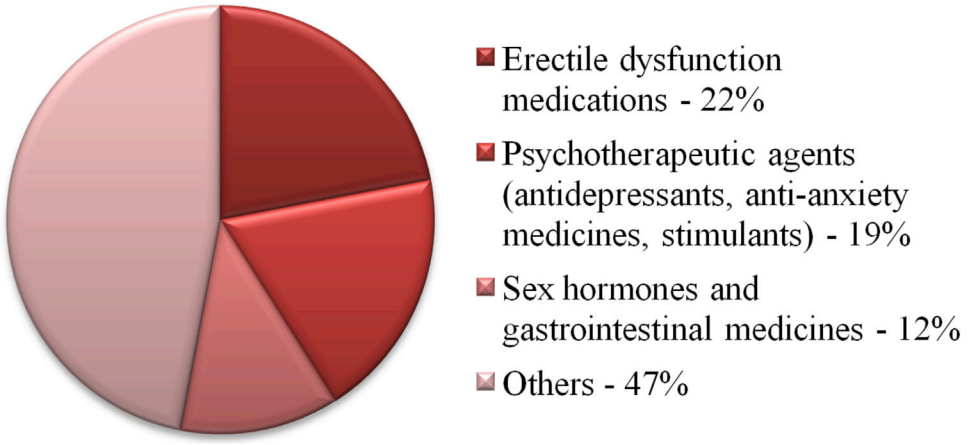

FIGURE 1
Distribution of drugs into pharmacological groups of products collected during Interpol's global Pangea XVI 2023 campaign [3].

supplements for men's sexual performance were purchased from an e-commerce platform (Ho et al., 2022). Although these products were advertised as containing only herbal ingredients, sildenafil citrate was also detected in each. This was confirmed using several techniques, including ATR-FTIR. Measurements performed using this technique confirmed the presence of bands characteristic of sildenafil citrate, corresponding to N-H stretching, N-H bending, S=O symmetrical and asymmetric stretching, C–N stretching. Two of the products were unregistered generic tablets and one was a falsified medical product.

R.S. Ortiz et al. demonstrated the application of this technique using a diamond crystal for the rapid identification of falsified medicinal products containing phosphodiesterase type 5 inhibitors (Ortiz et al., 2013). The results revealed similarities between the mixtures used to prepare various counterfeit products. Similar findings were reported in a study of the same products on samples collected by law enforcement agencies in Poland (Piorunska-Sedlak and Stypulkowska, 2021). ATR-FTIR can also be used as an auxiliary technique accompanying the main research method. Products obtained from questionable online pharmacies in the Czech Republic were examined using Raman spectroscopy and mapping, but the results of identifying the qualitative composition were additionally confirmed by measurements in infrared spectroscopy (Spalovska et al., 2021).

In falsified drugs, active ingredients often originate from illegal sources. These ingredients may differ in efficacy from the original if they are in a different salt form or may pose additional risks if they contain impurities. Even a negative result of a test confirming the identity of an API without the possibility of identification due to database limitations may constitute valuable information. P.H.J. Keizers et al. after excluding the presence of sildenafil citrate by ATR-FTIR and confirming the presence of sildenafil by LC-MS decided to take the next step. They used several additional advanced techniques, including high-resolution tandem mass spectrometry, Raman microscopy, melting point analysis, and NMR spectroscopy, to demonstrate that sildenafil in the form of a mesylate, instead of citrate, can be found as an active ingredient in the illegal market (Keizers et al., 2016).

ATR-FTIR data can be further processed using numerous computational and chemometric methods. By applying singular value decomposition to calculate the wavenumber importance index, Brito et al. proposed a novel method for wavenumber selection (Brito et al., 2020). This method aimed to classify authentic and falsified drugs containing sildenafil and tadalafil citrate. A combination of these types of proceedings was also presented by other researchers (Mittal et al., 2021). Examination and analysis of results from over 400 antibiotic samples led to the development of a classification method aimed at detecting and identifying specific solid dosage forms of antibiotics. The combination of data recorded using the attenuated total reflection technique with the partial least squares–discriminant analysis method can be a useful tool for distinguishing between less and more sophisticated falsified Durateston® products (Brazilian product containing an anabolic steroid) in a study of 96 samples (Neves et al., 2017).

IR spectroscopy can be used not only for qualitative analysis but also for quantitative analysis. A well-designed method can differentiate between substandard and falsified products. Researchers in the United Kingdom developed such a method using preparations containing paracetamol as an example (Lawson et al., 2018).

Not only synthetic drugs but also herbal medicines are subject to falsification. An Indonesian study presented an approach for the quantification and classification of herbal medicine products adulterated with synthetic drugs (prednisone and metamizole) by combining ATR-FTIR with multivariate calibration and discriminant analysis (Fatmarahmi et al., 2022).

The analysis of falsified drugs does not have to focus solely on the form of the active ingredients. Drug falsification also involves packaging, which can be used to assess the authenticity. M.R. Bin Salim et al. utilized this approach to study the blister packaging

materials of paracetamol samples (Bin Salim et al., 2021). In another packaging study, a technique was used for the chemical analysis of vial label paper, flip-off caps, and cello tape on vial labels and stoppers (Degardin al., 2019). Additional techniques, such as Raman spectroscopy and microscopy, optical microscopy, and X-ray fluorescence spectroscopy, have also been employed. The combination of these tools enabled the examination of 31 falsified vials and revealed unexpected connections between counterfeits, which may be useful for supporting ongoing investigations.

2.3 Application of ATR-FTIR technique in analyzing pharmacologically active ingredients in other products

IR spectroscopic identification methods are applied not only to study medicinal products but also to analyze other substances that affect the human body, including new psychoactive substances (NPS), narcotic, and psychotropic substances.

In Poland, IR spectral analysis has been applied for the rapid differentiation of structural isomers among NPS (Piorunska-Sedlak and Stypulkowska, 2020). The combination of ATR-FTIR technique and computational methods has broad applications in analyzing various other substances. J. Hughes et al. described method for the rapid identification and quantification during police operations and seizures (Hughes et al., 2013). A thoroughly developed and validated method can be used as an inexpensive, fast, and mobile alternative to expensive and labor-intensive processes. Darie et al. analyzed spectra to classify various drugs of abuse, including hallucinogens, cannabinoids, and opioids, using machine learning models, such as support vector machines and eXtreme Gradient Boosting (Darie et al., 2023). An interesting application of spectral data involves the identification and selection of compounds that can be used as surrogates for opioids in the development and training of spectroscopic sensors. Compounds such as heroin, fentanyl, and carfentanil have been studied to enhance the safety of drug enforcement officer training (Daniels et al., 2022). Chemometric models also enable the use of spectroscopic data to determine the origin of drugs based on impurity profiles, characteristic of specific synthetic pathways. McKeown et al. described the application of the orthogonal partial least squares-discriminant analysis model to the fentanyl precursors N-phenethyl-4-piperidone and 4-anilino-N-phenethylpiperidine (McKeown et al., 2023). The combination of experimental and computational approaches in the analysis of atomic locality for selected vibrational models and well-known compounds, such as variously substituted piperidine, facilitates the detection of novel derivatives in illicit drug-related samples and supports the identification of fentanyl and its analogs, including salts, in environmental samples (Shan et al., 2022). Due to the sensitivity of this technique to polymorphisms, it is often used in studies of APIs. Combined with Raman spectroscopy and computational methods, this technique has proven useful for identifying different polymorphic forms of pyrazinamide in mixtures (Zhou et al., 2024).

A different case was reported by J. Coelho Neto et al. They examined colorful tablets sold as ecstasy (MDMA) (3,4-methylenedioxymethamphetamine) and found no traces of the declared MDMA (Neto et al., 2018). However, they detected spectral bands characteristic of sildenafil. The tablets were repainted genuine Brazilian products for the treatment of erectile dysfunction.

Another application was shown in quantitative analysis. Ramsay et al. described the role of ATR-FTIR as part of a multi-technology approach used to determine fentanyl in complex mixtures containing caffeine and fentanyl in illicit opioids (Ramsay et al., 2021).

The examples mentioned show that ATR-FTIR and Raman spectroscopy are often used together. They are complementary techniques in modern vibrational spectroscopy, as they are based on different phenomena: IR absorption and Raman scattering. Raman spectroscopy detects vibrational modes that involve changes in molecular polarizability, making it effective for analyzing non-polar bonds, while IR spectroscopy identifies modes associated with changes in dipole moments, making it sensitive to polar functional groups. Therefore, together they provide a more comprehensive molecular characterization of pharmaceutical compounds, excipients, and falsified drugs by capturing different vibrational features governed by distinct selection rules (Muro et al., 2015).

3 Usefulness and potential of the XRPD technique in pharmaceutical analysis

3.1 Basic properties of the XRPD technique and possible applications

Each crystalline substance is characterized by a distinct crystal system composed of regularly repeating structural elements, such as atoms, ions, and molecules. These elements form lattice planes, whose arrangement can act as a diffraction grating for radiation. The diffraction of radiation, in this case, X-rays, arises from interactions with the electron clouds of atoms. Depending on the specific arrangement of the atoms, the incident radiation can be either enhanced or diminished in the crystal lattice. The amplification condition requires that the path difference between two diffracted X-ray waves must be an integral multiple of the wavelength, a principle described by Bragg's law (European Pharmacopoeia, 2022). When this requirement is fulfilled, strongly reflected X-rays are produced at specific angles and recorded as a function of the angle to produce diffraction patterns. The positions and intensities of the peaks can be analyzed because they are characteristic of different crystalline substances.

XRPD is a highly effective analytical technique with a long history of use. For years, it has been used to analyze and characterize crystalline structures, providing information on both active pharmaceutical ingredients and excipients. Other advantageous application of the method is detection of changes in polymorphic structure of the substance, as indicated by numerous research papers (Thakral et al., 2018; Spiliopoulou et al., 2020; Rodríguez et al., 2021). This is crucial because different polymorphic forms can have different properties that affect the bioavailability, stability, and manufacturing of API

(Ainurofiq et al., 2020). Differences in polymorphic forms can be clear indicators of falsified products because legitimate drugs are manufactured under strict controls to maintain consistency in their crystalline forms. Moreover, this technique can detect variations in excipients and coatings, thereby distinguishing between genuine and counterfeit medicines. As a nondestructive analytical tool, it supports the pharmaceutical industry in quality control, regulatory compliance, and the development of novel therapeutic agents, thereby enhancing overall drug discovery and development.

3.2 Application of XRPD technique in the analysis of falsified and substandard drugs

XRPD offers substantial development potential for the detection and prevention of drug falsification, which is an area of growing concern in pharmaceutical regulations and consumer safety. This method provides a highly accurate means of verifying the authenticity of various medications, especially when the reference diffraction pattern of the original product is available.

XRPD is a technique used to analyze drugs for erectile dysfunction. Such investigations were evaluated in Poland, covering the topic of falsification of the well-known medication Viagra® containing sildenafil citrate. Substantial differences in diffraction patterns have been observed between authentic and falsified products (Piorunska-Sedlak and Stypulkowska, 2021; Maurin et al., 2007). Moreover, E Deconinck et al. employed chemometric models to distinguish between tadalafil and sildenafil citrate samples from different manufacturers, which can help in determining the API sources (Deconinck et al., 2022; 2023). The aforementioned London-based study also provided valuable insights into the physical form of the active ingredient, its phase transitions, and the potential impact on product performance through the use of simultaneous differential scanning calorimetry and XRPD techniques (Ho et al., 2022). Similar investigations have been carried out on other medications, for example, on the anti-ulcer medication omeprazole (Rebiere et al., 2022), and also to differentiate between genuine and counterfeit medicines claiming to contain acetylsalicylic acid and ascorbic acid (Jendrzejewska et al., 2018). These examples illustrate the broad applicability of this technique in pharmaceutical authentication.

To increase revenue, falsified drug producers frequently use cheaper alternatives for both active pharmaceutical ingredients and excipients. These alternatives may be of inferior quality, ineffective, or even hazardous, posing serious health risks to consumers. Research on drugs containing paracetamol has shown that XRPD can effectively reveal quality inconsistencies between different pharmaceutical products with the same active ingredients and distinguish polymorphic forms of paracetamol in different drug formulations (Oloyede et al., 2023; Jendrzejewska et al., 2020). This is particularly important because legitimate pharmaceuticals are produced under tightly controlled conditions to ensure that the crystalline form of the active ingredient remains consistent across all batches. Any deviation in these forms may suggest that the product is falsified or substandard. The ability of XRPD to identify these subtle yet critical differences makes it a valuable tool in fighting drug falsification.

3.3 Application of XRPD in the analysis of pharmacologically active ingredients in other products

The application of XRPD extends beyond the identification of falsified drugs. It can be applied not only to final products but also during the pre-approval drug studies. Stability studies are pivotal in the pharmaceutical industry for estimating the long-term behavior of substances. Environmental conditions such as temperature (Kumar and Jha, 2017), light exposure, and humidity (Ng et al., 2022) can cause changes in the crystalline structure of APIs and excipients, thereby affecting the stability, efficacy, and safety of medicines. Phase transitions, amorphization, and recrystallization are phenomena that may occur (Jojart-Laczkovich et al., 2016). Understanding these changes is essential for establishing proper storage conditions and identifying degradation products or impurities, which can optimize formulations. Amorphous drugs often exhibit higher solubility and dissolution rates than their crystalline counterparts (Kapoor et al., 2023).

Therefore, studies using XRPD to monitor changes in medicines are very popular, leading to many applications, such as in the field of co-amorphous formulations. M. Ruponen et al. analyzed furosemide with arginine and P-glycoprotein inhibitor drugs (Ruponen et al., 2021), while other scientists evaluated the stability of amorphous olanzapine and its co-amorphous form with saccharin (da Costa et al., 2022). There was also a Danish research conducted on co-amorphous systems consisting of naproxen, arginine, and lysine (Wostry et al., 2020). An investigation into diabetes treatment in this area showed that mixing poorly soluble nateglinide with metformin hydrochloride enhanced the dissolution rate of nateglinide. The amorphization and stabilization of this form in the mixture were confirmed, leading to increased drug release and the potential for improved therapy in patients with diabetes (Wairkar and Gaud, 2016). Other studies focused on developing inclusion complexes of meloxicam with β-cyclodextrin-based nanosponges that should enhance solubility, stability, and prolong drug release. The crystalline form of meloxicam converts into an amorphous state through complexation with nanosponges, which is a new approach in terms of drug release (Shende et al., 2015). Similar studies were conducted in Poland on inclusion complexes of ketoprofen (Betlejewska-Kielak et al., 2021) and flurbiprofen (Betlejewska-Kielak et al., 2023) with β-cyclodextrin, proving the formation of a complex.

Determining which crystalline form of the compound occurs in a given drug is crucial. In this regard, XRPD technique experiments were carried out with segesterone acetate, a drug used as a contraceptive (Aragon et al., 2021), flavonoids such as taxifolin (Terekhov et al., 2020), and antiepileptic drug levetiracetam (Xu et al., 2015). In a previously mentioned study of different polymorphic forms of pyrazinamide, XRPD was used for identification (Zhou et al., 2024).

Another interesting topic that has attracted increasing attention is the production and distribution of NPS. These substances are typically sold online and marketed as fertilizers, bath salts (Altun and Cok, 2020; Riley et al., 2020), and research chemicals (Hohmann et al., 2014; Thornton et al., 2019). XRPD can be a useful tool for identifying NPS not only in the form of pure substances but also in

TABLE 2 Applications of ATR-FTIR and XRPD techniques in the study of products and compounds with pharmacological activity.

Technique	Subject of study		References
	Category	Reason for using/substance	
Falsified and substandard			
ATR-FTIR	Falsified herbal supplements	Men's sexual performance	Ho et al. (2022)
	Authentic and falsified medicinal products	Blister packaging materials	Bin Salim et al. (2021), Degardinet al. (2019)
	Authentic/falsified medicinal products	Pain relievers (paracetamol)	Lawson et al. (2018)
	Falsified medicinal products	Erectile dysfunction disorder drugs (Phosphodiesterase-5 Inhibitors- PDE5-i)	Ortiz et al. (2013), Piorunska-Sedlak and Stypulkowska (2021), Spalovska et al. (2021)
	Falsified API		Keizers et al. (2016)
ATR-FTIR/ chemometric	Authentic/falsified medicinal products		Brito et al. (2020)
		An anabolic steroid	Neves et al. (2017)
	Medicinal products	Antibiotics	Mittal et al. (2021)
	Authentic and falsified herbal medicinal products	Pain relievers	Fatmarahmi et al. (2022)
XRPD	Falsified herbal supplements	Men's sexual performance	Ho et al. (2022)
	Substandard medicinal products	Pain relievers (paracetamol)	Oloyede et al. (2023), Jendrzejewska et al. (2020)
	Falsified medicinal products	Acetylsalicylic acid and ascorbic acid	Jendrzejewska et al. (2018)
	Falsified medicinal products	Erectile dysfunction disorder drugs (Phosphodiesterase-5 Inhibitors- PDE5-i)	(Piorunska-Sedlak and Stypulkowska, 2021) Maurin et al. (2007)
XRPD/chemometric	Authentic/substandard/falsified API		(Deconinck et al., 2022; 2023)
		Omeprazole	Rebiere et al. (2022)
Illegal and others			
ATR-FTIR	Illegal products/authentic/falsified medicinal products	MDMA/PDE5-i	Neto et al. (2018)
	Illegal products	Heroin, fentanyl, and carfentanil surrogates	Daniels et al. (2022)
		New psychoactive substances- NPS	Piorunska-Sedlak and Stypulkowska (2020)
		Fentanyl	Ramsay et al. (2021)
ATR-FTIR/ chemometric		New psychoactive substances- NPS	Darie et al. (2023)
		Methamphetamine	Hughes et al. (2013)
		Fentanyl precursors	McKeown et al. (2023)
		Fentanyl and analogs	Shan et al. (2022)
	API (polymorphic forms)	Pyrazinamide	Zhou et al. (2024)
XRPD	API (co-amorphous formulations)	Furosemide with arginine and P-glycoprotein inhibitor drugs	Ruponen et al. (2021)
		Olanzapine with saccharin	da Costa et al. (2022)
		Naproxen and arginine with lysine	Wostry et al. (2020)
		Nateglinide with metformin hydrochloride	Wairkar and Gaud (2016)
	API (inclusion complexes)	Meloxicam with β-cyclodextrin-based nanosponges	Shende et al. (2015)
		Ketoprofen with β-cyclodextrin	Betlejewska-Kielak et al. (2021)
		Flurbiprofen with β-cyclodextrin	Betlejewska-Kielak et al. (2023)
	API (polymorphic forms)	Segesterone acetate	Aragon et al. (2021)

(Continued on following page)

TABLE 2 (*Continued*) Applications of ATR-FTIR and XRPD techniques in the study of products and compounds with pharmacological activity.

Technique	Subject of study		References
	Category	Reason for using/substance	
		Taxifolin	Terekhov et al. (2020)
		Levetiracetam	Xu et al. (2015)
	Illegal products	New psychoactive substances- NPS	Jurasek et al. (2019)
XRPD/chemometric	API (polymorphic forms)	Pyrazinamide	Zhou et al. (2024)

street mixtures containing both organic and inorganic impurities (Jurasek et al., 2019).

4 Discussion and future outlook

Attenuated total reflectance- Fourier transform infrared spectroscopy and X-ray powder diffraction are nondestructive analytical techniques that allow direct measurement of samples with minimal preparation, thus preserving their original composition. Both techniques are noninvasive, simple, and reproducible, enabling the identification of both the main and auxiliary components. The combination of the techniques enables the rapid and accurate identification of contaminants or falsified substances, including salts, co-crystals, mixtures, and various polymorphic forms (Table 2), although both techniques require access to databases or reference materials. Therefore, they are well suited for rapid screening tests and identification of known compounds registered in databases. Negative results of database searches direct further research towards the use of other techniques for identifying unknown substances or detecting low concentrations of compounds, such as LC-MS or NMR. Whereas ATR-FTIR has long been established for its speed and simplicity, the importance of XRPD has grown due to advances in miniaturization and faster analysis. They play relevant roles in confirming the identity and authenticity of products, highlighting their importance in ensuring product safety and quality across regulatory and industrial settings.

Author contributions

AM: Conceptualization, Formal Analysis, Investigation, Visualization, Writing–original draft. KP: Writing–review and editing, Conceptualization, Formal Analysis, Investigation, Visualization, Writing–original draft. JM: Writing–review and editing. AB: Funding acquisition, Supervision, Writing–review and editing.

Funding

The author(s) declare that financial support was received for the research, authorship, and/or publication of this article. The publication was co-financed by the state budget under the program of the Minister of Education, and Science called “Science for the Society II”, project number NdS-II/SN/0270/2023/01, amount of funding 10269 PLN; total value of the project 1956000 PLN.

Conflict of interest

The authors declare that the research was conducted in the absence of any commercial or financial relationships that could be construed as a potential conflict of interest.

Generative AI statement

The author(s) declare that no Generative AI was used in the creation of this manuscript.

Publisher’s note

All claims expressed in this article are solely those of the authors and do not necessarily represent those of their affiliated organizations, or those of the publisher, the editors and the reviewers. Any product that may be evaluated in this article, or claim that may be made by its manufacturer, is not guaranteed or endorsed by the publisher.

References

Ainurofiq, A., Dinda, K. E., Pangestika, M. W., Himawati, U., Wardhani, W. D., and Sipahutar, Y. T. (2020). The effect of polymorphism on active pharmaceutical ingredients: a review. *Int. J. Res. Pharm. Sci.* 11 (2), 1621–1630. doi:10.26452/ijrps.v11i2.2044

Altun, B., and Cok, I. (2020). Psychoactive bath salts and neurotoxicity risk. *Turk. J. Pharm. Sci.* 17 (2), 235–241. doi:10.4274/tjps.galenos.2018.40820

Aragon, F. F. H., Haeck, C. M., Morais, P. C., and Variano, B. (2021). Polymorphism characterization of segesterone acetate: a comprehensive study using XRPD, FT-IR and Raman spectroscopy. *Int. J. Pharm.* 596, 120234. doi:10.1016/j.ijpharm.2021.120234

Betlejewska-Kielak, K., Bednarek, E., Budzianowski, A., Michalska, K., and Maurin, J. K. (2021). Comprehensive characterisation of the ketoprofen-β-cyclodextrin inclusion complex using X-ray techniques and NMR spectroscopy. *Molecules* 26 (13), 4089. doi:10.3390/molecules26134089

Betlejewska-Kielak, K., Bednarek, E., Budzianowski, A., Michalska, K., and Maurin, J. K. (2023). Comprehensive characterisation of the flurbiprofen/β-cyclodextrin

inclusion complex using X-ray techniques and NMR spectroscopy. *J. Mol. Struct.* 1285, 135450. doi:10.1016/j.molstruc.2023.135450

Bin Salim, M. R., Widodo, R. T., and Noordin, M. I. (2021). Fast detection of counterfeit paracetamol by the analysis of blister plastic materials using fourier transform infrared spectroscopy (FTIR) and differential scanning calorimetry (DSC). *Glob. Res. J. Chem.* 5 (1), 53–59.

Brito, J. B. G., Bucco, G. B., John, D. K., Ferrão, M. F., Ortiz, R. S., Mariotti, K. C., et al. (2020). Wavenumber selection based on Singular Value Decomposition for sample classification. *Forensic Sci. Int.* 309, 110191. doi:10.1016/j.forsciint.2020.110191

Chauhan, A., and Chauhan, P. (2014). Powder XRD technique and its applications in science and technology. *J. Anal. Bioanal. Tech.* 5. doi:10.4172/2155-9872.1000212

da Costa, N. F., Daniels, R., Fernandes, A. I., and Pinto, J. F. (2022). Downstream processing of amorphous and Co-amorphous olanzapine powder blends. *Pharmaceutics* 14 (8), 1535. doi:10.3390/pharmaceutics14081535

Daniels, G. C., Whitener, K. E., Smith, Ch. D., Giordano, B. C., and Collins, G. E. (2022). Assessment of opioid surrogates for spectroscopic testing (Part III). *Forensic Chem.* 30, 100443. doi:10.1016/j.forc.2022.100443

Darie, I.-F., Anton, S. R., and Praisler, M. (2023). Machine learning systems detecting illicit drugs based on their ATR-FTIR spectra. *Inventions* 8 56, 56. doi:10.3390/inventions8020056

Deconinck, E., Courselle, P., Raimondo, M., Grange, Y., Rebière, H., Mihailova, A., et al. (2022). GEONs API fingerprint project: selection of analytical techniques for clustering of sildenafil citrate API samples. *Talanta* 239, 123123. doi:10.1016/j.talanta.2021.123123

Deconinck, E., Raimondo, M., Borioni, A., Grange, Y., Rebière, H., Mihailova, A., et al. (2023). Clustering of tadalafil API samples according to their manufacturer in the context of API falsification detection. *J. Pharm. Sci.* 112 (11), 2834–2842. doi:10.1016/j.xphs.2023.05.015

Degardin, K., Jamet, M., Guillemain, A., and Mohn, T. (2019). Authentication of pharmaceutical vials. *Talanta* 198, 487–500. doi:10.1016/j.talanta.2019.01.121

European Pharmacopoeia (2021). Absorption spectrophotometry, infrared. Available at: https://pheur.edqm.eu/app/11-4/content/11-4/20224E.htm?highlight=on&terms=20224 (Accessed December 30, 2024).

European Pharmacopoeia (2022). Characterisation of crystalline solids by XRPD. Available at: https://pheur.edqm.eu/app/11-4/content/default/20933E.htm (Accessed November 22, 2024).

Fatmarahmi, D. C., Susidarti, R. A., Swasono, R. T., and Rohman, A. (2022). Application of FTIR-ATR spectroscopy in combination with multivariate analysis to analyze synthetic drugs adulterant in ternary mixtures of herbal medicine products. *Indones. J. Pharm.* 33 (1), 63–71. doi:10.22146/ijp.2609

Ho, H. M. K., Xiong, Z., Wong, H. Y., and Buanz, A. (2022). The era of fake medicines: investigating counterfeit medicinal products for erectile dysfunction disguised asherbal supplements. *Int. J. Pharm.* 617, 121592. doi:10.1016/j.ijpharm.2022.121592

Hohmann, N., Mikus, G., and Czock, D. (2014). Effects and risks associated with novel psychoactive substances: mislabeling and sale as bath salts, spice, and research chemicals. *Dtsch. Ärzteblatt Int.* 111 (9), 139–147. doi:10.3238/arztebl.2014.0139

Hughes, J. M., Ayoko, G., Collett, S., and Golding, G. (2013). Rapid quantification of methamphetamine: using attenuated total reflectance fourier transform infrared spectroscopy (ATR-FTIR) and chemometrics. *PLOS ONE* 8 (7), e69609. doi:10.1371/journal.pone.0069609

INTERPOL (2023). Global illicit medicines targeted by INTERPOL operation. Available at: https://www.interpol.int/News-and-Events/News/2023/Global-illicit-medicines-targeted-by-INTERPOL-operation (Accessed October 29, 2024).

Jendrzejewska, I., Goryczka, T., Pietrasik, E., Klimontko, J., and Jampilek, J. (2020). X-Ray and thermal analysis of selected drugs containing acetaminophen. *Molecules* 25 (24), 5909. doi:10.3390/molecules25245909

Jendrzejewska, I., Zajdel, P., Pietrasik, E., Barsova, Z., and Goryczka, T. (2018). Application of X-ray powder diffraction and differential scanning calorimetry for identification of counterfeit drugs. *Monatsh Chem.* 149, 977–985. doi:10.1007/s00706-018-2193-z

Jojart-Laczkovich, O., Katona, G., Aigner, Z., and Szabo-Revesz, P. (2016). Investigation of recrystallization of amorphous trehalose through hot-humidity stage X-ray powder diffraction. *Eur. J. Pharm. Sci.* 95, 145–151. doi:10.1016/j.ejps.2016.08.003

Jurasek, B., Bartunek, V., Huber, S., and Kuchar, M. (2019). X-Ray powder diffraction - a non-destructive and versatile approach for the identification of new psychoactive substances. *Talanta* 195, 414–418. doi:10.1016/j.talanta.2018.11.063

Kapoor, D. U., Singh, S., Sharma, P., and Prajapati, B. G. (2023). Amorphization of low soluble drug with amino acids to improve its therapeutic efficacy: a state-of-art-review. *AAPS PharmSciTech* 24 (8), 253. doi:10.1208/s12249-023-02709-2

Keizers, P. H. J., Bakker, F., Ferreira, J., Wackers, P. F. K., van Kollenburg, D., van der Aa, E., et al. (2019). Benchtop NMR spectroscopy in the analysis of substandard and falsified medicines as well as illegal drugs. *J. Pharm. Biomed.* 178, 112939. doi:10.1016/j.jpba.2019.112939

Keizers, P. H. J., Wiegard, A., Bastiaan, J., and Venhuis, B. J. (2016). The quality of sildenafil active substance of illegal source. *J. Pharm. Biomed.* 131, 133–139. doi:10.1016/j.jpba.2016.08.027

Kumar, N., and Jha, A. (2017). Temperature excursion management: a novel approach of quality system in pharmaceutical industry. *Saudi Pharm. J.* 25 (2), 176–183. doi:10.1016/j.jsps.2016.07.001

Lawson, G., Ogwu, J., and Tanna, S. (2018). Quantitative screening of the pharmaceutical ingredient for the rapid identification of substandard and falsified medicines using reflectance infrared spectroscopy. *PLOS ONE* 13 (8), e0202059. doi:10.1371/journal.pone.0202059

Maurin, J. K., Plucinski, F., Mazurek, A. P., and Fijalek, Z. (2007). The usefulness of simple X-ray powder diffraction analysis for counterfeit control—the Viagra® example. *J. Pharm. Biomed.* 43 (4), 1514–1518. doi:10.1016/j.jpba.2006.10.033

McKeown, H. E., Rook, T. J., Pearson, J. R., and Jones, O. A. H. (2023). Investigations into fentanyl precursors method classification by handheld Fourier transform infrared and Raman spectroscopy combined with multivariate statistical analysis. *Forensic Chem.* 33, 100476. doi:10.1016/j.forc.2023.100476

Mittal, M., Sharma, K., and Rathore, A. (2021). Checking counterfeiting of pharmaceutical products by attenuated total reflection mid-infrared spectroscopy. *Spectroc. Acta Pt. A-Molec. Biomolec. Spectr.* 255, 119710. doi:10.1016/j.saa.2021.119710

Muro, C. K., Doty, K. C., Bueno, J., Halámková, L., and Lednev, I. K. (2015). Vibrational spectroscopy: recent developments to revolutionize forensic science. *Anal. Chem.* 87 (1), 306–327. doi:10.1021/ac504068a

Neto, J. C., Faraco, R. F. P., Alves, C. F., Castro, S. M. M., and Machado, Y. (2018). Genuine sildenafil tablets sold in Brazil disguised as MDMA. *Forensic Sci. Int.* 283, e8–e12. doi:10.1016/j.forsciint.2017.12.006

Neves, D. B., Talhavini, M., Braga, J. W., Zacca, J. J., and Caldas, E. D. (2017). Detection of counterfeit Durateston using Fourier transform infrared spectroscopy and partial least squares: discriminant analysis. *J. Braz. Chem. Soc.* 28, 1288–1296. doi:10.21577/0103-5053.20160293

Ng, L. H., Ling, J. K. U., and Hadinoto, K. (2022). Formulation strategies to improve the stability and handling of oral solid dosage forms of highly hygroscopic pharmaceuticals and nutraceuticals. *Pharmaceutics* 14 (10), 2015. doi:10.3390/pharmaceutics14102015

Oloyede, O. O., Alabi, Z. O., Akinyemi, A. O., Oyelere, S. F., Oluseye, A. B., and Owoyemi, B. C. D. (2023). Comparative evaluation of acetaminophen form (I) in commercialized paracetamol brands. *Sci. Afr.* 19, e01537. doi:10.1016/j.sciaf.2022.e01537

Ortiz, R. S., de Cássia Mariotti, K., Fank, B., Limberger, R. P., Anzanello, M. J., and Mayorga, P. (2013). Counterfeit Cialis and Viagra fingerprinting by ATR-FTIR spectroscopy with chemometry: can the same pharmaceutical powder mixture be used to falsify two medicines? *Forensic Sci. Int.* 226 (1–3), 282–289. doi:10.1016/j.forsciint.2013.01.043

Piorunska-Sedlak, K., and Stypulkowska, K. (2020). Strategy for identification of new psychoactive substances in illicit samples using attenuated total reflectance infrared spectroscopy. *Forensic Sci. Int.* 312, 110262. doi:10.1016/j.forsciint.2020.110262

Piorunska-Sedlak, K., and Stypulkowska, K. (2021). Selectivity of identification of compounds from the group of phosphodiesterase-5 inhibitors (PDE-5i) in falsified products from the Polish market using attenuated total reflectance Fourier transform infrared spectroscopy and X-ray powder diffraction. *Sci. and Justice* 61 (6), 714–722. doi:10.1016/j.scijus.2021.08.008

Ramsay, M., Gozdzialski, L., Larnder, A., Wallace, B., and Hore, D. (2021). Fentanyl quantification using portable infrared absorption spectroscopy. A framework for community drug checking. *Vib. Spectrosc.* 114, 103243. doi:10.1016/j.vibspec.2021.103243

Rao, A. S., Dileep, B., and Madhusudhan, B. (2023). A review on "pharmaceutical analysis in the modern era: advanced analytical methods". *J. Nov. Res. Devel.* 8 (10), a876–a881.

Rebiere, H., Grange, Y., Deconinck, E., Courselle, P., Acevska, J., Brezovska, K., et al. (2022). European fingerprint study on omeprazole drug substances using a multi analytical approach and chemometrics as a tool for the discrimination of manufacturing sources. *J. Pharm. Biomed.* 208, 114444. doi:10.1016/j.jpba.2021.114444

Rebiere, H., Guinot, P., Chauvey, D., and Brenier, Ch. (2017). Fighting falsified medicines: the analytical approach. *J. Pharm. Biomed.* 142, 286–306. doi:10.1016/j.jpba.2017.05.010

Riley, A. L., Nelson, K. H., To, P., Lopez-Arnau, R., Xu, P., Wang, D., et al. (2020). Abuse potential and toxicity of the synthetic cathinones (i.e., "Bath salts"). *Neurosci. Biobehav. Rev.* 110, 150–173. doi:10.1016/j.neubiorev.2018.07.015

Rodríguez, I., Gautam, R., and Tinoco, A. D. (2021). Using X-ray diffraction techniques for biomimetic drug development, formulation, and polymorphic characterization. *Biomimetics* 6 (1), 1. doi:10.3390/biomimetics6010001

Ruponen, M., Kettunen, K., Santiago Pires, M., and Laitinen, R. (2021). Co-amorphous formulations of furosemide with arginine and P-glycoprotein inhibitor drugs. *Pharmaceutics* 13 (2), 171. doi:10.3390/pharmaceutics13020171

Sansone, A., Cuzin, B., and Jannini, E. A. (2021). Facing counterfeit medications in sexual medicine. A systematic scoping review on social strategies and technological solutions. *Sex. Med.* 9 (6), 100437. doi:10.1016/j.esxm.2021.100437

Shan, X., Lee, L., Clewes, R. J., Howle, Ch. R., Sambrook, M. R., and Clary, D. C. (2022). Computational analyses of the vibrational spectra of fentanyl, carfentanil and remifentanil. *Spectroc. Acta Pt. A-Molec. Biomolec. Spectr.* 270, 120763. doi:10.1016/j.saa.2021.120763

Shende, P. K., Gaud, R. S., Bakal, R., and Patil, D. (2015). Effect of inclusion complexation of meloxicam with β-cyclodextrin- and β-cyclodextrin-based nanosponges on solubility, *in vitro* release and stability studies. *Colloids Surf. B Biointerfaces* 136, 105–110. doi:10.1016/j.colsurfb.2015.09.002

Song, Y., Cong, Y., Wang, B., and Zhang, N. (2020). Applications of Fourier transform infrared spectroscopy to pharmaceutical preparations. *Expert Opin. Drug Deliv.* 17 (4), 551–571. doi:10.1080/17425247.2020.1737671

Spalovska, D., Pekarek, T., Kuchar, M., and Setnicka, V. (2021). Comparison of genuine, generic and counterfeit Cialis tablets using vibrational spectroscopy and statistical methods. *J. Pharm. Biomed.* 206, 114383. doi:10.1016/j.jpba.2021.114383

Spiliopoulou, M., Valmas, A., Triandafillidis, D.-P., Kosinas, C., Fitch, A., Karavassili, F., et al. (2020). Applications of X-ray powder diffraction in protein crystallography and drug screening. *Crystals* 10 (2), 54. doi:10.3390/cryst10020054

Terekhov, R. P., Selivanova, I. A., Tyukavkina, N. A., Ilyasov, I. R., Zhevlakova, A. K., Dzuban, A. V., et al. (2020). Assembling the puzzle of taxifolin polymorphism. *Molecules* 25 (22), 5437. doi:10.3390/molecules25225437

Thakral, N. K., Zanon, R. L., Kelly, R. C., and Thakral, S. (2018). Applications of powder X-ray diffraction in small molecule pharmaceuticals: achievements and aspirations. *J. Pharm. Sci.* 107 (12), 2969–2982. doi:10.1016/j.xphs.2018.08.010

Thornton, S. L., Darracq, M. A., Gugelmann, H. M., and Armenian, P. (2019). Surface internet marketplace presence and availability of NPS sold as research chemicals: a snapshot study. *Toxicol. Commun.* 3 (1), 67–74. doi:10.1080/24734306.2019.1648067

Wairkar, S., and Gaud, R. (2016). Co-amorphous combination of nateglinide-metformin hydrochloride for dissolution enhancement. *AAPS PharmSciTech* 17, 673–681. doi:10.1208/s12249-015-0371-4

Wostry, M., Plappert, H., and Grohganz, H. (2020). Preparation of Co-amorphous systems by freeze-drying. *Pharmaceutics* 12 (10), 941. doi:10.3390/pharmaceutics12100941

Xu, K., Xiong, X., Guo, L., Wang, L., Li, S., Tang, P., et al. (2015). An investigation into the polymorphism and crystallization of levetiracetam and the stability of its solid form. *J.Pharm. Sci.* 104 (12), 4123–4131. doi:10.1002/jps.24628

Zhou, J., Zhang, B., Gong, L., Hu, K., Yang, S., and Lu, Y. (2024). Quantitative analysis of pyrazinamide polymorphs in ternary mixtures by ATR-FTIR and Raman spectroscopy with multivariate calibration. *Vib. Spectrosc.* 130, 103625. doi:10.1016/j.vibspec.2023.103625

frontiers | Frontiers in Chemistry

TYPE Review
PUBLISHED 20 February 2025
DOI 10.3389/fchem.2025.1536222

OPEN ACCESS

EDITED BY
Constantinos K. Zacharis,
Aristotle University of Thessaloniki, Greece

REVIEWED BY
Xiaoping Wu,
Fuzhou University, China
Guinevere S. M. Lageveen-Kammeijer,
University of Groningen, Netherlands

*CORRESPONDENCE
Virginia Ghizzani,
virginia.ghizzani@iss.it,
virginia.ghizzani01@universitadipavia.it

RECEIVED 28 November 2024
ACCEPTED 22 January 2025
PUBLISHED 20 February 2025

CITATION
Ghizzani V, Ascione A, Gonnella F, Massolini G and Luciani F (2025) Exploring imaged capillary isoelectric focusing parameters for enhanced charge variants quality control.
Front. Chem. 13:1536222.
doi: 10.3389/fchem.2025.1536222

Exploring imaged capillary isoelectric focusing parameters for enhanced charge variants quality control

Virginia Ghizzani[1,2]*, Alessandro Ascione[1], Federico Gonnella[1], Gabriella Massolini[2] and Francesca Luciani[1]

[1]National Centre for the Control and Evaluation of Medicines (CNCF), Istituto Superiore di Sanità, Rome, Italy, [2]Department of Drug Sciences, University of Pavia, Pavia, Italy

Biopharmaceuticals are increasingly utilised in the treatment of oncological, inflammatory, and autoimmune diseases, largely due to their exceptional specificity in targeting antigens. However, their structural complexity, heterogeneity, and sensitivity pose crucial challenges in their production, purification, and delivery. Charge heterogeneity analysis, a Critical Quality Attribute of these biomolecules used in their Quality Control, is often performed using separative analytical techniques such as imaged capillary Isoelectric Focusing (icIEF). Recognized as a gold standard by the industry, icIEF leverages a pH gradient to provide high-resolution profiling of charge variants in biotherapeutics. In this review, critical experimental parameters for icIEF method development in the context of biotherapeutic drug development and QC will be discussed. Key aspects, including sample preparation, capillary properties, carrier ampholytes, stabilizers, and detection are examined, and supported by recent literature. Advances in icIEF technology and its expanding applications underline its robustness, reproducibility, and compliance with regulatory standards, affirming its pivotal role in ensuring the identity and consistency of biological products.

KEYWORDS

icIEF, charge heterogeneities, isoelectric point, biotherapeutics development, QC

1 Introduction

Biotherapeutics are becoming commonly used drugs for the treatment of several oncological, inflammatory, and autoimmune diseases principally due to their high specificity in target antigen binding, reducing the need for frequent dosing (Lechner et al., 2019, 1–17; Sharma et al., 2023, 18; Paul et al., 2024, 399). Many of the biotherapeutic molecules are monoclonal antibodies (mAbs), however, recently, several novel antibody-based biologic products have been engineered in order to improve potency, increase circulation half-life, expand functions, enable specific delivery of drugs and effector proteins to the site of action, and enhance tissue penetration. Examples of next-generation of antibody therapeutics include Fc fusion proteins, antibody-drug conjugates (ADC), bispecific antibodies (BsAbs) and antibody fragments. Today, more than 100 mAbs and ADCs have been approved as biotherapeutic products by the European Medicines Agency (EMA) and the Food and Drug Administration (FDA) (Carter and Rajpal, 2022, 2789). These biomolecules are often complex, heterogeneous, and fragile, which makes their

production, purification, and delivery challenging. Indeed, during their production in cell culture and storage, biotherapeutics are prone to Post-Translational Modifications (PTMs) such as deamidation, glycosylation, or oxidation which may produce charge heterogeneities. Since some charged-based variants can have an impact on pharmacokinetics, biological activity, and long-term storage, charge heterogeneity is considered a Critical Quality Attribute (CQA) by regulatory authorities which must be monitored during the biotherapeutics life cycle, to ensure their quality, efficacy, and safety. In fact, a CQA is a physical, chemical, biological, or microbiological property/characteristic that should be within an appropriate limit, range, or distribution to ensure the desired product quality (Pharmaceutical Development, 2022, ICH Harmonised Tripartite Guideline). CQAs variation, outside defined ranges, can have an impact on the final drug product (DP) safety and efficacy.

Quality Control (QC) of charge heterogeneity is commonly achieved using separative analytical techniques such as ion exchange chromatography (IEC) or traditional isoelectric focusing (IEF), particularly conventional capillary isoelectric focusing (cIEF) or imaged capillary isoelectric focusing (icIEF) (Lechner et al., 2019, 1–17). icIEF combines the principles of capillary electrophoresis (CE) and IEF to separate proteins based on the isoelectric point (pI) within a capillary, the separation of analytes occurs along the length of the capillary by direct imaging with a charge-coupled device (CCD) camera, without a mobilisation step as in conventional cIEF (Zhang et al., 2016, 148; Madren et al., 2022, 1050).

Compared to cIEF, icIEF allows faster separation, higher resolution, repeatability, and a simpler method development procedure. Moreover, it can be applied to biopharmaceutical QC due to its good sensitivity and robustness, thus being a useful tool to be used for annual marketing surveillance programs and the fight against counterfeit drugs. The icIEF protocols can be efficiently validated according to ICH guidelines. These advantages offer in the regulatory context a potential analytical platform for an effective detection of several PTMs-related charge-isoforms.

Recently, thanks to the increasing use of (i)cIEF, European Pharmacopoeia (Ph. Eur.) published a general text in which it is proposed a horizontal method to analyse mAb-based drugs and their charge variants, making appropriate technical distinctions between the classical and the imaged method (European Pharmacopoeia, 2023). In this framework, some interesting reviews have been published. Kahle and Wätzig have discussed the application of three electrophoretic based techniques, namely, cIEF, icIEF, and capillary zone electrophoresis for the analyses of protein charge variants (Kahle and Wätzig, 2018, 2492). The article defined the experimental conditions in icIEF methods development, such as concentration of carrier ampholytes (CAs), L-Arginine (L-Arg), pI Markers (pIMs), and urea, in QC of mAbs. More recently, Krebs et al. published a review on CE method development and validation including icIEF, emphasising that this is a mature technique that can be routinely applied in analytical laboratories, especially in the biopharmaceutical industry (Krebs et al., 2023, 1279). Another excellent review has been published in Trends in Analytical Chemistry mainly focused on the current developments of icIEF technologies including higher sensitivity detection mode (fluorescence and chemiluminescence) and combination of icIEF with mass spectrometry (MS) detection. Applications of icIEF in the pharmaceutical industry and in research laboratories were also discussed by Wu (Wu J. et al., 2022, 150). In the current state of the art, icIEF is an elected analytical method for determining pIs and charge heterogeneity profiles to guarantee the QC during the entire life cycle for mABs, BsAb, ADCs and biotherapeutic proteins (Kinoshita et al., 2013, 76; Tardif et al., 2023, 124633; Sutton et al., 2024, 5450–5458; Wu et al., 2024a) (Figure 1). In literature are reported different validation studies and QC methods for biotherapeutics published by industry users and researchers of icIEF technology (Wu et al., 2018, 2091–2098; Li et al., 2020, 3836–3843). For mAbs, icIEF methods are typically used as identity and/or purity assays in the pharmaceutical industry. The uniqueness of the charge heterogeneity profile of a mAb product is used for identity, commonly coupled to other analytical techniques, such as peptide mapping or bioassays. In the purity assay, the pI value and percentage of each charge variant of a mAb are determined. The combination of the two values of all peaks is the charge profile of the mAb, which is often used in formulation studies and product QC (Wu et al., 2024a). Product identity is one of the release testing requirements that need to be established to ensure no misidentification of drugs.

In this review, we will focus on the icIEF advancements and experimental conditions to be considered during method development for biotherapeutics drug development and QC. An overview of major performance parameters, such as sample preparation and additives, capillary properties, CAs, anodic and cathodic stabilizers, and detection modes will be discussed with the support of well-established literature and articles of the last decade. The developments of this technology and the more novel applications indicate that icIEF is a robust, reproducible, and regulatory-compliant

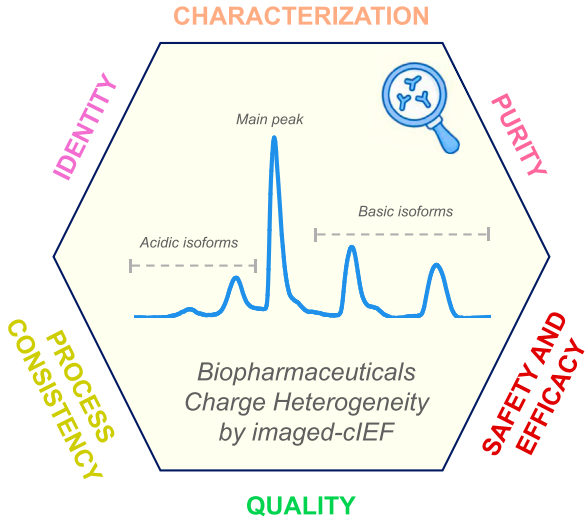

FIGURE 1
Illustrative schematic diagram showing the valuable insights obtained with icIEF charge variants analysis that support the characterization, identification, purity assessment, and process consistency of biotherapeutics. These attributes are critical for evaluating the quality, efficacy, and safety of drug products, thereby contributing significantly to their development and QC.

method for ensuring the identity and consistency of biological products (Ahluwalia et al., 2018, 271).

2 icIEF technique

icIEF is an industry's high-resolution gold-standard separative technique based on a pH gradient and is employed for the evaluation of charge variants profiles of biotherapeutic (Madren et al., 2022, 1050–1058). It can be considered the latest evolution of the outdated IEF separation technique, a group of analytic methodologies that operates in the presence of an electric field and has emerged as a tool for detailed charge-based analysis of complex molecules, especially biological drugs. Similarly to the other IEF techniques, it exploits the properties of ampholytic components, which are molecules acting as weak acids and bases, to separate them in the presence of an electric field. The electrophoretic mobility of these species will change in the presence of a pH gradient, slowing migration in the region near their pI value, by definition the pH level where the net charge of the species is zero. In the case of protein molecules, the process of separation is based on the composition of the exposed amino acids and charged residues, which behave in a manner analogous to weak acids and bases. It is crucial to acknowledge that the pI value determined through (i)cIEF techniques is regarded as an "apparent" pI, since experimental conditions influence it. This distinction stems from the observed divergence between experimentally measured values and theoretical predictions, typically derived from the primary sequence of the molecule (Ascione et al., 2024, 2313737).

While the initial application of this separative approach was the polyacrylamide gel-based IEF (gIEF), the cIEF was first developed in the early 1980s thanks to the pioneering work of Hjertedal and Zhu (Hjertén and Zhu, 1985, 265–270). Further relevant work was given, for instance, by Chen A. B.'s research group (Jochheim et al., 2001, 59–65). However, the earliest iteration of icIEF occurred approximately a decade later, in the early 1990s, with the progressive work of Wu and Pawliszyn, (1994) research group, who innovated the method by introducing whole capillary imaging (real-time monitoring of the separation phase) instead of a single point of detection (Wu and Pawliszyn, 1992, 219–224, 1994, 867–873). However, similarly to all related IEF techniques, multiple parameters must be considered in order to ensure the success of the method, as will be discussed in the relevant sections of this review (Figure 2; Table 1).

Technically in icIEF, as in cIEF, a designed mixture of amphoteric molecules, called CAs, is used to generate a pH gradient when an electric field is applied between the end of the capillary, which enables the analytes to move along the capillary until they reach their pI value. Within this context, the focusing time constitutes another pivotal parameter that must be methodically delineated during the method development to ensure the attainment of an optimal separation and, concomitantly, a reliable estimate of the measured pI values. Insufficient focusing time may result in some charged species not reaching their isoelectric point, thus leading to incomplete separation. Conversely, excessive focusing time may cause a shift in the peaks due to undesirable factors such as a residual effect of the EOF or the secondary occurring of pH gradient instability.

Considering its fundamental principles, it is evident that the genesis and development of reliable ampholyte formulations to generate stable pH gradients has been a pivotal aspect in the evolution and application of this separative technique (Righetti et al., 1997, 91–104). The implementation of the methodology within the capillary framework has been demonstrated to result in a notable enhancement in the resolution that permits differentiation between the most closely related charge variants, accompanied by a considerable reduction in both focusing time and

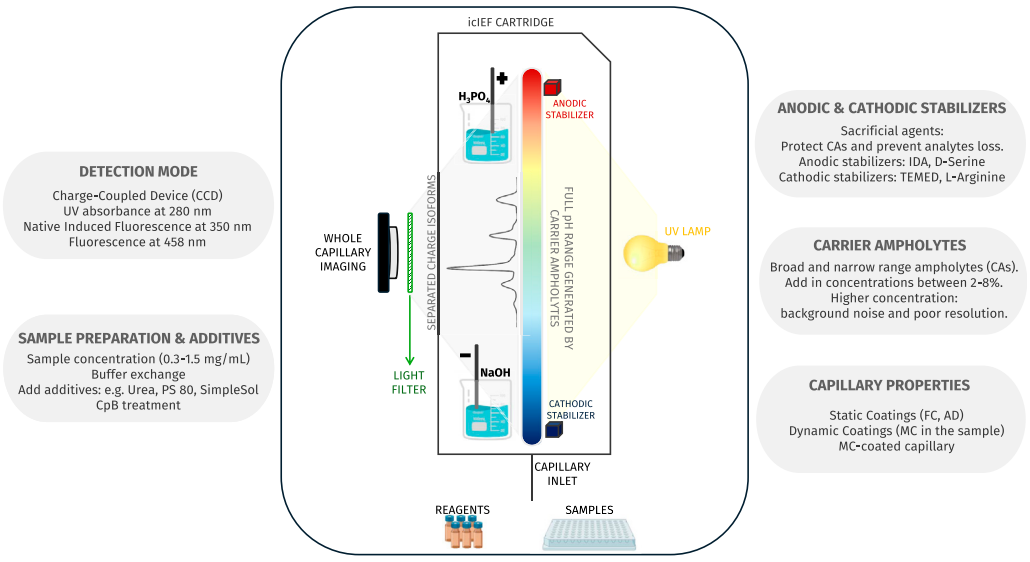

FIGURE 2
The figure provides a detailed scheme of icIEF technology which is able to detect the entire capillary, thereby allowing real-time monitoring of analyte charge variants separation. Additionally, the figure gives an overview of the factors that influence the method's performance.

TABLE 1 Summary of main critical aspects to be addressed during an icIEF method development.

Factor	Parameter	Aim	Influence on the analysis	Drawbacks
Capillary coatings	Fluorocarbon (FC)	Suppressed EOF	Improve resolution and peak shape	
	Acrylamide (AD)	Reduced EOF Reduced adsorption of biomolecules		
	Methylcellulose (MC)	Reduced EOF		MC not compatible with MS analysis, could produce spikes and clogs
Sample preparation	Concentration (not < 0.2 mg/mL)	Experimental setting based on LOD_{ABS} and LOD_{FLUO}	Suitable sensitivity	
	Buffer Exchange	Removing interferences from sample matrix	Reduced spikes and artefacts	
	Additives (Urea, NDSB, Glycine, SimpleSol)	Enhanced solubility, avoid precipitation and aggregation	Repeatability, reliability, reproducibility	Could produce peak shifts and spikes
Carrier ampholytes	Broad-range	pH gradient more versatile and widely utilised		
	Narrow-range	Tailored analysis for specific biomolecules	Enhanced resolution	Longer focusing time needed
	Total concentration (ranging 2%-8%)	Method optimization	Enhanced separation	>4 % could increase background noise
Anodic and cathodic stabilizers	Highly acidic pI value (IDA, Serine-D)	Reduced anodic drift	Stable pH gradient, enhanced repeatability, and reproducibility	High concentration negatively affect resolution
	Highly basic pI value (L-Arg, TEMED)	Reduced cathodic drift		
Focusing time	Sample-tailored (ranging 4-15 minutes)	Method optimization	Enhanced separation	Too short time: incomplete focusing. Too long time: not reliable pI values, lost pI Markers and/or analytes, artefacts and spikes
Detection mode	Absorbance	Signal acquisition tuning	Standard detection	Higher background noise
	Fluorescence		Higher sensitivity and resolution, decreased need of buffer exchange, spikes recognition	More limited available type of pI Markers

the amount of samples required (by order of few µL), which are considered advantageous aspects for the routine monitoring of pharmaceutical products. While these significant advantages are shared between cIEF and icIEF, the latter actually represents a further evolution of the conventional one with additional advantages, notably in terms of automation and faster analysis. In fact, this improvement renders the mobilisation step unnecessary, which is instead a prerequisite for conventional cIEF in order to push the analytes, once separated, towards the detector (for details, please see section 2.5).

Furthermore, icIEF technique can guarantee adequate sensitivity, enabling the detection of low abundance isoforms, with limit of detections (LODs) between 3 µg/mL and 0.7 µg/mL, depending on the detection mode (absorbance or fluorescence), as reported by the device manufacturer (Improving Charge Variant, 2000).

The icIEF has also proven to offer an optimal approach for the relative quantification of individual species (percentage area) or absolute levels, over the primordial gIEF technology, provided that adequate standards are available (Sosic et al., 2008, 4368).

As a consequence of the aforementioned advantages, icIEF is currently one of the leading methods in the industry for the analysis of biotherapeutics charge variants (Zhang et al., 2017b, 1–7). The technology of icIEF instruments has improved over the years and icIEF is now an indispensable tool in therapeutic protein development and manufacturing. The robustness and reproducibility of an icIEF instrument (iCE280) has been first evaluated in intercompany studies (Salas-solano et al., 2012, 3124) more than 10 years ago. The results from this study, whose statistical analysis was performed based on the ISO 5725-2 Guide principles, showed that icIEF is a reliable technology and largely met industry standards to assess charge heterogeneity of therapeutic proteins. Nevertheless, validation of the icIEF following the guidelines established by the International Council for Harmonization (ICH) remains to be addressed. In 2018, an interlaboratory icIEF method validation, involving 10 laboratories in eight independent Chinese companies using

iCE3 instrument with improvements in the autosampler and injector, was carried out. The method validation was performed following the ICH guideline on the analytical procedure (specificity, precision, accuracy, linearity, range, limit of quantification (LOQ), and robustness) using a typical therapeutic mAb, with a single main peak at a pI of approximately 8.5. Taking all parameters together, the obtained results validate the use of the icIEF methodology as both an identity assay and purity assay in protein charge characterization (Wu et al., 2018, 2091–2098).

More recently, additional improvements to the icIEF equipment have resulted in the Maurice® instrument by ProteinSimple, which utilises a pre-assembled cartridge leading to reduced instrument setup time. In an interesting application note, two different icIEF instruments, iCE3 system and the latest version Maurice®, were compared to understand if both equipment give comparable responses in terms of percentage of mAbs charge isoforms. A method validation was performed to estimate both method performances, concerning precision and LOQ and it has been concluded that both instruments display comparable performance in charge isoforms characterization of mAbs (Tavernier et al., 2022).

To demonstrate the comparability between iCE3 and Maurice, a global multi-lab study was carried out with a team of 19 companies (biopharmaceutical companies, diagnostics companies, and regulatory agencies located in the United States, Europe, and China). NISTmAb reference material and a programmed death-ligand 1 (PD-L1) fusion protein were analysed using both the iCE3 and Maurice instruments. Intra- and interlaboratory precision and robustness of the icIEF method for the two different molecules on both instruments were evaluated. The obtained results showed that both the iCE3 and the Maurice systems can robustly perform icIEF to monitor charge heterogeneity of monoclonal antibodies and fusion proteins. The electropherograms of the NISTmAb and the rhPD-L1-Fc are consistent across all laboratories and between both the two instruments. Identical apparent pI values (RSD values of less than 0.3% on both instruments) for the main isoform and comparable relative peak areas for the acidic, main, and basic isoforms for the NISTmAb were found (charged variants percent peak area values for both instruments less than 1.02% across different laboratories). Both instruments produce comparable quantitative results for rhPD-L1-Fc (Madren et al., 2022, 1050–1058).

From an alternative perspective, Ascione et al. recently documented and discussed the parallel analysis of a panel of antibody products employing cIEF and icIEF systems, performed within the framework of the Ph. Eur. activities concerning the development of 'horizontal standards' for the QC of mAbs. This work showed that, despite the utilisation of comparable experimental conditions, inconsistencies emerge in the measured charge profile and isoelectric points between the two (i)cIEF systems, as shown in Figure 3. The reasons for this discrepancy are thought to be due to intrinsic differences between the instrumentations or to the commonly accepted practice of using too few pIMs as internal calibrators, leading to small deviations due to the assumption of linearity of the pH gradient along the capillary. As a consequence, it was concluded that, currently, cIEF and icIEF may not be considered directly interchangeable, and presented a thoughtful analysis of the implications of this from both an analytical and a normative perspective (Ascione et al., 2024, 2313737).

2.1 Capillary properties

Fused-silica capillaries used in conventional cIEF have silanol groups whose pK varies between pH 3.5 and 8. These slightly acidic groups generate a double layer at the capillary wall that plays an important role in developing the electroosmotic flow (EOF) (Yao

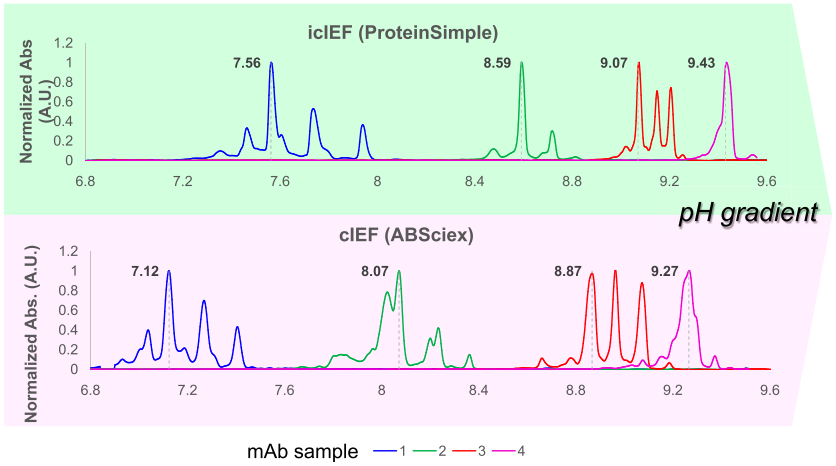

FIGURE 3
Systematic inconsistencies in measured pIs and charge distribution profiles have been observed when comparing cIEF and icIEF techniques across a selection of four mAbs with pI values ranging from 6.8 to 10. This set of therapeutic mAbs was analysed under similar experimental conditions. The electropherograms, obtained respectively by icIEF and cIEF (ProteinSimple and ABSciex), according to their own calibration curves, were scaled on the same pH range (normalized ABS signal vs. pI), to obtain comparable results. Reproduced and modified with permission from the ref. (Ascione et al., 2024, 2313737), Copyright 2024, Taylor and Francis Group, LLC. (This work is licensed under CC BY-NC-ND 4.0. To view a copy of this license, visit https://creativecommons.org/licenses/by-nc-nd/4.0/).

et al., 1993, 21–29). Large proteins can contain positive charge regions that are electrostatically attracted to the negatively charged silanol groups on the capillary inner surface. During icIEF separation, the EOF generated along the capillary by the adsorption may interfere with the separation of proteins according to their pIs (Štěpánová and Kašička, 2022, p. 339447; Duša et al., 2023, p. 117018). Therefore, neutral coating technologies based on hydrophobic fluorocarbon (FC) or hydrophilic acrylamide (AD), both of which are chemically linked to the capillary wall (static coating), have been widely employed to suppress EOF and enhance the efficiency of protein separation by icIEF (Kwok et al., 2023a, no. 5). However, the residual negatively charged silanol groups, which the coatings cannot fully shield, tend to adsorb the proteins, resulting in low separation efficiency and poor repeatability. Neutral polymers such as methylcellulose (MC) are usually added to the protein sample solution containing proteins and ampholytes to create a dynamic coating to improve the resolution and peak shape, especially for complex proteins (Kwok et al., 2023b, no. 5). The use of MC has some drawbacks such as the production of spikes due to bubble generation and frequent capillary clogs during the separation. Moreover, MC easily produces the contamination of MS ion source when carrying out icIEF-MS direct coupling (Permanent methylcellulose, 2023, coated cartridges achieves iCIEF free from polymers as dynamic coating for straight forward characterization of protein drugs - Technical note, Advanced Electrophoresis solutions). In a research article by Kwok et al., a bilayer polymerization strategy was developed for the static coating of MC in the capillary and the MC-coated capillary was employed to analyse charge variants of different types of complex biotherapeutics. It was observed that the peaks of the fusion protein were acidic (range of pI 4.0-6.5), the BsAb demonstrated rather basic pIs (around 9.5) for the main protein and its four isoforms, lastly the ADC sample showed basic properties (range of pIs 8.7–9.2) for major peaks. The new icIEF method demonstrated high repeatability, outstanding separation efficiency, and excellent pI measurements. The removal of MC from the experimental workflow greatly improved the compatibility with MS; thus, the MC-coated capillary was successfully used for the icIEF-MS characterization of protein charge variants for a diverse set of protein therapeutics (Kwok et al., 2022, 2).

2.2 Sample preparation and additives

In the analysis of biopharmaceutical products, sample preparation is an important part of icIEF method development. For example, mAbs formulations can contain high concentrations (10–100 g/L) of the mAbs and relatively high concentrations of buffers, salts, and excipients (e.g., sucrose, polysorbate 80), thus the samples must be appropriately processed in order to minimise the influence of concentration and excipients on the performances.

Depending on the initial concentration of the biomolecule to be analysed, the sample concentration should be adjusted taking into account the sensitivity of the instrumentation (as declared by the manufacturer) as well as the LOD/LOQ of the specific employed analytical method. Methods like dialysis or centrifugal filtration (using filters with a molecular weight cut-off) are commonly exploited to exchange the sample buffer in order to avoid unwanted matrix effect. The second approach can also be used, if necessary, to change the protein concentration to make it suitable for icIEF analysis. The sample buffer used must be chosen carefully to ensure that the pH gradient established along the capillary ensures a stable pI value. Typically, the buffers used are weak acidic or near neutral with low ionic strength, to avoid a denaturing process. Buffer exchange is considered a critical step to remove matrix components (Dadouch et al., 2021, 4) which might interfere with the icIEF analysis. In this regard, even the general chapter published in the Ph. Eur. on (i)cIEF analysis for recombinant therapeutic mAbs, provides a general recommendation to carry out a desalting step (using a common 20 mM Tris buffer at pH 8.0), aiming at removing any possible interferences related to the original formulation components of the analyte (2.5.44. Capillary Isoelectric Focusing for Recombinant Therapeutic Monoclonal Antibodies, 2023).

In a study by Abbood, the effects of varying the final concentration of maytansinoid-antibody samples (ADC) on charge variant separation were investigated (Abbood, 2023, 8150143). The samples were examined at 0.3, 0.5, 0.8, 1, and 1.5 mg/mL, and a shift to higher pI values was observed at higher concentrations. This phenomenon is likely attributable to the increased presence of auxiliary components, such as histidine, sucrose, and glycine, within the sample formulation, which may influence the linearity of the pH gradient. The optimal pH gradient linearity was observed within the concentration range of 0.3–1 mg/mL of maytansinoid-antibody. In a research article by Tardif et al., a Principal Component Analysis (PCA) was employed to evaluate the potential impact of sample concentration and excipients on the electrophoretic profile that could serve as a fingerprint for unambiguous analytes (mAbs) identification (Tardif et al., 2023, 124633). Infliximab was diluted with ultrapure water or Polysorbate 80 (PS 80). Higher quantities of PS 80 were selected in comparison to those typically employed in hospital settings (0.1%–2%) in order to ascertain its lack of influence on the differentiation of mAbs. The objective was to highlight discrimination by comparing three concentrations of Infliximab (0.5, 1.0, 1.5 mg/mL) with 1 mg/mL of Nivolumab. PCA is capable of distinguishing between individuals based on the concentration of Infliximab, with a score of 71%. Furthermore, a Partial Least-Squares Discriminant Analysis (PLS-DA) model, based on previously processed electropherograms, is effective in attributing samples to the appropriate mAb cluster, without any concentration or excipient effects.

icIEF has been explored as a product identity analytical method by Ahluwalia et al. The research group evaluated the possible challenges which can be encountered during the set-up of a product identity method for mAbs and their related products with icIEF. The work emphasises that to ensure reliable results, it is essential that the sample maintains its native form and that aggregation is avoided (Ahluwalia et al., 2018, 271).

In a protocol by ProteinSimple the treatment of mAbs with carboxypeptidase B (CpB) and its challenges during the procedure is discussed. CpB cleavages specifically the C-terminal lysine residues, modifying the aspect of the charge isoforms profile. Recently, in literature it has been reported that C-terminal lysine could adversely affect mAbs complement-dependent cytotoxicity (CDC) (Van Den Bremer et al., 2015, 672-680). A desalting process before the CpB treatment is useful to avoid certain formulation components inhibiting the enzyme activity. Furthermore, it is known that several

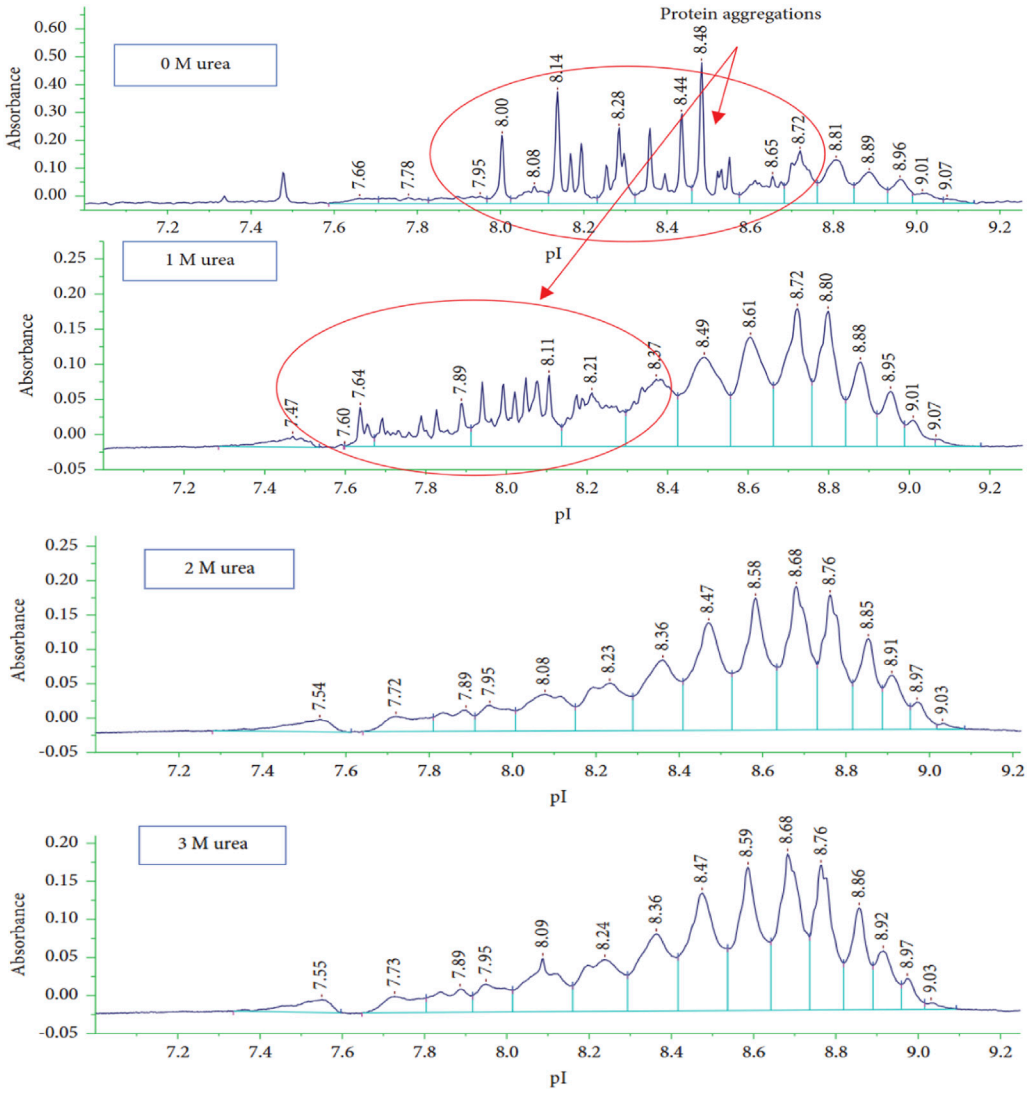

FIGURE 4
icIEF analysis of maytansinoid-antibody under different concentrations of urea (0, 1, 2, and 3 M) to study its effect on charge variants separation. The presence of the additive improves the resolution of the electropherogram, in fact 2 M of urea is chosen to obtain an optimal separation of the sample. Reproduced with permission from the ref. (Abbood, 2023, 8150143), Copyright 2024, John Wiley & Sons. (This work is licensed under CC BY-NC-ND 4.0. To view a copy of this license, visit https://creativecommons.org/licenses/by-nc-nd/4.0/).

pIMs which contain arginine or lysine residues could undergo CpB digestion, causing an imprecise calibration of icIEF pIs measurements. In this published protocol, Adalimumab is used as a mAb example to demonstrate the importance of desalting before the digestion with CpB. ProteinSimple showed that in order to minimise unexpected digestion of basic pIMs, inhibiting the CpB enzyme activity, two different pathways should be followed: a cooling process at 4°C or the addition of citric acid after the CpB treatment (ProteinSimple, 2018).

In icIEF it is essential to use additives for enhancing analytes solubility. Near their pI value, proteins can aggregate or precipitate due to low solubility, affecting the reproducibility of charge profiles and generating spikes during the analysis. Additives act principally as solubilizer agents, the most common example is urea, which reduces the possibility of hydrogen bond formation, avoiding protein aggregation and precipitation and helping with their solubilization (Leng et al., 2024, 343176; Turner and Schiel, 2018, 2079–2093). In literature many research articles study the effects of urea on charge variants analysis by (i)cIEF. The presence of urea can decrease signal intensity or lead to a position shift of the main peak (Kinoshita et al., 2013, 76–83); it can also have an impact on the focusing time and voltage settings (Mack et al., 2009, 4049–4058).

In a recent article, the impact of different amounts of urea, ranging from 0 M to 3 M, added to a sample of ADC product, maytansinoid-humanised anti-EphA2 antibody, was evaluated (Abbood, 2023, 8150143). The results showed (Figure 4) that the addition of urea to the sample matrix improved the characterization of the charge isoforms of the sample, but also that at 1 M urea concentration spikes were generated probably due to aggregation. Charge variants profile was stable at urea concentrations above 2 M, which was chosen as the best analysis condition even if pI values

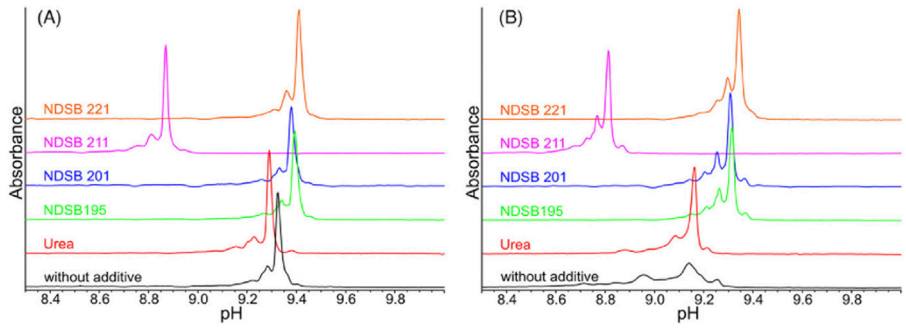

FIGURE 5
icIEF electropherograms of an IgG1 mAb **(A)** and a ZweimAb **(B)** using different types of NDSBs at 0.5 M, as additives compared to urea in concentration of 3 M or without any additive. NDSB 195 shows excellent properties, thus a suitable stabilizing additive for the specific icIEF protocol. Reproduced with permission from the ref. (Meudt et al., 2024, 1295–1306), Copyright 2024, John Wiley & Sons. (This work is licensed under CC BY-NC-ND 4.0. To view a copy of this license, visit https://creativecommons.org/licenses/by-nc-nd/4.0/).

were moderately decreased and the viscosity of the sample matrix was increased.

Chemicals with urea's structural similarities, such as formamide and N-ethylurea have been reported in literature as able to enhance method robustness during icIEF analysis of difficult-to-denature proteins. Zhang et al. noted that urea and sucrose are not sufficient to obtain a robust charge profile of a typical fusion protein in icIEF assay. They suggested using formamide, since the results obtained with this additive showed that it significantly improved the robustness and repeatability of the icIEF assay (Zhang et al., 2017b, 1–7), making it a very good alternative. In a second paper, Zhang's group studied the effect of different types of denaturing agents such as urea, formamide and non-detergent sulfobetaine mixed with taurine (NDSB-T). The results indicate that only NDSB enhances the repeatability, while NDSB-T can maintain very hydrophobic antibodies in their native condition during icIEF analysis, providing more accurate information during charge heterogeneity characterization. The novel matrix formula containing NDSB-T may be a valuable tool for proteins incompatible with conventional icIEF matrices (Zhang et al., 2017a, 13).

As we have discussed above, unfolding, miss-folding, and aggregation can result in a deteriorated charge variant analysis. In a recent work (Meudt et al., 2024, 1295–1306) four different types of NDSBs, namely, NDSB 195, NDSB 201, NDSB 211, and NDSB 221, were tested as alternative stabilising additives for the analysis of mAbs and complex bispecific IgG-like mAbs (Figure 5). It was found that NDSB 195, at 500 mM concentration, exhibited excellent properties for icIEF applications. The platform provides good resolution and linearity to resolve charge species and reliably determines the pI of the considered analytes.

Another reagent has been reported to solubilize PEGylated proteins in a new icIEF method developed to improve the resolution of charge variants (Zhang et al., 2020, 735). Analysis of charge variants of PEGylated protein drugs is a challenging task since the PEGylation process inevitably increases the structural complexity of the conjugated protein. The addition of glycine to the icIEF matrix enabled the separation of co-migrated charge variants of PEGylated protein A. However, the addition of glycine causes significant baseline interferences reducing the assay quantitation and detection limit for basic charge variants. The issue was resolved through the addition of taurine, whose zwitterionic form competes with glycine for binding to the capillary wall. This effectively reduces matrix-induced baseline interference, allowing precise integration and quantification of basic charge variants. The precision of the newly developed method with the use of glycine-taurine sample matrix (Gly-T) was confirmed by multiple injections and multiple sample preparations of PEGylated protein A. The precision of the multiple sample preparation, evaluated by the standard deviation of the percentage peak area for acidic, main, and basic groups was very good (standard deviation 0.3%, 0.5%, and 0.3%, respectively). Linearity and accuracy studies, as well as sample stability, were carried out: linearity was confirmed with an R2 greater than 0.98; accuracy was calculated as a percentage of recovery (93.2%–109.9%, 98.0%–101.9%, and 94.6%–107.3%, respectively, for acidic group, main peak, and basic group) and resulted conform to ICH guideline. LOQ and LOD of the new icIEF method, using Gly-T matrix, were determined and confirmed to be 0.028 mg/mL and 0.008 mg/mL, respectively. Robustness and stability studies were also performed. The proposed icIEF method enables the analysis of charge variants of PEGylated proteins and antibodies and allows to capture the changes made during PEGylation and purification processes.

A non-denaturing versatile protein stabilizer (SimpleSol) was used to perform icIEF analysis of fusion proteins that are otherwise prone to aggregation or precipitation (Wu G. et al., 2022, 114505). The obtained data suggest that SimpleSol can be used as a versatile protein stabilizer in platform methods for icIEF analysis of fusion proteins as reproducible peak patterns could be acquired. The developed platform method can be used as the starting point when high resolution is required, avoiding the need for lengthy method development. The icIEF method can be applied as an identity and purity assay for fusion proteins in the biopharmaceutical industry as the results are reproducible in peak group area percentage and apparent pI determination.

In a recent article by Leng et al. different concentrations of urea were evaluated to analyse charge variants profile of ADCs (Leng et al., 2024, 343176). Drug-to-antibody ratio (DAR) ADCs of

various values (ranging 4–8) and payload linker chemistry were considered, and it turned out that the concentration of urea gave different results depending on DAR value and payload linker. For DAR = 8 ADC with a payload-linker containing a PEG subunit the addition of 3 M or 5 M urea into the sample led to poor separation while 8 M of urea showed an increased number of peaks, generating fragments favoured by a denaturing environment. Thus, SimpleSol, a ProteinSimple additive used to solubilize proteins, was studied finding an enhanced separation of the profile with the addition of 40% or 50% of SimpleSol. The research demonstrated how SimpleSol, which is a non-ionic surfactant, is more effective in the interaction with PEG-containing linker, avoiding possible precipitation and or aggregation forms.

We can summarise that in icIEF analysis, urea is normally used to improve the repeatability of charge variants separations in proteins and antibodies and to measure more stable pI value, however sometimes other additives should be considered, regarding the type of biotherapeutic under analysis.

2.3 Carrier ampholytes

Carrier ampholytes (CAs) are essential components in IEF techniques. They are added to samples to generate a stable pH gradient into the capillary, enabling analytes separation based on their pI. Usually, CAs are aliphatic oligo-amino oligo-carboxylic acid molecules of different lengths and or branching (200–1,200 Da) and their electrophoretic properties differ in base to their supplier (Righetti, 1983; Righetti et al., 2007, 3799–3810; Kristl et al., 2014). CAs have been marketed under trade names such as Pharmalyte, Servalyt, and AESlyte. The quality of an icIEF analysis for biotherapeutics charge variants evaluation is highly dependent on the type of carrier ampholytes utilised in terms of baseline signal, pH gradient linearity and pI measurement (Kwok et al., 2022, 2).

Commonly, CAs are added in total concentrations between 2% and 8% to the samples and broad-range CAs – such as Pharmalytes 3-10, can be mixed with narrow-range ones to improve resolution. Moreover, the total concentration of Pharmalytes, as well as their assortment, can greatly influence the focusing time required for proper separation of the analytes. Thus, careful research for the best CA brand selection, the right amounts and the reciprocal ratios of CAs is necessary to achieve the best compromise in establishing the best pH gradient along which the analytes charge variants can be separated (Michels et al., 2012, 5380–5386). An important aspect to be considered in the selection of CA is the CA-specific background during the analysis. In fact, it was observed that when CAs are at a concentration above 3%-4%, the background noise of the analysis increases, influencing peak integration from baseline fluctuations. The problem occurs with both UV and fluorescent detection.

AESlytes are CAs developed for the high-resolution and enhanced characterization of complex protein therapeutics such as BsAbs, viral and fusion proteins and ADCs which demonstrate a reduction in the background noise (AES Advanced Electrophoresis Solutions Ltd, 2016). This type of CAs was used in a research article by Kwok et al. aimed at studying the charge variants profiles of different commercial fusion proteins and biosimilars with high repeatability. Furthermore, narrow-range pH AESlytes were considered during icIEF-MS analysis to optimise the resolution and to obtain more reliable and accurate charge variants profiles (Kwok et al., 2022, 2).

Pharmalytes were used in a research article by Abbood to evaluate maytansinoid-antibody charge isoforms. In this study it was observed that the charge variants of the sample (pIs ranging between 7.5 and 9.0) shifted simultaneously with the calibration pI marker 9.50, in a sample mixture of 4% broad range 3–10 Pharmalyte. With the addition of the narrow-range 8-10.5 Pharmalyte (reciprocal ratio 1:1), the maytansinoid-antibody charge variants were differentiated from the pI marker 9.50 (Abbood, 2023, 8150143).

Besides Pharmalytes and AESlytes, Servalyts are another type of CAs used. Servalytes have been used for the charge heterogeneity characterization of fusion protein therapeutics. An icIEF platform method was developed for fusion proteins with pI values ranging from four to 8 (Wu G. et al., 2022, 114505). In this work, a wide pH range ampholyte, Servalyt 2–9 was used. The resolution of some fusion proteins was improved by the addition, into the preexisting carrier ampholytes mix of the platform method, of supplemental carrier ampholytes tailored for that molecule's pI. In a more recent research article by Leng et al., Servalytes demonstrated to favour electrophoretic separation of high DAR ADCs charge variants, due to their sulfonate groups (Leng et al., 2024, 343176). A combination of 1% Servalyt 2%–11% and 3% Servalyt 9–11 was studied, and a better separation of the profile was obtained. However, the ADC-4 main peak showed a pI around 8.5–8.6, out of the linear pH gradient range. Servalyt 9–11 acts as a basic spacer, shifting the charge variants profile to the acidic pH range. The study demonstrated that narrow-range Servalytes are required to increase the pH gradient and achieve a linear pH gradient for the separation. Lastly, Leng et al. evidenced how the combination of Servalytes and SimpleSol allows a better separation of ADC charge variants, with charge masking effect from the payload-linker and the high DAR.

The important role of CAs was demonstrated in the development of an icIEF method for charge heterogeneity characterization of therapeutic mAbs and BsAb with pI values ranging from 6 to 10, a variety of different broad- and narrow-range ampholytes and combinations thereof were investigated. A CAs combination of Pharmalyte 5–8 and Pharmalyte 8–10.5 showed a highly linear pH gradient and covered a suitable pH range. The article also reported the advantages and disadvantages of CAs covering different pH ranges and obtained from different manufacturers (Meudt et al., 2024, 1295–1306).

It can be stated that narrower ampholytes (ΔpH < 1.0) usually can increase peak resolution, thus leading to a better separation of charge variants. This was the case of PEGylated proteins icIEF analysis, where the use of narrow range ampholytes (Pharmalyte 4–6.5 and Pharmalyte 5–8) allowed a slightly better separation of charge variants but was not enough to resolve the broad co-migrating peaks due to the masking effect of PEG chain surrounding proteins. Thus, a novel icIEF matrix (Gly-T) provides an excellent solution for charge variant analysis of PEGylated proteins (Zhang et al., 2020, 735).

All these studies showed that optimal CAs should guarantee good linearity of the pH gradient in a wide pH range, low protein interactions, reproducible protein separation, low UV absorbance in order to minimize electropherogram background noise, low background noise to obtain high sensitivity during icIEF-MS analysis.

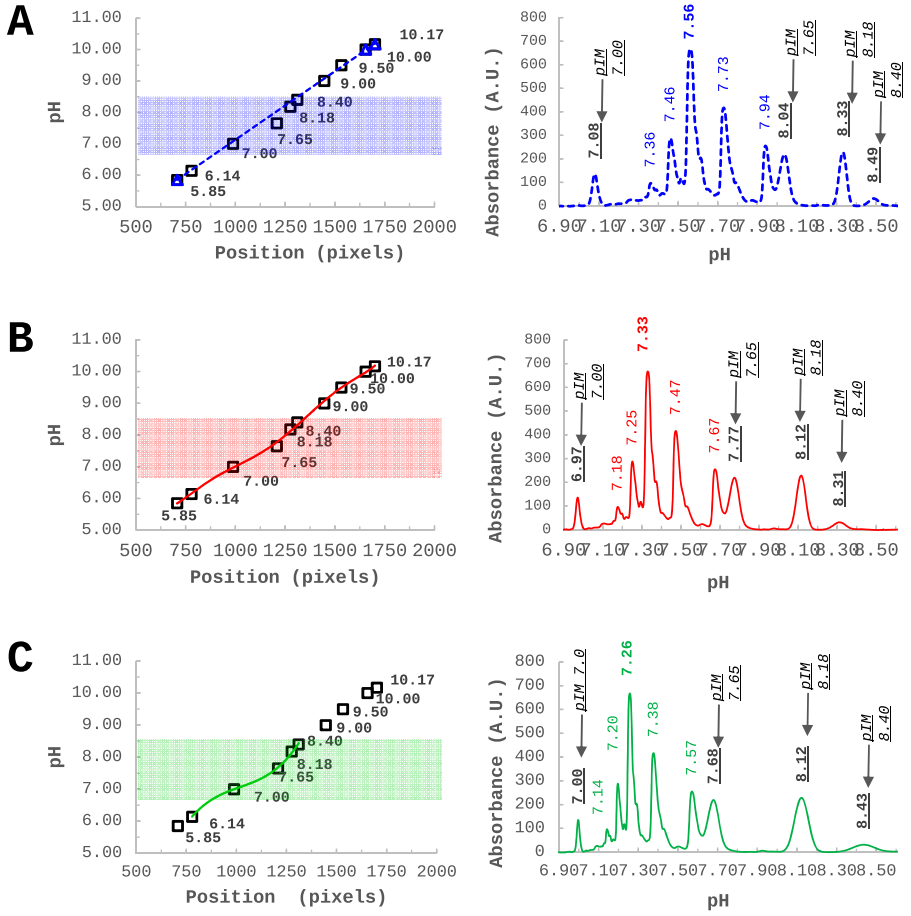

FIGURE 6
Infliximab - charge variants characterization through icIEF - analysed together with 10 pIMs, along the pH gradient. **(A)** Commonly used approach of linear calibration using three external pIMs as internal calibrators. **(B)** A non-linear calibration curve using 10 pIMs. **(C)** A non-linear calibration curve optimized in a narrow window by using five pIMs out of 10. Reproduced with permission from the ref. (Belfiore et al., 2024, 28087), Copyright 2024, Springer Nature Limited. (This work is licensed under CC BY-NC-ND 4.0. To view a copy of this license, visit https://creativecommons.org/licenses/by-nc-nd/4.0/).

Regardless of the type of ampholytes used, in (i)cIEF techniques pI values of the analyte are calculated after internal calibration. This calibration is commonly obtained with two or three pIMs, flanking the analyte, assuming a linear dependence throughout the pH gradient between pI values and migration time (cIEF) or position (in pixels) along the capillary (icIEF). In this context, Belfiore and Ascione et al. shared their experience with the ProteinSimple-Maurice™ apparatus and proposed an innovative calibration approach for iciEF in order to obtain more reliable and objective (close to theoretical) pI measurements, thus exploring the concept of univocal charge identity (Belfiore et al., 2024, 28087). The proposed new calibration approach may help to reconcile discrepancies in the pI obtained for the same sample from different devices. The assumption of a linear calibration curve, currently enforced by both icIEF and cIEF analysis software, introduces unpredictable errors in the expected pI values, across the pH gradient, despite Pearson's determination coefficient is very close to one. To address this issue, they proposed to use a non-linear regression approach to enable recalibration of the data, as shown in Figure 6. Importantly, while assuming a linear calibration implies a constant resolution over the pH gradient, the non-linear regression reveals an actual non-homogeneous resolution along the gradient. Accordingly, they demonstrated the possibility of investigating the resolution power across the entire capillary to identify the optimal focusing conditions and CAs combination for a specific purpose.

The approach described above offers intriguing insights and aims to make possible the objective estimation of pI. The state-of-the-art of currently available softwares integrated in (i)ciEF instruments renders the above approach not yet applicable to routine control activities. At the moment, the high-level standardization effort of Ph. Eur. is recognized, delivering reliable reference for the application of (i)cIEF methodology to the control of biopharmaceuticals (2.5.44. Capillary Isoelectric Focusing for Recombinant Therapeutic Monoclonal Antibodies, 2023).

2.4 Anodic and cathodic stabilizers

In icIEF the analyte charge variants are focused along the desired pH region. Furthermore, a phenomenon called cathodic or anodic

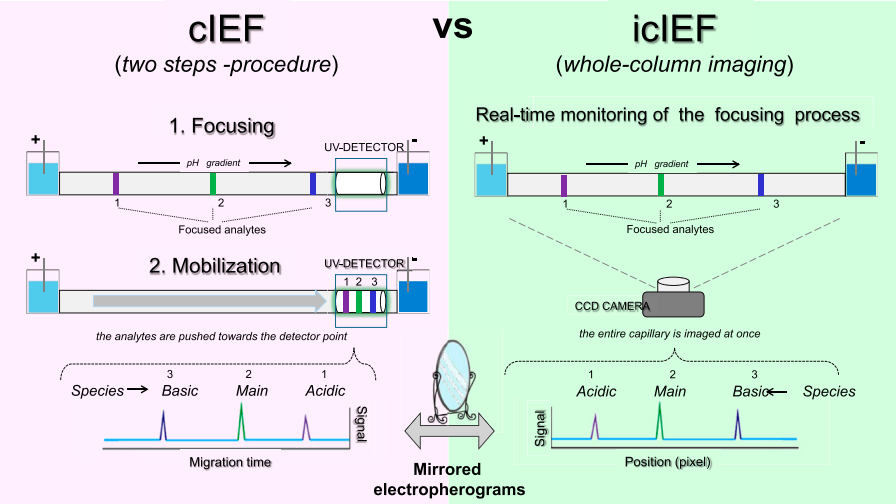

FIGURE 7
Schematic representation of the key technical differences between cIEF and icIEF, regarding data acquisition and resulting electropherograms.

drift (loss of basic and acidic CAs) could occur during the focalization process, negatively impacting repeatability and reproducibility (Tardif et al., 2023, 124633). Anodic and cathodic stabilizers, also known as sacrificial agents or spacers, act as buffering zones at the ends of the capillary, compressing and stabilising the pH gradient.

The main characteristic of a cathodic stabilizer is to have a pI value below the catholyte solution but above pH 10 (Kristl et al., 2014). L-Arg is an amphoteric amino acid (pI ~ 10.76), known to suppress EOF in capillary electrophoresis and to stabilise the cathodic zone of the capillary (Kristl and Stutz, 2014, 148). Commonly, in icIEF technique L-Arg is used at concentrations ranging from 5 to 10 mM. When a narrow-range CA is added to the sample preparation, an anodic stabilizer should also be used. The main propriety is to possess a pI value above the anolyte solution but below pH 3. The most used anodic spacer is iminodiacetic acid (IDA) which is a dicarboxylic acid amine that has a pI value around 2.2 (Kristl et al., 2014) and is used at concentrations around 5-10 mM. These sacrificial agents protect CAs from leaving the capillary and avoid the analytes loss during the separation. The right quantity of these reagents must be optimised to ensure no interference as high concentrations could impact the total resolution (Kristl and Stutz, 2014, 148; Kristl et al., 2014; Kahle and Wätzig, 2018, 2492).

There are other sacrificial agents known in literature such as tetramethylethylenediamine (TEMED), which acts as a cathodic stabilizer because it is a highly basic organic compound. Another anodic stabilizer is Serine-D which has a pI of around 5.68 (Mohan and Lee, 2002, 271–276). In an article by Tardif et al. different concentrations (ranging from 0% to 5%) of those stabilizers were tested to demonstrate their efficiency. This work concluded that to prevent a good separation of the analytes with a good resolution, TEMED and Serine-D have to be added into the sample preparation respectively in concentrations of 1.2% and 2.4% (Tardif et al., 2023, 124633). The effect of anodic and cathodic stabilizers on icIEF analysis is significant. Indeed, in a research article by Kahle et al. which aims to gain a comprehensive understanding of icIEF technique through the application of a DoE approach, three concentrations of L-Arg (0, 5, and 10 mM) have been studied (Kahle et al., 2019, 2382–2389). It was observed that by increasing L-Arg concentrations, the resolution decreases probably due to the correlation to a reduced separation length into the capillary. The high quantity of L-Arg is accumulated at the cathodic extremity of the capillary, causing a compressed pH gradient. L-Arg significantly influences resolution power, peak position, and peak count, but it does not affect the apparent pI measured.

2.5 Detection mode

The key distinction between icIEF and traditional cIEF lies in the detection step. icIEF detection method results in a significant reduction in method development time while maintaining the established advantages of high resolution, high throughput and minimal solvent consumption. In conventional cIEF, following the focusing of protein isoforms at their respective isoelectric points in a long capillary (20-60 cm), the so-called mobilisation step is required, whereby the separated species are mobilised towards the detection point, typically located at one end of the capillary. However, the mobilisation step, which is typically conducted chemically or by controlled pressure, can result in several limitations, including prolonged analysis time, distortion of the pH gradient and even occasional uneven resolution as a consequence of the unequal speed of mobilisation (Mao and Pawliszyn, 1999, 93–110). The aforementioned issues are circumvented by icIEF. In fact, in icIEF technique, the separation process occurs within a capillary of a relatively short length (4-5 cm) that is stabilised within a cartridge, while a CCD camera is positioned to capture images of the entire capillary structure. This configuration enables the real-time detection of the target protein within the capillary, thereby facilitating a markedly higher analytical speed. The two different modes of detection are reflected in a different visualization of the separated species

(Figure 7). In cIEF, the more basic variants will appear first in the electropherogram since they pass through the detector first; in this system, the detected signals are displayed as a function of migration time, with the basic and acidic variants to the left and right of the main species respectively (Figure 7, left). Instead in icIEF, the entire capillary is imaged, and the peaks are plotted as a function of their position in pixels along the capillary, thus resulting in an electropherogram in which the acid species are displayed on the left and the basic species are on the right (Figure 7, right). In practical terms, apart from the anticipated similarity in shape, the arrangement of the peaks in the electropherograms of the two systems will be specular (Ascione et al., 2024, 2313737).

As previously stated, the latest generation of icIEF instruments generally guarantees high sensitivity, which is an essential prerequisite for detecting low abundance variants; however, the power level of this attribute is largely dependent on the technology used for detection. Absorption imaging detection is the most practical at present due to its quantitative ability and universal characteristics, even if various types of imaging detectors have been developed including refractive index gradient, and laser-induced fluorescence (LIF). Usually, icIEF technique is based on protein absorption at 280 nm but nowadays instruments add native induced fluorescence (NIF) detection around 350 nm (Li et al., 2021, 462043) to enhance its capabilities. The detection process by native fluorescence is achieved through the measurement of the fluorescence emission of the aromatic group of tryptophan, a naturally fluorescent amino acid. Since this is a label-free detection, baselines are highly cleaner and less sensitive to CAs interference, as these species do not fluoresce between 320 and 450 nm. Furthermore, as stated in a ProteinSimple Application Note this sensitivity allows to avoid sample concentration or desalting, reducing sample preparation time. As outlined in this Application Note, working with native fluorescence would allow to reduce or completely remove urea during sample preparation (Improving Charge Variant, 2000). The Maurice-ProteinSimple instrument introduced a fluorescence detection filter at 458 nm which is particularly useful for ADC characterization. In fact, as it is reported in literature, if an enhanced fluorescence intensity is observed at 458 ± 30 nm, ADC samples might be analysed by icIEF fluorescence at 458 nm. This detection enables the quantification of the conjugated drug to be conducted independently of the antibody, for each charge variant. In a study case presented in a ProteinSimple Protocol, Alexa® 350 fluorescent dye was conjugated at different dye-to-protein molar ratios to simulate different DARs (ProteinSimple, 2019). This study evidenced how the fluorescent conjugate can be imaged as a standalone entity, independent of the protein signal. Furthermore, the dye and antibody peaks can be attributed by overlapping the absorption and fluorescence profiles. As reported in an excellent research article by Li et al. icIEF-UV fluorescence is an auspicious technique even to characterise recombinant human ErythroPOietin (rhEPO) charge variants in DPs, without sample treatment (Li et al., 2021, 462043). The sensitivity of the combination of UV and native fluorescence was sufficient to detect low concentrations of rhEPO, while maintaining the separation power of the icIEF technique which allows to avoid interference from excipients. A method validation was performed on a commercial DP sample, following ICH guidelines, and demonstrated a 100-fold higher sensitivity in comparison to icIEF-UV but also to CZE-UV techniques.

Simultaneous monitoring of the capillary using both absorbance and fluorescence detection has been used during the analysis of fixed-dose combination (FDC) products containing different mAbs (Candreva et al., 2022, 1701–1709). It was observed that UV absorbance is ideal for analysing the charge isoforms of the high-concentration component, while native fluorescence is suited for detecting the variants of the low-concentration component.

Furthermore, as suggested by Belfiore and Ascione et al. modern icIEF devices' capability to measure signals in both absorbance and fluorescence modes, can be exploited in order to strengthen the calibration by using multiple pIMs as internal calibrators (Belfiore et al., 2024, 28087). Assuming that an ever-widening range of differently visible pIMs (in one channel and in both) will soon be available on the market, this would make it possible to obtain a kind of independent 'two-channel electropherogram', without any interference for sample analysis: in other words, an optimal internal calibration curve and a clean-molecule electropherogram would be obtained simultaneously for each injection.

3 icIEF-MS: a novel orthogonal approach

In addition to a charge variant profiling obtained with icIEF technique coupled to UV and fluorescent detectors, mass spectrometry (MS) analyses can be also desirable to acquire identification of these charged species. icIEF-MS approach can offer significant potential in the biopharmaceutical sector, where charge variant analysis and peak identification are essential for research and development activities, including mAb-based drugs screening, purification process optimization, formulation studies, stability assessments, QC testing, and Investigational New Drug (IND)-enabling studies (Mack et al., 2019, 3084).

icIEF-MS analysis can be performed through offline fractionation, where collected fractions are processed with MS-compatible materials, before being introduced into the MS, for detailed and enhanced characterization. The advanced preparative icIEF system enables the simultaneous isolation and analysis of specific protein charge variants. Additionally, it can be directly integrated with MS, providing fractionated protein samples for immediate characterization (Maráková et al., 2023, e2300244). The newly directly coupled icIEF-MS technique represents a significant advancement in the field of high-resolution separation of therapeutic charge variants, enabling the quantification and identification of their individual components and the interpretation of their structural differences. This integrated method (Figure 8) is useful and adaptable for characterizing various biotherapeutics, such as fusion proteins, bispecific antibodies (BsAbs), and antibody-drug conjugates (ADCs) (He et al., 2022, 1215).

A recent study by Wu et al. introduced a novel integrated approach combining icIEF-MS for the analysis of a set of therapeutic mAb charge variants (Wu et al., 2023, 2548–2560). In this work, both icIEF-MS and strong cation exchange-MS (SCX-MS) techniques were optimised to characterise charge heterogeneity,

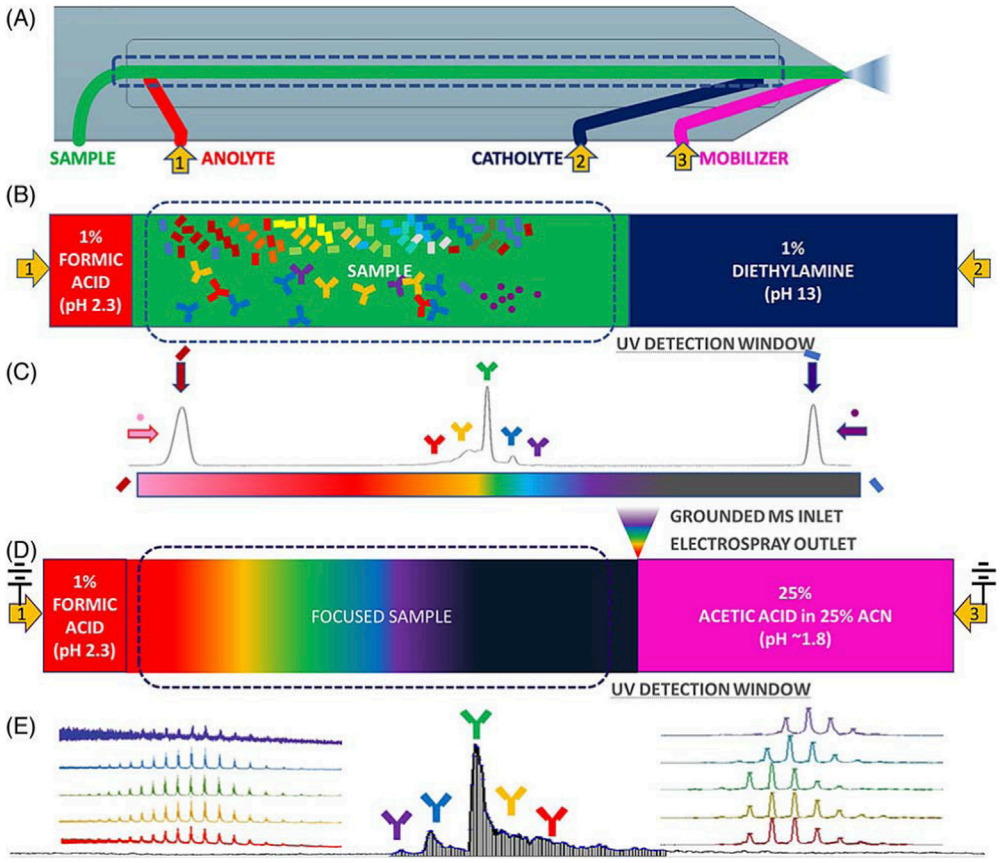

FIGURE 8
Coupled icIEF-MS workflow for the analysis of therapeutic intact protein. **(A)** Scheme of the microfluidic separation and ionization chip with electrospray outlet, inlets for solvents, and electrodes at anode, cathode, and mobilizer. **(B)** Path of the separation phase (anolyte, sample and catholyte solutions). **(C)** Focused sample and pIMs electropherogram (UV ABS). **(D)** Scheme of the initiation of mobilization and ESI of the separated sample. **(E)** Time-resolved base peak intensity plot with inset normalized raw and deconvoluted mass spectra. Reproduced with permission from the ref. (He et al., 2022, 1215), Copyright 2024, Springer Nature Limited. (This work is licensed under CC BY-NC-ND 4.0. To view a copy of this license, visit https://creativecommons.org/licenses/by-nc-nd/4.0/).

with a particular focus on comparing their performance through methodological validation. The results demonstrated that, while SCX-MS offered higher throughput, icIEF-MS performed higher sensitivity, reduced carryover, precise protein identification, and enhanced resolution in protein separation. However, despite its advantages, icIEF-MS presents several challenges in the analysis of protein charge variants. The study highlighted issues with repeatability, complex and often trial-and-error optimization processes, and difficulties related to compatibility with MS ion sources. Notably, the chip-based icIEF-MS technique relies on chemical mobilisation for MS detection, which can induce instability in the pH gradient, leading to reduced reproducibility. The analytical platform developed in this study was thoroughly validated across sensitivity, repeatability, carryover effects, and capillary lifespan, ensuring robust and consistent results The same research group aimed to study fusion proteins' charge isoforms with a dedicated analytical platform (Wu G. et al., 2022, 114505). This work presented a novel approach for the comprehensive characterization of etanercept analogues in QC and manufacturing processes, utilising AESlyte and allowing an enhanced resolution also of the complex glycosylation patterns. The study compared icIEF profiles with the output of HPLC-HRMS peptide mapping and PTMs analysis, finding an agreement between the two techniques which could be used for the production and QC of fusion proteins.

Native MS (nMS) has recently emerged for the analysis of large biomolecules, allowing the characterization of protein complexes and their structural features in a solution environment that closely mimics their native state. nMS allows the study of noncovalent protein assemblies while retaining their biological relevance. Zhang's research group developed a whole workflow of icIEF-MS strategy for a rapid fingerprint of intact proteins which demonstrated to be reliable and accurate and provided a comprehensive and innovative technology for protein drug QC monitoring and in-depth characterization (Zhang et al., 2023a, 114961). In another research article by the same group, the whole icIEF-MS workflow for protein heterogeneity was performed within 45 min. Moreover, the developed icIEF-MS configuration was capable of adapting to an icIEF-based fraction collection model (Figure 9), thereby enabling the analyst to carry out supplementary in-depth characterisation techniques, such as peptide mapping by HPLC and LC-MS/MS. The established

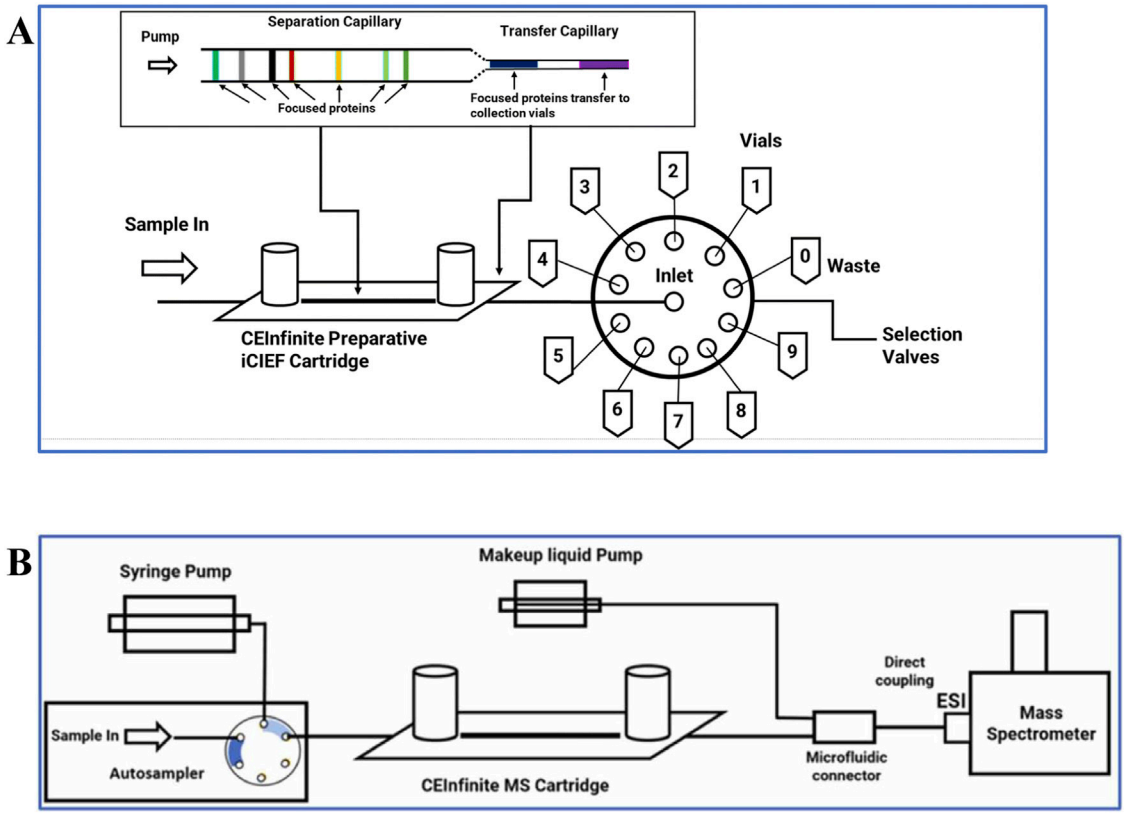

FIGURE 9
Configuration of **(A)** an icIEF-based fraction collection model by preparative icIEF and **(B)** online icIEF-HRMS. Reproduced with permission from the ref. (Kwok et al., 2023b, 411–418), Copyright 2024, © The Royal Society of Chemistry. (This work is licensed under CC BY-NC-ND 4.0. To view a copy of this license, visit https://creativecommons.org/licenses/by-nc-nd/4.0/).

methodology was highly sensitive and accurate, during the heterogeneity evaluation of mAb and ADC. icIEF-HRMS can provide a promising, accurate and rapid strategy for the differentiation and identification of protein charged variants, supporting the rapid growth and need of biotherapeutics (Zhang et al., 2023b, 115178). In a more recent paper, Zhang et al. used the icIEF-MS approach to analyse the charge variants of cysteine-linked ADCs, which are crucial during drug development. Two distinct cysteine-linked ADCs were examined: Polatuzumab vedotin, a novel ADC with promising therapeutic applications, and Brentuximab vedotin, the first FDA-approved ADC of this kind. One of the key achievements in this research work is the development of an optimised icIEF buffer system, which ensures the native conformation of cysteine-linked ADCs during the analysis, enabling a more accurate charge variant profiling (Zhang et al., 2024).

Furthermore, Wu et al. evaluated an advanced online coupling of icIEF-MS under near-native conditions, specifically designed for the in-depth characterization of cysteine-linked ADCs (Wu et al., 2024c, 465353). The characterization of cysteine-linked ADCs presents significant challenges due to the presence of interchain disulfide bonds that are reduced during payload conjugation, as well as the non-covalent interactions between the antibody light and heavy chains. However, despite the potential advantages of icIEF-MS, characterising cysteine-linked ADCs remains difficult because maintaining the integrity of the conjugated structure for intact MS analysis requires native conditions, and the associated parameters must be carefully optimised. By keeping the cysteine-linked ADCs in their near-native state, the developed method enabled high-resolution MS detection without compromising the integrity of the conjugated structure. In an article by Mack et al. the icIEF-MS technique was evaluated for the characterization of Trastuzumab charge variants, in its intact state. In this study, five major glycoforms in a single assay of 15 min were detected and 33 distinct molecular species were separated by the icIEF-MS technique. This allowed the identification and monitoring of several CQAs in a single exhaustive analysis (Mack et al., 2019, 3084).

Recent advancements have introduced new microfluidic chip-based icIEF systems directly coupled with MS, further improving the precision and efficiency of charge variant peak identification. In an article by He et al. the comparability of the measured pI values and the relative charge isoforms distribution between icIEF-MS technique and a routinely utilised methodology is demonstrated (He et al., 2022, 1215). Different IgG mAbs subclasses along a pI range between 7.3 and 9.0 were evaluated. Thanks to the high-performance icIEF-MS system, low abundance PTMs were also detected. In this study acidic and basic shifts were noticed,

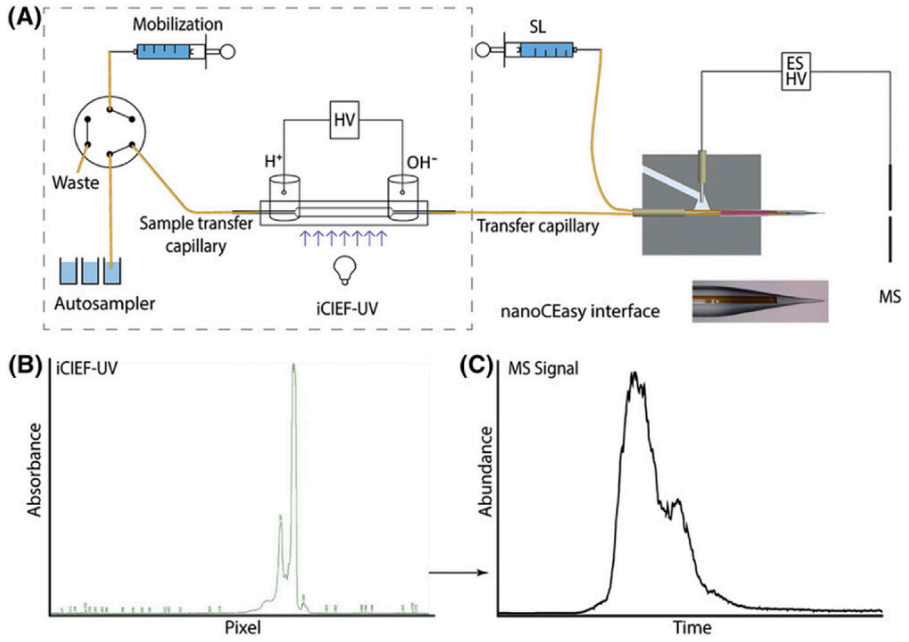

FIGURE 10
(A) Scheme of the CEInfinite with icIEF cartridge connected with the nanoCEasy ESI–MS interface. **(B)** iCIEF–UV profile of 2 mg/mL Trastuzumab. **(C)** Base peak electropherogram m/z 1500–4000 of Trastuzumab with Orbitrap Fusion Lumos. Reproduced with permission from the ref. (Schlecht et al., 2022, 540), Copyright 2024, John Wiley & Sons. (This work is licensed under CC BY-NC-ND 4.0. To view a copy of this license, visit https://creativecommons.org/licenses/by-nc-nd/4.0/).

corresponding to additions of sialic acids and unprocessed lysine residues, respectively, due to a primary structural characterization of the IgG2 mAb subclass. The icIEF-MS analysis was able to detect particularly low abundance glycoforms (e.g., G0, G0F-GlcNAc). Moreover, Schlecht's working group set up a direct icIEF-MS coupling procedure, via nanoCEasy interface, enabling a successful application for narrow charge variant profile of Trastuzumab (Figure 10). The study investigated crucial parameters (e.g., sample concentration, ampholytes concentration, etc.) which could affect the charge variants profiling. The obtained parameter values were a functional starting point and needed to be optimised depending on the MS system used. To avoid loss of peaks during the detection, low mobilisation flow rate and ampholyte concentration >3% are required (Schlecht et al., 2022, 540).

In a research article by Ostrowski et al. a novel method for the rapid, multi-attribute characterization of BsAbs using an enhanced microfluidic chip-based integrated icIEF-MS technology. The improved approach utilizes a nebulization gas at the electrospray tip of the microchip during the delivery into the MS (Ostrowski et al., 2022, 378). This icIEF-MS platform developed allows a direct and simultaneous analysis of multiple CQAs of BsAbs and the characterization of the charge variants in their native state with a high-resolution power. Furthermore, the use of a microfluidic chip system allowed a faster and more efficient analytical process, reducing sample volume and improving the throughput.

Recently, the already cited Wu's research group has carried out a lot of in-depth analysis on icIEF-MS to characterise SARS-CoV-2 recombinant vaccine, combined with different separative analytical techniques (Wu et al., 2024b, 342349). Due to the higher complexity of the vaccine, compared to mAbs, Wu's research group decided to eliminate the glycans by using PNGaseF. The obtained results demonstrated the crucial role of high-resolution CAs during icIEF-MS separation and its importance to obtain a fast identify of the recombinant vaccine complexity, like those used in the fight against COVID-19. This work emphasises the necessity of high-resolution analytical methods for ensuring the consistency and quality of vaccines.

4 icIEF relevance in biopharmaceutical context: advanced applications

Industry users apply icIEF methods for the verification of identity and purity at the level of characterization and drug substance (DS)/DP release. This technique is an optimal tool to monitor the heterogeneity profile of mAb products, which provides insights into the purity of the molecule and, in combination with peptide mapping to detect primary sequence and potency testing to address functional activity, deliver a comprehensive picture of product identity.

A research article demonstrated the challenges that can come across while establishing a product identity method for a mAb (pI~7.9) and 10 in-house mAbs products with close pI range (pI~7.0–8.5) using icIEF method (Ahluwalia et al., 2018, 271). mAbs were analysed by icIEF method under native, enzymatic and reduced conditions and a unique three-point identity criteria tool (visual comparison, pI of individual peaks and ΔpIs) was applied to distinguish mAb1 from the other in-house mAbs. A reduction approach followed by icIEF showed higher potential for

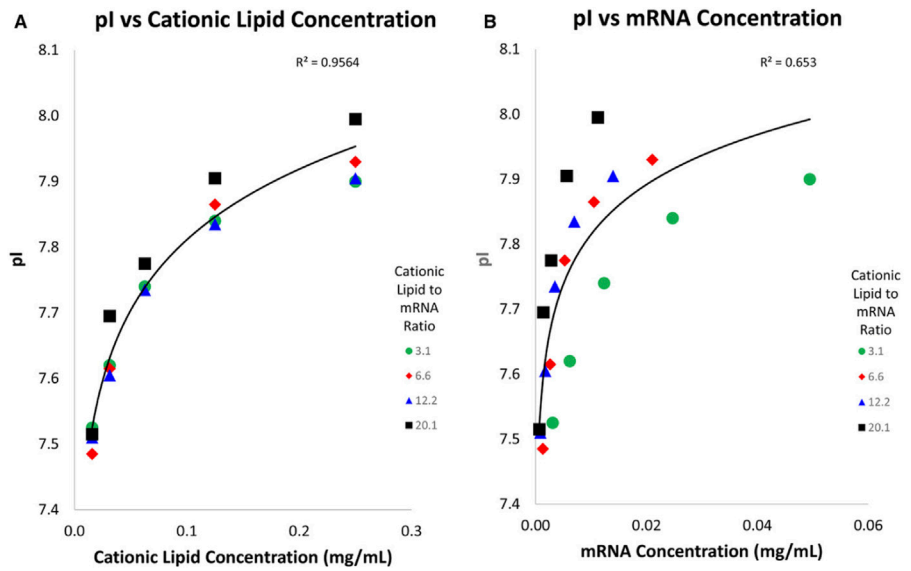

FIGURE 11
Graphics of LNP pI against cationic lipids **(A)** and mRNA concentration **(B)**: different LNP batches containing different cationic lipids to mRNA ratios. The apparent pI was found to have a strong correlation to cationic lipids concentration but a weaker correlation to mRNA concentration. Reproduced with permission from the ref. (Loughney et al., 2019, 2602–2609), Copyright 2024, John Wiley & Sons. (This work is licensed under CC BY-NC-ND 4.0. To view a copy of this license, visit https://creativecommons.org/licenses/by-nc-nd/4.0/).

establishing identity for mAb product as compared to native and enzymatic digestion approach.

An icIEF analytical method has been set up with the aim of obtaining the characterization of a novel humanised anti-EphA2 antibody conjugated to a maytansine derivative charge variant (Abbood, 2023, 8150143). A validation protocol of the optimised icIEF method was carried out and a good inter-day repeatability with the following RSD values: <1% (pI), <8% (% peak area), and 7% (total peak areas) was demonstrated. Indeed, this optimised icIEF method has been applied to evaluate the quality of a discovery batch of maytansinoid-mAb, in comparison to its naked antibody.

In addition, icIEF can be employed to assess the surface charge of lipid nanoparticle (LNP)-based mRNA vaccines (Loughney et al., 2019, 2602–2609). This technique is capable of differentiating the pI of LNPs that contain one or more types of ionizable lipids, aiding in the verification of LNP identity during manufacturing processes. As a quantitative method, icIEF also provides insights into the stability of LNPs, making it applicable for both process optimization and formulation development of mRNA vaccines. Furthermore, it can distinguish between LNPs that incorporate various cationic lipids, serving as a useful tool for confirming the identity but also to study the correlation between LNP apparent pI and cationic lipids and mRNA concentrations. Four different batches of LNP containing different cationic lipid to mRNA ratios were subjected to icIEF analysis (Figure 11). The results indicate that the cationic lipid is situated on the surface of the LNP, while the mRNA is located within. This is a reasonable assumption, given that the LNP fulfils the function of a hydrophobic protective barrier, thereby protecting the mRNA.

Two distinct icIEF approaches have been developed, as reported in the literature, to evaluate the quality and stability of mRNA vaccines, particularly those encapsulated in LNPs. These methods are effective for characterising the stability of mRNA-loaded LNPs under different conditions, such as varied storage temperatures, freeze-thaw cycles, and lipid compositions, and are capable of detecting batch-to-batch variability. Overall, icIEF analysis has proven to be highly suitable for characterising mRNA vaccines. It has been an essential analytical tool during the COVID-19 pandemic and will continue to play a significant role in the development of future mRNA-based products (Krebs et al., 2022, 1971–1983). The assessment of batch-to-batch consistency is of pivotal importance in the context of regulatory compliance. Consequently, other research groups developed robust and reproducible methodologies for the fulfilment of these tasks. Indeed, Sutton et al. developed and optimised an icIEF method for an in-house recombinant humanised IgG1k mAb expressed in Chinese Hamster Ovary (CHO) cells (Sutton et al., 2024, 5450–5458). Its purpose was to assess different lots consistency in terms of pIs and peak area percentage of main peak, acidic and basic isoforms. Furthermore, the method was employed to analyse different batches of Herceptin (Trastuzumab) produced in the European Union (EU) and the United States (US).

Recently, an icIEF method has been developed and tailored for the characterization of high DAR ADCs charge heterogeneity. The study showed how this optimised icIEF condition is able to quantify charge variants with higher precision and resolution but also improved sensitivity. The method lets to differentiate contributions from the protein and payload-linker (Leng et al., 2024, 343176).

icIEF has been investigated as a potential multi-attribute method (MAM) for a detailed characterization and QC of BsAbs in a recent article (Wu et al., 2024a). This work demonstrated that icIEF is able, detecting and quantifying BsAbs charge isoforms, to provide detailed insights on their biophysical characteristics, providing an

identity, purity and impurity assay. The method was validated and the native fluorescence detection was used to achieve good sensitivity (down to 4 μg/mL LOQ). The proposed icIEF method is able to measure pI values and quantify the relative abundance of each charge isoform as well as the impurities of homodimer mAb, generated during BsAb assembly. The research group studied the use of icIEF for optimising BsAbs production conditions in order to decrease the number of unwanted heterogeneities. Furthermore, a novel workflow has recently been presented to correlate the charge isoforms of a BsAb to its function. This approach involves the use of icIEF-MS and surface plasmon resonance (SPR) techniques (Bio-Techne, n.d.). The work investigated a therapeutic BsAb, named Mosunetuzumab to determine affinity and binding kinetics of different charge species. High-purity fractions of the BsAb were collected from the icIEF instrument and examined with SPR to comprehend their affinity to ligands CD3 and CD20. This method outlines the significance of utilising advanced techniques during the development and QC of biotherapeutics.

A notable application of icIEF is its use in characterising charge isoforms of FDC products. Combination therapies involving two or more therapeutic mAbs have gained prominence in oncology and the need for accurate characterization of these complex formulations has grown. In a recent study, an optimised icIEF methodology was developed to allow simultaneous quantification of acidic and basic charge variants in FDC products containing two different mAb isotypes (IgG1 and IgG4), each with distinct pI values (Candreva et al., 2022, 1701–1709). The developed icIEF approach is a QC-friendly solution, adhering to critical acceptance criteria outlined by the ICH, including sensitivity, specificity, linearity, and repeatability. By employing a dual-detection approach, this method ensures high accuracy and reproducibility, even for complex mAb mixtures.

5 Conclusion

icIEF technique is an indispensable tool for protein product monitoring and is becoming the platform method of choice for analysing protein charge heterogeneity due to its high-resolution power, quantitative capabilities, robustness, fast analysis times and automation. It can be stated that icIEF is certainly a consolidated technique for monitoring the heterogeneity of the charge variants and the quality of proteins and mAb-based drugs, but the application horizons of icIEF are constantly broadening. Recently, more tailored icIEF approaches in the characterization of ADCs, BsAbs, fusion proteins and LNPs are described in literature. The analysis of more complex proteins has magnified some technical difficulties of icIEF such as protein solubility, pH gradient resolution, capillary wall adsorption and pI reproducibility. Although the method's development is rapid, numerous parameters must be considered such as CAs, additives selection, anodic and cathodic stabilizers to optimise charge variants separation (Table 1). At present, there is a wide collection of both broad and narrow range CAs with different molecular properties that can be leveraged to optimize icIEF resolution for specific samples. Other important aspects in icIEF method optimization are sample preparation and capillary properties. For example, there are durable and specialized hydrophilic coatings (made from MC) that can reduce some issues such as bubble formation and capillary clogging, thus expanding the samples that can be analysed by icIEF.

The wide range of variables that can influence this analytical method make it a good candidate for the development of Analytical Quality by Design (AQbD) approaches, according to ICH Q14 guideline, to develop platform methods able to control charge heterogeneity of specific molecular classes (e.g., mAbs). This may be a great advantage to manufacturers, where standardization of the analysis is made initially as a platform and then transferred by reduced validation exercise to more molecules from the same class. This approach is interesting since its potential to reduce time and costs of the development phase is evident.

From the point of view of equipment, we have witnessed a notable technological development of icIEF, starting with the introduction of fluorescence detectors capable of guaranteeing greater sensitivity, followed by instruments that combines icIEF with MS, allowing a rapid identification of intact charge variants.

It can be underlined that, at present, the correct interpretation of icIEF data requires expertise. In future, applications of artificial intelligence (AI) in managing complex icIEF data sets will be expected to play an important role, particularly in understanding the impact of charged variants on product performances. All technological and digital advances will make icIEF more and more a powerful tool throughout all stages of biotherapeutic development and manufacturing, ensuring the safety and efficacy of biopharmaceutical products.

Author contributions

VG: Conceptualization, Visualization, Writing–original draft. AA: Visualization, Writing–original draft. FG: Writing–review and editing. GM: Funding acquisition, Supervision, Writing–review and editing. FL: Funding acquisition, Supervision, Writing–review and editing.

Funding

The author(s) declare that financial support was received for the research, authorship, and/or publication of this article. This work was supported by Ministero dell'Università e della Ricerca Scientifica: PRIN project (QubyD4Prot) Prot. 2022AF8KZ3. Virginia Ghizzani PhD grant is funded by Istituto Superiore di Sanità (XXXVIII Cycle in Chemical and Pharmaceutical Sciences and Industrial Innovation, University of Pavia).

Conflict of interest

The authors declare that the research was conducted in the absence of any commercial or financial relationships that could be construed as a potential conflict of interest.

Generative AI statement

The author(s) declare that no Generative AI was used in the creation of this manuscript.

Publisher's note

References

Abbood, A. (2023). Optimization of the imaged cIEF method for monitoring the charge heterogeneity of antibody-maytansine conjugate. *J. Anal. Methods Chem.* 2023, 1–10. doi:10.1155/2023/8150143

Ahluwalia, D., Belakavadi, M., Das, T. K., and Katiyar, A. (2018). A three-point identity criteria tool for establishing product identity using icIEF method. *J Chromatogr B Analyt Technol Biomed Life Sci*, 1083, 271. 277. doi:10.1016/j.jchromb.2018.02.042

Ascione, A., Belfiore, M., Vesterinen, J., Buda, M., Holtkamp, W., and Luciani, F. (2024). Charge heterogeneity of therapeutic monoclonal antibodies by different cIEF systems: views on the current situation. *MAbs* 16, 2313737. doi:10.1080/19420862.2024.2313737

Belfiore, M., Ascione, A., Ghizzani, V., Di Meo, S., and Luciani, F. (2024). A new paradigm for optimized experimental design in cIEF platforms aimed at an accurate robust and reliable mAbs charge-variant assessment. *Sci. Rep.* 14, 28087. doi:10.1038/s41598-024-79108-5

Bio-Techne (n.d.) A novel icIEF fractionation and SPR-based workflow for correlating the charge structure to the function of a bispecific antibody. Available at: https://resources.bio-techne.com/bio-techne-assets/docs/literature/7678776428-icIEF-fractionation-and-SPR-workflow.pdf.

Candreva, J., Esterman, A. L., Ge, D., Patel, P., Flagg, S. C., Das, T. K., et al. (2022). Dual-detection approach for a charge variant analysis of monoclonal antibody combination products using imaged capillary isoelectric focusing. *Electrophoresis* 43, 1701–1709. doi:10.1002/elps.202200026

Carter, P. J., and Rajpal, A. (2022). Designing antibodies as therapeutics. *Des. antibodies as Ther.* 185, 2789–2805. doi:10.1016/j.cell.2022.05.029

Dadouch, M., Ladner, Y., and Perrin, C. (2021). Analysis of monoclonal antibodies by capillary electrophoresis: sample preparation, separation, and detection. *Sep. Detect.* 8, 4. doi:10.3390/separations8010004

European Pharmacopoeia (2023). 2.5.44. Capillary isoelectric focusing for recombinant therapeutic monoclonal antibodies. European Pharmacopoeia 11.8. Available at: https://pheur.edqm.eu/app/11-8/content/default/20544E.htm.

Duša, F., Kubesová, A., Šalplachta, J., and Moravcová, D. (2023). Capillary isoelectric focusing – the role of markers of isoelectric point and recent applications in the field. 162, 117018. doi:10.1016/j.trac.2023.117018

He, X., Elnaggar, M., Ostrowski, M. A., Guttman, A., Gentalen, E., and Sperry, J. (2022). Evaluation of an icIEF-MS system for comparable charge variant analysis of biotherapeutics with rapid peak identification by mass spectrometry. *Electrophoresis* 43, 1215–1222. doi:10.1002/elps.202100295

Hjertén, S., and Zhu, M. (1985). Adaptation of the equipment for high-performance electrophoresis to isoelectric focusing. *J. Chromatogr. A* 346, 265–270. doi:10.1016/S0021-9673(00)90512-0

Improving Charge Variant (2000). *Improving charge variant analysis with Maurice native fluorescence - ProteinSimple application note*. Available at: https://chayon.co.kr/email/2020/20-0305_maurice/appnote/10.pdf.

Jochheim, C., Novick, S., Balland, A., Mahan-Boyce, J., Wang, W.-C., Goetze, A., et al. (2001). *Separation of Enbrel® (rhuTNFR: Fc) isoforms by capillary isoelectric focusing*. doi:10.1007/978-3-322-83021-0_7

Kahle, J., Stein, M., and Wätzig, H. (2019). Design of experiments as a valuable tool for biopharmaceutical analysis with (imaged) capillary isoelectric focusing. *Electrophoresis* 40, 2382–2389. doi:10.1002/elps.201900162

Kahle, J., and Wätzig, H. (2018). Determination of protein charge variants with (imaged) capillary isoelectric focusing and capillary zone electrophoresis. *Electrophoresis* 39, 2492–2511. doi:10.1002/elps.201800079

Kinoshita, M., Nakatsuji, Y., Suzuki, S., Hayakawa, T., and Kakehi, K. (2013). Quality assurance of monoclonal antibody pharmaceuticals based on their charge variants using microchip isoelectric focusing method. *J. Chromatogr. A* 1309, 76–83. doi:10.1016/j.chroma.2013.08.021

Krebs, F., Burger, U., Dörks, S., Kramer, M., and Wätzig, H. (2022). Two quality and stability indicating imaged CIEF methods for mRNA vaccines. *Electrophoresis* 43, 1971–1983. doi:10.1002/elps.202200123

Krebs, F., Zagst, H., Stein, M., Ratih, R., Minkner, R., Olabi, M., et al. (2023). Strategies for capillary electrophoresis: method development and validation for pharmaceutical and biological applications—updated and completely revised edition. *Electrophoresis* 44, 1279–1341. doi:10.1002/elps.202300158

Kristl, T., Stutz, E.-H., Wenz, C., and Rozing, G. (2014). Principles and applications of capillary isoelectric focusing. Available at: https://www.agilent.com/cs/library/primers/public/5991-1660EN.pdf (Accessed November 18, 2024).

Kristl, T., and Stutz, H. (2014). Comparison of different mobilization strategies for capillary isoelectric focusing of ovalbumin variants. *J. Sep. Sci.* 38, 148–156. doi:10.1002/jssc.201400890

Kwok, T., Chan, S. L., Shi, J., Zhou, M., Schaefer, A., Bo, T., et al. (2023a). Imaged capillary isoelectric focusing employing fluorocarbon and methylcellulose coated fused silica capillary for characterization of charge heterogeneity of protein biopharmaceuticals. *Sep. Sci. Plus* 6. doi:10.1002/sscp.202200160

Kwok, T., Chan, S. L., Zhou, M., Schaefer, A., Bo, T., Huang, T., et al. (2022). High-efficient characterization of complex protein drugs by imaged capillary isoelectric focusing with high-resolution ampholytes. *Sep. Sci. Plus* 6. doi:10.1002/sscp.202200142

Kwok, T., Zhou, M., Schaefer, A., Bo, T., Li, V., Huang, T., et al. (2023b). Fractionation and online mass spectrometry based on imaged capillary isoelectric focusing (icIEF) for characterizing charge heterogeneity of therapeutic antibody. *Anal. Methods* 15, 411–418. doi:10.1039/D2AY01670B

Lechner, A., Giorgetti, J., Gahoual, R., Beck, A., Leize-Wagner, E., and François, Y.-N. (2019). Insights from capillary electrophoresis approaches for characterization of monoclonal antibodies and antibody drug conjugates in the period 2016–2018. 1–17. doi:10.1016/j.jchromb.2019.05.014

Leng, C., Sun, S., Lin, W., Pavon, J. A., Gennaro, L., Gunawan, R. C., et al. (2024). Imaged capillary isoelectric focusing method development for charge variants of high DAR ADCs. *Anal. Chim. Acta X.* 1328, 343176. doi:10.1016/j.aca.2024.343176

Li, X., Shi, X., Qin, X., Yu, L., Zhou, Y., and Rao, C. (2020). Interlaboratory method validation of imaged capillary isoelectric focusing methodology for analysis of recombinant human erythropoietin. *Anal. Methods* 12, 3836–3843. doi:10.1039/D0AY00823K

Li, X., Yu, L., Shi, X., Rao, C., and Zhou, Y. (2021). Capillary isoelectric focusing with UV fluorescence imaging detection enables direct charge heterogeneity characterization of erythropoietin drug products. *J. Chromatogr. A* 1643, 462043. doi:10.1016/j.chroma.2021.462043

Loughney, J. W., Minsker, K., Ha, S., and Rustandi, R. R. (2019). Development of an imaged capillary isoelectric focusing method for characterizing the surface charge of mRNA lipid nanoparticle vaccines. *vaccines* 40, 2602–2609. doi:10.1002/elps.201900063

Mack, S., Arnold, D., Bogdan, G., Bousse, L., Danan, L., Dolnik, V., et al. (2019). A novel microchip-based imaged CIEF-MS system for comprehensive characterization and identification of biopharmaceutical charge variants. *Electrophoresis* 40, 3084–3091. doi:10.1002/elps.201900325

Mack, S., Cruzado-Park, I., Chapman, J., Ratnayake, C., and Vigh, G. (2009). A systematic study in CIEF: defining and optimizing experimental parameters critical to method reproducibility and robustness. *Electrophoresis* 30, 4049–4058. doi:10.1002/elps.200800690

Madren, S., Mcelroy, W., Schultz-kuszak, K., Boumajny, B., Shu, Y., Sautter, S., et al. (2022). Global intercompany assessment of ICIEF platform comparability for the characterization of therapeutic proteins. *Electrophoresis* 43, 1050–1058. doi:10.1002/elps.202100348

Mao, Q., and Pawliszyn, J. (1999). Capillary isoelectric focusing with whole column imaging detection for analysis of proteins and peptides. *J. Biochem. Biophys. Methods* 39, 93–110. doi:10.1016/s0165-022x(99)00006-8

Maráková, K., Opetová, M., and Tomašovský, R. (2023). Capillary electrophoresis-mass spectrometry for intact protein analysis: pharmaceutical and biomedical applications (2018–March 2023). *J. Sep. Sci.* 46, e2300244. doi:10.1002/jssc.202300244

Meudt, M., Pannek, M., Glogowski, N., Higel, F., Thanisch, K., and Knape, M. J. (2024). CE methods for charge variant analysis of mAbs and complex format biotherapeutics. *Electrophoresis* 45, 1295–1306. doi:10.1002/elps.202300170

Michels, D. A., Tu, A. W., McElroy, W., Voehringer, D., and Salas-Solano, O. (2012). Charge heterogeneity of monoclonal antibodies by multiplexed imaged capillary isoelectric focusing immunoassay with chemiluminescence detection. *Anal. Chem.* 84, 5380–5386. doi:10.1021/ac3008847

Mohan, D., and Lee, C. S. (2002). Extension of separation range in capillary isoelectric focusing for resolving highly basic biomolecules. *J. Chromatogr. A* 979, 271–276. doi:10.1016/S0021-9673(02)01442-5

Ostrowski, M. A., Mack, S., Ninonuevo, M., Yan, J., Elnaggar, M., Gentalen, E., et al. (2022). Rapid multi-attribute characterization of intact bispecific antibodies by a

microfluidic chip-based integrated icIEF-MS technology. *MS Technol.* 44, 378–386. doi:10.1002/elps.202200165

Paul, S., Konig, M. F., Pardoll, D. M., Bettegowda, C., Papadopoulos, N., Wright, K. M., et al. (2024). Cancer therapy with antibodies. *Nat. Rev. Cancer* 24, 399–426. doi:10.1038/s41568-024-00690-x

Permanent methylcellulose (MC) (2023). Coated cartridges achieves iCIEF free from polymers as dynamic coating for straight forward characterization of protein drugs - technical note. *Adv. Elecrtophoresis solutions*. Available at: https://aeslifesciences.com/wp-content/uploads/2022/08/CEInfinite-Tech-Note-MC-coating-cartridge.pdf.

Pharmaceutical Development (2022). ICH harmonised tripartite guideline. Available at: https://database.ich.org/sites/default/files/Q8%28R2%29%20Guideline.pdf (Accessed October 10, 2024).

ProteinSimple (2018). Analysis of monoclonal antibodies with carboxypeptidase B. Available at: https://resources.bio-techne.com/bio-techne-assets/docs/protocols/analysis-of-monoclonal-antibodies-with-carboxypeptidase-b-revb.pdf.

ProteinSimple (2019). Analysis of ADC mimics by icIEF with 458 nm fluorescence detection. Available at: https://resources.bio-techne.com/bio-techne-assets/docs/protocols/pl7-0066-reva-analysis-adc-mimics-by-maurice-protocol.pdf.

Righetti, P. G. (1983). *Isoelectric focusing: theory, methodology, and applications*. Amsterdam: Elsevier Biomedical Press. Available at: https://onesearch.nihlibrary.ors.nih.gov/discovery/fulldisplay?vid=01NIH_INST:NIH&docid=alma9910012857795046 86&lang=en&context=L&adaptor=Local%20Search%20Engine (Accessed November 27, 2024).

Righetti, P. G., Gelfi, C., and Conti, M. (1997). Current trends in capillary isoelectric focusing of proteins. *Curr. trends Capill. isoelectric Focus. proteins* 699, 91–104. doi:10.1016/S0378-4347(96)00208-3

Righetti, P. G., Simó, C., Sebastiano, R., and Citterio, A. (2007). Carrier ampholytes for IEF, on their fortieth anniversary (1967-2007), brought to trial in court: the verdict. *Electrophoresis* 28, 3799–3810. doi:10.1002/elps.200700232

Salas-solano, O., Kennel, B., Park, S. S., Roby, K., Sosic, Z., Boumajny, B., et al. (2012). Robustness of iCIEF methodology for the analysis of monoclonal antibodies: an interlaboratory study. *J. Sep. Sci.* 35, 3124–3129. doi:10.1002/jssc.201200633

Schlecht, J., Moritz, B., Kiessig, S., and Neusüß, C. (2022). Characterization of therapeutic mAb charge heterogeneity by iCIEF coupled to mass spectrometry (iCIEF–MS). *iCIEF–MS* 44, 540–548. doi:10.1002/elps.202200170

Sharma, P., Joshi, R. V., Pritchard, R., Xu, K., and Eicher, M. A. (2023). Therapeutic antibodies in medicine. *Molecules* 28, 6438. doi:10.3390/molecules28186438

Sosic, Z., Houde, D., Blum, A., Carlage, T., and Lyubarskaya, Y. (2008). Application of imaging capillary IEF for characterization and quantitative analysis of recombinant protein charge heterogeneity. *Electrophoresis* 29, 4368–4376. doi:10.1002/elps.200800157

Štěpánová, S., and Kašička, V. (2022). Applications of capillary electromigration methods for separation and analysis of proteins (2017–mid 2021) – a review. *A Rev.* 1209, 339447. doi:10.1016/j.aca.2022.339447

Sutton, H., Hong, F., Han, X., and Rauniyar, N. (2024). Analysis of therapeutic monoclonal antibodies by imaged capillary isoelectric focusing (icIEF). *icIEF* 16, 5450–5458. doi:10.1039/d4ay00836g

Tardif, C., Jaccoulet, E., Bellec, J.-F., Surroca, Y., Talbot, L., Taverna, M., et al. (2023). Imaged capillary isoelectric focusing associated with multivariate analysis: a powerful tool for quality control of therapeutic monoclonal antibodies. *Talanta* 260, 124633. doi:10.1016/j.talanta.2023.124633

Tavernier, V., Butré, C., and Delobel, A. (2022). *Capillary isoelectric focusing (icIEF) bridging study between iCE3 and Maurice equipment*. Available at: https://www.quality-assistance.com/capillary-isoelectric-focusing-icief-bridging-study-between-ice3-and-maurice-equipment.

Turner, A., and Schiel, J. E. (2018). Qualification of NISTmAb charge heterogeneity control assays. *Anal. Bioanal. Chem.* 410, 2079–2093. doi:10.1007/s00216-017-0816-6

Van Den Bremer, E. T., Beurskens, F. J., Voorhorst, M., Engelberts, P. J., De Jong, R. N., Van Der Boom, B. G., et al. (2015). Human IgG is produced in a pro-form that requires clipping of C-terminal lysines for maximal complement activation. *MAbs* 7, 672–680. doi:10.1080/19420862.2015.1046665

AES Advanced Electrophoresis Solutions Ltd (2016). White paper: Critical reagents for successful iCIEF. Available at: https://aeslifesciences.com/wp-content/uploads/2022/10/White-paper.pdf (Accessed November 15, 2024).

Wu, G., Du, J., Xu, G., Li, M., and Yu, C. (2024a). Possibility of using the imaged capillary isoelectric method as a multi-attribute method for bispecific antibodies. *Electrophoresis* 45, 1665–1672. doi:10.1002/elps.202400066

Wu, G., Du, J., Yu, C., Fu, Z., Zhang, X., Wang, L., et al. (2024b). Mass spectrometry study on SARS-CoV-2 recombinant vaccine with comprehensive separation techniques to characterize complex heterogeneity. *Anal. Chim. Acta X.* 1297, 342349. doi:10.1016/j.aca.2024.342349

Wu, G., Yu, C., Wang, W., Du, J., Fu, Z., Xu, G., et al. (2023). Mass spectrometry-based charge heterogeneity characterization of therapeutic mAbs with imaged capillary isoelectric focusing and ion-exchange chromatography as separation techniques. *Anal. Chem.* 95, 2548–2560. doi:10.1021/acs.analchem.2c05071

Wu, G., Yu, C., Wang, W., and Wang, L. (2018). Interlaboratory method validation of icIEF methodology for analysis of monoclonal antibodies. *Electrophoresis* 39, 2091–2098. doi:10.1002/elps.201800118

Wu, G., Yu, C., Wang, W., Zhang, R., Li, M., and Wang, L. (2022a). A platform method for charge heterogeneity characterization of fusion proteins by icIEF. *Anal. Biochem.* 638, 114505. doi:10.1016/j.ab.2021.114505

Wu, G., Zhang, X., Wang, X., Du, J., Li, M., Xu, G., et al. (2024c). In-depth characterization of a cysteine-linked ADC disitamab vedotin by multiple LC-MS analysis methods and cutting-edge imaged capillary isoelectric focusing coupled with native mass spectrometry. *J. Chromatogr. A* 1736, 465353. doi:10.1016/j.chroma.2024.465353

Wu, J., Mcelroy, W., Pawliszyn, J., and Heger, C. D. (2022b). Imaged capillary isoelectric focusing: applications in the pharmaceutical industry and recent innovations of the technology. 150. 116567. doi:10.1016/j.trac.2022.116567

Wu, J., and Pawliszyn, J. (1992). High-performance capillary isoelectric focusing with a concentration gradient detector. *Anal. Chem.* 64, 219–224. doi:10.1021/ac00026a023

Wu, J., and Pawliszyn, J. (1994). Dual detection for capillary isoelectric focusing with refractive index gradient and absorption imaging detectors. *Anal. Chem.* 66, 867–873. doi:10.1021/ac00078a018

Yao, X.-W., Wu, D., and Regnier, F. E. (1993). Manipulation of electroosmotic flow in capillary electophoresis, *J. Chromatogr. A, Manip. electroosmotic flow Capill. Electrophor.* 636, 21–29. doi:10.1016/0021-9673(93)80052-A

Zhang, X., Chemmalil, L., Ding, J., and Li, Z. (2020). A novel approach enables imaged capillary isoelectric focusing analysis of PEGylated proteins. *Electrophoresis* 41, 735–742. doi:10.1002/elps.201900406

Zhang, X., Chemmalil, L., Ding, J., Mussa, N., and Li, Z. (2017a). Imaged capillary isoelectric focusing in native condition: a novel and successful example. *Anal. Biochem.* 537, 13–19. doi:10.1016/j.ab.2017.08.014

Zhang, X., Chen, T., Li, V., Bo, T., Du, M., and Huang, T. (2023a). Cutting-edge mass spectrometry strategy based on imaged capillary isoelectric focusing (icIEF) technology for characterizing charge heterogeneity of monoclonal antibody. *Anal. Biochem.* 660, 114961. doi:10.1016/j.ab.2022.114961

Zhang, X., Kwok, T., Zhou, M., Du, M., Li, V., Bo, T., et al. (2023b). Imaged capillary isoelectric focusing (icIEF) tandem high resolution mass spectrometry for charged heterogeneity of protein drugs in biopharmaceutical discovery. *J. Pharm. Biomed. Anal.* 224, 115178. doi:10.1016/j.jpba.2022.115178

Zhang, X., Voronov, S., Mussa, N., and Li, Z. (2017b). A novel reagent significantly improved assay robustness in imaged capillary isoelectric focusing. *Anal. Biochem.* 521, 1–7. doi:10.1016/j.ab.2016.12.013

Zhang, X., Wu, G., Du, M., Bo, T., Chen, T., and Huang, T. (2024). Imaged capillary isoelectric focusing coupled to high-resolution mass spectrometry (icIEF-MS) for cysteine-linked antibody-drug conjugate (ADC) heterogeneity characterization under native condition. *Electrophoresis* 45, 1915–1926. doi:10.1002/elps.202400083

Zhang, Z., Perrault, R., Zhao, Y., and Ding, J. (2016). SpeB proteolysis with imaged capillary isoelectric focusing for the characterization of domain-specific charge heterogeneities of reference and biosimilar Rituximab. *J Chromatogr B Analyt Technol Biomed Life Sci*, 1020, 148. 157. doi:10.1016/j.jchromb.2016.03.031

frontiers | Frontiers in Chemistry

TYPE Original Research
PUBLISHED 26 February 2025
DOI 10.3389/fchem.2025.1534216

OPEN ACCESS

EDITED BY
Federica Aureli,
National Institute of Health (ISS), Italy

REVIEWED BY
Sulaymon Eshkabilov,
North Dakota State University, United States
Estefania Alfaro Mejia,
University of Puerto Rico at Mayagüez, Puerto Rico
Jinhuan Xu,
Qilu University of Technology, China

*CORRESPONDENCE
Wei Zhang,
weizcaas@126.com
Xueyuan Bai,
baixy1212@163.com

RECEIVED 25 November 2024
ACCEPTED 30 January 2025
PUBLISHED 26 February 2025

CITATION
Ran J, Xu H, Wang Z, Zhang W and Bai X (2025) Non-destructive analysis of *Ganoderma lucidum* composition using hyperspectral imaging and machine learning. *Front. Chem.* 13:1534216. doi: 10.3389/fchem.2025.1534216

Non-destructive analysis of *Ganoderma lucidum* composition using hyperspectral imaging and machine learning

Jing Ran, Hui Xu, Zhilong Wang, Wei Zhang* and Xueyuan Bai*

Northeast Asia Institute of Traditional Chinese Medicine, Changchun University of Chinese Medicine, Changchun, Jilin, China

Background: *Ganoderma lucidum* is a widely used medicinal fungus whose quality is influenced by various factors, making traditional chemical detection methods complex and economically challenging. This study addresses the need for fast, noninvasive testing methods by combining hyperspectral imaging with machine learning to predict polysaccharide and ergosterol levels in *Ganoderma lucidum* cap and powder.

Methods: Hyperspectral images in the visible near-infrared (385–1009 nm) and short-wave infrared (899–1695 nm) ranges were collected, with ergosterol measured by high-performance liquid chromatography and polysaccharides assessed via the phenol-sulfuric acid method. Three machine learning models—a feedforward neural network, an extreme learning machine, and a decision tree—were tested.

Results: Notably, the extreme learning machine model, optimized by a genetic algorithm with voting, provided superior predictions, achieving R^2 values of 0.96 and 0.97 for polysaccharides and ergosterol, respectively.

Conclusion: This integration of hyperspectral imaging and machine learning offers a novel, nondestructive approach to assessing *Ganoderma lucidum* quality.

KEYWORDS

polysaccharide, ergosterol, hyperspectral imaging, machine learning model, medicinal fungus

1 Introduction

Ganoderma lucidum, a member of the Ganodermataceae family, is classified as a white-rot fungi (Wang T. T. et al., 2024). This species primarily grows in tropical, subtropical, and temperate climates. As one of the leading producers, China has developed a large-scale *Ganoderma lucidum* planting industry. This fungus is rich in specific bioactive components, including polysaccharides, triterpenes, proteins, and sterols (Cör et al., 2022). *Ganoderma lucidum*, known for its remarkable antioxidant, antibacterial, tumor-inhibiting, and anti-inflammatory effects, holds a significant position in the healthcare and nutrition market. This is attributed to its three primary functions: nourishment, treatment, and tonification. As awareness of the quality of *Ganoderma lucidum* increases, it becomes evident that its quality is significantly affected by many factors, including producing area, cultivation environment, harvest conditions, and so on. Researchers have developed various quality control techniques for *Ganoderma lucidum*, including UV-Vis spectrophotometry (Jiang

et al., 2018) and nuclear magnetic resonance (Wang M. et al., 2024) spectroscopy for analyzing polysaccharides, high-performance liquid chromatography (HPLC) for assessing triterpenoid acids (Zeng et al., 2023) and ergosterol (Liu et al., 2011), HPLC-ELSD lipid profiling (Xia et al., 2023), and high-performance capillary electrophoresis for nuclear glycoside content analysis (Dai et al., 2002). Although these methods can be employed to determine the chemical composition of *Ganoderma lucidum*, traditional detection techniques have limitations, including complexity, time consumption, destructiveness, and sensitivity to standard experimental procedures.

Advancements in spectral technology have significantly improved non-destructive testing methods. Consequently, researchers have quantitatively analyzed polysaccharides and triterpene compounds in *Ganoderma lucidum* (Zhang and Huang, 2021; Zhang, 2020) alongside rapid identification of *Ganoderma lucidum* varieties (Yang et al., 2017) through near-infrared fingerprint technology. Near-infrared spectroscopy works by measuring samples that absorb near-infrared light, which provides insight into their chemical composition and physical properties. However, this technique typically offers lower spatial resolution and is limited to spectroscopic information. Hyperspectral imaging technology (HSI)—a novel analytical method—integrates traditional imaging with spectroscopy to simultaneously capture spatial and spectral information of samples. This technology offers several advantages: it is non-contact, non-destructive, fast, and capable of providing a large amount of information. It holds significant potential for applications across agriculture, food, medicine, and other fields. Machine learning, an important branch of artificial intelligence, automatically extracts features from large datasets and learns rules by creating predictive models to accurately predict or classify unknown samples. Xu et al. employed principal component analysis (PCA) to extract feature bands and utilized a support vector machine for modeling moldy walnuts (Xu et al., 2022). Xiao et al. developed an SVM model using feature wavelengths extracted via PCA and convolutional neural networks, achieving results comparable to or better than those of the full-wavelength model (Xiao et al., 2020). Li et al. extracted 13 characteristic wavelengths using a stacked autoencoder and achieved optimal predictive performance in a GA-ELM model, with an R^2 value of 0.97 (Li et al., 2023a). This study achieved an overall classification accuracy of 93%. Furthermore, Li et al. successfully used the SNV-SPA-LS-SVM algorithm to detect protein content in mulberry leaves. This method effectively assessed leaf quality, yielding an RPD value of 3.83 and an $R^2$for protein detection (Li et al., 2023b).

The researchers captured hyperspectral images of wheat flour in the range of 968–2576 nm and developed models using partial least squares discriminant analysis and SVM based on characteristic wavelengths. The results indicate that the nonlinear discriminant model outperformed the linear model in classifying the wheat flour grades. Furthermore, the MSC-UVE-CARS-PSO-SVM model provides superior prediction performance, achieving 100% accuracy in the calibration and validation sets (Zhang et al., 2023). Alfaro-Mejía et al. propose an unsupervised deep learning model for endmember extraction and fractional abundance map estimation from the HSI (Alfaro-Mejía et al., 2023). Other scholars have used a fast and compact Hybrid CNN to process HSI data for bloodstain identification and classification (Butt et al., 2022). Hou et al. proposed a hyperspectral imagery classification model based on self-supervised contrastive learning (SSCL),where conventional spectral-spatial features and deep models are combined to improve the classification accuracy (Hou et al., 2021). Advancements in HSI and machine learning algorithms are further improving their application in the quality detection of *Ganoderma lucidum*. For example, Pan et al. and other researchers developed a prediction model by collecting hyperspectral images of *Ganoderma lucidum* spore powder samples with varying wall-breaking rates (Pan et al., 2024). The model incorporated spectral preprocessing and characteristic band extraction. The combination of Savitzky-Golay smoothing and competitive adaptive reweighted feature band selection together with partial least squares yielded the best prediction performance. This technique successfully enabled a rapid, non-destructive testing approach for determining the wall-breaking rate of *Ganoderma lucidum* spore powder. Additionally, other researchers have employed visible-near infrared HSI to pre-detect polysaccharide content in *Ganoderma lucidum* fruiting bodies. *Ganoderma lucidum* polysaccharide content has been accurately predicted by collecting hyperspectral images, conducting spectral preprocessing, extracting characteristic bands, and utilizing partial least squares modeling (Liu Y. et al., 2021). The concentration of 15 inorganic elements, including lead, in the entire fruiting body of *Ganoderma lucidum* was higher than those in the caps (Liu et al., 2023). Furthermore, while the caps contain higher concentrations of ganoderic acid A (Huang et al., 2017) and ganoderic acid B (Shi et al., 2013), infrared spectroscopy indicates that the levels of amino acids, peptides, and proteins in *Ganoderma lucidum* were higher than those in the caps (Huang et al., 2015).

In a previous hyperspectral study of *Ganoderma lucidum* polysaccharides, only the cap was collected. However, differences in the distribution of chemical compositions in *Ganoderma lucidum* may result in inaccurate model predictions. Therefore, hyperspectral

TABLE 1 Samples of *Ganoderma lucidum*.

Origins	Numbers	Identification
Jilin Fusong	4	A1
Jiaohe, Jilin	3	A2
Huadian, Jilin	1	A3
Jilin City, Jilin Province	3	A4
Tonghua, Jilin	3	A5
Anqing, Anhui	1	B2
Bozhou, Anhui	3	B3
Tai'an, Shandong	3	C1
Liaocheng, Shandong	1	C2
Jixi, Heilongjiang	3	D
Longquan, Zhejiang	1	E
Baise, Guangxi	3	F
Linzhi, Tibet	3	G

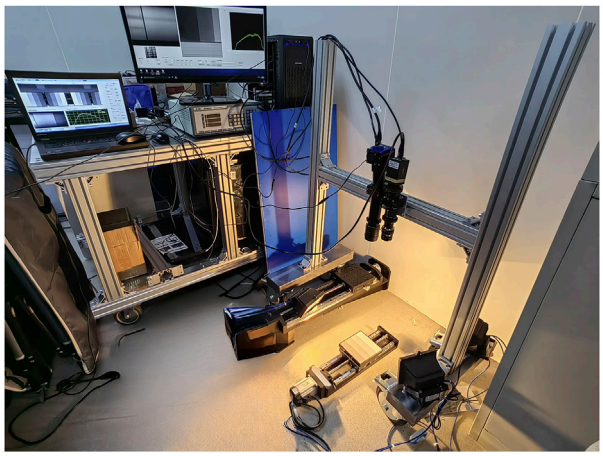

FIGURE 1
Hyperspectral imaging system.

images of *Ganoderma lucidum* caps and powder were collected, and the hyperspectral data were preprocessed using genetic algorithms and principal component analysis, and three kinds of machine learning models, BPNN, ELM, and DT, of the original spectral data and the preprocessed spectral data, were established for the prediction of the chemical content of the samples of different morphologies of *Ganoderma lucidum*, and the best prediction models were screened out by comparing different algorithms with each other. It aims to provide a new method for non-destructive testing of *Ganoderma lucidum* quality.

2 Materials and methods

2.1 Sample preparation and hyperspectral image acquisition

In this study, 32 fruiting bodies of *Ganoderma lucidum* were collected from 13 production areas. Table 1 provides detailed information. Upon collection, the *Ganoderma lucidum* cap was immediately crushed into powder, which was pressed onto A4 paper to coin-sized shapes for consistent hyperspectral image acquisition under the same conditions. During the collection, the indoor temperature was kept at approximately 25°C. Each sample was photographed three times, and the average spectrum was calculated from the original spectral data.

The HSI system used for image acquisition adopts a dual-light source set-up, consisting of a grating splitter, charge-coupled device, an IMPERX 1920 × 1080 visible near-infrared camera (lens: Kowa 35 mm focal length), Guohui 640 × 512 short-wave infrared camera (lens: AZURE 50 mm focal length), halogen light sources, electric platform, and computer. The experimental equipment was provided by the Changchun Institute of Optics and Precision Machinery, Chinese Academy of Sciences (Figure 1).

Calibration images were collected (Reddy et al., 2023) before acquiring the hyperspectral images to correct for any variations in light source intensity and dark current, ensuring accurate spectral data (Dai et al., 2023). The calibration formula is in the following Equation 1.

$$R = \frac{I_{raw} - I_{dark}}{I_{white} - I_{dark}} \quad (1)$$

where R is the calibrated reflectance image, I_{raw} is the original reflectance image, I_{dark} represents the blackboard reference image, and I_{white} is the whiteboard reference image.

Figure 2 Provides a schematic overview of the analysis process, including the acquisition of spectral data and model development.

2.2 Region of interest extraction and sample set division

The region of interest was manually delineated using ENVI5.3 software, selecting three pixels and calculating their average values as the spectral reflectance for each sample. Overall, 128 regions of interest were extracted from 32 *Ganoderma lucidum* cap (GLC) and powder (GLP), which were randomly divided into training and prediction sets at a ratio of 115:13 for subsequent modeling.

2.3 Measurement of chemical composition

2.3.1 Polysaccharides

To measure polysaccharide content, 1.0 g of the fruiting body powder of *Ganoderma lucidum* collected from the hyperspectral images was weighed, and 40 mL of pure water was added. The mixture was then boiled for 2 h, fixed volume to 50 mL, and filtered. The filtrate (5 mL) was added to 25 mL of anhydrous ethanol, followed by overnight precipitation. The mixture was centrifuged at 5000 rpm for 25 min. The resulting supernatant was discarded, and the residue was dissolved in 25 mL of water. The solution (1 mL) was thoroughly mixed with water to 2 mL, and the absorbance was determined according to the phenol sulfate method. The determination was repeated three times, and the average value was calculated.

2.3.2 Ergosterol

A 1.0 g sample of the powder collected from the HSI was dissolved in 20 mL of methanol, thoroughly mixed, and sonicated for 1 h. Following filtration, the ergosterol content in *Ganoderma lucidum* was determined using HPLC. The HPLC conditions were as follows: an Agilent Eclipse Plus C18 column (4.6 mm × 250 mm,5 μm), flow rate of 1.0 mL/min, detection wavelength of 282 nm, injection volume of 10 μL, column temperature of 30°C, and methanol as mobile phase.

2.4 Hyperspectral data processing methods

Hyperspectral data is high-dimensional and nonlinear, often containing large volumes of information, noise, redundancy, and collinearity, all of which complicate analysis (Chen et al., 2024; Sun et al., 2024). Using full-spectrum modeling not only increases the complexity of model training but also causes overfitting. Therefore,

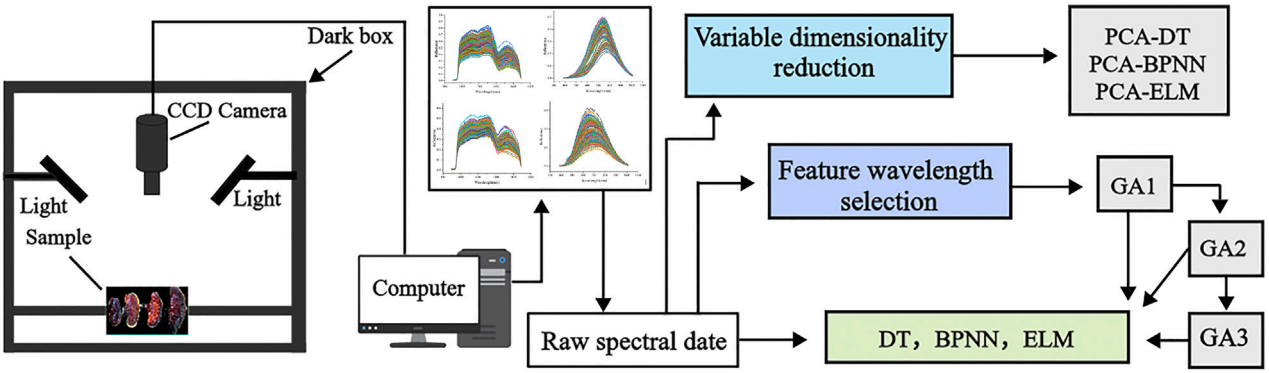

FIGURE 2
Schematic diagram of *Ganoderma lucidum* sample program analysis.

reducing variables and selecting relevant wavelengths are essential for enhancing classification accuracy and simplifying computations.

2.4.1 Variable dimensionality reduction

Dimensionality reduction is an essential preprocessing step in data mining with broad applications, particularly for spectral data. PCA is a commonly used unsupervised learning method.

PCA uses an orthogonal transformation to convert observed data represented by linearly correlated variables into a smaller set of linearly independent variables, known as principal components. Principal components with high interpretive value retain most of the critical information from hyperspectral images (Xiao et al., 2020; Ye et al., 2022).

2.4.2 Characteristic wavelength selection

A GA is an optimization method inspired by the principles of natural selection and Darwinian evolution theory. Following the "survival of the fittest" principle, GA uses the "network" to find the global optimal solution by simulating the biological evolution process (Zhang et al., 2024). Using "minimum error" as the evolutionary criterion, the optimal solution is searched in the global scope (Wang et al., 2021). Compared with the inverse gradient descent method, GA can search multiple solutions within the solution space simultaneously without requiring differential operation. This makes GA highly robust and widely applicable (Wang et al., 2023). We propose two methods for selecting feature wavelengths using GA. The first is iterative feature selection, which reduces the number of wavelengths over multiple iterations, refining the quality of the selected wavelengths. The second approach uses voting-based feature selection, where multiple runs are performed, and the wavelengths selected most frequently are designated as the characteristic wavelength. The roulette wheel selection strategy was used to select the most fit individual. Additionally, single-point crossover was implemented to improve the search process. The variation operator uses the fundamental bitwise variation and sets the variation probability to 0.05. This setting helped prevent the algorithm from getting stuck in a local optimum. It also enhanced its ability to perform global searches. These genetic operators collaborate to help the algorithm discover a better combination of features in the feature selection process, which ultimately improves the final model's performance.

2.5 Model construction and evaluation

2.5.1 BP neural network

A back propagation (BP) neural network is a multilayer feed forward network and one of the most widely used neural network architectures (Figure 3). Each BP neural network (Yu and Sun, 2024) consists of an input, hidden, and output layer, where there can be one or more hidden layers (He and Zhou, 2022). The core concept of a BP neural network is to adjust the connection weight of the network through the backpropagation error, thus minimizing the output error. However, in complex networks, training can often become trapped in local minimum (Yuan et al., 2009). Additionally, the performance of BP neural networks largely depends on the settings of hyperparameters, such as the learning rate and number of hidden layers and neurons. If the learning rate is too high, training may become unstable, while too low may cause slow or stalled training. Increasing hidden layers or nodes can reduce error and improve model generalization, simultaneously increasing neural network complexity, extending learning time, and may eventually cause overfitting. Overfitting makes the model prone to getting trapped in a local minimum, ultimately degrading its e performance. Conversely, reducing the number of hidden layers may prevent the network from achieving sufficient accuracy or cause underfitting. Therefore, balancing the number of nodes is essential for optimizing model performance, minimizing overfitting, and achieving a robust fit (Liu et al., 2016). In this study, we configure the BPNN with the following parameters: the hidden layer contains 100 neurons, the maximum number of iterations is set to 1000, the initial learning rate is 0.01, the activation function is the tanh, and the solver is the lbfgs algorithm.

2.5.2 Decision tree

A decision tree (DT) is a machine-learning model that uses a hierarchical tree structure composed of a root node, several internal nodes, and leaf nodes to represent decision rules and classification outcomes. The root node serves as the starting point of the tree, each internal node represents a feature attribute or judgment condition (Xu et al., 2022), and the leaf node represents the final prediction result (Figure 4). The decision tree recursively partitions the dataset until the stopping condition is met, thus forming a prediction model (Li M. Y., 2024). Model stability generally increases with a lower

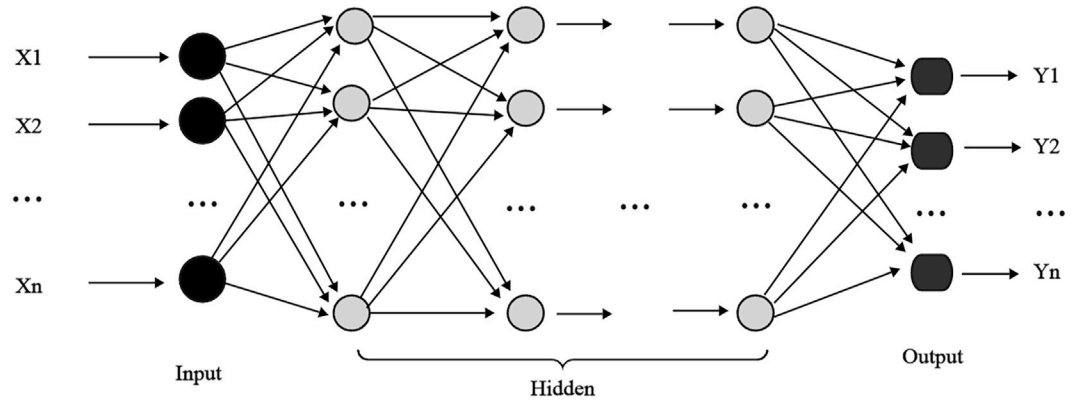

FIGURE 3
Topology diagram of backpropagation neural network.

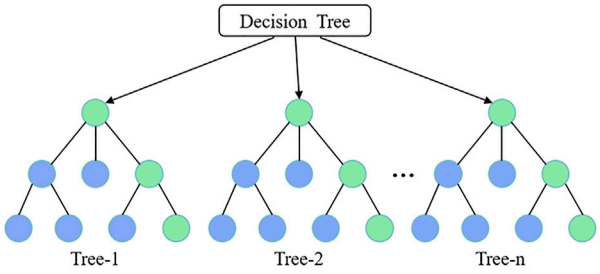

FIGURE 4
Topology diagram of the decision tree.

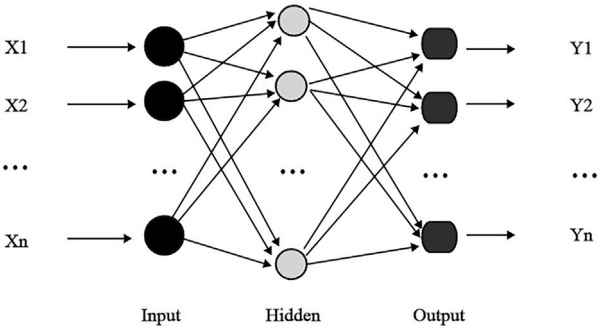

FIGURE 5
Topology diagram of the extreme learning machine.

learning rate. Additionally, the complexity of the model is influenced by the tree depth and number of splits: as complexity increases, more decision trees are required, which increases training time and storage requirements (Zhang et al., 2024).

2.5.3 Extreme learning machine

Extreme learning machine (ELM) is a single-layer feedforward neural network consisting of an input, a hidden, and an output layer (Figure 5), known for its strong performance in classification and regression (Jia et al., 2024; Huang et al., 2006; Liu et al., 2022; Feng et al., 2024). The principle of the ELM is to map the input data into a high-dimensional feature space to establish an optimal hyperplane that best represents the relationship between inputs and outputs (Li P. X., 2024). Unlike traditional feedforward neural networks, ELM reduces complexity by avoiding iterative learning and parameter tuning, transforming the training into a simple matrix inversion problem. Hidden layer weights and thresholds are assigned randomly, while output layer weights are directly calculated, bypassing gradient descent. Therefore, ELM significantly reduces training time and offers high learning efficiency, accuracy, and ease of parameter adjustment (Chen and Wang, 2019; Lu et al., 2024; Liu T. et al., 2021).

2.6 Model evaluation

The training set determination coefficient (R_T^2), verification set determination coefficient (R_V^2), and mean square error (MSEP) are utilized as indicators to determine the model performances. All the models ran 10 times for averaging to ensure the robustness of the model evaluation. The closer the determination coefficient (R^2) is to 1, the better the fitting effect of the model (Li et al., 2023c). Among them, $R^2 > 0.90$ indicates excellent prediction ability of the model, $0.81 < R^2 < 0.90$ suggests good prediction performance of the model, and $0.60 < R^2 < 0.80$ shows that the model is general but still useable for prediction. The MSEP is employed to determine the deviation between the predicted and real values. A larger R^2 and a smaller MSEP indicates higher accuracy and better stability of the model (Cui et al., 2017).

3 Results

3.1 Chemical composition content

By mapping the average content of *Ganoderma lucidum* polysaccharides and ergosterol (Figure 6), the polysaccharide

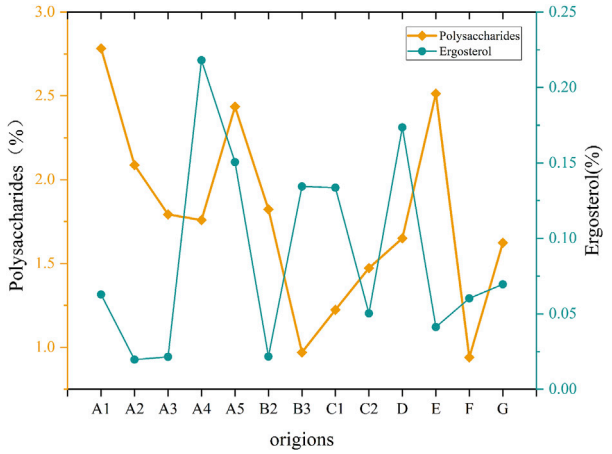

FIGURE 6
Diagram of chemical composition content in *Ganoderma lucidum* samples.

content in Bozhou, Anhui, and Baise, Guangxi, was <1.0%, which was the lowest among all the producing areas. In contrast, ergosterol content was relatively high in Longquan, Zhejiang, and Fusong, Jilin Province, with the highest levels found in Jilin City, Jilin Province. These findings suggest significant variation in *Ganoderma lucidum* contents across different areas; however, traditional separation and detection methods were time-consuming and complex. Furthermore, the performance of each component differs across production areas, complicating the evaluation of *Ganoderma lucidum* quantity based solely on a single component. Therefore, using hyperspectral technology to predict the content and assess the quality of *Ganoderma lucidum* may be highly valuable.

3.2 Spectral characteristics

The spectral reflectance of the GLC and GLP showed similar trends in different wavelength bands, but their reflectance values exhibited significant differences (Figure 7). The average reflectance of the GLC was higher than that of the GLP. In the range of the VNIR band, the reflectance map of the GLC appeared delaminated, owing to structural variation, such as surface roughness and texture. After crushing, the sample exhibited high uniformity, causing this delamination effect to disappear and shifting the position of the absorption peak accordingly. Absorption peaks were observed near 1100, 1300, and 1520 nm in the SWIR band; the peak at 1100 nm may be related to the second overtone of N-H stretching, while that

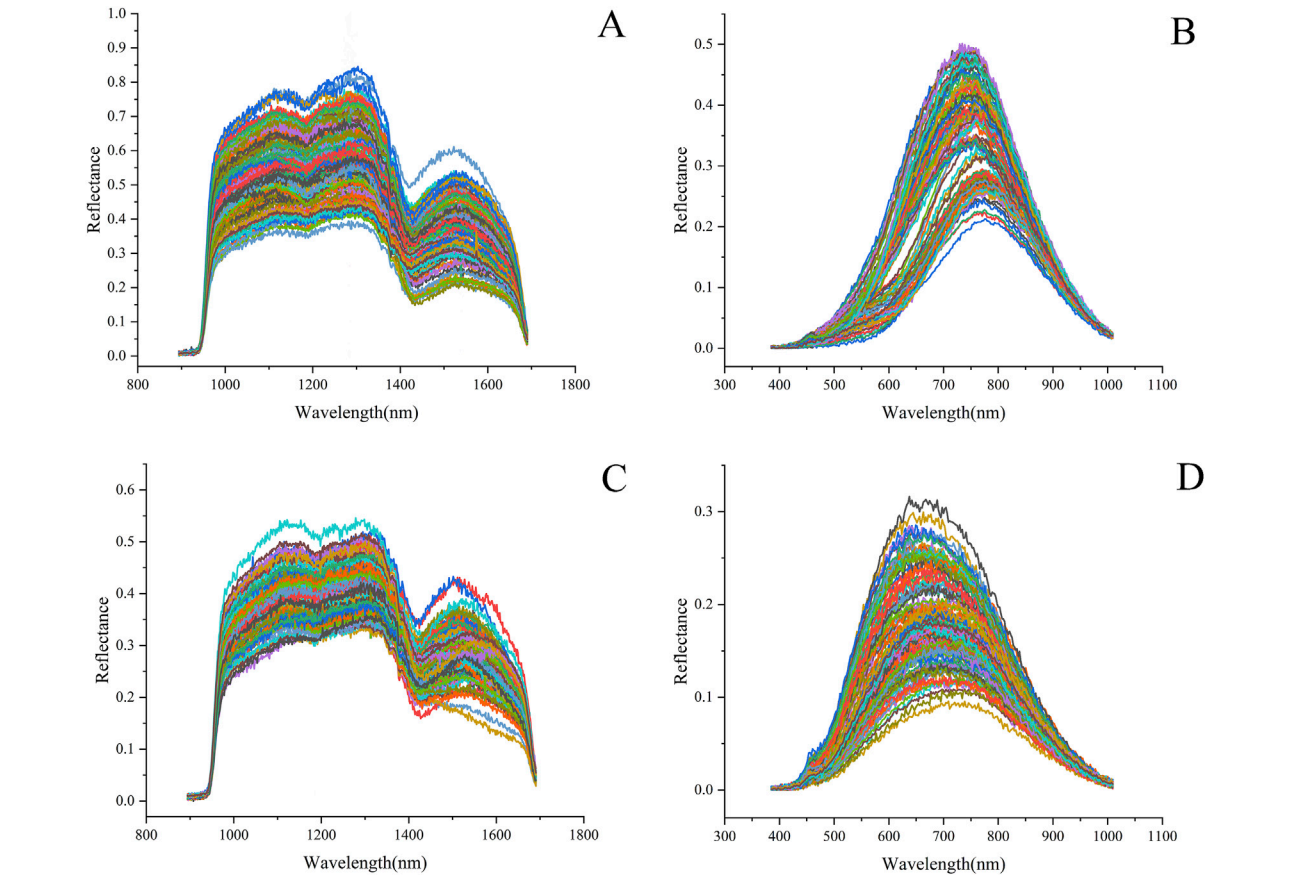

FIGURE 7
Spectral reflectance map of *Ganoderma lucidum* samples: **(A)** GLC spectrum in the range of SWIR and **(B)** VNIR. **(C)** GLP spectrum in the range of SWIR and **(D)** VNIR.

TABLE 2 Predictive analysis based on original spectral modeling.

		SWIR						VNIR					
		GLC			GLP			GLC			GLP		
		R_P^2	MSEP	R_T^2	R_P^2	MSEP	R_T^2	R_P^2	MSEP	R_T^2	R_P^2	MSEP	R_T^2
polysaccharides	DT	0.79	0.16344	0.93	0.43	0.54344	0.86	0.70	0.39496	0.92	0.72	0.13792	0.94
	BP	0.90	0.06663	0.96	0.91	0.04238	0.98	0.92	0.11338	0.95	0.96	0.03277	0.97
	ELM	0.94	0.08107	0.90	0.92	0.08555	0.92	0.92	0.02883	0.93	0.91	0.06044	0.93
ergosterol	DT	0.77	0.00090	0.96	0.28	0.00116	0.92	0.92	0.00024	0.96	0.86	0.00047	0.98
	BP	0.91	0.00045	0.94	0.94	0.00041	0.96	0.92	0.00024	0.95	0.90	0.00030	0.99
	ELM	0.91	0.00059	0.93	0.91	0.00029	0.93	0.96	0.00033	0.96	0.92	0.00041	0.92

at 1300 nm may be attributed to the second overtone of C-H stretching. A local minimum is observed near 1200 and1430 nm; the trough at 1200 nm may correspond to the ergosterol absorption band in *Ganoderma lucidum* (Delwiche et al., 2019), and those at 1430 and 1520 nm may be related to the first overtone of O-H stretching.

3.3 Modeling and analysis

Through the modeling of polysaccharide and ergosterol contents in the GLC and GLP (Table 2), the training accuracy of all models was >0.90, demonstrating strong performance. However, model effects varied significantly across different band ranges. In the SWIR band range, the BPNN and ELM models performed better than those of the other models. The prediction of DT model results showed that the GLC contained significantly higher levels of polysaccharides and ergosterol compared to that of the GLP. The prediction accuracy for the GLP was below 0.43, which was insufficient for effective prediction. In the BP model, the accuracy for predicting polysaccharides in the GLP slightly exceeded that of the GLC, while the model achieved the highest accuracy for predicting ergosterol, with an R^2 value of 0.94.

In the VNIR band range, the BP model showed the optimal prediction effect for polysaccharides in the GLP, achieving an $R^2$of 0.96. In contrast, the ELM model predicted ergosterol in the GLC with an R^2 of 0.96. The performance of the DT model for GLP significantly exceeded that of the SWIR band, particularly in predicting ergosterol.

3.4 Characteristic wavelength selection

3.4.1 Result of characteristic wavelength selection

Two methods for feature-wavelength selection were proposed in this study using the GA. The first method, iterative feature selection, is conducted thrice to obtain different sets of feature wavelengths (Figure 8). The second method is voting feature selection. The second technique, voting feature selection, involves selecting 50 results with a determination coefficient >0.7. The wavelength that appears most frequently is selected as the feature wavelength, matching the count obtained from the iterative feature selection. Polysaccharides select more characteristic wavelengths than ergosterols in the VNIR band. This may be because polysaccharides are polymeric compounds composed of multiple monosaccharide molecules connected by glycosidic bonds that contain numerous functional groups (e.g., OH). Its chemical structure is complex, with various intramolecular and intermolecular interaction types, such as hydrogen bonds and van der Waals forces, which increase the overlap of the spectra. Consequently, identifying the characteristic wavelengths becomes challenging, and the number of these wavelengths is larger.

3.4.2 Characteristic wavelength modeling results

This study employed two GA to extract the characteristic wavelengths and established three models: BPNN, ELM, and DT. The first was used to predict polysaccharides (Table 3). The training accuracy of all models was >0.81, and the MSEP of the verification set was minimal, indicating good performance. When using two types of GA selection across different wavelength ranges, the prediction accuracy for GLC and GLP surpasses that of the characteristic wavelength voting method. In the SWR range, the prediction accuracy of the three models under voting conditions ranked as follows: ELM > BPNN > DT. The ELM model showed the best prediction performance for GLC and GLP, with R^2 values of 0.96 and 0.95, respectively. The DT model of the GLC performed worse than the original model under two types of GA conditions. However, the prediction accuracy of iterative feature selection is significantly higher than that of voting, with R^2 values > 0.61. For GLP, the prediction accuracy of the DT model was better than that of the original model when using the voting GA. Across all three models, the prediction accuracy for GLC was higher than that of GLP. In the VNIR range, the prediction accuracy of the DT model was significantly higher than that of SWIR, increasing from 0.23 to 0.90 by the third iteration of GLC. The prediction accuracies of the two GA methods were significantly higher than those of the original models. The prediction accuracy of the three models was consistent within the SWIR range. The GLC achieved the highest prediction accuracy with an R^2 value of 0.96 in the ELM model under the voting GA condition. Overall, for GLC, the average R^2 values were 0.82 for iterative GA selection and 0.90 for voting GA, while for GLP, the values were 0.82 and 0.88, respectively.

All models for predicting ergosterol levels (Table 4) achieved a training accuracy >0.93, the MSEP of the verification set was

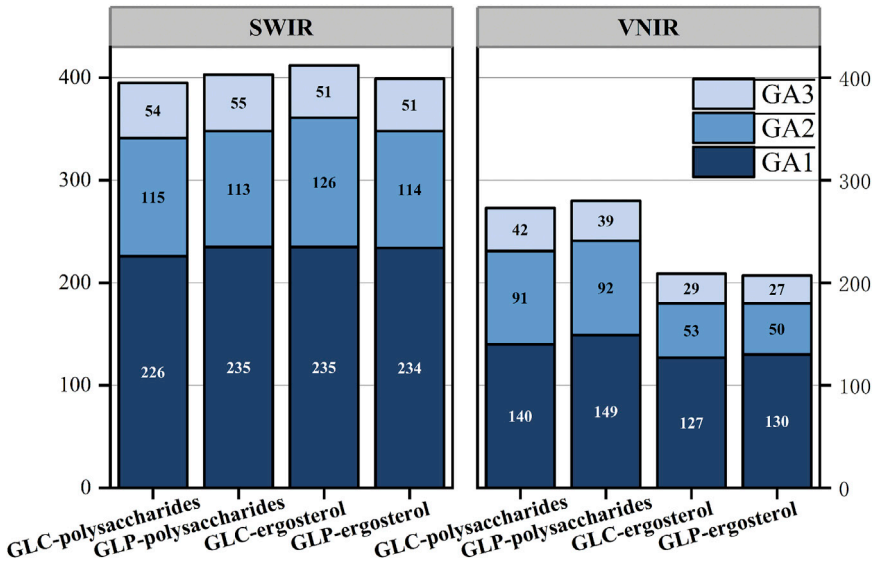

FIGURE 8
Number of characteristic wavelengths.

TABLE 3 Modeling and prediction results of polysaccharides based on different GA characteristic wavelength extraction methods.

			SWIR						VNIR					
			GLC			GLP			GLC			GLP		
			R_P^2	MSEP	R_T^2	R_P^2	MSEP	R_T^2	R_P^2	MSEP	R_T^2	R_P^2	MSEP	R_T^2
Iteration	GA1	DT	0.43	0.37866	0.86	0.22	0.41046	0.85	0.85	0.12045	0.92	0.72	0.21023	0.93
		BP	0.88	0.08973	0.90	0.90	0.09160	0.94	0.92	0.05908	0.93	0.92	0.13836	0.96
		ELM	0.95	0.05354	0.95	0.95	0.04008	0.97	0.96	0.02238	0.98	0.94	0.13313	0.95
	GA2	DT	0.47	0.36487	0.81	0.5	0.29792	0.82	0.84	0.09545	0.89	0.82	0.08886	0.92
		BP	0.91	0.10084	0.91	0.94	0.03787	0.94	0.92	0.07607	0.93	0.91	0.04212	0.95
		ELM	0.92	0.07141	0.96	0.91	0.05589	0.91	0.96	0.04511	0.97	0.93	0.04819	0.94
	GA3	DT	0.23	0.62163	0.81	0.73	0.12729	0.81	0.9	0.00020	0.9	0.73	0.13908	0.94
		BP	0.84	0.19085	0.88	0.94	0.05518	0.96	0.92	0.06307	0.93	0.9	0.12113	0.92
		ELM	0.94	0.05664	0.94	0.88	0.09554	0.94	0.92	0.14226	0.96	0.85	0.34920	0.92
Vote	GA1	DT	0.62	0.41219	0.87	0.61	0.15264	0.81	0.86	0.05895	0.95	0.86	0.44724	0.83
		BP	0.94	0.04855	0.94	0.92	0.06101	0.95	0.96	0.05150	0.96	0.95	0.03769	0.96
		ELM	0.96	0.02695	0.96	0.95	0.04940	0.95	0.96	0.04319	0.98	0.94	0.07691	0.95
	GA2	DT	0.76	0.08397	0.84	0.69	0.10474	0.82	0.91	0.07629	0.92	0.91	0.03906	0.94
		BP	0.94	0.03086	0.94	0.94	0.05594	0.95	0.94	0.01371	0.94	0.93	0.08137	0.95
		ELM	0.96	0.03483	0.96	0.95	0.03872	0.95	0.96	0.03272	0.97	0.94	0.03446	0.97
	GA3	DT	0.76	0.11890	0.88	0.73	0.17983	0.83	0.91	0.07568	0.91	0.76	0.17893	0.93
		BP	0.95	0.08343	0.93	0.94	0.04940	0.96	0.95	0.03238	0.96	0.9	0.12855	0.88
		ELM	0.96	0.04188	0.97	0.95	0.08341	0.92	0.94	0.06976	0.97	0.89	0.22995	0.92

TABLE 4 Modeling and prediction results of ergosterol based on different GA characteristic wavelength extraction methods.

			SWIR						VNIR					
			GLC			GLP			GLC			GLP		
			R_P^2	MSEP	R_T^2	R_P^2	MSEP	R_T^2	R_P^2	MSEP	R_T^2	R_P^2	MSEP	R_T^2
Iteration	GA1	DT	0.73	0.00084	0.97	0.21	0.00302	0.85	0.87	0.00030	0.92	0.87	0.00051	0.98
		BP	0.86	0.00060	0.94	0.92	0.00047	0.96	0.92	0.00044	0.93	0.81	0.00079	0.98
		ELM	0.94	0.00017	0.95	0.92	0.00039	0.93	0.94	0.00021	0.95	0.92	0.00027	0.96
	GA2	DT	0.79	0.00018	0.93	0.54	0.00183	0.91	0.79	0.00079	0.87	0.94	0.00031	0.95
		BP	0.9	0.00036	0.91	0.94	0.00014	0.95	0.92	0.00026	0.93	0.87	0.00044	0.92
		ELM	0.95	0.00020	0.97	0.93	0.00015	0.95	0.93	0.00036	0.95	0.88	0.00149	0.94
	GA3	DT	0.73	0.00058	0.94	0.46	0.00283	0.86	0.77	0.00077	0.83	0.91	0.00037	0.98
		BP	0.94	0.00033	0.95	0.92	0.00043	0.94	0.91	0.00040	0.91	0.92	0.00058	0.93
		ELM	0.95	0.00048	0.97	0.92	0.00283	0.94	0.9	0.00105	0.94	0.89	0.00186	0.94
Vote	GA1	DT	0.75	0.00056	0.92	0.62	0.00119	0.92	0.89	0.00039	0.92	0.88	0.00045	0.94
		BP	0.94	0.00017	0.94	0.95	0.00013	0.97	0.95	0.00019	0.97	0.93	0.00025	0.98
		ELM	0.95	0.00015	0.96	0.93	0.00020	0.94	0.97	0.00033	0.98	0.94	0.00027	0.94
	GA2	DT	0.8	0.00037	0.88	0.74	0.00134	0.89	0.86	0.00041	0.90	0.94	0.00026	0.98
		BP	0.94	0.00024	0.94	0.95	0.00030	0.96	0.95	0.00044	0.95	0.94	0.00026	0.96
		ELM	0.95	0.00019	0.97	0.95	0.00043	0.96	0.97	0.00013	0.98	0.94	0.00060	0.96
	GA3	DT	0.86	0.00029	0.93	0.61	0.00192	0.91	0.88	0.00097	0.89	0.8	0.00060	0.97
		BP	0.94	0.00041	0.95	0.83	0.00067	0.93	0.96	0.00020	0.99	0.89	0.00052	0.91
		ELM	0.95	0.00063	0.97	0.91	0.00086	0.96	0.92	0.00032	0.96	0.86	0.00131	0.93

minimal, demonstrating effective training. In the SWIR range, the DT model performs worse than that of the BPNN and ELM models. The iterative GA prediction accuracy for ergosterol in GLP was <0.54, and the accuracy of GA1 was lower than that of the original model, with an R^2 value of only 0.21. The DT model selected by the three-voting GA outperformed the original model, achieving an R^2 value > 0.61. In contrast, the ELM model in GA3 exhibited a lower performance compared to that of the iterative model. The prediction effect of the three models of GLC under voting GA was ranked as ELM > BPNN > DT, with the ELM achieving the highest accuracy at 0.95. In the iterative GA selection, the BPNN model performed worse than the original model inGA1andGA3, and only the DT model in GA2 outperformed the original model. In the VNIR range, the DT model developed using GLP demonstrated superior performance than that of the SWIR range. The prediction accuracy of the three models assessed in the voting GA3 was slightly lower than that of the iterative GA3. The predictive performance of the three models utilizing GLC *w*as consistent with the SWIR findings, ranking as follows: ELM > BPNN > DT, with ELM achieving the highest prediction accuracy of 0.97. Overall, the average R^2 of the iterative GA model based on the characteristic wavelengths of the GLC was 0.87; however, the voting GA model achieved 0.91. The iterative GA model using the characteristic wavelengths of GLP resulted in an R^2 of 0.82, compared to an R^2 of 0.87 for the voting GA model. In summary, the predictions for ergosterol and polysaccharides are consistent across different models, with the model employing characteristic wavelengths selected by voting GA being the most effective. Among them, the predictive performance of ELM in the GA1 and GA2 in the VNIR band was the highest, with R^2 of 0.97.

3.4.3 Variable dimension reduction

The first five principal components for analysis were retained in this study. Only the DT model in the SWIR band improved the predictions of polysaccharides and ergosterol in the fruiting body powder (Table 5), increasing R^2 from 0.43 to 0.28 to 0.63 and 0.70, respectively. The predictive results from the other models were inferior to those of the original model, the ELM model achieved MSEP of 3.02734 and 2.49455 for polysaccharide prediction of GLP in SWIR and VNIR bands, respectively, probably because PCA is generally more effective for linear data; however, most hyperspectral data exhibit high-order correlations, affecting dimensionality reduction outcomes.

3.5 Visualization of polysaccharide and ergosterol content

We collected a complete hyperspectral image of *Ganoderma lucidum* with a stalk (Figure 9) and visualized the distribution of polysaccharide and ergosterol content. The results showed that the

TABLE 5 Modeling and prediction results based on variable dimensionality reduction methods.

		SWIR						VNIR					
		GLC			GLP			GLC			GLP		
		R_P^2	MSEP	R_T^2	R_P^2	MSEP	R_T^2	R_P^2	MSEP	R_T^2	R_P^2	MSEP	R_T^2
polysaccharides	DT	0.50	0.49257	0.80	0.63	0.12218	0.72	0.54	0.17276	0.72	0.71	0.17911	0.85
	BP	0.32	0.38350	0.57	0.55	0.14353	0.81	0.57	0.25815	0.64	0.34	0.37401	0.43
	ELM	0.60	0.45253	0.83	0.53	3.02734	0.91	0.69	0.43786	0.95	0.38	2.49455	0.95
ergosterol	DT	0.62	0.00132	0.82	0.70	0.00114	0.74	0.68	0.00101	0.73	0.86	0.00039	0.93
	BP	0.48	0.00183	0.56	0.57	0.00096	0.66	0.58	0.00121	0.80	0.76	0.00087	0.76
	ELM	0.61	0.06103	0.89	0.53	0.01555	0.95	0.65	0.00445	0.92	0.74	0.00282	0.96

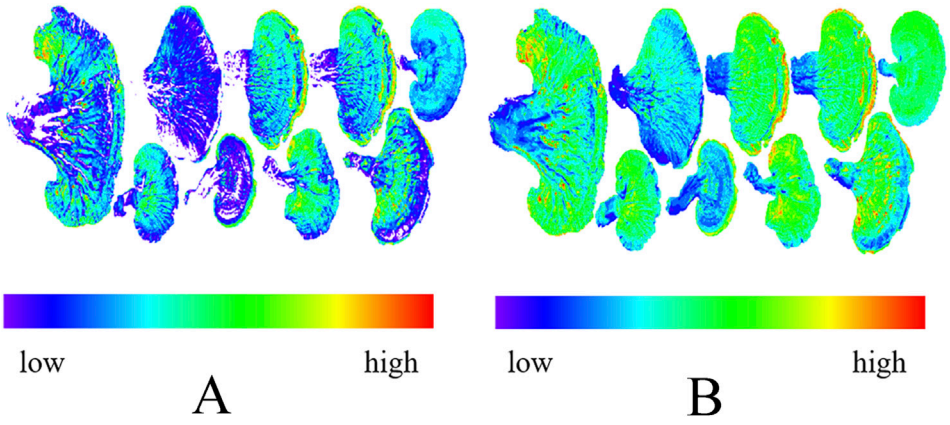

FIGURE 9
PCA diagram of *Ganoderma lucidum*. **(A)** Polysaccharides and **(B)** ergosterol.

polysaccharide content of the *Ganoderma lucidum* stalk was significantly lower than that of the *Ganoderma lucidum* cap. The average levels of polysaccharide and ergosterol decreased following pulverization, which may explain why predictive accuracy for GLP was lower than that of the GLC. Additionally, pulverization improves sample homogeneity, increasing the spectral reflectance and potentially reducing prediction accuracy.

The whole *Ganoderma lucidum* fruiting body maintains its natural morphology and tissue structure, which may play a role in the synthesis, storage, and release of its active components. The structural integrity allows for interactions among various compounds, creating a relatively stable system that protects active components from environmental factors, such as oxidation. In contrast, pulverizing *Ganoderma lucidum* disrupts this natural structure, increasing its surface area and making it more susceptible to external factors, causing the degradation of active components and affecting predictive accuracy.

4 Discussion

HSI was used in this study to predict the chemical composition of the GLP and GLC. The results showed that the average predictive ability of the GLC was better than that of GLP. HSI technology was used to determine calcium and other trace elements in wheat grains and flour (Zhang et al., 2010). The results showed that the prediction accuracy of wheat grains was higher than that of wheat flour. This is consistent with the findings of the present study, in which intact samples yielded better predictions.

In the original BPNN and ELM models, polysaccharides and ergosterols achieved high prediction accuracies, $R^2 > 0.9$. However, in the GLP range of the SWIR band, the DT model showed a lower prediction accuracy, $R^2 < 0.43$, particularly ergosterol, with an R^2 of only 0.28. Furthermore, the predictive performance across models in the SWIR band is inferior to that in the VNIR band,and the MSEPs of the three models are significantly higher in the SWIR band. This may be attributed to the visible light and part of the near-infrared spectrum included in the VNIR band, providing extensive information on the color, texture, and chemical composition of objects. The SWIR band, while valuable, does not provide as abundant spectral information as that in the VNIR band. Common environmental substances, such as soil (Li et al., 2023a), show strong spectral responses in the VNIR band, and chlorophyll exhibits pronounced absorption features in the VNIR band (Sun et al., 2022). Additionally, the VNIR reflectance spectrum is less affected by water (Yang et al., 2023). VNIR band sensor

technology is well-developed, facilitating data acquisition and processing with high spatial and spectral resolution. This technology has been extensively validated and applied in agriculture, forestry, geology, and environmental monitoring. In contrast, data from the SWIR band tends to be more complex, often resulting in large datasets that require more sophisticated algorithms to eliminate noise and manage other processing challenges. Therefore, advanced techniques are typically needed to handle SWIR data effectively. In summary, the VNIR band provides a better predictive performance than the SWIR band owing to its richer spectral content, higher data quality, and simpler processing methods, making it suitable for several applications.

In this study, characteristic wavelengths extracted through different GA methods were used to construct the predictive model. In most cases, models based on the characteristic wavelength performed better than those of the original model. The GA effectively extracts feature wavelengths, reducing noise and minimizing redundant input data, aligning with findings from other studies. Additionally, GA voting offers distinct advantages over GA iteration, probably owing to the inherent randomness in GA iteration processes, such as the initial population generation, crossover, and mutation, which may lead to inconsistent results. Each run can yield significantly different results, and the algorithm may become trapped in local optimal solution. Owing to its sequential nature, where each iteration depends on the previous results, greatly affected by the final results. In contrast, GA voting aggregates multiple independent GA results, favoring solutions that perform well across numerous runs, thus reducing the influence of randomness., This approach enhances the reliability and stability of the results, increasing the likelihood of finding a global optimal solution. The voting approach can efficiently screen for superior solutions and may achieve improved outcomes without requiring extensive iterations.

PCA dimensionality reduction often underperforms relative to the original model, likely because of its limited ability to capture the inherent structure and complexity of nonlinear data (Baytas et al., 2016). Additionally, the high sensitivity of PCA leads to deviations in the principal components, highlighting the need for data preprocessing to mitigate these deviations. Moreover, PCA reduces data dimensions by projection, potentially leading to the loss of some information. Furthermore, PCA assumes independence among input features. However, when features are highly correlated, PCA may fail to capture all data variances, negatively affecting the performance of the reduced-dimensional model.

This study examines how different feature wavelength extraction and regression algorithms perform in analyzing the chemical composition of Ganoderma lucidum in various states. The results indicate that the model combining feature wavelength extraction with machine learning algorithms effectively predicts the chemical components of Ganoderma lucidum. Among them, the ELM model built by GLC after voting feature selection was the most effective for polysaccharides and ergosterol prediction table. This study highlights the effectiveness of hyperspectral imaging in the SWIR and VNIR ranges for quickly evaluating quality parameters in Ganoderma lucidum and has potential applications in other traditional Chinese medicines. These findings offer important insights that could advance innovative approaches in this field and serve as a reference method for quality control in traditional Chinese medicines.

The application of HSI technology in traditional Chinese medicine (TCM) is well-documented and widely studied, but studies focused on *Ganoderma lucidum* remain limited. Despite the achievements made in this study, some limitations persist, such as a small sample size, variability in origin and strain, and the initial stages of model parameter optimization. Especially the small sample size of only 13 samples in the test set presents numerous challenges for model evaluation, generalization performance assessment, and data mining analysis. Therefore, future research should consider expanding the sample size to improve the accuracy and reliability of the results. Studies should also examine *Ganoderma lucidum* from diverse production areas and varieties, incorporate predictions for additional chemical components, and further refine model parameters.

HSI is a powerful analytical technology with broad application prospects and development potential. Simultaneously, the integration of artificial intelligence and big data expands the application of HSI technology, especially in fields of TCM, such as authenticity identification, quality evaluation, and origin traceability. It can also support monitoring of cultivation, harvest, and processing of TCM. HSI contributes to quality control and production process optimization, making outstanding contributions to standardizing TCMs.

Data availability statement

Data will be made available by the authors on request.

Author contributions

JR: Writing–original draft, Visualization. HX: Data curation, Writing–review and editing. ZW: Software, Writing–review and editing. WZ: Funding acquisition, Supervision, Writing–review and editing. XB: Investigation, Resources, Writing–review and editing.

Funding

The author(s) declare that financial support was received for the research, authorship, and/or publication of this article. This work was supported by the Science and Technology Development Plan Project of Jilin Province (20210204146YY), and the National Key Research and Development Program of Ministry of Science and Technology of China (2021YFD1600900, 2021YFD1600903-02).

Conflict of interest

The authors declare that the research was conducted in the absence of any commercial or financial relationships that could be construed as a potential conflict of interest.

Generative AI statement

The author(s) declare that Generative AI was used in the creation of this manuscript. Generative AI techniques were used in this study to aid in text generation. During the course of the study, we used OpenAI's ChatGPT model to translate and polish the initial drafts. The main purpose of using generative AI was to improve writing efficiency and help us explore different ways of expression and argument construction.

Publisher's note

References

Alfaro-Mejía, E., Manian, V., Ortiz, J. D., and Tokars, R. P. (2023). A blind convolutional deep autoencoder for spectral unmixing of hyperspectral images over waterbodies. *Front. Earth Sci.* 11, 1229704. doi:10.3389/feart.2023.1229704

Baytas, I. M., Lin, K., Wang, F., Jain, A. K., and Zhou, J. (2016). Stochastic convex sparse principal component analysis. *EURASIP J. Bioinform Syst. Biol.* 2016, 15. doi:10.1186/s13637-016-0045-x

Butt, M. H. F., Ayaz, H., Ahmad, M., Li, J. P., and Kuleev, R. (2022). A fast and compact hybrid CNN for hyperspectral imaging-based bloodstain classification. *Congr. Evol. Comput.* 2022, 1–8. doi:10.1109/CEC55065.2022.9870277

Chen, L. T., Liu, Z. X., Lan, Y., Ma, X., and Wang, R. J. (2024). Research on rice variety identification based on hyperspectral technology and principal component analysis. *J. Agric. Sci. Technol.* doi:10.13304/j.nykjdb.2023.0640

Chen, Y. Y., and Wang, Z. B. (2019). Cross components calibration transfer of NIR spectroscopy model through PCA and weighted ELM-based TrAdaBoost algorithm. *Chemom. Intelligent Laboratory Syst.* 192, 192103824–103824. doi:10.1016/j.chemolab.2019.103824

Cör, A. D., Knez, Ž., and Knez, M. M. (2022). Antioxidant, antibacterial, antitumor, antifungal, antiviral, anti-inflammatory, and nevro-protective activity of Ganoderma lucidum: an overview. *Front. Pharmacol.* 13, 934982. doi:10.3389/FPHAR.2022.934982

Cui, X., Song, Q. J., Zhang, Y. Y., Xu, G., Meng, B. P., et al. (2017). Estimation of soil organic carbon content in alpine grassland using hyperspectral data. *Acta Prataculturae Sin.* 10, 23–32.

Dai, C., Sun, J., Huang, X., Zhang, X., Tian, X., Wang, W., et al. (2023). Application of hyperspectral imaging as a nondestructive technology for identifying tomato maturity and quantitatively predicting lycopene content. *Foods* 12 (15), 2957. doi:10.3390/FOODS12152957

Dai, J., Lu, J., Lin, R. C., and Liu, W. Y. (2002). Determination of nucleosides in siweilingzhi mixture by HPCE. *China J. Chin. Materia Medica* 09, 28–31.

Delwiche, S. R., Rodriguez, T. I., Rausch, S. R., and Graybosch, R. A. (2019). Estimating percentages of fusarium-damaged kernels in hard wheat by near-infrared hyperspectral imaging. *J. Cereal Sci.* 87, 18–24. doi:10.1016/j.jcs.2019.02.008

Feng, H., Chen, Y., Song, J., Lu, B., Shu, C., Qiao, J., et al. (2024). Maturity classification of rapeseed using hyperspectral image combined with machine learning. *Plant Phenomics* 06, 0139. doi:10.34133/PLANTPHENOMICS.0139

He, Z., and Zhou, S. (2022). BPNN-based behavioral modeling of the S-parameter variation characteristics of PAs with frequency at different temperatures. *Micromachines (Basel)* 13 (11), 1831. doi:10.3390/MI13111831

Hou, S., Shi, H., Cao, X., Zhang, X., and Jiao, L. (2021). Hyperspectral imagery classification based on contrastive learning. *IEEE Trans. Geoscience Remote Sens.* 2021 (60), 1–13. doi:10.1109/TGRS.2021.3139099

Huang, D. L., Chen, X. K., and Xu, Y. Q. (2015). Analysis of different parts of ganoderma tsugae by fourier transform infrared spectroscopy. *J. Anal. Sci.* 31 (01), 59–62. doi:10.13526/j.issn.1006-6144.2015.01.013

Huang, G. B., Zhu, Q. Y., and Siew, C. K. (2006). Extreme learning machine: theory and applications. *Neurocomputing* 70 (01), 489–501. doi:10.1016/j.neucom.2005.12.126

Huang, W. K., Huang, Q. W., Guo, Z. X., and Zhang, W. T. (2017). Determination on ganoderic acid A in ganoderma lucidum with different growth stages and different parts by HPLC. *Edible Fungi China.* 01, 60–62. doi:10.13629/j.cnki.53-1054.2017.01.013

Jia, Z. Z., Du, M. H., and Wang, P. X. (2024). Tool condition monitoring based on extreme learning machine and genetic algorithm. *Nat. Sci.* Available at: http://kns.cnki.net/kcms/detail/53.1223.N.20240424.1556.002.html.

Jiang, W., Zhou, G. S., Chen, X. P., Ye, H., Qiao, Z., Bai, G. G., et al. (2018). Content determination of polysaccharides, triterpenoids and sterols of ganoderma lucidum pieces by ultraviolet-visible spectrophotometry. *China Pharm.* 14, 15–18.

Li, M. Y. (2024a). Research on multi-factor stock selection model based on decision tree. *Prod. Res.* 02, 145–149. doi:10.19374/j.cnki.14-1145/f.2024.02.023

Li, P. X. (2024b). Research on construction cost prediction of construction Project based on extreme iearning machine. *Total Corros. Control* (08), 92–94. doi:10.13726/j.cnki.11-2706/tq.2024.08.084.03

Li, X., Li, Z., Qiu, H., Chen, G., and Fan, P. (2023a). Soil carbon content prediction using multi-source data feature fusion of deep learning based on spectral and hyperspectral images. *Chemosphere* 336, 139161. doi:10.1016/J.CHEMOSPHERE.2023.139161

Li, X., Peng, F., Wei, Z., Han, G., and Liu, J. (2023b). Non-destructive detection of protein content in mulberry leaves by using hyperspectral imaging. *Front. Plant Sci.* 14, 1275004. doi:10.3389/FPLS.2023.1275004

Li, X., Wei, Z., Peng, F., Liu, J., and Han, G. (2023c). Non-destructive prediction and visualization of anthocyanin content in mulberry fruits using hyperspectral imaging. *Front. Plant Sci.* 14, 1137198. doi:10.3389/FPLS.2023.1137198

Liu, H., Ma, D. M., Liu, X. K., and Wang, J. Y. (2016). Forecasting incidence of hand-foot-mouth disease with the ARIMA-BPNN combination model. *Mod. Prev. Med.* 16, 11–14+22.

Liu, J. J., Huang, W. H., Lv, M. L., Si, J. P., Guo, B. L., and Li, S. J. (2011). Determination of ergosterol in ganoderma lucidum from different varieties and cultured tree species by HPLC. *J. Chin. Med. Mater.* 02, 30–33. doi:10.13863/j.issn1001-4454.2011.02.007

Liu, T., Xu, T. Y., Yu, F. H., Yuan, Q. Y., Guo, Z. H., and Xu, Bo (2021a). A method combining ELM and PLSR (ELM-P) for estimating chlorophyll content in rice with feature bands extracted by an improved ant colony optimization algorithm. *Comput. Electron. Agric.* 186, 106177. doi:10.1016/J.COMPAG.2021.106177

Liu, X. L., Liang, G. Y., Yang, Y., Wei, F. X., Zhang, Q. H., and Deng, T. F. (2023). Analysis of inorganic elements and nutrient components in different parts of Ganoderma Lucidum from Guizhou. *J. Xinyang Normal Univ. Nat. Sci. Ed.* 01, 45–51.

Liu, Y., Long, Y., Liu, H., Lan, Y., Long, T., Kuang, R., et al. (2021b). Polysaccharide prediction in Ganoderma lucidum fruiting body by hyperspectral imaging. *Food Chem. X* 13, 100199. doi:10.1016/J.FOCHX.2021.100199

Liu, Y., Wang, L. H., Yang, L. B., and Liu, X. M. (2022). Drought prediction based on an improved VMD-OS-QR-ELM model. *PLoS One* 17 (01), e0262329. doi:10.1371/JOURNAL.PONE.0262329

Lu, C., Dong, Y. N., and Qiu, X. H. (2024). An online study model based on ELM algorithm. *Intelligent Comput. Applications* 06, 116–124. doi:10.20169/j.issn.2095-2163.240615

Pan, Z. C., Zhong, Y., Fang, L., Qi, Z. C., Xu, J., Liang, Z. S., et al. (2024). A rapid, hyperspectral-based method for determining sporoderm-broken rate of ganoderma lucidum spore powder. *Chin. J. Mod. Appl. Pharm.* (06), 38–44. doi:10.13748/j.cnki.issn1007-7693.20231852

Reddy, P., Panozzo, J., Guthridge, K. M., Spangenberg, G. C., and Rochfort, S. J. (2023). Single seed near-infrared hyperspectral imaging for classification of perennial ryegrass seed. *Sensors (Basel)* 23, 1820. doi:10.3390/S23041820

Shi, F. M., Tong, X. R., Ding, Z. M., Sun, C., and Liu, W. S. (2013). Difference analysis of active components content in different medicinal parts of three species of ganoderma lucidum. *China Med. Pharm.* 21, 43–45+50.

Sun, J., Yao, K., Cheng, J., Xu, M., and Zhou, X. (2024). Nondestructive detection of saponin content in Panax notoginseng powder based on hyperspectral imaging. *J. Pharm. Biomed. Anal.* 242, 116015. doi:10.1016/J.JPBA.2024.116015

Sun, W., Liu, S., Zhang, X., and Zhu, H. (2022). Performance of hyperspectral data in predicting and mapping zinc concentration in soil. *Sci. Total Environ.* 824, 153766. doi:10.1016/J.SCITOTENV.2022.153766

Wang, H., Zhu, H., Bi, L., Xu, W., Song, N., Zhou, Z., et al. (2023). Quality grading of river crabs based on machine vision and GA-BPNN. *Sensors (Basel)* 23 (11), 5317. doi:10.3390/S23115317

Wang, M., Liu, Y. P., Pei, L., and Li, B. (2024a). Application of nuclear magnetic resonance hydrogen spectroscopy in quality control of ganoderma polysaccharides. *Edible Fungi China.* 02, 91–98. doi:10.13629/j.cnki.53-1054.2024.02.014

Wang, T. T., Xu, J., and Liu, X. L. (2024b). Research progress on ganoderma cultivation. *J. Fungal Res.* 01, 98–106. doi:10.13341/j.jfr.2023.1678

Wang, Y. F., Zhang, L. J., and Duan, H. P. (2021). Hydraulic performance optimization of radial diffuser multistage pump based on genetic algorithm-back propagation neural network. *Sci. Technol. Eng.* 04, 144–150.

Xia, F. N., Guan, X. Y., Chen, S. D., Chen, Q. Y., Zhang, Y. F., and Yang, X. B. (2023). Fingerprint analysis and content determination of lipid components in ganoderma lucidum spore powder by HPLC-ELSD. *Acta Edulis Fungi* 06, 56–63. doi:10.16488/j.cnki.1005-9873.2023.06.006

Xiao, Q., Bai, X., Gao, P., and He, Y. (2020). Application of convolutional neural network-based feature extraction and data fusion for geographical origin identification of radix astragali by visible/short-wave near-infrared and near infrared hyperspectral imaging. *Sensors (Basel)* 20 (17), 4940. doi:10.3390/s20174940

Xu, J., Xu, D., Bai, X., Yang, R., and Cao, J. (2022). Non-destructive detection of moldy walnuts based on hyperspectral imaging technology. *Molecules* 27 (20), 6776. doi:10.3390/MOLECULES27206776

Yang, J., Xian, L., Zhong, T. S., Wei, L. N., Li, Y. R., and Fu, H. Y. (2017). Rapid identification of different kinds of Ganoderma lucidum based on near infrared spectroscopy fingerprint information. *Lishizhen Med. Mater. Medica. Res.* 28 (06), 1359–1361.

Yang, Y., Nan, R., Mi, T., Song, Y., Shi, F., Liu, X., et al. (2023). Rapid and nondestructive evaluation of wheat chlorophyll under drought stress using hyperspectral imaging. *Int. J. Mol. Sci.* 24 (6), 5825. doi:10.3390/IJMS24065825

Ye, W., Yan, T., Zhang, C., Duan, L., Chen, W., Song, H., et al. (2022). Detection of pesticide residue level in grape using hyperspectral imaging with machine learning. *Foods* 11, 1609. doi:10.3390/FOODS11111609

Yu, Y., and Sun, D. L. (2024). Research on corrosion rate prediction of buried pipeline based on PCA-BPNN model. *J. Lanzhou Univ. Technol.* 04, 66–74.

Yuan, S. Q., Shen, Y. L., Zhang, J. F., and Yuan, J. P. (2009). *Performance predicting of centrifugal pumps with compound impeller based on improved BP neural network*. Transactions of the Chinese Society for Agricultural Machinery 09, 31+83–86.

Zeng, F. Q., Lu, M. L., Xue, Z. W., and Peng, N. (2023). Analysis of 18 main triterpenoids in basidiomata of Ganoderma lingzhi by HPLC. *Mycosystema* 11, 142–152. doi:10.13346/j.mycosystema.230095

Zhang, M., Huang, Y. K., Yuan, Q. D., Zhao, H. X., Huang, L. Y., and Guo, D. L. (2024). Study on modeling and prediction of carbon paper base paper properties based on GA-BPNN algorithm. *China Pulp and Pap.* 43 (01), 121–127.

Zhang, M. H., Zhang, Y., Zhang, Z. Q., Da, H., Li, L., and Jia, Y. C. (2024). Permafrost distribution innortheast China based on boosting regression tree. *J. Harbin Inst. Technol.* Available at: http://kns.cnki.net/kcms/detail/23.1235.T.20240624.1556.014.html.

Zhang, Q. Q. (2020). *Analytical study of triterpenoids from Ganoderma lingzhi fruiting bodies through infrared spectrocopy*. University of Science and Technology of China. doi:10.27517/d.cnki.gzkju.2020.001539

Zhang, Q. Q., and Huang, Q. (2021). Quantitative analysis of Ganoderma polysaccharides content in fruiting bodies by near-infrared spectroscopy. *Mycosystema* 01, 257–265. doi:10.13346/j.mycosystema.200218

Zhang, S., Yin, Y., Liu, C., Li, J., Sun, X., and Wu, J. (2023). Discrimination of wheat flour grade based on PSO-SVM of hyperspectral technique. *Spectrochim. Acta A Mol. Biomol. Spectrosc.* 302, 123050. doi:10.1016/J.SAA.2023.123050

Zhang, Y., Shi, R., Rezaul, K. M., Zhang, F., and Zou, C. (2010). Iron and zinc concentrations in grain and flour of winter wheat as affected by foliar application. *J. Agric. Food Chem.* 58 (23), 12268–12274. doi:10.1021/jf103039k

frontiers | Frontiers in Chemistry

TYPE Original Research
PUBLISHED 19 March 2025
DOI 10.3389/fchem.2025.1536858

OPEN ACCESS

EDITED BY
Federica Aureli,
National Institute of Health (ISS), Italy

REVIEWED BY
Eric Deconinck,
Sciensano (Belgium), Belgium
Maria Cristina Gaudiano,
National Institute of Health (ISS), Italy

*CORRESPONDENCE
Agata Blazewicz,
a.blazewicz@nil.gov.pl

RECEIVED 29 November 2024
ACCEPTED 27 January 2025
PUBLISHED 19 March 2025

CITATION
Blazewicz A, Poplawska M, Daniszewska B, Piorunska K and Karynski M (2025) Illegal and falsified medicines self-administrated in not approved post-cycle therapy after the cessation of anabolic-androgenic steroids – qualitative analysis. *Front. Chem.* 13:1536858. doi: 10.3389/fchem.2025.1536858

Illegal and falsified medicines self-administrated in not approved post-cycle therapy after the cessation of anabolic-androgenic steroids – qualitative analysis

Agata Blazewicz*, Magdalena Poplawska, Beata Daniszewska, Karolina Piorunska and Michal Karynski

Falsified Medicines and Medical Devices Department, National Medicines Institute, Warsaw, Poland

Background: The term post-cycle therapy (PCT) often appears in bodybuilding forums in the context of anabolic-androgenic steroids (AAS) cessation. To reduce the negative impact of AAS on the hormonal system, unapproved PCT is used, which consist of medications that help restore hormonal balance. The most used medicinal products are selective estrogen receptor modulators (SERMs), aromatase inhibitors (AIs), and preparations containing human chorionic gonadotropin (hCG). These substances are prohibited in sports by the World Anti-Doping Agency.

Methods: Between January 2020 and the end of August 2024, 601 samples seized by the police and prosecutor's office from the illegal market, intended for use as performance-enhancing drugs (PEDs), were tested at the Polish Official Medicines Control Laboratory. Samples were analyzed using accredited methods, including liquid chromatography coupled with high-resolution hybrid mass spectrometry and X-ray powder diffraction, to estimate PCT drug prevalence among other PED samples. In total, 411 (68.4%) samples declaring to contain AAS, 63 (10.5%) declaring to contain substances used in PCT, and 127 (21.1%) other PEDs were tested.

Results: Among the PCT drug samples, 33.3%, 25.4%, and 41.3% indicated the presence of SERMs (tamoxifen and clomiphene), AIs (anastrozole, letrozole, and exemestane), and other substances (hCG, cabergoline, and mesterolone), respectively according to the label. However, not all samples were consistent with the declarations. In 65.1% of the samples, the declared active pharmaceutical

Abbreviations: AAF, adverse analytical finding; AAS, anabolic-androgenic steroid; AI, aromatase inhibitor; API, active pharmaceutical ingredient; EDTA-Na, ethylenediaminetetraacetic acid sodium salt; ER, estrogen receptor; DTT, dithiothreitol; hCG, human chorionic gonadotropin; LC-MS, liquid chromatography-mass spectrometry; LC-QTOF-MS/MS, high-resolution hybrid quadrupole-TOF mass spectrometry coupled with high performance liquid chromatography; MS, mass spectrometry; OMCL, Official Medicines Control Laboratory; PCT, post-cycle therapy; PDE-5i, phosphodiesterase-5 inhibitor; PED, performance-enhancing drug; PTFE, polytetrafluoroethylene; Q, quadrupole; SARM, selective androgen receptor modulator; SERM, selective estrogen receptor modulator; SERD, selective estrogen receptor degrader; TOF, time-of-flight; WADA, World Anti-Doping Agency; XRPD, X-ray powder diffraction.

ingredients (APIs) were present, whereas in 34.9%, they were not. Furthermore, among the samples in which the declared API was found, 58.7% contained only the declared API, while 6.4% included an additional undeclared API. Conversely, among the samples without the declared API, 20.6% contained neither a declared API nor any API, while 14.3% had other undeclared APIs.

Conclusion: We have shown that illicit drugs used in PCT may be substituted, adulterated, or contain no active ingredients. Our results indicate that in view of the high prevalence of illicit AAS use, the self-administration of unapproved PCT using illegal and falsified medicines is dangerous and can be considered a potential threat to consumer health.

KEYWORDS

anabolic androgenic steroids, AAS, post-cycle therapy, PCT, falsified medicines, cessation of AAS, SERMs, AIs

1 Introduction

Anabolic-androgenic steroids (AAS) stimulate protein synthesis, leading to increased skeletal muscle mass and strength (anabolic effect). They are also responsible for the development of male secondary sexual characteristics (androgenic effect) (Hoffman and Ratamess, 2006). AAS have selected therapeutic uses, including male hypogonadism, anemia, and osteoporosis treatment. However, their anabolic effects have led to widespread non-medical use, especially among young adults engaged in athletic activities as performance-enhancing drugs (PEDs) (de Ronde and Smit, 2020; McCabea et al., 2007). Furthermore, AAS are banned according to the List of Prohibited Substances and Methods of the World Anti-Doping Agency (WADA) (World Anti-Doping Agency, 2024c).

Uncontrolled use of substances from the AAS group for non-medical purposes is associated with a high risk of adverse effects on the liver and the reproductive, musculoskeletal, cardiovascular, and central nervous systems. Exogenous AAS inhibit endogenous testosterone production, and discontinuation of their use is often associated with a prolonged decrease in testosterone secretion (Kanayama et al., 2015; Rasmussen et al., 2016; Shankara-Narayana et al., 2020). AAS-induced hypogonadism is a serious problem, and complete recovery is difficult in most cases (Vilar Neto et al., 2021). It can take months or years for the testosterone levels to return to normal after AAS cessation (Kanayama et al., 2015; Shankara-Narayana et al., 2020). Men who stop taking AAS may experience decreased libido, erectile dysfunction, fatigue, and depression symptoms (Kanayama et al., 2015; Rasmussen et al., 2016). Since no evidence-based recommendations for safe AAS withdrawal management currently exist, some users self-administer non-approved post-cycle therapy (PCT) to stimulate endogenous testicular function (Griffiths et al., 2017; Grant et al., 2023a).

The substances used in PCT are administered in the treatment of male hypogonadism unrelated to androgen abuse (Grant et al., 2024). However, PCT is recommended in bodybuilding forums for men who have discontinued testosterone or other androgenic hormones. Moreover, the PCT protocol differs depending on the individual group. Recreational AAS users (men without hormone therapy indications) predominantly start with optimal testosterone levels, aiming to quickly improve their physique. However, they experience a decrease in endogenous testosterone production owing to AAS use, which manifests, among others, as erectile dysfunction and spermatogenesis suppression, resulting in testicular atrophy, and infertility. PCT is believed to prevent testicular atrophy and inhibits feminization processes, such as gynecomastia. PCT can become even more important when high AAS doses are used or when multiple AAS are administered simultaneously.

To restore endogenous testosterone, mainly aromatase inhibitors (AIs), selective estrogen receptor modulators (SERMs), and human chorionic gonadotropin (hCG) are used (Karavolos et al., 2015; Bonnecaze et al., 2021). AIs and SERMs are relatively new doping agents, similar to selective androgen receptor modulators (SARMs) (Hackney, 2018).

In the 2024 WADA Prohibited List (World Anti-Doping Agency, 2024c) Section 4: "hormone and metabolic modulators," AIs (Subsection S4.1) and anti-estrogenic substances, including anti-estrogens and SERMs (Subsection S4.2), are prohibited at all times (in- and out-of-competition). In Subsection S2.2.1, chorionic gonadotropin is listed as a testosterone-stimulating peptide in males.

Aromatase is an enzyme that converts testosterone to estradiol (the most potent estrogen form) and androstenedione to estrone (Kang et al., 2017). As aromatase mediates estrogen production, its inhibition with chemical molecules is considered an effective treatment for estrogen receptor (ER)-positive breast cancer. Moreover, AIs are used off-label to reduce circulating estradiol levels, thereby inhibiting the negative feedback of AAS use, limiting excessive testosterone release. Therefore, AIs play a role in minimizing the side effects associated with elevated estradiol levels in men, including gynecomastia (Basaria, 2010). AIs can be divided into two groups based on their chemical structure: steroidal (analogs of androstenedione, exemestane, formestane, and testolactone), which provide irreversible aromatase inhibition, and non-steroidal (anastrozole and letrozole), which provide reversible inhibition (Ahmad, 2015). The main AIs currently used include the new-generation letrozole, anastrozole, and exemestane, which can be administered orally.

The anti-estrogenic compounds mentioned in the WADA list can be divided into two groups: SERMs (bazedoxifene, clomiphene, cyclofenil, ospemifene, raloxifene, tamoxifen, and toremifene) and selective estrogen receptor degraders (SERDs), of which fulvestrant is a representative. Fulvestrant is the first SERD approved for clinical use to treat advanced and metastatic breast cancer. SERMs are non-steroidal estradiol analogs with mixed agonist-antagonist effects on

ERs and are used in osteoporosis and breast cancer treatment (Jordan, 2004). Tamoxifen was the first SERM used to treat ER-positive breast cancer (Hackney, 2018). Clomiphene and cyclofenil are also older SERMs (although perhaps less selective than tamoxifen) (Heuberger and Cohen, 2019). In approved medicines, clomiphene is a mixture of two isomers: cis (Z-isomer or zuclomiphene) and trans (E-isomer or enclomiphene). Enclomiphene is anti-estrogenic, whereas zuclomiphene manifests moderate estrogenic and anti-estrogenic effects (Girase et al., 2023). Raloxifene is a new SERM developed for osteoporosis that appears to prevent breast cancer (Lewis and Jordan, 2005). Similar to AIs, SERMs are used off-label to alleviate the side effects of excess estradiol. The main antiestrogenic substances can be administered orally.

In addition, other medicines are recommended on bodybuilding forums during PCT. hCG is used by bodybuilders and athletes at the end of an AAS cycle to prevent muscle tissue breakdown. hCG directly stimulates Leydig cells to produce and release intratesticular testosterone by binding to the luteinizing hormone/choriogonadotropin receptor (Rizzuti et al., 2023). Moreover, hCG maintains spermatogenesis during gonadotropin suppression (Bond et al., 2022). However, according to bodybuilder forums, hCG is also important in restoring testicles to their normal size, as often, after a period of AAS use, an athlete's testicles can shrink. Chorionic gonadotropin is a heterodimeric glycoprotein composed of two non-covalently bound subunits. The α subunit of hCG is structurally identical to the α subunits of gonadotropins secreted by the pituitary gland. The β subunit differs in its amino acid sequence from other gonadotropins and is hCG-specific. However, posttranslational modifications with eight potential glycosylation sites in the hCG structure result in a wide range of hCG glycoforms.

When administering 19-nortestosterone derivatives with significant progestogenic activity (nandrolone and trenbolone), cabergoline is recommended. Cabergoline is an ergot alkaloid derivative used to treat hyperprolactinemia, prolactinoma, and Parkinson's disease. It effectively inhibits prolactin secretion and is therefore used by men during PCT to prevent gynecomastia. Bromocriptine, an ergot alkaloid derivative used to treat hyperprolactinemia, has a structure and activity similar to cabergoline. Mesterolone is used not only to increase androgen levels in athletes as an AAS but also for its supposed intrinsic aromatase enzyme antagonist properties as an anti-estrogen (Llewellyn, 2017). To the best of our knowledge, there is only one available source (outside of sports blogs and forums) that provides information on aromatase inhibition by mesterolone (Llewellyn, 2017).

Medicines used in PTC may cause serious side effects, including blood clots, stroke, and endometrial cancer in women taking SERMs (Hackney, 2018). The main adverse events reported by male AAS users to SERMs (clomiphene and tamoxifen) were decreased libido and erectile dysfunction (24%), acne (21%), fatigue (19%), mood disorders (13%), visual disturbances (5%), arthralgia (4%), insomnia (4%), and hot flushes (2%). Two men reported serious adverse drug reactions (hepatic cytolysis requiring hospitalization and abdominal pain requiring a visit to the emergency department) (Rochoy et al., 2022). In another study based on website data, AAS users reported tamoxifen side effects such as blurred vision, dizziness, headaches, and reduced libido (Karavolos et al., 2015). The main adverse events reported on AIs (anastrozole, letrozole, and exemestane) were decreased libido (27%), arthralgia (24%), mood disorders (12.5%), asthenia (10%), headaches (6%), anxiety (4.5%), and palpitations (3%). Three men reported serious adverse drug reactions requiring an emergency department visit (gross hematuria, palpitations, and urticaria) (Rochoy et al., 2022). According to other study AAS users reported arthralgia as an AI side effect (Karavolos et al., 2015). Furthermore, hCG can cause or aggravate gynecomastia (Rahnema et al., 2014). Adverse effects of chronic dopamine agonist (cabergoline) use include headaches, orthostatic hypotension, nausea, and sometimes cardiac valvular disease (Bonnecaze et al., 2021).

Owing to restrictions on the purchase of AAS and PCT products, an international black market for such preparations has developed. Unfortunately, because AAS cycles and PCTs are carried out outside the supervision of the doctor, most often using illegally traded products, they can be considered a potential threat to consumer health. The availability of illegally sold medicines has become a challenge in recent decades. For many years, falsified medicines have been traded worldwide; however, this has become increasingly easier owing to the increased availability of medicines and open channels of trade, including online sales. In addition to drug trafficking, pharmaceutical crime is of interest to organized criminal groups, and many factors contribute to the falsification of medicines. It is generally stated that over 50% of medical products sold through websites other than established online pharmacies can be classified as falsified medical products (Deconinck et al., 2021). The World Health Organization distinguishes between three categories of poor-quality medical products: substandard, unregistered/unlicensed, and falsified (World Health Organization, 2018).

The necessity of identifying unknown and undeclared substances in illegal and falsified products requires the constant development of techniques used for analytical research in forensic or control laboratories to perform analyses for public authority needs. Mass spectrometry (MS) has long been used for the identification and determination of the molecular structure of organic compounds (Khalikova et al., 2024). Different analyzers used in high resolution MS, including time of flight (TOF), and Orbitrap enable the determination of the elemental composition (assignment of the most probable sum formula) of a compound by measuring the exact mass and comparing the isotopic profile of the obtained spectrum with the theoretical profile. In many cases, the analysis of fragmentation spectra allows for the determination of the structural formula of the compound or elements of its structure. In the identification of unknown compounds, the use of high-resolution hybrid quadrupole (Q)-TOF, additionally coupled with high performance liquid chromatography (LC-QTOF-MS/MS) is irreplaceable (Johansson et al., 2014; Rebiere et al., 2017). However, to confirm the structure of the unknown compounds, especially those for which reference materials are not available, nuclear magnetic resonance (NMR) spectrometry is recommended (Johansson et al., 2014; Rebiere et al., 2017; dos Santos Ribeiro et al., 2021). X-ray powder diffraction (XRPD) enables the identification of crystalline substances, including both active pharmaceutical ingredients and excipients, that can be lost during dissolution and filtration when preparing samples for

other analytical techniques. It also allows the determination of the form in which a compound is present, whether as a salt or a co-crystal. The Polish Official Medicines Control Laboratory (OMCL), upon request by police, customs, or other enforcement groups, regularly tests AAS and other PEDs submitted to the laboratory using accredited methods such as LC-QTOF-MS/MS and XRPD.

Although a growing body of literature on PCT and user characteristics associated with PCT use exists (Griffiths et al., 2017; Bonnecaze et al., 2021; Grant et al., 2023a), data on the quality of medications used within PCT are limited, in contrast to AAS quality (Graham et al., 2009; Frude et al., 2020; Magnolini et al., 2022). This study aimed to estimate the prevalence of medicines used for non-approved PCT among other PED samples and to identify declared and undeclared substances in illicit samples to check whether they were in accordance with the declaration. In this report, we describe the results of these studies to raise awareness that illegal and falsified products that pose a risk to consumer health exist in the European market.

2 Materials and methods

2.1 Scope

Samples declared as containing substances intended to enhance sports performance, such as AAS, other PEDs, or substances used after the AAS cycle to mitigate side effects, were included. Active ingredient identification was conducted for all samples, however only the results for the PCT samples are presented in this study. Substances of abuse banned by the WADA List (World Anti-Doping Agency, 2024c), such as stimulants from Section S6, narcotics from S7, and cannabinoids from S8, were excluded. In addition, phosphodiesterase-5 inhibitors (PDE-5i), popular among AAS users, were excluded, although they were thought to increase libido after AAS cessation.

2.2 Samples and timeframe

All samples were obtained between January 2020 and the end of August 2024 from the illegal supply chain seized by the police, prosecutor offices, customs, or other enforcement groups. Products were collected from illicit distribution sites for medicinal products, online stores, individual mail shipments, and prisons.

2.3 Chemicals

Methanol and acetonitrile, both of purity suitable for LC–MS, were purchased from Merck Millipore (LiChrosolv; Darmstadt, Germany) or Honeywell (Seelze, Germany), formic acid and ammonium bicarbonate for LC-MS from Honeywell, dithiothreitol (DTT) from Pierce Biotechnology (Rockford, IL, United States), iodoacetamide from Sigma-Aldrich (St. Louis, MO, United States), and trypsin from Roche Diagnostics (Mannheim, Germany). Ultrapure water (18.2 MΩ cm resistivity, Arium Comfort H2O-I-1-UV-T from Sartorius, Goettingen, Germany) or LC-MS grade water (LiChrosolv, Merck KGaA) was used throughout.

Reference standards: anastrozole, cabergoline, clomiphene citrate, letrozole, mesterolone, and raloxifene hydrochloride (EDQM, Strasbourg, France); tamoxifen citrate (Sigma Aldrich, Saint Louis, MO, United States); exemestane (USP, Rockville, MD, United States); EDTA (Chempur, Piekary Śląskie, Poland); WHO International Standard for hCG; and medicinal product Pregnyl (N.V. Organon, Netherlands).

2.4 Sample preparation

For LC–QTOF-MS/MS analysis, 1 mg of powder or homogenized tablet was dissolved or extracted using 5 mL of a 1:1:1 (v/v/v) mixture of water/methanol/acetonitrile, assisted by ultrasonication for 10 min, and afterwards filtered by a Whatman 0.2 µm pore size polytetrafluoroethylene (PTFE) filter medium (GE Healthcare, Chicago, IL, United States). The filtrate was diluted to suitable concentrations when necessary. Samples suspected to contain hCG were dissolved in water and cleaned by centrifugation.

For XRPD analysis, the powder samples or homogenized tablets were placed in circular plastic holders (1.5 mm deep, 25 mm in diameter) and leveled with a microscope slide. These holders were designed to minimize background interference.

2.5 Apparatus and parameters

2.5.1 LC-QTOF-MS/MS

The parameters of LC-QTOF-MS/MS methods depended on the equipment on which the analyses were carried out. Two screening methods and hCG detection methods (intact and tryptically digested) were applied. Chromatographic and mass spectrometric parameters are summarized in the Table 1. In each method solvents A and B comprising of water-acetonitrile-formic acid (90:10:0.1, v/v/v) and methanol-acetonitrile-formic acid (90:10:0.1, v/v/v), respectively were used.

2.5.1.1 Small molecules analysis

Compounds in the samples analyzed between 2020 and 2023 were identified using a high-performance liquid chromatograph (Ultimate 3,000 system from Dionex, Thermo Fisher Scientific, Waltham, MA, United States) coupled with a high-resolution micrOTOF-QII hybrid mass spectrometer (Bruker Daltonik, Bremen, Germany). The screening method described in our previous study (Poplawska et al., 2020) was applied with the LC and MS parameters described in the Table 1. TOF analyzer was calibrated prior to each sample using a solution of sodium formate.

Compounds in the samples analyzed in 2024 were identified using a liquid chromatograph with quadrupole TOF mass spectrometer (LCMS9050-Q-TOF, Shimadzu Corporation, Kyoto, Japan). Chromatographic and mass spectrometric parameters of this screening method are summarized in the Table 1. A calibration segment with a sodium formate solution was included in each sample run to ensure high mass accuracy.

TABLE 1 Summarized chromatographic and mass spectrometric parameters of analytical methods applied in the study.

Methods	Screening method used in 2020–2023	Screening method used in 2024	hCG detection (tryptically digested)	hCG detection (intact)
LC parameters				
Column	Hypersil GOLD C18 analytical column 100 × 2.1 mm, 3 µm particle size with a guard column (both from Thermo Fisher Scientific)	Shim-pack Velox C18 150 × 2.1 mm, 1.8 µm particle size (Shimadzu)	Shim-pack Velox C18 150 × 2.1 mm, 1.8 µm particle size (Shimadzu)	Supelco BIOshell A400 Protein C4 column 100 × 2.1 mm, 3.4 µm particle size (Merck KGaA)
Gradient program	0–2 min—10%B 2–7 min—10–90%B 7–10 min—90%B 10–12 min—90–10%B 12–14 min—10%B	0–2 min—0%B 2–9 min—0–90%B 9–11 min—90%B 11–12 min—90–0%B 12–15 min—0%B	0–2 min—0%B 2–60 min—0–60%B 60–65 min—100%B 65–68 min—0%B	0–2 min—0%B 2–50 min—0–32%B 50–54 min—32%B 54–55 min—32–0%B 55–60 min—0%B
Oven temperature	40°C	40°C	40°C	70°C
Flow rate	0.15 mL min^{-1}	0.35 mL min^{-1}	0.20 mL min^{-1}	0.30 mL min^{-1}
PDA	200–320 nm	190–400 nm	190–400 nm	200–320 nm
MS parameters				
ESI source	drying gas flow rate: 8.0 L min^{-1} dry heater: 180°C capillary voltage: 4500 V (pos)/3200 V (neg) end plate offset: −500 V	drying gas flow rate: 10.0 L min^{-1} nebulizing gas flow rate: 3.0 L min^{-1} heating gas flow rate: 10.0 L min^{-1} interface temperature: 300°C DL temperature: 250°C heat block: 400°C interface voltage: 4,000 V (pos)/ 3,500 V (neg)	drying gas flow rate: 10.0 L min^{-1} nebulizing gas flow rate: 3.0 L min^{-1} heating gas flow rate: 10.0 L min^{-1} interface temperature: 300°C DL temperature: 250°C heat block: 400°C interface voltage: 4,000 V (pos)	drying gas flow rate: 9.0 L min^{-1} nebulizer: 1.6 Ba dry heater: 200°C capillary voltage: 4500 V (pos) end plate offset: −500 V
MS mode	full scan mode (m/z 50–1,500) Auto-MS/MS with five Precursor Ions (intensity order)	full scan mode (m/z 50–1,500) DDA with six MS/MS events (intensity order)	full scan mode (m/z 200–1,500) DDA with six MS/MS events (intensity order) detected in a range of m/z 100–2,200	full scan mode (m/z 900–3,000) without MS/MS events
CE	Linear gradient: m/z 200–20eV m/z 400–25 eV m/z 800–35 eV	35V ± 20V	20V ± 5V	-

pos – positive ionization mode; neg – negative ionization mode; MeOH, methanol; ACN, acetonitrile; CE, collision energy; DDA, Data Dependent Analysis algorithm; DL, desolvation line.

Both targeted and non-targeted data analysis was applied. In the first step, a targeted screening was conducted using an in-house database to find known compounds potentially present in the sample. This was followed by a thorough data analysis for unidentified components of the sample. Retention times, full scans, and MS/MS spectra were compared with those obtained from the analysis of reference standards or suitable databases such as PubChem or MassBank, which are public repositories of mass spectra.

2.5.1.2 Large molecules analysis

Regarding samples suspected of containing large peptides or proteins, the HPLC column was changed to a Supelco BIOshell A400 Protein C4 column (10 cm × 2.1 mm; 3.4 µm particle size; Merck KGaA, Darmstadt, Germany), MS settings of the screening method used in 2020–2023 were switched to high-mass detection (m/z 700–3,000) and the ESI-L LCMS Tuning Solution (Agilent Technologies) was used for calibration, whereas, in the screening method used in 2024 the data acquisition range was changed to m/z 100–3,000, and a sodium iodide solution was used for MS calibration.

2.5.1.3 Intact hCG analysis

Samples purported to contain hCG were subjected to direct LC-QTOF-MS/MS analysis without prior pretreatment. Analyses were performed using an Ultimate 3000 HPLC system (Dionex) coupled with a micrOTOF-QII system. The settings described in the Table 1 were adjusted according to the conditions described by other researchers (Camperi et al., 2018).

2.5.1.4 hCG tryptic digestion

One mg of the sample was dissolved in 200 µL of 50 mM ammonium carbonate. Then, 5 µL of 200 mM DTT was added and incubated for 40 min at 60°C; subsequently, 5 µL of 1 M iodoacetamide was added and incubated for 1 h, at room temperature and protected from light. At the end of this step, 20 µL of 200 mM DTT was added before digestion with 50 µL trypsin overnight, at 37°C. The enzymatic reaction was stopped by

adding 5 µL of formic acid, and the sample was filtered by 0.2 µm PTFE filters. LCMS9050-Q-TOF analyses were conducted using similar parameters as in screening method described above, except for the gradient program. Details are provided in the Table 1. Raw data were directly loaded into Peaks Studio 11 software (Bioinformatics Solutions Inc., Canada), which enables peptide and protein identification, *de novo* peptide sequencing, and database searches. Carbamidomethylation was set as a fixed modification, whereas methionine oxidation, asparagine and glutamine deamination, and glycosylation options were set as variable modifications, according to published data (Lebede et al., 2021). Trypsin was defined as the cleavage enzyme; a maximum of two missed cleavages and three variable posttranslational modifications per peptide were allowed. The precursor and fragment mass error tolerances were set to 10 ppm and 0.1 Da, respectively.

The intact hCG analysis revealed several hCGα glycoforms; however, hCGβ was not detected owing to a poor ionization in the ESI source and high heterogeneity of hCGβ isoforms, consistent with previously published studies (Camperi et al., 2018). Nevertheless, various studies reported that an extensive pre-purification (Toll et al., 2006) or specific solid-phase extraction (Goumenou et al., 2025) yielded a mass spectrum of the intact subunit β. To resolve the hCGβ detection problem, a tryptic digestion of the sample, monitoring of the peptide or peptides unique for hCGβ, and using them as hCG markers were applied in several studies (Gam et al., 2003; Lund et al., 2012). Here, we performed tryptic digestion of potential hCG-containing samples and applied the PEAK Studio software with a database search to identify the protein. Even without introducing a post-translation glycosylation option, the hCGβ subunit could be detected in the Pregnyl sample (reference sample) with a 67% sequence coverage. When potential glycosylation was allowed in the settings, the sequence was covered in 98%.

2.5.2 XRPD

All XRPD experiments were performed using a Bruker AXS D8 Advanced diffractometer equipped with a copper X-ray tube and a Våntec position-sensitive detector. The instrument operated at 40 kV and 40 mA, generating monochromatic CuKα radiation. Data collection was conducted in θ-θ mode following the Bragg–Brentano method, within the 2 θ range of 4.8°–60°, using a step size of 0.011° and a time per step of 424 s. The collected diffraction patterns were subjected to background correction and standard smoothing, and the resulting data were analyzed using DIFFRAC.EVA V4.1 software, comparing them to both the PDF-2 commercial database and an in-house reference library.

2.6 API identification

Qualitative composition tests were conducted using LC-QTOF-MS/MS and XRPD methods to identify components, especially those that were not declared. Retention times, full scans, and MS/MS spectra (for LC-QTOF-MS/MS) or diffractograms (for XRPD) were compared with those obtained from the analysis of reference standards or suitable databases such as PubChem, MassBank, or PDF-2, which are public repositories of mass spectra or commercial databases of diffraction patterns, respectively.

Samples were tested for the presence of AIs (2-androstenol (5α-androst-2-en-17-ol), 2-androstenone (5α-androst-2-en-17-one), 3-androstenol (5α-androst-3-en-17-ol), 3-androstenone (5α-androst-3-en-17-one), 4-androstene-3,6,17 trione (6-oxo), aminoglutethimide, anastrozole, androsta-1,4,6-triene-3,17-dione (androstatrienedione), androsta-3,5-diene-7,17-dione (arimistane), exemestane, formestane, letrozole, and testolactone), and anti-estrogenic substance (bazedoxifene, clomiphene, cyclofenil, fulvestrant, ospemifene, raloxifene, tamoxifen, and toremifene) prohibited by WADA.

In addition, the samples were screened for other AIs and anti-estrogenic substances presence because the WADA list is open and not limited to the above-mentioned substances.

3 Results

3.1 Classification of samples by declaration of the label

A total of 601 samples declared as containing PEDs were obtained. Our classification of the various PED substances, based on the packaging declaration, resulted in three main groups: AAS, medicines used in PCT, and other PEDs. Most of the samples (n = 411, 68.4%) indicated AAS presence; however, 63 (10.5%) were intended for PCT, and 127 (21.1%) were declared as containing other PEDs (Figure 1.). These substances are briefly described as follows:

3.1.1 AAS

Reporting the identified AAS results was not the subject of this study, except for mesterolone, which bodybuilders use as a PCT drug. Therefore, mesterolone was included as a PCT substance. Other AAS were only counted as AAS according to the packaging declaration for this project.

3.1.2 Other PEDs

This group included other substances prohibited by WADA, such as non-approved substances (BPC-157) from Section S0, other anabolic agents (clenbuterol and SARMs) from Subsection S0, S1.2, peptide hormones and their releasing factors (AOD-9604, hGH 176-191, CJC-1295, ibutamoren, ipamorelin, and growth hormone-releasing peptide) from S2.2, growth factors and growth factor modulators (thymosin-ß4 and its derivative TB-500) from S2.3, beta-2 agonists (salbutamol and indacaterol) from S3, metabolic modulators (meldonium, GW1516, SR9009, SR9011, and insulins) from Section S4.4, and thyroid hormones.

3.1.3 PCT drugs

This group comprises AIs, SERMs, and other PCT substances, such as hCG, cabergoline, and mesterolone. The results of the analyses of these samples are presented in the following sections.

PCT drugs were declared in 63 samples (10.5%). Of the 63 samples, SERMs were declared in 21 (3.5%), AIs in 16 (2.7%), and other PCT substances in 26 (4.3%) (Figure 1).

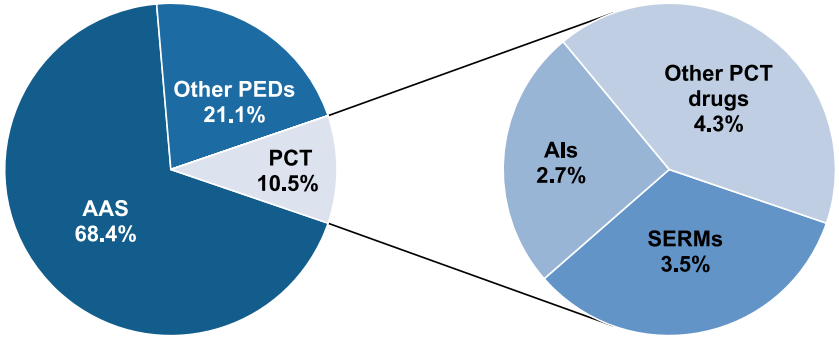

FIGURE 1
Distribution of samples (2020–2024) based on the substance declaration on the packaging.

3.2 Annual comparison of PEDs samples (2020–2024)

The numbers of the three types of samples provided for each year are summarized in Figure 2.

3.3 Dosage forms of the PCT samples

Almost all the PCT samples had a pharmaceutical product appearance. However, some products had strange battery-like appearances with the writing "get more power" and signs "+" and "-" on both sides. Most of the tested samples (74.6%, n = 47) were in tablet form intended for oral administration (Figure 3), while 25.4% were presented as powders for injections (n = 16).

3.4 Packaging and product authentication of the PCT samples

Most packaging was without leaflets (71%; n = 45); however, 18 samples (29%) had leaflets, including 13 in Greek, 2 in Turkish, 1 in English, and 2 in Polish. Some of the external product packaging contained anti-counterfeit markings, located on stickers under the scratch-off label with "the anti-counterfeit number" and instructions: "*Scratch coating on the anti-counterfeiting label to get the anti-counterfeit number. Visit our website to check its authenticity,*" "*Before use, please authenticate your product at our website (link), authentication code, scratch here*" or "*Please use the Authentication system to verify the products you use are real, each time. This is the only way to ensure you are not using a fake product and the product is safe to use.*" After verification on the manufacturer's website, the products are confirmed as authentic with messages such as "*This serial number exists. You got the real product.*" Many evidential products did not meet the labeling requirements for original medicinal products (including no batch number, list of excipients, full manufacturer name, information leaflets, and permit number on the packaging). Moreover, mistakes were mainly in the names of active pharmaceutical ingredients (APIs), such as *exemastene* instead of exemestane, *anastrazole* instead of anastrozole, and others.

3.5 AI identification

Among the 63 samples, three AI APIs (anastrozole, letrozole, and exemestane) were identified using LC-QTOF-MS/MS (Table 2). These substances are used in small doses (mostly 1 mg anastrozole, 2.5 mg letrozole, and 12.5 mg exemestane); therefore, the concentration was too low for XRPD.

3.5.1 Letrozole

Letrozole-containing products on the market include Femara, Aromek, Clarzole, Etruzil, Lametta, and Letrozole. During this study, only two samples with declared letrozole were tested, and both contained the declared API. An example of the letrozole spectrum is shown in Figure 4. However, one letrozole sample contained undeclared exemestane and yohimbine traces (Figure 5). In addition, we identified letrozole as an undeclared API in three samples that were declared to contain anastrozole. One sample contained only letrozole, another contained letrozole with stanozolol, and the third contained letrozole with ostarine (Table 2).

3.5.2 Anastrozole

Anastrozole-containing products on the market include Arimidex, Anastrozol, Anastrozole, Atrozol, and Egistrozol. Seven samples with declared anastrozole were tested; four contained the declared API, two contained only the declared API, the third with the declared API contained undeclared tamoxifen, oxandrolone, ligandrol, and cardarine traces, while the fourth product contained tamoxifen. In contrast, three samples were incorrectly labeled, and the declared API was absent. These samples contained letrozole instead of anastrozole. One sample contained letrozole only, the second contained letrozole and ostarine, and the third contained stanozolol. None of the products tested in this study contained anastrozole as an undeclared active substance (Table 2).

An example of anastrozole spectrum is presented in Figure 4C. Although letrozole and anastrozole share structural similarity and they eluate at the same retention time, their ionization ability in ESI source is completely different. Letrozole ionizes in both positive and negative ionization modes, while anastrozole undergoes only positive ionization.

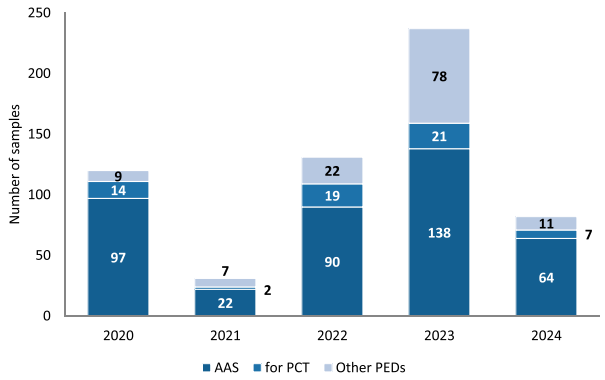

FIGURE 2
Number of samples from different PED groups submitted at Polish OMCL each year. All, n = 601; 2020, n = 120; 2021, n = 31; 2022, n = 131; 2023, n = 237, 2024, n = 82. *Data for 2024 is only through 31 August 2024.

3.5.3 Exemestane

Exemestane-containing products on the market include Aromasin, Etadron, Glandex, Symex, and Exemestane. Seven samples with declared exemestane content were tested, all of which contained the declared API. However, we found exemestane as an undeclared API in two samples, one with declared chlorodehydromethyltestosterone and undeclared oxandrolone, and the other with declared letrozole and undeclared yohimbine traces (Figure 5; Table 2).

3.6 Identification of SERMs and anti-estrogens

All results are summarized in Table 2.

3.6.1 Tamoxifen

Tamoxifen-containing products on the market include Tamoxifen, Zymoplex, and Nolvadex. Seven samples with declared tamoxifen were tested; five contained the declared API, while two were incorrectly labeled, and the declared API was absent. One of these false samples contained ethylenediaminetetraacetic acid disodium salt dihydrate (EDTA-Na), whereas the other sample contained no API. Furthermore, we found tamoxifen as undeclared API in seven samples, together with chlorodehydromethyltestosterone, stanozolol, anastrozole, oxandrolone, ligandrol, or cardarine (Table 2).

Two sample X-ray diffractograms of the tamoxifen samples are presented in Figure 6.

In sample no. 1 with declared tamoxifen, tamoxifen presence was not confirmed by LC-QTOF-MS/MS or XRPD; instead, another crystalline component, the EDTA-Na salt, was identified (Figure 6A). In sample no. 2, the diffraction measurement results allowed unequivocal tamoxifen identification in the form of citrate (Figure 6B).

3.6.2 Raloxifene

No samples with declared raloxifene were seized. However, in three samples declared as containing AAS or BPC-157, in addition to the declared API, contamination with undeclared raloxifene was present, together with chlorodehydromethyltestosterone, ibutamoren, and SR9009 (Table 2).

3.6.3 Clomiphene

Clomiphene-containing products on the market include Clostilbegyt, Clomiphene Citrate 50, Clomid-50, and Terpafen-50. Fourteen samples with declared clomiphene were tested. Half of the samples contained the declared API, while half were incorrectly labeled, and the declared API was absent. In most of these (n = 4) fake samples, we identified no API, whereas another contained methyltestosterone and stanozolol, the second contained tadalafil and sildenafil, and the third contained methandienone and

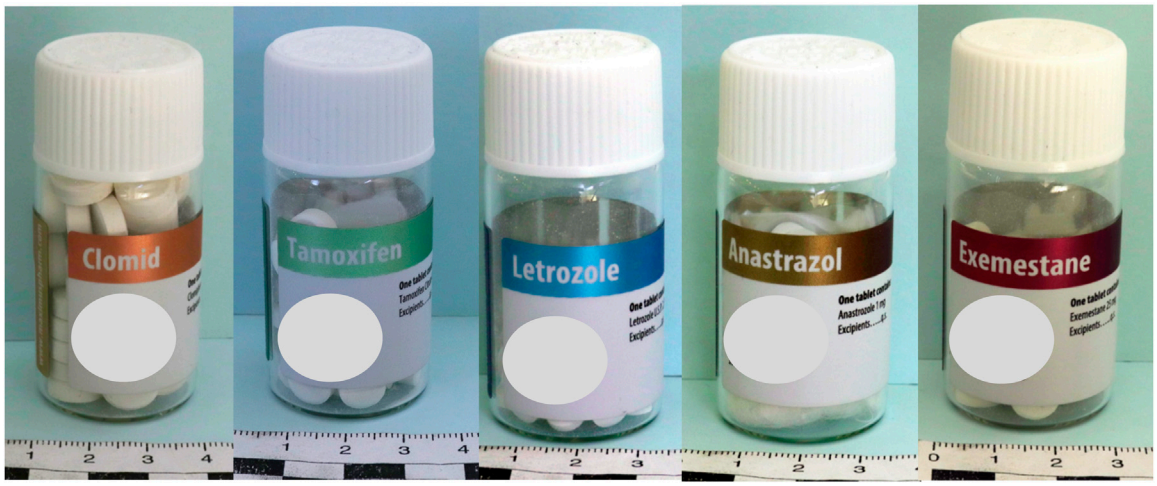

FIGURE 3
Examples of PCT samples in tablet forms.

TABLE 2 List of seized products and identified active substance(s) in the study.

Item	Product labeling—declared API	Declared API identified	Undeclared API(s) identified
Products with aromatase inhibitors			
1	Letrozole	yes	exemestane, yohimbine
2	Letrozole	yes	no
3-4	Anastrozole	yes	no
5	Anastrozole	yes	tamoxifen, oxandrolone, ligandrol, cardarine
6	Anastrozole	yes	tamoxifen
7	Anastrozole	no	letrozole
8	Anastrozole	no	letrozole, stanozolol
9	Anastrozole	no	letrozole, ostarine
10-16	Exemestane	yes	no
Products with anti-estrogenic substances			
17-21	Tamoxifen	yes	no
22	Tamoxifen	no	EDTA-Na
23	Tamoxifen	no	no
24-30	Clomiphene	yes	no
31-34	Clomiphene	no	no
35	Clomiphene	no	methyltestosterone, stanozolol
36	Clomiphene	no	tadalafil, sildenafil
37	Clomiphene	no	methandienone, sildenafil
Products with other substances used in PCT			
38-40	Cabergoline	yes	no
41	Cabergoline	yes	stanozolol
42	Cabergoline	no	no
43	Cabergoline	no	sildenafil
44-45	Mesterolone	yes	no
46	Mesterolone	no	stanozolol, sildenafil
47	Mesterolone	no	no
48-57	hCG	yes	no
58-63	hCG	no	no
Products with undeclared API for PCT			
64	Chlorodehydromethyltestosterone	yes	exemestane, oxandrolone
65	Chlorodehydromethyltestosterone	yes	tamoxifen
66	Oxandrolone	no	tamoxifen
67	Oxandrolone	yes	tamoxifen, chlorodehydromethylotestosterone
68	Oxandrolone	yes	tamoxifen, stanozolol
69	Liotyronine	no	tamoxifen
70	BPC-157	yes	raloxifene, ibutamoren, SR9009

(Continued on following page)

TABLE 2 (*Continued*) List of seized products and identified active substance(s) in the study.

Item	Product labeling—declared API	Declared API identified	Undeclared API(s) identified
71-72	Chlorodehydromethyltestosterone	yes	raloxifene
73	Dapoxetine	yes	clomiphene
74-75	Tadalafil	yes	clomiphene, dapoxetine
76	Sildenafil	yes	clomiphene
77	Cardarine	yes	clomiphene

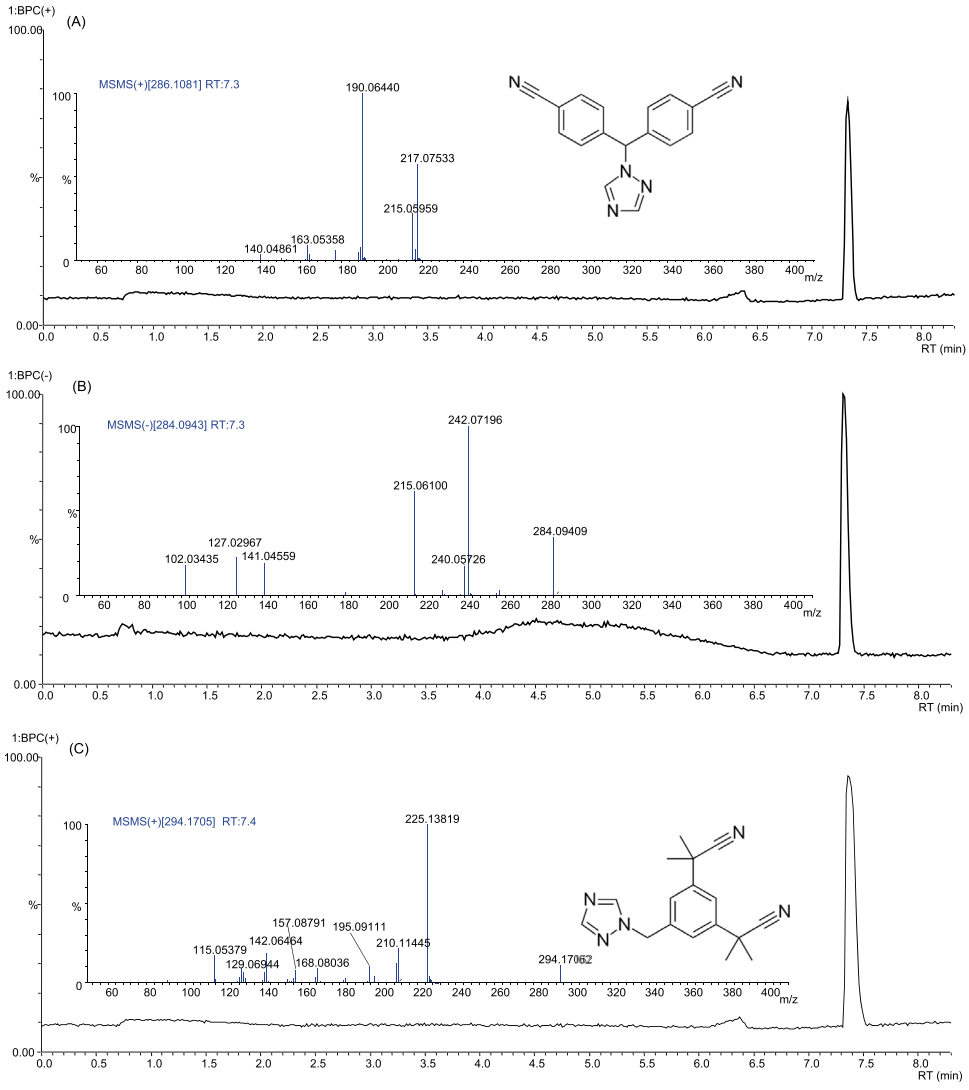

FIGURE 4
Base peak chromatograms and product ion spectra of letrozole in positive ion mode **(A)**, negative ion mode **(B)** and of anastrozole in positive ion mode **(C)**.

sildenafil. We identified clomiphene as an undeclared API in five samples, together with tadalafil, sildenafil, dapoxetine, and cardarine (Table 2).

3.7 Other PCT substances identification

All results are summarized in Table 2.

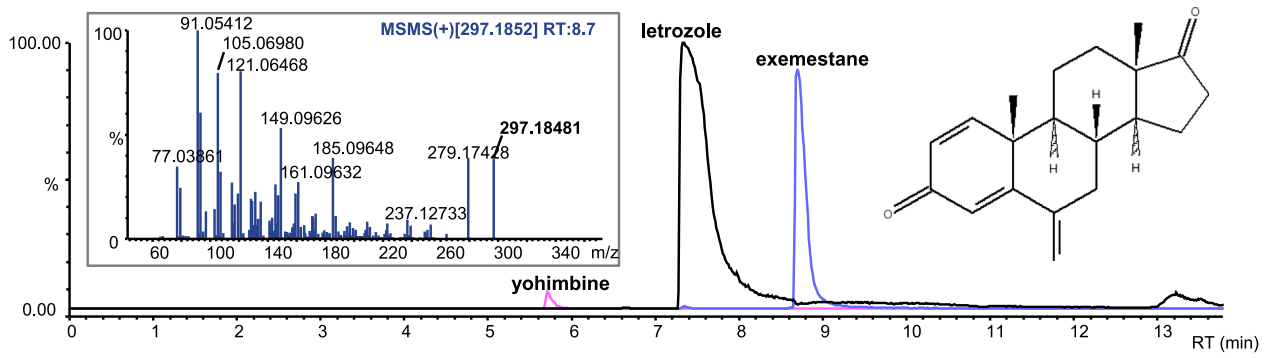

FIGURE 5
Extracted-ion chromatograms (ESI+) of the sample with letrozole and undeclared exemestane and yohimbine traces; product ion spectrum of exemestane.

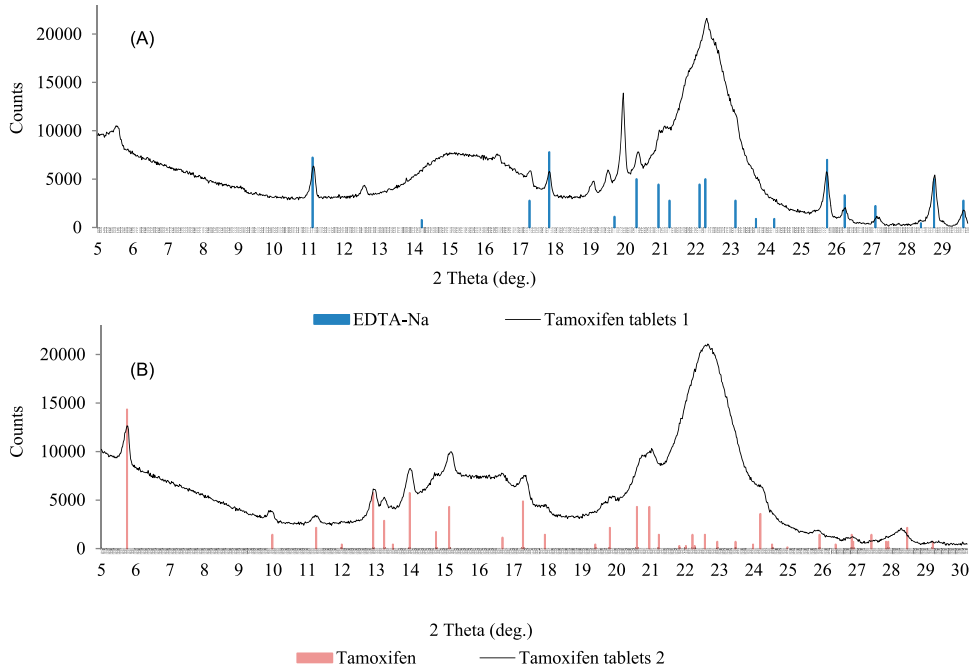

FIGURE 6
X-Ray diffractograms of tamoxifen samples; tablets without declared tamoxifen but with EDTA-Na **(A)**; tablets with declared tamoxifen citrate **(B)**.

3.7.1 Cabergoline

Cabergoline-containing medicinal products on the market include Dostinex and Cabaser. Six samples with declared cabergoline were tested; four contained the declared API, while two samples were incorrectly labeled, and the declared API was absent. One of these fake samples contained no API, whereas sildenafil contamination was identified in another. Stanozolol was detected in one sample with declared and identified cabergoline (Figure 7). We did not find cabergoline as an undeclared API in any of the samples (Table 2).

3.7.2 Mesterolone

Mesterolone-containing products on the market include Proviron (at different doses). Four samples with declared mesterolone were tested; two contained the declared API, while two were incorrectly labeled, and the declared API was absent. We identified stanozolol and sildenafil in one of the fake samples and no API in the other. We did not find mesterolone to be an undeclared API in any of the samples (Table 2).

3.7.3 hCG

hCG-containing products on the market include Pregnyl, Vir-Provigil, Ovigil, HCG 5000 IU, Gonadonax 5,000, Chorgon Human Chorionic, Puretrig-5000 IU. Sixteen samples with declared hCG were tested; 10 contained the declared API, while 6 were incorrectly labeled, the declared API was absent, and only mannitol was identified. We did not find hCG as an undeclared API in any sample; however, because of the special identification method, not all samples were screened for hCG (Table 2).

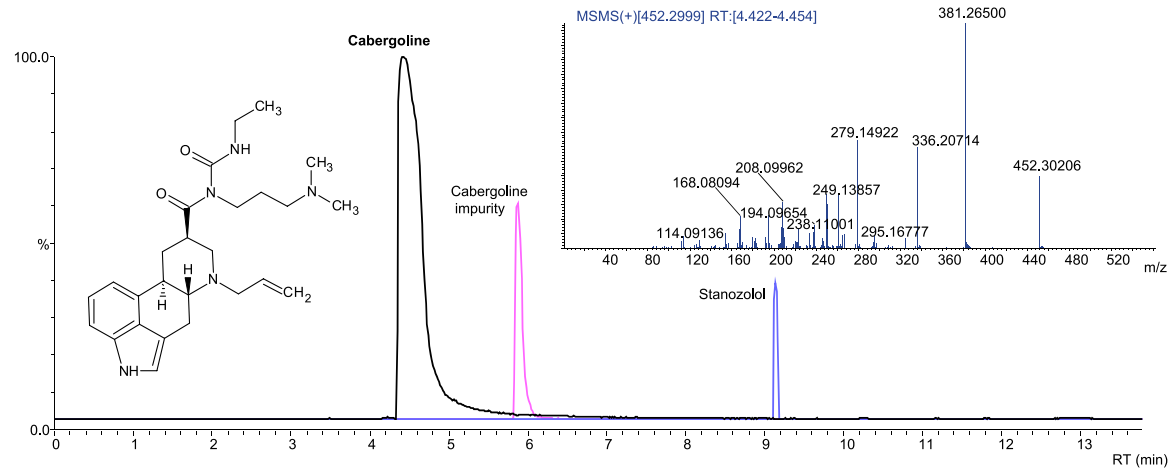

FIGURE 7
Extracted-ion chromatogram (ESI+) of the sample with cabergoline and stanozolol; product ion spectrum of cabergoline.

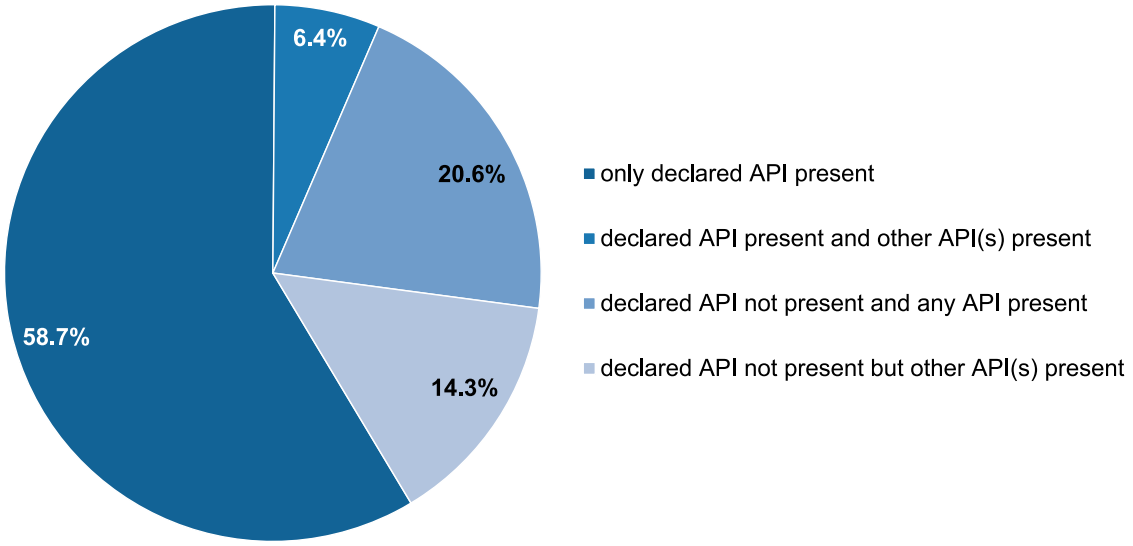

FIGURE 8
Occurrence of detected APIs within 63 PCT samples.

3.8 Declared and undeclared API(s) in the PCT samples

Approximately 59% of the PCT samples were correctly labeled, whereas 41% were incorrectly labeled according to the presence of the declared active substances.

As described in the previous sections, not all samples were consistent with this declaration. In 65.1% of the PCT samples, the declared API was present, whereas it was absent in 34.9%. Furthermore, in 58.7% of the samples, only the declared API was present, whereas 6.4% contained an additional undeclared API. Conversely, in 20.6% of the samples, neither a declared API nor any API was identified; however, in 14.3% of the samples, other undeclared APIs were identified (Figure 8).

Nine different substances were declared as PCT medicines in the samples and, in order of occurrence frequency, they were hCG (n = 16), clomiphene (n = 14), tamoxifen (n = 7), exemestane (n = 7), anastrozole (n = 7), cabergoline (n = 6), mesterolone (n = 4), and letrozole (n = 2).

In 20 samples, we identified undeclared API used in PCT. Six of these were declared as containing other PCT drugs (of 63); however, 14 other samples should contain only AAS or other substances according declaration (Table 2). Nevertheless, 14 samples declared as containing only AAS and other substances contained undeclared PCT medicines, including tamoxifen (n = 5), clomiphene (n = 5), raloxifene (n = 3), and exemestane (n = 1) (Table 2).

A summary of the declared and undeclared APIs in PCT samples is shown in Figure 9.

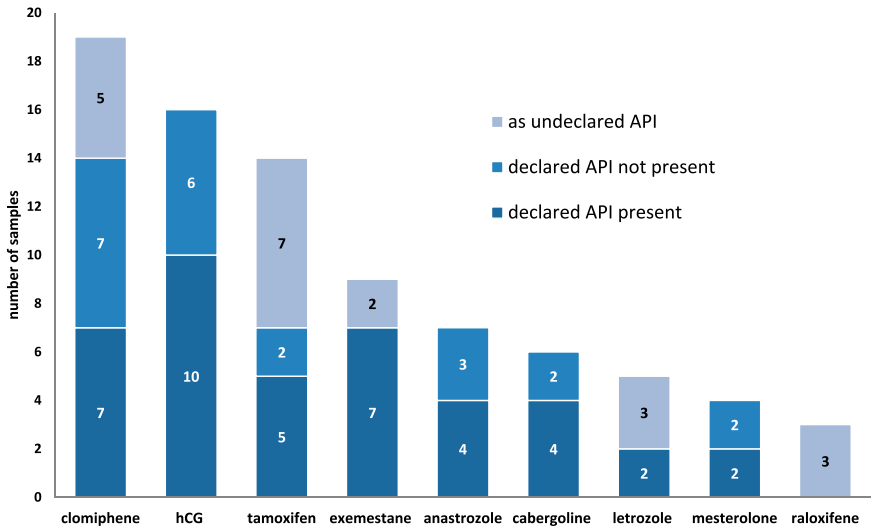

FIGURE 9
Occurrence of the APIs for PCT in the samples.

4 Discussion

Between January 2020 and the end of August 2024, 601 PED samples seized by the police and prosecutor's office from the illegal market were submitted for testing at the Polish OMCL. The fewer samples in 2021 were mainly due to the COVID-19 pandemic in 2020, as samples that reached the laboratory were usually seized much earlier. In contrast, the number of samples received in 2024 was lower; however, this was because the samples were counted only until the end of August. New samples are continually tested in the laboratory, and we typically receive more samples in the second half of the year than in the first half. More than a hundred samples were seized and sent to the Polish OMCL, where they are waiting for analysis.

It is not surprising that AAS products constituted the largest group in each year between 2020 and 2024 (average: 68.4%); however, the number decreased from 80.8% in 2020 to 58.2% in 2023. The year 2024 can only be assessed after completion. Nevertheless, a significant number of AAS products are expected to be analyzed in 2024 because illicit sites that distribute huge quantities of anabolic agents (located in Poland) have recently been tracked down by the police (Centralne Biuro Sledcze Policji, 2023; Centralne Biuro Sledcze Policji, 2024). AAS were also the most dominant group among all analyzed products used as PEDs in other studies (Begley et al., 2017; Deconinck et al., 2021; Magnolini et al., 2022).

Conversely, the number of other PED samples increased (mean 21.1%) from 7.5% in 2020 to 32.9% in 2023. This could be due to a significant increase in interest in SARMs (Deconinck et al., 2021; Gaudiano et al., 2024; Holubeck et al., 2024) or peptide hormones and their releasing factors, growth factor modulators, and metabolic modulators. SARMs have become particularly popular recently among PED users because they are not "steroids" and, therefore, have less stigma attached to them, have lower risks of needle sticks and blood-borne diseases, and appear more legal (Chakrabarty et al., 2021).

Since AAS use is still very popular, the users self-administer post-cycle drugs after an AAS cycle to mitigate the side effects. Self-administration of PCT medicines was reported by 73% of men discontinuing AAS in Scotland between 2015 and 2022 (Grant et al., 2023a) and by 80% of 100 male athletes in the Netherlands between 2015 and 2018 (Smit et al., 2021). However, in an online survey conducted between December 2021 and February 2023, 56.5% of the 470 respondents recruited through advertisements on websites related to AAS use reported PCT use when stopping AAS (Grant et al., 2023b).

In our study, PCT medications constituted 6.5% of samples in 2021, 14.5% in 2022, and 8.5% in 2024 (average, 10.5%). There was a stagnant interest in PCT drugs, as recently demonstrated by other researchers (Holubeck et al., 2024). However, they will not disappear from the market when AAS are still used.

Of the 63 samples, SERMs were declared in 21 (33.3%), AIs in 16 (25.4%), and other PCT substances in 26 (41.3%). Nine different substances were declared or identified as undeclared PCT drugs in the samples and, in order of occurrence frequency, they were clomiphene, hCG, tamoxifen, exemestane, anastrozole, cabergoline, letrozole, mesterolone, and raloxifene (Figure 9). The compounds most frequently encountered in our study were consistent with those described by other researchers. Grant et al. demonstrated that the most popular drugs used for PCT were clomiphene (77%), tamoxifen (75%), and hCG (74%) (Grant et al., 2023a). Notably, hCG was also used during AAS cycle and as a PCT drug together with tamoxifen and clomiphene in 47%, while anastrozole was self-reported by only 4% of respondents. However, according to results of a web-based survey between August 2019 and April 2020 within 2,385 AAS users (Bonnecaze et al., 2020), the main PED used during AAS cycle were anastrozole (48%), tamoxifen (31%), exemestane (30%), and hCG (29%), whereas tamoxifen (40%), clomiphene (32%), hCG (26%), anastrozole (16%), exemestane (9%), letrozole (3%), and cabergoline/bromocriptine (1.6%) were

used as PCT; however, 33% of them reported no PCT medicine use. In another study (Smit et al., 2021), tamoxifen (70%), clomiphene citrate (54%), and hCG (55%) were mostly used as PCT drugs. Other researchers analyzed 1792 posts published between 2013 and 2019 on the bodybuilding forum among AAS users, and 845 posts concerned SERMs while 571 concerned AIs (Rochoy et al., 2022).

All the analyzed PCT samples looked like medicines, which may give users confidence in the product quality despite coming from the illegal market. Some evidential product packaging contained anti-counterfeit markings and hints on how to verify product authenticity on the manufacturer's website. Notably, this is a common "anti-counterfeiting" procedure for manufacturers who illegally produce medicinal products. However, data on the packaging of these products often contain inaccurate information on their composition, origin, performance, and use, which might mislead consumers.

Only over half of the samples were consistent with the declaration. The discrepancies between the label and content can be divided into whether the product contained a similar PED, a completely different API, an additional API, or contained no API. Undeclared pharmacologically active substances in illegal and falsified products can cause extreme harm to public health and pose a serious threat to human life. It is not surprising that there are counterfeits that do not contain API, especially since pharmaceutical API, such as hCG, is expensive compared to other doping agents such as AAS.

Although only three anti-estrogenic substances banned by WADA were identified in this study, clomiphene, tamoxifen, and raloxifene, it should be remembered that other banned substances from the S4.2 group, such as bazedoxifene, cyclofenil, fulvestrant, ospemifene, or toremifene, may also be present in illegal samples purchased by athletes (Okano et al., 2022). Bazedoxifene, ospemifene, and toremifene are newer-generation SERMs that are expected to soon become more popular in the illegal market. Bazedoxifene and ospemifene have been included in the WADA Prohibited List since January 2020. According to blogs, toremifene under the Fareston brand name is even preferred as a modern and safer SERM than tamoxifen and clomiphene; however, it is not yet commonly sold in the black market. In contrast, cyclofenil (Fertodur) is not as commonly used as clomiphene and tamoxifen, which have dominated this drug category for many decades. The SERD fulvestrant is also not yet widely available in the black market (Llewellyn, 2017). This may be due to the fact that it is very expensive, administered as an injection, and must be stored in a refrigerator. Therefore, it is important to note that falsifications without an API can be expected.

Similar to the anti-estrogenic group, only three AIs banned by WADA were identified in this study: letrozole, anastrozole, and exemestane. Notably, other banned substances from the S4.1 group, such as aminoglutethimide, arimistane, formestane, or testolactone, may also be present in illegal samples purchased by athletes. However, letrozole, anastrozole, and exemestane are newer-generation AIs that dominate the drug category. Aminoglutethimide and testolactone (Teslac) were the first generation of non-selective irreversible AIs; however, they are no longer commonly used in clinical medicine. Formestane is a newer AI used as an injection solution and is not widely available in the athletic community (Llewellyn, 2017).

Substances from the newer generations have started appearing among athletes. Within the class S4 of "hormone and metabolic modulators" of the WADA Prohibited List, 39% of the adverse analytical findings (AAF) reported in 2020 resulted from SERMs (tamoxifen and clomiphene) and another 29% from AIs (letrozole, anastrozole, exemestane, and adrostatrienedione) (World Anti-Doping Agency, 2022). In 2021, the numbers of AAF were 33% from SERMs (tamoxifen and clomiphene) and 15% from AIs (anastrozole, letrozole, adrostatrienedione, armistane, and 2-androstenone) (World Anti-Doping Agency, 2024a). Further, the numbers were 35% from anti-estrogenic substances (tamoxifen, clomiphene, fulvestrant, toremifene, and raloxifene) and 20% from AIs (letrozole, anastrozole, exemestane, adrostatrienedione, and armistane) in 2022 (World Anti-Doping Agency, 2024b).

Among the other PCT drugs, bromocriptine, which is similar to the popular cabergoline, an ergot alkaloid derivative used to treat hyperprolactinemia, is less common than cabergoline among AAS users during PCT owing to its many side effects, such as low blood pressure, dizziness, confusion, and nausea.

The effectiveness and purity of PCT drugs are concerns for many users (Grant et al., 2023b). Although many AAS users believe that PEDs are safe for long-term use, the vast majority would stop using AAS if they experience a serious health problem (Bonnecaze et al., 2020). In another study was reported that respondents believed that confirming substance legality would encourage safer practices and reduce potentially dangerous side effects (Piatkowski et al., 2023).

Polypharmacy associated with AAS and PCT drugs may have serious harmful effects on those engaged in such practices, which constitutes a serious public health concern (Sagoe et al., 2015). Moreover, illegal and falsified products used in PCT may interact with other medications or affect preexisting disease development or treatment.

Although these medications are legally available only with the prescription of a doctor, they can be bought without a prescription on the Internet. In another study researchers analyzed posts on a bodybuilding forum concerning SERMs and AIs, revealing that a minority of users were able to obtain PCT medication through a pharmacy (5% clomiphene, 5% tamoxifen, 6% anastrozole, 8% exemestane, and 22% letrozole) (Rochoy et al., 2022). Only 5% of AAS users reported consulting physicians. However, many of them (25% of SERM and 33% of AI users) reported having a blood test to monitor levels of gonadotropins, estradiol, and total, free, and bioavailable testosterone and to adjust AI doses during AAS treatment. It should be emphasized that in another survey (Grant et al., 2023b), most respondents believed that PCT should be prescribed under the supervision of a physician. However, no recommended treatment for AAS cessation currently exists. PCT use after discontinuing AAS treatment reduced the desire to reuse AAS, withdrawal symptoms, and suicidal thoughts by 60%, 60%, and 50%, respectively (Grant et al., 2023b). However, SERM, AI, or prolactin inhibitor use during PCT remains an unproven practice (Bond et al., 2022). Some researchers were unable to demonstrate any beneficial

effect of PCT medications; therefore, the use of these agents should be discouraged (Smit et al., 2021).

Owing to the high prevalence of illicit steroid use, the self-administration of unapproved PCT using illegal and falsified medicines is dangerous and can be considered a potential threat to consumer health. Pharmaceutical and drug-related crimes are problems that the modern world struggles with. The increasing scale of this phenomenon, dynamic changes in the market for falsified and illegally traded products, and threats to the health and life of people receiving such products imply the urgency of systematic monitoring of both legal and illegal chains of medicinal products.

We have shown that the illicit drugs used in PCT are of poor quality; they may be substituted, contain no active ingredients, or be adulterated. Our results indicate that in view of the high prevalence of illicit AAS use, the self-administration of unapproved PCT using illegal and falsified medicines is dangerous and can be considered a potential threat to consumer health.

4.1 Limitations

This study had some limitations. Because only qualitative analysis was performed, the exact doses of illicit PCT drugs were unknown. Therefore, even samples where the labeled API was confirmed may not be consistent with the declaration because of variations in API concentrations, which may have health implications for consumers.

Not only APIs but also declared excipients were analyzed, mainly by XRPD; however, without the full composition of the analyzed products (known only as legal medicinal products), confirming compliance with the declaration was not possible.

Data availability statement

The raw data supporting the conclusions of this article will be made available by the authors, without undue reservation.

Author contributions

AB: Conceptualization, Data curation, Formal Analysis, Funding acquisition, Investigation, Methodology, Project administration, Resources, Supervision, Validation, Visualization, Writing–original draft, Writing–review and editing. MP: Investigation, Methodology, Writing–review and editing, Writing–original draft, Data curation, Validation, Visualization. BD: Investigation, Writing–review and editing, Methodology. KP: Investigation, Writing–review and editing, Methodology, Writing–original draft, Visualization. MK: Writing–review and editing, Writing–original draft.

Funding

The author(s) declare that financial support was received for the research, authorship, and/or publication of this article. The publication was co-financed by the state budget under the program of the Minister of Education, and Science called "Science for the Society II," project number NdS-II/SN/0270/2023/01, amount of funding 56,952 PLN total value of the project 1,956,000 PLN.

Acknowledgments

The authors would like to thank the other employees of Falsified Medicines and Medical Devices Department of National Medicines Institute for their assistance with preparing photographic documentation of samples and preparing samples for analysis.

Conflict of interest

The authors declare that the research was conducted in the absence of any commercial or financial relationships that could be construed as a potential conflict of interest.

Generative AI statement

The author(s) declare that no Generative AI was used in the creation of this manuscript.

Publisher's note

References

Ahmad, I., and Shagufta, (2015). Recent developments in steroidal and nonsteroidal aromatase inhibitors for the chemoprevention of estrogen-dependent breast cancer. *Eur. J. Med. Chem.* 102, 375–386. doi:10.1016/j.ejmech.2015.08.010

Basaria, S. (2010). Androgen abuse in athletes: detection and consequences. *J. Clin. Endocrinol. Metab.* 95 (4), 1533–1543. doi:10.1210/jc.2009-1579

Begley, E., McVeigh, J., Hope, V., Bates, G., Glass, R., Campbell, J., et al. (2017). *Image and performance enhancing drugs: 2016 national survey results.* Liverpool: Liverpool John Moores University.

Bond, P., Smit, D. L., and de Ronde, W. (2022). Anabolic–androgenic steroids: how do they work and what are the risks? *Front. Endocrinol.* 13, 1059473. doi:10.3389/fendo.2022.1059473

Bonnecaze, A. K., O'Connor, T., and Aloi, J. A. (2020). Characteristics and attitudes of men using anabolic androgenic steroids (AAS): a survey of 2385 men. *Am. J. Men's Health* 14 (6), 1557988320966536. doi:10.1177/1557988320966536

Bonnecaze, A. K., O'Connor, T., and Burns, C. A. (2021). Harm reduction in male patients actively using anabolic androgenic steroids (AAS) and performance-enhancing

drugs (PEDs): a review. *J. Gen. Intern. Med.* 36 (7), 2055–2064. doi:10.1007/s11606-021-06751-3

Camperi, J., Combes, A., Guibourdenche, J., Guillarme, D., Pichon, V., Fournier, T., et al. (2018). An attempt to characterize the human Chorionic Gonadotropin protein by reversed phase liquid chromatography coupled with high-resolution mass spectrometry at the intact level. *J. Pharm. Biomed. Anal.* 161, 35–44. doi:10.1016/j.jpba.2018.07.056

Centralne Biuro Sledcze Policji (2023). Jedna z najwiekszych akcji w historii CBSP wymierzona w przestepczosc farmaceutyczna. Available at: https://cbsp.policja.pl/cbs/aktualnosci/239660,Jedna-z-najwiekszych-akcji-w-historii-CBSP-wymierzona-w-przestepczosc-farmaceuty.html (Accessed October 16, 2024).

Centralne Biuro Sledcze Policji (2024). Nielegalnie produkowali i sprzedawali przez Internet leki. *CBSP zatrzymalo 11 Osob*. Available at: https://cbsp.policja.pl/cbs/aktualnosci/251579,Nielegalnie-produkowali-i-sprzedawali-przez-Internet-leki-CBSP-zatrzymalo-11-oso.html (Accessed October 16, 2024).

Chakrabarty, R., Grainger, J., Goebel, C., Brooker, L., and George, A. (2021). "For research use only": a comprehensive analysis of SARMs and related IPEDs purchased on local Australian websites between 2017 and 2018. *Perform. Enhanc. Health* 9 (3-4), 100201. doi:10.1016/j.peh.2021.100201

Deconinck, E., Vanhee, C., Keizers, P., Guinot, P., Mihailova, A., Syversen, P. V., et al. (2021). The occurrence of non-anatomical therapeutic chemical-international nonproprietary name molecules in suspected illegal or illegally traded health products in Europe: a retrospective and prospective study. *Drug Test. Anal.* 13 (4), 833–840. doi:10.1002/dta.3001

de Ronde, W., and Smit, D. L. (2020). Anabolic androgenic steroid abuse in young males. *Endocr. Connect.* 9 (4), R102–R111. doi:10.1530/EC-19-0557

dos Santos Ribeiro, H. S., Dagnino, D., and Schripsema, J. (2021). Rapid and accurate verification of drug identity, purity and quality by 1H NMR using similarity calculations and differential NMR. *J. Pharm. Biomed. Anal.* 199, 114040. doi:10.1016/j.jpba.2021.114040

Frude, E., McKay, F. H., and Dunn, M. (2020). A focused netnographic study exploring experiences associated with counterfeit and contaminated anabolic-androgenic steroids. *Harm. Reduct. J.* 17 (42), 42. doi:10.1186/s12954-020-00387-y

Gam, L. H., Tham, S. Y., and Latiff, A. (2003). Immunoaffinity extraction and tandem mass spectrometric analysis of human chorionic gonadotropin in doping analysis. *J. Chromatogr. B Anal. Technol. Biomed. Life Sci.* 792 (2), 187–196. doi:10.1016/s1570-0232(03)00264-2

Gaudiano, M. C., Aureli, F., Manna, L., Borioni, A., Maccelli, A., Raimondo, M., et al. (2024). Illegal products containing selective androgen receptor modulators purchased online from Italy: health risks for consumers. *Sex. Med.* 12 (2), qfae018. doi:10.1093/sexmed/qfae018

Girase, T., Patil, J., Tatiya, A., Patil, D., and Patil, M. (2023). Clomiphene citrate as nanomedicine assistance in ovulatory disorders and its hyphenated techniques. *Mater. Procee.* 14 (1), 6. doi:10.3390/IOCN2023-14505

Goumenou, A., Chendo, C., Combes, A., Fournier, T., Pichon, V., and Delaunay, N. (2025). Evaluation of Jacalin lectin sorbents for the extraction of the human chorionic gonadotropin glycoforms prior to analysis by nano liquid chromatography-high resolution mass spectrometry. *J. Pharm. Biomed.* 252, 116525. doi:10.1016/j.jpba.2024.116525

Graham, M. R., Ryan, P., Baker, J. S., Davies, B., Thomas, N. E., Cooper, S. M., et al. (2009). Counterfeiting in performance- and image-enhancing drugs. *Drug Test. Anal.* 1 (3), 135–142. doi:10.1002/dta.30

Grant, B., Campbell, J., Pradeep, A., Burns, A. D., Bassett, P., Abbara, A., et al. (2023a). Factors predicting normalization of reproductive hormones after cessation of anabolic-androgenic steroids in men: a single center retrospective study. *Eur. J. Endocrinol.* 6 (189), 601–610. doi:10.1093/ejendo/lvad164

Grant, B., Hyams, E., Davies, R., Minhas, S., and Jayasena, C. N. (2024). Androgen abuse: risks and adverse effects in men. *Ann. N. Y. Acad. Sci.* 1538, 56–70. doi:10.1111/nyas.15187

Grant, B., Kean, J., Vali, N., Campbell, J., Maden, L., Bijral, P., et al. (2023b). The use of post-cycle therapy is associated with reduced withdrawal symptoms from anabolic-androgenic steroid use: a survey of 470 men. *Subst. Abuse Treat. Prev. Policy.* 18 (1), 66. doi:10.1186/s13011-023-00573-8

Griffiths, S., Henshaw, R., McKay, F. H., and Dunn, M. (2017). Post-cycle therapy for performance and image enhancing drug users: a qualitative investigation. *Perform. Enhanc. Health* 5 (3), 103–107. doi:10.1016/j.peh.2016.11.002

Hackney, A. C. (2018). Hormone and metabolic modulators. *Perform. Enhancing Drugs, Hormones Sport*, 77–89. doi:10.1016/b978-0-12-813442-9.00007-9

Heuberger, J. A. A. C., and Cohen, A. F. (2019). Review of WADA prohibited substances: limited evidence for performance-enhancing effects. *Sports Med.* 49 (4), 525–539. doi:10.1007/s40279-018-1014-1

Hoffman, J. R., and Ratamess, N. A. (2006). Medical issues associated with anabolic steroid use: are they exaggerated? *J. Sports Sci. Med.* 5 (2), 182–193. Available at: https://pmc.ncbi.nlm.nih.gov/articles/PMC3827559/.

Holubeck, P. A., Eksi, A. C., Gillett, K., O'Hara, J., McGoldrick, D. J., Brown, D. R., et al. (2024). Social interest data as a proxy for off-label performance-enhancing drug use: implications and clinical considerations. *Cureus* 16 (1), e52011. doi:10.7759/cureus.52011

Johansson, M., Fransson, D., Rundlöf, T., Huynh, N.-H., and Arvidsson, T. (2014). A general analytical platform and strategy in search for illegal drugs. *J. Pharm. Biomed. Anal.* 100, 215–229. doi:10.1016/j.jpba.2014.07.026

Jordan, V. C. (2004). Selective estrogen receptor modulation: concept and consequences in cancer. *Cancer Cell* 5 (3), 207–213. doi:10.1016/s1535-6108(04)00059-5

Kanayama, G., Hudson, J. I., DeLuca, J., Isaacs, S., Baggish, A., Weiner, R., et al. (2015). Prolonged hypogonadism in males following withdrawal from anabolic-androgenic steroids: an under-recognized problem. *Addiction* 110 (5), 823–831. doi:10.1111/add.12850

Kang, H., Xiao, X., Huang, C., Yuan, Y., Tang, D., Dai, X., et al. (2017). Potent aromatase inhibitors and molecular mechanism of inhibitory action. *Eur. J. Med. Chem.* 1 (143), 426–437. doi:10.1016/j.ejmech.2017.11.057

Karavolos, S., Reynolds, M., Panagiotopoulou, N., McEleny, K., Scally, M., and Quinton, R. (2015). Male central hypogonadism secondary to exogenous androgens: a review of the drugs and protocols highlighted by the online community of users for prevention and/or mitigation of adverse effects. *Clin. Endocrinol. (Oxf)* 82 (5), 624–632. doi:10.1111/cen.12641

Khalikova, M., Jireš, J., Horáček, O., Douša, M., Kučera, R., and Nováková, L. (2024). What is the role of current mass spectrometry in pharmaceutical analysis? *Mass Spectrom. Rev.* 43 (43), 560–609. doi:10.1002/mas.21858

Lebede, M., Di Marco, F., Esser-Skala, W., Hennig, R., Wohlschlager, T., and Huber, C. G. (2021). Exploring the chemical space of protein glycosylation in noncovalent protein complexes: an expedition along different structural levels of human chorionic gonadotropin by employing mass spectrometry. *Anal. Chem.* 93, 10424–10434. doi:10.1021/acs.analchem.1c02199

Lewis, J. S., and Jordan, V. C. (2005). Selective estrogen receptor modulators (SERMs): mechanisms of anticarcinogenesis and drug resistance. *Mutat. Res.* 591 (1-2), 247–263. doi:10.1016/j.mrfmmm.2005.02.028

Llewellyn, W. (2017). *Anabolics*. 11th ed. Vahlt LLC.

Lund, H., Løvsletten, K., Paus, E., Halvorsen, T. G., and Reubsaet, L. (2012). Immuno-MS based targeted proteomics: highly specific, sensitive, and reproducible human chorionic gonadotropin determination for clinical diagnostics and doping analysis. *Anal. Chem.* 84, 7926–7932. doi:10.1021/ac301418f

Magnolini, R., Falcato, L., Cremonesi, A., Schori, D., and Bruggmann, P. (2022). Fake anabolic androgenic steroids on the black market – a systematic review and meta-analysis on qualitative and quantitative analytical results found within the literature. *BMC Public Health* 22, 1371. doi:10.1186/s12889-022-13734-4

McCabea, S. E., Brower, K. J., West, B. T., Nelson, T. F., and Wechsler, H. (2007). Trends in non-medical use of anabolic steroids by U.S. college students: results from four national surveys. *Drug Alcohol Dependence* 90, 243–251. doi:10.1016/j.drugalcdep.2007.04.004

Okano, M., Sato, M., and Kageyama, S. (2022). Detection of bazedoxifene, a selective estrogen receptor modulator, in human urine by liquid chromatography-tandem mass spectrometry. *Drug Test. Anal.* 14, 1995–2001. doi:10.1002/dta.3225

Piatkowski, T., Puljevic, C., Francis, C., Ferris, J., and Dunn, M. (2023). They sent it away for testing and it was all bunk: exploring perspectives on drug checking among steroid consumers in Queensland, Australia. *Int. J. Drug. Policy* 119, 104139. doi:10.1016/j.drugpo.2023.104139

Poplawska, M., Bednarek, E., Naumczuk, B., and Blazewicz, A. (2020). Identification and structural characterization of three psychoactive substances, phenylpiperazines (pBPP and 3,4-CFPP) and a cocaine analogue (troparil), in collected samples. *Forensic Toxicol.* 40, 132–143. doi:10.1007/s11419-021-00597-4

Rahnema, C. D., Lipshultz, L. I., Crosnoe, L. E., Kovac, J. R., and Kim, E. D. (2014). Anabolic steroid–induced hypogonadism: diagnosis and treatment. *Fertil. Steril.* 101 (5), 1271–1279. doi:10.1016/j.fertnstert.2014.02.002

Rasmussen, J. J., Selmer, C., Østergren, P. B., Pedersen, K. B., Schou, M., Gustafsson, F., et al. (2016). Former abusers of anabolic androgenic steroids exhibit decreased testosterone levels and hypogonadal symptoms years after cessation: a case-control study. *PLoS One* 11 (8), e0161208. doi:10.1371/journal.pone.0161208

Rebiere, H., Guinot, P., Chauvey, D., and Brenier, Ch. (2017). Fighting falsified medicines: the analytical approach. *J. Pharm. Biomed.* 142, 286–306. doi:10.1016/j.jpba.2017.05.010

Rizzuti, A., Alvarenga, C., Stocker, G., Fraga, L., and Santos, H. O. (2023). Early pharmacologic approaches to avert anabolic steroid-induced male infertility: a narrative review. *Clin. Ther.* 45 (11), e234–e241. doi:10.1016/j.clinthera.2023.09.003

Rochoy, M., Danel, A., Chazard, E., Gautier, S., and Berkhout, C. (2022). Doping with aromatase inhibitors and oestrogen receptor modulators in steroid users: analysis of a forum to identify dosages, durations and adverse drug reactions. *Therapie* 77 (6), 683–691. doi:10.1016/j.therap.2022.03.004

Sagoe, D., McVeigh, J., Bjørnebekk, A., Essilfie, M. S., Andreassen, C. S., and Pallesen, S. (2015). Polypharmacy among anabolic-androgenic steroid users: a descriptive metasynthesis. *Subst. Abuse Treat. Prev. Policy.* 10, 12. doi:10.1186/s13011-015-0006-5

Shankara-Narayana, N., Yu, C., Savkovic, S., Desai, R., Fennell, C., Turner, L., et al. (2020). Rate and extent of recovery from reproductive and cardiac dysfunction due to androgen abuse in men. *J. Clin. Endocrinol. Metab.* 105 (6), 1827–1839. doi:10.1210/clinem/dgz324

Smit, D. L., Buijs, M. M., de Hon, O., den Heijer, M., and de Ronde, W. (2021). Disruption and recovery of testicular function during and after androgen abuse: the HAARLEM study. *Hum. Reprod.* 36 (4), 880–890. doi:10.1093/humrep/deaa366

Toll, H., Berger, P., Hofmann, A., Hildebrandt, A., Oberacher, H., Lenhof, H. P., et al. (2006). Glycosylation patterns of human chorionic gonadotropin revealed by liquid chromatography-mass spectrometry and bioinformatics. *ELECTROPHORESIS* 27, 2734–2746. doi:10.1002/elps.200600022

Vilar Neto, J. D. O., da Silva, C. A., Bruno da Silva, C. A., Pinto, D. V., Caminha, J. D. S. R., de Matos, R. S., et al. (2021). Anabolic androgenic steroid-induced hypogonadism, a reversible condition in male individuals? *A Syst. Rev. –Andrologia* 53, e14062. doi:10.1111/and.14062

World Anti-Doping Agency (2022). Data from: 2020 anti-doping testing figures. Available at: https://www.wada-ama.org/sites/default/files/2022-01/2020_anti-doping_testing_figures_en.pdf.

World Anti-Doping Agency (2024a). Data from: 2021 anti-doping testing figures. Available at: https://www.wada-ama.org/sites/default/files/2024-02/2021_anti-doping_testing_figures_en_v2.pdf.

World Anti-Doping Agency (2024b). Data from: 2022 anti-doping testing figures. Available at: https://www.wada-ama.org/sites/default/files/2024-04/2022_anti-doping_testing_figures_en.pdf.

World Anti-Doping Agency (2024c). *The world anti-doping code 2024*. International Standard. Prohibited List 2024. Available at: https://www.wada-ama.org/sites/default/files/2023-09/2024list_en_final_22_september_2023.pdf.

World Health Organization (2018). Substandard and falsified medical products. Available at: http://www.who.int/news-room/fact-sheets/detail/substandard-and-falsified-medical-products (Accessed October 19, 2024).

frontiers | Frontiers in Chemistry

TYPE Original Research
PUBLISHED 25 April 2025
DOI 10.3389/fchem.2025.1551189

OPEN ACCESS

EDITED BY
Serban Moldoveanu,
Independent Researcher, Greensboro, NC, United States

REVIEWED BY
Haji Muhammad,
Federal Urdu University of Arts, Sciences and Technology Islamabad, Pakistan
Muhammad Hassan Yousaf,
Lahore Garrison University, Pakistan

*CORRESPONDENCE
Aktham Mestareehi,
aktham.mestareehi@med.wayne.edu

RECEIVED 07 January 2025
ACCEPTED 24 March 2025
PUBLISHED 25 April 2025

CITATION
Mestareehi A (2025) Comprehensive and robust stability-indicating reversed phase high performance liquid chromatography (RP-HPLC) method for Rivaroxaban: synergistic integration of infrared spectroscopy and clinical pharmacology insights.
Front. Chem. 13:1551189.
doi: 10.3389/fchem.2025.1551189

Comprehensive and robust stability-indicating reversed phase high performance liquid chromatography (RP-HPLC) method for Rivaroxaban: synergistic integration of infrared spectroscopy and clinical pharmacology insights

Aktham Mestareehi [1,2,3]*

[1]Department of Applied Pharmaceutical Sciences and Clinical Pharmacy, Faculty of Pharmacy, Isra University, Amman, Jordan, [2]Department of Pharmaceutical Sciences, School of Pharmacy and Health Sciences, Wayne State University, Detroit, MI, United States, [3]Department of Pharmaceutical Sciences, School of Pharmacy, Northeastern Illinois University, Chicago, IL, United States

Introduction: Rivaroxaban is an anticoagulant medication that targets a key stage in the blood clotting process, preventing the formation and growth of clots. It is commonly used to prevent thrombosis or inhibit the enlargement of existing clots. Rivaroxaban functions as a Factor Xa inhibitor and is indicated for reducing the risk of stroke and systemic embolism in patients with non-valvular atrial fibrillation, treating deep vein thrombosis (DVT) and pulmonary embolism (PE), as well as reducing the risk of recurrent DVT and PE, and prophylaxis of DVT, which may lead to PE in patients undergoing knee or hip replacement surgery.

Methods: A robust, precise, and selective reversed-phase high-performance liquid chromatography (HPLC) method was developed and validated for analyzing Rivaroxaban in raw materials. Isocratic elution at a flow rate of 1 mL/min was performed using a Thermo ODS Hypersil C18 column (4.6 × 250 mm, 5 µm) at ambient temperature. The mobile phase consisted of monobasic potassium phosphate at pH 2.9 and acetonitrile in a 70:30 (v/v) ratio, with UV detection at 249 nm.

Results: Linearity was established in the concentration range of 50–1,000 ppm (R^2 = 0.999), and the retention time for Rivaroxaban was approximately 12 min. The percentage relative standard deviation (RSD) for precision and accuracy was consistently below 2.0%, ensuring method reliability. Solution stability studies confirmed the stability of Rivaroxaban over the analysis period, as no peak loss, degradation, or additional peaks were observed between the first and last injections. Furthermore, forced degradation studies were conducted under various stress conditions, including acid and base hydrolysis, as well as hydrogen peroxide oxidation. The method successfully resolved Rivaroxaban from its degradation products, demonstrating its stability-indicating capability.

Conclusion: Rivaroxaban is a novel oral anticoagulant that selectively and directly inhibits factor *Xa*. A method has been developed and validated for its analysis, adhering to guidelines from the International Conference on Harmonisation (ICH) and the U.S. Pharmacopeia (USP). The validation process assessed parameters such as specificity, robustness, linearity, accuracy, precision, limit of detection (LOD), and limit of quantitation (LOQ). The LOD for impurities and degradants was determined to be 0.3 ppm, while the LOQ was 1 ppm. This stability-indicating method is highly suitable for routine quality control and analytical applications in both raw materials and finished drug products, owing to its simplicity, efficiency, and robustness.

KEYWORDS

Rivaroxaban, high-performance liquid chromatography (HPLC), specificity, linearity, accuracy, precision, limit of detection (LOD), limit of quantitation (LOQ)

Introduction

Rivaroxaban is an oral, oxazolidinone based anticoagulant that acts as a selective, direct inhibitor of Factor Xa. It is commonly prescribed to prevent venous thromboembolism in adult patients following total knee or hip replacement surgery (Janssen Pharmaceuticals, 2011). Rivaroxaban was originally developed by Bayer and is marketed in the United States by Janssen Pharmaceuticals, a division of Johnson and Johnson. It was the first orally administered direct factor Xa inhibitor to become available (Fernandez et al., 2021). Rivaroxaban is rapidly absorbed, reaching peak plasma concentrations within 2–4 h after tablet administration. Its oral bioavailability is high (80%–100%) for the 10 mg dose, regardless of food intake, and is similarly high for the 15 mg and 20 mg doses when taken with food (Janssen Pharmaceuticals, 2011). A synthetic form of Rivaroxaban has been developed, utilizing (R)-epichlorohydrin as a key chiral intermediate (R)-Epichlorohydrin was reacted with sodium cyanate (NaOCN) to produce (R)-chloromethyl-2-oxazolidinone, with bromobenzene serving as the primary starting material (Yuan et al., 2014).

Rivaroxaban, the active ingredient in XARELTO tablets, has the molecular formula $C_{19}H_{18}ClN_3O_5S$ and a molecular weight of 435.89 g/mol. Its structural formula is shown in Figure 1 and purity ≥99. Rivaroxaban's chemical name is (5-Chloro-N-({(5S)-2-oxo-3-[4-(3-oxomorpholin-4-yl) phenyl]-1,3-oxazolidin-5-yl} methyl) thiophene-2- carboxamide) (Yuan et al., 2014). It is an odorless, non-hygroscopic, white to yellowish powder that exists as a pure (S)-enantiomer. It has a melting point of 228°C–229°C and a boiling point of approximately 732.6°C ± 60.0°C. The compound's density is 1.460 g/cm^3. It exhibits an optical rotation [α]D of −34 to −44 (c = 0.3 in DMSO) and has a pKa of 13.36 (Mueck et al., 2014). Classified under the Biopharmaceutical Classification System as a low-solubility, high-permeability compound (Class 2), rivaroxaban has limited pH-independent solubility in aqueous media (5–7 mg/L; pH 1–9) but is slightly soluble in polyethylene glycol 400 (2,431 mg/L) (Mueck et al., 2014). Additionally, each XARELTO tablet contains 10 mg, 15 mg, or 20 mg of Rivaroxaban. Inactive ingredients include Hypromellose, magnesium stearate, lactose monohydrate, croscarmellose sodium, microcrystalline cellulose, and sodium lauryl sulfate. Additionally, each tablet is coated with a film coating mixture tailored for the 10 mg, 15 mg, and 20 mg strengths (Janssen Pharmaceuticals, 2011; FDA, 2014).

Abbreviations: ACN, Acetonitrile; Avg, Average; C18, Column having octadecyl chain of Carbon atom; FDA, Food and Drug Administration; HCl, hydrochloric acid; HPLC, High Performance Liquid Chromatography; ICH, International Conference on Harmonization; pKa, Ionization constant; LC, Liquid Chromatography; LOD, Limit of Detection; LOQ, Limit of Quantitation; µL, Micro liter; µg/mL, Microgram per Milliliter; min, Minutes; N, Normality; Mg, Milligram; ppm, Parts per million; ODS, Octadecylsilane; pH, negative logarithm of H+ concentration; RP-HPLC, Reversed Phase High Performance Liquid Chromatography; RSD, Relative Standard Deviation; RT, Retention time; r^2, Correlation of coefficient; STD, Standard Deviation; UV, Ultraviolet.

Clinical pharmacology

Xarelto (Rivaroxaban) is an anticoagulant that works by directly inhibiting factor Xa, a key enzyme in the blood coagulation cascade. By blocking factor Xa, Xarelto prevents the conversion of prothrombin to thrombin, thereby inhibiting clot formation. Since it does not require a cofactor like anti-thrombin III, it is considered a direct and specific factor Xa inhibitor. This mechanism makes Xarelto effective in preventing and treating conditions like deep vein thrombosis (DVT), pulmonary embolism (PE), and stroke in patients with non-valvular atrial fibrillation (Weitz and Bates, 2005).

The absolute bioavailability of Xarelto 10 mg is 80%–100%, unaffected by food, so it can be taken with or without food. For the 20 mg dose, bioavailability is 66% but taking it with food increases bioavailability significantly (39% increase in AUC and 76% increase in Cmax). Therefore, Xarelto 15 mg and 20 mg must be taken with the evening meal. The peak plasma concentrations (Cmax) of Rivaroxaban occur 2–4 h after intake (Mueck et al., 2011).

Rivaroxaban has a plasma protein binding of approximately 92%–95%, with albumin being the main protein binding component. The steady-state volume of distribution in healthy individuals is around 50 L. (Janssen Pharmaceuticals, 2011) About 51% of an administered dose is recovered as metabolites, with 30% excreted in the urine and 21% in feces. The major metabolic pathways involve oxidative degradation via enzymes like CYP3A4/5, CYP2J2, and hydrolysis. The predominant form of Rivaroxaban in plasma is the unchanged drug, with no major active circulating metabolites (Janssen Pharmaceuticals, 2011; Mueck et al., 2011).

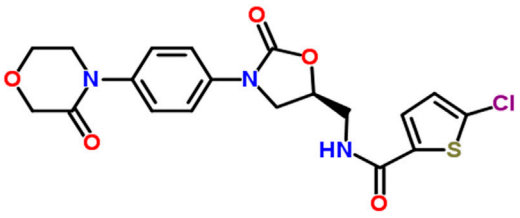

FIGURE 1
The chemical structure of Rivaroxaban (National Center for Biotechnology Information, 2024).

Approximately 66% of the drug is excreted in urine (36% unchanged), and 28% is excreted in feces (7% unchanged). Rivaroxaban is primarily excreted via active tubular secretion (approximate 5:1 ratio compared to glomerular filtration). The terminal elimination half-life of Rivaroxaban is 5–9 h in healthy subjects aged 20–45 years. The drug has a low systemic clearance (about 10 L/h) in healthy volunteers following intravenous administration (Janssen Pharmaceuticals, 2011; Mueck et al., 2011). This profile of Xarelto underscores its high bioavailability for lower doses, while its absorption, metabolism, and excretion are influenced by food intake and renal function. In clinical studies, it has been observed that elderly individuals tend to have higher plasma concentrations of Rivaroxaban compared to younger people. This is primarily due to a reduction in total body and renal clearance in the elderly population. Specifically, the mean AUC (area under the curve) values for Rivaroxaban are approximately 50% higher in older adults. Additionally, the terminal elimination half-life of Rivaroxaban is extended in the elderly, ranging from 11 to 13 h, compared to 5–9 h in younger individuals. These changes in pharmacokinetics are important to consider when prescribing Rivaroxaban to elderly patients, as they may be at an increased risk of accumulation of the drug, requiring potential adjustments to dosing (Janssen Pharmaceuticals, 2011; FDA, 2014; Mueck et al., 2011).

Xarelto (Rivaroxaban) should be discontinued at least 24 h before any surgical procedure to reduce the risk of bleeding. This precaution is important because Rivaroxaban is an anticoagulant and stopping it before surgery helps lower the risk of excessive bleeding during the procedure. After the surgery or procedure, Xarelto should be resumed as soon as possible, depending on the patient's condition and the type of surgery performed. If the patient is unable to take Xarelto by mouth after the procedure, a parenteral anticoagulant (such as heparin) may be administered until oral anticoagulation can be resumed. This ensures continued thromboprophylaxis while avoiding complications related to bleeding (Janssen Pharmaceuticals, 2011; Mueck et al., 2011).

Overdose of Xarelto (Rivaroxaban) can lead to hemorrhage due to its anticoagulant effects. However, systemic exposure does not significantly increase with single doses above 50 mg because of limited absorption at higher doses. In the event of an overdose with bleeding, it is crucial to immediately stop Xarelto and initiate appropriate therapy to manage the bleeding. If the overdose is recent, activated charcoal may be administered to reduce further absorption of the drug from the gastrointestinal tract. Reversal agents such as Andexanet alfa or procoagulant treatments may be considered, depending on the severity of the bleeding and available resources. Close monitoring and supportive care are essential to managing any complications associated with Xarelto overdose (Janssen Pharmaceuticals, 2011; National Center for Biotechnology Information, 2024). The most common side effects of Xarelto (Rivaroxaban) are related to its anticoagulant properties, which increase the risk of bleeding. These include bleeding events, itching (pruritus), pain in the arms or legs, and muscle pain (myalgia). (Janssen Pharmaceuticals, 2011; FDA, 2014).

The liver plays a crucial role in blood coagulation by synthesizing most of the clotting factors and inhibitors of the coagulation pathway (Mestareehi and Abu-Farsakh, 2024). Individuals with hepatic impairment have a reduced ability to synthesize these coagulation factors, which can increase their risk of bleeding due to impaired hemostasis. The severity of hepatic impairment is commonly classified using the Child–Pugh system, with grade A indicating mild impairment, grade B moderate impairment, and grade C severe impairment (Kubitza et al., 2013). Studies have shown that the reduction in clotting factor levels closely correlates with the severity of hepatic impairment as determined by the Child–Pugh score. Additionally, hepatic impairment can influence the pharmacokinetics of drugs metabolized by the liver, potentially leading to increased drug exposure and necessitating dose adjustments for affected patients (Verbeeck, 2008).

Several liquid chromatographic methods have been reported for the quantitation of Rivaroxaban in pharmaceutical dosage forms. One method developed by K. Chandra Sekhar, P. Satya Vani, and Narendra Devanaboyina, focuses on the use of Reverse-Phase High-Performance Liquid Chromatography (RP-HPLC). In this method, separation is achieved on a C18 column (250 × 4.6 mm, 5 µm) at ambient temperature. The mobile phase consists of a mixture of acetonitrile, methanol, and 0.1% phosphoric acid (90:8:2), with the pH adjusted to 4.06. The flow rate is 1.5 mL/min, and absorbance is measured at 234 nm. The linear detection range is from 50 to 200 µg/mL. The method was validated according to ICH guidelines. Rivaroxaban eluted at a retention time of 3.315 min, but early elution may mask the presence of degradants and impurities. Notably, no forced degradation stability studies were conducted, so the impact of degradation products on the chromatographic results was not assessed (Sekhar et al., 2012).

Another method, developed by Mustafa Celebier, Tuba Recber, and Sacide Altinoz, describes a new RP-HPLC method for estimating Rivaroxaban in pharmaceutical dosage forms. This method uses a Luna C18 column (250 mm length, 4.6 mm internal diameter, 5 µm particle size) with a mobile phase consisting of acetonitrile and water (55:45), a flow rate of 1.2 mL/min, and a column temperature of 40°C. Absorbance is performed at 249 nm, and the linear detection range is from 0.005 to 40.0 µg/mL. The method was also validated in accordance with ICH guidelines. Rivaroxaban eluted at a retention time of 3.37 min. However, the very low linear concentration range (from 0.005 to 40.0 µg/mL) used for forced degradation studies is problematic and not recommended for method development. This approach may lead to errors and does not adequately assess the stability of the drug or the presence of degradation products, highlighting the need for a more reliable stability-indicating method. As a result, the absence of

a comprehensive stability-indicating method was identified as a significant limitation of this approach (Çelebier TRb et al., 2013). While many studies have focused on the separation and stability of Rivaroxaban raw material, there has been a lack of research on the development of an RP-HPLC method for simultaneous separation and stability-indicating analysis of Rivaroxaban in its pharmaceutical dosage form. To fill this gap, the purpose of the current research is to develop a simple, fast, precise, and accurate RP-HPLC stability-indicating method specifically for Xarelto Tablets®. The method will be validated according to ICH (International Council for Harmonisation) and FDA guidelines to meet regulatory standards for quality control and stability testing. This development aims to provide a reliable tool for analyzing the stability of Rivaroxaban in tablet form, ensuring its potency, safety, and efficacy over time.

Materials and methodology

Chemicals and reagents

Rivaroxaban USP, CAS: 366789-02-8, Lot No: F10350; hydrochloric acid 12 N, Fisher Scientific,CAS A144-212, Lot No,135238; sodium hydroxide, EM Science, Lot No, 33257-344; Sodium Acetate, Fisher Scientific,CAS S210-500; Acetonitrile (ACN) HPLC Grade, Fisher Scientific,CAS 7778-77; Potassium Phosphate Monobasic, Merck & CO.; Potassium Phosphate Dibasic, ACROSORGANIC CAS7758-11-4, Lot No,A0340250; Potassium Dihydrogen Phosphate, Fluka Chemika, lot no, 290682-490; phosphoric acid (85%) J.T Baker, Lot No, 33397; Glacial acetic acid, Mallinckrodt Inc., CAS 2504-5X6, Lot No., 3532 KBPR; hydrogen peroxide 30%, Fisher Scientific, CAS 7722-84-1, Lot No 094115; hydrogen peroxide 3%, Fisher Scientific, CAS 7722-84-1, Lot No 094115; Deionized Water (in house system); pH Buffer Standards: 4.0, Fischer Scientific, Lot No.,122994; pH Buffer Standards: 7.0, Fischer Scientific, Lot No.,127454; pH Buffer Standards: 9.0, Fischer Scientific, Lot No., 123465.

Chromatography equipment

The analysis was conducted using Agilent HPLC system, which consisted of the following components:

- 1,100 Series HPLC System with DAD Detector, Agilent Technologies.
  - ➢ G1322A Degasser, Serial # JP05033159,
  - ➢ G1311A Quaternary Pump Serial # DE111155886,
  - ➢ G1329A ALS (Thermostat Auto sampler), Serial # DE11115876,
  - ➢ G1316A Column Thermostat, Serial # DE11123026,
  - ➢ G1365B DAD (Diode Array Detector), Serial # DE11101219
- 1,100 Series HPLC System with VWD (UV/VIS Detector), Agilent Technologies.
  - ➢ G1322A Degasser, Serial # JP05033683,
  - ➢ G1311A Quaternary Pump Serial # DE11115504,
  - ➢ G1329A ALS (Thermostat Auto sampler), Serial # DE11116580,
  - ➢ G1316A COLCOM, Serial #DE14927164,
  - ➢ G1314A VWD (Variable Wavelength Detector), Serial # JP92113753
- ChemStation Data Acquisition System for LC, Agilent Technologies.
- Thermo ODS Hypersil C18 (4.6 × 250 mm, 5 µm), Part No; 30105-254630, Serial No; 0153571S.

Additional equipment

- UV/VIS Spectrophotometer, Hitachi U-2910. Serial No, 2656-003
- Thermo Nicolet IR 200 Spectrometer
- pH Meter, Accumet Research, Fisher Scientific, Serial No AR93311993
- Sonicator/Ultrasonic, T21
- Analytical Balance, Mettler Toledo, Model xp205, s#1129211544
- Lab-line Instrument Inc. Oven (Model: 3512, 800 W, 50/60 Hz, 120 V)
- UV Light, Spectroline, Model ENF-260C, Serial#1358236
- Hot plate/Stirrer, Corning, Model PC-420, Serial No.420505018647
- Disposable Syringe Filter, Nylon Acordis CR 25 mm 0.2 µm, HPLC Certified.
- Filter 0.45 µm PVDF (polyvinylidene difluoride) Membrane.
- pH 0 −13.0 stripes, J.T Baker Inc.,4403-01

Chromatographic conditions

The chromatographic conditions for the analysis of Rivaroxaban are detailed in Table 1 below. These optimized conditions facilitate efficient separation with a short analysis time, ensuring precise quantification and reliable detection.

Solution preparation procedures

Comprehensive details on sample preparation, mobile phase composition, and analytical procedures employed in this study are provided in the Supplementary Materials under Supplementary Procedures for reproducibility and further reference.

Stock solution of Rivaroxaban (10,000 ppm)

Weigh 500 mg of Rivaroxaban and transfer it into a 50 mL volumetric flask. Add 25 mL of ACN: DI water (70:30 v/v) and sonicate for 20 min or until Rivaroxaban is completely dissolved. Complete the volume to the mark with ACN: DI water (70:30 v/v) and shake it thoroughly.

Stock solution of Rivaroxaban (1,000 ppm)

Transfer 5.0 mL of stock solution Rivaroxaban (10,000 ppm) into a 50 mL volumetric flask. Complete the volume to the mark with ACN: DI water (70:30 v/v) and shake it thoroughly.

TABLE 1 Optimized chromatographic conditions for rivaroxaban analysis.

Parameters	Conditions
Column	Thermo ODS Hypersil C18 (4.6 × 250 mm, 5 µm)
Mobile Phase	ACN: BUFFER (25 Mm potassium phosphate buffer monobasic pH 2.9) (30:70)
RT (retention time)	12.1 ± 0.235 min
Flow Rate	1 mL/min
Sample Injector	15 µL loop
Detection Wavelength	249 nm
Column Temperature	Ambient

Mobile phase B (100% acetonitrile)

Transfer 1,000 mL of ACN into the mobile phase reservoir and sonicate for 20 min to remove air bubbles.

Mobile phase A (buffer pH 2.9)

To prepare 1 L of 25 mM potassium phosphate monobasic solution at pH 2.90.

Weigh 3.40 g of Potassium Phosphate Monobasic and transfer it into a 1,000 mL beaker. Add 1,000 mL of DI water and stir until buffer salt is completely dissolved. Place a calibrated pH probe into the solution and adjust the pH by slowly adding phosphoric acid dropwise. Stop once the desired pH of 2.9 is reached. Filter the buffer by using (0.45 µm membrane filter) and sonicate for 20 min to remove any air bubbles.

Method development and optimization

In HPLC method development, understanding the sample's hydrophilicity or hydrophobicity is essential, as it guides the choice of stationary and mobile phases and other parameters for optimal separation (Siraj et al., 2024; Mestareehi, 2024). For hydrophobic compounds like Rivaroxaban, reverse-phase HPLC (RP-HPLC) is typically preferred, which uses a nonpolar stationary phase and a polar mobile phase, favoring the retention of hydrophobic analytes (ICH ICoH, 2005). The primary objective of this research was to develop a straightforward, efficient, selective, and precise isocratic RP-HPLC method tailored to determine Rivaroxaban in its raw form. This method also aimed to separate Rivaroxaban from its impurities and any degradation products, eliminating the need for additional separation steps. Several parameters were explored to establish the ideal conditions, focusing on achieving a high theoretical plate number (indicating column efficiency), well-defined peak shapes, minimal peak tailing for raw materials, and effective separation of Rivaroxaban from impurities and degradation products. The following studies were conducted to optimize these aspects, ensuring reliable and reproducible results.

Solubility studies of Rivaroxaban

The initial step in developing an HPLC method for analyzing Rivaroxaban involved determining its solubility in various solvents to identify an appropriate diluent. Rivaroxaban was tested for solubility in acetonitrile (ACN), methanol, deionized (DI) water, and combinations of these solvents. Approximately 1 mg of Rivaroxaban was dissolved in 3 mL each of ACN, DI water, and methanol individually, but it was found to be insoluble in these solvents alone. However, it was fully soluble in a mixture of 75:25 v/v ACN: DI water. Based on this result, a 70:30 v/v ACN: DI water mixture was chosen as the diluent for preparing Rivaroxaban solutions in further studies, as it provided sufficient solubility while being compatible with the HPLC method. The findings from this solubility testing are summarized in Supplementary Table S1.

Infrared (IR) study for Rivaroxaban

Infrared (IR) spectroscopy is among the most employed spectroscopic techniques for qualitative analysis, particularly useful for identifying chemical functional groups in various compounds. In the case of Rivaroxaban, IR spectroscopy serves as an effective tool to verify the presence and structure of specific functional groups within its raw material. The IR spectrum provides a "molecular fingerprint" by detecting vibrations in molecular bonds, allowing chemists to confirm the authenticity and purity of the compound. This method is particularly advantageous for confirming the structural integrity of Rivaroxaban and identifying any potential contaminants or impurities through their unique IR absorption patterns (ICH ICoH, 2005).

Weigh about 100 mg of Potassium Bromide (KBr) and 2 mg of Rivaroxaban raw materials. Mix the finely ground solid sample with powdered potassium bromide and press the mixture under high pressure. Potassium Bromide (KBr) under the pressure melts and seals the compound into a matrix. The result is a thin disk. KBr plates must be inserted into a holder to be analyzed by IR-Spectrometer.

The infrared spectrum of Rivaroxaban provides an idea of functional group, from left hand side, the spectrum exhibits at medium absorbing peak at about 3,350 cm^{-1} for N—H stretching frequencies, amides show a very strong band for the C=O group that appears at 1,644.45 cm^{-1}. Ester shows a very strong band for the C=O group that appears at 1733.43 cm^{-1}. The C=C stretching bands for aromatic rings appear between 1,600 cm^{-1} and 1,400 cm^{-1}. Primary chloride absorbs at 544.63 cm^{-1}. The infrared (IR) spectrum of Rivaroxaban is illustrated in Figure 2. The chemical functional groups were identified and listed below in Table 2.

Detector wavelength selection

Stock solution of Rivaroxaban (20 ppm)

Transfer 1.0 mL of stock solution of Rivaroxaban (1,000 ppm) into a 50 mL volumetric flask. Complete the volume to the mark with ACN: DI water (70:30 v:v) and shake it thoroughly.

To determine the optimal wavelength for Rivaroxaban analysis, 1 mL of a 20 ppm Rivaroxaban stock solution was transferred to a 1 cm quartz cuvette. The solution was scanned over a range of 200–400 nm using a Hitachi UV-VIS double-beam spectrometer as seen in Supplementary Figure S1. The scan revealed maximum absorbance peaks at 200 nm and 249 nm. However, 249 nm was selected as the analytical wavelength because it offered less noise

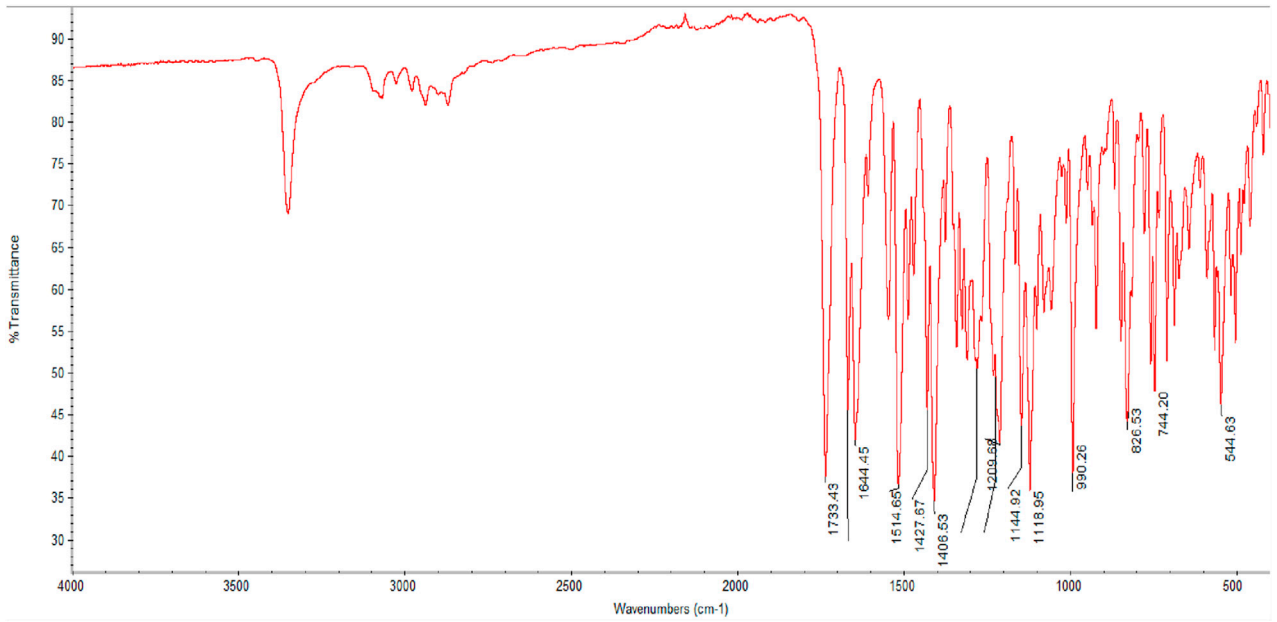

FIGURE 2
Infrared (IR) spectrum of Rivaroxaban using Thermo Nicolet IR 200 Spectrometer.

TABLE 2 IR correlation chart for rivaroxaban.

Frequency (cm^{-1})	Structural unit	Type of vibration	Intensity
3,350	Amide	N—H Stretch	Medium
1,733.43	Ester	C=O Stretch	Strong
1,644.45	Amide	C=O Stretch	Strong
1,514.65	Aromatic	C=C Stretch	Strong
1,500	Amine	Bend	Medium
1,427.64	Methylene	Scissoring	Strong
1,144.92	Ester	C—O Stretch	Strong
544.63	Chloride	C—Cl Stretch	Strong

compared to the shorter wavelength of 200 nm, enhancing the accuracy and stability of the measurements. This wavelength choice ensures clearer, more reliable data for quantitative analysis in this study.

Column selection

The second step in HPLC method development involved selecting the optimal column for Rivaroxaban analysis. Six different C18 columns were initially cleaned and conditioned by flushing them with solvents in the following sequence 50:50 v/v ACN: H_2O, 75:25 v/v ACN: H_2O, and 100% ACN. Each solvent mixture was passed through the columns for 30 min at a flow rate of 1 mL/min. This cleaning process helped achieve the appropriate peak shape, tailing, and theoretical plate number for Rivaroxaban. According to the International Council for Harmonisation (ICH) guidelines, acceptable peak shape requires a tailing factor between 0.9 and 2.0. These procedures are in line with standard practices for analytical method validation, as outlined in ICH guideline Q2(R2) on validation of analytical procedures. Additionally, the column should have a theoretical plate number (N) greater than 2,000 to ensure adequate resolution and efficiency for analytical separation (ICH ICoH, 2005). Each HPLC column was utilized twice for different tests. Prior to each use, we implemented rigorous cleaning and equilibration procedures to maintain column integrity and prevent cross-contamination. Details about each tested column are provided in Supplementary Table S2. In this study, 1,000 ppm of Rivaroxaban was injected into the HPLC system to evaluate the performance of six different C18 columns, as illustrated in Supplementary Figure S2. The columns were maintained at ambient temperature using a column thermostat, thereby enhancing the reliability and reproducibility of the analytical results.

TABLE 3 Column selection results.

Column #	Column C18	Retention times (min)	Tailing factor	Number of theoretical plates
1	Phenomenex (4.6 × 150 mm, 5 µm)	9.423	1.50	6,128
2	WATER (4.6 × 150 mm, 5 µm)	9.460	0.78	6,968
3	Agilent Zorbax (4.6 × 250 mm, 5 µm)	7.814	1.30	2,516
4	WATER (4.6 × 250 mm, 5 µm)	11.893	0.976	5,709
5	Phenomenex (4.6 × 250 mm, 5 µm)	15.727	1.219	4,168
6	Thermo Hypersil ODS (4.6 × 250 mm, 5 µm)	11.448	0.940	7,890

All six columns were evaluated under the same chromatographic conditions, including flow rate, injection volume, temperature, and mobile phase, to maintain consistency in the method development process. The results indicated that Column #2 did not meet the ICH acceptance criteria due to a tailing factor below 0.90, which suggested inadequate peak symmetry. Column #3 achieved a tailing factor of 1.30 and a theoretical plate count of 2,516, which met ICH requirements but was lower in performance compared to other columns. Columns 1, 4, 5, and 6 all demonstrated satisfactory numbers of theoretical plates and acceptable tailing factors. Ultimately, Column #6 was selected for further studies, as it provided the most favorable performance. With a tailing factor of 0.94 and 7,890 theoretical plates, Column #6 demonstrated superior efficiency and peak shape relative to the other columns. Detailed information on each column tested is presented in Table 3.

Selection pH of the mobile phase

Controlling pH in a reverse-phase HPLC system is critical to maintaining stable retention times and selectivity, particularly with silica-based columns where free silanol groups on the stationary phase can adsorb basic compounds, leading to unwanted secondary interactions, peak tailing, and poor peak shape. This is especially relevant for Rivaroxaban, a weak base that could interact with the silanol groups through hydrogen bonding, resulting in tailing that interferes with quantification accuracy. Adjusting the pH to 2.9 keeps the silanol groups protonated, reducing their potential interactions with Rivaroxaban, and improving both retention stability and peak shape.

In this study, a 1,000 ppm Rivaroxaban solution was injected under various pH conditions (2.9, 5.0, and 7.0) using a mobile phase consisting of ACN (phase B) at a 70:30 v/v ratio with the buffer (phase A), as shown in Figure 3. The chromatograms confirmed that pH 2.9 was optimal, minimizing secondary interactions and enhancing chromatographic performance. Supplementary Table S3 summarizes these findings, showing only slight differences in retention time, tailing factor, and theoretical plates across the tested pH levels. However, pH 2.9 provided the highest number of theoretical plates, indicating superior column efficiency and separation, as illustrated in Figure 3. Thus, potassium phosphate monobasic buffer at pH 2.9 was chosen for subsequent method development and validation, achieving an effective balance between retention, peak quality, and chromatographic performance.

Isocratic elution studies

Optimizing method validation often involves adjusting the isocratic elution composition. Different ratios of buffer (pH 2.9) and acetonitrile (ACN) were explored to achieve a retention time of approximately 10–13 min, allowing enough time for impurities and degradants to be separated before the main peak. In this study, a 1,000 ppm standard solution of Rivaroxaban was analyzed using various ratios of buffer pH 2.9 (mobile phase A) and ACN (mobile phase B) (v/v). The resulting chromatograms, shown in Figure 4, summarize the retention times, peak areas, and tailing factors, detailed in Supplementary Table S4. When using a 50:50 v/v ratio of buffer pH 2.9 and ACN, Rivaroxaban eluted at 4.55 min, which was too short for effective separation, especially for degradation studies. Further testing with different ACN to buffer ratios ultimately demonstrated that a 70:30 v/v ratio yielded an optimal retention time near 12 min for Rivaroxaban, allowing for more efficient separation of potential impurities and degradants. Therefore, the 70:30 v/v buffer pH 2.9: ACN ratio was selected as the optimal mobile phase composition for further analysis, ensuring improved chromatographic performance. Detailed chromatograms and conditions are presented in Figure 4, with supporting results in Supplementary Table S4.

Selection of injection volume

Injections of 25 µL and 20 µL of Rivaroxaban led to peak splitting due to saturation of the column's packing material, resulting in volume overload. This overload effect can compromise peak integrity by causing distortion, impacting the accuracy of quantitative analysis. To prevent these issues, the injection volume was reduced to 15 µL, which allowed for clear, well-defined peaks without overloading the column. This optimized volume was chosen for subsequent method development to ensure consistent, reliable chromatographic results. The chromatograms reflecting these adjustments, along with the chromatographic conditions, are shown in Supplementary Figure S3.

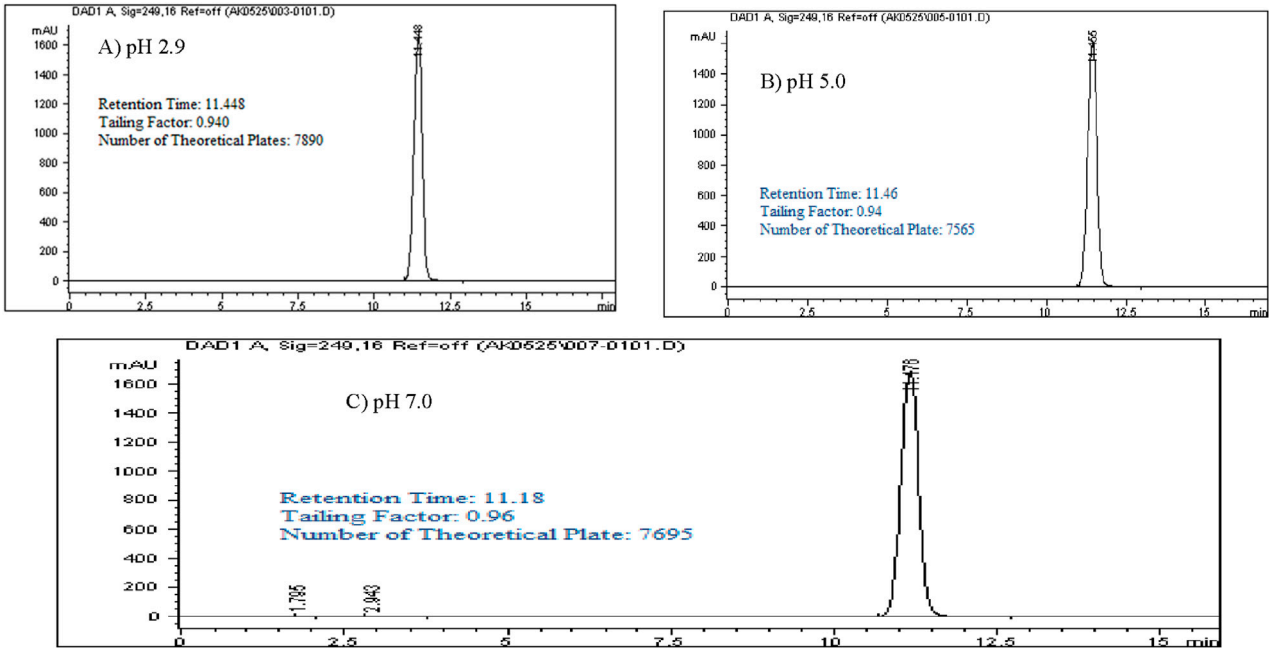

FIGURE 3
Chromatograms with a mobile phase concentration of 30:70 ACN/buffer pH. **(A)** pH 2.9: 25 mM potassium phosphate buffer monobasic pH 2.9. **(B)** pH 5.0: 25 mM sodium acetate buffer pH 5.0. **(C)** pH 7.0: 25 mM dibasic potassium phosphate buffer pH 7.0. Chromatographic conditions: Isocratic elution, mobile phase 30:70 ACN/buffer, flow rate 1.0 mL/min, detection wavelength at 249 nm, ambient temperature, 15 µL injection volume thermo hypersil ODS C_{18} (4.6 × 250 mm, 5 µm) column.

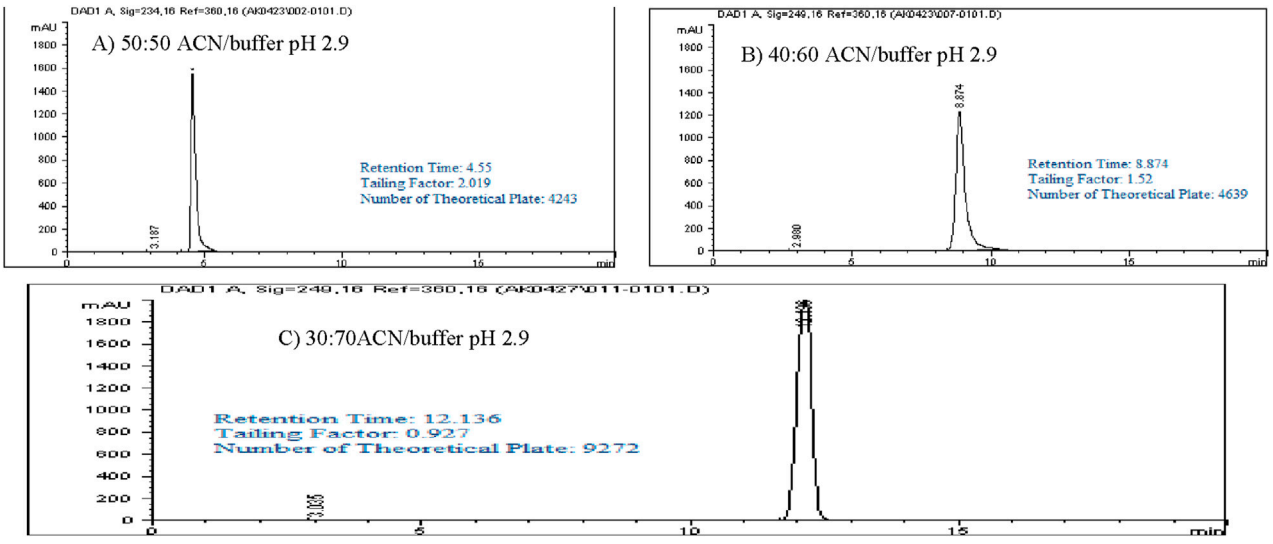

FIGURE 4
Chromatograms of Rivaroxaban with a different mobile phase concentration of ACN/buffer. **(A)** 50:50 ACN/buffer pH 2.9. **(C)** 30:70 ACN/buffer pH 2.9. **(B)** 40:60 ACN/buffer pH 2.9. Chromatographic conditions: Isocratic elution, mobile phase ACN/25 mM potassium phosphate buffer monobasic pH 2.9, flow rate 1.0 mL/min, detection wavelength at 249 nm, ambient temperature, 15 µL injection volume, thermo hypersil ODS C_{18} (4.6 × 250 mm, 5 µm) column.

Nominal concentration selection

To determine the nominal concentration for Rivaroxaban analysis, a calibration curve was established within the linear response range of the detector. Calibration curves are essential in analytical method validation, as they ensure that the detector's response to various concentrations of the analyte is consistent and proportional. By selecting concentrations within this linear range, the analysis becomes more accurate and reliable, minimizing potential errors due to detector saturation or nonlinearity at higher concentrations.

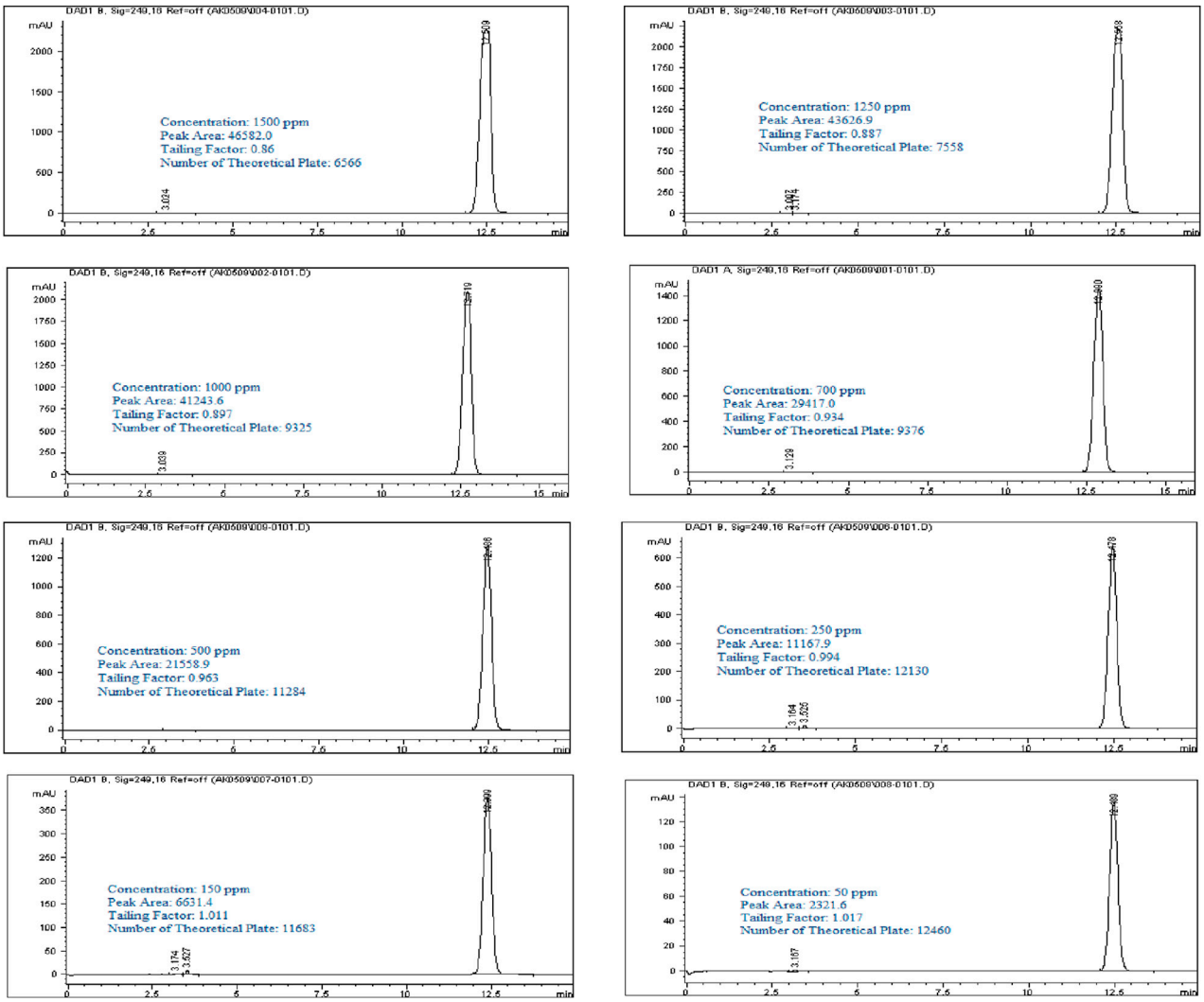

FIGURE 5
Chromatograms of Rivaroxaban for nominal concentration Selection. Chromatographic conditions: Isocratic elution, mobile phase 30:70 ACN/25 mM potassium phosphate buffer monobasic pH 2.9, flow rate 1.0 mL/min, detection wavelength at 249 nm, ambient temperature, 15 µL injection volume, thermo hypersil ODS C_{18} (4.6 × 250 mm, 5 µm) column.

Stock solution of Rivaroxaban (10,000 ppm)

Weigh 500 mg of Rivaroxaban and transfer it into a 50 mL volumetric flask. Add 25 mL of ACN: DI water (70:30 v/v) and sonicate for 20 min or until Rivaroxaban completely dissolved. Complete the volume to the mark with ACN: DI water (70:30 v/v) and shake it thoroughly.

A stock solution of Rivaroxaban at a concentration of 10,000 ppm was used to prepare a series of diluted solutions with concentrations of 1,500 ppm, 1,250 ppm, 1,000 ppm, 700 ppm, 500 ppm, 250 ppm, 150 ppm, and 50 ppm (shown in Supplementary Materials). These serial solutions were analyzed by injecting them into the HPLC system under the optimized isocratic elution conditions. The chromatograms, chromatographic conditions, and peak areas corresponding to each concentration can be viewed in Figure 5, with the peak area results summarized in Table 4. This approach allows for accurate calibration and validation across a range of concentrations, ensuring reliable quantitation in further analysis.

It was observed that the concentrations of 1,500 ppm and 1,250 ppm fell outside the linear response range of the detector, as shown in Figure 6A. Therefore, the linearity test confirmed a linear response within the concentration range of 50–1,000 ppm. A calibration curve for Rivaroxaban was created by plotting peak area against concentration, yielding a high linear correlation coefficient of 0.9995, as depicted in Figure 6B. To determine the nominal concentration, a concentration at 70% of the highest value within the linear range was selected. Consequently, 700 ppm was chosen as the nominal concentration and will serve as the reference concentration for further method development studies. This ensures accurate and consistent results within the linear response range of the detector, optimizing the method's reliability and precision.

Mixed degradation study (acid, base, and oxidation)

The objective of the mixed degradation study was to assess the capability of the developed HPLC method to effectively

TABLE 4 Summary of nominal concentration selection.

Sample #	Concentration (ppm)	Peak area (mAu)
1	1,500	46,582
2	1,250	43,626.9
3	1,000	41,244
4	700	29,417
5	500	21,558.9
6	250	11,168
7	150	6,631.4
8	50	2,321.6

separate Rivaroxaban from all potential degradants and impurities, ensuring accurate quantification and purity assessment (ICH ICoH, 2005; United States pharmacopeia X, 1990). For this study, a control sample of 700 ppm was prepared from a 3,500 ppm stock solution of Rivaroxaban and injected into the HPLC system to establish a baseline for comparison. This control sample chromatogram, shown in Figure 7A, allows for calculating the percent degradation of Rivaroxaban after mixed degradation conditions are applied, confirming that the method can distinguish between the active ingredient and any degradative by products.

Transfer 1 mL of each the stress degraded solutions that produced less than 10% degradation (0.01 N HCl for 24 h, 0.01 N NaOH for 1 h, and 0.05% H_2O_2 for 24 h), into a test tube. Mix the solution thoroughly and filter with (0.45 µm membrane filter) before injected into the HPLC system. The chromatogram of Rivaroxaban from mixture degradation study is shown in Figure 7B.

The study showed that Rivaroxaban's primary degradants eluted at retention times of 8.3, 9.0, and 9.4 min. These peaks were completely separated from the main Rivaroxaban peak, which eluted at approximately 12 min, confirming the method's capacity to distinctly resolve the active ingredient from its degradation products. This separation ensures that the developed HPLC method is suitable for accurately identifying and quantifying Rivaroxaban without interference from degradants. The detailed degradation results for each study condition are summarized in Table 5.

Method validation

To ensure compliance with Good Laboratory Practice (GLP) and Good Manufacturing Practice (GMP), the developed analytical

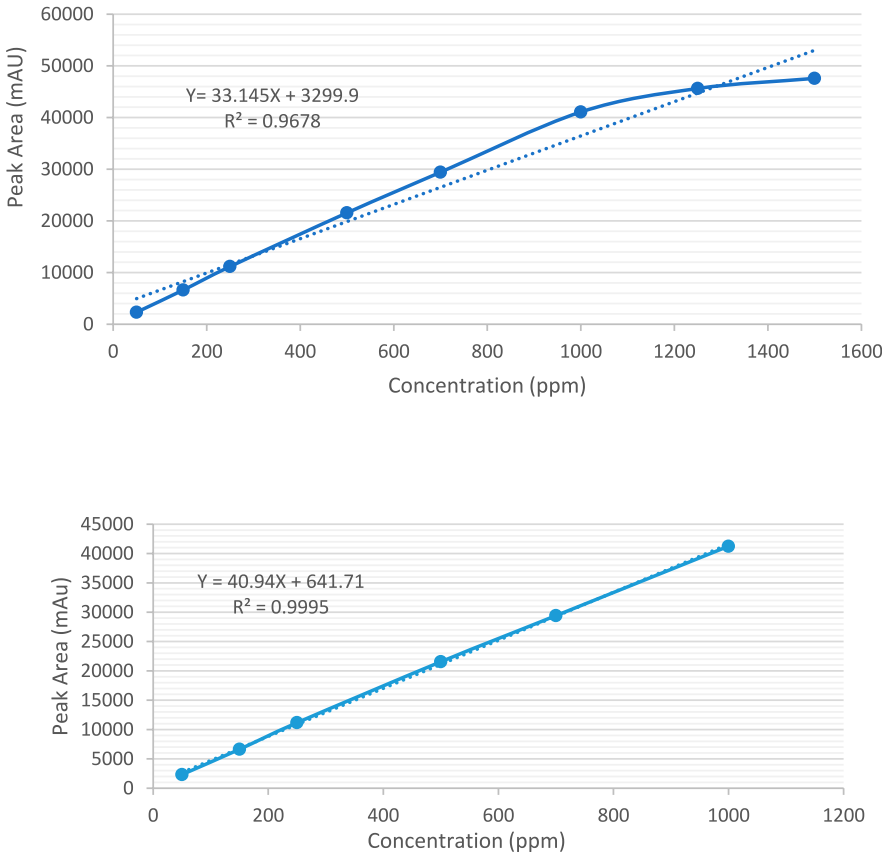

FIGURE 6
(A) Calibration curve for the quantification of Rivaroxaban across a concentration range of 50 ppm–1,500 ppm. **(B)** Calibration curve for the quantification of Rivaroxaban across a concentration range of 50 ppm–1,000 ppm.

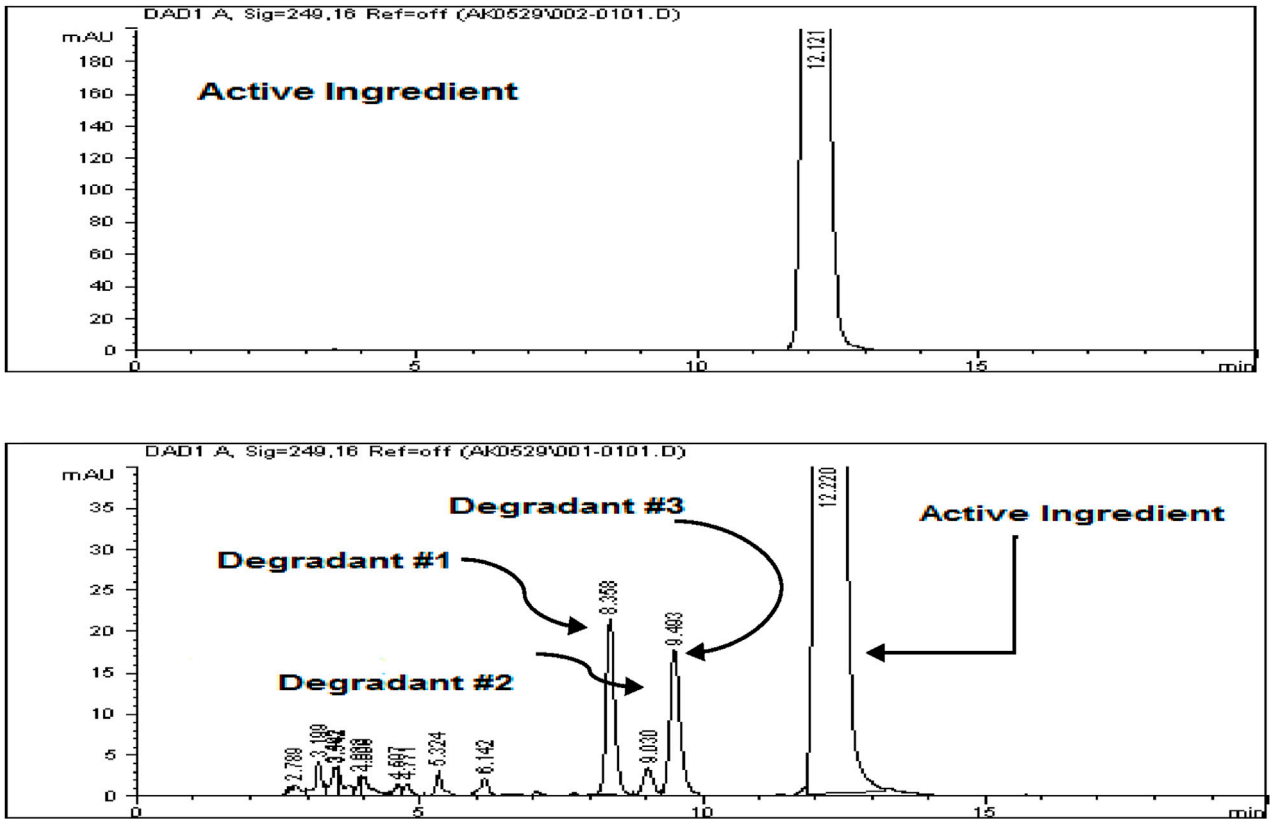

FIGURE 7
(A) Chromatograms of Rivaroxaban 700 ppm control solution used for degradation study. **(B)** Zoomed in chromatogram of the optimized mixed degradation study. Chromatographic conditions: Isocratic elution, mobile phase 30:70 ACN/25 mM potassium phosphate buffer monobasic pH 2.9, flow rate 1.0 mL/min, detection wavelength at 249 nm, ambient temperature, 15 µL injection volume, thermo hypersil ODS C_{18} (4.6 × 250 mm, 5 µm) column.

TABLE 5 Mixed degradation study results under optimized chromatographic conditions.

Stress condition	Exposed time	Temperature (°C)[a]	Color	Peak area	% degradation
None	None	None	Clear	29,894.4	----
0.01 N HCl	24 h	75	Clear	26,868.3	8.80
0.01 N NaOH	One hour	75	Clear	27,074.50	8.10
0.05% H_2O_2	24 h	75	Clear	28,837.0	6.50
Mixture solution	-	-	Clear	27,144.12	9.20

[a]Heat it on a heating block at 75°C for the specified duration.

method must meet the validation requirements outlined by several authoritative guidelines, such as the ICH (International Conference on Harmonization) guidelines Q2A and Q2B (ICH ICoH, 2005), the FDA (U.S. Food and Drug Administration) (FDA, 2004), and the USP (U.S. Pharmacopeia) (United States pharmacopeia X, 1990). The following key validation parameters were evaluated to confirm the method's reliability and accuracy:

- System Suitability Test (SST): This verifies that the HPLC system meets the desired analytical standards before sample analysis, ensuring consistent performance.
- Specificity: Ensures that the method can clearly distinguish Rivaroxaban from impurities and degradants, demonstrating it is free from interference.
- Method Robustness: Assesses the method's reliability under varied conditions, such as slight changes in pH or solvent composition.
- Solution Stability: Confirms that the Rivaroxaban solution remains stable over the testing period without degradation.
- Linearity and Range: Establishes that the method produces accurate results over a specified concentration range.
- Method Accuracy and Precision: Includes:
  - Method Precision: Reproducibility of results within the same method over time.
  - Injection Precision: Consistency of injection volumes and peak areas.
  - Intermediate Precision: Method reliability across different days and analysts.

- Limit of Detection (LOD) and Limit of Quantitation (LOQ): Defines the minimum concentration at which impurities or degradants can be reliably detected and quantified. This comprehensive validation, following ICH and FDA guidelines, ensures the method's suitability for high-quality, reproducible analysis of Rivaroxaban.

System suitability

System suitability test (SST) is a vital component of HPLC analysis as recommended by the ICH Q2R1 guidelines. It ensures that the HPLC system and related components such as equipment, software, electronics, and samples are operating correctly and consistently. System suitability tests help establish that the method's performance is reliable before analyzing samples, ensuring high data integrity and accuracy. The key SST parameters and acceptance criteria for HPLC, as specified by the guidelines, are (ICH ICoH, 2005):

- Relative standard deviation (RSD) of response of replicate injections NMT 1%
- Relative standard deviation (RSD) of retention time of replicate injections NMT 1%
- Number of theoretical plates MT 2000
- Tailing factor between 0.9 and 2
- Capacity factor greater than 2
- Resolution values greater than 2.0
- % Drift $\leq$ 2

These criteria collectively confirm that the HPLC system is suitable for analysis and can reliably deliver accurate and reproducible results. By meeting these benchmarks, laboratories can ensure the precision, accuracy, and consistency of their analyses as per regulatory standards.

Standard solutions preparation for system suitability

Stock standard solution of Rivaroxaban (10,000 ppm)

Weigh 500 mg of Rivaroxaban and transfer it into a 50 mL volumetric flask. Add 25 mL of ACN: DI water (70:30 v/v) and sonicate for 20 min or until Rivaroxaban is completely dissolved. Complete the volume to the mark with ACN: DI water (70:30 v/v) and shake it thoroughly.

Working standard solution of Rivaroxaban (700 ppm) #1

Transfer 3.5 mL of stock solution Rivaroxaban (10,000 ppm) into a 50 mL volumetric flask. Complete the volume to the mark with ACN: DI water (70:30 v/v) and shake it thoroughly.

Working standard solution of Rivaroxaban (700 ppm) #2

Transfer 3.5 mL of stock solution Rivaroxaban (10,000 ppm) into a 50 mL volumetric flask. Complete the volume to the mark with ACN: DI water (70:30 v/v) and shake it thoroughly.

System suitability tests were performed by injecting the working standard solutions of Rivaroxaban (labeled as #1 and #2) to confirm the reliability and consistency of the HPLC system. The working standard solution #1 was injected six times consecutively, as illustrated in Figure 8, while solution #2 was injected twice, as shown in Figure 8. The results from these injections were used to calculate key system suitability parameters, including the %RSD of peak area and retention time for Rivaroxaban #1 (six injections) and Rivaroxaban #2 (two injections). This metric ensures consistent peak responses and retention times. Tailing Factor and Number of Theoretical Plates were calculated for each peak to assess peak shape and column efficiency.

The percentage drift (% Drift) was calculated by using equation below:

$$\%\,\text{Drift} = \frac{\text{As} - \text{Ac}}{\text{As}}\ \text{x}\ 100$$

where $\mathbf{A_S}$ is the average peak area of six replicate injection of working standard solution #1 and $\mathbf{A_C}$ is the average peak area of two replicate injections of working standard solution #2.

The percent relative standard deviations were calculated by using equation below.

$$\%\,\text{RSD} = \frac{S}{Xave} x100$$

where %RSD is the relative standard deviation, S is the standard deviation, $Xave$ is the average value of measurements.

$$S = \sqrt{\frac{1}{n-1}\sum_{i=1}^{N}(x_i - \bar{x})}$$

where S is the standard deviation, x_i is the value of measurement i, x is the average value of measurements and N is the number of measurements.

Specificity

Specificity measures the ability of a method to accurately identify and quantify the target analyte, Rivaroxaban, in the presence of degradants, impurities, and other related compounds within the sample matrix. The specificity of an analytical method ensures that it effectively isolates the analyte peak from other components without interference. Acceptance Criteria for Specificity are The peak purity factor should exceed 990, indicating a pure peak without co-elution, Peaks must be well-separated, with a resolution greater than 2 to confirm baseline separation, and No interference from impurities, degradants, or related substances should affect the peak of interest, Rivaroxaban (ICH ICoH, 2005). This study aims to confirm that the method is specifically measuring the Rivaroxaban peak with accurate concentration, clearly separated from any degradants or impurities.

Mixed degradation samples were prepared by combining 1 mL each from acid, base, and oxidative degradation solutions with degradation levels under 10%: 0.01 N HCl (8.8% degradation over 24 h), 0.01 N NaOH (8.1% degradation for 1 hour), and 0.05% H_2O_2 (6.5% degradation over 24 h). The solutions were combined, thoroughly mixed, and filtered through a 0.45 µm membrane filter. The sample was then injected into an Agilent 1100 HPLC system equipped with a Diode Array Detector (DAD).

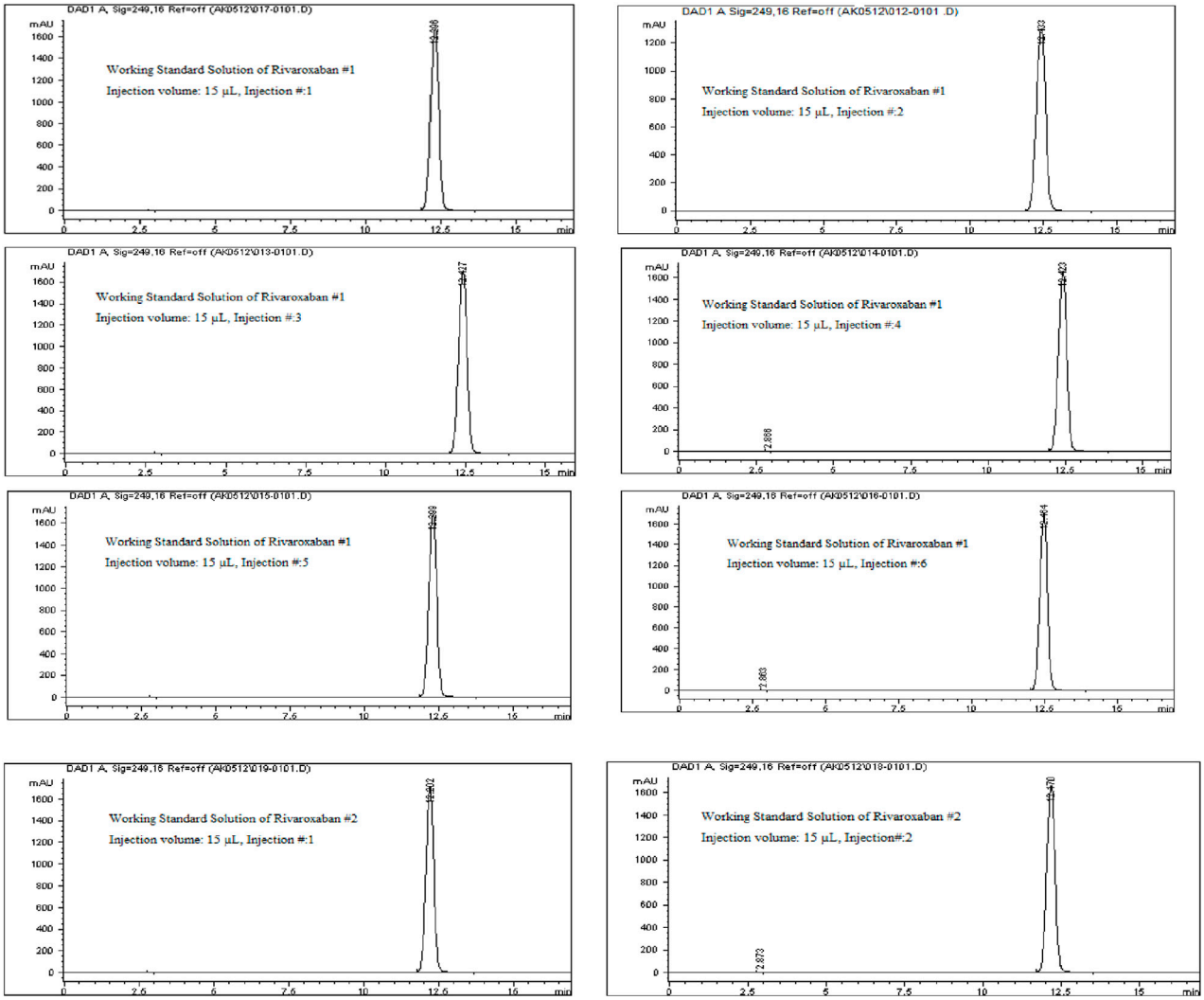

FIGURE 8
Chromatograms of the working standard solution for Rivaroxaban from System Suitability Study #1 and System Suitability Study #2. Chromatographic conditions: Isocratic elution, mobile phase 30:70 ACN/25 mM potassium phosphate buffer monobasic pH 2.9, flow rate 1.0 mL/min, detection wavelength at 249 nm, ambient temperature, 15 µL injection volume, thermo hypersil ODS C_{18} (4.6 × 250 mm, 5 µm) column.

Method Robustness

The robustness of an analytical method tests its ability to remain consistent and unaffected by minor, deliberate changes in parameters. This is a key part of method validation under ICH guidelines, as it helps ensure that the method performs reliably under varied conditions in practical applications (ICH ICoH, 2005). In this study, robustness was assessed by adjusting five critical parameters:

- Buffer pH: (2.9 ± 0.2)
- Flow Rate: (1.0 ± 0.2 mL/min)
- Wavelength: (249 ± 2 nm)
- % B Composition: (30 ± 5% B)
- Volume injected: (15 ± 2 μ L)

The acceptance criteria for robustness are listed below (ICH ICoH, 2005):

- Tailing factor between 0.9 and 2.0
- Number of Theoretical plates ≥ 2,000
- All peaks should be separated from the peak of interest by RS > 2.0

Mobile phase A (buffer pH 2.9)

To prepare 1 L of 25 mM potassium phosphate monobasic solution at pH 2.90.

Weigh 3.40 g of potassium phosphate monobasic and transfer it into a 1,000 mL beaker. Add 1,000 mL of DI water and stir until buffer salt is completely dissolved. Place a calibrated pH probe into the solution and adjust the pH by slowly adding phosphoric acid dropwise. Stop once the desired pH of 2.9 is reached. Filter the buffer by using (0.45 µm membrane filter) and sonicate for 20 min to remove any air bubbles.

For further analysis, additional mobile phases with buffer pH adjustments were prepared at pH 3.1 and pH 2.7, following the same method previously established. Each prepared mobile

phase was introduced individually into the HPLC system to assess their impact on the retention and peak shape of the analyte. This allowed for comparison of chromatographic performance at slightly different pH values to ensure robustness and fine-tune separation parameters. This step helps confirm that the method provides consistent results across slight variations in buffer pH, which is essential for method validation.

Transfer 1 mL of each of the stress degraded solutions that produced less than 10% degradation (0.01 N HCl for 24 h, 0.01 N NaOH for 1 h and 0.05% H_2O_2 for 24 h) into a test tube. Mix the solution thoroughly and filter with (0.45 µm membrane filter) before injecting into the Agilent 1100 HPLC system with Diode Array Detector (DAD).

Solution stability

The purpose of solution stability testing is to assess how the analyte of interest, in this case Rivaroxaban, responds over time to various environmental factors such as temperature, light, and humidity (Administration FaD, 2003). By examining these influences, solution stability ensures accurate and reliable quantification of the analyte in routine analysis, which is crucial for method validation.

Solution stability was evaluated by measuring the percent change in the peak area over time, comparing the initial (immediate) injection with subsequent injections at 24, 48, and 72 h. This method helps to detect any degradation or instability in the analyte under different storage or testing conditions. The % change in peak area was calculated using the following formula:

$$\%\ \text{Change in area} = \frac{At - Ai}{Ai} x100$$

A_t is a Peak Area at different time t and A_i is a Peak Area at initial time i.

No new peaks or lost peaks should appear in the chromatographic profile between the first and last injections, indicating no significant degradation or instability in the solution over the course of the analysis (ICH ICoH, 2005).

Linearity and range for active ingredient (Rivaroxaban)

To assess the linearity of Rivaroxaban, a stock solution of 5,000 ppm was used to prepare a serial dilution series with concentrations of 850 ppm, 800 ppm, 750 ppm, 700 ppm, 650 ppm, 600 ppm, 550 ppm, and 500 ppm. Each solution was injected into the HPLC system under the established optimum conditions, and their chromatograms, along with relevant chromatographic parameters, are shown in Figure 9. The corresponding peak area results are detailed in Table 6.

For the linearity, the correlation coefficient for Rivaroxaban must be at least 0.999 to meet acceptance criteria, ensuring that the relationship between concentration and detector response is linear within the tested range. This high threshold confirms the method's reliability for quantitative analysis across the concentration range.

Stock solution of Rivaroxaban (5,000 ppm)

Weigh 250 mg of Rivaroxaban and transfer it into a 50 mL volumetric flask. Add 25 mL of ACN: DI water (70:30 v/v) and sonicate for 20 min until Rivaroxaban is completely dissolved. Complete the volume to the mark with ACN: DI water (70:30 v/v) and shake it thoroughly.

A stock solution of Rivaroxaban with a concentration of 5,000 ppm was used to prepare a series of diluted solutions at concentrations of 850 ppm, 800 ppm, 750 ppm, 700 ppm, 650 ppm, 600 ppm, 550 ppm, and 500 ppm (shown in Supplementary Materials). These solutions were analyzed using HPLC under optimized isocratic elution conditions. The resulting chromatograms, chromatographic parameters, and corresponding peak areas for each concentration are presented in Figure 9, with a summary of peak area results provided in Table 7.

Accuracy

The accuracy of the developed HPLC method was evaluated to assess how closely the measured values align with the true or theoretical values. To determine accuracy, Rivaroxaban solutions were prepared in triplicate at 80%, 100%, and 120% of the nominal concentration (700 ppm) for the active ingredient. The acceptance criteria for method accuracy were defined as follows: For the active ingredient, the percent recovery should be between 95% and 105% of the theoretical value. These criteria ensure that the method can reliably and accurately quantify the active ingredient, as well as any impurities and degradants, across a range of concentrations.

To assess the accuracy of the developed method for the active ingredient, a stock solution of Rivaroxaban (5,000 ppm) was diluted to prepare samples with concentrations of 850 ppm, 700 ppm, and 500 ppm. These samples were then analyzed by injecting them into the HPLC system, and the corresponding peak areas were recorded. The percentage recovery of the active ingredient was calculated using the linear regression equation derived from the calibration curve, Y = 41.716X + 971.04, as shown in Figure 10. Here: y represents the peak area of the injected sample, and x corresponds to the concentration of Rivaroxaban in ppm. Using this equation, the calculated concentration could be compared to the theoretical concentration to determine the percent recovery for each sample. These results are summarized in Table 8, which shows that the method meets the accuracy criteria by achieving recoveries within the acceptable range of 95%–105%.

$$\textbf{Percentage Recovery} = \frac{\textit{Csample}}{\textit{Cstandard}} \textbf{x100}$$

Csample: Measured concentration of the sample obtained from linear regression equation.

Cstandard: Actual concentration of the prepared sample.

Triplicate samples at each concentration level (850 ppm, 700 ppm, and 500 ppm) were injected into the HPLC system to ensure precision and accuracy in the results. The corresponding chromatograms for these injections, along with detailed chromatographic conditions, are presented in Supplementary Figures S10–S12. These figures illustrate the method's reproducibility and the stability of the results across multiple

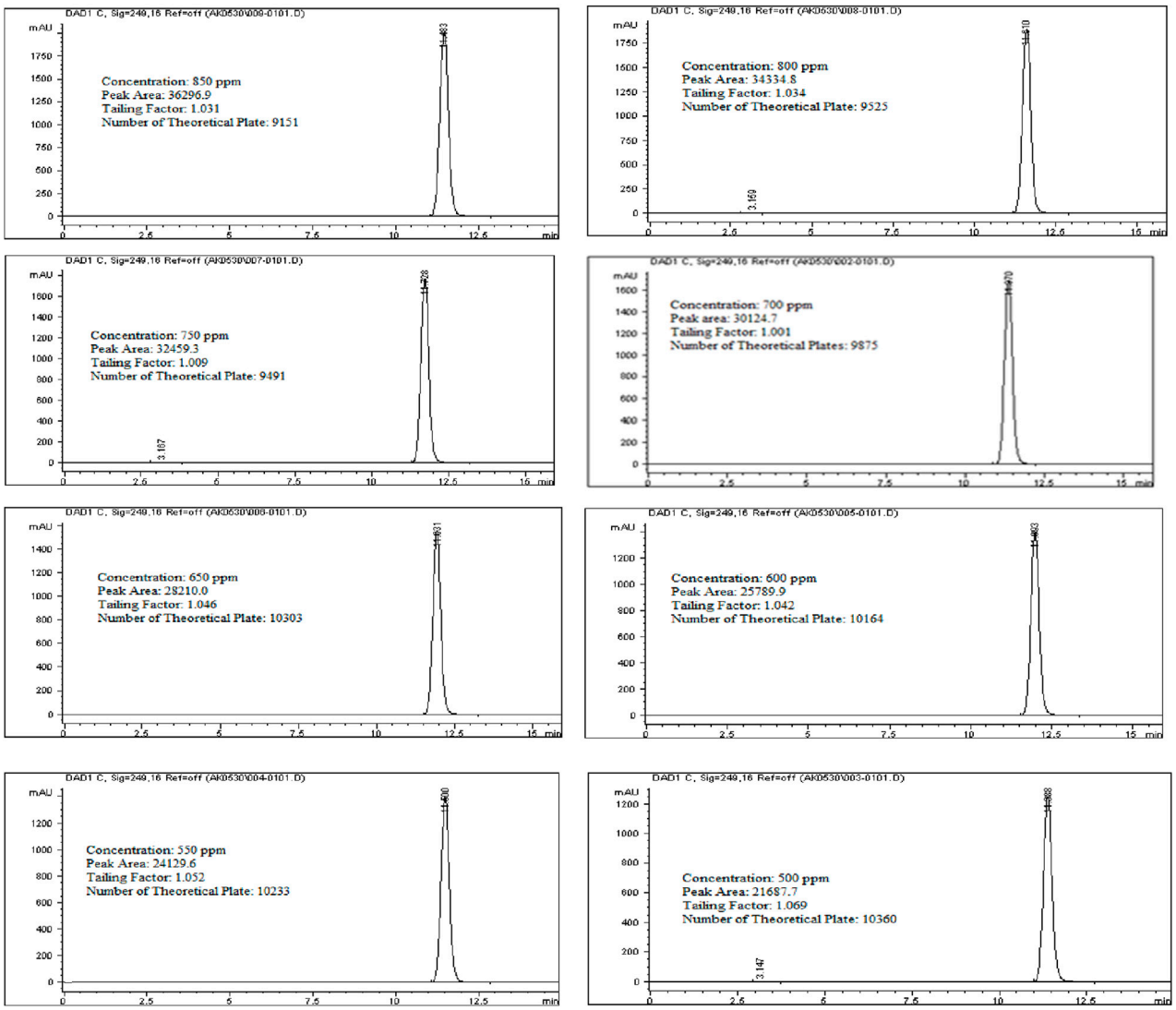

FIGURE 9
Chromatograms for linearity and range study for Rivaroxaban active ingredient. Chromatographic conditions: Isocratic elution, mobile phase 30: 70 ACN/25 mM potassium phosphate buffer monobasic pH 2.9, flow rate 1.0 mL/min, detection wavelength at 249 nm, ambient temperature, 15 µL injection volume, thermo hypersil ODS C_{18} (4.6 × 250 mm, 5 µm) column.

injections, confirming that the developed method meets the required accuracy and reliability standards for quantifying Rivaroxaban at various concentration levels.

Method precision

The precision of an analytical method reflects the consistency and reliability of the measurements taken under the same conditions, defined by how closely multiple measurements of the same concentration match each other. According to the International Council for Harmonisation (ICH) guidelines, precision is categorized into three main levels (ICH ICoH, 2005):

1. Repeatability: This refers to the closeness of results when the same analyst performs multiple injections or measurements of the same sample, using the same instrument and method over a short period of time.
2. Intermediate Precision: Also known as within-laboratory precision, it assesses variations within the same lab but includes different conditions, such as different days, analysts, or instruments.
3. Reproducibility: This measures the precision between laboratories, indicating how well the method performs across different labs.

Each level of precision provides important insights into the method's robustness and consistency in diverse settings, ensuring that results are reliable and reproducible.

Repeatability (method precision)

Repeatability evaluates the method's reliability by determining the variability that may arise from sample

TABLE 6 Limit of detection study results.

Sample #	Concentration (ppm)	Peak area	Retention time	Signal to noise ratio
1	10.0	415.81	11.54	117.2
2	5.0	185.54	11.90	41.0
3	2.0	107.47	11.47	31.7
4	1.5	69.40	11.49	18.1
5	1.3	60.13	11.62	16.2
6	1.0	51.91	11.79	10.80
7	0.90	40.63	12.0	7.50
8	0.50	25.17	11.75	6.20
9	0.40	17.58	11.76	5.70
10	0.30	12.85	11.85	4.0
11	0.20	9.91	11.83	2.6

TABLE 7 Linearity results for rivaroxaban active ingredient.

Sample #	Concentration (ppm)	Peak area (mAu)
1	850	36,296.9
2	800	34,334.8
3	750	32,459.3
4	700	30,124.7
5	650	28,210
6	600	25,789.9
7	550	24,130.9
8	500	21,687.7

preparation errors by the same analyst under identical operating conditions. This level of precision helps assess the method's sensitivity to minor operational changes, ensuring consistent and reliable results. The acceptance criteria for method precision are stringent, as per regulatory standards. Specifically, the % Relative Standard Deviation (%RSD) of the peak area for the compound of interest should not exceed 1% (NMT 1%).

To assess repeatability for Rivaroxaban's active ingredients, six separate samples of a 700 ppm concentration were prepared and injected into the HPLC system using the method's optimized chromatographic conditions, as illustrated in Supplementary Figure S13. The % Relative Standard Deviation (% RSD) of peak areas for these injections was then calculated to confirm the consistency and reliability of the method. Meeting the repeatability criteria, as outlined in the acceptance guidelines, demonstrates that the method consistently yields precise measurements for the target compound under the same experimental conditions.

Stock solution of Rivaroxaban (700 ppm)

Weigh 35 mg of Rivaroxaban and transfer it into a 50 mL volumetric flask. Add 25 mL of ACN: DI water (70:30 v/v) and sonicate for 20 min or until Rivaroxaban is completely dissolved. Complete the volume to the mark with ACN: DI water (70:30 v/v) and shake it thoroughly.

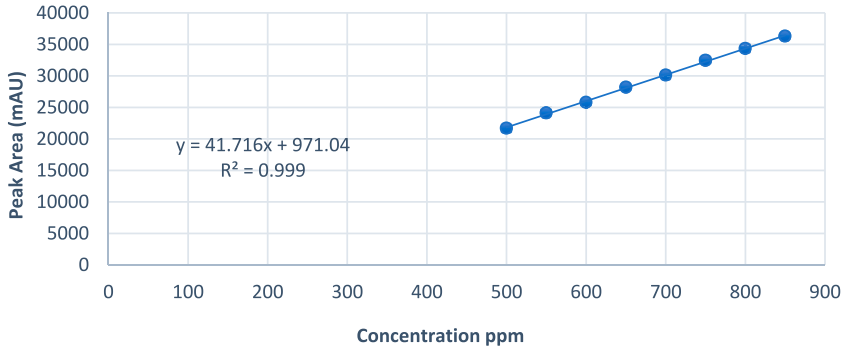

FIGURE 10
Peak area vs. concentration plot of Rivaroxaban for linearity study.

TABLE 8 Limit of quantitation study results.

Sample #	Concentration (ppm)	Peak area	Retention time	Signal to noise ratio
1	1.0	50.44	11.58	11.8
2	1.0	51.55	11.68	11.0
3	1.0	52.44	11.70	11.7
4	1.0	49.97	11.70	10.7
5	1.0	52.18	11.68	12.1
6	1.0	52.03	11.63	11.2
7	1.0	51.56	11.58	12.2
8	1.0	51.16	11.50	10.6
9	1.0	52.13	11.53	10.8
10	1.0	51.73	11.55	10.5
Average		51.52		11.26
Standard deviation		0.793		0.64
%RSD		1.54		5.68

Injection precision

Injection precision assesses the consistency of the method regarding instrument-related errors, including potential variability from the column, injector, detector, and integration device during sample injection. According to the acceptance criteria, the % RSD for the peak area of Rivaroxaban should not exceed 1%. To demonstrate injection precision for the active ingredient, a single Rivaroxaban sample at 700 ppm was prepared and injected six times into the HPLC system under optimized conditions. As shown in Supplementary Figure S14, the % RSD of the peak areas was calculated and found to meet the required acceptance criteria, confirming the method's reliability in terms of injection precision.

Stock solution of Rivaroxaban (700 ppm)

Weigh 35 mg of Rivaroxaban and transfer it into a 50 mL volumetric flask. Add 25 mL of ACN: DI water (70:30 v/v) and sonicate for 20 min or until Rivaroxaban is completely dissolved. Complete the volume to the mark with ACN: DI water (70:30 v/v) and shake it thoroughly.

A single Rivaroxaban sample at a concentration of 700 ppm was prepared and injected six times into the HPLC system under optimized chromatographic conditions. The peak areas were measured, and the % RSD for injection precision was calculated. The results, shown in Supplementary Table S7, met the acceptance criteria for injection precision, confirming that the method is consistent and precise for the Rivaroxaban active ingredient.

Intermediate precision (robustness)

Intermediate precision for the Rivaroxaban analytical method was assessed by evaluating the consistency of results across variations in conditions, such as different analysts, dates, instruments, and columns. According to the acceptance criteria for intermediate precision, the % RSD of peak area for Rivaroxaban raw material should not exceed 1.5%. To determine the reproducibility of the method under varying conditions, six samples of 700 ppm Rivaroxaban were prepared. These samples were injected into different HPLC systems, with different columns, under the same developed method but using different equipment and on different dates. The chromatograms and conditions for the analysis are presented in Supplementary Figure S15, and the results for the peak areas are detailed in Supplementary Table S8.

Stock solution of Rivaroxaban (5,000 ppm)

Weigh 250 mg of Rivaroxaban and transfer it into a 50 mL volumetric flask. Add 25 mL of ACN: DI water (70:30 v/v) and sonicate for 20 min or until Rivaroxaban is completely dissolved. Complete the volume to the mark with ACN: DI water (70:30 v/v) and shake it thoroughly.

Stock solution of Rivaroxaban (700 ppm)

Transfer 7.0 mL of stock solution Rivaroxaban (5000 ppm) into a 50 mL volumetric flask. Complete the volume to the mark with ACN: DI water (70:30 v/v) and shake it thoroughly.

Intermediate precision parameters for the developed method are as follows:

- HPLC: 1100 Series HPLC system with MWD (UV/VIS Detector), Agilent Technologies
- Separation Mode: Isocratic (Reversed-Phase Separation)
- Column: Water XTERRA RP-18 (4.6 × 250 mm, 5 µm)
- Mobile Phase: Solvent A: 25 mM potassium phosphate monobasic buffer 2.9

Solvent B: 100% ACN

- Solvent Strength: (70:30 v/v) Buffer: ACN

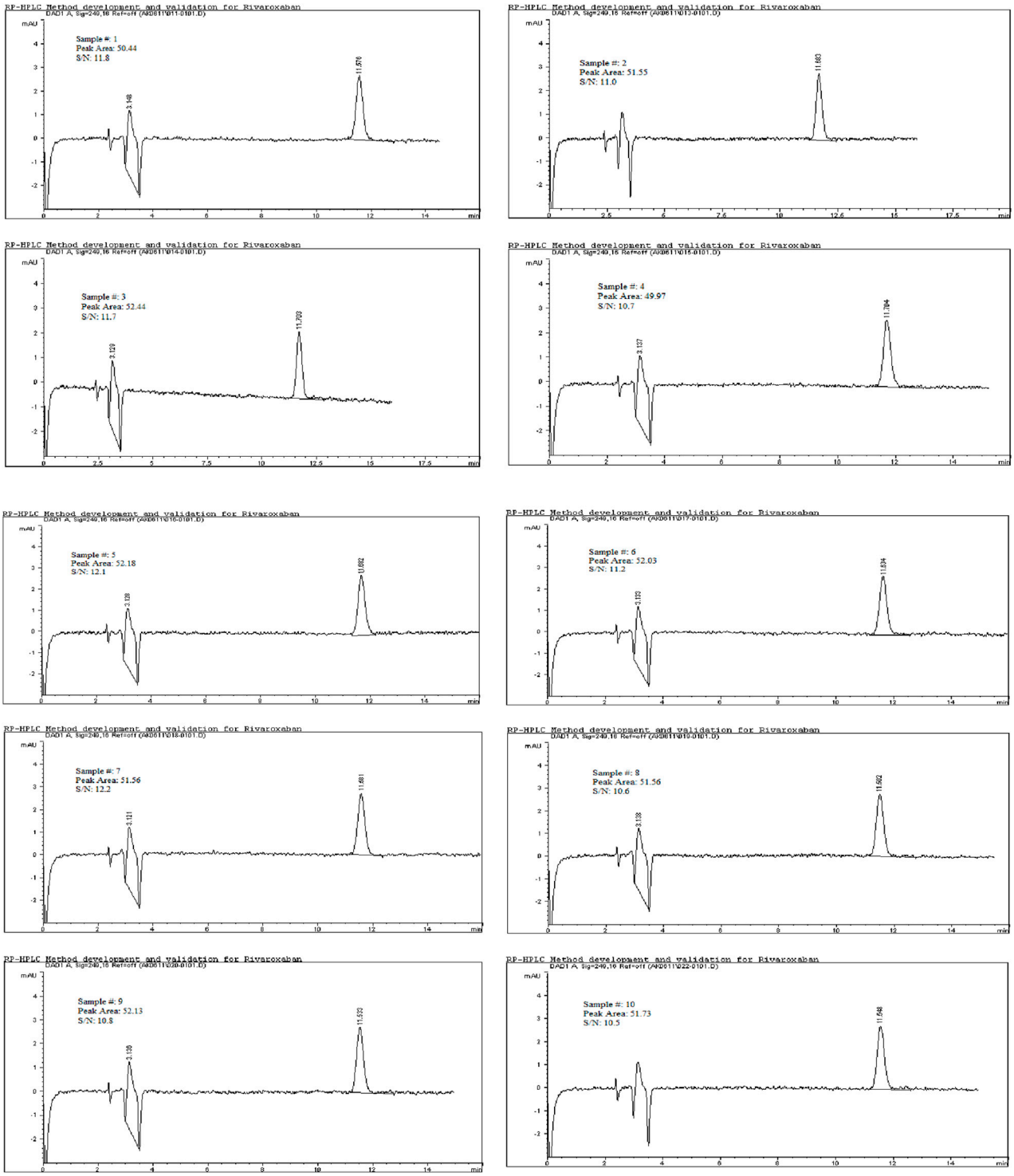

FIGURE 11
Chromatograms for limit of quantitation study for 1.0 ppm. Chromatographic conditions: Isocratic elution, mobile phase 30:70 ACN/25 mM potassium phosphate buffer monobasic pH 2.9, flow rate 1.0 mL/min, detection wavelength at 249 nm, ambient temperature, 15 µL injection volume, thermo hypersil ODS C_{18} (4.6 × 250 mm, 5 µm) column.

- Absorbance: 249 nm
- Flow Rate: 1.0 mL/min
- Injection Volume: 15 µL
- Column Temperature: Ambient
- Run Time: 18 min

Limit of detection (LOD)

The limit of detection (LOD) was evaluated to determine the minimum concentration of analyte in a sample that can be reliably detected, though not necessarily quantified precisely. This was done

TABLE 9 System suitability results for working standard solution for rivaroxaban# 1 and rivaroxaban #2.

Standard #1 injection	Retention time	Peak area (mAU)	Plate count	Tailing factor
1	12.296	31,205.2	9,959	0.945
2	12.433	31,043.9	10,489	0.943
3	12.427	31,211.1	10,657	0.943
4	12.423	31,094.6	10,167	0.954
5	12.299	31,022.4	10,197	0.951
6	12.464	30,954.3	10,599	0.950
Average	12.39	31,042.35		
STDEV	0.073	102.45		
Retention Time % RSD	0.59			
Peak Area % RSD		0.33		
% Drift	−0.22			
Standard # 2 injection				
1	12.202	31,014.6	10,521	0.958
2	12.170	31,256.4	9,537	0.957
Average	12.19	31,109.90		
STDEV	0.02	134.77		
Retention Time % RSD	0.19			
Peak Area % RSD		0.43		

using Rivaroxaban as a surrogate for impurities and degradants. LOD was determined based on the signal-to-noise ratio, with the acceptance criterion being a signal-to-noise ratio of ≥3.

Stock solution of Rivaroxaban (5,000 ppm)

Weigh 250 mg of Rivaroxaban and transfer it into a 50 mL volumetric flask. Add 25 mL of ACN: DI water (70:30 v/v) and sonicate for 20 min or until Rivaroxaban is completely dissolved. Complete the volume to the mark with ACN: DI water (70:30 v/v) and shake it thoroughly.

Stock solution of Rivaroxaban (10 ppm)

Transfer 0.1 mL of stock solution Rivaroxaban (5000 ppm) into a 50 mL volumetric flask. Complete the volume to the mark with ACN: DI water (70:30 v/v) and shake it thoroughly.

Limit of quantitation (LOQ)

To determine the limit of quantitation (LOQ) for Rivaroxaban, a series of dilutions were prepared, and the signal-to-noise ratios were calculated based on a 5,000 ppm stock solution. The LOQ was initially estimated at 1.0 ppm, as indicated by the results in Table 8, where the signal-to-noise ratio for this concentration met the acceptance criterion of ≥10 and % RSD ≤10. To confirm the LOQ, a 1.0 ppm Rivaroxaban solution was prepared and injected ten times into the HPLC system. The resulting chromatograms, shown in Figure 11, provided further data on the signal-to-noise ratio and allowed for the determination of precision. The results from these injections are summarized in Table 8, where the signal-to-noise ratio was found to meet the acceptance criteria. Additionally, the % RSD for this concentration was ≤10%, confirming that 1.0 ppm is the LOQ for the developed method.

Results and discussion

Rivaroxaban is an oral anticoagulant that directly inhibits factor Xa, thereby preventing clot formation. It is commonly prescribed to reduce the risk of stroke in patients with non-valvular atrial fibrillation and to prevent deep vein thrombosis (DVT) following hip or knee replacement surgeries (Alam et al., 2023; Mestareehi et al., 2021). Several RP-HPLC methods have been developed for quantifying rivaroxaban in pharmaceutical forms. One method utilized a Phenomenex Luna C18 column (250 × 4.6 mm, 5 µm) at 40°C, with an acetonitrile-water (55:45 v/v) mobile phase, a 1.2 mL/min flow rate, and detection at 249 nm. Rivaroxaban eluted at 3.37 min, and the method was validated per ICH guidelines (Sekhar et al., 2012). Another study employed a HiQSil C18 column (250 × 4.6 mm, 5 µm) at room temperature, using a methanol-water (65:35 v/v) mobile phase, a 1.4 mL/min flow rate, and detection at 249 nm. The retention time was 3.12 min, and the method was validated for accuracy and precision (Çelebier TRb et al., 2013). Notably, many existing methods lack comprehensive

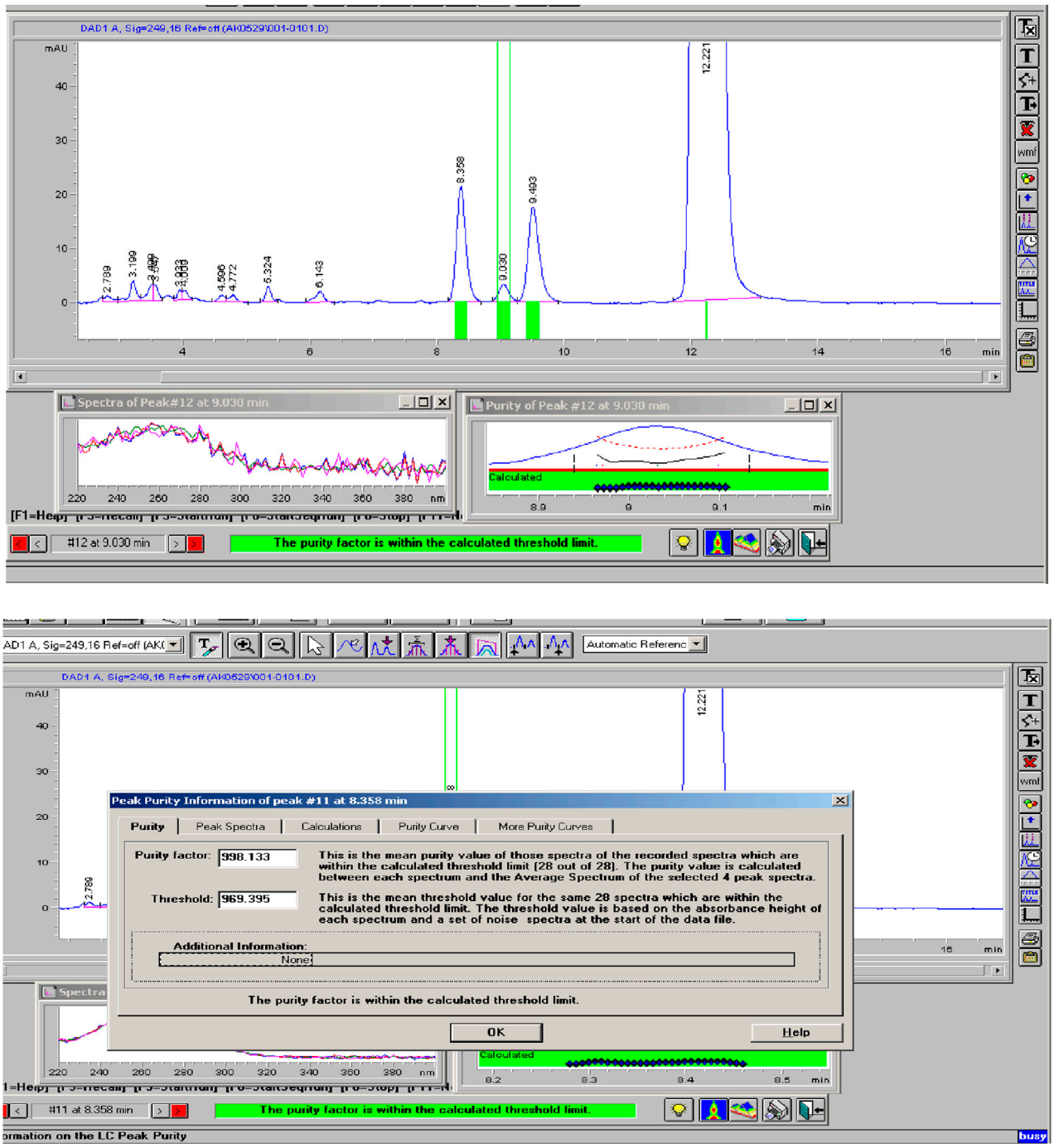

FIGURE 12
Peak purity of Rivaroxaban degraded to 9.2%. Chromatographic conditions: Isocratic elution, mobile phase 30:70 ACN/25 mM potassium phosphate buffer monobasic pH 2.9, flow rate 1.0 mL/min, detection wavelength at 249 nm, ambient temperature, 15 µL injection volume, thermo hypersil ODS C_{18} (4.6 × 250 mm, 5 µm) column.

stability-indicating analyses, underscoring the need for methods that assess rivaroxaban's stability in tablet formulations to ensure potency, safety, and efficacy.

The results of the system suitability test, as outlined in Table 9, indicate that all peaks achieved complete resolution with a tailing factor close to 1, demonstrating optimal peak shape. The number of theoretical plates exceeded 9,000, which reflects high column efficiency and satisfactory separation. The %RSD values for peak area and retention time of six replicate injections from working standard solution #1 were 0.33% and 0.59%, respectively. For working standard solution #2, the %RSD values for peak area and retention time from two replicate injections were 0.43% and 0.19%, respectively. These low %RSD values demonstrate the system's repeatability and precision. Additionally, the percent

TABLE 10 Method robustness results variations for mixed degradation sample.

Parameters	Conditions	Retention time (min.)	Tailing factor	Peak area (mAU)	Number of theoretical plates
pH of buffer	2.7	11.3	1.05	30,365	12,566
	2.9	12.2	1.04	31,341	14,771
	3.1	11.95	1.05	30,855	14,135
Flow rate mL/min	0.8	14.16	1.04	35,135	16,018
	1	12.2	1.05	31,341	14,771
	1.2	10.2	1.05	25,578	13,922
Wavelength	247	12.29	1.05	30,627	14,959
	249	12.2	1.05	31,341	14,771
	251	12.08	1.06	31,187	14,433
% B composition	25	17.67	0.98	29,665.0	16,990
	30	12.2	1.05	31,341	14,771
	35	8.23	1.13	27,703	10,774
Injection volume (μ L)	13	12.2	1.06	27,899	15,601
	15	12.2	1.05	31,341	14,771
	17	12.38	1.03	34,776	13,973

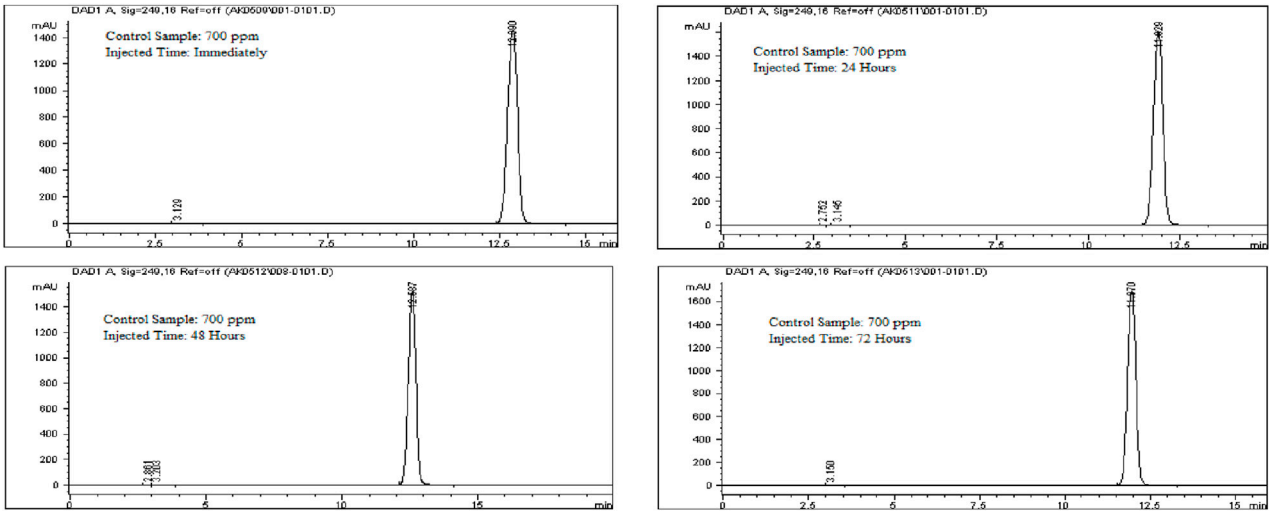

FIGURE 13
Chromatograms for solution stability study for Rivaroxaban 700 ppm. Chromatographic conditions: Isocratic elution, mobile phase 30:70 ACN/25 mM potassium phosphate buffer monobasic pH 2.9, flow rate 1.0 mL/min, detection wavelength at 249 nm, ambient temperature, 15 µL injection volume, thermo hypersil ODS C_{18} (4.6 × 250 mm, 5 µm) column.

drift was below 1%, indicating stability and minimal variability between working standard solutions. These results meet the acceptance criteria for system suitability according to ICH guidelines, confirming that the system performs reliably. This test was conducted prior to analyzing other parameters to ensure system readiness for accurate data generation in subsequent studies.

The Rivaroxaban peak was observed at a retention time of 12.20 min, with three additional major peaks from degradation products at 8.358, 9.030, and 9.493 min. All peaks were well-resolved from the Rivaroxaban peak, meeting the specificity requirement for resolution. Moreover, the peak purity factor exceeded the threshold, confirming that the main Rivaroxaban peak was free from interference. The specificity study demonstrated that the method accurately isolates and quantifies Rivaroxaban in the presence of degradants and impurities. Chromatographic evidence, including a purity chromatogram and a 3D image of Rivaroxaban, is provided in Figure 12 and Supplementary Figure S4, respectively, showcasing the

TABLE 11 Accuracy results for rivaroxaban active ingredient.

Concentration (ppm)	Peak area	Percent recovery	Average percent recovery	% RSD
500	21,723.1	99.6	99.7	0.32
	21,803.0	100.0		
	21,671.1	99.4		
700	29,970.3	99.4	99.4	0.21
	30,033.1	99.6		
	29,909.8	99.2		
850	36,278.4	99.7	100.5	0.74
	36,623.0	101.1		
	36,798.9	100.6		

method's efficacy in meeting ICH and FDA guidelines (ICH ICoH, 2005).

The robustness study results are summarized in Table 10. All results adhered to ICH guidelines. The tailing factor ranged between 0.9 and 2, and the number of theoretical plates exceeded 2,000. The method demonstrated robustness against minor variations in solvent strength, flow rate, buffer pH, wavelength, and injection volume. Chromatograms from the robustness study and corresponding chromatographic conditions are shown in Supplementary Figures S5–S9.

To evaluate solution stability, a 700 ppm Rivaroxaban solution was freshly prepared from a 10,000 ppm stock solution and immediately injected into the HPLC system. The same 700 ppm solution was reinjected at 24, 48, and 72 h. Chromatograms and chromatographic conditions are displayed in Figure 13. No new peaks or peak loss was observed in the chromatographic profiles between the first and last injections, indicating no significant degradation or instability of the solution during the analysis as shown in Supplementary Table S5.

Eight concentrations of Rivaroxaban standard solutions (850 ppm, 800 ppm, 750 ppm, 700 ppm, 650 ppm, 600 ppm, 550 ppm, and 500 ppm) were prepared to assess linearity, with each concentration injected individually into the HPLC system. The recorded peak areas for each concentration are presented in Table 7. A calibration curve was constructed by plotting peak areas against concentrations. The resulting linear regression equation demonstrated a correlation coefficient of 0.9990, as shown in Figure 10. This value meets the acceptance criterion for linearity, confirming the HPLC method's reliability and linear response across the tested concentration range. These findings validate the method's suitability for quantitative analysis of the active ingredient.

Each sample of Rivaroxaban (850 ppm, 700 ppm, and 500 ppm) was prepared in triplicate, injected into the HPLC system, and analyzed for peak area to calculate percent recovery. The accuracy study results, summarized in Table 11, indicate that all tested concentrations of the active ingredient met the acceptance criteria. These results confirm the method's accuracy for determining Rivaroxaban, with percent recovery within the specified range, validating its reliability for quantifying the active ingredient in raw material.

To evaluate the repeatability of the analytical method for rivaroxaban, six individual samples at a concentration of 700 ppm were prepared and injected into the HPLC system under optimized chromatographic conditions, as depicted in Supplementary Figure S13. The percent relative standard deviation (%RSD) of the peak areas from these injections was calculated to assess the method's precision. According to ICH guidelines, a %RSD not more than 2.0% is typically acceptable for repeatability in analytical methods. Compliance with this criterion demonstrates that the method consistently provides precise measurements for rivaroxaban under the same experimental conditions.

Six individual samples of Rivaroxaban (700 ppm) were prepared and analyzed using the HPLC system under optimized chromatographic conditions. The peak areas for each injection were recorded, and the % RSD was calculated to evaluate the method's precision. As presented in Supplementary Table S6, the % RSD values met the acceptance criteria for injection precision, confirming the method's reliability in consistently measuring peak areas across repeated injections. Additionally, a single Rivaroxaban sample (700 ppm) was injected six times into the HPLC system under identical conditions to further assess injection precision. The % RSD was determined, and as shown in Supplementary Table S7, the results complied with the acceptance criteria, reinforcing the method's precision for quantifying the active ingredient. Moreover, to assess intermediate precision, six separate Rivaroxaban samples (700 ppm) were prepared and injected into a different HPLC system. The % RSD of the peak areas was calculated, and the results, detailed in Supplementary Table S8, met the acceptance criteria. These findings confirm that the method consistently produces reliable results under varying laboratory conditions, as specified in the validation protocol.

The limit of detection (LOD) for Rivaroxaban was determined by preparing serial dilutions from a 5,000 ppm stock solution, with concentrations ranging from 10.0 ppm, 5.0 ppm, 2.0 ppm, 1.5 ppm, 1.0 ppm, 0.90 ppm, 0.50 ppm, 0.40 ppm, 0.30 ppm, and 0.2 ppm. Each solution was injected into the HPLC system, and the resulting chromatograms (shown in Figure 14) were analyzed to calculate the signal-to-noise ratios. The results, presented in Table 6, indicate that the 0.3 ppm concentration yielded a signal-to-noise ratio of 4.0. Based on this finding, 0.3 ppm was selected

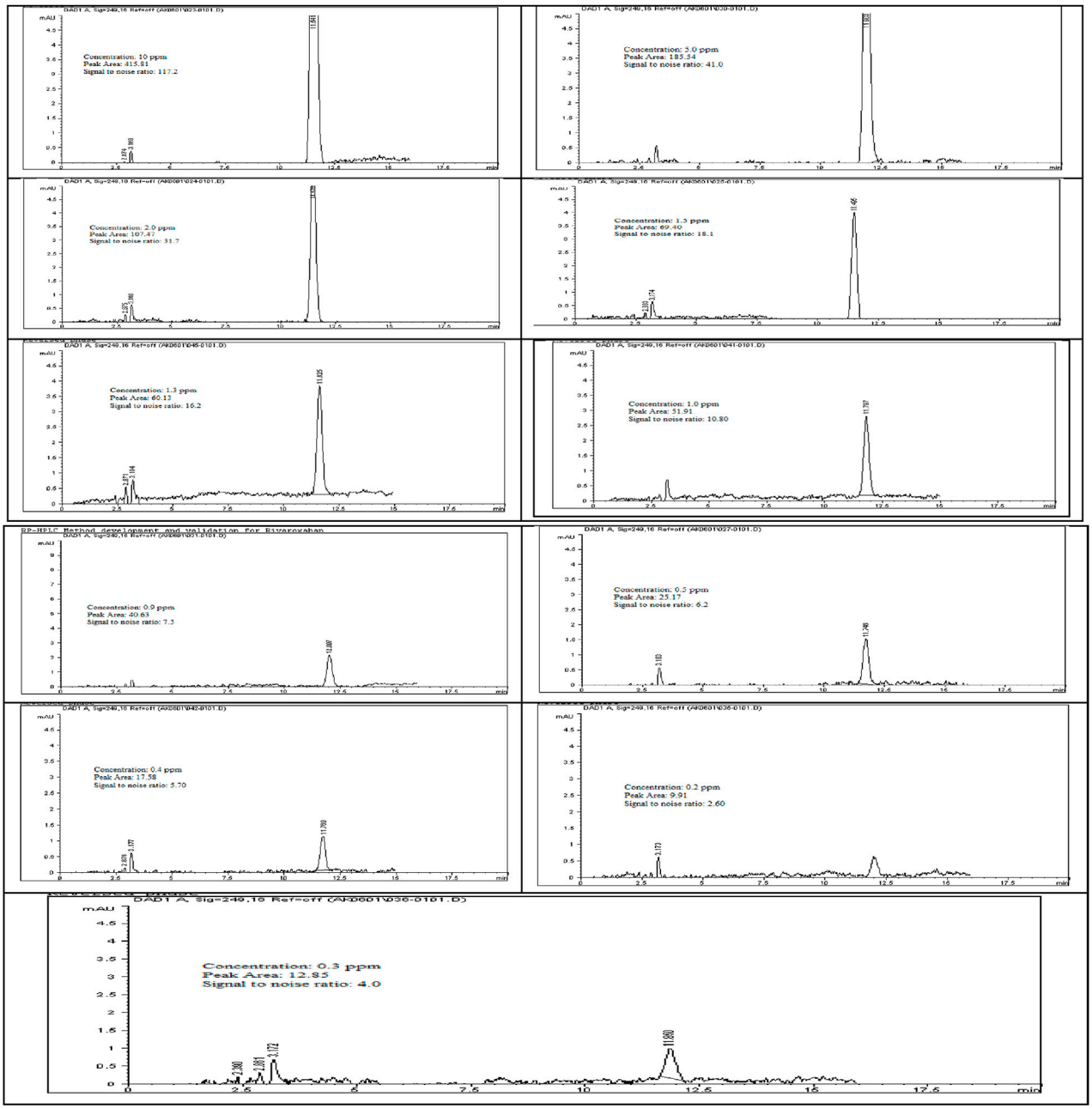

FIGURE 14
Chromatograms for limit of detection (LOD) of Rivaroxaban. Chromatographic conditions: Isocratic elution, mobile phase 30:70 ACN/25 mM potassium phosphate buffer monobasic pH 2.9, flow rate 1.0 mL/min, detection wavelength at 249 nm, ambient temperature, 15 µL injection volume, thermo hypersil ODS C_{18} (4.6 × 250 mm, 5 µm) column.

as the LOD for the developed method, meeting the acceptance criterion of a signal-to-noise ratio of ≥3. Additionally, to assess the limit of quantitation (LOQ) for Rivaroxaban, a 1 ppm solution was prepared and injected ten times into the HPLC system. The resulting chromatograms were analyzed to evaluate the peak areas, and the signal-to-noise ratios were calculated. The % RSD (relative standard deviation) of the peak areas was determined to be 1.54%, which is well within the acceptance criteria for the LOQ, where the % RSD should be ≤ 10%. These results confirm that the 1.0 ppm concentration meets the criteria for LOQ, indicating that the developed method is precise enough for quantification at this low concentration.

To confirm our results for the Limit of Detection (LOD) and Limit of Quantitation (LOQ), the International Council for Harmonisation (ICH) recommends various approaches, depending on the instrument used for analysis, the nature of the analyte, and the suitability of the method. One acceptable approach is the standard deviation of the response and the slope of the calibration curve (ICH ICoH, 2005; Ravisankar and Sankar, 2015). The formulas for calculating LOD and LOQ are:

$$LOD = 3.3X\left(\frac{\sigma}{S}\right) \text{ and } LOQ = 10X\left(\frac{\sigma}{S}\right)$$

where, σ = standard deviation of the response and S = slope of the calibration curve.

From the linearity test, we calculated σ = 96.07 and S = 971.04. Applying the respective formulas yielded an LOD of 0.33 ppm and an LOQ of 0.99 ppm, which closely aligns with our signal-to-noise ratio results (LOD = 0.31 ppm, LOQ = 1 ppm). These calculations comply with the guidelines established by the ICH and USP for analytical method validation.

Conclusion

A reversed-phase HPLC method has been successfully developed and validated for the quantitative of Rivaroxaban in raw materials and pharmaceutical dosage forms. The method employs isocratic elution with an optimized mobile phase consisting of 25 mM potassium phosphate monobasic buffer (pH 2.9) and acetonitrile (70:30, v/v), delivered at a flow rate of 1.0 mL/min. The separation was performed using a Thermo Hypersil ODS C18 column (4.6 × 250 mm, 5 µm) on an Agilent Technologies 1,100 Series HPLC system, equipped with a multi-wavelength diode array detector (MWD/DAD). The injection volume was set to 15 µL, with detection carried out at 249 nm under ambient temperature conditions.

The results of the system suitability test (SST) confirmed that all chromatographic peaks achieved complete resolution, with a tailing factor close to 1, indicating excellent peak symmetry and optimal column efficiency. The theoretical plate count exceeded the recommended threshold, demonstrating high column performance and separation efficiency. The method exhibited high specificity, with no detectable interference from excipients, degradation products, or other impurities. Solution stability studies showed no evidence of peak loss, degradation, or additional peaks between the first and last injections, confirming the stability of Rivaroxaban in the prepared solutions over the analysis period. Furthermore, the peak purity factor exceeded the acceptance threshold, ensuring that the Rivaroxaban peak remained free from spectral overlap or co-eluting impurities.

The method demonstrated excellent linearity over the validated concentration range, with a correlation coefficient (R^2) of 0.9990, indicating a strong linear relationship between concentration and peak response. The calculated limit of detection (LOD) was 0.3 ppm, supported by a signal-to-noise ratio of 4.0, which meets the regulatory acceptance criterion of ≥3. The LOQ was also 1 ppm, ensuring precise and reproducible quantification at lower analyte concentrations.

A comprehensive validation was performed in accordance with FDA, USP, and ICH guidelines (ICH Q2 (R1)), assessing key parameters such as system suitability, specificity, linearity, accuracy, precision, robustness, solution stability, LOD, and LOQ. The method demonstrated high accuracy, with recovery values within the acceptable range (98.0%–102.0%), and precision, with %RSD values consistently below 2.0%, confirming the reproducibility of the results. Robustness testing confirmed the method's reliability under deliberate variations in chromatographic conditions, such as mobile phase composition, flow rate, column temperature, and detection wavelength. This validated, stability-indicating HPLC method is highly suitable for routine quality control, stability studies, and pharmaceutical analysis of Rivaroxaban in both raw materials and finished dosage forms. Its simplicity, sensitivity, high throughput, and robustness make it an optimal choice for regulatory-compliant analytical applications in pharmaceutical laboratories. Additionally, its ability to detect potential degradants and impurities further supports its applicability in stability testing and formulation development.

Data availability statement

The original contributions presented in the study are contained in the article and/or the Supplementary Material. Further inquiries can be directed to the corresponding author.

Ethics statement

The data utilized in this study were exclusively derived from our own datasets, based on the results obtained from our samples. Furthermore, it is important to highlight that the study was conducted with the approval and consent of the institutional ethics committee.

Author contributions

AM: Conceptualization, Formal Analysis, Funding acquisition, Methodology, Resources, Software, Supervision, Validation, Visualization, Writing – original draft, Writing – review and editing.

Funding

The author(s) declare that no financial support was received for the research and/or publication of this article.

Acknowledgments

We sincerely thank Northeastern Illinois University for providing faculties to carry out research work. In addition, thanks to all the authors who contributed to this article and to the publisher for supporting this article.

Conflict of interest

The author declares that the research was conducted in the absence of any commercial or financial relationships that could be construed as a potential conflict of interest.

Generative AI statement

The author(s) declare that no Generative AI was used in the creation of this manuscript.

Publisher's note

All claims expressed in this article are solely those of the authors and do not necessarily represent those of their affiliated organizations, or those of the publisher, the editors and the reviewers. Any product that may be evaluated in this article, or claim that may be made by its manufacturer, is not guaranteed or endorsed by the publisher.

Supplementary material

The Supplementary Material for this article can be found online at: https://www.frontiersin.org/articles/10.3389/fchem.2025.1551189/full#supplementary-material

References

Administration FaD (2003). *Guidance for industry Q1A(R2) stability testing of new drug substances and products*.

Alam, I., Nadir Ali, S., Qayoom, A., Bibi, R., Aqeel, M., and Muhammad, H. (2023). Green liquid chromatographic method for simultaneous determination of metformin, linagliptin and rivaroxaban: tablet manufacturing and application to *in-vitro* dissolution studies. *Microchem. J.* 193, 109025. doi:10.1016/j.microc.2023.109025

Çelebier Trb, M., Koçak, E., and Altınöz, S. (2013). RP-HPLC Method development and validation for estimation of Rivaroxaban in pharmaceutical dosage forms. *Braz. J. Pharm. Sci.*, 49 (2), 359–366. doi:10.1590/S1984-82502013000200018

FDA. Xarelto approval history. (2014).

FDA (2004). *Validation of chromatographic methods*. Linda: Center for Drug Evaluation and Research NPN.

Fernandez, S., Lenoir, C., Samer, C. F., and Rollason, V. (2021). Drug-drug interactions leading to adverse drug reactions with rivaroxaban: a systematic review of the literature and analysis of VigiBase. *J. Pers. Med.* 11 (4), 250. doi:10.3390/jpm11040250

(ICH) ICoH (2005). *Validation of analytical procedures: methodology Q2(R1)*. ICH Guidance for Industry. Available online at: https://database.ich.org/sites/default/files/Q2%28R1%29%20Guideline.pdf

Janssen Pharmaceuticals, I. (2011). *Xarelto (Rivaroxaban) prescription blood thinner*. Titusville, NJ, United States: Janssen Pharmaceuticals, Inc.

Kubitza, D., Roth, A., Becka, M., Alatrach, A., Halabi, A., Hinrichsen, H., et al. (2013). Effect of hepatic impairment on the pharmacokinetics and pharmacodynamics of a single dose of rivaroxaban, an oral, direct Factor Xa inhibitor. *Br. J. Clin. Pharmacol.* 76 (1), 89–98. doi:10.1111/bcp.12054

Mestareehi, A. (2024). Global gene expression profiling and bioinformatics analysis reveal downregulated biomarkers as potential indicators for hepatocellular carcinoma. *ACS Omega* 9 (24), 26075–26096. doi:10.1021/acsomega.4c01496

Mestareehi, A., and Abu-Farsakh, N. (2024). Impact of protein phosphatase expressions on the prognosis of hepatocellular carcinoma patients. *ACS Omega* 9 (9), 10299–10331. doi:10.1021/acsomega.3c07787

Mestareehi, A., Zhang, X., Seyoum, B., Msallaty, Z., Mallisho, A., Burghardt, K. J., et al. (2021). Metformin increases protein phosphatase 2A activity in primary human skeletal muscle cells derived from lean healthy participants. *J. Diabetes Res.* 2021 (1), 1–6. doi:10.1155/2021/9979234

Mueck, W., Lensing, A. W., Agnelli, G., Decousus, H., Prandoni, P., and Misselwitz, F. (2011). Rivaroxaban: population pharmacokinetic analyses in patients treated for acute deep-vein thrombosis and exposure simulations in patients with atrial fibrillation treated for stroke prevention. *Clin. Pharmacokinet.* 50 (10), 675–686. doi:10.2165/11595320-000000000-00000

Mueck, W., Stampfuss, J., Kubitza, D., and Becka, M. (2014). Clinical pharmacokinetic and pharmacodynamic profile of rivaroxaban. *Clin. Pharmacokinet.* 53 (1), 1–16. doi:10.1007/s40262-013-0100-7

National Center for Biotechnology Information (2024). *PubChem compound summary for CID 9875401. Rivaroxaban*. Bethesda, MD, United States: U.S. National Library of Medicine, National Institutes of Health.

Ravisankar, P., and Sankar, R. (2015). A review on step-by-step analytical method validation. *IOSR J. Pharm.* (5), 7–19.

Sekhar, K. C., Vani, P. S., Lakkshami, A. D., Devi, C. L. L., Barik, A., and Narendra, D. (2012). A new method and validation for analysis of rivaroxaban in formulation by RP-HPLC. *Narendra Devanaboyina Res Desk* 1 (1). 24–33.

Siraj, Z., Adil, O., Amin, B., and Tahiri, I. (2024). *Development and validation of assay method for the estimation of moxifloxacin in bulk and pharmaceutical formulations by RP-HPLC2024*.

United States pharmacopeia X (1990). *The United States Pharmacopeia—The National Formulary*. United States Pharmacopeial Convention, Inc.: Rockville, MD, 1225

Verbeeck, R. K. (2008). Pharmacokinetics and dosage adjustment in patients with hepatic dysfunction. *Eur. J. Clin. Pharmacol.* 64 (12), 1147–1161. doi:10.1007/s00228-008-0553-z

Weitz, J. I., and Bates, S. M. (2005). New anticoagulants. *J. Thromb. Haemost.* 3 (8), 1843–1853. doi:10.1111/j.1538-7836.2005.01374.x

Yuan, J., Liu, K., Li, L., Yuan, Y., Liu, X., and Li, Y. (2014). A novel synthesis of the oxazolidinone antithrombotic agent rivaroxaban. *Molecules* 19 (9), 14999–15004. doi:10.3390/molecules190914999

frontiers | Frontiers in Chemistry

TYPE Original Research
PUBLISHED 29 April 2025
DOI 10.3389/fchem.2025.1578126

OPEN ACCESS

EDITED BY
Anna Borioni,
National Institute of Health (ISS), Italy

REVIEWED BY
Yulong Zhu,
Anhui University of Chinese Medicine, China
Maria Cristina Gaudiano,
National Institute of Health (ISS), Italy

*CORRESPONDENCE
Yue-Hua Chen,
chenyuehua527@126.com
Hui-Peng Song,
songhuipeng15@163.com

RECEIVED 17 February 2025
ACCEPTED 10 April 2025
PUBLISHED 29 April 2025

CITATION
Zhang X-R, Chen Y-H, Zhang J-N, Wang W-Y, Sun R-B, Ding Z-X, Zhang H, Xie M, Kang T-G and Song H-P (2025) Discrimination of poisonous and medicinal plants with similar appearance (*Asarum heterotropoides* vs. *Cynanchum paniculatum*) via a fusion method of E-nose, E-tongue, LC-HR-Q-TOF-MS/MS, and electrochemical fingerprint spectra. *Front. Chem.* 13:1578126.
doi: 10.3389/fchem.2025.1578126

Discrimination of poisonous and medicinal plants with similar appearance (*Asarum heterotropoides* vs. *Cynanchum paniculatum*) via a fusion method of E-nose, E-tongue, LC-HR-Q-TOF-MS/MS, and electrochemical fingerprint spectra

Xin-Ru Zhang[1], Yue-Hua Chen[1]*, Jia-Nuo Zhang[1], Wen-Yu Wang[1], Rui-Bo Sun[1], Zi-Xuan Ding[1], Hui Zhang[1], Ming Xie[1], Ting-Guo Kang[1] and Hui-Peng Song[1,2]*

[1]Key Laboratory for Identification and Quality Evaluation of Traditional Chinese Medicine of Liaoning Province, Liaoning University of Traditional Chinese Medicine, Dalian, China, [2]Key Laboratory of Ministry of Education for TCM Viscera-State Theory and Applications, Liaoning University of Traditional Chinese Medicine, Shenyang, China

Introduction: The similarity in appearance of poisonous and medicinal plants, such as Asarum heterotropoides (AH) and Cynanchum paniculatum (CP), poses safety risks due to frequent confusion. Since AH contains toxic ingredients, the traditional methods of olfactory and gustatory identification cannot be used to distinguish AH from CP.

Methods: To differentiate them systematically, we proposed a novel strategy based on dual electronic sensors (DES) and dual fingerprint spectra (DFS). The DES included two intelligent sensors, namely the E-nose and E-tongue, which differentiated AH and CP based on odor and taste, respectively. DFS comprised chemical fingerprint spectra obtained through LC-HR-Q-TOF-MS/MS and electrochemical fingerprint spectra derived from the Belousov-Zhabotinsky reaction, differentiating AH and CP by their specific and overall compositions, respectively. To our knowledge, this was the first time that the E-nose, E-tongue, LC-HR-Q-TOF-MS/MS, and the Belousov-Zhabotinsky reaction were combined to identify AH and CP.

Results and discussion: With the E-nose, we identified 25 major odor components in AH and 12 odor components in CP in a single run of 140 s. Using the E-tongue, bitterness and astringency were identified as their primary taste differences. Furthermore, 91 compounds in AH and 90 compounds in CP were identified through LC-HR-Q-TOF-MS/MS. Both AH and CP shared nitrogenous compounds, volatile oils, organic acids, and lignans. However, AH uniquely contained coumarins and flavonoids, while CP contained steroidal

compounds and saccharides. Notably, AH also possessed distinct toxic components, specifically aristolactam I, aristolochic acid D, and safrole. Based on the Belousov-Zhabotinsky reaction, we obtained the electrochemical fingerprint spectra of AH and CP, thereby facilitating further distinction between these two herbs. Through the combination of electrochemical fingerprint spectra with principal component analysis (PCA) or orthogonal partial least squares-discriminant analysis (OPLS-DA), the accuracy of this method reached 100%. Through the fusion strategy, the odors, tastes, components, and electrochemical properties of AH and CP have been systematically analyzed.

KEYWORDS

medicinal plants, electronic nose, electronic tongue, mass spectrometry, Belousov-Zhabotinsky reaction

1 Introduction

Confusion and misuse frequently occur among medicinal plants with highly similar appearances (Xin et al., 2022). This phenomenon not only impacts the efficacy of medications but also poses potential threats to patients' health. The underground parts of *Asarum heterotropoides* (AH) and *Cynanchum paniculatum* (CP), as two herbal medicines with remarkable medicinal value and highly similar appearances, serve as typical examples of such issues. AH is widely used to treat symptoms such as colds, rhinitis, and coughs, while CP can effectively alleviate stomachaches and toothaches (Zhang et al., 2021). Given their significant differences in pharmacological functions, misusing one for the other can lead to severe consequences. Notably, AH contains poisonous components such as aristolochic acid-like ingredients which has been classified as a Group I cancer-causing agent by the World Health Organization. Its misuse or overdosage can trigger a series of adverse reactions or even lead to life-threatening conditions. Additionally, due to AH's significantly higher market price compared to CP, some unethical merchants may intentionally adulterate AH with CP for sale. This further poses challenges to the authentication of these two medicinal plants. To effectively prevent the confusion and misuse, there is an urgent need to adopt modern technologies and establish reliable strategies to discriminate them from multiple angles.

Electronic sensory technologies have demonstrated unique advantages in the identification of medicinal plants. Electronic nose (E-nose) and electronic tongue (E-tongue) are two representative electronic sensory technologies (Tibaduiza et al., 2024; Wang S. et al., 2022). The E-nose perceives and analyzes volatile odors by simulating the human olfactory system. Using E-nose, Zhang et al. differentiated raw *Magnolia officinalis* and ginger-processed *M. officinalis* and identified 16 possible odor components (Zhang et al., 2022). Lu et al. employed E-nose combined with gas chromatography-mass spectrometry to identify 40 aroma components from chamomile (Lu et al., 2024). In another example, the adulterants and geographical origins of *Ziziphi Spinosae* were successfully identified by E-nose and headspace gas chromatography-mass spectrometry (Zhang et al., 2023). Similarly, as an intelligent taste recognition tool, the E-tongue has also been widely applied in the field of medicinal plants. For example, Lei et al. conducted comprehensive evaluations of the aroma and taste of bear bile powder and its common counterfeit by E-nose and E-tongue technologies (Lei et al., 2023). Xing et al. determined the taste characteristics of *Polygonum multiflorum* using E-tongue and revealed the relationship between tastes and components (Xing et al., 2021). Wang et al. studied the correlation between the fragrance, taste, and effective components of *Gastrodiae Rhizoma* by E-nose and E-tongue (Wang B. et al., 2022). In summary, the rapid development of E-nose and E-tongue technologies provides a new approach for the identification of morphologically similar medicinal plants.

Chemical fingerprint spectra based on liquid chromatography-mass spectrometry (LC-MS) is one of the effective strategies for the analysis of chemical components in medicinal plants (Chen et al., 2021; Liang et al., 2022). In recent years, this technique has been increasingly and widely applied in this field. For instance, Bao et al. revealed at least 18 different chemical components in *Coptidis Rhizoma* by using UPLC-Q/TOF-MS (Bao et al., 2024). Mei et al. identified 50 components in *Spatholobi Caulis* by LC-Triple TOF-MS (Mei et al., 2021). Batsukh et al. utilized LC-IT-TOF-MS/MS in conjunction with multivariate statistical analysis to identify 30 compounds from *Divaricate Saposhnikoviae* (Batsukh et al., 2020). With this method, researchers can obtain detailed fingerprint spectra and abundant information on chemical components. Although LC-MS is effective in the identification of medicinal plants, it comes with drawbacks like expensive equipment and lengthy data analysis. In recent years, electrochemical fingerprint spectra has emerged and developed rapidly (Lan et al., 2023). Compared to LC-MS, electrochemical fingerprint spectra offers advantages including cheap instrumentation, simple sample treatment and short detection time, making it an effective complement to LC-MS. Furthermore, it can intuitively reflect the overall characteristic information of medicinal plants. The principle indicates that during the electrochemical reaction process, the chemical components in different medicinal plants will elicit unique changes, leading to characteristic fingerprint spectra. Zeng et al. utilized fingerprint spectra on the basis of three-electrode system to differentiate *Coptidis Rhizoma* from its adulterants (Zeng and Jiang, 2022). Tarighat et al. used fingerprint spectra based on cyclic voltammetry to classify and identify Lamiaceae herbs such as mint and lavender (Tarighat et al., 2023). Liu et al. discovered significant differences in the fingerprint spectra of *Astragali Radix* from various provinces through differential pulse voltammetry (Liu and Yan, 2023). However, electrochemical fingerprint spectra commonly identify medicinal plants from the overall

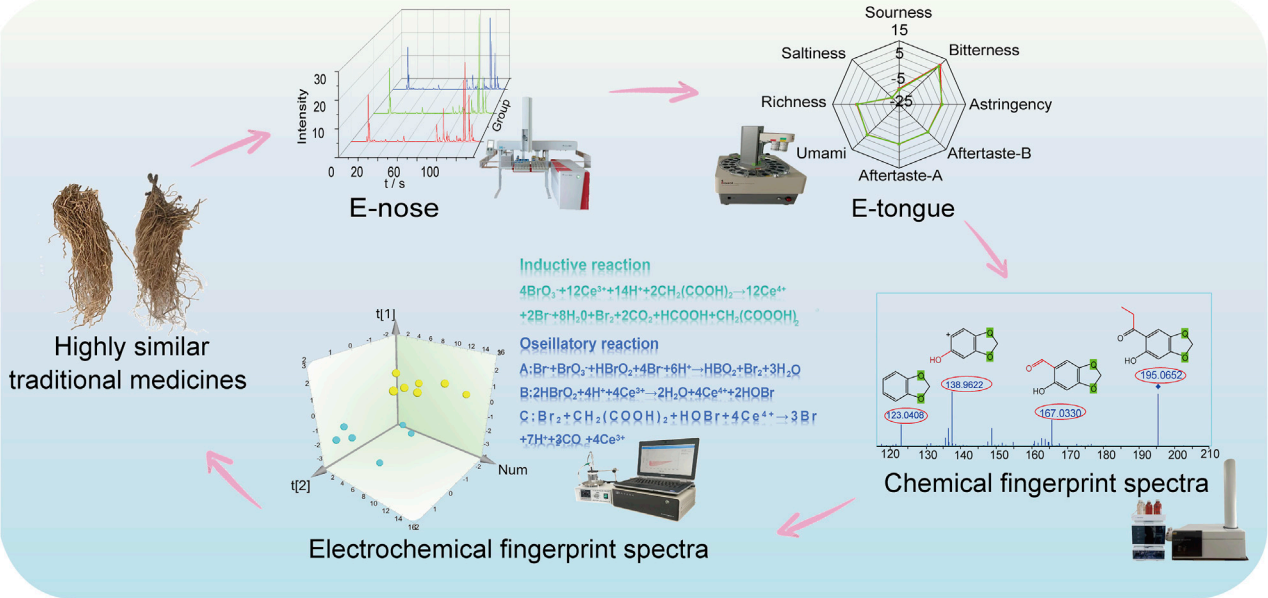

FIGURE 1
A four-step technical route for differentiation of AH and CP.

components, lacking specificity for individual components. It seems that the combination of LC-MS and electrochemical fingerprint spectra is an ideal method for the analysis of medicinal plants. Currently, there are few reports on the combination of the two methods.

In this study, a novel strategy combining dual electronic sensors (DES) and dual fingerprint spectra (DFS) was proposed for differentiating AH and CP. This strategy emphasized the integration of electronic sensory technology and fingerprint spectra analysis. On the one hand, E-nose and E-tongue were utilized to differentiate AH and CP from the perspectives of odor and taste, respectively. On the other hand, chemical fingerprint spectra obtained through LC-HR-Q-TOF-MS/MS and electrochemical fingerprint spectra derived from the Belousov-Zhabotinsky reaction were employed to differentiate AH and CP, focusing on specific chemical components and overall characteristic information, respectively. Furthermore, the electrochemical fingerprint spectra was combined with PCA and OPLS-DA to ensure a 100% accurate differentiation between AH and CP. Through the implementation of the DES and DFS strategy, a comprehensive and systematic differentiation of AH and CP from multiple angles was achieved.

2 Materials and methods

2.1 Reagents and materials

Seven different batches of AH were purchased from the regional medicinal herb trading center of Anguo City, Hebei Province (batches: 07230307, 07230401, 07230504, 07230604, 07230702, 07230801, 07230905). Seven different batches of CP were purchased from the regional medicinal herb trading center of Lu'an City, Anhui Province (batches: 23060201, 23070304, 23080302, 23090203, 23100402, 23110501, 23120204). The chemical standards including asarinin (PS010871), methyl eugenol (PS001191), (1R)-(+)-α-pinene (PS230925-10), (+)-3-carene (PS230926-01), eucalyptol (PS020906), carvacrol (PS230925-13), α-terpineol (PS020226), paeonol (PS000281), hesperidin (PS010632), chlorogenic acid (PS010694), o-hydroxyacetophenone (PS230925-14), p-hydroxyacetophenone (PS020038), palmitic acid (PS020930), and oleic acid (PS020507) were all purchased from Chengdu Push Bio-technology Co., Ltd. Vanillic acid (MUST-23012113), caffeic acid (MUST-23061118), and (−)-β-pinene (MUST-2392216) were purchased from Chengdu Must Biotechnology Co., Ltd. The purity of all the above compounds was above 98%. Purified water was purchased from Wahaha Group Co., Ltd. (Hangzhou, China). H_2SO_4 (20111014) was purchased from Sinopharm Chemical Reagent Co., Ltd. $CH_2(COOH)_2$ (M813041) was purchased from Macklin Co., Ltd. $(NH_4)_2SO_4{\cdot}Ce(SO_4)_2$ (20230601) was purchased from Tianjin Damao Chemical Reagent Co., Ltd. $KBrO_3$ (20160107) and LC-grade methanol (20241101) were purchased from Tianjin Kermel Chemical Reagent Co., Ltd. LC-grade acetonitrile (JB145430) and MS-grade formic acid (20171008) were purchased from Merck (Darmstadt, Germany).

2.2 Sample preparation

The roots and rhizomes of AH and CP were powdered and passed through a sieve. Then 0.5 g of sample was weighed and mixed with 10 mL of methanol for a 40-min ultrasonic extraction (F-050 type, Fuyang ultrasonic cleaner). After centrifugation (LC-LX-H185C type, Lichen Co., Ltd.) at 14,000 rpm for 5 min, the supernatant was used for LC-HR-Q-TOF-MS/MS analysis.

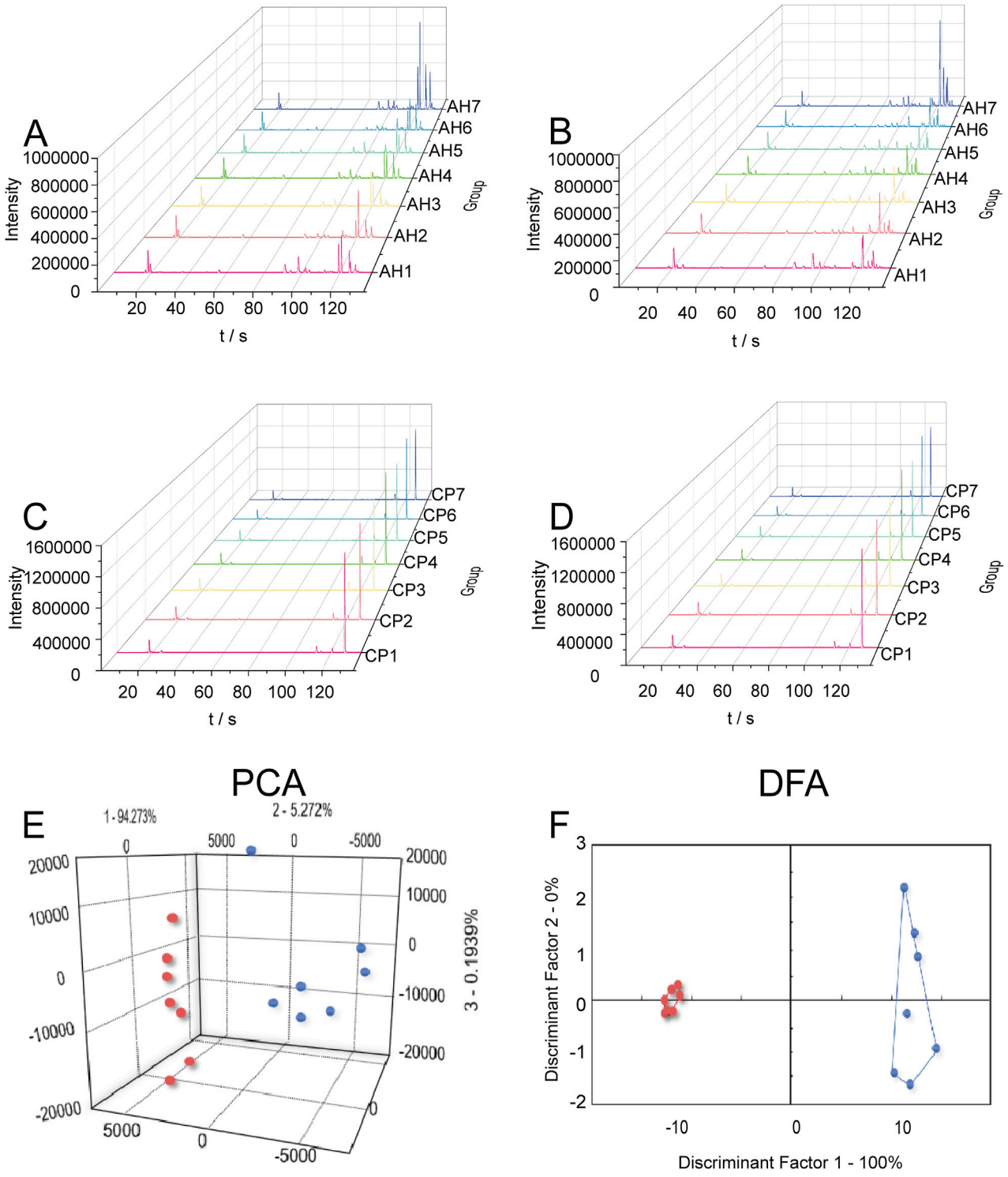

FIGURE 2
Odor chromatograms of AH on MXT-5 **(A)** and MXT-1701 **(B)**. Odor chromatograms of CP on MXT-5 **(C)** and MXT-1701 **(D)**. PCA **(E)** and DFA **(F)** for distinguishing between AH and CP based on E-nose.

Another 0.5 g of sample powder was weighed and mixed with 10 mL of deionized water for a 30-min ultrasonic extraction. The extract was filtered and diluted tenfold for E-tongue analysis. The powders of medicinal plants were directly used for electrochemical analysis. Prior to E-nose analysis, both dried AH and CP samples were processed into uniform small segments (1 cm in length) to ensure morphological standardization. Each headspace vial was filled with 1.0 g of the processed sample material. This standardization procedure aimed to unify both morphology and mass, thereby reducing variations in the detection of volatile components.

10.3389/fchem.2025.1578126

TABLE 1 Possible compounds and sensory descriptions of AH and CP.

	Molecular formula	Reserved parameter		Possible compound	Correlation index	Sensory description	AH	CP
		MXT-5	MXT-1701					
1	$C_{11}H_{24}$	1098	1097	Terpinolene	98.92	Star anise; oranges; fresh fruits; herbaceous plant; pine tree, plastic, sweet, woody scent	+	
2	$C_{10}H_{18}O_2$	1474	1688	Gamma-decalactone	98.76	Coconut; greasy; fresh; fruity (dry); lactones; greasy; oily (fresh); peach; sweet; candlesmell		+
3	$C_{15}H_{32}$	1486	1488	Pentadecane	96.78	Alkane; heteroalcohols; freshly mowed	+	
4	$C_{12}H_{24}O_2$	1417	1488	Methy lundecanoate	96.24	Brandy; greasy; fruits; greasy; sweet; thesmellofcandles; wine	+	
5	$C_{10}H_{22}$	953	963	4-ethyl-octane	95.84		+	
6	$C_{12}H_{26}$	1146	1130	Decane	95.47	Oak; apple; greasy; fruits; grass; freshly mowed; luxuriant		+
7	$C_6H_{10}O$	802	893	(Z)-3-hexenal	95.41			+
8	$C_{10}H_{16}O$	1147	1288	Camphor	94.61	Greasy; freshly mowed; greenpepper; mushrooms; pepper; butter	+	+
9	$C_{13}H_{20}O$	1405	1559	Alpha-ionone	94.43	Fragrant with oil or spices; cedar; floral or botanical; fruits; dovetail; sweet; tropical; the violet; warm; woody scent		+
10	$C_5H_{10}O$	664	740	2-methyl butanal	94.32	Almonds; apple; charred; burning (strong); asphyxiating; coco; coffee; fermented or brewed; fruits; freshly mowed; iodoform; malt; musty smell; nutty; powerful; agreasy smell of incense; acidity	+	
11	$C_{13}H_{28}$	1307	1286	Tridecane	94.27	Alkane; oranges; fruits; heteroalcohols; hydrocarbon	+	+
12	C_4H_8O	600	693	Butan-2-one	94.16	Acetone; butter; cheese; chemistry; chocolate; the atmosphere; aromatic; fruits; gaseous; cheerful; spicy; sharp; sweet	+	
13	$C_5H_8O_2$	943	1097	4-pentanolide	93.90	Fennel; coco; herbaceous; sweet; tobacco; warm; woody scent	+	
14	C_3H_6O	459	559	Propanal	93.85	Acetaldehyde; coco; earthy; the atmosphere; nutty; plastics; spicy; solvent	+	
15	$C_{10}H_{14}O$	1182	1338	Cymen-8-ol	93.60	Cherry; oranges; coumarin; floral or botanical; fruits; fruity (sweet); musty smell; sweet		+
16	C_8H_{18}	683	681	2,2,4-trimethyl pentane	93.27	Gasoline	+	+
17	$C_6H_{14}O$	802	893	2-hexanol	93.05	Cauliflower; chemistry; greasy; fruits; terpene; wine	+	
18	$C_7H_{10}O_3$	1190	1445	5-ethyl-3-hydroxy-4-methyl-2(5H)-furanone	92.35	Brown sugar; butterscotch; caramel; fruits; fruity (sweet); maple; nutty; condiments; spicy; sweet	+	
19	$C_{10}H_{16}$	1037	1078	Limonene	91.55	Oranges; freshly mowed; pine tree	+	+
20	C_5H_{12}	518	485	Pentane	87.72	Alkane; gasoline		+
21	C_8H_{18}	769	789	3-methylheptane	86.20	Green plants; sweet	+	
22	$C_{10}H_{10}O_2$	1407	1560	(E)-methyl cinnamate	83.67		+	
23	$C_{13}H_{26}O_2$	1533	1607	Methyl dodecanoate	83.01	Coconut; creamy; greasy; floral or botanical; fruits; mushrooms; soap; sweet; the smell of candles; waxy	+	

(Continued on following page)

10.3389/fchem.2025.1578126

TABLE 1 (*Continued*) Possible compounds and sensory descriptions of AH and CP.

	Molecular formula	Reserved parameter		Possible compound	Correlation index	Sensory description	AH	CP
		MXT-5	MXT-1701					
24	$C_{10}H_{12}O_2$	1244	1358	Ethyl phenylacetate	82.62	Fennel; cinnamon; coco; floral or botanical; fruits; honey; rose; spicy; sweet; candlesmell	+	
25	C_2H_4O	433	499	Acetaldehyde	81.05	Aldehyde group; the atmosphere; fresh; fruits; cheerful; piquant	+	+
26	$C_{10}H_{16}$	995	1069	Alpha-phellandrene	73.02	Orange; freshly cut grass scent; mint flavor; spicy; terpene aroma; pine resin; woody scent	+	
27	$C_{10}H_{16}$	995	1069	Myrcene	72.96	Sesame oil aroma; spice fragrance; airy; fruity; geranium; lemon; metallic; musty; plastic; pleasant; resinous; soapy; spicy; sweet; woody scent	+	
28	$C_{10}H_{16}$	995	1069	(+)-alpha-phellandrene	72.65	Dill flavor	+	
29	$C_{15}H_{24}$	1577	1627	1-phenyl-nonane	77.81		+	
30	C_9H_{20}	928	873	Nonane	76.80	Alkane; heteroalcohols; gasoline		+
31	$C_{10}H_{18}O$	1235	1358	3-decen-2-one	68.65	Unctuous	+	
32	$C_3H_6O_2$	484	596	Methy lacetate	52.09	Blackcurrant; the atmosphere; aromatic; fruits; fruity (sweet); cheerful; solvent; sweet	+	

2.3 Setup and conditions of E-nose

The E-nose (Alpha MOS SA Heracles NEO) was employed for analysis, equipped with an automatic sampling device, an ultra-fast gas chromatography (GC) unit, two flame ionization detectors (FID), and two columns of different polarities (MXT-5 and MXT-1701). The volume of a headspace vial was 20 mL and the sample weight was 1.0 g. Seven batches of samples were prepared and each sample was subjected to three replicate measurements. The injection volume was set at 4,000 μL, with an incubation temperature of 60°C and an incubation time of 20 min. The injection speed was 125 μL/s, lasting for 45 s. The inlet temperature was maintained at 200°C, while the trap temperature was set at 40 °C. Hydrogen was used as the carrier gas at a flow rate of 1.0 mL/min. The trap time was 50 s, and the final temperature of the trap was 240°C. The initial column temperature was 50°C. The temperature was programmed to ramp up from 0.5°C/s to 90°C, followed by an increase of 4°C/s to 250°C, where it was held for 15 s. The acquisition time was 137 s, and the FID gain was set at 12. A mixture of n-alkanes (C_6–C_{16}) was used as the chemical reference.

2.4 Setup and conditions of E-tongue

The sensors (AAE, CT0, CA0, C00, AE1) and reference electrodes of the E-tongue (INSET Intelligent Sensor Technology, Inc. Taste Sensing System SA402B) were separately immersed in the reference solution (30 mmol/L potassium chloride and 0.3 mmol/L tartaric acid) and 3.33 mol/L potassium chloride solution for 24 h for activation. Calibration was performed using the reference solution, followed by the measurement of the umami, saltiness, sourness, bitterness, astringency, and richness of seven batches of samples at a room temperature of 25°C. After a brief rinse with the reference solution, sensors C00 and AE1 were used to determine residual tastes (bitter and astringent aftertaste). The data acquisition time was 30 s, with a total of 4 cycles collected. Due to significant fluctuations in the data from the first cycle, this cycle's data was excluded from the analysis. Data from the second to fourth cycles were retained. Each batch was analyzed in triplicate, and the mean of triplicate measurements was adopted for subsequent analysis.

2.5 Conditions of LC-HR-Q-TOF-MS/MS

The chemical compositions of AH and CP were analyzed using an Agilent LC-6500 series Q-TOF liquid chromatography-mass spectrometry system. The separation column was an Agilent Phenyl-Hexyl column (4.6 × 50 mm, 3.5 μm). The mobile phase consisted of 0.1% formic acid in water (A) and acetonitrile (B). The flow rate was set at 0.5 mL/min. The injection volume was 1 μL. Gradient elution was performed as follows: 0–8 min, 5%–5% B; 8–20 min, 5%–20% B; 20–40 min, 20%–60% B; 40–45 min, 60%–95% B; 45–50 min, 95%–95% B. The Q-TOF-MS/MS system was used for analysis in positive or negative ion mode. The operational parameters were set as follows: drying gas temperature at 200°C, drying gas flow rate at 11 L/min, nebulizer gas pressure at 35 psi, sheath gas temperature at 350°C, sheath gas flow rate at 8 L/min, capillary voltage at 4,000 V, *m/z* range from 100 to 1,000, nozzle voltage at 1,000 V, fragmentation voltage at 120 V, and collision energy at 30 eV. Auto MS/MS was used for data acquisition. Compounds with available chemical reference standards could be accurately identified by comparing their retention times, molecular ions, and secondary fragment ions with those of the reference standards. For unknown compounds, a combined approach that utilized both self-built compound libraries and

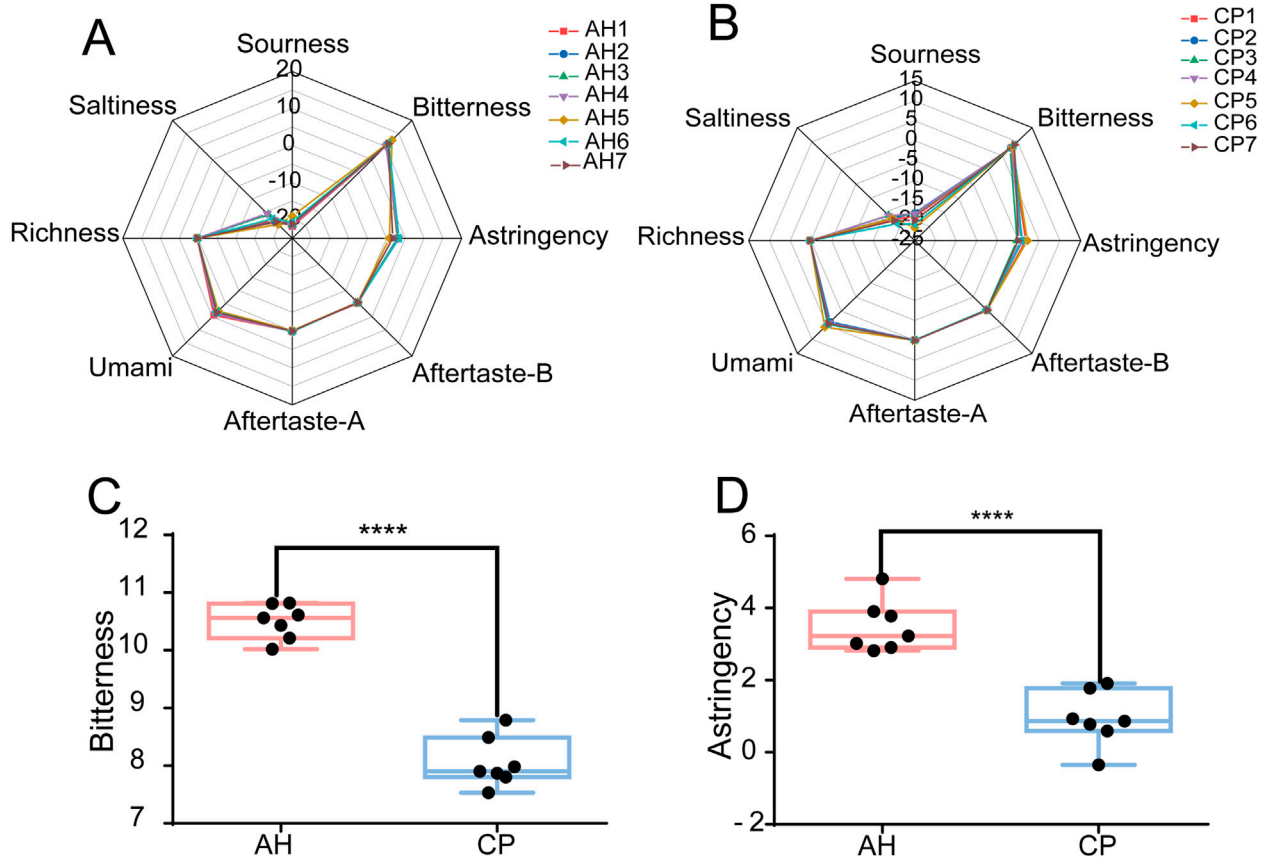

FIGURE 3
Electronic tastes of AH **(A)** and CP **(B)**. Comparison of bitterness **(C)** and astringency **(D)** between AH and CP.

public compound databases was employed for structural elucidation. On one hand, a mass spectrometry database for AH and CP was compiled from relevant literature, encompassing chemical formulas, molecular ions, fragment ions, and other related parameters (Wang et al., 2023; Wen et al., 2014; Zhang et al., 2021; Mao et al., 2017; Gao et al., 2019; Chen et al., 2023; Hu et al., 2025; Yu et al., 2016). On the other hand, public databases such as PubChem, METLIN, ChemSpider, and mzCloud spectral library were used for the structural comparison of the compounds.

2.6 Setup and conditions of electrochemical fingerprint spectra

The Belousov-Zhabotinsky reaction was conducted in a continuously stirred reactor (85–2 type, Changzhou Yuexin Instrument Manufacturing Co., Ltd.). A graphite electrode was used as the reference electrode, and a platinum electrode was used as the indicator electrode. To the reactor, 0.4 g of sample powder, 24 mL of H_2SO_4 solution (3 mol/L), 12 mL of $CH_2(COOH)_2$ solution (1 mol/L), and 6 mL of $(NH_4)_2SO_4$·$Ce(SO_4)_2$ solution (0.1 mol/L) were added. The temperature of the reaction system was controlled at 310 K. After stirring at a constant speed of 600 r/min for 5 min, 6 mL of $KBrO_3$ solution (0.2 mol/L) was rapidly injected through a syringe to initiate the reaction. Immediately, the data acquisition program was started to record the electrochemical fingerprint spectrum until the oscillation of electric potential disappeared.

2.7 Statistical analysis

To analyze Q-TOF data, Agilent MassHunter was employed. The Heracles NEO E-nose was controlled via Alpha Soft, wherein principal component analysis (PCA) and discriminant factor analysis (DFA) were implemented for data processing. The AroChemBase database was used to identify volatile compounds and obtain sensory description. Origin 2021 was utilized to generate fingerprint spectra for E-nose, radar charts for E-tongue, and electrochemical fingerprint spectra for Belousov-Zhabotinsky reaction. GraphPad Prism 6 was applied to generate box plots. SIMCA was utilized to perform PCA and orthogonal partial least squares discriminant analysis (OPLS-DA).

3 Result and discussion

3.1 Technical route

AH and CP are commonly used but easily confused medicinal plants due to their highly similar appearance. Due to the presence

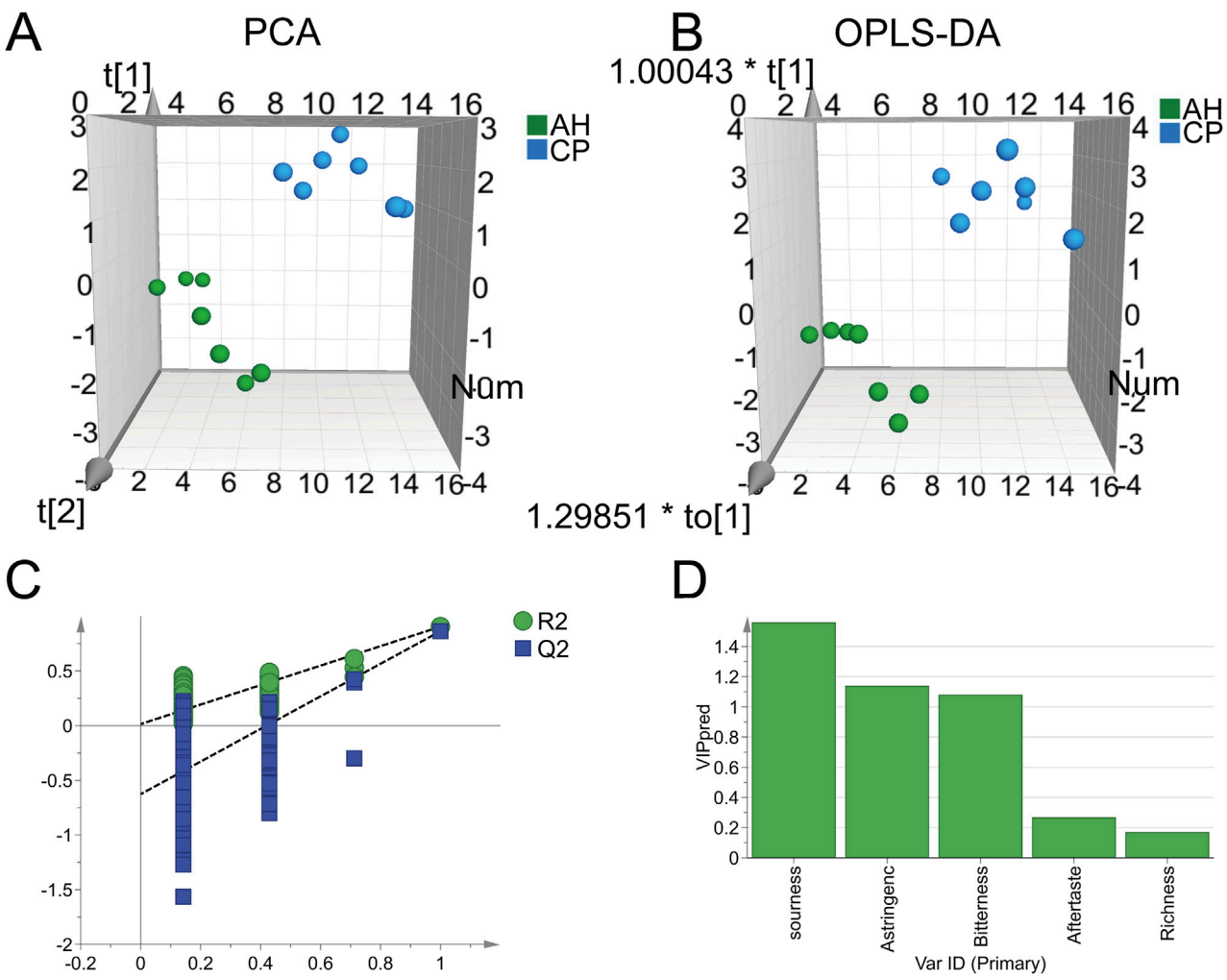

FIGURE 4
PCA **(A)** and OPLS-DA **(B)** of AH and CP based on electronic tastes. The permutation test **(C)** and VIP values **(D)** of OPLS-DA.

of toxic ingredients in AH, the conventional methods of identification through smell and taste cannot be employed to differentiate AH from CP. To achieve this, a four-step technical route utilizing dual electronic sensors (DES) and dual fingerprint spectra (DFS) was proposed for the first time (Figure 1). Firstly, an E-nose was applied to capture characteristic gas information, with PCA and DFA adopted to distinguish them further. Secondly, an E-tongue was utilized to obtain characteristic tastes, with radar charts and box plots used to analyze their taste differences. The strategy of DES could overcome the shortcomings of the traditional methods of olfactory and gustatory identification which could not be used for the identification of toxic medicinal plants. Thirdly, LC-HR-Q-TOF-MS/MS was employed to analyze the differences in chemical compositions between AH and CP, yielding their chemical fingerprint spectra. Fourthly, the Belousov-Zhabotinsky reaction was utilized to acquire electrochemical fingerprint spectra, differentiating them from the perspective of electrochemical properties. By integrating E-nose, E-tongue, chemical fingerprint spectra, and electrochemical fingerprint spectra, a systematic and multi-angled differentiation between AH and CP was achieved.

3.2 E-nose analysis

Using the Heracles NEO ultra-fast gas-phase E-nose, odor chromatograms for AH and CP were established on two types of chromatographic columns: MXT-5 and MXT-1701 (Figure 2). It was evident that each sample could be analyzed within 140 s, demonstrating remarkable efficiency. Through comparison with the Arochembase database, 25 odor components were identified in AH and 12 odor components in CP. Table 1 provides detailed information on the compounds and their odor descriptions. Five compounds, including camphene, tridecane, 2,2,4-trimethylpentane, limonene, and acetaldehyde, were found to be shared by AH and CP. These compounds were associated with a range of odor descriptions, such as freshly cut grass, fruity, aromatic, spicy, alkane-like, acidic, and petrol-like notes. The unique components in AH, such as pyridine, butylbutanoate,

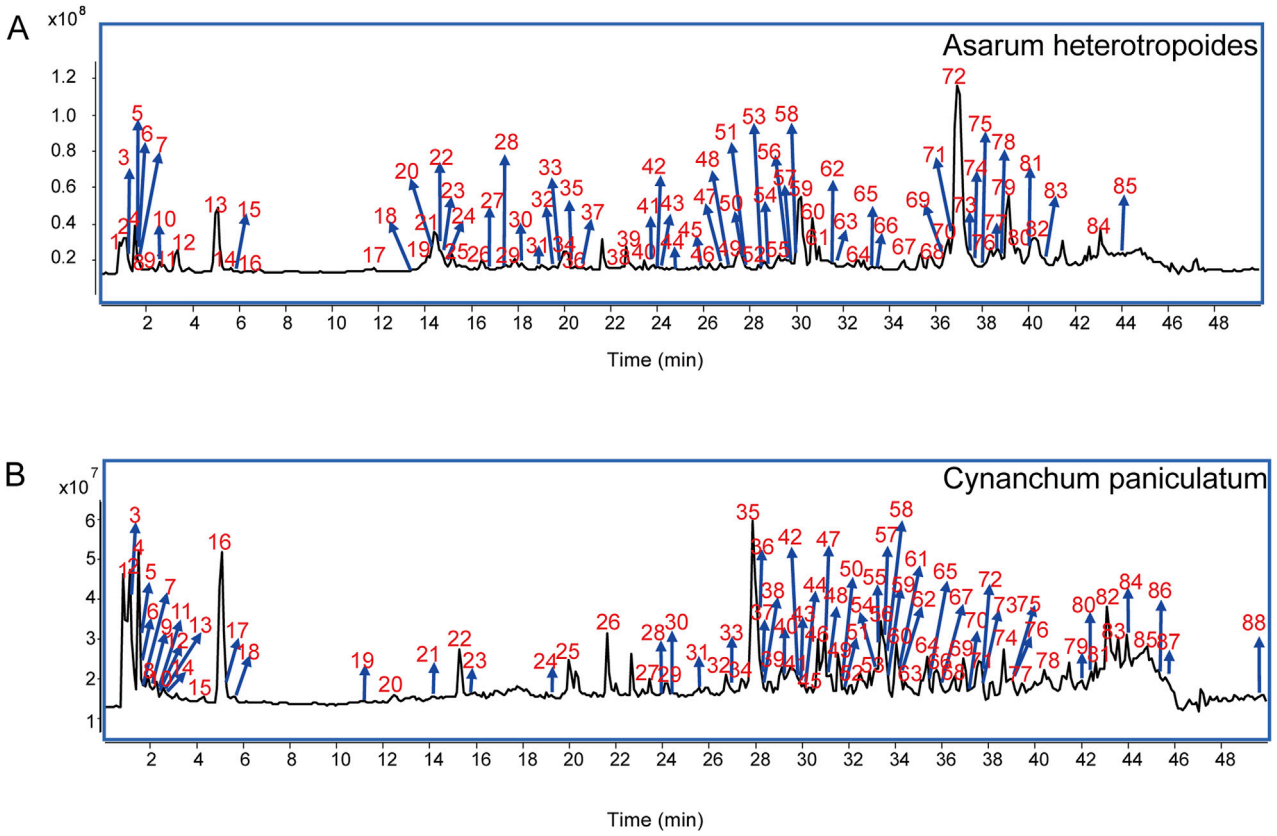

FIGURE 5
Total ion chromatograms of AH **(A)** and CP **(B)** in positive ion mode.

o-chlorotoluene, pentadecane, and butan-2-one, were primarily characterized by notes of freshly cut grass, alkane-like qualities, and spicy aromas. CP contained unique components like gamma-decalactone, hexane, (Z)-3-hexenal, alpha-ionone, and cymen-8-ol, which exhibited petrol-like, greasy, and sweet odors. While there were similarities in the odor descriptions of AH and CP, they also possessed distinct characteristics that set them apart.

To further distinguish AH from CP, the chromatographic peaks obtained by the E-nose were used as influencing factors for PCA (Figure 2E) and DFA (Figure 2F). In the PCA model, the first principal component (PC1) contributed 94.183%, while the second principal component (PC2) contributed 4.729%. The cumulative contribution rate of the principal components reached 98.912%, indicating that AH and CP could be well distinguished. In the DFA model, the horizontal and vertical coordinates represented the first discriminant factor (DF1) and the second discriminant factor (DF2), respectively. The DF1 in Figure 2F was 100%, suggesting that DFA could better distinguish AH and CP samples based on odor characteristics. The result demonstrated that the E-nose combined with DFA was effective to distinguish AH from CP from the perspective of odor. The efficiency of this method was demonstrated in two aspects. On the one hand, plant samples used for E-nose analysis did not require grinding and extraction, thus offering significant advantages in sample pretreatment. On the other hand, the single analysis time for each plant sample was 140 s, which significantly shortened the analysis time compared to traditional methods.

3.3 E-tongue analysis

The taste values of AH and CP samples were measured using an E-tongue, and radar charts were constructed based on the signals collected by the sensors (Figures 3A,B). While an initial observation suggested a similar overall shape in the radar charts, a closer analysis revealed significant differences ($P < 0.05$) between AH and CP in terms of bitterness, astringency, sourness, aftertaste-A, and richness, as shown in Figures 3C,D and Supplementary Figure S1. The taste response range of the E-tongue encompasses the following: sourness (−13 to 12), bitterness (0–25), astringency (0–25), and saltiness (−6–19). Importantly, only values falling within these ranges could reflect the corresponding taste. Notably, the bitterness and astringency of AH were significantly higher than those of CP, suggesting that these two tastes could serve as key discriminators between the two samples.

PCA and OPLS-DA were employed to further differentiate between AH and CP. As shown in Figures 4A,B, the samples of AH and CP could be clearly separated from each other. The PCA model achieved R^2 and Q^2 values of 0.869 and 0.607, respectively. Furthermore, the OPLS-DA model demonstrated R^2X, R^2Y, and Q^2 values of 0.93, 0.936, and 0.895, respectively. These parameters confirm the reliability of the results. To further validate the credibility of the model, a permutation test was performed (Figure 4C). Ideally, the R^2Y intercept and Q^2Y intercept of a valid model should not have exceeded 0.4 and 0.05, respectively

10.3389/fchem.2025.1578126

TABLE 2 Identification of compounds in AH by LC-HR-Q-TOF-MS/MS.

No.	t_R (min)	m/z (Error,ppm)	Formula	Fragmentions (m/z)	Identification
1	0.959	175.1194 (-2.57)^{H}	$C_6H_{14}N_4O_2$	130.0955,116.0700,112.0863	L-arginine
2	1.072	138.0553 (-2.52)^{H}	$C_7H_7NO_2$	123.0653,122.4088	Anthranilic acid
3	1.123	137.0600 (-2.16)^{H}	$C_8H_8O_2$	120.0783,121.0817	Ortho-hydroxyacetophenone[a]
4	1.508	137.0600 (-2.16)^{H}	$C_8H_8O_2$	120.0297,121.0733	4-hydroxyacetophenone[a]
5	1.553	180.1019 (0.03)^{NH4}	$C_{10}H_{10}O_2$	150.0546,124.0504,110.0365	Safrole
6	1.586	166.0863 (-0.27)^{H}	$C_9H_{11}NO_2$	122.0690,107.0485,151.1898	Phenylalanine
7	1.602	152.0704 (1.36)^{H}	$C_8H_9NO_2$	110.0338,135.0296	Acetaminophen
8	1.681	121.0648 (-0.07)^{H}	C_8H_8O	107.0724,103.0543	4-methylbenzaldehyde
9	2.182	180.1019 (0.03)^{NH4}	$C_{10}H_{10}O_2$	124.0508,110.0624	Isosafrole
10	2.339	229.0319 (-1.34)^{H}	$C_5H_4N_6O_5$	138.9636,122.0160,111.8917	6,8-dinitro-3,5-dihydrotetrazolo [1,5-a]pyridin-5-ol
11	2.668	166.0863 (-0.27)^{H}	$C_9H_{11}NO_2$	122.0855,108.0424,107.0496	Dimethylanthranilate
12	3.413	353.0847 (5.7)^{H}	$C_{16}H_{16}O_9$	177.0058,160.9132,118.9029	4-methylumbelliferyl glucuronide
13	5.033	200.0478 (-5.05)^{H}	$C_{12}H_7O_3$	157.0412,129.0443	6-formylnaphthalene-2-carboxylate
14	5.625	205.0969 (1.25)^{H}	$C_{11}H_{12}N_2O_2$	146.8926,132.0806,118.0647	Tryptophan
15	5.691	188.0707 (-0.51)^{H}	$C_{11}H_9NO_2$	188.0707,118.0647	3-indoleacrylic acid
16	6.856	136.0617 (0.53)^{H}	$C_5H_5N_5$	120.0381,107.0746	Adenine
17	11.657	330.1699 (0.26)^{H}	$C_{19}H_{23}NO_4$	207.0798,177.0787,164.8723,150.0901	Reticuline
18	13.885	379.1000 (6.24)^{H}	$C_{18}H_{18}O_9$	217.8755,189.8638,161.8689,185.0418,171.9442	Geshoidin
19	14.000	177.0545 (0.68)^{H}	$C_{10}H_8O_3$	151.0544,111.0370,134.0348	Hymecromone
20	14.113	147.0440 (0.38)^{H}	$C_9H_6O_2$	118.0407,102.0479	2-benzofurancarboxaldehyde
21	14.403	273.0757 (0.18)^{H}	$C_{15}H_{12}O_5$	181.0626,155.0234,153.0177,147.0438,137.9719	(2S)-naringenin
22	14.447	314.1758 (-2.32)	$C_{19}H_{24}NO_3^+$	209.0954,167.0830,179.0888,153.0692	Magnocurarine
23	14.683	344.1856 (0.10)^{H}	$C_{20}H_{25}NO_4$	192.1013,162.0670,138.0625,108.0558	Cilomilast
24	14.906	314.1758 (-2.32)	$C_{19}H_{24}NO_3^+$	209.0950,167.0799,179.0884,153.0698	Lotusine
25	15.251	177.0545 (0.68)^{H}	$C_{10}H_8O_3$	121.0261,109.9687,105.0331	7-methoxycoumarin
26	16.461	236.1643 (0.87)^{H}	$C_{14}H_{21}NO_2$	165.0687,121.0644	Spectraban
27	16.694	344.1856 (0.10)^{H}	$C_{20}H_{25}NO_4$	207.0785,177.0749,147.8670,139.9561	Laudanine
28	17.584	231.0626 (-0.43)^{H}	$C_9H_6N_6O_2$	148.9010,110.9477	4-[5-(Pyridin-3-yl)-1,2,4-oxadiazol-3-yl]-1,2,5-oxadiazol-3-amine
29	17.881	353.1207 (6.80)^{H}	$C_{17}H_{20}O_8$	207.9798,177.8574,164.8723,146.8601	RhytidchromoneD
30	18.153	314.1758 (-2.32)	$C_{19}H_{24}NO_3$	209.0950,167.0832,179.0903,153.0691	(R)-oblongine
31	19.196	236.1643 (0.87)^{H}	$C_{14}H_{21}NO_2$	123.0438,107.0485	Meprylcaine
32	19.398	201.1634 (1.88)^{H}	$C_{15}H_{20}$	187.1392,159.1155,145.0995,131.0846	3,4-dihydrocadalene
33	19.479	268.1328 (1.51)	$C_{17}H_{18}NO_2$	251.1069,219.0783,236.0822,191.0844	Unknown
34	20.165	435.1289 (-0.75)^{H}	$C_{21}H_{22}O_{10}$	273.0748,181.0637,153.0179	(2S)-naringenin-5-O-beta-D-glucopyranoside
36	20.238	273.0757 (0.18)^{H}	$C_{15}H_{12}O_5$	181.0615,155.0236,153.0179,147.0444,137.8857	(2R)-naringenin
35	20.255	597.1824 (-1.68)^{H}	$C_{27}H_{32}O_{15}$	435.1288,273.0756	(2R)-naringenin5,7-di-O-glucoside
37	20.467	278.1746 (1.70)^{H}	$C_{16}H_{23}NO_3$	128.8733,112.9887,152.9022	Cordypyridone B

(Continued on following page)

TABLE 2 (*Continued*) Identification of compounds in AH by LC-HR-Q-TOF-MS/MS.

No.	t_R (min)	m/z (Error,ppm)	Formula	Fragmentions (m/z)	Identification
38	22.487	215.0678 (0.34)^{Na}	$C_{11}H_{12}O_3$	175.0678,144.0570,114.9631	Myristicin
39	22.836	304.1883 (0.05)^{Na}	$C_{16}H_{27}NO_3$	222.0666,179.0847,165.0698,205.0649	Scalusamide A
40	23.237	304.1883 (0.05)^{Na}	$C_{16}H_{27}NO_3$	248.8163,164.0674	3,3-dimethyl-1-[(2S)-2-pentanoylpyrrolidin-1-yl]pentane-1,2-dione
41	23.814	282.1488 (0.21)^{NH4}	$C_{18}H_{16}O_2$	265.1211,250.0973,235.0750,219.0797	Unknown
42	23.839	265.1223 (0.02)^{H}	$C_{16}H_{18}O_2$	153.0688,108.9738,122.9137	1,2-bis(3-methylphenoxy)ethane
43	24.071	304.1883 (0.05)^{Na}	$C_{16}H_{27}NO_3$	206.8651,164.0700,136.8765	3-acetyl-5-hydroxy-4,5-dimethyl-1-octyl-2-pyrrolone
44	24.696	304.1883 (0.05)^{Na}	$C_{16}H_{27}NO_3$	231.8412,180.8673	Ethyl1-(3-cyclopentylpropanoyl)piperidine-4-carboxylate
45	25.939	336.1229 (0.40)^{H}	$C_{20}H_{17}NO_4$	320.0908,292.0961,184.9388	N-(biphenyl-4-ylmethyl)-3-hydroxy-6-methyl-4-oxo-4H-pyran-2-carboxamide
46	26.254	387.1413 (6.55)^{H}	$C_{21}H_{22}O_7$	302.8310,276.8630,202.8263,176.0397	Sen-byakangelicol
47	26.749	291.1295 (1.42)^{H}	$C_{10}H_{18}N_4O_6$	247.0652,203.0687,159.0353	L-argininosuccinic acid
48	27.021	387.1413 (6.55)^{H}	$C_{21}H_{22}O_7$	289.1100,188.8615,161.0210	Edultin
49	27.426	226.1799 (1.13)^{H}	$C_{13}H_{23}NO_2$	144.8945,100.9319	Cyclohexyln-cyclohexylcarbamate
50	27.615	183.1012 (2.04)^{H}	$C_{10}H_{14}O_3$	168.0745,153.0537,125.0594,137.0592,152.0812	3,4,5-trimethoxytoluene
51	27.665	205.0832 (0.17)^{H}	$C_8H_8N_6O$	137.9020,122.9628,106.9811	2-[(e)-(2H-tetrazol-5-ylhydrazinylidene)methyl]phenol
52	27.688	168.0778 (1.77)^{H}	$C_9H_{11}O_3$	152.0611,109.0283,137.0060	(3,4-dimethoxyphenyl)methanolradical
53	28.561	179.0700 (1.52)^{H}	$C_{10}H_{10}O_3$	135.9491,108.9598,121.0283	Trans-4-methoxycinnamic acid
54	28.646	308.0557 (-1.14)^{H}	$C_{17}H_9NO_5$	222.0650,278.0566,250.0593,280.0596,252.0642	17-hydroxy-3,5-dioxa-11-azapentacyclo [10.7.1.02,6.08,20.014,19]icosa-1(19),2(6),7,12(20),13,15,17-heptaene-9,10-dione
55	29.223	183.1013 (1.49)^{H}	$C_{10}H_{14}O_3$	168.0745,153.0537,125.0594,137.0592,152.0812	2,4,6-trimethoxytoluene
56	29.616	228.1955 (1.34)^{H}	$C_{13}H_{25}NO_2$	158.0950,144.0575,100.9321	Cyclohexyl-carbamic acidhexylester
57	29.634	250.1774 (0.28)^{H}	$C_{11}H_{19}N_7$	166.1208,155.8579,112.8977	Metazine
58	30.108	209.0809 (-0.31)^{H}	$C_{11}H_{12}O_4$	176.0447,161.0231	2-methoxyl-methylenedioxypropiophenone
59	30.182	308.0557 (-1.14)^{H}	$C_{17}H_9NO_5$	222.0637,278.0567,250.0595,280.0616,252.0634	7-hydroxy-3,5-dioxa-11-azapentacyclo [10.7.1.02,6.08,20.014,19]icosa-1(20),2(6),7,12,14,16,18-heptaene-9,10-dione
60	30.815	338.0665 (-1.74)^{H}	$C_{18}H_{11}NO_6$	294.0460,265.0489,250.0261,206.0595	4-[(z)-[2-(1,3-benzodioxol-5-yl)-5-oxo-1,3-oxazol-4-ylidene] methyl]benzoic acid
61	30.983	318.3005 (-0.72)^{H}	$C_{18}H_{39}NO_3$	192.8404,164.8297,136.9307	Phytosphingosine
62	31.506	205.0969 (1.25)^{H}	$C_{11}H_{12}N_2O_2$	176.0463,122.0709	Ethotoin
63	31.512	195.0652 (-0.08)^{H}	$C_{10}H_{10}O_4$	167.0330,138.9622,123.0408	Kakuol
64	32.667	294.0760 (0.29)^{H}	$C_{17}H_{11}NO_4$	279.0521,251.0571,264.0656,236.0693	Aristolactam I
65	33.292	318.3005 (-0.72)^{H}	$C_{18}H_{39}NO_3$	192.8434,164.8287,136.9309	2-aminooctadecane-1,3,4-triol
66	33.462	302.3052 (0.52)^{H}	$C_{18}H_{39}NO_2$	246.8158,176.9090,106.0860	Sphinganine
67	34.616	222.1850 (1.09)^{H}	$C_{14}H_{23}NO$	101.9493,152.1066,191.0324	N-isobutyl-2E,4E,8Z-decatrienamide
68	35.844	219.1741 (1.11)^{H}	$C_{15}H_{22}O$	178.0759,150.0992,122.0691,163.1103,123.0798	Nootkatone
69	36.445	250.2165 (0.16)^{H}	$C_{16}H_{27}NO$	140.8710,112.9899,100.0754	(2E,4E)-1-(pyrrolidin-1-yl)dodeca-2,4-dien-1-one
70	36.558	219.1741 (1.11)^{H}	$C_{15}H_{22}O$	191.0859	Longiverbenone
71	36.564	224.2013 (-1.83)^{H}	$C_{14}H_{25}NO$	167.0813	Pellitorine

(Continued on following page)

TABLE 2 (*Continued*) Identification of compounds in AH by LC-HR-Q-TOF-MS/MS.

No.	t_R (min)	m/z (Error,ppm)	Formula	Fragmentions (m/z)	Identification
72	37.175	249.2077 (4.09)^H	$C_{16}H_{26}NO$	178.1300,151.1344,155.1157	N-methylmeptazinol
73	37.334	248.2014 (-2.06)^H	$C_{16}H_{25}NO$	167.8590,152.1068	N-isobutyl-2E,4E,8Z,10E-dodecatetraenamide
74	37.576	337.1075 (-1.34)^H	$C_{20}H_{16}O_5$	321.0957,267.0612,237.0545	Psoralidin
75	37.911	248.2014 (-2.06)^H	$C_{16}H_{25}NO$	167.1264,152.1066	N-isobutyl-2E,4E,8Z,10Z-dodecatetraenamide
76	38.392	250.2165 (0.16)^H	$C_{16}H_{27}NO$	153.1093,127.0939,116.0588	Dodeca-2E,4E,8Z-trienoic acidisobutylamide
77	38.522	248.2014 (-2.06)^H	$C_{16}H_{25}NO$	167.8582,152.1066	N-isobutyl-2E,4Z,8Z,10E-dodecatetraenamide
78	38.714	284.1986 (-1.37)^H	$C_{16}H_{27}O_4$	171.8515,116.0529,128.8711	Monododecylmaleate
79	39.258	274.2171 (-2.05)^H	$C_{18}H_{27}NO$	120.0886,107.0853	8-acetyl-2-(dipropylamino)tetralin
80	39.620	296.1987 (-1.66)^H	$C_{17}H_{27}O_4$	196.7978,153.9014,127.0712	(E)-5-cyclohexyl-2-[2-[(2-methylpropan-2-yl)oxy]-2-oxoethyl]pent-2-enoate
81	40.125	252.2326 (-1.63)^H	$C_{16}H_{29}NO$	154.1219,112.0753,128.1425,102.0904	(2E,4E)-N-isobutyl-2,4-dodecadienamide
82	40.198	274.2171 (-2.05)^H	$C_{18}H_{27}NO$	120.0534,107.0491	7-(N,N-Dipropylamino)-5,6,7,8-tetrahydronaphtho (2,3-b) dihydro-2,3-furan
83	40.509	276.2324 (-0.76)^H	$C_{18}H_{29}NO$	176.1107,146.0701,107.0850	(1S,2R)-5-methoxy-1-methyl-N,N-dipropyl-1,2,3,4-tetrahydronaphthalen-2-amine
84	42.875	359.1265 (3.59)^H	$C_{23}H_{18}O_4$	345.1991,253.1547,177.9723,147.0110	7-(benzyloxy)-3-(4-methoxyphenyl)-4H-chromen-4-one
85	44.208	415.0429 (4.69)^H	$C_{23}H_{10}O_8$	268.0054,241.9654,165.0678,149.0265	5-[4-[(1,3-dioxo-2-benzofuran-5-yl)oxy]benzoyl]-2-benzofuran-1,3-dione

Na, $[M + Na]^+$; H, $[M + H]^+$; NH_4, $[M + NH_4]^+$.
[a]The compounds were identified by comparing with reference substances.

(Wang et al., 2024). In this case, the R^2Y intercept and Q^2Y intercept were 0.113 and −0.666 respectively, indicating the results were credible. A VIP value greater than 1 was considered a criterion for differential variables (Wang et al., 2024). As shown in Figure 4D, the VIP values for bitterness and astringency exceeded this threshold, which was consistent with the previous findings. Consequently, the results suggested that the E-tongue could effectively differentiate between AH and CP from the perspective of tastes. The necessity of employing E-tongue analysis was underscored by two aspects: (1) AH contained toxic components such as aristolochic acid-like ingredients, thus traditional taste-testing methods could lead to poisoning; (2) The taste of CP was unpleasant and nauseating, making taste-testing methods unsuitable as well.

3.4 Chemical fingerprint spectra based on LC-HR-Q-TOF-MS/MS

3.4.1 Identification of chemical compositions

The chemical compositions of AH and CP were analyzed using LC-HR-Q-TOF-MS/MS. As a result, 91 compounds were identified in AH, comprising 32 nitrogen-containing compounds, 28 volatile oils, 11 organic acids, 6 coumarins, 5 flavonoids, 3 lignans, and 6 other compounds. Notably, ortho-hydroxyacetophenone, 4-hydroxyacetophenone, vanillic acid, and asarinin were confirmed by comparison with their respective chemical standards. The total ion chromatogram (TIC) of AH in positive ion mode is presented in Figure 5A, with detailed compound information listed in Table 2. For negative ion mode, the TIC and compound information are shown in Supplementary Figure S2 and Supplementary Table S1, respectively. Similarly, 90 compounds were identified from CP, including 22 steroidal compounds, 24 nitrogen-containing compounds, 14 volatile oils, 10 organic acids, 8 saccharides, 2 lignans, and 10 other compounds. Among these, paeonol was positively identified by comparison with its chemical standard. The TIC of CP extract in positive ion mode is depicted in Figure 5B, and the corresponding compound information is presented in Table 3. For negative ion mode, the TIC and compound information are shown in Supplementary Figure S3 and Supplementary Table S2, respectively. The discussion on the MS/MS fragmentation patterns of compounds in AH and CP is as follows.

3.4.2 Fragmentation patterns of main compositions in AH

Safrole (Figure 6A) was taken as an example of volatile oils for illustration. The quasi-molecular ion at *m/z* 180 initially underwent methoxy group cleavage to eliminate a molecule of CH_2O, generating an ion at *m/z* 150. This process might have involved the formation of an allylic carbocation intermediate. Subsequently, the ion at *m/z* 150 underwent rearrangement within the conjugated double bond system, eliminating C_2H_2 to yield an ion at *m/z* 124. Finally, this fragment underwent either cleavage of the aromatic ring side-chain CH_2 group or exocyclic rearrangement to form the stable

10.3389/fchem.2025.1578126

TABLE 3 Identification of compounds in CP by LC-HR-Q-TOF-MS/MS.

No.	tR (min)	m/z (Error,ppm)	Formula	Fragmentions (m/z)	Identification
1	1.007	469.2150 (2.58)^{H}	$C_{23}H_{48}O_8$	207.0872,181.1031	2-[(E)-4-(2-hydroxy-2-tricyclo [9.4.0.03,8]pentadeca-1 (15),3,5,7,9,11,13-heptaenyl)but-2-enyl]tricyclo [9.4.0.03,8]pentadeca-1 (15),3,5,7,9,11,13-heptaen-2-ol
2	1.087	398.1664 (-1.79)^{H}	$C_{14}H_{21}N_8O_6$	180.0641,164.0709	Methyl 3-o-(2-acetamido-2-deoxy-b-D-galactopyranosyl)-a-D-galactopyranoside
3	1.158	365.1061 (-1.95)^{Na}	$C_{12}H_{22}O_{11}$	186.9692,203.0519	Melibiose
4	1.399	365.1061 (4.77)^{H}	$C_{20}H_{43}NO_4$	179.1147,164.0699,150.0893	2-[(2S,3R,4R,5R,6R)-4,5-diacetyloxy-6-(acetyloxymethyl)-3-hydroxyoxan-2-yl]oxyacetic acid
5	1.535	268.1045 (-1.76)^{H}	$C_{10}H_{13}N_5O_4$	136.0617,121.0752	Adenosine
6	1.551	182.0814 (-1.27)^{H}	$C_9H_{11}NO_3$	136.0755,119.0734	D-Thr-OH
7	1.648	294.1547 (0.10)^{H}	$C_{12}H_{23}NO_7$	234.9316,147.0539,117.9572	1,2-O-dimethyl-4-[2,4-dihydroxy-butyramido]-4,6-dideoxy-alpha-D-mannopyranoside
8	1.681	276.1420 (-0.13)^{H}	$C_{12}H_{21}NO_6$	190.0614,148.9078	Triethanolaminetriacetate
9	1.936	420.198 (-0.82)^{H}	$C_{17}H_{29}N_3O_9$	258.1306,198.1222,126.0581	Ethyl(2S,4R,5R)-5-azido-4-(methoxymethoxy)-6-[5-(methoxymethoxy)-2-methyl-1,3-dioxan-4-yl]oxane-2-carboxylate
10	1.945	201.0732 (-0.68)^{H}	$C_5H_8N_6O_3$	158.0701,128.9388,113.9639	2-[(E)-[amino-(4-amino-1,2,5-oxadiazol-3-yl) methylidene]amino]oxyacetamide
11	2.145	298.1396 (0.50)^{H}	$C_{13}H_{15}N_3O_5$	179.0685,122.0610	Hippuryl-glycyl-glycine
12	2.256	420.1980 (-0.82)^{H}	$C_{17}H_{29}N_3O_9$	288.1544,203.0967,159.0642	2-[2-[bis(carboxymethyl)amino]ethyl-[2-[carboxymethyl-(3-methyl-2-oxobutyl)amino]ethyl] amino]acetic acid
13	2.321	283.1402 (-5.16)^{H}	$C_{11}H_{22}O_8$	223.1172,163.0966,103.0537	(2R,5R)-3,4-bis(methoxymethoxy)-5-(methoxymethoxymethyl)oxolan-2-ol
14	2.530	214.1186 (6.38)^{H}	$C_{11}H_{17}O_4$	174.8792,116.9289	2-o-allyl-3,4-O-isopropylidenearabinopyranosylradical
15	4.342	253.1294 (-4.48)^{H}	$C_{10}H_{20}O_7$	179.9909,149.9065,123.0985	2,3-butanediolglucoside
16	5.240	200.0478 (-5.05)^{H}	$C_{12}H_7O_3$	156.0382,128.0163	2-naphthalen-1-yl-2-oxoacetate
17	5.658	188.0706 (0.03)^{H}	$C_{11}H_9NO_2$	171.0617,143.0721,118.0645,104.0489	3-indoleacrylic acid
18	5.723	297.1557 (-4.41)^{H}	$C_{12}H_{24}O_8$	203.9758,149.0712	Caryophyllose
19	11.239	273.1915 (2.27)^{H}	$C_{12}H_{24}N_4O_3$	174.8691,131.0996,130.0973	4-amino-1-[(3-amino-propyl)-isopropyl-carbamoyl]-pyrrolidine-3-carboxylic acid
20	12.490	313.1249 (-8.31)^{H}	$C_{22}H_{16}O_2$	236.8742,144.8656,128.8721	6-(4-hydroxy-phenyl)-1-phenyl-naphthalen-2-ol
21	14.174	362.2407 (1.20)^{H}	$C_{16}H_{27}N_9O$	169.9317,140.9187,211.8761,126.9461	2-[[4-[2-(dimethylamino)ethylamino]-6-ethyl-1,3,5-triazin-2-yl]amino]-N-ethyl-3-methylimidazole-4-carboxamide
22	15.304	483.1475 (-7.61)^{H}	$C_{29}H_{22}O_7$	229.0671,257.0607,215.0571,171.0257	2-oxopropane-1,3-diylbis (3-phenoxybenzoate)
23	15.810	437.2351 (0.78)^{H}	$C_{16}H_{32}N_6O_8$	219.8877,191.0225,147.9832	2-[[1-[2-[1,1-bis(carboxymethylamino)ethyl-methylamino]ethyl-methylamino]-1-(carboxymethylamino)ethyl]amino]acetic acid
24	19.387	399.1408 (0.86)^{H}	$C_{18}H_{18}N_6O_5$	311.0778,178.0652,148.8566,134.9326	N6-methoxy-2-[(2-pyridinyl)ethynyl]adenosine
25	19.965	399.1408 (0.86)^{H}	$C_{18}H_{18}N_6O_5$	353.1377,220.8733,206.1003	N-[3-[4-(hydroxycarbamoyl)phenoxy]propyl]-6-oxo-2-pyrazol-1-yl-1h-pyrimidine-5-carboxamide
26	21.655	701.4939 (6.85)^{H}	$C_{42}H_{68}O_8$	557.0080,412.9373	5-[[(1S,3aS,5aR,5bR,7aR,9S,11aR,11bR,13aR,13bR)-9-(5-hydroxy-3-methyl-5-oxo-pentanoyl)oxy-1-isopropyl-5a,5b,8,8,11a-pentamethyl-1,2,3,4,5,6,7,7a,9,10,11,11b,12,13,13a,13b-hexadecahydrocyclopenta [a]chrysen-3a-yl]methoxy]-3-methyl-5-oxo-pentanoic acid

(Continued on following page)

TABLE 3 (*Continued*) Identification of compounds in CP by LC-HR-Q-TOF-MS/MS.

No.	tR (min)	m/z (Error,ppm)	Formula	Fragmentions (m/z)	Identification
27	23.492	475.3258 (1.57)^{H}	$C_{25}H_{46}O_8$	279.8175,221.9363	(5-acetyloxy-3,4-diheptoxy-6-methoxyoxan-2-yl) methylacetate
28	23.814	219.1008 (3.93)^{H}	$C_{12}H_{27}NO_2$	165.1682,137.0588,120.9529	Chuanxiongol
29	24.180	297.2206 (2.34)^{H}	$C_{21}H_{28}O$	221.1308,185.1308,169.1003	Phenol,2,4-bis(1,1-dimethylethyl)-6-(phenylmethyl)-2,4-di-tert-butyl-6-benzylphenol
30	24.197	679.3301 (-0.13)^{Na}	$C_{33}H_{52}O_{13}$	679.3290,517.2774,312.0463,297.2187	Cynapanoside G
31	25.532	308.2213 (2.34)^{H}	$C_{18}H_{29}NO_3$	251.1494,193.1422,138.0851,123.0668,109.0517	Betaxolol
32	26.747	291.1297 (0.73)^{H}	$C_{10}H_{18}N_4O_6$	247.0651,176.1423,160.0386	L-argininosuccinic acid
33	27.038	443.1671 (1.28)^{Na}	$C_{22}H_{28}O_8$	291.4742,260.8591,230.0843,146.1015,154.0119	(−)-lyoniresinol
34	27.469	266.1721 (1.07)^{H}	$C_{17}H_{17}N_2O$	180.9167,154.0762,152.8657	(2S,4S)-4-azido-1-((S)-2,6-diaminohexanoyl) pyrrolidine-2-carbonitrile
35	27.806	167.0702 (0.43)^{H}	$C_9H_{10}O_3$	125.0588,111.0394,137.0425	Paeonol*
36	27.973	262.0157 (5.24)^{H}	$C_6H_9NO_9$	218.1872,202.9778,144.9735	Glycolatenitrogen
37	28.094	167.0702 (0.43)^{H}	$C_9H_{10}O_3$	153.0692,137.0221,121.0642,111.0388	Isopaeonol
38	28.163	167.0702 (0.43)^{H}	$C_9H_{10}O_3$	153.0674,123.0697,109.0275	Ethylparaben
39	29.077	979.4513 (-0.40)^{Na}	$C_{47}H_{72}O_{20}$	979.4491,817.0969,673.3171	Komaroside O
40	29.226	250.1773 (0.68)^{H}	$C_{12}H_{25}O_5$	193.0993,136.0314	Metazine
41	29.538	250.1773 (0.68)^{H}	C12H25O_5	168.8645,141.0679,113.9636	[4,6-bis(ethylamino)-1,3,5-triazin-2-yl]-propan-2-ylcyanamide
42	29.604	228.1953 (2.23)^{H}	$C_{13}H_{25}NO_2$	130.8979,116.9627,102.9469	4-nonanoylmorpholine
43	29.827	250.1773 (0.68)^{H}	$C_{12}H_{25}O_5$	168.9394,141.8710,113.9628	Ethyl-(4-ethylamino-6-isopropylamino-[1,3,5]triazin-2-yl)-cyanamide
44	30.084	250.1773 (0.68)^{H}	$C_{12}H_{25}O_5$	235.8168,151.9062	8-(6-aminohexyl)-amino-adenine
45	30.379	285.2894 (2.25)^{H}	$C_{17}H_{36}N_2O$	173.9206,117.0710	Tetrabutylurea
46	30.665	274.2742 (-0.53)^{H}	$C_{16}H_{35}NO_2$	230.2460,106.0859	N-lauryldiethanolamine
47	30.921	979.4513 (-0.40)^{Na}	$C_{47}H_{72}O_{20}$	979.4499,817.3955,673.3178,299.0703	Komaroside U
48	30.990	318.3003 (-0.09)^{H}	$C_{18}H_{39}NO_3$	164.8291,150.1119,106.0649	2,2'-((2-(dodecyloxy)ethyl)imino)bisethanol
49	31.416	993.4648 (1.82)^{Na}	$C_{48}H_{74}O_{20}$	933.4630,833.4395	Marstenacisside A3
50	31.607	817.4020 (-4.92)^{Na}	$C_{41}H_{62}O_{15}$	673.3181,383.1164	Glaucoside D
51	31.672	979.4513 (-0.40)^{Na}	$C_{47}H_{72}O_{20}$	979.4501,817.3950,673.3165,299.0700	Achyranthoside C
52	32.170	316.2842 (1.33)^{H}	$C_{18}H_{37}NO_3$	246.8668,176.0696,162.8314	N,N-bis(2-hydroxypropyl)dodecanamide
53	32.883	304.2632 (0.96)^{H}	$C_{20}H_{33}NO$	191.1254,149.0471,248.2005	Fenpropimorph
54	33.147	831.4144 (-0.81)^{Na}	$C_{42}H_{64}O_{15}$	655.3060,297.1291	(+)-divaroside
55	33.341	817.4020 (-4.92)^{Na}	$C_{41}H_{62}O_{15}$	673.3206,543.2544	Cynapanoside C
56	33.376	963.4573 (-1.38)^{Na}	$C_{41}H_{62}O_{15}$	801.4019,657.3241,299.0692	Cynatratoside D
57	33.448	302.3051 (0.85)^{H}	$C_{18}H_{39}NO_2$	302.3051,260.2358,246.1843,232.1683,218.1529,190.1215	Sphinganine

(Continued on following page)

TABLE 3 (*Continued*) Identification of compounds in CP by LC-HR-Q-TOF-MS/MS.

No.	tR (min)	m/z (Error,ppm)	Formula	Fragmentions (m/z)	Identification
58	33.580	963.4573 (-1.38)^{Na}	$C_{47}H_{72}O_{19}$	657.3232,299.0692	Cynatratoside E
59	33.653	817.4020 (-4.92)^{Na}	$C_{41}H_{62}O_{15}$	673.3181,543.2543,383.1164	Cynapanoside F
60	34.094	817.4020 (-4.92)^{Na}	$C_{41}H_{62}O_{15}$	673.3181,543.2543,383.1164	Glaucoside C
61	34.109	977.4718 (-0.16)^{Na}	$C_{48}H_{74}O_{19}$	917.4468,817.4185	Marstenacisside A2
62	34.151	335.219 (0.00)^{H}	$C_{16}H_{26}N_6O_2$	265.0644,249.1262,233.0831,177.8611	2-(6-(isobutylamino)-2-(pentylamino)-9H-purin-9-yl) acetic acid
63	34.454	817.4020 (-4.92)^{Na}	$C_{41}H_{62}O_{15}$	673.3181,543.2543,383.1164	Hirundigoside C
64	35.168	831.4144 (-0.81)^{Na}	$C_{42}H_{64}O_{15}$	671.3278	Cynapanoside E
65	35.321	437.1936 (2.10)^{H}	$C_{23}H_{20}N_{10}$	356.2191,210.9564	3-(1-Methylpyrazol-4-yl)-6-[1-[5-(1-methylpyrazol-4-yl)triazolo [4,5-b]pyrazin-3-yl]ethyl]quinoline
66	35.481	831.4144 (-0.81)^{Na}	$C_{42}H_{64}O_{15}$	655.3441,435.2209	Deoxoglycyrrhizin
67	35.843	303.0629 (7.57)^{H}	$C_{19}H_{10}O_4$	199.0295,158.8591,130.9570	3-benzoylnaphtho [1,2-b]furan-4,5-dione
68	35.939	831.4144 (-0.81)^{Na}	$C_{42}H_{64}O_{15}$	441.2081,329.1572	Gitaloxin
69	36.932	801.4041 (-1.18)^{Na}	$C_{41}H_{62}O_{14}$	657.3234,527.2597,383.1818	Cynanoside K
70	37.12	277.1436 (3.35)^{H}	$C_{16}H_{22}O_4$	263.7807,235.9707,149.0153,121.0289,105.0333	1,2-benzenedicarboxylic acid
71	37.591	366.3366 (0.15)^{H}	$C_{23}H_{43}NO_2$	212.0646,212.0646,117.0681	Semiplenamide A
72	37.690	801.4041 (-1.18)^{Na}	$C_{41}H_{62}O_{14}$	657.3234,527.2597,383.1818	Cynanoside J
73	37.768	279.2317 (0.56)^{H}	$C_{18}H_{30}O_2$	199.8904,159.9928,131.0850	Linolenic acid
74	38.656	815.4195 (-0.85)^{Na}	$C_{42}H_{64}O_{14}$	755.3959,715.3654,655.3442	3-O-S2-11α-O-acetyl-l2β-O-tigloyl-tenacigenin B
75	38.730	277.2159 (1.11)^{H}	$C_{18}H_{28}O_2$	237.9916,183.0341,143.0845	Stearidonic acid
76	39.010	295.2265 (0.92)^{H}	$C_{18}H_{30}O_3$	167.8593,141.9124	13-keto-9Z,11E-octadecadienoic acid
77	39.483	295.2265 (0.92)^{H}	$C_{18}H_{30}O_3$	295.2265,238.8623,208.9628,151.0278	2-{2-[4-(1,1,3,3-tetramethylbutyl)phenoxy]ethoxy} ethanol
78	40.394	301.141 (-0.83)^{H}	$C_{14}H_{16}N_6O_2$	244.9672,164.9589,148.9675	8-amino-2-furan-2-yl-[1,2,4]triazolo [1,5-a]pyrazine-6-carboxylic acidbutylamide
79	41.801	291.1297 (0.73)^{H}	$C_{10}H_{18}N_4O_6$	247.1354,231.1099,160.1096,189.0018	(2S)-2-[[amino-[[(4S)-4-amino-4-carboxybutyl]amino] methylidene]amino]butanedioic acid
80	42.503	425.2152 (4.23)^{H}	$C_{22}H_{32}O_8$	266.0295,211.0616,152.1410	Didrovaltrate
81	42.598	282.2794 (-0.92)^{H}	$C_{18}H_{35}NO$	158.0583,102.0910	Oleamide
82	42.807	359.1259 (5.27)^{H}	$C_{23}H_{18}O_4$	333.1705,257.9660,213.9605	2-allyl-4,6-dibenzoylresorcinol
83	43.548	284.295 (-0.74)^{H}	$C_{18}H_{37}NO$	228.3951,158.9754,116.0496	Octadecanamide
84	44.068	415.0432 (3.97)^{H}	$C_{23}H_{10}O_8$	268.0060,177.9745,149.0278	5-[4-[(1,3-Dioxo-2-benzofuran-5-yl)oxy]benzoyl]-2-benzofuran-1,3-dione
85	44.796	423.3241 (3.92)^{H}	$C_{29}H_{42}O_2$	337.1505,255.1688,215.0875,201.1629	(3R,4S,4aR,6aR,6bS,14aR,14bR)-4-(hydroxymethyl)-4,6a,6b,11,12,14b-hexamethyl-1,2,3,4a,5,6,7,8,14,14a-decahydropicen-3-ol

(Continued on following page)

TABLE 3 (*Continued*) Identification of compounds in CP by LC-HR-Q-TOF-MS/MS.

No.	tR (min)	m/z (Error,ppm)	Formula	Fragmentions (m/z)	Identification
86	45.406	291.1297 (0.73)^{H}	$C_{10}H_{18}N_4O_6$	247.0667,189.1625,160.0363	Argininosuccinate
87	45.606	471.106 (3.07)^{H}	$C_{27}H_{18}O_8$	310.1218,177.1196,162.0399	Methyl 4-[bis(4-hydroxy-2-oxochromen-3-yl)methyl] benzoate
88	49.667	291.1297 (0.73)^{H}	$C_{10}H_{18}N_4O_6$	247.0628,231.1112,160.0414	(N (omega)-L-arginino)succinic acid

Na, $[M + Na]^+$; H, $[M + H]^+$.
*The compounds were identified by comparing with reference substance.

terminal product ion at *m/z* 110. This fragmentation pathway revealed the stepwise dissociation characteristics of the methoxy group, conjugated double bonds, and aromatic ring structure in the safrole molecule.

Asarinin (Figure 6B) was taken as an example of lignans for illustration. Initially, it started from its quasi-molecular ion at *m/z* 353 and lost a molecule of CH_2O, generating an ion at *m/z* 323. It then lost another molecule of CH_2O, forming an ion at *m/z* 293. Subsequently, the ion at *m/z* 293 lost a molecule of $C_{10}H_6O_2$, producing an ion at *m/z* 135. Ultimately, the ion at *m/z* 135 underwent another fragmentation, resulting in the loss of a molecule of CH_3 and yielding an ion at *m/z* 120. In addition, there was another fragmentation pathway that started from the quasi-molecular ion at *m/z* 353, where it lost a molecule of $C_7H_4O_2$, generating an ion at *m/z* 233 (Hu et al., 2025).

(2S)-naringenin (Figure 6C) was taken as an example of flavonoids for illustration. It started from its quasi-molecular ion at *m/z* 273. By losing a molecule of C_6H_4O, this ion transformed into a fragment ion at *m/z* 181. Subsequently, this fragment ion further fragmented and lost a molecule of CO, generating an ion at *m/z* 153. Immediately thereafter, the ion at *m/z* 153 lost an OH group, forming an ion at *m/z* 137. Additionally, there was another fragmentation pathway that started from the fragment ion at *m/z* 181, where it directly lost a molecule of C_2H_2, producing an ion at *m/z* 155 (Wen et al., 2014).

Aristolactam I (Figure 6D) was taken as an example of amides for illustration. It started from its quasi-molecular ion at *m/z* 294. By losing a molecule of CH_3, it generated an ion at *m/z* 279. Subsequently, it lost a molecule of CO, resulting in an ion at *m/z* 251. In addition, there was another fragmentation pathway that started from the quasi-molecular ion at *m/z* 294. In this pathway, the ion lost a molecule of CH_2O, producing an ion at *m/z* 264. Finally, this ion at *m/z* 264 lost a molecule of CO, yielding an ion at *m/z* 236 (Mao et al., 2017).

Aristolochic acid (Figure 6E) was taken as an example of phenanthrenes for illustration. It began with the quasi-molecular ion at *m/z* 356. By losing a molecule of NO_2 and a molecule of COO^-, it generated an ion at *m/z* 266. Subsequently, this ion at *m/z* 266 further fragmented and lost a molecule of CH_2O, forming an ion at *m/z* 236. Additionally, there was another fragmentation pathway that began with the quasi-molecular ion at *m/z* 356. In this pathway, the ion lost a molecule of COOH, a molecule of CO_2, and a molecule of NO_2, producing an ion at *m/z* 221 (Yu et al., 2016).

3.4.3 Fragmentation patterns of major types of compounds in CP

Glaucoside C (Figure 6F) was taken as an example of steroids for illustration. The initial quasi-molecular ion at *m/z* 817 underwent cleavage by losing a molecule of $C_7H_{12}O_3$, generating an ion at *m/z* 673. This likely corresponded to the rupture of a glycosidic bond or an ester bond in the molecule, resulting in the detachment of a saccharide or ester group containing 7 carbon atoms, 12 hydrogen atoms, and 3 oxygen atoms. Subsequently, the ion at *m/z* 673 underwent further fragmentation by eliminating a molecule of $C_6H_{10}O_3$, producing an ion at *m/z* 543. This step might similarly have involved the cleavage of another saccharide unit or related functional group. Following this, the ion at *m/z* 543 underwent additional fragmentation through the loss of another $C_6H_{10}O_3$ molecule, yielding a terminal ion at *m/z* 383. The fragments lost at each step were structural glycosyl units, and these fragmentation processes gradually revealed the structural information of the molecule.

Melibiose (Figure 6G) was taken as an example of saccharides for illustration. The quasi-molecular ion at m/z 365 underwent cleavage at the α-1,6-glycosidic bond, primarily through two distinct fragmentation pathways. In the first pathway, glycosidic bond cleavage was accompanied by elimination of a hexose unit ($C_6H_{11}O_6$), resulting in a dehydrated monosaccharide fragment at m/z 185. In the second pathway, direct elimination of the $C_6H_{11}O_6$ moiety occurred without hydroxyl group removal, yielding a hydroxyl-retained monosaccharide fragment at m/z 202. These observations suggested that heterolytic cleavage of hydrogen bonds played a critical role in differentiating the fragmentation pathways. Additionally, the intermediate ion observed at m/z 349 (formed via deoxygenation) indicated the loss of a hydroxyl oxygen atom from the sugar ring, generating an unsaturated structure. This structural rearrangement likely facilitated fragmentation pathway branching through intracyclic double bond reorganization.

3.4.4 Component comparison of AH and CP

By comparing the chemical compositions of AH and CP, we could observe significant differences as well as shared components between them. AH primarily comprised nitrogenous compounds, volatile oils, organic acids, coumarins, flavonoids, and lignans. Notably, AH contained unique coumarins and flavonoids that were rare in CP, which exhibited a broad spectrum of pharmacological activities. For example, 7-methoxycoumarin ameliorated hepatotoxicity in rats induced by carbon tetrachloride and spatial memory impairment in ovariectomized Wistar rats induced by scopolamine (Sancheti et al., 2013; Zingue et al., 2018). Naringenin alleviated non-alcoholic fatty liver disease by suppressing the NLRP3/NF-κB pathway and prevented cardiomyopathy through targeting HIF-1α in mice (Wang et al.,

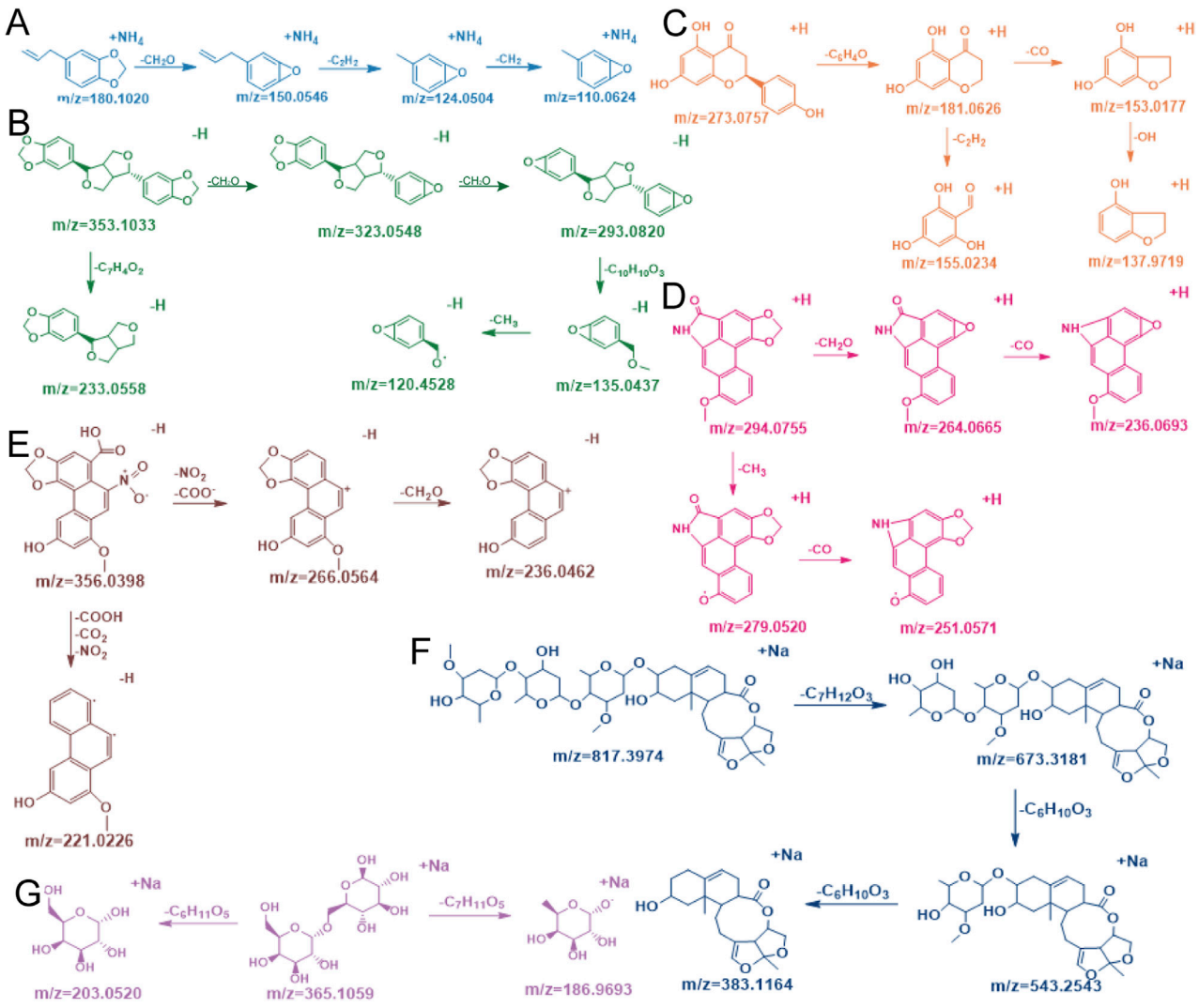

FIGURE 6
Compound cracking pathways for safrole **(A)** asarinin **(B)** (2S)-naringenin **(C)** aristolactam I **(D)** aristolochic acid **(E)** glaucoside C **(F)** and melibiose **(G)**.

2020; Pan et al., 2024). Furthermore, some components in AH exhibited potent toxicity, including aristolactam I, aristolochic acid D, and safrole. Studies demonstrated that aristolactam I accumulated extensively in renal cells and induced nephrotoxicity (Au et al., 2023), while aristolochic acid D triggered lymphocyte infiltration and renal fibroproliferation (Xian et al., 2021). Additionally, safrole exerted hepatotoxicity through the cytochrome P450 enzyme CYP1A2 (Hu et al., 2019). In contrast, the chemical composition of CP mainly included steroidal compounds, nitrogenous compounds, volatile oils, organic acids, saccharides, and lignans. Among them, CP contained unique steroidal compounds and saccharides that were absent in AH, exemplified by glaucoside C and melibiose. Glaucoside C alleviated atopic dermatitis by inhibiting the mitogen-activated protein kinase (Fleitas et al., 2022), while melibiose ameliorated cerebral ischemia/reperfusion injury through regulating autophagic flux (Wu et al., 2021). Despite the chemical differences between AH and CP, they shared common components, such as L-argininosuccinic acid and sphinganine. The results indicated that LC-HR-Q-TOF-MS/MS could differentiate AH and CP from the perspective of chemical compositions.

3.5 Electrochemical fingerprint spectra based on Belousov-Zhabotinsky reaction

Although LC-HR-Q-TOF-MS/MS was utilized for analyzing the components of medicinal plants, it also had limitations. On the one hand, it was impossible to identify all the components in medicinal plants. On the other hand, complex data analysis required a considerable amount of time. Therefore, it was necessary to establish a simpler method from the perspective of holistic chemistry, namely, electrochemical fingerprint spectra based on the Belousov-Zhabotinsky reaction. The principle, influencing factors, and model accuracy of this method were as follows.

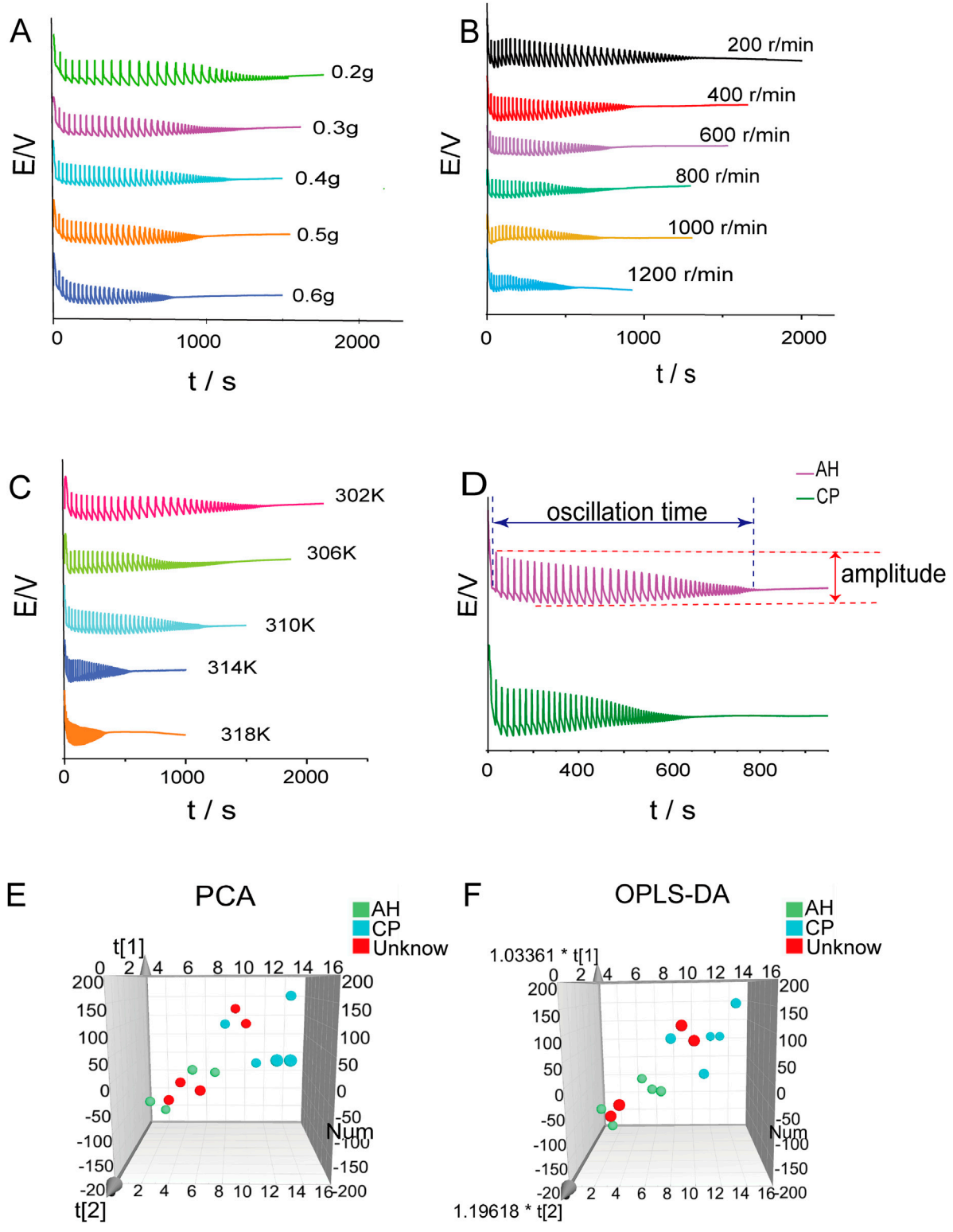

FIGURE 7
The effects of sample mass **(A)** rotation speed **(B)** and temperature **(C)** on the Belousov-Zhabotinsky oscillation reaction. Electrochemical fingerprint spectra of AH and CP under the same condition **(D)**. Principal component analysis **(E)** and orthogonal partial least squares discriminant analysis **(F)** of AH and CP.

3.5.1 Principle of electrochemical reactions

Electrochemical fingerprint spectra, as a part of nonlinear chemistry, was capable of characterizing the overall chemical properties of medicinal plants. It arose from oscillations in autocatalytic reactions, revealing fluctuations in the concentrations of certain substances. The principle of this reaction encompassed the consumption of bromide ions (Br^-), the oxidation of cerium ions (Ce^{3+}), and the regeneration of bromide ions (Br^-). The cycle of bromide ion consumption and regeneration drove the oscillatory system (Wang et al., 2024). The whole components in medicinal plants influenced these reactions, offering novel representations of their chemical properties. For instance, the distinct redox-active components in AH and CP (e.g., ortho-hydroxyacetophenone and paeonol) could influence the oxidation process of Ce^{3+}. To ensure the integrity of the phytochemical components, the plant powder was directly involved in the reaction without prior extraction.

3.5.2 Factors influencing Belousov-Zhabotinsky reaction

The effects of sample mass, rotation speed, and temperature on the Belousov-Zhabotinsky oscillation reaction were investigated. In Figure 7A, the electrochemical fingerprint spectra of AH powder with varying masses (0.2g, 0.3g, 0.4g, 0.5g, 0.6g) are presented. The characteristic parameters of these spectra were summarized in Supplementary Table S3. Notably, as the mass of the AH powder increased, a discernible trend emerged: the oscillation time gradually decreased, accompanied by a reduction in amplitude. The electrochemical fingerprint spectra of AH powder at stirring speeds ranging from 200 to 1200 r/min (in increments of 200 r/min) are shown in Figure 7B. The characteristic parameters of these spectra were summarized in Supplementary Table S4. As the stirring speed increased, the oscillation time shortened progressively, while the amplitude decreased correspondingly. In Figure 7C, the electrochemical fingerprint spectra of AH at experimental temperatures ranging from 302 to 318 K (in increments of 4 K) were illustrated. The characteristic parameters of these spectra are listed in Supplementary Table S5. As the experimental temperature increased, the oscillation time shortened progressively, while the amplitude decreased correspondingly. It could be seen that the AH powder caused regular changes in the Belousov-Zhabotinsky oscillation reaction. The rotation speed and temperature had a significant influence on this reaction, which should be strictly controlled during the experiment.

3.5.3 Electrochemical fingerprint spectra of AH and CP

The comparison between the electrochemical fingerprint spectra of AH and CP is illustrated in Figure 7D. It could be observed that the oscillation time of AH was significantly longer than that of CP, whereas the maximum amplitude of CP was notably larger than that of AH. To further differentiate the two medicinal plants, the PCA method was employed. The scatter plot is presented in Figure 7E, which shows the separation of AH and CP. The R^2X and Q^2 values of this model, at 0.687 and 0.591 respectively, indicated the reliability of the model. Furthermore, the OPLS-DA method was utilized to differentiate between these two medicinal plants (Figure 7F). The result was consistent with that obtained from PCA. The R^2X, R^2Y, and Q^2 values of this model, standing at 0.568, 0.924, and 0.751 respectively, demonstrated the reliability of the outcomes. To assess the accuracy of the model, four unknown samples were analyzed, including two distinct AH samples and two distinct CP samples that had each been independently prepared. The results showed that the unknown samples could be accurately classified into their designated areas, demonstrating a 100% accuracy rate. Compared to LC-HR-Q-TOF-MS/MS, electrochemical fingerprint spectra exhibited the following significant advantages: (1) it allowed for direct analysis of plant powder without extraction, thus simplifying the operation; (2) the analysis time was short, and the data processing was simple. Therefore, it can be concluded that electrochemical fingerprint spectra can be effectively utilized to distinguish between AH and CP.

3.6 Integrated analysis of data and methods

AH and CP had very similar appearances, and they were often confused in the market. Given that AH contained toxic ingredients, and both AH and CP had irritating odors and tastes, traditional sensory identification methods, such as nose-sniffing and mouth-tasting, could not accurately distinguish between them. Furthermore, these methods might cause discomfort to the human body. Therefore, we used E-nose and E-tongue to distinguish between the two poisonous and medicinal plants. The E-nose provided the shortest analysis time among all technologies, enabling it to rapidly complete sample testing within 140 s. More importantly, it did not require extraction of samples and the plants could be directly used for analysis, greatly simplifying the operation process. In the PCA and DFA models, the reliability of the E-nose reached 98.912% and 100%, respectively, fully demonstrating its accuracy. The E-nose further disclosed that both AH and CP contained unpleasant ingredients. Specifically, AH included terpinolene, alpha-phellandrene, and camphor, which imparted flavors of anise, plastic, spiciness, and pepper. These ingredients might induce headaches and discomfort. On the other hand, CP contained camphor with a distinct, stimulating peppery taste that could also cause discomfort. At the same time, the E-tongue also revealed that the tastes of components in these two plants were bitter and astringent. In the PCA model, the R^2 and Q^2 values of the E-tongue were 0.869 and 0.607, respectively, indicating that the model had good predictive ability and stability. The R^2X, R^2Y, and Q^2 values of the OPLS-DA model were 0.93, 0.936, and 0.895, respectively, further confirming the reliability of the results. Through LC-Q-TOF MS, we found that the bitter and astringent components in AH might be asarinin, N-isobutyl-2E,4E,8Z,10E-dodecatetraenamide, etc., while the bitter and astringent components in CP might be paeonol, etc. Due to the different components of AH and CP, their effects on the Belousov-Zhabotinsky reaction were also different. Based on the electrochemical fingerprint of the reaction, we achieved 100% accurate differentiation between AH and CP. By integrating data from E-nose, E-tongue, LC-HR-Q-TOF-MS/MS, and electrochemical fingerprint spectra, this study provided a diverse perspective based on odor, taste, and chemical

composition, thereby providing powerful technical support for accurately distinguishing between AH and CP. It should be noted that the current study focused specifically on AH samples from Anguo City and CP samples from Lu'an City, which represented the mainstream sources of these medicinal plants in the Chinese herbal market. This study was based on a market survey revealing an adulteration practice in which AH (Anguo City) was adulterated with CP (Lu'an City) for illicit profit. Given that the quality of medicinal plants is influenced by geographical origins, growth stages, and plant parts, the impacts of these factors on the current methodology require further systematic and in-depth investigation.

In the field of medicinal plant identification, current techniques such as microscopic identification, DNA barcoding, and near-infrared spectroscopy exhibited distinct characteristics and inherent limitations when applied individually. Microscopic identification enabled rapid and cost-effective differentiation, but some microscopic characteristics lacked sufficient specificity to support accurate identification (Xu et al., 2015). Although DNA barcoding provided specific genetic information, it suffered from low resolution in distinguishing closely related species (Zhu et al., 2022). Near-infrared spectroscopy required minimal sample preparation, but its accuracy was susceptible to interference from factors such as moisture content and particle size (Yin et al., 2019). These limitations highlighted the inadequacy of a single method to address the complex demands of medicinal plant identification. In this study, E-nose, E-tongue, LC-HR-Q-TOF-MS/MS, and electrochemical fingerprint spectra were combined to distinguish the visually similar plants AH and CP. Actually, each method possessed distinct strengths and limitations. E-nose analysis required no sample extraction and could be completed within 3 minutes. However, its detectable targets were restricted to volatile compounds. E-tongue could substitute for human sensory evaluation in detecting the taste of toxic plants, but it was unable to distinguish specific taste components. LC-HR-Q-TOF-MS/MS could resolve chemical components, but data processing required a considerable amount of time. Electrochemical fingerprint spectra offered simple data processing with high accuracy. However, it could only reflect the plant's electrochemical properties from a holistic perspective. Therefore, through complementary integration of these technologies, the limitations of individual methods were mitigated, and their strengths synergistically enhanced.

4 Conclusion

A novel strategy, incorporating dual electronic sensors (DES) and dual fingerprint spectra (DFS), was proposed for the authentication and differentiation of the highly similar poisonous and medicinal plants, AH and CP. The E-nose was utilized to identify 25 odor components in AH and 12 in CP within 140 s, effectively distinguishing the aroma profiles of the two plants. The E-tongue, combined with chemometrics, revealed that bitterness and astringency were the key differentiating tastes. Through the use of LC-HR-Q-TOF-MS/MS for chemical fingerprint spectra, 91 compounds in AH and 90 compounds in CP were identified. To further differentiate AH and CP, electrochemical fingerprint spectra based on the Belousov-Zhabotinsky reaction were established, achieving a 100% accuracy rate. In summary, this study represented the first instance of integrating E-nose, E-tongue, LC-HR-Q-TOF-MS/MS, and Belousov-Zhabotinsky reaction for the authentication and differentiation of highly similar poisonous and medicinal plants.

Data availability statement

The original contributions presented in the study are included in the article/Supplementary Material, further inquiries can be directed to the corresponding authors.

Ethics statement

Written informed consent was obtained from the individual(s) for the publication of any potentially identifiable images or data included in this article.

Author contributions

X-RZ: Methodology, Software, Writing – original draft, Writing – review and editing. Y-HC: Funding acquisition, Methodology, Supervision, Writing – original draft. J-NZ: Validation, Writing – review and editing. W-YW: Formal Analysis, Writing – review and editing. R-BS: Validation, Writing – review and editing. Z-XD: Writing – review and editing, Software. HZ: Writing – review and editing, Funding acquisition, Methodology. MX: Supervision, Writing – review and editing. T-GK: Writing – review and editing, Supervision. H-PS: Conceptualization, Supervision, Funding acquisition, Investigation, Writing – original draft.

Funding

The author(s) declare that financial support was received for the research and/or publication of this article. This study was supported by National Natural Science Foundation of China (82173935), Liaoning Natural Science Foundation (2024-MSLH-297), Shenyang Youth Science and Technology Innovation Talent Cultivation Project - U35 Top Youth Project (RC230846), Liaoning Provincial Education Department project (JYTMS20231826 and JYTQN2023455), and Youth Scientific and Technological Innovation Team Project (2024-JYTCB-080).

Conflict of interest

The authors declare that the research was conducted in the absence of any commercial or financial relationships that could be construed as a potential conflict of interest.

Generative AI statement

The author(s) declare that no Generative AI was used in the creation of this manuscript.

Publisher's note

All claims expressed in this article are solely those of the authors and do not necessarily represent those of their affiliated organizations, or those of the publisher, the editors and the reviewers. Any product that may be evaluated in this article, or claim that may be made by its manufacturer, is not guaranteed or endorsed by the publisher.

Supplementary material

The Supplementary Material for this article can be found online at: https://www.frontiersin.org/articles/10.3389/fchem.2025.1578126/full#supplementary-material

References

Au, C.-K., Ham, Y.-H., and Chan, W. (2023). Bioaccumulation and DNA adduct formation of aristolactam I: unmasking a toxicological mechanism in the pathophysiology of aristolochic acid nephropathy. *Chem. Res. Toxicol.* 36 (2), 322–329. doi:10.1021/acs.chemrestox.2c00415

Bao, M., Bu, Q., Pan, M., Xu, R., Chen, Y., Yang, Y., et al. (2024). Coptidis rhizoma extract alleviates oropharyngeal candidiasis by gC1qR-EGFR/ERK/c-fos axis-induced endocytosis of oral epithelial cells. *J. Ethnopharmacol.* 331, 118305. doi:10.1016/j.jep.2024.118305

Batsukh, Z., Toume, K., Javzan, B., Kazuma, K., Cai, S., Hayashi, S., et al. (2020). Metabolomic profiling of Saposhnikoviae Radix from Mongolia by LC-IT-TOF-MS/MS and multivariate statistical analysis. *J. Nat. Med.* 74 (1), 170–188. doi:10.1007/s11418-019-01361-0

Chen, Y., Bi, J., Xie, M., Zhang, H., Shi, Z., Guo, H., et al. (2021). Classification-based strategies to simplify complex traditional Chinese medicine (TCM) researches through liquid chromatography-mass spectrometry in the last decade (2011–2020): theory, technical route and difficulty. *J. Chromatogr. A* 1651, 462307. doi:10.1016/j.chroma.2021.462307

Chen, Y., Li, S., Wang, D., Yuan, W., Xu, K., Wang, J., et al. (2023). Combinatorics-based chemical characterization and bioactivity comparison of different parts of traditional Chinese medicinal plants through LC-Q-TOF-MS/MS, multivariate statistical analysis and bioassay: Marsdenia tenacissima as an example. *J. Chromatogr. B* 1228, 123850. doi:10.1016/j.jchromb.2023.123850

Fleitas, M. M. D., Kim, S. S., Kim, N. K., and Seo, S. R. (2022). Cynanoside F controls skin inflammation by suppressing mitogen-activated protein kinase activation. *Antioxidants* 11 (9), 1740. doi:10.3390/antiox11091740

Gao, M., Jia, X., Huang, X., Wang, W., Yao, G., Chang, Y., et al. (2019). Correlation between quality and geographical origins of Cortex Periplocae, based on the qualitative and quantitative determination of chemical markers combined with chemical pattern recognition. *Molecules* 24 (19), 3621. doi:10.3390/molecules24193621

Hu, L., Wu, F., He, J., Zhong, L., Song, Y., and Shao, H. (2019). Cytotoxicity of safrole in HepaRG cells: studies on the role of CYP1A2-mediated ortho-quinone metabolic activation. *Xenobiotica* 49 (12), 1504–1515. doi:10.1080/00498254.2019.1590882

Hu, Y., Zhang, J., Yang, H., Liu, C., Li, Y., Bi, Q., et al. (2025). Chemical profiling and comparative analysis of different parts of Asarum heterotropoides using SPME-GC-QTOF-MS and LC-Orbitrap-MS. *J. Pharm. Biomed. Anal.* 252, 116502. doi:10.1016/j.jpba.2024.116502

Lan, L., Yang, T., Fan, J., Sun, G., and Zhang, H. (2023). Anti-inflammation activity of Zhizi Jinhua Pills and overall quality consistency evaluation based on integrated HPLC, DSC and electrochemistry fingerprints. *J. Ethnopharmacol.* 311, 116442. doi:10.1016/j.jep.2023.116442

Lei, K., Yuan, M., Li, S., Zhou, Q., Li, M., Zeng, D., et al. (2023). Performance evaluation of E-nose and E-tongue combined with machine learning for qualitative and quantitative assessment of bear bile powder. *Anal. Bioanal. Chem.* 415, 3503–3513. doi:10.1007/s00216-023-04740-5

Liang, C., Yao, Y., Ding, H., Li, X., Li, Y., and Cai, T. (2022). Rapid classification and identification of chemical components of Astragali radix by UPLC-Q-TOF-MS. *Phytochem. Anal.* 33 (6), 943–960. doi:10.1002/pca.3150

Liu, X., and Yan, Z. (2023). Identification of geographical origins of Astragalus membranaceus in China using electrochemical fingerprinting. *Int. J. Electrochem. Sci.* 18, 100183. doi:10.1016/j.ijoes.2023.100183

Lu, J., Jiang, Z., Dang, J., Li, D., Yu, D., Qu, C., et al. (2024). GC-MS combined with fast GC E-nose for the analysis of volatile components of chamomile (Matricaria chamomilla L.). *Foods* 13 (12), 1865. doi:10.3390/foods13121865

Mao, W., Gao, W., Liang, Z., Li, P., Zhao, Z., and Li, H. (2017). Characterization and quantitation of aristolochic acid analogs in different parts of Aristolochiae Fructus, using UHPLC-Q/TOF-MS and UHPLC-QqQ-MS. *Chin. J. Nat. Med.* 15 (5), 392–400. doi:10.1016/S1875-5364(17)30060-2

Mei, Y., Wei, L., Tan, M., Wang, C., Zou, L., Chen, J., et al. (2021). Qualitative and quantitative analysis of the major constituents in Spatholobi Caulis by UFLC-Triple TOF-MS/MS and UFLC-QTRAP-MS/MS. *J. Pharm. Biomed. Anal.* 194, 113803. doi:10.1016/j.jpba.2020.113803

Pan, J., Meng, L., Li, R., Wang, Z., Yuan, W., Li, Y., et al. (2024). Naringenin protects against septic cardiomyopathy in mice by targeting HIF-1α. *Biochem. Biophys. Res. Commun.* 704, 149613. doi:10.1016/j.bbrc.2024.149613

Sancheti, S., Sancheti, S., and Seo, S.-Y. (2013). Ameliorative effects of 7-methylcoumarin and 7-methoxycoumarin against CCl_4-induced hepatotoxicity in rats. *Drug Chem. Toxicol.* 36 (1), 42–47. doi:10.3109/01480545.2011.648329

Tarighat, M. A., Abdi, G., Tarighat, F. A., and Bayatiyani, K. S. (2023). Authentication and identification of Lamiaceae family with cyclic voltammetry fingerprint-PCA-LDA and determination of the used phenolic contents for classification using chromatographic analyses. *Talanta* 265, 124894. doi:10.1016/j.talanta.2023.124894

Tibaduiza, D., Anaya, M., Gómez, J., Sarmiento, J., Perez, M., Lara, C., et al. (2024). Electronic tongues and noses: a general overview. *Biosensors* 14 (4), 190. doi:10.3390/bios14040190

Wang, B., Sun, Y., Pei, W., Zhang, H., and Kang, T. (2022b). A new method for studying the mechanism of "Feature Identification based quality assessment" of Traditional Chinese Medicine, taking Gastrodiae Rhizoma as an example. *Heliyon* 8, e10354. doi:10.1016/j.heliyon.2022.e10354

Wang, M., Zhang, S., Guo, N., Xv, H., Wang, A., Li, X., et al. (2023). Quality evaluation of standard decoction prepared from powder of Asari Radix et Rhizoma. *World J. Tradit. Chin. Med.* 18, 2121–2127.

Wang, Q., Ou, Y., Hu, G., Wen, C., Yue, S., Chen, C., et al. (2020). Naringenin attenuates non-alcoholic fatty liver disease by down-regulating the NLRP3/NF-κB pathway in mice. *Br. J. Pharmacol.* 177 (8), 1806–1821. doi:10.1111/bph.14938

Wang, S., Lin, Z., Zhang, B., Du, J., Li, W., and Wang, Z. (2022a). Data fusion of electronic noses and electronic tongues aids in botanical origin identification on imbalanced Codonopsis Radix samples. *Sci. Rep.* 12, 19120. doi:10.1038/s41598-022-23857-8

Wang, S., Yang, T., Guo, P., Lan, L., and Sun, G. (2024). A new method to comprehensively evaluate the quality of Tianma Toutong tablets by multiple fingerprints combined with quantitative analysis and prescription analysis. *J. Pharm. Biomed. Anal.* 242, 116008. doi:10.1016/j.jpba.2024.116008

Wen, H., Gao, H., Qi, W., Xiao, F., Wang, L., Wang, D., et al. (2014). Simultaneous determination of twenty-two components in Asari Radix et Rhizoma by ultra performance liquid chromatography coupled with quadrupole time-of-flight mass spectrometry. *Planta Med.* 80 (18), 1753–1762. doi:10.1055/s-0034-1383296

Wu, Z., Zhang, Y., Liu, Y., Chen, X., Huang, Z., Zhao, X., et al. (2021). Melibiose confers a neuroprotection against cerebral ischemia/reperfusion injury by ameliorating autophagy flux via facilitation of TFEB nuclear translocation in neurons. *Life* 11 (9), 948. doi:10.3390/life11090948

Xian, Z., Tian, J., Zhang, Y., Meng, J., Zhao, Y., Li, C., et al. (2021). Study on the potential nephrotoxicity and mutagenicity of aristolochic acid IVa and its mechanism. *Biomed. Pharmacother.* 142 112081. doi:10.1016/j.biopha.2021.112081

Xin, T., Li, R., Lou, Q., Lin, Y., Liao, H., Sun, W., et al. (2022). Application of DNA barcoding to the entire traditional Chinese medicine industrial chain: A case study of Rhei Radix et Rhizoma. *Phytomedicine* 105, 154375. doi:10.1016/j.phymed.2022.154375

Xing, Y., Yan, Z., Li, Y., Teka, T., Pan, G., Dou, Z., et al. (2021). An effective strategy for distinguishing the processing degree of Polygonum multiflorum based on the analysis of substance and taste by LC-MS, ICP-OES and electronic tongue. *J. Pharm. Biomed. Anal.* 205, 114328. doi:10.1016/j.jpba.2021.114328

Xu, Y., Song, W., Zhou, P., Li, P., and Li, H. (2015). Morphological and microscopic characterization of five commonly-used testacean traditional Chinese medicines. *Acta Pharm. Sin. B* 5 (4), 358–366. doi:10.1016/j.apsb.2015.03.014

Yin, L., Zhou, J., Chen, D., Han, T., Zheng, B., Younis, A., et al. (2019). A review of the application of near-infrared spectroscopy to rare traditional Chinese medicine. *Spectrochim. Acta A Mol. Biomol. Spectrosc.* 221, 117208. doi:10.1016/j.saa.2019.117208

Yu, J., Ma, C., Wang, X., Shang, M., Hattori, M., Xu, F., et al. (2016). Analysis of aristolochic acids, aristololactams and their analogues using liquid chromatography tandem mass spectrometry. *Chin. J. Nat. Med.* 14 (8), 626–640. doi:10.1016/S1875-5364(16)30074-7

Zeng, J., and Jiang, Y. (2022). Identification of coptis chinensis and its counterfeits via electroanalysis-based fingerprint. *Int. J. Electrochem. Sci.* 17, 221262. doi:10.20964/2022.12.90

Zhang, J., Li, M., Zhang, Y., Qin, Y., Li, Y., Su, L., et al. (2023). E-eye, flash GC E-nose and HS-GC-MS combined with chemometrics to identify the adulterants and geographical origins of Ziziphi Spinosae Semen. *Food Chem.* 424, 136270. doi:10.1016/j.foodchem.2023.136270

Zhang, K., Wang, J., Fan, X., Zhu, G., Lu, T., and Xue, R. (2022). Discrimination between raw and ginger juice processed Magnoliae officinalis cortex based on HPLC and Heracles NEO ultra-fast gas phase electronic nose. *Phytochem. Anal.* 33 (5), 722–734. doi:10.1002/pca.3123

Zhang, Y., Li, S., Liang, Y., Liu, R., Lv, X., Zhang, Q., et al. (2021). A systematic strategy for uncovering quality marker of Asari Radix et Rhizoma on alleviating inflammation based chemometrics analysis of components. *J. Chromatogr. A* 1642, 461960. doi:10.1016/j.chroma.2021.461960

Zhong, X., Tian, J., Zhang, Y., Meng, J., Zhao, Y., Li, C., et al. (2021). Study on the potential nephrotoxicity and mutagenicity of aristolochic acid IVa and its mechanism. *Biomed. Pharmacother.* 142, 112081. doi:10.1016/j.biopha.2021.112081

Zhu, S., Liu, Q., Qiu, S., Dai, J., and Gao, X. (2022). DNA barcoding: an efficient technology to authenticate plant species of traditional Chinese medicine and recent advances. *Chin. Med.* 17 (1), 112. doi:10.1186/s13020-022-00655-y

Zingue, S., Foyet, H. S., Djiogue, S., Ezo'o, Y. E., Abaïssou, H. H. N., Fachagbo, P., et al. (2018). Effects of Ficus umbellata (Moraceae) aqueous extract and 7-methoxycoumarin on scopolamine-induced spatial memory impairment in ovariectomized Wistar rats. *Behav. Neurol.* 2018, 1–14. doi:10.1155/2018/5751864

frontiers | Frontiers in Chemistry

TYPE Original Research
PUBLISHED 23 July 2025
DOI 10.3389/fchem.2025.1594567

OPEN ACCESS

EDITED BY
Kevin Honeychurch,
University of the West of England,
United Kingdom

REVIEWED BY
Mukaddes Gürler,
Hacettepe University, Türkiye
Auwal Musa,
University of the West of England,
United Kingdom
Pallavi Choudhary,
GOI, India

*CORRESPONDENCE
Fahad S. Aldawasri,
fahad386@gmail.com

RECEIVED 16 March 2025
ACCEPTED 08 July 2025
PUBLISHED 23 July 2025
CORRECTED 07 August 2025

CITATION
Alamri FM, Alshmmari SK, Altamimy MA, Al Othaim IA, Alshehri YM, Alafraa RM, Almalki AD, Alkhalifah TA, Sahlabji T, Idris AM, Al-Hamoud H, Jamous YF and Aldawasri FS (2025) Investigation of illicit pregabalin in seized samples from Saudi Arabia.
Front. Chem. 13:1594567.
doi: 10.3389/fchem.2025.1594567

Investigation of illicit pregabalin in seized samples from Saudi Arabia

Fatimah M. Alamri[1,2], Sultan K. Alshmmari[3], Monerah A. Altamimy[3], Ibrahim A. Al Othaim[3], Yahya M. Alshehri[3], Rayed M. Alafraa[4], Ahmed D. Almalki[4], Turki A. Alkhalifah[4], Taher Sahlabji[1], Abubakr M. Idris[1,5], Haitham Al-Hamoud[6], Yahya F. Jamous[7] and Fahad S. Aldawasri[3]*

[1]Department of Chemistry, College of Science, King Khalid University (KKU), Abha, Saudi Arabia, [2]Department of Chemistry, College of Science, University of Bisha (UB), Bisha, Saudi Arabia, [3]Saudi Food & Drug Authority (SFDA), Riyadh, Saudi Arabia, [4]General Directorate of Narcotics Control, Ministry of Interior (MOI), Riyadh, Saudi Arabia, [5]Research Center for Advanced Materials Science (RCAMS), King Khalid University, Abha, Saudi Arabia, [6]Institute of Refining and Petrochemical Technologies, Energy and Industry Sector, King Abdulaziz City for Science and Technology (KACST), Riyadh, Saudi Arabia, [7]Institute of Health Technologies and Preventive Medicine—Health Sector, King Abdulaziz City for Science and Technology (KACST), Riyadh, Saudi Arabia

Introduction: Pregabalin (PGL) is a medication that is prescribed for controlling specific neurological-related symptoms. Due to its abuse in multiple countries, PGL has been classified as a controlled substance by authorities, including the Saudi Food and Drug Authority (SFDA).

Methods: This study developed a validated ultra-performance liquid chromatography-photodiode array detector (UPLC-PDA) method to quantify PGL in 40 seized samples (35 capsules, 5 powders). A complementary liquid chromatography-tandem mass spectrometry (LC-MS/MS) method was used to detect potential adulterants.

Results: The UPLC-PDA method demonstrated linearity (r = 0.9973) for PGL quantification (0.50–3.00 mg/mL), with an accuracy of 96%–102%. The RSD% values were 0.63% and 1.03% for intra-day and inter-day precision, respectively. Analysis of the five powder samples revealed a relative inconsistency in PGL content (107.91%–114.55%). Moreover, it showed higher variability in PGL content (RSD 1.16%–5.30%), suggesting possible adulteration or poor manufacturing. Furthermore, the results of the nuclear magnetic resonance (NMR) showed an acceptable purity for the powder samples. On the other hand, among 35 capsules, 5 (14.29%) exceeded pharmacopeial limits (95%–105% PGL content), while 6 (17.14%) contained <95% PGL.

Discussion: These results demonstrate significant variability in PGL content and the presence of adulterants, underscoring the need for robust analytical methods in forensic chemistry. Furthermore, the LC-MS/MS method detected adulteration of PGL with codeine, paracetamol, and gabapentin in 2.9% of the analyzed capsules, suggesting custom mixing by perpetrators. In general, 31.43% of these samples failed to meet quality standards and contained substances beyond declared contents that posed toxicity risks, revealing inadequacies in illicit drug production and circulation. The UPLC-PDA method offers a rapid, validated approach for PGL quantification, while LC-MS/MS enhances adulterant detection, supporting forensic and quality control applications.

KEYWORDS

pregabalin, forensic analysis, abused drugs, seized samples, counterfeit drugs, adulterants, ultra-performance liquid chromatography, tandem mass spectrometry

1 Introduction

Pregabalin (PGL), a gabapentinoid, is an antiepileptic and analgesic that modulates voltage-gated calcium channels to treat neuropathic pain and epilepsy (Kriikku and Ojanperä, 2021). It is chemically named (*S*)-(+)-3-(aminomethyl)-5-methylhexanoic acid ($C_8H_{17}NO_2$) (Figure 1) with a molecular weight of 159.23 g/mol. PGL has a white, crystalline solid form (Toth, 2014). In December 2004, the Food and Drug Agency (FDA) in the United States of America (United States) approved PGL for the treatment of neuropathic pain associated with diabetic peripheral neuropathy and postherpetic neuralgia. Since then, PGL has been approved in the United States and Europe for the treatment of these symptoms (Tassone et al., 2007). In Europe, PGL has also received regulatory approval to treat a variety of clinical conditions, as it demonstrates a wide range of therapeutic utility. Subsequently, PGL has also been recommended as a medication for seizures, neuropathic pain states, and anxiety-related disorders. PGL serves as a valuable adjunctive option for individuals with partial epilepsy as well (Asomaning et al., 2016). Furthermore, it works by slowing down nerve activity in the brain and spinal cord. On the contrary, PGL commonly causes dizziness, drowsiness, blurred vision, and dry mouth (Mutalabisin et al., 2021). It can produce euphoria and relaxation (Kriikku and Ojanperä, 2021; Evoy et al., 2017), increasing its significant risks of abuse, which include respiratory depression, dependence, and, in rare cases, severe allergic reactions. Overdose may cause seizures, coma, or dangerously low blood pressure (Alelwani et al., 2021).

PGL has emerged as a drug of abuse owning to several factors such as its intoxicating effects, potential to enhance the euphoric and sedative effects of other CNS depressants (e.g., opioids, benzodiazepines), ability to self-treat pain/withdrawal symptoms, accessibility as a generic medication and its association with opioid abuse. Moreover, the prevalence of non-medical use of PGL is expected due to its affordable price (Buttram and Kurtz, 2020). PGL was among the top-selling medications globally in 2017. During the year 2018, in England, more than 14 million PGL prescriptions were issued. This was probably driven by refraining from opioid analgesics. In April 2019, the United Kingdom reported significant gabapentinoid-related deaths due to misuse, highlighting their abuse potential (Mathieson et al., 2020). In this context, it is worth mentioning the definition of the term abuse, which is defined as "the substance that is used for nontherapeutic purposes to obtain psychotropic (e.g., euphoric, sedative, or anxiolytic) effects" (Smith et al., 2013).

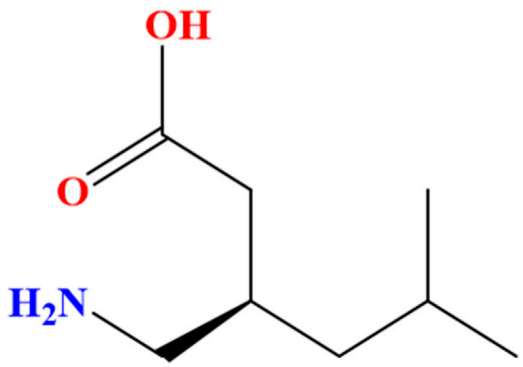

FIGURE 1
Chemical structure of the (S)-enantiomer of pregabalin [(S)-(+)-3-(aminomethyl)-5-methylhexanoic acid].

Based on the above-mentioned data, there are growing concerns about the abuse, addiction, intoxication, and even fatalities associated with PGL. Accordingly, PGL was classified in December 2017 by the Saudi Food and Drug Authority (SFDA) as one of the controlled prescription drugs that has been facing issues of abuse and illegal trafficking (Althunian et al., 2022).

It is noteworthy that PGL has been considered subject to abuse when formulated with various substances. Several samples, which contained numerous substances and manufactured by unauthorized factories for non-medical purposes, were seized in some countries. Common compounds detected alongside PGL included cannabis products, opioids (e.g., morphine, hydromorphone and codeine), semi-synthetic analogues (e.g., hydrocodone), and over-the-counter medications (e.g., paracetamol and naproxen) (Teker et al., 2024). In connection to this, health risks linked to the abuse of PGL with other compounds are considered serious. As PGL is known to depress the Central Nervous System (CNS), its use with other CNS depressants significantly elevates the danger of severe toxicity and mortality. When combined with opioids, cannabis products, and other depressing agents, PGL loses its therapeutic efficacy and considerably enhances the risk of severe adverse effects or potentially fatal outcomes (Elliott et al., 2017). Hence, developing selective analytical methods for PGL in the presence of various additives is highly desirable to be applied at forensic, toxicological, and pharmaceutical laboratories.

It is well-known that pharmaceutical analysis relies heavily on liquid chromatography (LC). Unfortunately, direct LC analysis of PGL faces some challenges, including a lack of chromophores, interference with excipients that absorb at similar wavelengths, and instability due to oxidative degradation (Mutalabisin et al., 2021; Kritikos et al., 2022). As a result, identification and quantification of PGL are considered a hurdle during initial routine procedures for laboratory screening. These analytical challenges necessitate the development of more efficient assay methods, particularly for confirmation analysis of PGL when it is suspected to contribute to adverse clinical presentations or toxicities (Mutalabisin et al., 2021). In this context, a limited number of analytical methods were developed for PGL quantification in various sample matrices for clinical and forensic applications. LC with mass spectrometric detections (MS), including tandem MS and TOF-MS methods, are dominant in the literature. Through these methods, PGL levels were examined in various human samples, including blood (Mata and Davis, 2022; Nahar et al., 2017; De La Vega et al., 2019), plasma (Almalki et al., 2021), urine (Mata and Davis, 2022; Almalki et al., 2021; Wang and Xu, 2019; Pelander et al., 2010), saliva (Wang and Xu, 2019), gastric contents (Mata and Davis, 2022), vitreous humor (Pelander et al., 2010), liver and brain tissues (Mata and Davis, 2022). Environmental analysis of urban sewage samples for determination of PGL was also reported using LC-MS/MS (Gurke et al., 2015). In addition, high-performance liquid chromatography (HPLC) with fluorescence and UV

FIGURE 2
Representative seized pregabalin samples showing physical variability: **(A)** Capsules with differing shapes/colours where be difficult to trace, and **(B)** Powder formulations with inconsistent solid state.

detection have been reported for PGL assay in human plasma for therapeutic drug monitoring (Martinc et al., 2014) as well as bulk and tablet formulations for forensic investigations (Vinutha Ko et al., 2017; Khanage et al., 2014). Recent studies have well-documented PGL misuse, particularly among polydrug users and opioid-dependent individuals (Kriikku and Ojanperä, 2021). To that end, some regulatory warnings and mortality data have further confirmed its abuse potential (Mathieson et al., 2020; Elliott et al., 2017).

This study provides analytical data on locally seized PGL samples. Furthermore, the study aims to identify PGL contents and purity levels along with potential adulteration. The study combines two analytical methods, i.e., ultra-performance liquid chromatography with photodiode array detector (UPLC-PDA) and LC-MS/MS. The HPLC-UV method recommended by the British Pharmacopoeia (BP) (British Pharmacopoeia, 2022) was upgraded to UPLC-PDA and then validated. Then, the new method was applied for PGL assay in capsule and powder samples while an LC-MS/MS method was performed for confirmation of the adulterated seized samples.

2 Materials and methods

2.1 Sampling

The forensic samples examined in the current study were seized by the General Directorate of Narcotics Control (GDNC), Saudi Arabia. The seized samples consisted of 35 capsules and 5 powder forms suspected to contain PGL. The capsules varied in shape, colour, and form, while the powders were likely intended for clandestine capsule production (Figure 2). All samples were handled under proper chain-of-custody protocols and stored at room temperature in a dark place to preserve sample integrity for analytical testing.

2.2 Chemicals and reagents

PGL reference standard (purity ≥99.90%) was obtained from HPC Standards GmbH (Germany). HPLC-grade acetonitrile, formic acid, and ammonium formate were purchased from Sigma-Aldrich (Germany), while potassium dihydrogen orthophosphate and

TABLE 1 The gradient elution protocol for the UPLC-PDA method.

Time (min)	Mobile phase a (%v/v)	Mobile phase B (%v/v)
0	100	0
1.1	100	0
4.4	60	40
5.6	60	40
6.6	100	0
8.6	100	0

sodium hydroxide were sourced from Fisher Scientific (United Kingdom). Purified water was prepared using a Duo™ water purification system from Avidity Science™ (United States).

2.3 Instrumentation

A Waters® ACQUITY UPLC-PDA system was used for separation, equipped with a Phenomenex C18 column (2.1 × 50 mm, 1.8 µm). For mass spectrometry investigation, a Thermo Scientific® LC-MS/MS system was used. Structural nuclear magnetic resonance (NMR) elucidation was performed by JEOL JNM-ECA600II NMR (deuterium oxide (D_2O) solvent, tetramethylsilane (TMS) as a reference).

2.4 Sample preparation

Powder samples (~20 mg) were dissolved in 10 mL of water: acetonitrile (90:10), while capsule contents were extracted in 50 mL of the same solvent. All samples were agitated for 10 min (1,000 rpm), filtered through a 0.22 µm nylon syringe filter, and analyzed in triplicate for quality control.

The NMR sample was prepared by accurately dissolving 5 mg of PGL powder sample in 0.5 mL of D_2O without filtration. The resulting solution was transferred into a 5 mm NMR tube for spectral acquisition under standard operating conditions.

2.5 Standard solution preparation

The stock solution of PGL (5.0 mg/mL) was prepared by dissolving appropriate amounts in acetonitrile:water (10:90) solution. Working solutions of PGL were prepared from the stock solution by further dilution with acetonitrile:water (10:90) solution at concentrations of 0.50, 0.75, 1.00, 1.25, 1.50, 2.00, and 3.00 mg/mL.

2.6 Chromatographic system conditions

For the UPLC-PDA method, the separation was achieved into a Phenomenex 2.1 mm ID, 50 mm C18 column with particle size 1.8 µm. A gradient elution was applied using a mobile phase composed of Solution A and Solution B in a 9:1 ratio, respectively. The composition was varied over time to effectively separate PGL from any potential impurities or adulterants (Table 1). While solution-B was acetonitrile, solution-A was potassium dihydrogen orthophosphate (0.272% w/v) adjusted at a pH of 5.9 with 1 M sodium hydroxide. The mobile phase was delivered at a flow rate of 0.5 mL/min with a total runtime of 8.6 min. The column temperature was set at 40^0 C. The sample volume was adjusted at 3 µL. The PDA detector was set at 210 nm wavelength.

For the LC-MS/MS method, an isocratic elution with two mobile phases was applied. Mobile phase C was composed of acetonitrile with 0.1% formic acid and mobile phase D was composed of 5 mmol of ammonium format in 0.1% (v/v) formic acid. Mobile phases C and D were used at a constant ratio (20:80) during the analysis. The method was conducted in the positive ionization mode. The specific mass transitions were monitored to detect the target compounds (Table 2).

2.7 Method validation

The HPLC assay method for PGL, which was recommended by the British Pharmacopoeia (BP) (British Pharmacopoeia, 2022), was upgraded to a UPLC-PDA method. The linearity, accuracy, precision, limits of detection (LOD) and quantification (LOQ) were validated according to International Council for Harmonisation (ICH) guidelines (Abraham et al., 2010).

The calibration curve was prepared using seven calibrators over a concentration range of 0.50–3.00 mg/mL for PGL and injected into the UPLC system, with each concentration analyzed in triplicate (n = 3). Linear regression was used to plot peak area versus concentration. The linear range was assessed visually from the calibration curve and by calculating the correlation coefficient (r).

Specificity was assessed by injecting blank and placebo solutions, ensuring no interfering peaks appeared at the retention time of the target analyte. Carry-over was evaluated by injecting blank solvent (acetonitrile: water, 10:90) immediately following the highest calibration standard (3.00 mg/mL), with acceptance criteria requiring signal in blanks to be <20% of the LOQ for specificity and ≤5% of the upper calibration limit for carry-over.

The accuracy was calculated using Equation 1. The precision was determined as the relative standard deviation (RSD%) of replicate measurements at various concentrations, calculated using Equation 2. Intraday precision was assessed via three replicates for each of three different concentrations (0.75, 1.25,

TABLE 2 The composition of mobile phase elution of LC-MS/MS.

Time (min)	Flow (mL/min)	Mobile phase C (%v/v)	Mobile phase D (%v/v)	Curve
0	0.5	20	80	5
2	0.5	20	80	5
2	Stop Run			

and 2.00 mg/mL) in one run. Inter-day studies analyzed three replicates per concentration of (0.75, 1.25, and 2.00 mg/mL) across six consecutive days.

$$Accuracy\ (\%) = \frac{Calculate\ concentration}{Nominal\ Concentration}\ X\ 100 \quad (1)$$

$$RSD\% = \frac{Standard\ deviation\ of\ peak\ areas\ (SD)}{Mean\ peak\ areas}\ X\ 100 \quad (2)$$

The LOD and LOQ were established based on the calibration curve parameters by using the standard deviation of response (SD) and slope (S) obtained from linear regression of the seven-point calibration curve as per Equations 3, 4, according to ICH Q2 (R1).

$$LOD = 3.3(SD/S) \quad (3)$$

$$LOQ = 10(SD/S) \quad (4)$$

Statistical analyses were performed using Empower™ (Waters) and XCalibur™ (Thermo) software, with supplementary calculations conducted in Microsoft Excel.

3 Results and discussion

3.1 UPLC-PDA Method validation

The upgrading of the PGL assay method from HPLC to UPLC resulted in significant reductions in analysis run time from 17.0 min down to 8.6 min. The sampling frequency was improved from 2 samples/h using the HPLC method to 4 samples/h using the UPLC method; an advantage resulted in better laboratory productivity. It is also known that sample throughput is a critical aspect of forensic analysis that requires rapid analysis of urgent samples. Additionally, the use of UPLC method reduces chemical reagent consumption and waste generation; an issue that achieves a less environmentally harmful method. These benefits were obtained by decreasing the mobile phase flow rate from 1 mL/min using the HPLC method to 0.5 mL/min using the UPLC method. The sample injection volume was also reduced from 20 µL to just 3 µL. As a result, the total waste volume generated per sample is reduced significantly from 27.020 mL to 6.803 mL, representing a 74.8% reduction in waste volume. On the other hand, the UPLC system achieved enhanced separation efficiency at the optimized flow rate (0.5 mL/min), reducing the analysis time by 49.4% compared to HPLC (1.0 mL/min).

3.2 Analysis of powder samples

The linearity of the modified UPLC method was evaluated by analysing a series of calibration standards. The method was found to be linear (Figure 3), with a correlation coefficient (r) of 0.9973, in the concentration range of 0.50–3.00 mg/mL for PGL. Using the linear least square regression method of the seven-point calibration curve (r = 0.9973), the slope and intercept for PGL were found to be 86,620 and 15,433, respectively. Despite a narrow linear range, the calibration features a high slope value, indicating a good response to slight changes in the concentration. The RSD% value of repeated measurements was found to be 0.628%, suggesting good repeatability of the UPLC method. It is reported that the typically acceptable is <2% (United States Pharmacopeia, 2023). Notably, the SD of the slope was 2,787, while the SD of the intercept was 4,547, reflecting acceptable variability in the slope and intercept calculations. In addition, the standard error of the estimate was 5,807, being relatively low, indicating the closeness of the data points to the calibration curve. This confirms a good fit of the linear regression model to the calibration data.

The LOD and LOQ values based on residual SD of the regression line were 0.23 and 0.69 mg/mL, respectively. Both values of LOD and LOQ are suitable for pharmaceutical analysis as PGL is a major component in seized samples as well as pharmaceutical formulations.

The method validation demonstrated excellent specificity, with no detectable interfering peaks at the retention time of PGL (0.36 min) in the blank and placebo solutions. All blank injections showed signals below 20% of the LOQ (0.69 mg/mL), confirming the method's selectivity for pregabalin detection. Carry-over evaluation revealed minimal residual signal (<5% of the upper calibration limit) in blank solvent injections following the highest standard (3.00 mg/mL), indicating acceptable system cleanliness for high-throughput analysis. These results confirm the reliability of the method for analyzing seized samples, as any potential matrix effects or carry-over contamination would not significantly impact the quantification accuracy.

For system suitability, as shown in Table 3, six independent preparations of the PGL reference standard (2.00 mg/mL) were subjected to the modified UPLC method on day one. System suitability was confirmed by meeting the following acceptance criteria: peak area RSD% (<2%), retention time variation (<2%), theoretical plates (>2000), and peak asymmetry (0.9–1.5). Evidently, the observed RSD% of peak areas was 1.16%, demonstrating excellent intraday precision. Moreover, the RSD% of the peak areas was found to be 1.16%. This result shows good intraday precision. The accuracy ranged between 96% and 102% for PGL analysis. Collectively, the RSD% values were 0.63% and 1.03% for intra-day and inter-day precision, respectively, demonstrating excellent performance for both repeatability and reproducibility of the analytical method over the tested concentration range.

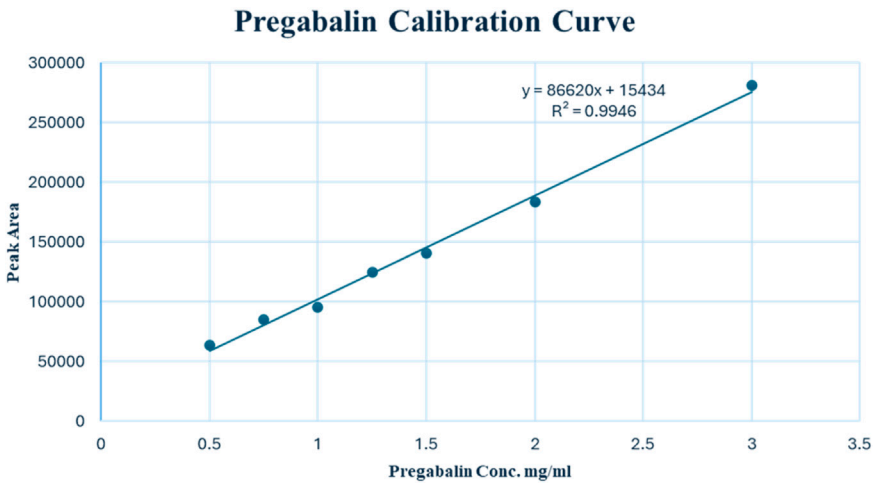

FIGURE 3
Calibration curve of pregabalin (0.50–3.00 mg/mL) by UPLC-PDA.

TABLE 3 System suitability of six independent preparations of PGL reference standard (2 mg/mL) for UPLC-PDA method.

Concentration of PGL reference standard (mg/mL)	Replicates	Mean area	SD	RSD%
2	6	184,747	2,142.5	1.16%

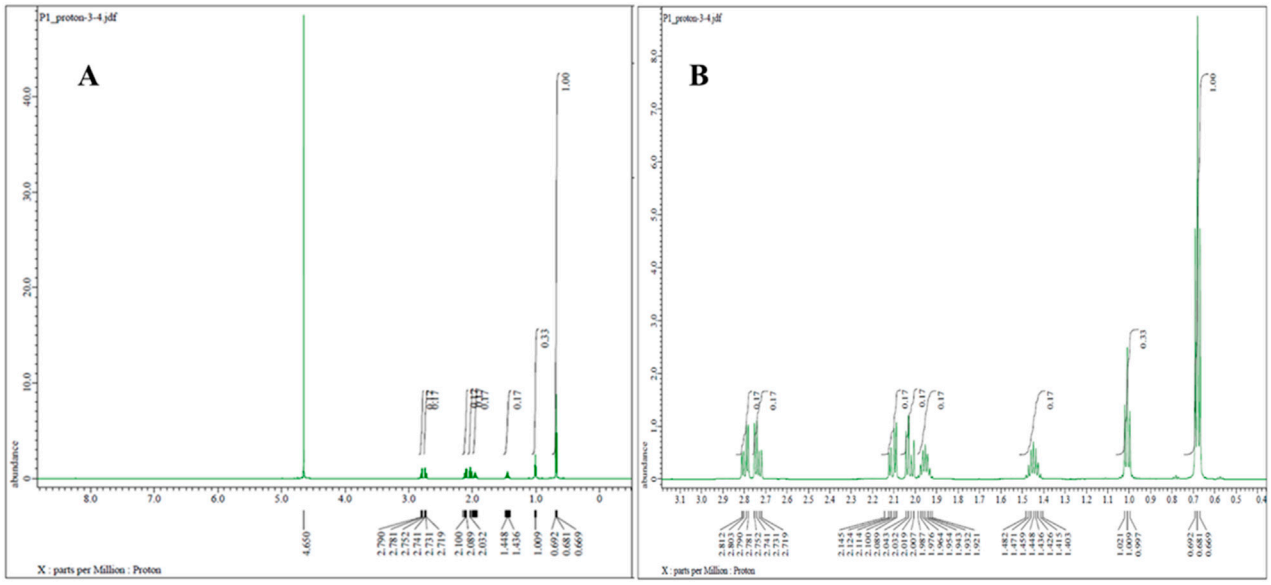

FIGURE 4
^{1}H NMR spectrum (600 MHz, D_2O) of pregabalin powder representative sample **(A)** with zoom-in from 1 to 3 ppm **(B)**, showing characteristic proton signals of pregabalin.

3.3 Analysis of capsule samples

The powder samples for raw material were visually investigated which demonstrated irrational results. A noticeable discrepancy was observed between different powder samples in terms of crystal size and shape. Irregular crystal structures were noticed compared to the well-defined structures typically expected for pure PGL. This observation might indicate a lack of homogeneity and potentially confirms poor manufacturing practices.

Proton NMR analysis for the five samples of the powder forms revealed comparable results in which all 14 alkyl protons in the PGL structure (Figure 1) were demonstrated in well-defined signals

TABLE 4 UPLC-PDA analysis of three independent preparations of each seized pregabalin powder sample.

Powder samples	Measured conc. (mg/mL)	PGL %	Mean	SD	RSD%
1P-1	2.051	109.66	114.55	6.07	5.30
1P-2	2.099	112.66			
1P-3	2.162	121.34			
2P-1	2.046	109.12	107.91	1.25	1.16
2P-2	2.044	107.98			
2P-3	2.023	106.63			
3P-1	2.103	111.01	111.84	2.19	1.96
3P-2	2.102	110.18			
3P-3	2.097	114.33			
4P-1	2.100	114.89	112.88	1.80	1.59
4P-2	2.063	111.44			
4P-3	2.104	112.32			
5P-1	2.09	109.92	111.25	1.95	1.75
5P-2	2.038	113.49			
5P-3	2.097	110.33			

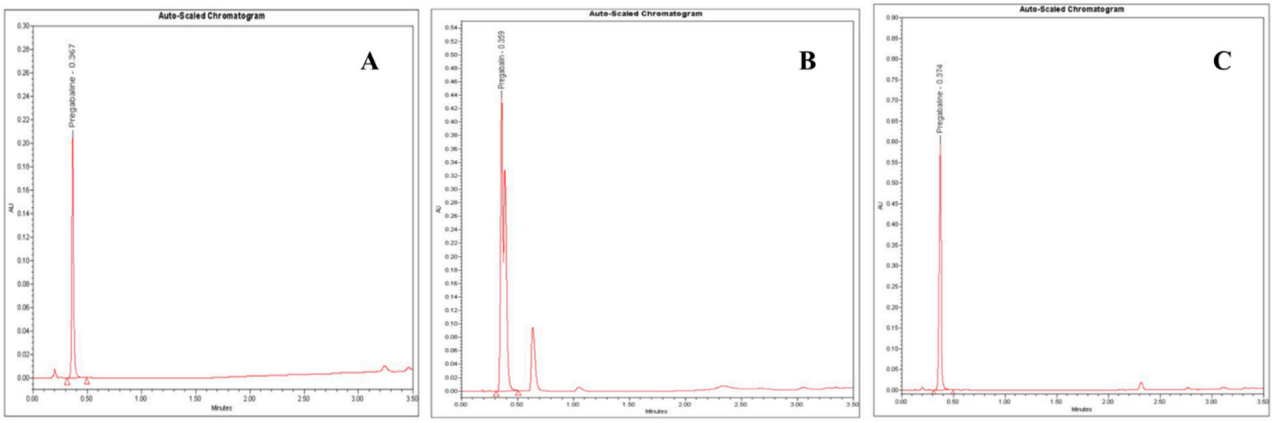

FIGURE 5
UPLC-PDA chromatograms of: **(A)** pregabalin standard (5.0 mg/mL), **(B)** an adulterated seized capsule sample showing pregabalin (Rt = 0.36 min) and unidentified impurities and **(C)** a seized pregabalin capsule sample. Chromatographic conditions: C18 column (2.1 mm ID, 50 mm, particle size 1.8 µm), mobile phase: buffer (pH 5.9): acetonitrile (9:1 ratio), flow rate 0.5 mL/min, column temperature at 40 °C and UV detection at 210 nm.

(Figure 4). These characterizations were in agreement with a typical NMR spectrum for PGL (Komisarek et al., 2022). This finding may illustrate acceptable purity in terms of PGL itself and not necessarily other adulterants or impurities. On the other side, the UPLC method was applied to the powder samples for quantitative analysis of PGL. As shown in Table 4, the analytical results of the powder samples for PGL showed higher concentrations than the reference standard (Figure 5A), suggesting the powders contained impurities/additional compounds other than the expected PGL. Notably, the United States Pharmacopeia (USP) recommended the acceptable range for PGL assay is 98%–102% on a dried basis. PGL concentrations above the recommended range suggest that the powder samples likely contain other substances.

Further contributing factors included potential adulteration, as additional chromatographic peaks beyond PGL implied other constituents (Figure 5B). Issues such as moisture absorption or degradation from inadequate storage conditions over time could also have unpredictably skewed measured values where PGL is susceptible to various degradation pathways, including hydrolysis, oxidation, thermal degradation, and photodegradation, which may contribute to the observed purity variations in seized samples. Hydrolysis can occur under acidic and alkaline conditions,

TABLE 5 UPLC-PDA analysis of seized pregabalin capsule samples. ND: not determined.

Capsule no.	Labelled capsule potency (mg)	Measured PGL concentration (mg/mg powder)	Total PGL content (mg) per capsule (mg/ capsule)	Assay of PGL%
1C	300	0.96	347.45	**115.82**
2C	150	0.65	148.28	98.85
3C	300	1.03	337.73	**112.58**
4C	150	0.75	154.15	102.77
5C	75	0.77	80.06	**106.74**
6C	75	0.80	75.13	100.17
7C	150	0.78	157.36	104.91
8C	150	0.78	155.53	103.69
9C	150	0.78	155.86	103.91
10C	75	0.84	81.57	**108.76**
11C	150	0.79	154.48	102.99
12C	150	0.70	150.60	100.40
13C	50	0.42	52.53	**105.06**
14C	300	1.02	300.22	100.07
15C	300	ND	ND	**ND**
16C	150	0.67	152.24	101.49
17C	150	0.68	155.49	103.66
18C	300	0.31	89.26	**29.75**
19C	150	0.35	77.96	**51.97**
20C	300	0.87	283.47	**94.49**
21C	300	0.94	301.95	100.65
22C	300	0.91	292.68	97.56
23C	75	0.57	72.83	97.11
24C	300	0.74	288.59	96.20
25C	300	0.77	310.10	103.37
26C	150	0.76	151.96	101.30
27C	150	0.77	154.77	103.18
28C	150	0.76	149.65	99.77
29C	50	0.28	46.34	**92.69**
30C	150	0.79	155.88	103.92
31C	300	0.78	309.90	103.30
32C	150	0.76	151.52	101.01
33C	300	0.94	300.46	100.15
34C	150	0.69	151.32	100.88
35C	300	0.60	280.75	**93.58**

Bold values indicate the seized capsule samples that did not satisfy the acceptable quality standard.

causing the ester bond in PGL to cleave, forming the acid and alcohol derivatives. In addition, thermal degradation results in the loss of a water molecule and oxidation in the presence of oxidizing substances like hydrogen peroxide and oxygen to form N-(3-carbamoylpropyl) isobutyric acid. This thermal degradant has a similar structure and could co-elute with PGL peak. Forced

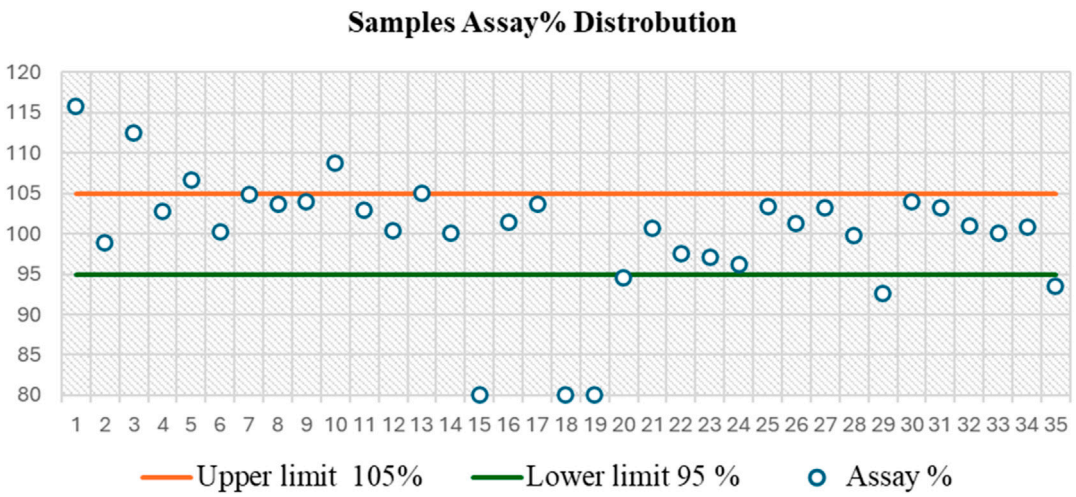

FIGURE 6
Control chart based on assay distribution between British Pharmacopoeia (BP) specifications (95%–105%) for the analysis of 35 capsule samples, as determined by the UPLC-PDA method, showing that 31.43% of these samples failed to meet the BP limit.

degradation studies, as per ICH guidelines, observed major degradation under basic hydrolysis and oxidation conditions, forming ten unknown oxidative impurities characterized using LC-MS, HR-MS and NMR. The proposed oxidative degradation pathway involves sequential formation of mono-hydroperoxide, cyclized hydroperoxide, dihydroperoxide and hydroxy derivatives that eventually degrade into multiple products (Vukkum et al., 2015). Issues related to purity, consistency, production quality control, and stability prevented the analytical results of the powder samples from aligning with the established reference values. A study (Sripathi et al., 2010) highlighted the importance of impurity characterization in manufacturing PGL pharmaceutical formulation to meet regulatory standards, safety and efficacy requirements. This recommendation aids in the optimization of manufacturing methods and reduces the formation of undesirable impurities. Another study reported that variations in the manufacturing process could result in significant differences in the uniformity of PGL formulations, which may have a reverse effect on patient safety (Gujral et al., 2009).

3.4 Method upgrading from HPLC to UPLC

The seized PGL capsule samples (n = 35) were examined for shape, size, and colour. These parameters provide initial clues about potential sources. In the current study, the investigation showed different shapes, colours, and forms. The comparison of the physical attributes of seized capsules to licensed product profiles helped in tracing some capsules back to major manufacturing facilities. The traceability of physical properties suggests that 21 seized samples were from four facilities, while 14 samples were difficult to trace. The presence of untraceable capsules suggests that they are counterfeit drugs randomly filled by unqualified illegal operators rather than legitimate pharmaceutical companies.

On the other side, the results of the PGL assay for the seized capsule samples (Figure 5C) using the UPLC-PDA method are shown in Table 5. The results revealed that five capsule samples containing PGL exceeded the range of 95%–105%, which is recommended by the BP. While most samples (68.57%) fell within the BP-recommended range (95%–105%), six showed the content of PGL below the range of 95%–105%. A control chart of the PGL contents following the BP limits is depicted in Figure 6. As shown, three samples (15C, 18C, and 19C) were found to be less than 80%. Additionally, three samples (20C, 29C, and 35C) were found to be below the lower limit (95%). Furthermore, five samples (1C, 3C, 5C, 10C, and 13C) exceeded the upper BP limit (105%). These results indicate that approximately one-third of the seized capsule samples did not satisfy the acceptable quality standard.

3.5 Analysis by LC-MS/MS

The UPLC-PDA method showed significant improvements over HPLC, reducing analysis time by 49.4% (from 17.0 to 8.6 min) and solvent waste by 74.8% (from 27.02 to 6.80 mL per sample). This was achieved through optimized parameters, including lowering the flow rate (from 1.0 to 0.5 mL/min) and decreasing the injection volume (from 20 to 3 μL), while doubling sample throughput from 2 to 4 samples per hour compared to HPLC.

This UPLC-PDA method achieved enhanced selectivity through its optimized chromatographic conditions. Importantly, the use of a 1.8 μm particle C18 column (50 × 2.1 mm) at 40°C improved peak sharpness and resolution compared to conventional HPLC, reducing peak widths and reducing co-elution risks. The method's selectivity was enhanced by the buffered mobile phase (minimizing peak tailing) and 210 nm detection (avoiding matrix interference), while the small particle size (1.8 μm) and low injection volume (3 μL) improved peak symmetry and resolution. Despite the high efficiency of UPLC, challenges in impurity retention were addressed through gradient optimization, ensuring that early-eluting polar compounds (hydrophobic interactions) were

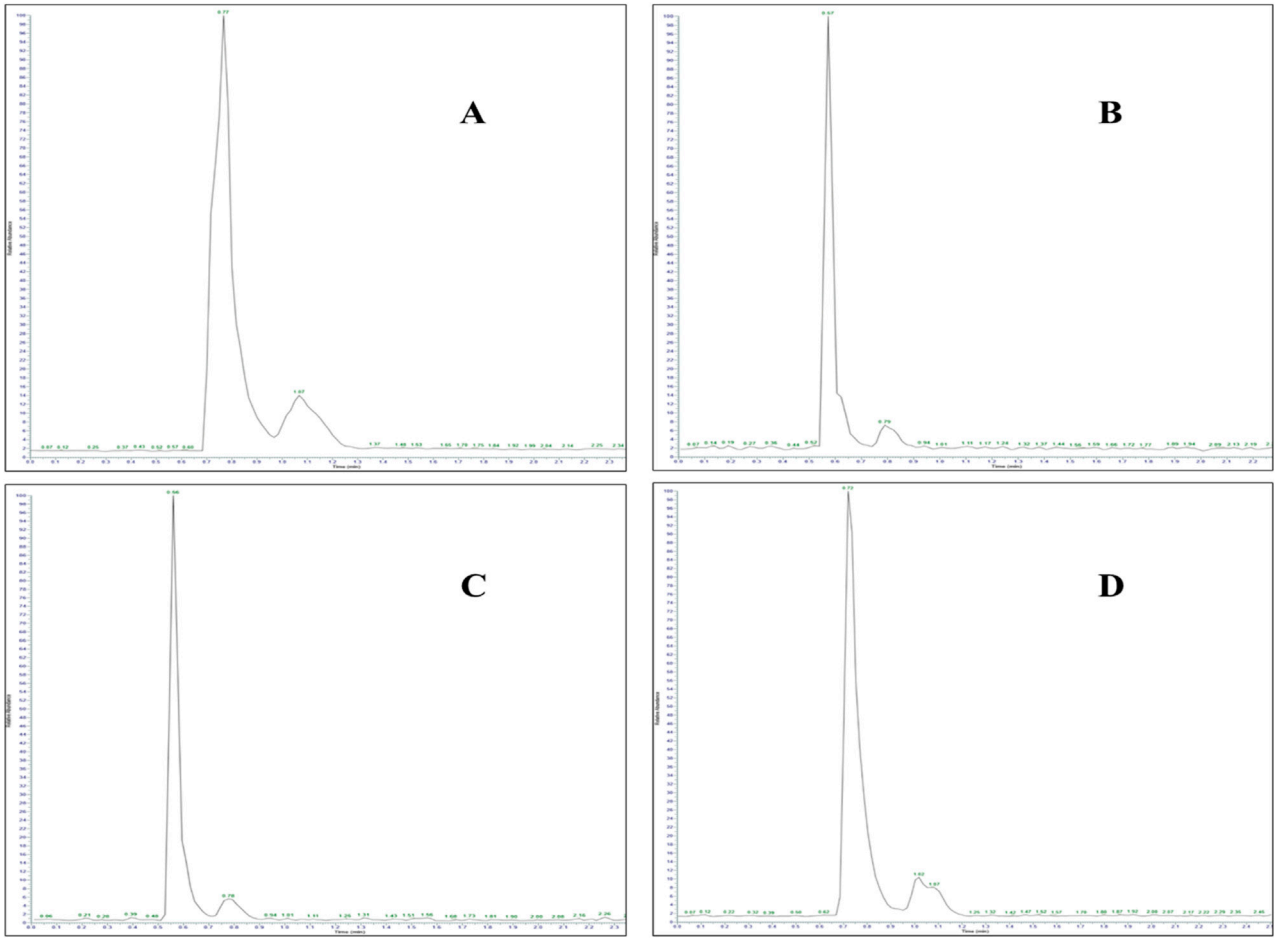

FIGURE 7
LC-MS/MS chromatogram of adulterated seized capsule sample containing **(A)** paracetamol (Rt: 0.77 min), **(B)** gabapentin (Rt: 0.57 min), **(C)** codeine (Rt: 0.56 min), and **(D)** pregabalin (Rt: 0.72 min).

resolved from the solvent front, while late-eluting nonpolar compounds were efficiently eluted within the 8.6 min runtime.

This approach not only improved separation efficiency but also met forensic requirements for rapid analysis and aligned with green chemistry principles by reducing solvent consumption while maintaining compliance with pharmacopeial standards.

3.6 Analysis by LC-MS/MS

LC-MS/MS analysis was performed to investigate the seized capsules and powder samples to identify any potential adulterants. The instrument was operated in multiple reaction monitoring (MRM) mode for targeted quantitative analysis. In the MRM mode, precursor and product ions are selected for each target analyte to achieve high selectivity and sensitivity.

Based on the molecular structures and fragmentation patterns, precursor and product ion transitions were selected for PGL and other common adulterants. These transitions were monitored in the mass spectrometer to detect and quantify analytes, if present, in the samples. Retention times and optimal collision energies were also determined from the analysis of standard solutions to allow the identification of peaks in the sample runs.

When sample extracts were injected into the LC column and eluted into the mass spectrometer, the transitions of PGL and monitored adulterants were automatically detected and peaks were produced in the chromatograms. By comparing retention times and peak areas to known standards, PGL, along with multiple adulterants in several seized capsule and powder samples, were distinguishable.

LC-MS/MS analysis revealed distinct fragmentation patterns characteristic of each analyte under optimized collision-induced dissociation (CID) conditions, validated against reference standards and published fragmentation patterns.

The analysis revealed the presence of codeine, paracetamol, and gabapentin in various capsule samples (Figures 7, 8). This result confirmed adulteration in clandestine samples. As shown in Figure 8 and Table 6, the protonated molecular ion of paracetamol ($[M + H]^+$ m/z: 152.1) was subjected to fragmentation, resulting in two diagnostic product ions when collision energies of 25 and 42eV were employed. The quantifier ion at m/z 110.1, arising from the elimination of the acetyl moiety (-$COCH_3$), and the qualifier ion at m/z 65.05, corresponding to the phenyl ring fragment. The mass

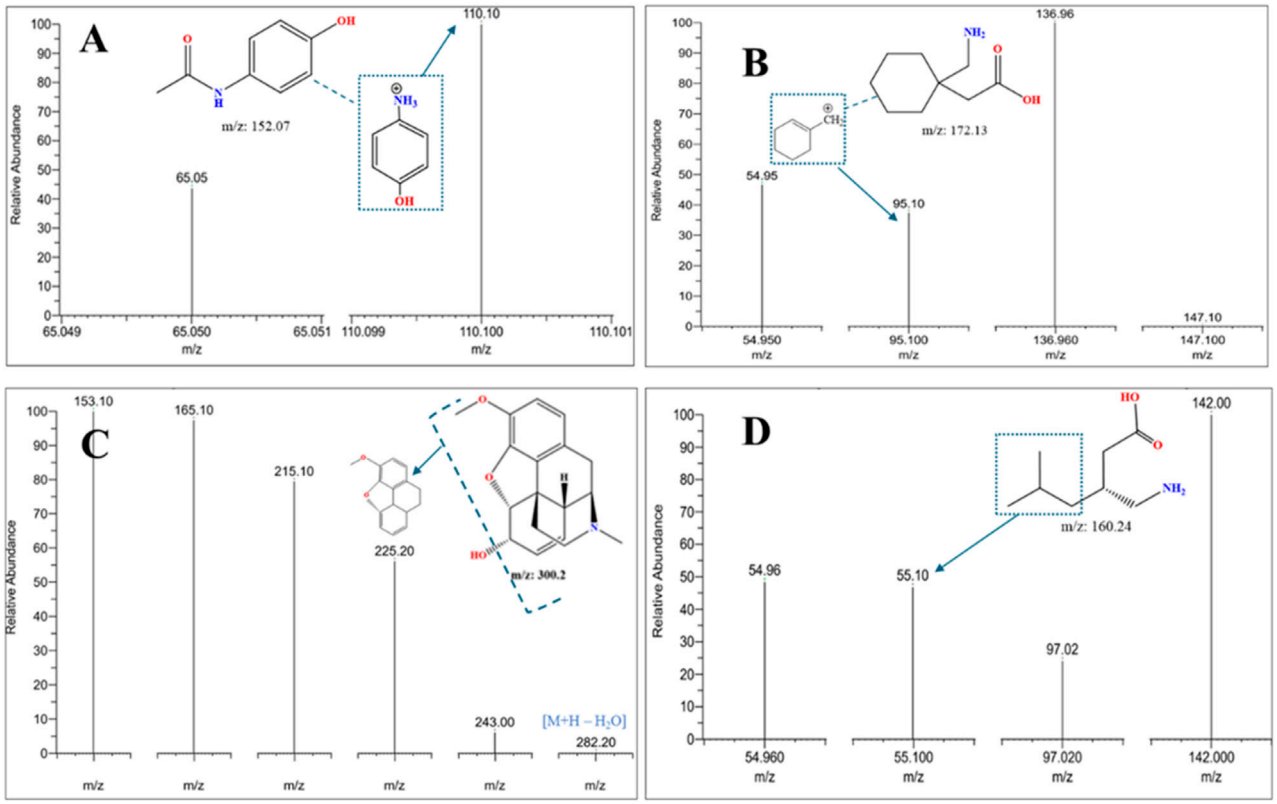

FIGURE 8
LC-MS/MS MRM mass spectra were acquired in positive ionization mode of fragmentation for an adulterated seized capsule sample containing **(A)** paracetamol, **(B)** gabapentin, **(C)** codeine, and **(D)** pregabalin, confirming the identity of co-formulated substances (paracetamol, gabapentin, codeine) in seized samples through MRM mass transitions.

spectral behaviour of gabapentin was characterized by its protonated molecular at m/z 172.09, generating product ions at m/z 147.1 due to the loss of NH_3, m/z 136.96 (sequential elimination of NH_3 and CH_2), and characteristic cyclohexyl-derived fragments observed included at m/z 95.1 and 54.95 with collision energies of 22 eV. On the other hand, codeine exhibited the most complex fragmentation profile, with its precursor ion $[M + H]^+$ at m/z 300.2 yielding multiple structurally significant transitions: m/z 282.2 due to the dehydration process, m/z 243 resulting from combined losses of CH_3OH and H_2O, m/z 225.2 related to morphinan ring fragment, and diagnostic phenanthrene-derived ions at m/z 165.1 and 153.1 using collision energies ranging from 23 to 50eV. Together with PGL, which demonstrated a molecular ion $[M + H]^+$ at m/z 160.09, exhibited sequential fragmentations to produce ions at m/z 142 (after H_2O elimination), m/z 97.02 (resulting from consecutive losses of NH_3 and CO_2), and diagnostic alkyl fragments at m/z 55.1 and 54.96 using collision energies 10,14 and 22eV. In addition to the above-mentioned interpretation, the mass spectra of those compounds were compared with those of standard reference materials for confirmation.

It is noteworthy to mention here that the presence of codeine as an adulterant with PGL can possibly cause respiratory failure (Bykov et al., 2020). Many organizations, such as the FDA, CDC, and DEA declared warnings against this practice (Bockbrader et al., 2010). Moreover, the appearance of other materials, such as paracetamol (Figure 8) in some capsules, indicates unsatisfactory manufacturing practices that do not meet specified quality standards. Some capsules reduced amounts of PGL intended to deceive consumers. The assay results for these capsules showed concentrations much lower than expected. However, quantitative assessment revealed that other capsules contained high concentrations of PGL beyond expected levels, posing risks of toxicity to users.

Results demonstrated that most samples of PGL capsules and powders were either counterfeit drugs or exceeded limits as per international pharmacopoeias, i.e., BP and USP (British Pharmacopoeia, 2022; United States Pharmacopeia, 2023). In conclusion, this study revealed that all uncontrolled drugs and illicit drug trafficking pose life-threatening dangers to consumers not only because of the active substances themselves but also to mixtures containing other compounds, particularly those from unknown or untraceable clandestine sources.

Thus, through utilizing MRM-LC-MS/MS and targeted analyte transitions, seized drug samples were successfully profiled, impurities were detected, and adulteration trends were uncovered - providing valuable data on the illegal market and risks to public health.

The current UPLC-PDA method offers significant advantages over previous HPLC-UV assays for PGL quantification in terms of total run time and sample preparation. It achieves complete chromatographic separation within a substantially shorter run time of 8.6 min, compared to a previous study (Mutalabisin et al., 2021), which reported HPLC-UV method with longer run times (15 min)

TABLE 6 LC-MS/MS performance displays the precursor and product in (m/z) from the mass spectrum of the adulterated sample.

Compound	Precursor ion (m/z)	Product ion (m/z)	Collision energy (v)
Paracetamol	152.1	65.05	35
	152.1	110.1	20
Pregabalin	160.09	54.96	22
	160.09	55.1	22
	160.09	97.02	14
	160.09	142	10
Gabapentin	172.09	54.95	22
	172.09	95.1	22
	172.09	136.96	14
	172.09	147.1	16.2
Codeine	300.2	153.1	50
	300.2	165.1	46
	300.2	215.1	23
	300.2	225.2	25.4
	300.2	243	37
	300.2	282.2	37

requiring derivatization with ninhydrin. This approach eliminates the need for derivatization, streamlining sample preparation and analysis time while minimizing potential sources of error associated with the derivatization process. The shorter run time enables higher throughput and increased efficiency, facilitating the analysis of a larger number of samples. The developed UPLC-PDA method demonstrates improved environmental sustainability compared to conventional HPLC-UV approaches through significant reductions in solvent consumption. The current method operates at an optimized flow rate of 0.5 mL/min, representing a 50% reduction from the previously reported HPLC-UV methods (1.0 mL/min) (Vinutha Ko et al., 2017; Khanage et al., 2014), while simultaneously decreasing the injection volume requirement. This enhancement in chromatographic efficiency aligns with the principles of green analytical chemistry by minimizing mobile phase usage and waste generation without compromising analytical performance. Additionally, the LC-MS/MS data further highlighted custom mixing of PGL with codeine, a trend noted in a previous study (Buttram and Kurtz, 2020) in illicit markets.

4 Conclusion

In this study, 40 seized samples (powder and capsule samples) were analysed using UPLC instrumentation. The capsules were traced to determine their manufacturing origin. Additionally, the obtained raw materials packaged in capsules were examined to understand their intended marketing. The content of these capsules had been adulterated, with adulterated samples showing concentrations inconsistent with registered amounts at the regulatory bodies.

Various capsule samples contained mixtures of PGL and codeine, a derivative of morphine that can cause serious respiratory failure. Moreover, results included either low drug amounts intended to mislead consumers or high concentrations beyond expected levels, posing toxicity risks. Overall, the analytical examination revealed poor practices in smuggled pharmaceuticals threatening public health and safety. These current chromatographic methods demonstrated significant performance characteristics for detecting PGL in seized samples and showed reliable quantitative and qualitative analysis. The analytical capabilities allowed simultaneous detection of multiple compounds, including pregabalin, codeine, gabapentin and paracetamol. This multi-compound detection feature proved crucial in identifying adulterants and determining sample authenticity. The chromatographic separation, combined with LCMS confirmation, provided accurate and dependable results for both powder and capsule formulations, making it an ideal tool for forensic analysis and quality control purposes.

Data availability statement

The original contributions presented in the study are included in the article/supplementary material, further inquiries can be directed to the corresponding author.

Author contributions

FtA: Writing – original draft, Data curation. SA: Methodology, Formal Analysis, Writing – original draft. MA: Validation,

Methodology, Writing – original draft. IA: Writing – review and editing, Supervision, Project administration. YA: Conceptualization, Writing – original draft, Visualization, Resources. RA: Supervision, Resources, Writing – original draft. AA: Resources, Writing – original draft, Supervision. TA: Supervision, Writing – original draft, Project administration. TS: Validation, Formal Analysis, Writing – review and editing. AI: Supervision, Writing – review and editing, Data curation, Visualization. HA-H: Writing – original draft, Funding acquisition, Resources. YJ: Formal Analysis, Writing – original draft, Resources. FhA: Writing – review and editing, Project administration.

Funding

The author(s) declare that financial support was received for the research and/or publication of this article. Researchers would like to extend their appreciation to the Saudi Food and Drug Authority (SFDA) for funding the publication of this project. Authors also extend their appreciation to the Deanship of Research and Graduate Studies at King Khalid University for funding this work through a large group research project under grant number (RGP2/475/46).

Acknowledgments

The authors at the Saudi Food and Drug Authority (SFDA) are grateful to the General Directorate of Narcotics Control (GDNC) in Saudi Arabia for supporting this research and providing seized samples of PGL. F. MA would like to thank King Khalid University for allowing her to study for a PhD degree as well as the Saudi Food and Drug Authority (SFDA) for providing the opportunity to carry out this work at the Drug Laboratory, SFDA.

Conflict of interest

The authors declare that the research was conducted in the absence of any commercial or financial relationships that could be construed as a potential conflict of interest.

Correction note

A correction has been made to this article. Details can be found at: 10.3389/fchem.2025.1674670.

Generative AI statement

The author(s) declare that no Generative AI was used in the creation of this manuscript.

Publisher's note

All claims expressed in this article are solely those of the authors and do not necessarily represent those of their affiliated organizations, or those of the publisher, the editors and the reviewers. Any product that may be evaluated in this article, or claim that may be made by its manufacturer, is not guaranteed or endorsed by the publisher.

References

Abraham, J. (2010). "International conference on harmonisation of technical Requirements for registration of pharmaceuticals for human use," in *Handbook of Transnational economic governance regimes*. Editors C. Tietje and A. Brouder (Leiden: Brill | Nijhoff), 1041–1053. doi:10.1163/ej.9789004163300.i-1081.897

Alelwani, W., Alkhazindar, A., Alqumaysh, B., Kutbi, D., Tayeb, R., and Altobaiqi, R. (2021). Pregabalin abuse and toxicity and related factors. *Int. Res. J. Med. Med. Sci.* 9, 34–42. doi:10.30918/irjmms.91.21.015

Almalki, A. H., Ali, N. A., Elroby, F. A., El Ghobashy, M. R., Emam, A. A., and Naguib, I. A. (2021). ESI–LC–MS/MS for therapeutic drug monitoring of binary mixture of pregabalin and tramadol: human plasma and urine applications. *Separations* 8, 21. doi:10.3390/separations8020021

Althunian, T. A., Alomran, M. I., Alsagri, G. M., Alrasheed, M. M., and Alshammari, T. M. (2022). The impact of regulatory restrictions on pregabalin use in Saudi Arabia: an interrupted time series analysis. *Drug Saf.* 31, 577–582. doi:10.1002/pds.5408

Asomaning, K., Abramsky, S., Liu, Q., Zhou, X., Sobel, R. E., and Watt, S. (2016). Pregabalin prescriptions in the United Kingdom: a drug utilisation study of the Health Improvement Network (THIN) primary care database. *Int. J. Clin. Pract.* 70, 380–388. doi:10.1111/ijcp.12791

Bockbrader, H. N., Wesche, D., Miller, R., Chapel, S., Janiczek, N., and Burger, P. (2010). A comparison of the pharmacokinetics and pharmacodynamics of pregabalin and gabapentin. *Clin. Pharmacokinet.* 49, 661–669. doi:10.2165/11536200-000000000-00000

British Pharmacopoeia (2022). Pregabalin capsules. Available online at: https://www.pharmacopoeia.com/ (Accessed May 20, 2023).

Buttram, M. E., and Kurtz, S. P. (2020). Preliminary evidence of pregabalin misuse among prescription and/or illicit opioid (Mis)users. *J. Psychoact. Drugs* 52, 172–175. doi:10.1080/02791072.2020.1734695

Bykov, K., Bateman, B. T., Franklin, J. M., Vine, S. M., and Patorno, E. (2020). Association of gabapentinoids with the risk of opioid-related adverse events in surgical patients in the United States. *JAMA Netw. Open* 3, e2031647. doi:10.1001/jamanetworkopen.2020.31647

De La Vega, H., Fox, K., Pardi, J., Santiago-Tirado, W., and Cooper, G. (2019). Validation of a high-throughput screening and quantification method for the determination of gabapentinoids in blood using a combination of LC-TOF-MS and LC-MS-MS. *J. Anal. Toxicol.* 43, 696–702. doi:10.1093/jat/bkz070

Elliott, S. P., Burke, T., and Smith, C. (2017). Determining the toxicological significance of pregabalin in fatalities. *J. Forensic Sci.* 62, 169–173. doi:10.1111/1556-4029.13263

Evoy, K. E., Morrison, M. D., and Saklad, S. R. (2017). Abuse and misuse of pregabalin and gabapentin. *Drugs* 77, 403–426. doi:10.1007/s40265-017-0700-x

Gujral, R. S., Haque, S. M., and Shanker, P. (2009). Development and validation of pregabalin in bulk, pharmaceutical formulations and in human urine samples by UV Spectrophotometry. *Int. J. Biomed. Sci.* 5, 175–180. doi:10.59566/IJBS.2009.5175

Gurke, R., Rossmann, J., Schubert, S., Sandmann, T., Rößler, M., Oertel, R., et al. (2015). Development of a SPE-HPLC–MS/MS method for the determination of most prescribed pharmaceuticals and related metabolites in urban sewage samples. *J. Chromatogr. B Biomed. Sci. Appl.* 990, 23–30. doi:10.1016/j.jchromb.2015.03.008

Khanage, S., Kale, D., Mohite, P., and Deshmukh, V. (2014). Reversed phase high performance liquid chromatographic method for simultaneous estimation of pregabalin and aceclofenac in tablet formulation (Acenac-N). *J. Rep. Pharma. Sci.* 3, 184. doi:10.4103/2322-1232.222561

Komisarek, D., Haj Hassani Sohi, T., and Vasylyeva, V. (2022). Co-crystals of zwitterionic GABA API's pregabalin and phenibut: properties and application. *Cryst. Eng. Comm.* 24, 8390–8398. doi:10.1039/D2CE01416E

Kriikku, P., and Ojanperä, I. (2021). Pregabalin and gabapentin in non-opioid poisoning deaths. *Forensic Sci. Int.* 324, 110830. doi:10.1016/j.forsciint.2021.110830

Kritikos, N., Iliou, A., Kalampaliki, A. D., Gikas, E., Kostakis, I. K., Michel, B. Y., et al. (2022). Chemometrically assisted optimization of pregabalin fluorescent derivatization reaction with a novel xanthone analogue and validation of the method for the determination of pregabalin in bulk via a plate reader. *Molecules* 27, 1954. doi:10.3390/molecules27061954

Martinc, B., Roškar, R., Grabnar, I., and Vovk, T. (2014). Simultaneous determination of gabapentin, pregabalin, vigabatrin, and topiramate in plasma by HPLC with fluorescence detection. *J. Chromatogr. B Biomed. Sci. Appl.* 962, 82–88. doi:10.1016/j.jchromb.2014.05.030

Mata, D. C., and Davis, J. F. (2022). Simultaneous quantitative analysis of 39 common toxicological drugs for increased efficiency in an ante- and postmortem laboratory. *Forensic Sci. Int.* 334, 111246. doi:10.1016/j.forsciint.2022.111246

Mathieson, S., Lin, C.-W. C., Underwood, M., and Eldabe, S. (2020). Pregabalin and gabapentin for pain. *BMJ* 369, m1315. doi:10.1136/bmj.m1315

Mutalabisin, F., Helaluddin, A. B. M., Sengupta, P., Mohamed, F., and Chatterjee, B. (2021). Quantitation of pregabalin by HPLC-UV method using ninhydrin derivatization: development and validation. *Curr. Pharm. Anal.* 17, 165–171. doi:10.2174/1573412916666191114120213

Nahar, L., Smith, A., Patel, R., Andrews, R., and Paterson, S. (2017). Validated method for the screening and quantification of baclofen, gabapentin and pregabalin in human post-mortem whole blood using protein precipitation and liquid chromatography–tandem mass spectrometry. *J. Anal. Toxicol.* 41, 441–450. doi:10.1093/jat/bkx019

Pelander, A., Ristimaa, J., and Ojanperä, I. (2010). Vitreous humor as an alternative matrix for comprehensive drug screening in postmortem toxicology by liquid chromatography-time-of-flight mass spectrometry. *J. Anal. Toxicol.* 34, 312–318. doi:10.1093/jat/34.6.312

Smith, S. M., Dart, R. C., Katz, N. P., Paillard, F., Adams, E. H., Comer, S. D., et al. (2013). Classification and definition of misuse, abuse, and related events in clinical trials: ACTTION systematic review and recommendations. *Pain* 154, 2287–2296. doi:10.1016/j.pain.2013.05.053

Sripathi, S., Somesetti, N. R., Veeramalla, R., Challa, N. R., Peddi, S. R., and Karnati, V. R. (2010). Synthesis and characterization of impurities of an anticonvulsant drug, Pregabalin. *Arkivoc* 2010, 266–275. doi:10.3998/ark.5550190.0011.a22

Tassone, D. M., Boyce, E., Guyer, J., and Nuzum, D. (2007). Pregabalin: a novel γ-aminobutyric acid analogue in the treatment of neuropathic pain, partial-onset seizures, and anxiety disorders. *Clin. Ther.* 29, 26–48. doi:10.1016/j.clinthera.2007.01.013

Teker, C., Aslan, R., İpekçi, C., Tokdemir, M., and Akgür, S. A. (2024). Pregabalin qualitative detection in Turkish forensic cases between 2017 to 2018. *J. Psychoact. Drugs* 56, 380–386. doi:10.1080/02791072.2023.2226138

Toth, C. (2014). Pregabalin: latest safety evidence and clinical implications for the management of neuropathic pain. *Ther. Adv. Drug Saf.* 5, 38–56. doi:10.1177/2042098613505614

United States Pharmacopeia (2023). USP monographs: pregabalin. Available online at: https://www.uspnf.com/official-text/proposal-statuscommentary/uspnf-2023 (Accessed May 20, 2023).

Vinutha Kommineni, K. P. R. C., and S, V. U. M. P. (2017). Development of A new stability indicating rp-hplc method for simultaneous estimation of saxagliptine and dapagliflozin and its validation as per ICH guidelines. *IAJPS*. doi:10.5281/ZENODO.892231

Vukkum, P., Babu, J. M., and Muralikrishna, R. (2015). Stress degradation behavior of pregabalin, identification of degradation impurities and development of stability indicating UPLC method. *Int. J. Pharm. Sci. Res.* 6, 2241. doi:10.13040/IJPSR.0975-8232.6(6).2241-57

Wang, J., and Xu, B. (2019). Quantitation of neurotransmitter GABA analogue drugs pregabalin and gabapentin in oral fluid and urine samples by liquid chromatography Tandem Mass Spectrometry. *J. Med. Discov.* 4, 1–8. doi:10.24262/jmd.4.2.19018

frontiers | Frontiers in Chemistry

TYPE Original Research
PUBLISHED 15 October 2025
DOI 10.3389/fchem.2025.1597784

OPEN ACCESS

EDITED BY
Sabina Susmel,
University of Udine, Italy

REVIEWED BY
Huangfan Xie,
Southwest Medical University, China
Naomi Kanzato,
Okinawa Southern Medical Center, Japan

*CORRESPONDENCE
Maria Cristina Gaudiano,
mariacristina.gaudiano@iss.it

†These authors have contributed equally to this work and share last authorship

RECEIVED 21 March 2025
ACCEPTED 21 July 2025
PUBLISHED 15 October 2025

CITATION
Aureli F, Gaudiano MC, Raimondo M, Maccelli A, Di Giorgio D, Gramazio M, Borioni A and Bartolomei M (2025) Quality assessment of "naturally occurring" high-percentage L-dopa commercial products proposed as dietary supplements on the Internet: from labeling to analytical findings.
Front. Chem. 13:1597784.
doi: 10.3389/fchem.2025.1597784

Quality assessment of "naturally occurring" high-percentage L-dopa commercial products proposed as dietary supplements on the Internet: from labeling to analytical findings

Federica Aureli[1], Maria Cristina Gaudiano[1]*, Mariangela Raimondo[1], Alessandro Maccelli[1], Domenico Di Giorgio[2], Marta Gramazio[2], Anna Borioni[1†] and Monica Bartolomei[1†]

[1]Chemical Medicines Unit, National Centre for the Control and Evaluation of Medicines, Istituto Superiore di Sanità, Rome, Italy, [2]Inspection and Certification Department, AIFA - Italian Medicines Agency, Rome, Italy

Introduction: Levodopa (L-dihydroxyphenylalanine or L-dopa) is a precursor of the neurotransmitter dopamine and is used in Parkinson's disease therapy. L-dopa dietary supplements are widely marketed as brain support. Among the L-dopa products claiming to contain botanical extracts, those from *Mucuna pruriens* are the most frequently offered on the Internet. The natural percentage of L-dopa in *M. pruriens* seeds or leaves varies from 1% to 7%, but extracts standardized at higher percentages of L-dopa are also available.

Methods: Four L-dopa products marketed as dietary supplements were purchased online and analyzed for labeling accuracy. The identification of L-dopa and the detection of undeclared pharmaceutical or nootropic ingredients were carried out via mass spectrometry (LC-MS Q-TOF). Nuclear magnetic resonance (NMR) spectroscopy was used to confirm the presence of L-dopa and quantify it. Furthermore, a Google Trends analysis was conducted to study interest in the terms "levodopa" and "brain supplements" and their Italian equivalents, over the last 10 years in Italy and globally.

Results: Visual inspection of labeling revealed that the extract of *M. pruriens*, which is not allowed in dietary supplements in Italy, was listed on three products, while the extract of *Vicia faba* was declared in one sample. Some labeling concerning the dosage of L-dopa was ambiguous. LC-MS and NMR analyses confirmed the presence of L-dopa in all the samples. No undeclared active pharmaceutical or nootropic ingredients were detected. The amount of L-dopa in the capsules was found to match the labeled dosage in some samples, but others were either overdosed or underdosed. Trend analysis indicated increasing interest in the terms "levodopa" and "brain supplements" both in Italy and worldwide.

Discussion: The obtained results showed evidence of potential risks related to consuming dietary supplements purchased online containing high-dose L-dopa. These risks arise from the inclusion of unauthorized botanical extracts, unclear

labeling, and inconsistencies between labeled and actual dosages. Given the observed increasing public interest in levodopa, these findings highlight the need to control this market and inform consumers and physicians about the risks of purchasing unauthorized online products.

KEYWORDS

mass spectrometry, nuclear magnetic resonance, L-dopa, dietary supplements, nootropic, plant extract, Parkinson's disease

1 Introduction

Levodopa (L-dihydroxyphenylalanine or L-dopa), belonging to the class of catecholamines, was discovered in the late 1950s to early 1960s and remains one of the most common therapies for treating motor symptoms in Parkinson's disease to this day (Hornykiewicz, 2017). As a precursor of the neurotransmitter dopamine, it is absorbed from the intestinal tract and crosses the blood–brain barrier via active transporters to reach the brain, where it is converted into dopamine (Rezak, 2007). The pharmacological efficacy of L-dopa decreases after a certain period of intake, which often requires the adjustment of therapies. The reported side effects of L-dopa include non-motor adverse effects such as i) nausea, vomiting, and dry mouth; ii) orthostatic hypotension, dizziness, headache, weakness, and somnolence; iii) cardiac dysrhythmias; and iv) hallucinations, chest pain, and depression and the motor adverse effects include motor fluctuations (on–off phenomenon) and dyskinesias (Bhushan et al., 2023; Mouchaileh and Hughes, 2020). To decrease the side effects, L-dopa is co-administered with carbidopa, entacapone, or benserazide (Katzung et al., 2024). The use of L-dopa preparations as nootropics or "brain support" is increasing due to the general increase in interest in products that enhance cognitive performance and improve mental focus and memory (Vanhee et al., 2025). Moreover, in bodybuilding forums, L-dopa dietary supplements are recommended alone or in combination with other nootropics to achieve dopaminergic stimulation or with 19-nor derivatives, such as trenbolone, to counteract dopamine depletion.

L-dopa can also be found in natural sources, particularly in plants of the Fabaceae family (e.g., beans, peas, faba beans, lentils, peanuts, and soybeans) (Boelens Keun et al., 2021), with Mucuna pruriens and its derived products being the most commonly promoted online for natural L-dopa supplementation. Different varieties of plants and individual parts of plant matrices (e.g., seeds and leaves) can contain various amounts of L-dopa. The natural concentration of L-dopa in *M. pruriens* ranges from less than 1% to 7% (Adebowale et al., 2005; Nishihara et al., 2005; Pulikkalpura et al., 2015; Soares et al., 2014). Faba bean shows a lower content of L-dopa on average, with quantities of < 1% in the leaf, flower, seeds, and pod extracts, which reach up to 3% in pod valves (Tesoro et al., 2024; Topal and Bozoğlu, 2016). Moreover, commercially available products marketed as vegetal preparations, also known as botanicals, or dietary supplements are sold online with high levels of L-dopa (15%, 25%, or practically pure products), indicating that they result from intensive extraction and concentration procedures or the addition of chemically synthesized pure active substance (Tesoro et al., 2022). In the European Union (EU), botanicals and botanical preparations can enter the market as food supplements or herbal medicinal products, provided they comply with the requirements set out in the respective food and medicinal legislation. The EU does not have a centralized authorization procedure for the use of botanicals and their derived preparations in food; instead, each Member State has developed national provisions to complement the general food regulatory framework. In Italy, the use of plant extracts and preparations in food supplements is currently regulated by the Ministerial Decree of 10 August 2018, which, among other provisions, sets out a list of permitted plants, either as a whole or as specific parts (seeds, leaves, etc.) (Ministero della Salute, 2018). This list is only relevant to plants/parts of plants and their derivatives (e.g., extracts or other preparations) with a history of significant food consumption before 1997; substances, preparations, and extracts obtained from the listed plants but without the cited history of consumption are considered novel foods (food that had not been consumed to a significant degree by humans in the EU before 15 May 1997) under Regulation (EU) 2015/2283 and, therefore, cannot be used prior to EU authorization.

Irrespective of their classifications and use, the illicit trade of commercial products containing undeclared/unauthorized pharmaceutical ingredients, nootropic agents, and unauthorized novel food is still increasing, and a variety of unauthorized products can be found on the Internet (Gaudiano et al., 2022; Gaudiano et al, 2024a; Gaudiano et al, 2024b; Vanhee et al., 2025). The safety profile of illegal products is unknown, posing a tangible health risk to consumers.

The identification and quantification of L-dopa in botanicals and botanical preparations proposed as dietary supplements is a crucial aspect in their quality assessment and for the verification of possible adulteration with other nootropic active ingredients that could be fraudulently added to these products. Different high-performance liquid chromatography (HPLC) and liquid chromatography–mass spectrometry (LC–MS) methods have been validated to quantify L-dopa in plant matrices (Kaced et al., 2024; Tesoro et al., 2022; Tesoro et al., 2023; Vora et al., 2018; Yumoto et al., 2022) and commercial *M. pruriens* products (Hasegawa et al., 2011; Soumyanath et al., 2018). Simpler methods such as high-performance thin-layer chromatography (HPTLC) have also been developed for the analysis of L-dopa in *M. pruriens* seed extract and its formulations (Aware et al., 2017; Modi et al., 2008; Pulikkalpura et al., 2015). Nuclear magnetic resonance (NMR) has been extensively used in the field of botanical health products analysis and quality control (Zhao et al., 2022), and quantitative NMR (q-NMR) has been applied for the analysis of L-dopa in *M. pruriens* seeds (Fernandez-Pastor et al., 2019).

Taking into account that L-dopa is an active ingredient with a consolidated use for the treatment of Parkinson's disease, the aim of

the present study was to assess the quality of products proposed as dietary supplements with declared L-dopa content and purchased via the Internet from retail websites accessible from Italy. Samples were evaluated for labeling and analyzed using an LC–MS screening method and NMR to identify L-dopa and assess possible adulteration with other nootropic and pharmaceutical active ingredients. Quantification of L-dopa in the products was performed by q-NMR to evaluate whether the actual amount of L-dopa complied with what was declared and whether it was compatible with the quantity derived from a natural extract. This research targets the first country-wide investigation of the illicit L-dopa online market in Italy. Finally, a study was conducted on web search trends for the terms "levodopa" and "brain supplements" and their Italian equivalents, comparing the situation in Italy with global trends.

2 Materials and methods

2.1 Selection of the retail websites

Websites accessible from Italy selling L-dopa "dietary supplements" were selected using the Google search engine using the Italian terms *"acquista integratori L-dopa in Italia"* (buy L-dopa dietary supplements in Italy) as the keywords. Websites based in Europe were prioritized for product purchases. Retail websites were chosen based on sale conditions: the possibility to pay by prepaid credit card and ship the product to Italy. These websites reported information in the Italian language; the IP addresses, investigated using the site https://www.iplocation.net/ip-lookup, were located in Italy (two sites), the Czech Republic (one site), and Germany (one site). The purchases were made by the Italian Medicines Agency.

The retail websites were selected if they explicitly mentioned products showing nootropic activities with claims such as "an exceptional extract that helps maintain a healthy nervous system," "a leading compound in Ayurvedic medicine," "guaranteed without synthetic additives," and "precursor of the neurotransmitter dopamine."

2.2 Samples and visual analysis

Four capsule products claiming to contain L-dopa from botanical extracts were purchased from four different manufacturers: three samples were labeled as naturally extracted from *M. pruriens*, and one sample was from *Vicia faba*. To avoid being traced as an official laboratory of control, the samples were sent to a private address. The samples were photographed and subjected to visual analysis of the packaging and labeling before instrumental analysis.

2.3 Trend of interest

The Italian and global trends of interest for the terms *"brain supplements"* and "*levodopa*" for "all categories" in the period from 01/12/2015 to 31/01/2025 were analyzed using the Google Trends application. Results are expressed as the relative normalized search volume numbers and are presented on a scale from 0 to 100, where 100 represents a maximum search interest at a given time and place. This tool allows investigating the popularity of a selected term in the specified period of time and region. The numbers reflect how many searches were performed for a particular term relative to the total number of searches performed using Google over time. Each point on the graph is divided by the highest point, which is conventionally set at 100 (Gaudiano et al, 2024a; Google, 2023). "*Levodopa*" was used in the searches for both the "World" and "Italy" regions, considering that the term is identical in English and Italian. Moreover, the term *"brain supplements"* was used for the "World," while the combined search terms *"integratori memoria + integratori concentrazione"* were used for Italy as these are used in everyday language to refer to common brain supplements.

2.4 LC–MS analysis

The identification analysis was performed using the same screening method reported elsewhere (Gaudiano et al, 2024a). In brief, a liquid chromatograph (Model 1290 from Agilent Technologies, Santa Clara, California) coupled with a high-resolution quadrupole time-of-flight mass spectrometer (Model 6520 from Agilent Technologies), equipped with a dual electrospray ionization (dual ESI) source working in both positive and negative mode, was used. All the operations, acquisition, and analysis of data were controlled using Agilent MassHunter Acquisition software version B.06.01 and processed using MassHunter Qualitative Analysis software version B.07.00. Each sample was analyzed in positive mode over the range of m/z = 50–1,200 in the extended dynamic range (2 GHz). The same condition was applied to negative mode. Accurate mass measurements were obtained by reference mass correction using masses at m/z 121.0509 (purine) and 922.0098 (hexakis (1H, 1H, 3H-tetrafluoropropoxy) phosphazene or HP-921) in positive ion mode and 112.9856 (trifluoroacetic anion) and 1,033.9881 (HP-921) in negative ion mode. All solvents and reagents were of LC–MS grade (Merck KGaA, Darmstadt, Germany). The reference standard L-dopa was purchased from Sigma-Aldrich (St Louis, MO, United States).

Chromatographic separation was carried out on a ZORBAX Extend-C18 Column (2.1 × 50 mm, 1.8 µm particle size) using a linear gradient elution from a high concentration of water (95:5 water/acetonitrile containing 0.1% formic acid) to a high concentration of organic solvent (5:95 water/acetonitrile containing 0.1% formic acid) over 15 minutes. The flow rate was set at 0.4 mL/min, and the injection volume was 1 µL. The column temperature was 35 °C, and the autosampler was thermostated at 10 °C. Mass spectrometer parameters were as follows: fragmentor, 100 V; nitrogen temperature, 300 °C; drying gas, 10 L/min; nebulizer, 40 psig; and VCap, 4,000 V. The high resolution of the instrument allowed for accurate measurement of ionic masses in MS mode and enabled the calculation of the chemical formulas of the molecules contained in the samples. Target MS/MS studies were performed by isolating $[M+H]^+$ or $[M-H]^-$ ions. The major fragments were obtained for the protonated/deprotonated molecule and compared with those produced for the standard under identical conditions. Fragmentation patterns were obtained at 20 V of

collision energy offset. Auto MS/MS analysis was used to screen for undeclared active pharmaceutical substances using the Agilent *MassHunter Forensics and Toxicology Personal Compound Database and Library* (*ForTox PCDL* B.07.01). The exact mass and ion fragmentation pattern of each detected compound were then compared with the PCDL library, which contains > 9,000 exact ion masses and > 3,000 ion fragmentation patterns, including common nootropic substances and active pharmaceutical ingredients.

For each product, the powder contained in a capsule was transferred to 50 mL or 100 mL volumetric flasks and dissolved with methanol. The solution was sonicated for 10 minutes and magnetically stirred for 1 hour. The solution was then diluted at a 1:10 ratio in acetonitrile/water (1:1 v/v) containing 0.1% formic acid and filtered through 0.22 µm PTFE filters in order to achieve an estimated L-dopa concentration of approximately 0.1 µg/µL for injection into the LC–MS system, based on the labeled content.

2.5 NMR analysis

The NMR experiments were performed on a Bruker AVANCE Neo 600 MHz Spectrometer (Bruker BioSpin GmbH, Germany), operating at 14.09 T and equipped with a Bruker iProbe 5 mm SmartProbe. The NMR data were collected and processed using TOPSPIN 4.1.3 and IconNMR software (Bruker BioSpin, United States). The samples were analyzed to confirm the presence of L-dopa in the capsules and determine its content.

2.5.1 Identification

An aliquot of the capsules' content corresponding to approximately one-quarter of the reported L-dopa content was dissolved in 1 mL of methanol-d4 (Sigma-Aldrich). The samples were vortexed for 1 minute and allowed to settle for 10 min. A measure of 0.6 mL of the supernatant was transferred into the NMR tube.

Identification was carried out using one- and two-dimensional Bruker's pulse programs: 1H-(zg), ^{1}H–^{1}H total correlation spectroscopy (TOCSY), ^{1}H–^{13}C heteronuclear single quantum coherence (HSQC, hsqcedetgpsisp2.3), and heteronuclear multiple bond correlation (HMBC, hmbcetgpl3nd).

2.5.2 Quantitative analysis

The choice of the internal standard/solvent system for q-NMR was based on the solubility of L-dopa and the standard and the good separation of their respective NMR signals in the spectra. L-dopa was extracted using a mixture of deuterium oxide (D 99.6%) and acetic acid-d4 (Cambridge Isotope Laboratories) according to the solubility data reported in the literature (Polanowska et al., 2019). Maleic acid (TraceCERT® Maleic Acid, Sigma-Aldrich, Milan, Italy), displaying a ^{1}H-NMR signal at 6.1 parts per million (ppm), was chosen as the internal reference standard. This compound was chosen as the internal standard because of the sharp singlet signal in a region of the NMR spectrum with no other signals and for its insensitivity to the matrix effects, solubility, and stability in a solution. The capsule powder from each sample was dissolved in acetic acid-d4/D_2O (20:80, v/v) at concentrations ranging from 5 mg/mL to 20 mg/mL of the capsule content, corresponding to approximately 0.5 mg/mL–13 mg/mL of labeled L-dopa content. The mixtures were vortexed for 1 min, sonicated for 15 min, and centrifuged at 10^4 rpm for 15 min. A volume of 0.7 mL of each solution was transferred into a vial containing 5 mg of maleic acid and vortexed for 2 min. Finally, the solutions were transferred to the NMR tubes for analysis.

q-NMR analysis was performed using the Bruker pulse program (zg) with the following settings: 32 scans, size of FID (TD) = 64K, spectral width (SW) = 25 ppm centered at (O1P) 4.70 ppm, and target probe temperature (TE) = 298.0 K. In addition, good signal intensity and recovery were ensured by the determination of the relaxation time (T1) and the calibration of the 90° pulse width (p1) prior to each analysis. The delay time D1, set at 7*T1 (60 s), allowed for 99.9% signal recovery. All spectra were apodized with an exponential function at 0.3 Hz, processed with zero filling (128 K), and subjected to phase adjustment and baseline correction. If necessary, manual phasing and baseline correction in selected spectral ranges were applied. Visual examination of the 2D NMR experiments (TOCSY, HSQC, and HMBC) confirmed that no interfering signals were present under the signals of L-dopa signals selected for quantification.

The reliability of the results was first based on the control of the equipment performance and the compliance to the requirements laid down in the European Pharmacopoeia (Ph. Eur.) and the ISO 17025:2017 system. At each analytical session, sensitivity (by checking the S/N), the homogeneity of the magnetic field (by the 1H-line shape test), and the 90° pulse length (related to the reproducibility of the measures) were assessed according to the manufacturer's acceptance criteria, and they support the suitability of the equipment for qNMRs in the applied range.

According to the Ph. Eur. monograph nuclear magnetic resonance spectrometry, a signal-to-noise ratio (S/N) of at least 150 allows peak integrations with a standard deviation of less than 1%. The S/N on the integrated signal of L-dopa in all the lower-concentration samples was higher than 150. As also required by the Ph. Eur., only signals with at least five digital points above the half-height were considered for quantification. This number of points ensures that the integrated signals are well-defined. Accuracy is also dependent on the spectra acquisition settings, which must ensure the full recovery of the integrated signals. This was achieved by a suitably long interscan delay (D1 = 60 s), which was experimentally determined for each sample. The accuracy also depends on the portion of the integration region. The NMR signals have a Lorentzian line shape that decays infinitely with a steepness value dependent on the full width at half height (FWHH) of each signal. Therefore, full signal integration is not realistic. Thus, the integration range of the sample and the reference standard signals was carefully selected. The FWHH of the L-dopa and maleic acid signals was measured, and the proportional regions corresponding to equal areas of the signals were integrated.

Once all the NMR experimental parameters were set correctly, the only factor that could affect the accuracy of the results was the efficiency of the L-dopa extraction from the matrix. This issue was addressed by checking the linearity of the results, as reported below. After preliminary experiments with methanol, which produced unsatisfactory results, the powder in the capsules was extracted using a 20% acetic acid-d4/D_2O solution. This approach was highly effective in distinguishing L-dopa from the other components.

10.3389/fchem.2025.1597784

TABLE 1 Findings of the visual inspection of labeling.

Sample #	1	2	3	4
Labeled vegetal extract content per cps[a]	420 mg	N.R[b]	400 mg	400 mg
Vegetal extract name	*Vicia faba*	*Mucuna pruriens*	*Mucuna pruriens*	*Mucuna pruriens*
Labeled % of L-dopa in the extract	25% (natural extract)	98%	15% (naturally occurring)	15%
Labeled L-dopa content per cps	105 mg	117 mg	N.R. (explicitly) [c]	N.R. (explicitly) [d]
Number of cps per serving	1 cps/die	1 cps/die	2 cps/die	5 cps/die
Labeled L-dopa content per serving	105 mg	117 mg	120 mg	N.R.[e] (explicitly) [e]
Labeled ingredients	*Broad bean extract (25% L-dopa), hydroxypropyl methyl cellulose (capsule), and D-a-tocopherol acetate (vitamin E)*	*Velvet bean extract (Mucuna pruriens) standardized 98% of L-dopa, anticaking: magnesium salts of fatty acids, silicon dioxide, and gelatine (capsule)*	*Amount per serving* *Mucuna extract (Mucuna* spp.*) (seed) (min. 15% L-dopa, naturally occurring) 800 mg* --- *L-dopa 120 mg* *Other ingredients: hypromellose (cellulose capsule), microcrystalline cellulose, and stearic acid (vegetable source)*	*Each vegetarian capsule contains 400 mg of the Mucuna pruriens extract standardized to 15% L-dopa* *Other ingredients: acacia gum and white rice flour*
Reported pharmacological activity	N.R.	N.R.	Brain support	N.R.
Reported manufacturing name and country	Yes (Germany)	Yes (SLO)	Yes (USA)	Only reported the country (United States) and EU distributor name
Reported batch number	Yes	Yes	Yes	Yes
Reported expiry date	Yes	Yes	Yes (as "Best be")	Yes
Reported warnings	Yes	Yes	Yes	Yes
Legal statement	N.R.	N.R.	*These statements have not been evaluated by the Food and Drug Administration. This product is not intended for diagnosing, treating, curing, or preventing any disease.*	N.R.
Language of labeling	English and German	English and Italian	English	English, French, and Portuguese

[a]Capsule.
[b]Not reported.
[c]Only reported the amount per serving (120 mg) and the serving size (two capsules) corresponding to an amount per capsule of 60 mg.
[d]"*Each vegetarian capsule contains 400 mg of Mucuna pruriens standardized to 15% L-dopa*" corresponding to an amount per capsule of 60 mg.
[e]Serving size: 2,000 mg *of Mucuna pruriens* extract standardized to 15% L-dopa corresponding to an amount per serving of 300 mg.

3 Results

3.1 Visual analysis

The results of the visual analysis of the samples are reported in Table 1. All samples, labeled as dietary supplements, were in capsules form and contained L-dopa extracts standardized from 15% to 98% (see images in Figure 1). The content of L-dopa for capsules was not clearly indicated in all the samples; in two samples (samples #3 and #4), the content was calculated on the basis of the reported percentage of L-dopa in the extract and the serving size. The labeled L-dopa content per serving ranged from 105 mg to 300 mg, with the last quantity exceeding the recommended initial daily dose for Parkinson's disease treatment (200 mg in combination with other active substances). In one case (sample #3), the use as "brain support" was explicitly reported. The manufacturer's name was absent in one case (in sample #4, only the country was reported). In one case only, labeling was provided also in Italian language. Samples #1, #3, and #4 did not report the part of the plants used to produce the extract. In three samples, the plant source of the extract was identified as *M. pruriens*. The content per capsule of the vegetal extract was reported only for three samples.

FIGURE 1
Photographs of the samples with details of the reported contents on the labels.

3.2 Trend of interest

Google Trends is a tool to evaluate the interest in a single product or product categories based on the frequency of related search terms on Google. Figure 2 shows the trend of interest % for the term *"brain supplements"* for the region *"World"* (A) and for the combined search terms *"integratori memoria + integratori concentrazione"* for *"Italy"* (B) on the upper panels and the trend of interest % for the term *"levodopa"* in the World (C) and in Italy (D) on the lower panels in the period from 01/12/2015 to 31/01/2025. In all cases, an upward tendency can be observed, with a practically linear mode for "levodopa" in Italy and a more marked increase in 2022 in the world. It should be highlighted that this result, showing the overall trend, does not discriminate among searches for levodopa medicinal products and dietary supplements or other types of searches (for research or study purposes). Nevertheless, the data showed evidence of a general increase in interest for this molecule and the related market of products, which was also confirmed by the trend for *"brain supplements"* and the corresponding Italian terms that showed an evident increment starting from 2022.

3.3 Identification of L-dopa by mass spectrometry

The presence of L-dopa was confirmed in all samples by LC–MS–Q-TOF analysis, as depicted in Table 2. Extracted ion chromatogram (EIC) for the expected positive molecular ion at 198.0761 ($[M + H]^+$) (see Supplementary Figure S1) showed correspondence of retention times compared to the L-dopa reference standard (Table 2). Moreover, accurate mass measurements obtained in positive mode by mass spectra extraction were in line with the theoretical mass, and the calculated error was <5 ppm in most cases. In sample #3, it was not possible to univocally assign the measured peak at 198.0895 to L-dopa; therefore, given the presence of an acidic moiety in the molecular structure of L-dopa, a negative mode analysis was tentatively used. A good correlation with the theoretical value of $[M–H]^-$ with a calculated error on mass accuracy <4 ppm was obtained. In order to consider the compound identified and avoid false positive assignment, MS/MS fragmentation experiments were carried out, and the compound was considered identified if the accurate mass and relative abundance of the five most abundant fragments matched those of the reference standard ±0.01 Da and 20%, respectively. Accurate mass measurements of fragment ions, along with their relative abundance, matched those of the reference standard in both the positive and negative modes. In positive mode, fragments at 181.050 (loss of $-NH_2$) and 152.070 (loss of $-CO_2H$) were recorded as shown in Figure 3, further strengthening the proper identification of L-dopa.

No additional approved or unapproved pharmaceutical drug substances among those investigated from the PCDL database were found, including an exact mass search of carbidopa, entacapone, and benserazide, which are typically associated with synthetic levodopa in medicinal therapies. In addition,

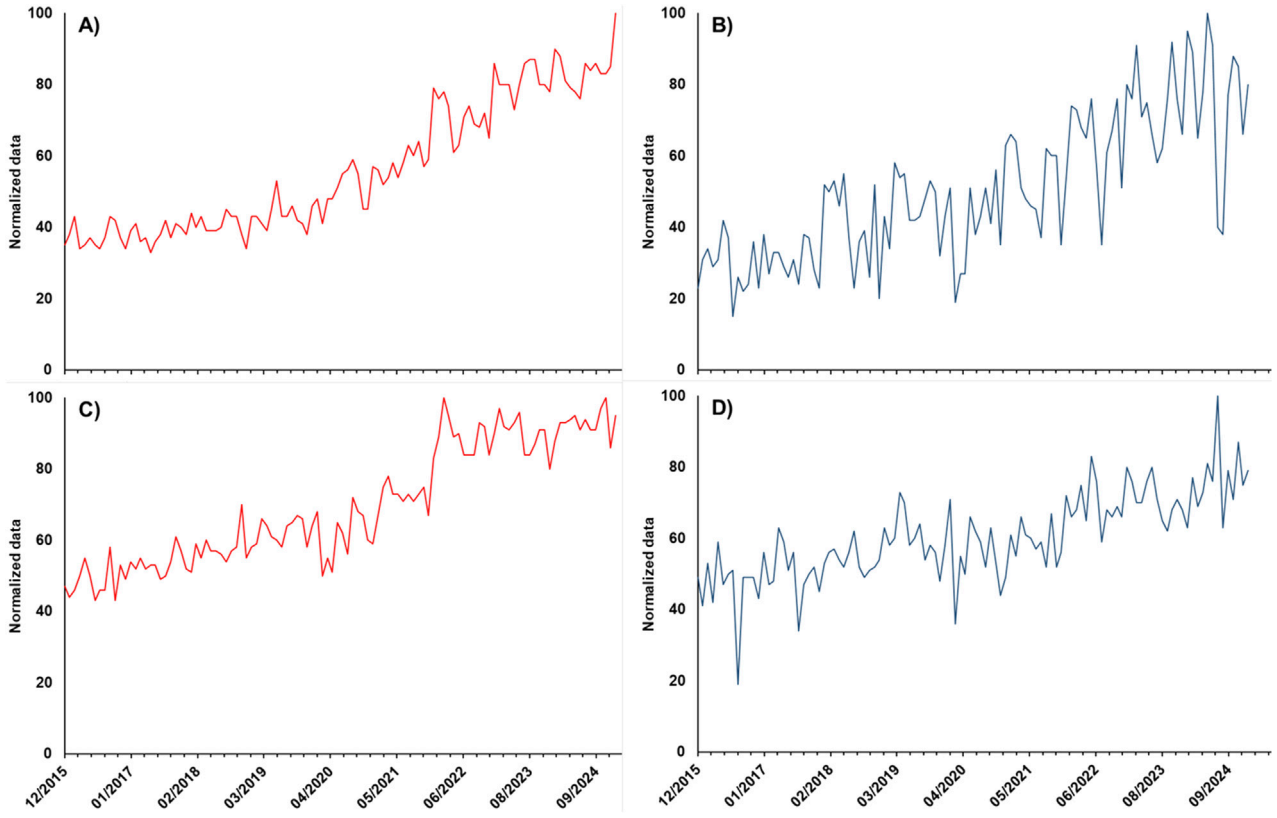

FIGURE 2
Trend of interest, obtained by the Google Trends application, for the search term "brain supplements" for the region "World" **(A)**, the combined search terms *"integratori memoria + integratori concentrazione"* for "Italy," **(B)** and the search term "levodopa" for the "World" **(C)** and "Italy" **(D)** for "all categories" in the period from 01/12/2015 to 31/01/2025. Normalization was carried out on the higher search volume obtained in the considered period.

samples were screened for the presence of natural compounds by extracting the molecular ion chromatograms at $(M+H)^+$ to rule out the use of synthetic levodopa as the only source of the active substance. Protonated species provisionally assigned to components such as arginine (molecular formula $C_6H_{14}N_4O_2$, extracted *m/z* 175.1195) and proline (molecular formula $C_5H_9NO_2$, extracted *m/z* 116.0712) were detected, accounting for examples of endogenous metabolites of Fabaceae water and methanol extracts (Sruthi et al., 2023; Tesoro et al., 2024). LC–MS screening and the NMR profiles supported the presence of natural extracts along with L-dopa in all samples.

3.4 Identification and determination of the L-dopa content by NMR

The one- and two-dimensional ^{1}H- and ^{13}C-NMR spectra of the samples in methanol-d4 (MeOD) confirmed the presence of L-dopa in all the samples. The identification was carried out based on interpretation and comparison to the literature (Alnoman, 2024; Fernandez-Pastor et al., 2019; Talebpour et al., 2004). The three typical aromatic signals for ^{1}H- and ^{13}C-NMR were found at δ 6.73 (d)-117.0 and 6.72 (s)-117.0 and 6.60 (dd) −121.5; due to the large number of compounds in the methanolic solution, no other signals attributable to L-dopa were visible.

Identification of L-dopa was also confirmed in the samples prepared for the quantification study. In this case, the extraction in the acetic acid-d4/D_2O mixture proved to be more selective toward L-dopa, and all the protons and carbons of the molecule were detectable. The ^{1}H-NMR spectra are shown in Figure 4, which includes the proton assignments for the same L-dopa sample dissolved in D_2O/acetic acid-d4 and MeOD. In the ^{1}H-NMR spectrum, signals ascribable to the aromatic protons d, e, and f were detected at δ 6.74 ppm (d, J = 2.1 Hz), 6.81 ppm (d, J = 8.0 Hz), and 6.65 ppm (dd, J = 8.0, 2.1 Hz), respectively. A more shielded signal at δ 3.84 ppm (dd, J = 8.0, 5.0 Hz) is attributable to proton *a*, whereas the b and c signals of the geminal protons in β with respect to the amine were identified in the two doublets at δ 3.07 pp (dd, J = 15.0, 8.0 Hz) and 2.91 ppm (dd, J = 15.0, 5.0 Hz). The protons a, b, and c in the spectrum with MeOD were not detectable.

In most cases, the one-dimensional proton spectra of plant extracts are highly populated and rich in signals, which may hinder identification and interfere with accurate quantification. The use of two-dimensional NMR ^{1}H–^{1}H and ^{1}H–^{13}C NMR experiments plays a fundamental role in the elucidation of molecular structures in mixtures without a database.

For q-NMR, L-dopa amounts were plotted against the corresponding powder weight, and the graphs were visually inspected for linearity. Bending of the linear curve at the higher concentration levels indicated that L-dopa had saturated the

TABLE 2 Retention time and accurate mass of molecular ions and fragments (in targeted mode) of the L-dopa peak in samples and in the reference standard obtained by LC–MS–Q-TOF analysis.

Sample #	RT[a] (minutes)	m/z ([M + H]$^+$) (Error, ppm[b])	m/z ([M − H]$^-$) (Error, ppm)	m/z of major fragment ions in positive mode (abundancies, %)	m/z of major fragment ions in negative mode (abundancies, %)
1	0.36	198.0761 (−0.18)	196.0612 (1.91)	**152.070 (base)**, 135.044 (61%), 139.039 (60%), 107.050 (40%), 111.044 (20%), 93.034 (17%), 163.040 (8%), and 140.041 (5%)	—
2	0.36	198.0760 (−0.49)	196.0612 (1.69)	**152.070 (base)**, 135.044 (62%), 139.039 (62%), 107.050 (43%), 111.045 (20%), 93.034 (16%), 163.038 (7%), and 140.042 (5%)	—
3	0.36	198.0895[d] (*67.65*)	196.0612 (3.87)	—	**135.044 (base)**, 122.037 (45%), 109.028 (22%), 74.024 (20%), 179.031 (10%), and 107.048 (7%)
4	0.36	198.0760 (0.43)	196.0606 (4.64)	**152.070 (base)**, 135.044 (61%), 139.039 (61%), 107.050 (42%), 111.044 (19%), 93.034 (18%), 163.038 (7%), and 140.042 (5%)	—
L-dopa Std[c]	0.36	198.0762 (−0.58)	196.0615 (1.86)	**152.071 (base)**, 135.044(72%), 139.039 (66%), 107.049 (51%), 111.043 (24%), 93.034 (16%), 163.039 (8%), and 140.041 (6%)	**135.044 (base)**, 122.036 (37%), 109.03(21%), 74.024 (18%). 179.039 (5%), and 107.0486 (5%)

[a]Retention time of the chromatographic peak.
[b]Parts per million.
[c]Standard.
[d]The positive ion was not univocally assigned to L-dopa, but the overall results allowed to univocally identify L-dopa.
Bold values represent the base peak.

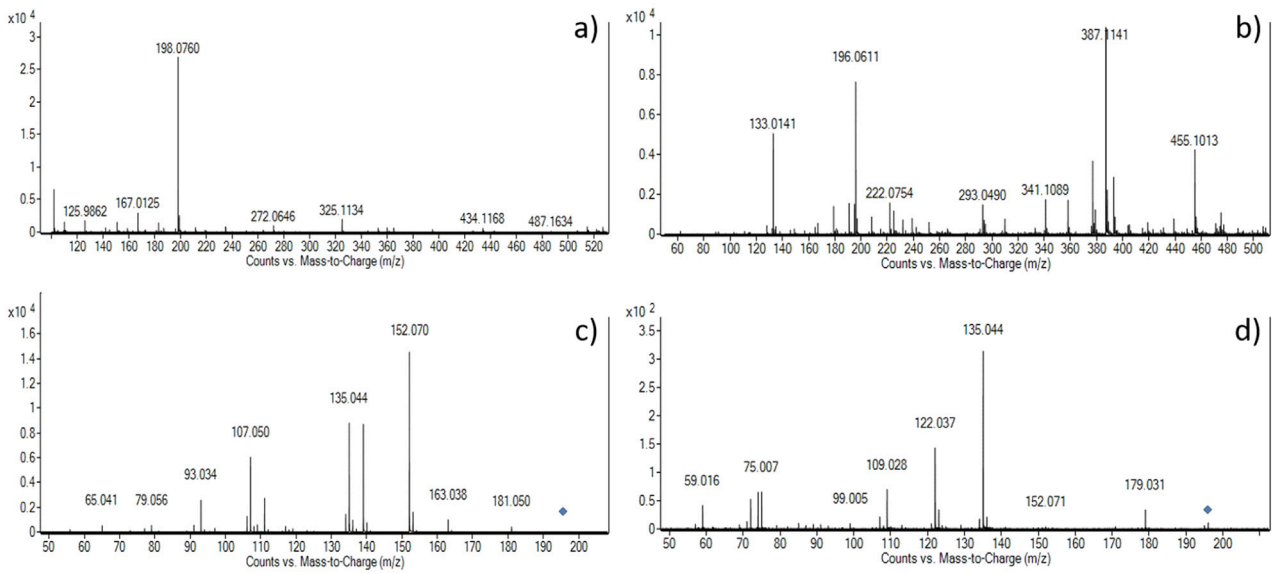

FIGURE 3
Mass spectra of the selected samples #4 **(a, c)** and #3 **(b, d)**. Upper panels depict mass spectra acquired in positive **(a)** and negative **(b)** modes, and the lower panels show the fragmentation pattern obtained at 20 V collision energy in positive **(c)** and negative **(d)** modes, respectively. The blue diamonds in panels c and d are the fragmented molecular ions $(M + H)^+$ = 198.0760 and $(M\text{-}H)^-$ = 196.0611, respectively.

extraction solvent, which compromised the reliability of the quantification results (data not shown). In this case, the extraction process was repeated using larger volumes of the extraction solvent. A regression analysis was performed on the linear plots. The value of R^2, the residuals (±2σ confidence interval), and the variance analysis ($F < 0.05$) confirmed a strong linear relationship between the L-dopa content and the powder amount, supporting quantitative extraction (Table 3). In conclusion,

10.3389/fchem.2025.1597784

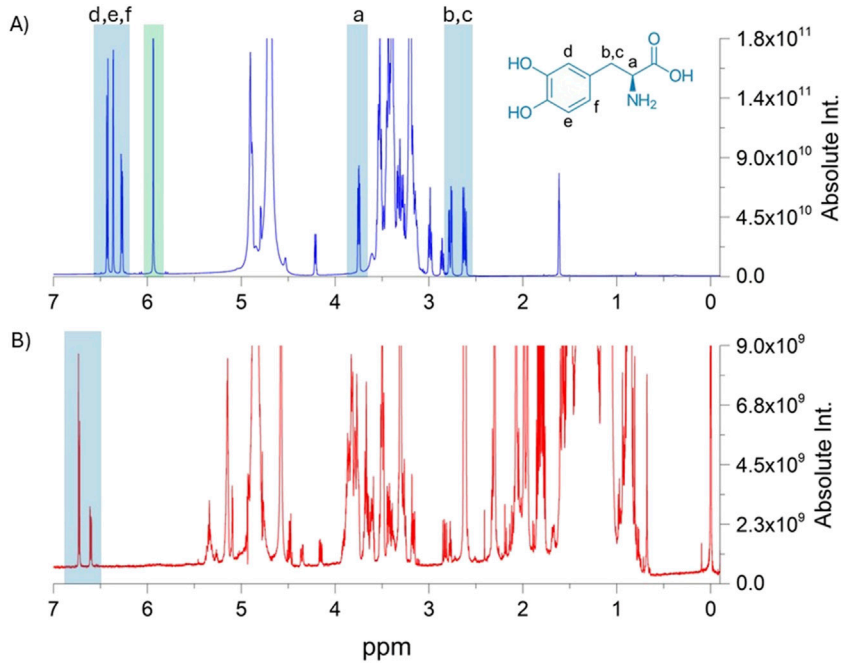

FIGURE 4
Comparison of the 1H-NMR spectra of the extraction procedures with the acid-d4/D2O mixture and MeOD in the upper **(A)** and lower **(B)** panels, respectively. In both profiles, involved L-dopa protons are highlighted in light blue boxes. The green box reports the signal of the internal standard, namely, maleic acid, which was used in q-NMR analysis.

TABLE 3 Found content of L-dopa by q-NMR analysis and values of the regression line.

Sample	mg of L-dopa/capsule	%RSD[1] (maximum acceptable limit)	Slope	Intercept	R^2	F
1	101 ± 8	8.0% (13.33%)	0.179	0.379	0.995	2.05E-3
2	56 ± 6	10.0% (16.7%)	0.253	0.184	0.996	1.45E-3
3	73 ± 5	8.4% (8.80%)	0.257	0.1286	0.993	1.74E-5
4	89 ± 2	3.0% (10.50%)	0.190	0.036	0.997	7.38E-5

[1]Relative standard deviation.

the accuracy was demonstrated by calculating the consistency of the results obtained at different concentrations in the linearity range. If extraction is non-quantitative, the L-dopa content result would not be proportional to the corresponding powder's weight. This approach is widely accepted in q-NMR experiments. In each sample, the L-dopa content per capsule was calculated using at least four different concentrations, and experiments were performed in two different analytical sessions.

The content found in each experiment was normalized to the average weight of the capsules' filling. For each sample, the RSD% (relative standard deviation) is reported in Table 3 with an evaluation of the maximum RSD% acceptable. Moreover, the two-tailed paired t-test with $\alpha = 0.05$ confirmed that the results among the four sample were not statistically different. This shows the reproducibility and precision of the extraction and q-NMR methods. The calculated t value for each comparison within the sample dataset was less than the tabulated t value of 3.182. The uniformity of the mass of the single-dose preparation was tested for each sample according to European Pharmacopoeia 2.9.5. The results confirmed good homogeneity of the capsule content weight, thus supporting the use of 10 capsules for the determination of the average weight.

The labeled and found L-dopa contents are reported in Table 4. Comparison of the found and labeled amounts of L-dopa in the capsules evidenced that the declared content is confirmed for sample #1. Sample #2 was found to be approximately 50% underdosed, and sample #3 and #4 resulted were overdosed by approximately 120% and 150%, respectively. These findings should be considered in light of consumer safety, particularly for sample #4, where the actual daily intake of L-dopa—based on the suggested number of capsules per day—corresponded to approximately 445 mg.

Finally, the percentages of L-dopa in the vegetal extracts were calculated considering the labeled content of the extract per capsule. The results, reported in Table 4, evidenced a percentage of 24% for sample # 1, matching the declared (25%), and percentages of 19% and 22% instead of the labeled 15% for samples # 3 and # 4, respectively. For sample # 2, the content of L-dopa reported was 98%; however, no information was present on the extract content.

10.3389/fchem.2025.1597784

TABLE 4 Found content of L-dopa and calculated percentage with respect to the reported content per capsule and with respect to the declared vegetal extract content. The actual daily intake was calculated based on the labeled serving size.

Samples	mg of L-dopa/capsule (found)	mg of L-dopa/capsule (declared or deduced)[a]	L-dopa/capsule (% found vs. declared or deduced)	% L-dopa/extract (declared)	Serving size[b] in mg of L-dopa (suggested)	Real daily intake in mg of L-dopa based on serving size
1	101 ± 8	105	96%	24%	105	93–109
2	56 ± 6	117	48%	N.R[c]	117	50–62
3	73 ± 5	60[d]	122%	19%	120	136–156
4	89 ± 2	60[d]	148%	22%	300	435–455

[a]This is the labeled content for samples 1 and 2. For samples 3 and 4, the content was deduced based on labeling, as reported in notes three and four of Table 1.
[b]The serving size is the suggested intake per day.
[c]Extract content not reported.
[d]The content per capsule is not declared. The mg of L-dopa/capsule was deduced according to notes three and four of Table 1.

Therefore, the calculation was not possible. The only sample that showed an L-dopa content nearly equal to the declared amount (both in terms of content per capsule and the reported extract percentage) was sample # 1, which was also the only containing the *Vicia Faba* extract.

4 Discussion

In the present work, botanical preparations proposed as L-dopa dietary supplements and marketed online in Italy were analyzed, and despite the limited number of samples, the results evidenced many different quality issues.

Three samples analyzed in this study contained an extract from a plant that is not allowed in dietary supplements in Italy (*M. pruriens*) (Ministero della Salute, 2018); L-dopa is not included in the list of nutrients and other substances with a nutritional or physiological effect permitted in food supplements in Italy (Ministero della Salute, 2022b), making the samples illegal for the Italian market. Moreover, this plant is also not authorized as a novel food in Europe and is reported in the compendium of botanicals prepared by the European Food Safety Authority, a database of botanicals that are reported to contain naturally occurring substances of possible concern for human health when present in food (EFSA, 2012). The extract employed in the fourth sample (#1) originated from a plant that is, in principle, allowed in Italy for botanical preparations (*V. faba*); however, there was no clear indication of the part of the plant used, hindering the univocal identification of the extract source that may be subject to cross-contamination between different parts of the plant, with a possible consequence on the quality and safety of the extract. More importantly, all the samples claimed to contain a standardized L-dopa extract with levels ranging from 15% to 98%. It should be noted that the natural content of L-dopa in *V. faba* is < 1%–3% (Tesoro et al., 2024; Topal and Bozoğlu, 2016), whereas the levels in *Mucuna* seeds that are conventionally used in Ayurvedic medicines can be assumed to be 1%–7% (Nishihara et al., 2005; Pulikkalpura et al., 2015; Soares et al., 2014). This indicates that the extracts are the results of technological processes focusing on the extraction and reintroduction at much higher levels of substances occurring at low levels in botanical components, with adjustments made by inert excipients or blending of batches (EFSA, 2009; European Pharmacopoeia, 2019). These practices deviate from the conventional and traditional processing method, thus raising concerns regarding the safe use of such products without prior authorization at the European regulatory level. The Italian authorities have clarified that plant preparations and extracts used in food supplements must have levels of active substances comparable to those in traditional methods to avoid falling under the Novel Food Regulation (Ministero della Salute, 2022a; Morán and Kilasoniya, 2024). More specifically, in the framework of the Novel Food Regulation, novel aspects of the production process should be characterized when it has not been used for food production within the EU before 15 May 1997. Therefore, a scientific assessment to guarantee the safety of the production process used in the manufacture of the product, including, e.g., information on raw materials and processing aids, processing steps and operational conditions, and safety assurance measures, should be carried out as part of the commercialization procedure (EFSA, 2009). The results presented in this study demonstrate that illicit L-dopa samples are circulating in Italy, which inherently pose risks to consumers. For instance, the most common adverse effects associated with the intake of *M. pruriens* include dyskinesias and other types of involuntary movements, nausea, vomiting, psychotic episodes, hallucinations, and paranoid ideas (AECOSAN, 2016). Furthermore, the Dutch National Institute for Public Health and the Environment (De Heer et al., 2024) provided evidence of health risks related to the consumption of dietary supplements containing extracts of *M. pruriens*, concluding that it is not possible to determine a safe dose for these extracts.

All samples were marketed by the producers for recreational use, claiming the nootropic effects of L-dopa, which is an active pharmaceutical substance. In bodybuilding forums, cocktails of different substances containing L-dopa at different dosages are claimed for physical stimulation and to enhance aggressiveness. In the same forums, it is reported that L-dopa can be combined with caffeine to increase dopaminergic stimulation and with epigallocatechin gallate and other nootropic molecules such as racetams, adrafinil, and taurine (original information obtained by the authors from Italian bodybuilding forums). Furthermore, the overdosage of levodopa supplements, along with the frequent concomitant intake of other supplements containing nootropic

substances such as caffeine, which synergistically interacts with levodopa and shortens the latency and increases the magnitude of the response, could represent a serious health risk to consumers (Deleu et al., 2006; Yu et al., 2006). The analyzed samples did not contain other nootropic or drug substances; however, this result is likely due to the limited number of samples analyzed; these findings also do not allow for speculation on geographical market differences or evolving manufacturing practices. The adulteration of these products cannot be ruled out and remains a potential risk to consumers, which should be addressed in wider surveillance studies covering Europe and Italy (Blazewicz A. et al., 2025; Gaudiano et al, 2024a; Vanhee et al., 2025).

The visual analysis evidenced severe deficiencies in labeling. This point should be stressed because unclear labeling can mislead consumers and lead to potential dosing errors. Moreover, even if the samples were sold in Italy through retail websites targeting the Italian market and providing information in Italian on their webpages, labeling was in Italian in only one sample. Quantitative NMR results, reported in Table 4, showed that the content per capsule was practically equal to the reported one (#1) in one sample, was approximately 50% of that labeled (#2) in another sample, and was significantly overdosed (approximately 120% in sample #3 and approximately 150% in sample #4) for the remaining two samples. The inconsistencies in the level of active compounds are aligned with previous findings on similar products bought online (Cohen et al., 2022; Soumyanath et al., 2018). Misdosing and ambiguous labeling are typical signs of the illegal market production (Gaudiano et al, 2024a; Gaudiano et al, 2024b; Gaudiano et al., 2022), where the quality criteria are barely met due to possible failures in production (e.g., inadequate purification processes), batch-to-batch inconsistencies, lack of good agricultural practice (e.g., pesticide residues), unsuitable starting and raw materials, and chemical and microbial contamination, including the potential presence of highly genotoxic aflatoxins.

This multicolored picture indicates that there is no certainty on the real content of L-dopa in these products, and the consumer can be exposed to very high dosages. Considering the number of capsules reported as "serving size" on the label, the observed variability is even more striking: from one product to another, the actual daily intake ranges from 56 mg to 445 mg. The content of L-dopa in the samples was relatively low to induce any therapeutic effect if considered individually; however, the suggested serving size resulted in an L-dopa intake close to or, in one case, even more than double the therapeutic dose for patients starting therapies with medicines containing L-dopa for Parkinson's disease (200 mg) (De Heer et al., 2024). This should be considered with caution since botanical preparations containing L-dopa can also be consumed by Parkinson's patients as a complement to standard pharmacological therapy (Cohen et al., 2021; Kispotta et al., 2024; Soumyanath et al., 2018). Health threats may originate from the interference with therapies, with consequences of developing severe dopamine dysregulation and resulting in patients' hospitalization (Lambea-Gil et al., 2021; Vanhee et al., 2025).

Additional data were also obtained from the analytical domain. The combination of high-resolution mass spectrometry and NMR used in this study has proven to be a useful tool to identify molecules even in the presence of complex mixtures. In this study, the complexity of the NMR spectra and the results of MS spectrometry suggest the presence of natural components, strengthening the hypothesis of the presence of a botanical extract in the samples, but it is not possible to indicate if the high content of L-dopa is only because of the extraction and concentration procedures or because of the additional presence of synthetic L-dopa. Moreover, the analytical methods used did not allow for the distinction between L-dopa and D-dopa, and we assumed that the detected molecule is the L-enantiomer based on the presumed natural origin of the extracts, as the D-enantiomer has not been found in dietary supplements containing *M. pruriens* (Hasegawa et al., 2013). This assumption can be considered a limitation of the study that would warrants further investigation, considering that a potential role for D-dopa in dopamine production has been proposed in the development of new therapeutic strategies for Parkinson's disease (Kawazoe T. et al., 2007). Moreover, as observed for other illegal products, it can be assumed that even for the same product, the variability among different batches could be high. Quantitative-NMR is a validated and reliable method for quantifying active ingredients, even in highly complex mixtures such as plant extracts, provided that at least one proton signal of the targeted molecule can be integrated without interference from overlapping signals. The advantage of this technique is the possibility to quantify any molecule containing paramagnetic atoms without a reference standard of the targeted molecule, which is, in the case of illegal products, a very useful tool.

Finally, the results of the present study should also be evaluated considering the information on the trend of interest for the terms "levodopa" and "brain supplements," as indicated by data from the Google Trends application. The search showed evidence of a general increase in interest in L-dopa in the studied time period, both worldwide and in Italy, with a specific search for these products as brain support. The market of food supplements has expanded in volume and variety over the last 20 years, confirming the belief that they are an important part of people's diets worldwide (Djaoudene et al., 2023). Italy is the leading market in Europe, with a share of 26% of the total turnover, followed by Germany (19%) and France (15%). The most prevalent sales channels are pharmacies, which are 78% of the total, followed by large-scale retail trade (with an incidence of 7.7%) and para-pharmacies (7.6%). Online channels account for 6.9% (Integratori and Salute, 2024). We have previously reported that illegal markets are fostered by the increase in interest in specific items (Gaudiano et al, 2024a); therefore, tracking the popularity of certain topics and products promotes the adoption of targeted quality assessments to tackle the phenomenon.

5 Conclusion

The results of this study provide evidence of the presence of commercial products proposed as dietary supplements claiming to contain botanical extracts that are highly concentrated in L-dopa and of plants (*M. pruriens*) not allowed in these products on the Internet market, which are accessible from Italy. The results of the visual inspection of labeling showed ambiguity on the amount of L-dopa per capsule and the identity of the manufacturers and the language not being accessible to Italian consumers. The analytical

findings showed the presence of L-dopa in all samples but in quantities that differed from those reported, resulting in dangerous overdoses when considering the suggested serving size. The limited number of samples of this study may undermine the transferability of the results on a wider base; however, research focused on specific geographic markets is still limited, raising the need for further studies engaged in understanding the nature and diffusion among users of certain practices in order to implement targeted regulatory measures. Despite the limited number of samples, the risk to the consumers was well-evidenced. Consumers may not have immediate access to information regarding the illegal use of *M. pruriens*, and the presence of these products in the online market encourages their use. Unclear labeling on the actual L-dopa content and the manufacturer's identity blurs traceability. The amount of L-dopa found in the capsules does not correspond to the labeled dose, and most importantly, in one case, it was higher than the therapeutic dose for patients starting therapies with medicines containing levodopa for Parkinson's disease.

These findings have significant implications for healthcare professionals who recommend food supplements as adjuvants in Parkinson's therapy and for general consumers seeking dopaminergic enhancement. In particular, efforts should be made to ensure that transparent information on dietary supplements sold online is readily accessible to consumers.

Data availability statement

The original contributions presented in the study are publicly available. This data can be found here: 10.6084/m9.figshare.30294385.

Author contributions

FA: Data curation, Formal Analysis, Investigation, Writing – original draft, Writing – review and editing, Conceptualization. MG: Writing – original draft, Formal Analysis, Supervision, Conceptualization, Data curation, Writing – review and editing, Methodology. MR: Formal Analysis, Writing – original draft, Writing – review and editing, Investigation. AM: Formal Analysis, Investigation, Writing – original draft, Writing – review and editing. DD: Funding acquisition, Writing – review and editing. MG: Writing – review and editing. AB: Formal Analysis, Writing – review and editing, Supervision, Writing – original draft, Methodology. MB: Conceptualization, Supervision, Writing – review and editing.

Funding

The author(s) declare that financial support was received for the research and/or publication of this article. This research was funded by the Italian Medicine Agency, grant agreement between Agenzia Italiana del Farmaco (AIFA) and Istituto Superiore di Sanità (ISS)-Disciplinare tecnico n.10.

Acknowledgments

The authors acknowledge Dr. Isabella Sestili, Head of the Chemical Medicines Unit for the scientific discussions and coordination of activities.

Conflict of interest

The authors declare that the research was conducted in the absence of any commercial or financial relationships that could be construed as a potential conflict of interest.

The author(s) declared that they were an editorial board member of Frontiers, at the time of submission. This had no impact on the peer review process and the final decision.

Generative AI statement

The author(s) declare that no Generative AI was used in the creation of this manuscript.

Publisher's note

All claims expressed in this article are solely those of the authors and do not necessarily represent those of their affiliated organizations, or those of the publisher, the editors and the reviewers. Any product that may be evaluated in this article, or claim that may be made by its manufacturer, is not guaranteed or endorsed by the publisher.

Supplementary material

The Supplementary Material for this article can be found online at: https://www.frontiersin.org/articles/10.3389/fchem.2025.1597784/full#supplementary-material

References

Adebowale, Y. A., Adeyemi, A., and Oshodi, A. A. (2005). Variability in the physicochemical, nutritional and antinutritional attributes of six mucuna species. *Food Chem.* 89, 37–48. doi:10.1016/j.foodchem.2004.01.084

AECOSAN (2016). *Report of the scientific committee of the Spanish agency for consumer affairs, food safety and nutrition (AECOSAN) on the risk of the use of seeds of* Mucuna pruriens *in craft products AECOSAN-2016-005*. Madrid: AECOSAN.

Alnoman, R. (2024). Design of chiral acidic molecularly imprinted polymer for the enantioselective separation of (±)-DOPA. *J. Chem. Technol. Biotechnol.* 99 (8), 1879–1888. doi:10.1002/jctb.7691

Aware, C., Patil, R., Gaikwad, S., Yadav, S., Bapat, V., and Jadhav, J. (2017). Evaluation of l-dopa, proximate composition with *in vitro* anti-inflammatory and antioxidant activity of Mucuna macrocarpa beans: a future drug for parkinson treatment, 7, 1097–1106. doi:10.1016/j.apjtb.2017.10.012

Bhushan, M., Akash, S., and Pettarusp, W. (2023). Adverse effects of medications used to treat motor symptoms of Parkinson's disease: a narrative review. *Ann. Mov. Disord.* 6, 45–57. doi:10.4103/aomd.aomd_37_22

Blazewicz, A., Poplawska, M., Daniszewska, B., Piorunska, K., and Karynski, M. (2025). Illegal and falsified medicines self-administrated in not approved post-cycle

therapy after the cessation of anabolic-androgenic steroids - qualitative analysis. *Front. Chem.* 2025 13, 1536858. doi:10.3389/fchem.2025.1536858

Boelens Keun, J. T., Arnoldussen, I. A., Vriend, C., and van de Rest, O. (2021). Dietary approaches to improve efficacy and control side effects of levodopa therapy in parkinson's disease. *A Syst. Rev.* 12, 2265–2287. doi:10.1093/advances/nmab060

Cohen, P. A., Avula, B., Wang, Y. H., Zakharevich, I., and Khan, I. (2021). Five unapproved drugs found in cognitive enhancement supplements. *Neurol. Clin. Pract.* 11, e303–e307. doi:10.1212/CPJ.0000000000000960

Cohen, P. A., Avula, B., Katragunta, K., and Khan, I. (2022). Levodopa content of *Mucuna pruriens* supplements in the NIH dietary supplement label database. *JAMA Neurol.* 79, 1085–1086. doi:10.1001/jamaneurol.2022.2184

De Heer, J. A., Buijtenhuijs, D., and de Wit-Bos, L. (2024). RIVM risk assessment of herbal preparations containing seed extracts of *Mucuna pruriens*. *RIVM Lett. Rep. 2024-0087*. doi:10.21945/RIVM-2024-0087

Deleu, D., Jacob, P., Chand, P., Sarre, S., and Colwell, A. (2006). Effects of caffeine on levodopa pharmacokinetics and pharmacodynamics in parkinson disease. *Neurology* 67, 897–899. doi:10.1212/01.wnl.0000233916.57415.9d

Djaoudene, O., Romano, A., Bradai, Y. D., Zebiri, F., Ouchene, A., Yousfi, Y., et al. (2023). A global overview of dietary supplements: regulation, market trends, usage during the COVID-19 pandemic, and health effects. *Health Eff.* 15, 3320. doi:10.3390/nu15153320

EFSA (2012). Compendium of botanicals reported to contain naturally occurring substances of possible concern for human health when used in food and food supplements. *EFSA J.* 10 (5), 2663. doi:10.2903/j.efsa.2012.2663

EFSAEFSA Scientific Committee (2009). Guidance on safety assessment of botanicals and botanical preparations intended for use as ingredients in food supplements. *EFSA J.* 7 (9), 1249. doi:10.2903/j.efsa.2009.1249

European Pharmacopoeia (2019). Herbal drug extracts. *Ph.Eur 11.0 04/2019*, 0765.

Fernandez-Pastor, I., Luque-Muñoz, A., Rivas, F., Medina-O'Donnell, M., Martinez, A., Gonzalez-Maldonado, R., et al. (2019). Quantitative NMR analysis of L-dopa in seeds from two varieties of *Mucuna pruriens*. *Phytochem. Anal.* 30, 89–94. doi:10.1002/pca.2793

Gaudiano, M. C., Bertocchi, P., De Orsi, D., Manna, L., Antoniella, E., Rodomonte, A., et al. (2022). A case of medicine in disguise: motion sickness patches sold as medical devices containing active pharmaceutical substances. *Ann. Ist. Super. Sanita* 58, 254–263. doi:10.4415/ANN_22_04_05

Gaudiano, M. C., Aureli, F., Manna, L., Borioni, A., Maccelli, A., Raimondo, M., et al. (2024a). Illegal products containing selective androgen receptor modulators purchased online from Italy: health risks for consumers. *Sex. Med.* 12, qfae018. doi:10.1093/sexmed/qfae018

Gaudiano, M. C., Aureli, F., Alfonsi, R., Rodomonte, A. L., Sestili, I., and Bartolomei, M. (2024b). Falsificazionedeimedicinali: daicasistoriciainuovi trend del fenomeno in Le attività di contrastodell'IstitutoSuperiore di Sanità. *Rapporti ISTISAN 24/15*. Roma: Istituto Superiore di Sanità.

Google (2023). Basics of google trends. Available online at: https://newsinitiative.withgoogle.com/it-it/resources/trainings/basics-ofgoogle-trends/(Accessed January 15, 2024).

Hasegawa, T., Ishii, T., Takahashi, K., Saijo, M., Fukiwake, T., Nagata, T., et al. (2011). Quantitative determination of L-dopa in dietary supplements containing *Mucuna pruriens* by high performance liquid chromatography. *Sci. Annu. Rep.* 60, 53–56.

Hasegawa, T., Takahashi, K., Fukiwake, T., Saijo, M., and Motoki, Y. (2013). Enantiomeric determination of DOPA in dietary supplements containing *Mucuna pruriens* by liquid chromatography/mass spectrometry. *Shokuhin Eiseigaku Zasshi* 54, 379–383. doi:10.3358/shokueishi.54.379

Hornykiewicz, O. (2017). L-dopa. *J. Park. Dis.* 7, S3–S10. doi:10.3233/JPD-179004

Integratori and Salute (2024). Integratori, un comparto in crescita. Available online at: https://www.integratoriebenessere.it/assemblea-annuale/#_ftnref3 (Accessed March 13, 2025).

Kaced, A., Belkacemi, L., Chemat, S., Taibi, N., Bensouici, C., Boussebaa, W., et al. (2024). Assessment of L-dopa, bioactive molecules and antioxidant activities of the local Algerian legume tadelaght (Vigna mungo l.Hepper) extract. *Food Biosci.* 61, 104902. doi:10.1016/j.fbio.2024.104902

Katzung, B. G., Farmacologia, V. T. W., and Clinica, G. e (2024). Italia: Piccin.

Kawazoe, T., Tsuge, H., Imagawa, T., Aki, K., Kuramitsu, S., and Fukui, K. (2007). Structural basis of D-dopa oxidation by D-amino acid oxidase: alternative pathway for dopamine biosynthesis. *Biochem. Biophys. Res. Commun.* 355, 385–391. doi:10.1016/j.bbrc.2007.01.181

Kispotta, S., Das, D., and Prusty, S. K. (2024). A recent update on drugs and alternative approaches for parkinsonism. *Neuropeptides* 104, 102415. doi:10.1016/j.npep.2024.102415

Lambea-Gil, A., María-Ángeles, R.-C., Horna-Cañete, L., and Horna-Cañete, L. (2021). Levodopa-induced dyskinesias related to Vicia faba ingestion in a parkinson's disease patient. *Neurol. India* 69, 1878–1879. doi:10.4103/0028-3886.333436

Ministero della Salute. (2018). DM 10 agosto 2018 "Disciplina dell'impiego negli integratori alimentari di sostanze e preparati vegetali e successivi aggiornamenti".

Ministero della Salute. (2022a). Nota ministeriale "Indicazioni sull'uso delle piante e delle loro parti negli integratori alimentari per garantire la sicurezza e tutela dei cittadini".

Ministero della Salute (2022b). Altri nutrienti e altre sostanze ad effetto nutritivo o fisiologico. Available online at: https://www.salute.gov.it/portale/alimentiParticolariIntegratori/dettaglioContenutiAlimentiParticolariIntegratori.jsp?lingua=italiano&id=1423&area=Alimenti%20particolari%20e%20integratori&menu=integratori (Accessed March 20, 2025).

Modi, K. P., Patel, N. M., and Goyal, R. K. (2008). Estimation of L-dopa from *Mucuna pruriens* LINN and formulations containing M. pruriens by HPTLC method. *Chem. Pharm. Bull. (Tokyo)* 56, 357–359. doi:10.1248/cpb.56.357

Morán, J., and Kilasoniya, A. (2024). Application of the "Novel Foods" regulation to botanicals in the european union. *Laws* 13, 10. doi:10.3390/laws13010010

Mouchaileh, N., and Hughes, A. J. (2020). Pharmacological management of Parkinson's disease in older people. *J. Pharm. Pract. Res.* 50, 445–454. doi:10.1002/jppr.1683

Nishihara, E., Parvez, M. M., Araya, H., Kawashima, S., and Fujii, Y. (2005). L-3-(3,4-Dihydroxyphenyl)alanine (L-dopa), an allelochemical exudedfrom velvetbean (*Mucuna pruriens*) roots. *Plant Growth Regul.* 45, 113–120. doi:10.1007/s10725-005-0610-x

Polanowska, K., Łukasik, R. M., Kuligowski, M., and Nowak, J. (2019). Development of a sustainable, simple, and robust method for efficient L-dopa extraction. *Molecules* 24, 2325. doi:10.3390/molecules24122325

Pulikkalpura, H., Kurup, R., Mathew, P. J., and Baby, S. (2015). Levodopa in *Mucuna pruriens* and its degradation. *Sci. Rep.* 5, 11078. doi:10.1038/srep11078

Rezak, M. (2007). Current pharmacotherapeutic treatment options in parkinson's disease. *Dis. Mon.* 53, 214–222. doi:10.1016/j.disamonth.2007.05.002

Soares, A. R., Marchiosi, R., Siqueira-Soares, R. d. C., Barbosa de Lima, R., Dantas dos Santos, W., and Ferrarese-Filho, O. (2014). The role of L-dopa in plants. *Plant. Signal. Behav.* 9, e28275. doi:10.4161/psb.28275

Soumyanath, A., Denne, T., Hiller, A., Ramachandran, S., and Shinto, L. (2018). Analysis of levodopa content in commercial *Mucuna pruriens* products using high-performance liquid chromatography with fluorescence detection. *J. Altern. Complement. Med.* 24, 182–186. doi:10.1089/acm.2017.0054

Sruthi, D., Jagannathan, A., Chandran, A. B., Rao, H. C. Y., and Jayabaskaran, C. (2023). Chromatography-mass spectrometry based chemical profiling of *Mucuna pruriens* (L.) DC. And its beneficial effect against hydrogen peroxide-induced oxidative stress in HEK 293T cells and breast cancer cells. *S. Afr. J. Bot.* 159, 85–97. doi:10.1016/j.sajb.2023.06.003

Talebpour, Z., Haghgoo, S., and Shamsipur, M. (2004). 1H nuclear magnetic resonance spectroscopy analysis for simultaneous determination of levodopa, carbidopa and methyldopa in human serum and pharmaceutical formulations. *Anal. Chim. Acta* 506 (1), 97–104. doi:10.1016/j.aca.2003.10.081

Tesoro, C., Lelario, F., Ciriello, R., Bianco, G., Di Capua, A., and Acquavia, M. A. (2022). An overview of methods for L-dopa extraction and analytical determination in plant matrices. *Separations* 9, 224. doi:10.3390/separations9080224

Tesoro, C., Lelario, F., Ciriello, R., Bianco, G., Acquavia, M. A., Montoro, P., et al. (2023). A validated LC–MS/MS method for quantitative determination of L-dopa in Fagioli di Sarconi beans (*Phaseolus vulgaris* L.). *J. Mass Spectrom.* 58, e4952. doi:10.1002/jms.4952

Tesoro, C., Lelario, F., Piscitelli, F., Di Capua, A., Della Sala, P., Montoro, P., et al. (2024). Vicia faba L. pod valves: a By-Product with high potential as an adjuvant in the treatment of parkinson's disease. *Molecules* 29, 3943. doi:10.3390/molecules29163943

Topal, N., and Bozoğlu, H. (2016). Determination of L-dopa L-3, 4-dihydroxyphenylalanine content of some faba bean Vicia faba L. *Genotypes* 22, 145–151. doi:10.1501/Tarimbil_0000001376

Vanhee, C., Deconinck, E., George, M., Hansen, A., Hackl, A., Wollein, U., et al. (2025). The occurrence of illicit smart drugs or nootropics in Europe and Australia and their associated dangers: results from a market surveillance study by 12 official medicines control laboratories. *J. Xenobiot.* 15 (3), 88. doi:10.3390/jox15030088

Vora, R., Joshi, A., and Joshi, N. (2018). Comparison of L-dopa content in three species of genus mucuna by different extraction techniques. *Ann. Plant Sci.* 7, 1973–1977. doi:10.21746/aps.2018.7.1.10

Yu, L., Schwarzschild, M. A., and Chen, J. F. (2006). Cross-sensitization between caffeine- and L-dopa-induced behaviors in hemiparkinsonian mice. *Neurosci. Lett.* 393, 31–35. doi:10.1016/j.neulet.2005.09.036

Yumoto, E., Yanagihara, N., and Asahina, M. (2022). The simple and rapid quantification method for L-3,4-dihydroxyphenylalanine (L-dopa) from plant sprout using liquid chromatography-mass spectrometry. *Plant. Biotechnol. (Tokyo)* 39, 199–204. doi:10.5511/plantbiotechnology.21.1126a

Zhao, J., Wang, M., Saroja, S. G., and Khan, I. A. (2022). NMR technique and methodology in botanical health product analysis and quality control. *J. Pharm. Biomed. Anal.* 207, 114376. doi:10.1016/j.jpba.2021.114376

Frontiers in Chemistry

Explores all fields of chemical science across the periodic table

Advances our understanding of how atoms, ions, and molecules come together and come apart. It explores the role of chemistry in our everyday lives - from electronic devices to health and wellbeing.

Discover the latest Research Topics

See more →

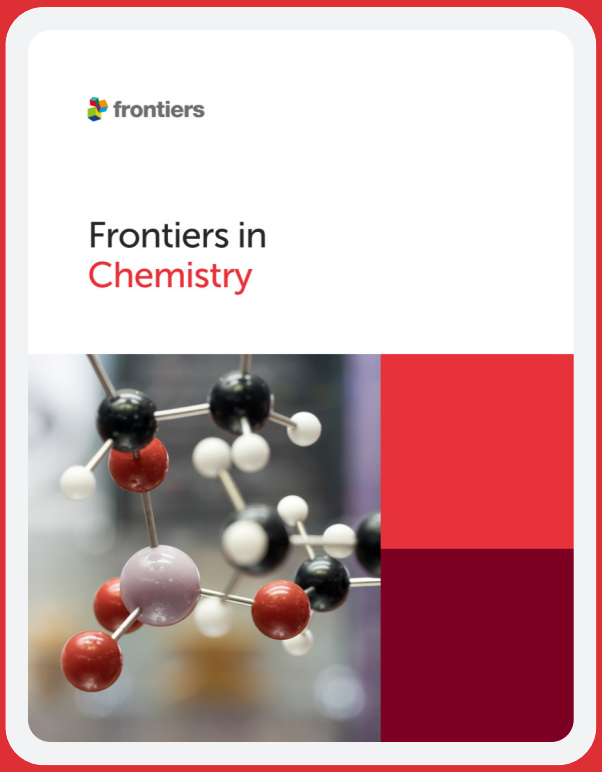

Frontiers

Avenue du Tribunal-Fédéral 34
1005 Lausanne, Switzerland
frontiersin.org

Contact us

+41 (0)21 510 17 00
frontiersin.org/about/contact